DOE/ER-0313/4

Fusion Reactor Materials

Semiannual Progress Report
for Period Ending
March 31, 1988

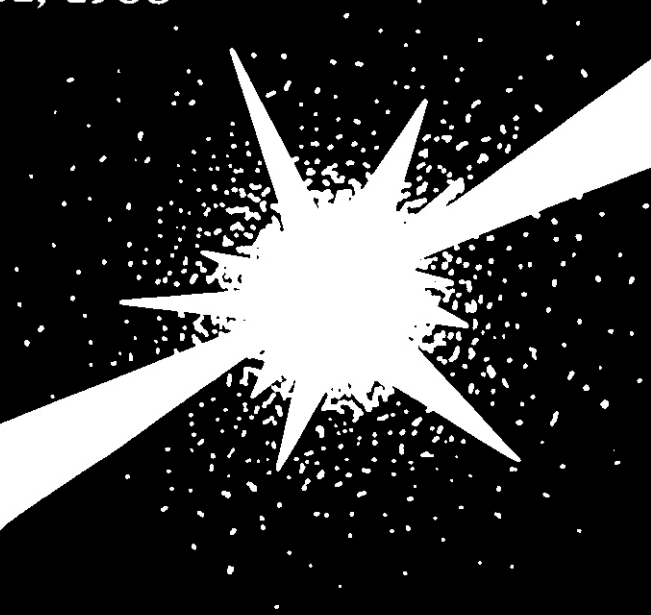

U. S. Department of Energy
Office of Fusion Energy

Printed in the United States of America Available from
National Technical Information Service
US Department of Commerce
5285 Port Royal Road Springfield Virginia 22161
NTIS price codes— Printed Copy A11 Microfiche A01

DOE/ER-0313/4
Distribution
Categories
UC-423, -424

FUSION REACTOR MATERIALS SEMIANNUAL PROGRESS REPORT FOR THE PERIOD ENDING MARCH 31, 1988

Date Published: August 1988

Prepared for
DOE Office of Fusion Energy

AT 15 02 00 0

Prepared by
OAK RIDGE NATIONAL LABORATORY
Oak Ridge, Tennessee 37831
operated by
MARTIN MARIETTA ENERGY SYSTEMS. INC.
for the
U.S. DEPARTMENT OF ENERGY
under Contract DE-AC05-840R21400

Reports previously issued in this series are as follows:

DOE/ER-0313/1	Period Ending September 30, 1986
DOE/ER-0313/2	Period Ending March 31, 1987
DOE/ER-0313/3	Period Ending September 30, 1987

FOREWORD

This is the fourth in a series of semiannual technical progress reports on fusion reactor materials. This report combines research and development activities which were previously reported separately in the following technical progress reports:

- Alloy Development for Irradiation Performance
- Damage Analysis and Fundamental Studies
- Special Purpose Materials

These activities are concerned principally with the effects of the neutronic and chemical environment on the properties and performance of reactor materials; together they form one element of the overall materials program being conducted in support of the Magnetic Fusion Energy Program of the U.S. Department of Energy. The other major element of the program is concerned with the interactions between reactor materials and the plasma and is reported separately.

The Fusion Reactor Materials Program is a national effort involving several national laboratories, universities, and industries. The purpose of this series of reports is to provide a working technical record for the use of the program participants, and to provide a means of communicating the efforts of materials scientists to the rest of the fusion community, both nationally and worldwide.

This report has been compiled and edited under the guidance of A. F. Rowcliffe, Oak Ridge National Laboratory, and D. G. Doran, Eattelle-Pacific Northwest Laboratory. Their efforts, the work of the publications staff in the Metals and Ceramics Division at ORNL, and the many persons who made technical contributions are gratefully acknowledged. T. C. Reuther, Reactor Technologies Branch, has responsibility within DOE for the programs reported on in this document.

G. M. Haas, Chief
Reactor Technologies Branch
Office of Fusion Energy

TABLE OF CONTENTS

1. IRRAOIATON FACILITIES, TEST MATRICES, AND EXPERIMENTAL METHODS

DESIGN AND FABRICATION OF HFIR-MFE RB* SPECTRALLY TAILORED IRRADIATION CAPSULES — A. W. Longest (Oak Ridge National Laboratory), J. E. Corum (Midwest Technical, Inc.), and D. W. Heatherly (Oak Ridge National Laboratory)

OBJECTIVE

The objective of this work is to design and fabricate irradiation capsules for testing magnetic fusion energy (MFE) first-wall materials in the High Flux Isotope Reactor (HFIR) removable beryllium (RB*) positions. Japanese and U.S. MFE specimens are being transferred to RB* positions following irradiation to 8 dpa at temperatures of 60, 200, 330. and 400°C in Oak Ridge Research Reactor (ORR) experiments ORR-MFE-6J and -7J.

SUMMARY

Design and fabrication of four HFIR-MFE RB* capsules (60, 200, 330, and 400°C) to accommodate MFE specimens preirradiated in spectrally tailored experiments in the ORR are proceeding satisfactorily. These capsule designs incorporate provisions for removal, examination. and re-encapsulation of the MFE specimens at intermediate exposure levels en route to a target exposure level of 30 displacements per atom (dpa). With the exception of the 60°C capsule, where the test specimens will be in direct contact with the reactor cooling water, the specimen temperatures (monitored by 21 thermocouples) will be controlled by varying the thermal conductance of a small gap region between the specimen holder and the containment tube. Hafnium sleeves will be used to tailor the neutron spectrum to closely match the helium production-to-atom displacement ratio (14 appm/dpa) expected in a fusion reactor first wall.

Design and preparation of fabrication drawings for the 60 and 330°C capsules and all generic capsule components and support facilities have now been completed. Assembly of the 60°C capsule is complete and the 330°C capsule is nearing completion. The irradiation of both capsules will begin when the HFIR returns to full power operation. Design and preparation of fabrication drawings for the 200 and 400°C capsules will be completed in 1988, and operation of these two capsules will follow the first two (60 and 330°C).

PROGRESS AND STATUS

Introduction

A series of spectrally tailored irradiation capsules are being designed and fabricated as part of the U.S./Japan collaborative program for testing MFE first-wall materials in mixed-spectrum fission reactors. The test specimens will be irradiated in the new RB* facility' of the HFIR.

The first four HFIR-MFE RB* capsules are designed to accomnodate Japanese and U.S. MFE specimens preirradiated to 8 dpa at temperatures of 60, 200, 330, and 400°C in the ORR spectrally tailored experiments ORR-MFE-6J and -75. Details of these ORR experiments, including descriptions of the test matrix, mechanical property specimens, and techniques of spectral tailoring, have been reported elsewhere.[2,3]

Spectral tailoring of the neutron flux to simulate in austenitic stainless steels the expected helium production-to-atom displacement ratio of 14 appm/dpa in the fusion reactor first wall is accomplished by varying the amount of neutron moderator and thermal neutron absorber materials surrounding the capsule. This controls the two-step ^{58}Ni thermal neutron reaction producing helium, while fast neutrons are simultaneously producing atomic displacements. In general, the neutron energy spectrum must be hardened as the irradiation progresses; this requires ongoing neutronics analysis support as provided for the ORR experiments. [4]

The HFIR-MFE RB* capsules are designed for insertion into any of the eight large-diameter holes (46 mm) of the HFIR RB* facility. Damage rates will increase from about 4 dpalyear in the ORR experiments to 8 dpal year in the HFIR RB* facility (based on 85 MW HFIR power).

Test specimen nominal loadings for the first four capsules are given in Table 1. Beginning with return of the HFIR to full power in 1988, these capsules will be irradiated in pairs (first the 60 and 330°C capsules, then the 200 and 400°C capsules) to a damage level of 20 dpa. After these four irradiations, the test specimens will be removed, examined, and approximately one-half of them re-encapsulated for irradiation to 30 dpa.

Table 1. Test specimen nominal loadings for the HFIR-MFE RB* capsules

Specimen Type	Number of specimens in capsule			
	60°C	200°C	330°C	400°C
Pressurized tube	39	26	45	39
Tube blank	9	9	9	9
Transmission electron microscopy tube				
Length (mm)				
SS-1 tensile	90	83	76	64
SS-3 tensile	54	54	15	15
Grodzinski fatigue	56	24	56	40
Crack growth	30	30	10	10
Rod tensile	0	0	4	0
Hourglass fatigue	0	0	0	5

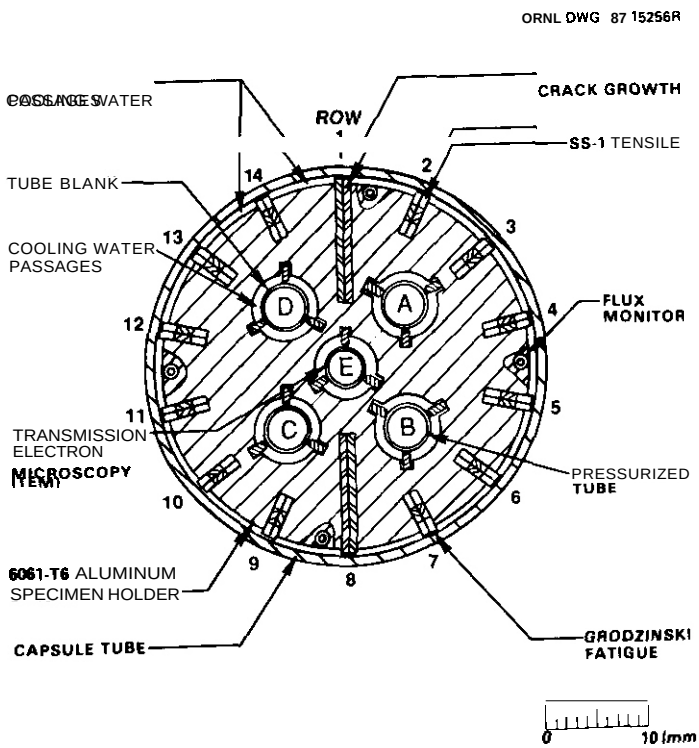

Fig. 1. Horizontal section through the HFIR-MFE-60J-1 capsule.

60°C Capsule

The 60°C capsule, designated HFIR-MFE-60J-1, is uninstrumented with the test specimens in contact with the reactor coolant water. A horizontal cross section through this capsule is shown in Fig. 1. Coolant flow channels are provided in this design to cool the capsule internally as well as externally. The various coolant passages were designed to permit water flow rates of 0.63 L/s over the capsule surface, 0.57 L/s between the capsule tube and the specimen holder, 0.076 L/s through the central specimen hole in the specimen holder, and 0.063 L/s through each of the other four specimen holes in the specimen holder. Resulting specimen temperatures are predicted to be within ±10°C of 60°C.

Assembly of the 60°C capsule has been completed, and the capsule has been placed in dry storage at the HFIR until the reactor returns to power. The radioactive test specimens were successfully loaded into the capsule in about one week. The specimen loading arrangement and the identification of the specimens in each position are given in Figs. 2 and 3, respectively.

330°C Capsule

The 330°C capsule (designated HFIR-MFE-330J-1) design was described in detail in the preceding progress report.[5] Assembly of this capsule has been completed to the point where it is ready for loading of the radioactive test specimens in the hot cell. Following the specimen loading and completion of the final closure weld at the hot cell, the capsule will be transferred to the HFIR and stored in the HFIR pool until the reactor returns to power.

400°C Capsule

Design of the 400°C capsule will be similar to the 330°C capsule and is scheduled to be completed by the end of 1988.

200°C Capsule

The 200°C capsule presents a special design problem because it is difficult to remove the large amount of gamma heat generated in the capsule while at the same time controlling the operating temperature at 200°C. As discussed in the preceding progress report,[5] several possible design concepts being considered for the 200°C capsule include: (1) an aluminum alloy specimen holder with a conventional temperature control gas gap which would be only about –0.029 mm thick at operating temperature, (2) use of a very low density material for the specimen holder, such as an aluminum foam product, which would permit use of a somewhat larger temperature control gas gap, (3) use of electric heaters for temperature control with gas gap thicknesses reduced to the minimum needed for assembly, so that operating temperature would be below 200°C under the condition of no heater power, and (4) use of a relatively large temperature control gas gap (–0.76 mm) filled with a binary (coarse/fine) mixture of metallic microspheres. In the latter concept, temperature would be controlled primarily by varying the inert gas pressure (and hence the mean free path of the gas molecules) in the particle bed to change its thermal conductance.

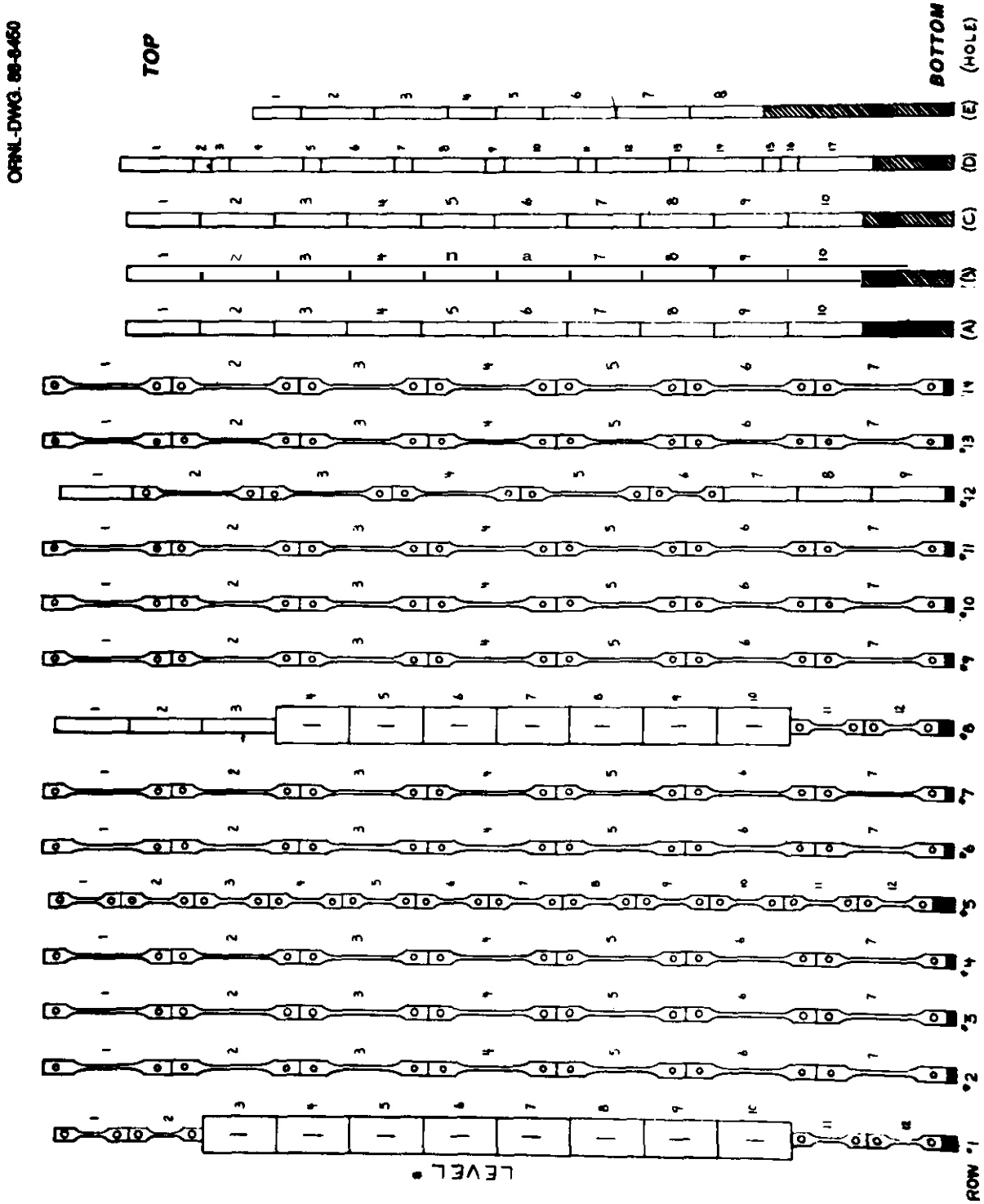

Fig. 2. Specimen loading arrangement in HFIR-MFE-60J capsule.

ORNL-DWG. 88-8451

	ROW 1	ROW 2	ROW 3	ROW 4	ROW 5	ROW 6	ROW 7	ROW 8	ROW 9	ROW 10	ROW 11	ROW 12	ROW 13	ROW 14	HOLE A	HOLE B	HOLE C	HOLE D	HOLE E
LEVEL 1	MH-13 MN-10	GFC-36 GFB-39	FL-38 E9-08	E4-08 B12-08	EK-21 HV-11	GFD-59 GFA-59	D-03 D-04	3700,01 3702,03	FL-60 ELW-8	GFD-39 GFA-36	E-808 E-308	DUMMY DUMMY	GFD-60 GFA-55	CL-60 CL-58	FA-58	3S-08	C2-C5	C3-A5	K-60
LEVEL 2	EC-11 EK-23	GFD-41 GFA-35	DL-41 E-609	DLA-8 B13-08	EK-28 AE-08	GFC-38 GFB-59	D-44 D-45	F300,01 F302,03	CLW-21 FL-61	GFA-34 GFD-38	HL-6 IL-7	GL-9 B-508	GFC-42 GFA-38	IL-6 B-308	PS-01	SA-17	SA-24	DUMMY	J-3
LEVEL 3	CGB-7 CGF-7	GFA-42 GFA-39	FL-35 DL-44	DLA-10 ML-6	EC-14 AE-17	GFC-56 GFA-60	EL-58 EL-57	3300,01 3802,03	KL-5 CLW-22	GFC-38 GFD-35	B-608 EL-37	FL-36 FL-37	GFD-36 GFB-34	DL-42 B-108	C4-C2	3C-08	3S-01	SA28-1	J-5
LEVEL 4	AT-16 CGF-9	GFC-37 GFD-40	GL-10 CL-39	GL-13 EL-38	AE-15 EL-07	GFC-60 GFB-55	DLW-19 ELW-6	CGA-10 CGA-8	CLW-20 DL-61	GFC-35 GFA-41	CLW-13 EL-41	CL-41 GL-12	GFA-37 GFA-43	E-108 B10-08	C2-B5	C3-A0	C3-B0	C1-B6	B
LEVEL 5	AH-08 AH-09	GFB-41 GFD-34	CLW-14 DL-38	B-708 KL-7	MH-11 AE-06	GFA-54 GFC-57	DLW-18 DLW-14	AT-15 CGF-8	DLA-11 EL-39	GFB-40 GFB-38	DL-39 CL-36	DL-60 DL-62	GFB-35 GFC-41	DL-40 CLW-16	3C-11	S3-A7	SA-49	3C12-1	C
LEVEL 6	CGA-9 AT-17	GFC-34 GFC-40	E10-08 CLW-15	B-208 B-908	MH-16 EC-13	GFD-58 GFB-57	ELW-7 FLW-14	CGE-10 AT-24	ML-7 GL-8	GFB-42 GFD-43	E-208 CL-40	DL-01 DX-01	GFB-43 GFD-42	DLA-13 ML-7	S1-A9	FA-24	FA-53	C3-A4	J-4
LEVEL 7	CGE-9 CGF-6	GFD-37 GFA-40	GL-11 KL-6	EL-40 EL-36	EK-26 AE-12	GFB-54 GFD-57	FLW-18 FLW-16	CGB-8 AH-04	E-509 DLA-12	GFB-37 GFB-36	B11-08 DLA-14	F400,01 F402,03	GFC-43 GFC-39	CL-38 CL-5	S2-A5	SA-54	C1-B5	PS14-1	J-1
LEVEL 8	AT-20 CGB-10				EK-25 HV-12			CGE-8 CGB-11				A700,01 A702,03			C1-C9	FA-36	FA-51	S2-A2	J-2
LEVEL 9	AT-19 CGE-11				HV-17 EC-12			AH-05 CGB-9				AA00,01 AA02,03			C2-B9	S1-A8	SA-55	S1A5-1	
LEVEL 10	CGB-6 CGA-11				MH-12 HV-09			AH-15 AH-14							SA-41	C1-A3	C2-B8	C2-B6	
LEVEL 11	HV-16 EK-27				AE-13 EL-04			EK-22 HV-15										CC-1	
LEVEL 12	AE-07 EC-15				MH-09 EC-10			EK-31 AE-14										PS-08	
LEVEL 13																		3S13-1	
LEVEL 14																		C3-A9	
LEVEL 15																		CB-1	
LEVEL 16																		CA-1	
LEVEL 17																		C3-C1	

Fig. 3. Specimen identification in HFIR-MFE-60J1 capsule.

A decision on the design concept to use for the 200°C capsule will be made soon. At this time, it appears that the choice will be between concepts 1 and 4 above. Additional thermal analyses will be made to fully evaluate concept 1 in view of the highly successful fabrication of the similar 330°C capsule specimen holder and containment tube parts. We plan to complete out-of-reactor development testing of concept 4 even if it is not selected for the 200°C capsule, so that data will be available for future consideration of its use. Should concept 4 be selected for the 200°C capsule, an in-reactor mockup capsule should be operated to fully demonstrate the workability of this new capsule temperature control concept.

FUTURE WORK

Design and preparation of fabrication drawings for the 200 and 400°C HFIR-MFE RB* capsules are sheduled to be completed by the end of 1988. Preparation of fabrication drawings for re-encapsulation of the MFE specimens after 20 dpa is scheduled to be completed in FY 1990.

Fabrication of parts for the 200 and 400°C capsules will continue into FY 1989.

REFERENCES

1. K. R. Thoms et al., "HFIR Irradiation Facilities Improvements — Completion of the HIFI Project," Proc. Third Intl. Conference on Fusion Reactor Materials (Karlsruhe, 1987); to be published in Journal of Nuclear Materials.

2. J. L. Scott et al., pp. 12–20 in ADIP Semiann. Prog. Rep., March 31, 1985, DOE/ER-0045/14, U.S. DOE, Office of Fusion Energy.

3. J. L. Scott et al., Second Annual Prog. Rep. on United States-Japan Collaborative Testing in the High Flux Isotope Reactor and the Oak Ridge Research Reactor, Sept. 30, 1985, ORNL/TM-10102.

4. R. A. Lillie, pp. 36–38 in Fusion Reactor Materials Semiann. Prog. Rep., Sept. 30, 1986, DOE/ER-0313/1, U.S. DOE, Office of fusion Energy.

5. A. W. Longest et al., "Design and Fabrication of HFIR-MFE RB* Spectrally Tailored Irradiation Capsules," Fusion Reactor Materials Semiann. Prog. Rep., Sept. 30, 1987, DOE/ER-0313/3, U.S. DOE, Office of Fusion Energy (in press).

STATUS OF U.S.-JAPAN COLLABORATIVE PROGRAM PHASE II HFIR TARGET CAPSULES - R. L. Senn (Oak Ridge National Laboratory)

OBJECTIVE

The objective of this program is to determine the response of various U.S. and Japanese austenitic stainless steels with different pretreatments and alloy compositions to the combined effects of displacement damage and helium generation at temperatures in the range of 300 to 600°C.

SUMMARY

The experiment matrix for Phase II HFIR target capsules (JP-9 through JP-16) was further revised to resolve certain discrepancies regarding specimen volume and position details. A thermal analysis to account for these changes was completed and the required new parts are on order. All eight capsules will be assembled and installed in the HFIR simultaneously beginning with the first full power operating cycle.

PROGRESS AND STATUS

Introduction

The program for U.S.-Japan collaborative testing of the Phase II HFIR target capsules consists of eight capsules, JP-9 through JP-16. In order to properly allocate specimen volumes, JP-15 was changed to incorporate four tensile bar specimens in place of four previously specified TEM specimen assemblies. Also, an additional sheet specimen was added to JP-14, replacing a TEM. A new thermal analysis was required for these changes, and new parts were ordered.

Experiment Matrix

The revised Phase II experiment matrix is shown in Fig. 1. As previously reported, these experiments incorporate transmission electron microscopy (TEM), tensile bar (TB), hourglass fatigue (F), SS-3 sheet tensile [T(2) and T(4)], and welded sheet (SHEET) specimens. Specimen material, design specimen temperatures, and the location of the various specimen holders are shown on the figure. The previously used position numbering system (from 1 at the top through 11 at the bottom) was modified by assigning positions 1A, 1B, etc., to the shorter specimens.

Thermal Analysis

As noted above, additional thermal analyses were required because of the revisions. Detailed results from these calculations are shown in Tables 1 and 2 for capsules JP-14 and -15, respectively.

Present Status

Parts for the eight new capsules are on hand except for the recently revised assemblies, which are on order. The various specimens are in preparation.

FUTURE WORK

Assembly of the eight capsules is planned for completion as soon as specimens are available. with installation in the HFIR at the earliest opportunity. Full power operation of the reactor is presently predicted to begin in October 1988.

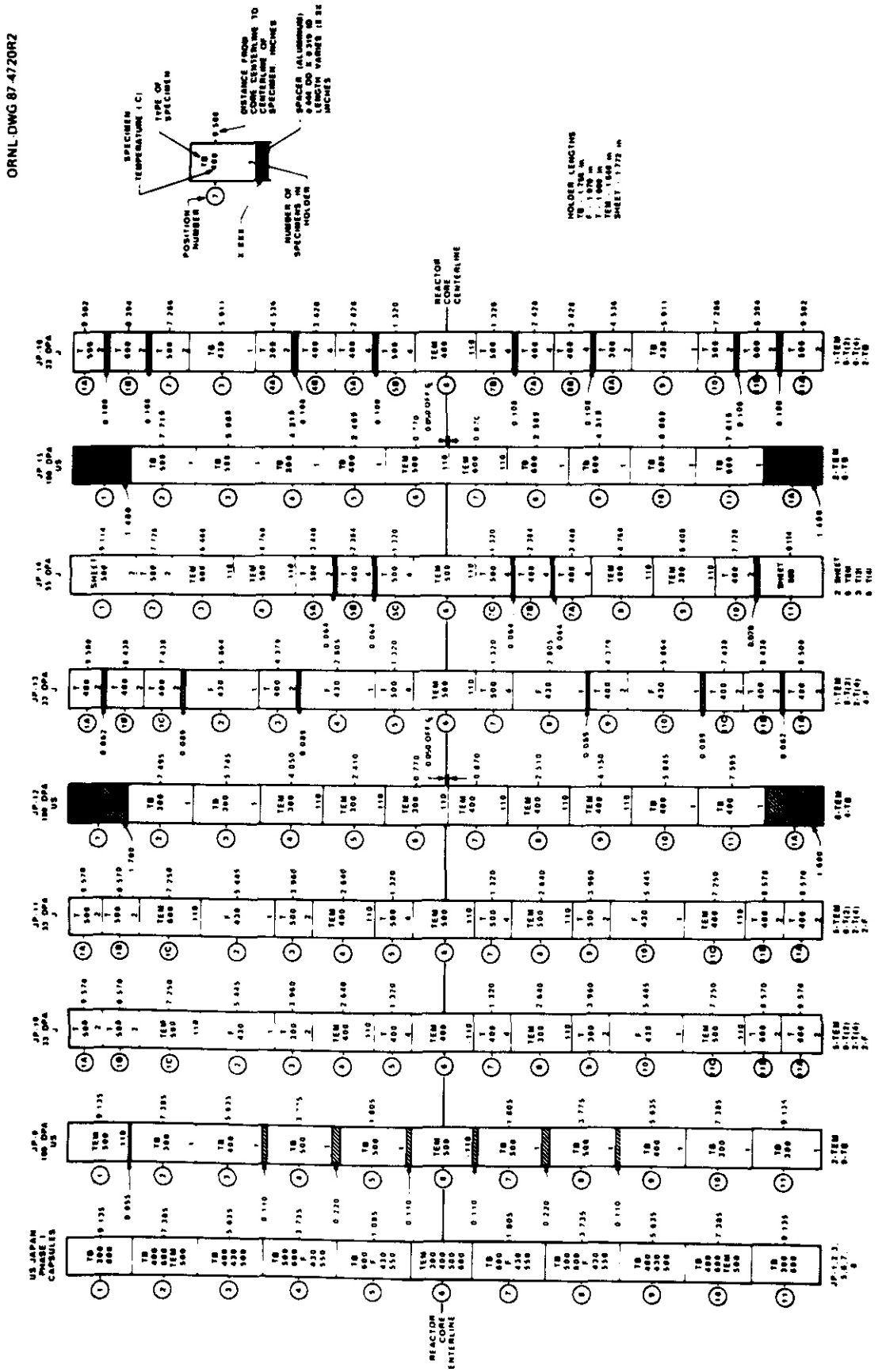

Fig. 1. U.S.-Japan Phase II capsule matrix.

Table 1. HFIR target capsule JP-14 thermal analysis

Position No.	Elevation from C_L (in.)	Heat Generation near HGEN SST (W/g)	HGEN Al (W/g)	Specimen Type**	Capsule JP-14 Specimen Temp. (°C)	Cold Gap (in.)
1	9.114	17.16	17.16	SHEET	500	0.0145
2	7.728	25.01	25.01	T(2)	500	0.0097
3	6.408	31.35	31.35	TEM	600	0.0267
4	4.768	37.67	37.67	TEM	500	0.0153
5A	3.448	41.51	41.51	T(2)	500	0.0057
5B	2.384	43.80	43.80	T(4)	400	0.0036
5c	1.320	45.37	45.37	T(4)	500	0.0052
6	0.000	46.30	46.30	TEM	500	0.0119
7c	1.320	45.37	45.37	T(4)	500	0.0052
7B	2.384	43.80	43.80	T(4)	400	0.0036
7A	3.448	41.51	41.51	T(4)	400	0.0038
8	4.768	37.67	37.67	TEM	400	0.0103
9	6.408	31.35	31.35	TEM	300	0.0075
10	7.728	25.01	25.01	T(2)	400	0.0065
11	9.114	17.16	17.16	SHEET	500	0.0145

** F = fatigue specimens, TEM = TEM disk specimens, TB = tensile bar specimens, T(2) = two SS-3 flat tensile specimens/holder, T(4) = four SS-3 flat tensile specimens/holder, SHEET = two welded sheet specimens/holder.

Note: Assumes 85 MW reactor power (85% neutronic heat) and same for bath aluminum and SST. J capsule. 55 dpa.

Table 2. HFIR target capsule JP-15 thermal analysis

Position No.	Elevation from C_L (in.)	Heat Generation HGEN SST (W/g)	HGEN Al (W/g)	Specimen Type**	Capsule JP-15 Specimen Temp. (°C)	Cold Gap (in.)
1	9.099	17.25	17.25		Aluminum spacer	
1T						0.0235
2	7.495	26.21	26.21	TB	500	0.0685
2B						0.0195
3T						0.0165
3	5.745	34.11	34.11	TB	500	0.0440
3B						0.0150
4T	4.715	37.85	37.85			0.0059
4	4.215	39.42	39.42	TB	300	0.0125
4B	3.715	40.83	40.83			0.0054
5T	2.965	42.64	42.64			0.0084
5	2.465	43.65	43.65	TB	400	0.0187
5B	1.965	44.50	44.50			0.0079
6T						
6	0.770	45.89	45.89	TEM	500	0.0120
6B						
7T						
7	0.870	45.81	45.81	TEM	600	0.0175
7B						
8T	2.065	44.35	44.35			0.0165
8	2.565	43.46	43.46	TB	600	0.0422
8B	3.065	42.42	42.42			0.0163
9T	3.815	40.56	40.56			0.0173
9	4.315	39.12	39.12	TB	600	0.0492
9B	4.815	37.52	37.52			0.0189
10T						0.0210
10	5.845	33.71	33.71	TB	600	0.0735
10B						0.0235
11T						0.0280
11	7.595	25.70	25.70	TB	600	0.1285
11B						0.0345
12	9.127	17.08	17.08		Aluminum spacer	

** F = fatigue specimens, TEM = TEM disk specimens, TB = tensile bar specimens, T(2) = two flat tensile specimenlholder. T(4) = four SS-3 flat tensile specimens/holder.

Note: Assumes 85 MW reactbr power (85% neutronic heat) and same for both aluminum and SST. U.S. capsule, 100 dpa; thermal analysis from CTR-58 work of I. I. Siman-Tov.

2. DOSIMETRY, DAMAGE PARAMETERS AND ACTIVATION CALCULATIONS

REDUCED ACTIVATION CALCULATIONS AT HANFORD - F. M. Mann. Westinghouse Hanford Company

OBJECTIVE

The objective of this work is to support the materials program by calculating the activation of materials proposed for future devices and of materials undergoing tests and by improving the codes and libraries involved in the calculations.

SUMMARY

Material activatlon is an inherent property of d-T fusion devices. Materials can be chosen. therefore. not only for their structural properties under irradiation but also for their favorable activatlon characteristics. Calculations of the long-term actlvatlon for various materials under ITER-like conditions show that the reduced activation materials being pursued would meet NRC Class C regulations for near surface disposal. Limits for each of the materials studied are determined by the presence of Mo and Nb (whether as a minor constituent or as impurities). Plans for improving the cross section and decay data libraries Involve the creation of a joint Dutch-U.K.-U.S. activation cross section library and in using the ENDF/B-VI libraries.

STATUS AND PROGRESS

Introduction

Because of its extensive libraries and ease of use, the REAC2[1] activatlon and transmutation code system has often been used to calculate the activation properties of proposed fusion materials. With the design for the ITER (International Thermonuclear Experimental Reactor) acceleratlng. questions concerning the actlvation of materials in such a device are being raised.

In order to improve the quality of the activatlon calculations. the cross section and decay data libraries need to be improved. Plans have been laid to accomplish this improvement. Most important in this task is the agreement among Harwell (England). Energy Centrum Nederland (Holland), and Hanford (U.S.) to create a joint activation 1ibrary.

Activatlon Calculations

To determine the activation under ITER-like conditions, material compositions of likely first wall materials were transmuted through the use of the REACZ code using the first wall STARFIRE flux. Using the U.S. alloy design experience as a guide. the activatlon of two ferritic steels (9Cr-1Mo and the reduced actlvatlon 9Cr-WV), two austenitic steels (AISI 316 and the reduced activation 12Cr-20Mn), and a vanadium alloy (V-15Cr-5Ti) were calculated for a 5 MW-y/m^2 exposure. The initial material compositions (see Table I) of the steels were supplied by Arthur Rowcliffe of ORNL, while the composition of the gvanadium alloy is a generic description.

Five timesteps were used to include the effects of multi-step reactions. The STARFIRE first wall spectrum was used since the ITER design is expected also to have water cooling. thus producing a first wall spectrum in ITER similar to that calculated for STARFIRE. Because the detalled tlme history of ITER is not presently known. the time history was assumed to be full power (3.6 MW/m^2) for 500 days. This assumed power history will not affect the conclusions for long term wastes. but will over-estimate short term wastes (i.e. those products having half-lives less than a year) relative to a calculation for a long time at low power.

Decay rate and dose rate as a function of decay tlme are shown in Figures 1 and 2. The 10 CFR 61 class C waste disposal rating is displayed in Figure 3. For all materials studied. Nb-94 (from Nb) and Tc-99 (from Mo) are the main sources of the waste disposal ratlng. This is even true for those materials where Mo and Nb are impurities. It should be noted. however. that the isotopes providing the most significant contrlbutlon to the long term decay rate (which Involves just the amount of material and its half-life) are other isotopes (Re186* from W for the steels) and C-14 for the vanadium allay. Nb-94 and Tc-99 are most significant In the waste ratlng because of their gamma emissions and their mobility in soil.

To determine the effect of longer irradiations. the calculations were repeated for a 10 year exposure, corresponding to 36 MW-yr/m^2. The results are shown in figures 4 through 6 and displayed in Tables II through VI. Although some departure away from a linear function of fluence is seen, it is small. At such a high exposure - about 450 dpa (which is beyond the capability of present materials) - the levels of Impurities must be greatly reduced to meet Class C disposal levels.

Library Improvement

The quality of all activation calculations depends on the quality of the cross section and decay data used. Because of the large amount of data used, only the most important data in the library can be evaluated so as to be of the highest quality. For example, the Re185 (n,gamma) Re186* cross section was initially estimated to be the same as the cross section to the ground state of Re186. However, because of its importance, an evaluation of the cross section was performed which shows that the cross section to the isomeric state is likely five orders of magnitude less.

To increase the quality of the data libraries, a plan was developed. Scientists from the Harwell Laboratory (England), the Energy Centrum Nederland (Holland), and the Hanford Laboratory have agreed to create a joint activation library for both national and ITER use. A format similar to that of ENDF-VI has been adopted. Calculations by Dr. William Wilson of the Los Alamos National Laboratory will be used to replace THRESH systematic calculations. Dr. Robin Forrest of Harwell will use the THRESH systematics computer code to calculate cross sections for short-lived isotopes and for isomers. The THRESH results are normalized by Harwell and ECN by experimental data and by improved systematics. The first release is expected to be in the fall of 1988. This library will then be processed into REACZ format. This summer, ENDF/B-VI evaluations will start to be released. For many of these evaluations, much effort was spent on activation reactions and these evaluations will also be added to the REACZ library. When the ENDFIE-VI decay library (supplied by Or. Charles Reich of INEL) is released, the REACZ decay data library will also be updated.

REFERENCES

1) F.M. Mann. Transmutation of Alloys in MFE Facilities as Calculated by REAC (A Computer Code System for Activation and Transmutation), HEDL-TME 81-37. Westinghouse Hanford Company, 1982.

Table I
Alloy Compositions (weight %)

Isotope	Fe 9Cr-1Mo	Fe Cr-WV	316	Fe 12Cr-20Mn	V 15Cr-5Ti
C	0.10	0.10	**0.06**	0.25	0.3
	0.05	0.005	0.01	0.005	0.7
					0.3
	0.15	0.15	**0.6**	0.20	
	0.02	0.02	0.02	**0.02**	
	0.01	0.01	0.01	0.01	
V	0.02	0.25	0.15	**0.15**	80.
Cr	9.0	9.0	16.8	**12.0**	15.
Mn	0.40	0.45	1.8	20.0	
Fe	88.8	87.9	64.5	66.3	**0.05**
Ni	**0.20**	0.01	13.5	0.01	
cu					0.3
Nb	0.08	0.0001	0.05	0.0001	
Mo	1.0	0.001	2.5	0.001	0.0006
Ta	0.01	0.08	**0.02**	**0.02**	
W	0.01	**2.0**	0.02	1.0	
Ti					5.0

Table II

Fe-9Cr-1Mo
Activation after 10 Year Decay

	5 MW-Y/m^2			36 MW-Y/m^2		
Isotope	Decay Rate(1)	Dose Rate(2)	Class C Waste(3)	Decay Rate(1)	Dose Rate(2)	Class C Waste(3)
Fe- 55	2.7e+0	(4)	0.	1.6e+1	(4)	0.
H - 3	1.3e-1	(4)	0.	3.0e+1	(4)	0.
Co- 60	5.6e-3	7.7e-3	0.	5.9e-2	8.0e-2	0.
Nb- 93*	4.4e-3	4.3e-5	(5)	2.4e-2	2.4e-4	(5)
Mn- 54	3.5e-3	1.8e-3	0.	6.3e-3	3.2e-3	0.
Ni- 63	6.7e-4	(4)	9.5e-2	4.8e-3	(4)	6.8e-1
Nb- 91	5.4e-4	(4)	(5)	4.0e-3	(4)	(5)
Mo- 93	5.2e-4	3.1e-5	1.8e+2	3.5e-3	2.1e-4	1.2e+2
V - 49	2.7e-4	(4)	0.	3.8e-4	(4)	0.
Tc- 99	2.3e-4	(4)	7.6e+0	7.4e-2	(4)	6.2e+2
Nb- 94	8.2e-5	7.9e-5	4.1e+2	5.3e-4	5.1e-4	2.4e+3
C - 14	6.1e-5	(4)	7.7e-2	4.3e-4	(4)	5.4e-1
co- 57	3.9e-5	3.7e-6	0.	4.6e-5	4.4e-6	0.
Ni- 59	6.8e-6	(4)	3.1e-2	4.6e-5	(4)	2.1e-1
Ta-179	3.8e-6	(4)	0.	5.7e-7	(4)	0.
Tc- 98	2.0e-6	(4)	(5)	7.2e-4	(4)	(5)
Tc- 97	1.3e-6	(4)	(5)	7.0e-4	(4)	(5)
Total	5.7e+0	9.6e-3	4.4e+2	4.7e+1	8.4e-2	3.2e+3
Ratio to 5MW-Y/m^2				8.2	8.8	7.0

1) units are (Curie/cm^3)
2) units are (Rem/hr-cm^3). Dose is air shielded at 1 meter from source
3) 10 CFR 61 values for metal are used to normalize decay rate
4) value is less than 1.0e-10
5) no value specified in 10 CFR 61

Table III
Fe-9Cr-WV
Activation after 10 Year Decay

	5 MW-Y/m^2			36 MW-Y/m^2		
Isotope	Decay Rate(1)	Dose Rate(2)	Class C Waste(3)	Decay Rate(1)	Dose Rate(2)	Class C Waste(3)
Fe- 55	5.6e+0	(4)	0.	1.6e+1	(4)	0.
H - 3	3.6e-2	(4)	0.	3.1e-1	(4)	0.
Mn- 54	3.6e-3	1.8e-3	0.	6.3e-3	3.2e-3	0.
Co- 60	1.7e-3	2.3e-3	0.	4.0e-2	5.5e-2	0.
V - 49	2.7e-4	(4)	0.	3.8e-4	(4)	0.
Ta-179	2.1e-4	(4)	0.	2.8e-5	(4)	0.
Hf-178*	4.1e-5	3.1e-5	(5)	9.3e-5	6.9e-5	(5)
Ni- 63	3.4e-5	(4)	5.0e-3	2.4e-4	(4)	3.4e-2
Re-186	1.0e-5	(4)	(5)	7.8e-5	(4)	(5)
Re-186*	1.0e-5	(4)	(5)	7.8e-5	(4)	(5)
Mn- 53	6.6e-6	(4)	1.2e-2	4.5e-5	(4)	7.5e-2
C - 14	6.1e-6	(4)	7.7e-3	4.3e-5	(4)	5.4e-2
Nb- 93*	5.4e-6	5.3e-8	(5)	2.9e-5	2.9e-7	(5)
Co- 57	2.0e-6	1.8e-7	0.	2.3e-6	2.2e-7	0.
Nb- 91	5.4e-7	(4)	(5)	4.0e-6	(4)	(5)
Mo- 93	5.2e-7	3.1e-8	1.8e-2	3.5e-6	2.1e-7	1.2e-1
Ni- 59	3.4e-7	(4)	1.5e-3	2.3e-6	(4)	1.0e-2
Tc- 99	2.3e-7	(4)	7.7e-3	7.4e-5	(4)	2.5e-1
P - 32	1.0e-7	(4)	(5)	9.5e-7	(4)	(5)
Si- 32	1.0e-7	(4)	(5)	9.5e-7	(4)	(5)
Nb- 94	1.0e-7	9.8e-8	5.1e-1	6.4e-7	6.2e-7	2.9
Tc- 98				7.2e-7	(4)	(5)
Tc- 97				7.0e-7	(4)	(5)
Na- 22				2.2e-8	3.1e-8	0.
Total	5.6e+0	4.2e-3	5.6e-1	1.6e+1	5.8e-2	5.7
Ratio to 5MW-Y/m^2				2.9	1.38	10.0

1) units are (Curie/cm^3)
2) units are (Rem/hr-cm^3). Dose is afr shielded at 1 meter from source
3) 10 CFR 61 values for metal are used to normalize decay rate
4) value is less than 1.0e-10
5) no value specified In 10 CFR 61

Table IV
AISI 316
Activation after **10** Year Decay

	5 MW-Y/m^2			36 MW-Y/m^2		
Isotope	Decay Rate(1)	Dose Rate(2)	Class C Waste(3)	Decay Rate(1)	Dose Rate(2)	Class C Waste(3)
Fe- **55**	4.3e+0	(4)	0.	1.2e+1	(4)	0.
H - 3	2.9e-1	(4)	0.	7.3e+1	(4)	0.
Co- **60**	2.8e-1	3.8e-1	0.	1.3e+0	1.8e+0	0.
Ni- **63**	4.5e-2	(4)	6.5e+0	3.2e-1	(4)	4.6e+1
Nb- **93***	3.6e-3	3.6e-5	(5)	2.5e-2	2.4e-4	(5)
Nb- **91**	1.3e-3	(4)	(5)	2.5e-2	(4)	(5)
Mo- **93**	1.3e-3	7.5e-5	4.3e+1	8.4e-3	5.0e-4	2.8e+2
co- **57**	2.6e-3	2.5e-4	0.	3.1e-3	2.9e-4	0.
Mn- **54**	2.5e-3	1.2e-3	0.	4.5e-3	2.3e-3	0.
Nb- **94**	6.0e-5	5.8e-5	2.8e+2	4.4e-4	4.3e-4	2.0e+3
Tc- **99**	5.5e-4	(4)	1.8e+1	1.8e-1	6.6e-10	6.0e+3
V - **49**	5.0e-4	(4)	0.	6.9e-4	(4)	0.
Ni- **59**	4.6e-4	(4)	2.1e+0	3.1e-3	2.9e-4	1.4e+1
C - **14**	1.2e-5	(4)	1.5e-2	8.6e-5	(4)	1.1e-1
Tc- **98**				1.7e-3	(4)	(5)
Tc- **97**				1.7e-3	(4)	(5)
Total	4.9e+0	3.8e-1	3.5e+2	8.7e+1	1.8e+0	8.3e+3
Ratio to 5MW-Y/m^2				18.	4.1	**24.0**

1) units are (**Curie/cm^3**)
2) units are (**Rem/hr-cm^3**). Dose **is air** shielded at **1** meter from source
3) **10** CFR **61** values for metal are **used** to normalize decay rate
4) value is less than **1.0e-10**
5) no value specified in **10** CFR **61**

Table V
Fe-12Cr-20Mn
Activation after 10 Year Decay

	5 MW-Y/m^2			36 MW-Y/m^2		
Isotope	Decay Rate(1)	Dose Rate(2)	Class C Waste(3)	Decay Rate(1)	Dose Rate(2)	Class C Waste(3)
Fe- 55	4.1e+0	(4)	0.	1.2e+1	(4)	0.
H - 3	3.6e-2	(4)	0.	3.0e-1	(4)	0.
Mn- 54	2.1e-2	1.1e-2	0.	2.6e-2	1.3e-2	0.
Co- 60	1.3e-3	1.8e-3	0.	3.0e-2	4.1e-2	0.
V - 49	3.5e-4	(4)	0.	4.9e-4	(4)	0.
Ta-179	9.8e-5	(4)	0.	1.3e-5	(4)	0.
Ni- 63	3.4e-5	(4)	4.8e-3	2.4e-4	(4)	3.4e-2
Hf-178*	1.9e-5	1.4e-5	(5)	3.9e-5	2.9e-5	(5)
C - 14	6.1e-6	(4)	7.7e-3	4.3e-5	(4)	5.4e-2
Re-186	5.1e-6	(4)	(5)	3.8e-5	(4)	(5)
Re-186*	5.1e-6	(4)	(5)	3.8e-5	(4)	(5)
Nb- 93*	5.4e-6	5.3e-8	(5)	2.9e-5	2.9e-7	(5)
Nb- 91	5.4e-7	(4)	(5)	4.0e-6	(4)	(5)
Mo- 93	5.2e-7	3.1e-8	1.8e-1	3.5e-6	2.1e-7	1.2e-1
Mn- 53	4.9e-6	(4)	8.2e-3	3.3e-5	(4)	5.5e-2
co- 57	2.0e-6	1.8e-7	0.	2.3e-6	2.2e-7	0.
Ni- 59	3.4e-7	(4)	1.5e-3	2.3e-6	(4)	1.0e-2
Tc- 99	2.3e-7	(4)	7.5e-3	7.4e-5	(4)	2.5
P - 32	1.0e-7	(4)	(5)	9.5e-7	(4)	(5)
Si- 32	1.0e-7	(4)	(5)	9.5e-7	(4)	(5)
Nb- 94	1.0e-7	9.8e-8	5.1e-1	6.4e-7	6.2e-7	2.9e+0
Tc- 98				7.2e-7	(4)	(5)
Tc- 97				7.0e-7	(4)	(5)
Na- 22				3.1e-8	4.1e-8	0.
Total	4.2e+0	1.2e-2	5.6e-1	1.3e+1	5.4e-2	5.7
Ratio to 5MW-Y/m^2				3.1	4.5	10.0

1) units are (Curie/cm^3)
2) units are (Rem/hr-cm^3). Dose is air shielded at 1 meter from source
3) 10 CFR 61 values for metal are used to normalize decay rate
4) value is less than 1.0e-10
5) no value specified in 10 CFR 61

Table VI
V-15Cr-5Ti
Activation after 10 Year Decay

	5 MW-Y/m^2			36 MW-Y/m^2		
Isotope	Decay Rate(1)	Dose Rate(2)	Class C Waste(3)	Decay Rate(1)	Dose Rate(2)	Class C Waste(3)
H - 3	4.1e-2	(4)	0.	3.8e-1	(4)	0.
V - 49	7.9e-4	(4)	0.	3.4e-3	(4)	0.
Fe- 55	6.2e-4	(4)	0.	1.9e-3	(4)	0.
Co- 60	1.5e-4	2.0e-4	0.	7.4e-4	1.0e-3	0.
Ni- 63	2.3e-5	(4)	3.0e-3	1.7e-4	(4)	7.4e-3
Mn- 54	7.3e-6	3.7e-6	0.	9.6e-6	4.9e-6	0.
Nb- 93*	4.0e-6	3.9e-8	(5)	2.4e-5	2.4e-7	(5)
Ta-179	2.9e-6	(4)	(5)	4.4e-7	(4)	(5)
C - 14	2.7e-6	(4)	3.3e-5	1.9e-5	(4)	2.3e-4
Co- 51	1.5e-6	1.4e-7	0.	1.7e-6	1.6e-7	0.
Hf-178*	5.2e-7	3.9e-7	(5)	3.2e-6	2.4e-6	(5)
Nb- 91	4.1e-7	(4)	(5)	3.0e-6	(4)	(5)
Mo- 93	4.0e-7	2.4e-8	1.3e-2	2.8e-6	1.6e-7	9.2e-2
Ni- 59	2.5e-7	(4)	1.1e-3	1.7e-6	(4)	7.3e-3
Tc- 99	1.6e-7	(4)	5.4e-3	4.5e-5	(4)	1.5e+0
Ar- 39	1.3e-7	(4)	(5)	7.1e-6	(4)	(5)
Ca- 45	8.2e-8	(4)	0.	9.1e-8	(4)	(5)
Nb- 94	4.8e-8	7.2e-8	2.4e-1	5.1e-7	5.0e-7	2.6e+0
K - 42				2.4e-6	3.6e-7	0.
Ar- 42				2.4e-6	(4)	(5)
Tc- 97				8.3e-7	(4)	(5)
Total	4.3e-2	2.1e-4	2.5e-1	3.9e-1	1.0e-3	4.1e+0
Ratio to 5MW-Y/m^2				9.1	4.8	10.8

1) units are (Curie/cm^3)
2) units are (Rem/hr-cm^3). Dose is air shielded at 1 meter from source
3) 10 CFR 61 values for metal are used to normalize decay rate
4) value is less than 1.0e-10
5) no value specified in 10 CFR 61

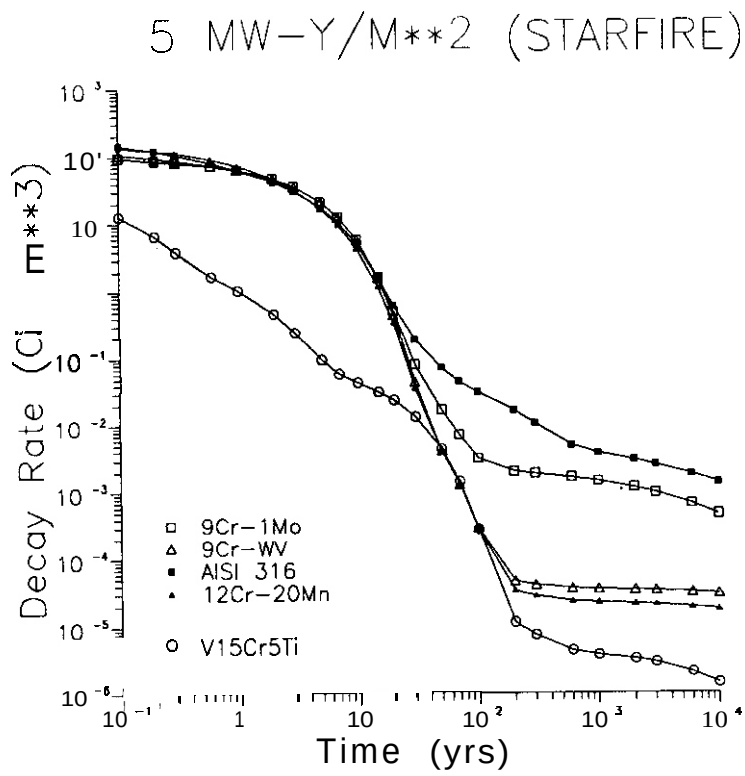

FIGURE 1. Decay Rate as a Function of Decay Time for 5 MW-y/m^2 Exposure

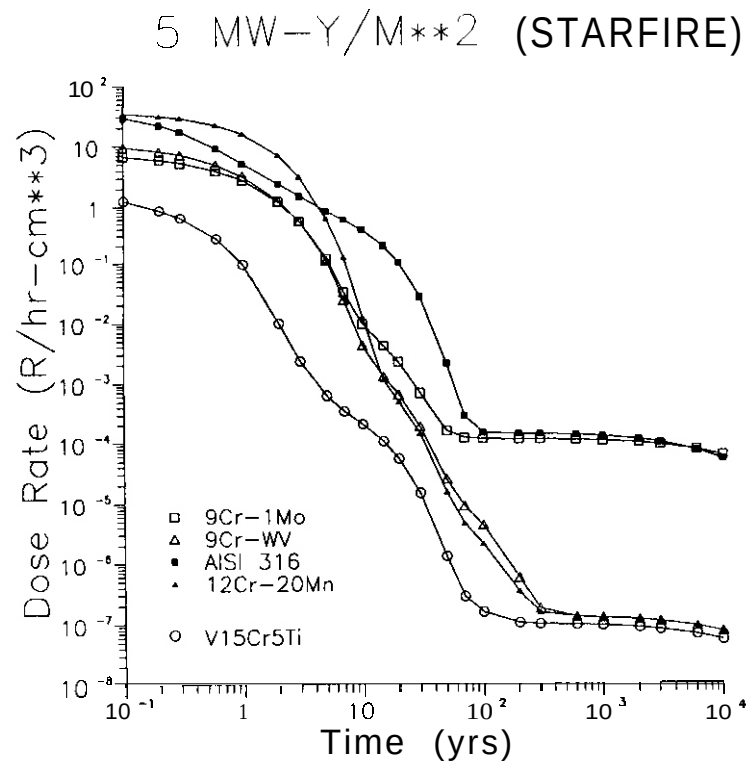

FIGURE 2. Dose Rate as a Function of Decay Time for 5 MW-y/m^2 Exposure

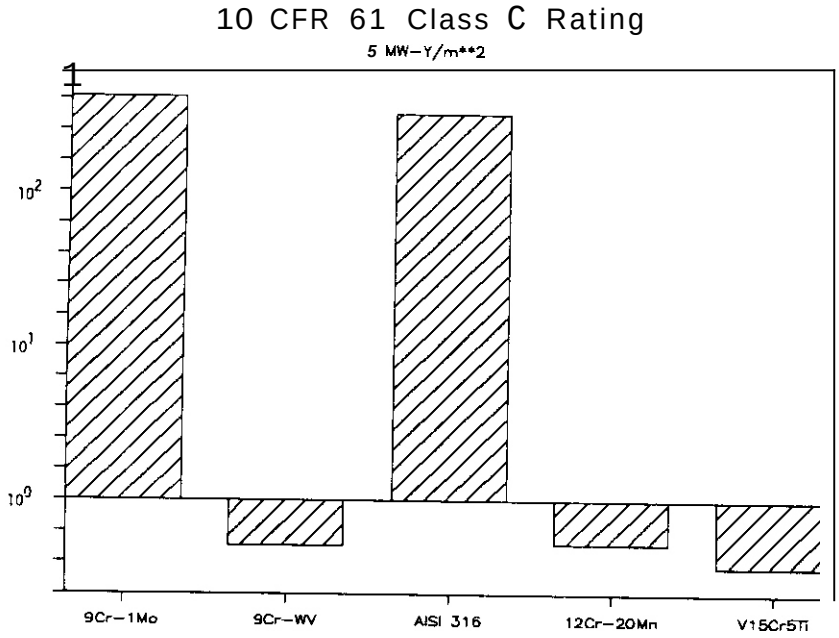

FIGURE 3. 10 CFR 61 Class C Waste Disposal Rating for 5 MW-y/m^2 Exposure

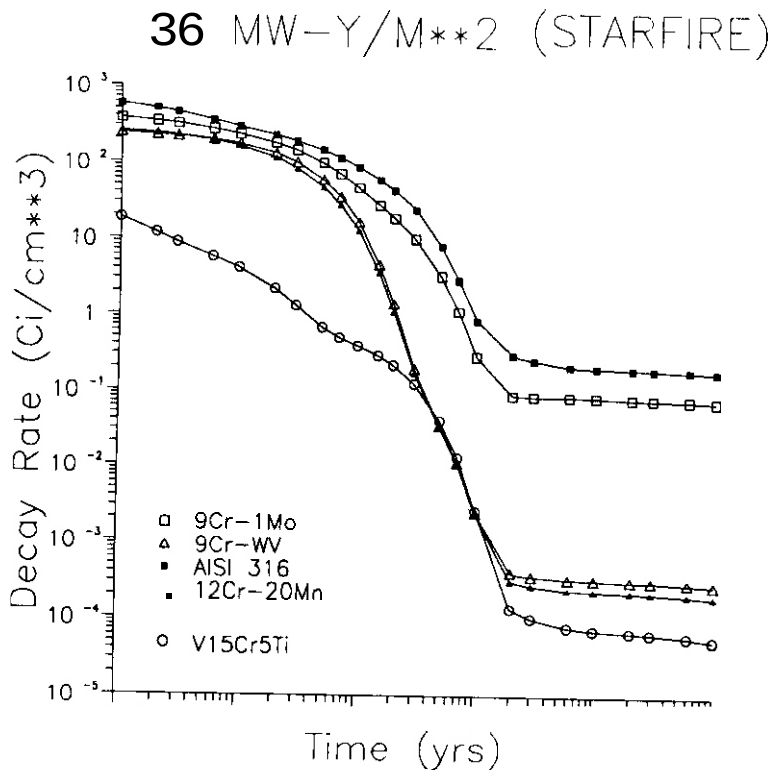

FIGURE 4. Decay Rate as a Function of Decay Time for 36 MW-y/m^2 Exposure

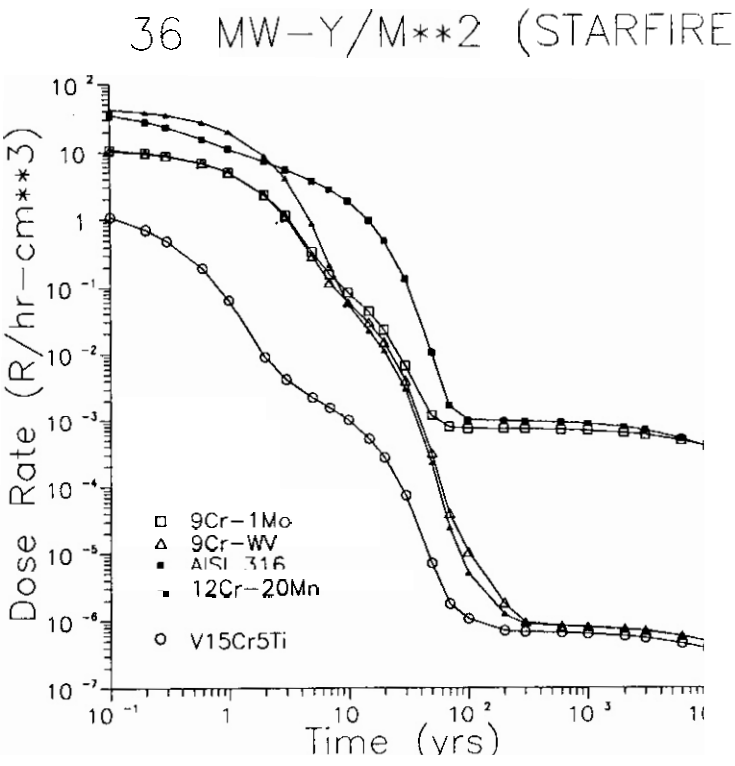

FIGURE 5. Dose Rate as a Function of Decay Time for 36 $MW\text{-}y/m^2$ Exposure

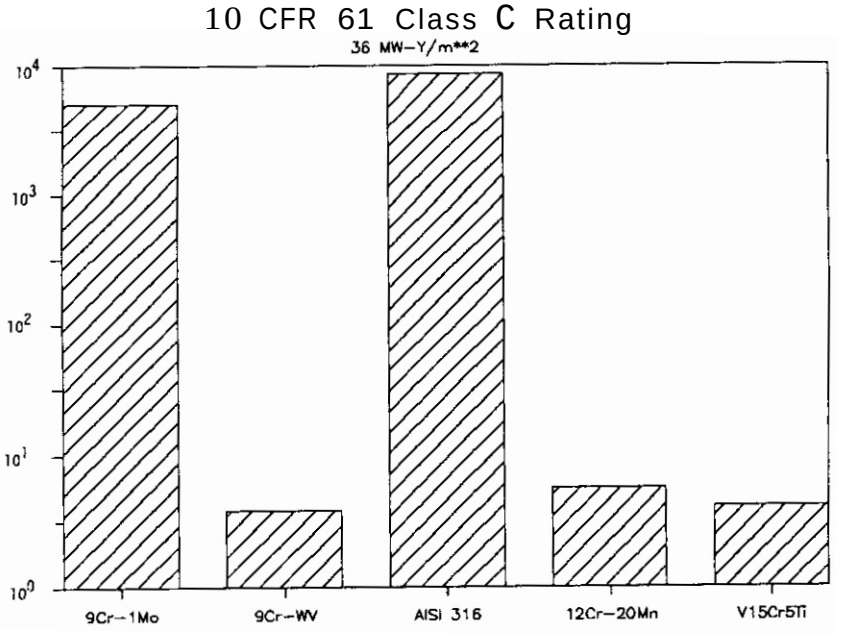

FIGURE 6. 10 CFR 61 Class C Waste Disposal Rating for 36 $MW\text{-}y/m^2$ Exposure

RADIATION DAMAGE CALCLLATIONS FOR COMPOUNC MATERIALS

-. R. Greenwood (Argonne National Laboratory)

OBJECTIVE

To develop displacement damage cross sections for compound materials.

SUMMARY

The SPECOMP computer code has been used to calculate neutron-induced displacement damage cross sections for compound materials, such as alloys, insulators, and ceramic tritium breeders for fusion reactors. These new calculations rely on recoil atom energy distributions which are stored in our SPECTER computer code master libraries. Calculations have been completed for stainless steel, vanadium alloys, ^{6}Li-compound tritium breeders, alumina, SiO_2, Cu_3Au, TaO, and NbTi superconducters. Cross sections are now being developed for other compounds: however, some research is needed to determine the proper threshold energies for many compounds.

PROGRESS AND STATUS

Until recently, it was only possible to use SPECTER1 to calculate displacement damage for pure elements. Damage in compounds has often been estimated assuming that the net damage will be given by the sum of elemental damage weighted by the atomic fraction of each species. It has long been recognized that this procedure is incorrect since the secondary displacement calculations must be done separately for each combination of recoiling atom and matrix material. For example, if we consider the compound Li_2O, then it is clear that a recoiling Li atom will have different probabilities for displacing Li and O atoms in the matrix. The mixed-atom damage functions (eg - Li on O and O on Li) are not available in SPECTER and hence are neglected in any linear combination of elemental damage. A further complication is that the displacement threshold energies will differ for each atomic species and the chemical compounds which they form. Consequently, a new computer code SPECOMP was developed to properly calculate damage for compound materials.

It must be noted that damage calculations for compounds are dependent on precise knowledge of the atomic abundances. In SPECOMP, we assume that atoms are uniformly distributed according to the theoretical density and crystalline structure. Hence, the probability that a recoiling atom will encounter a given type of matrix atom only depends on the atomic abundance of each species. If in fact atoms are segregated or clumped, then calculations must be redone for each local region. In the extreme case of segregation, damage may be more closely approximated by the elemental calculations in SPECTER. Impurities in a material could also have a significant effect. Hence, application of the damage cross sections described in this paper may require some characterization of the material.

The results of the SPECOMP calculations can be readily added to a master data file which can then be accessed by SPECTER. In this way, only one SPECOMP calculation need be done for a given compound material. SPECTER will then routinely calculate spectral-averaged displacements for this compound for any given neutron spectrum and length of irradiation. We are presently compiling SPECOMP calculations for a variety of compound materials and adding the results to the SPECTER libraries. Hence, in many cases users may not need to use SPECOMP at all, but only update their versions of the SPECTER computer code package to add the compound damage calculations subroutines and libraries.

If a compound has not been added to SPECTER, then users with access to SPECTER can run SPECOMP for any combination of the 38 elements for which recoil distributions are currently available. All SPECTER recoil distributions were calculated using the DISCS2 code using evaluated neutron data from ENOF/B-V.[3] The output dpa cross sections can then be readily added to SPECTER. It is also unfortunately true that SPECOMP calculations depend critically on the choice of displacement threshold energies chosen for each atomic species. In the case of pure elements, one can simply renormalize the dpa cross sections if you wish to change the displacement threshold energy. However, this is not possible for compound materials, as will be discussed later: consequently, it is necessary to redo the SPECOMP calculations for each choice of threshold energies. If calculations are desired for an atomic species not present in SPECTER, then it is necessary to run the DISCS2 code to prepare the needed libraries In SPECTER, prior to running SPECOMP. At present, SPECOMP is limited to 4 elements in a given compound: however, the code can easily be expanded.
The results of a calculation with SPECOMP include the energy-dependent displacement damage cross sections (dpa), as well as detailed listings of the secondary displacement functions, for each combination of recoil and matrix atoms. For convenience, a displacement cross section is also calculated from an atomic fraction-weighed sum of elemental damage, as given by SPECTER. It is important to note that the total dpa cross section given in SPECOMP does not distinguish the atomic species involved. For example, in the case of alumina, displacements may be either oxygen or aluminum atoms. The user can separate the displacements by atomic species, if desired, by referencing tables of displacements for each combination of recoil and matrix atoms. We should also point out that SPECOMP does not need to list the recoil atom energy distribution (pka) since these data are already available in SPECTER. The net recoil distribution for a compound,

independent of atomic species, can be obtained from an atom-weighted sum of the recoil distributions listed by SPECTER. Other damage parameters, such as gas production or kerma, also do not depend on the chemical species and values for compounds can be obtained as an atom-weighted sum from SPECTER.

SPECOMP has been used to calculate displacement damage cross sections for Li_2O, $LiAlO_2$, Al_2O_3, SiO_2, 316 stainless steel, NbTi, Cu_3Au, TaO, and V-15Cr-5Ti. These calculations assumed the displacement threshold energies of 10 eV for Li, 30 eV for O, 27 eV for Al, 25 eV for Si, 30 eV for Ti, 53 eV for Ta, 24 eV for Cu, 18 eV for Au, and 40 eV for the other elements. One of the purposes of this paper is to assess the importance of using SPECOMP to calculate damage in compounds, rather than using an atomic fraction-weighted sum of elemental damage, as calculated by SPECTER. To facilitate this comparison, we used the same displacement threshold energies in SPECOMP, as we normally use in SPECTER[1]. More realistically, we know that the displacement thresholds depend critically on the specific binding energies for a given compound and hence are usually very different from the energies used for an element. Unfortunately, we don't have a ready source of displacement energies for most compounds and further research is needed.

Displacement calculations for each combination of recoil and matrix atom are shown for Li_2O in figure 1. The net dpa cross section is shown in figure 2 where it is also compared to the atom-weighted sum of elemental damage from SPECTER. We note that the damage predicted by SPECOMP is typically 30-40% higher than would be expected from the elemental sum (see figure 4). As can be seen in figure 1, this difference is apparently due to an enhancement of the lithium secondary displacements from the oxygen primary recoils. If we look in detail, we find sharp differences between SPECOMP and SPECTER where we encounter peaks and valleys in the neutron cross sections for each element. This effect may be partly due to the differences in mass and partly due to the specific differences in displacement threshold energies.

Figure 3 shows a comparison of displacement damage from SPECOMP and SPECTER for 316 stainless steel. In this case, there is virtually no difference. This might be expected since the masses of the main atomic constituents are about the same, as are the displacement threshold energies.

In order to assess the importance of performing proper dpa calculations for compound materials, we have compared the results from SPECOMP with atom-fraction weighted sums of elemental damage from SPECTER. Figure 4 shows the energy-dependent ratios of the dpa cross sections (SPECOMP/SPECTER) for a variety of compounds. For a materials irradiation, only the net dpa value is important. Hence, Table I shows the spectral-averaged dpa ratios (SPECOMP/SPECTER) for a variety of neutron spectra. There are sizable differences for Li_2O, $LiAlO_2$, and TaO; however, ratios for the other compounds are close to 1. The largest differences seem to be for cases with sizable mass or threshold 'energy differences. In the case of HFIR, we note that the ratios are close to 1 for the Li compounds since the damage is dominated by the $^6Li(n,\alpha)$ reaction with the thermal neutrons. If this reaction is excluded. then the ratio increases to about 1.4. in aareement with the other facilities. For 316 stainless steel and the vanadium alloy, the dpa cross section-is virtually identical for SPECOMP and SPECTER, as shown in figure 3.

Three factors appear to be important in determining whether or not the SPECOMP calculations are significantly different from the atom-weighted sum of elemental damage, namely, relative atomic masses, threshold energies, and nuclear cross sections. The largest dpa differences in Table I occur for the lithium compounds and TaO, where both the masses and thresholds differ significantly. In the cases of alumina, SiO_2, 316 stainless steel, and the vanadium alloy, the masses and thresholds are all quite similar.

The nuclear cross sections can be important for several reasons. In the case of ^6Li, the (n,α) reaction completely dominates the damage below 0.1 MeV. Hence, the damage doesn't depend very much on which elements lithium is alloyed with. More generally, there are many instances in which the nuclear cross sections for one atomic species will dominate the damage productions. This can be seen in figures 1 and 4 where resonances or valleys in one cross section cause sharp differences between SPECOMP and SPECTER.

Effects caused by differences in displacement threshold energies are more difficult to assess. In our model of secondary displacements, there are no displacements below the threshold, 1 between the threshold and twice that energy, and a factor of $0.8/2E_d$ times the Lindhard damage energy at higher energies. This model leads to sharp breaks in the damage cross sections where the recoil atom energies are close to the threshold, especially when only one of the atoms in a compound is permitted to be displaced.

The importance of selecting proper displacement threshold energies can be readily demonstrated for the compound Li_2O. In Table I, the threshold for Li was 10 eV and O 30 eV. If we keep the O threshold at 30 eV and increase the Li threshold to 20 eV, then the spectral-averaged damage cross section in a ^{235}U fission spectrum decreases from 1074 barns to 621 barns. The ratio of dpa values predicted by SPECOMP to that from SPECTER decreases from 1.43 to 1.14. If we further increase the Li threshold value to 30 eV (same as O), then the SPECOMP dpa cross section further decreases to 471 barns and the ratio to SPECTER decreases to 0.98. Hence, we can see that the large difference in the thresholds is the primary contributing factor leading to the large increase in damage predicted by SPECOMP. It is difficult to generalize from this example since we appear to have very different effects for Cu_3Au and TaO where we have large differences in both mass and threshold energies. Clearly, further studies are needed to allow us to predict such effects.

FUTURE WORK

The SPECOMP computer code is available to SPECTER users and can be used to generate libraries of dpa cross sections for any combination of the 38 elements currently contained in SPECTER. The calculations can be run relatively quickly and cheaply on small computers since we make use of existing recoil spectra and do not need to access evaluated neutron cross sections. We are attempting to compile a library of dpa cross sections for a variety of alloys, insulators, and fusion tritium breeding materials. However, more research is needed to determine the proper displacement energies for each element in the compound.

REFERENCES

1. L. R. Greenwood and R. K Smither. SPECTER: Neutron Damage Calculations for Materials Irradiations, ANL/FPP/TM-197, 1985.

2. G. R. Odette and O. R. Dorian. Nucl. Technol. 29, 346 (1976).

3. Evaluated Neutron Data File, Version V, Part B, National Neutron Cross Section Center, Brookhaven National Laboratory, 1979.

Table I: DPA Ratio (SPECOMP/SPECTER)

Compound	Fission [a]	14 MeV	STARFIRE [b]	HFIR [c]	FFTF [d]
Li_2O	1.43	1.43	1.31	1.04	1.41
$LiAlO_2$	1.26	1.23	1.25	1.07	1.28
Al_2O_3	0.99	0.98	0.99	1.00	1.00
SiO_2	0.99	0.96	0.99	1.00	1.00
V-15Cr-5Ti	1.00	1.00	1.00	1.00	1.00
316 SS	1.00	1.00	1.00	1.00	1.00
Cu_3Au	0.98	0.98	0.98	0.99	0.99
Nb-Ti	0.99	1.00	0.99	0.99	0.99
TaO	0.89	1.16	0.96	0.86	0.80

[a] ^{235}U fission spectrum

[b] STARFIRE, first wall spectrum

[c] High Flux Isotopes Reactor, PTP, midplane

[d] Fast Flux Test Facility, mot, midplane

Dosimetry and Damage Analysis for the Omega West Reactor (LANL)

L. R. Greenwood (Argonne National Laboratory)

OBJECTIVE

To characterize reaction irradiation facilities and experiments in terms of neutron fluence, energy spectra, and radiation damage parameters.

SUMMARY

Neutron dosimetry measurements and damage calculations were completed for three experiments in the Omega West Reactor (LANL). These irradiations were conducted by Hanford Engineering Development Laboratory and were designed to compare radiation damage produced in a fission reactor spectrum with damage produced by 14 MeV neutrons at RTNS II.

PROGRESS and STATUS

Three experiments were conducted by Howard Heinisch (HEDL) at the Omega West Reactor at Los Alamos National Laboratory between May 21 and July 16, 1987. The experimental conditions were similar to those reported previously. [1,2,3] The irradiation histories and exposure parameters are listed below. The exposures are listed in full power hours at 8 MW reactor power.

Experiment	Dates	Exposure, FPH
9	5/21/87-5/22/87	12.97
10	5/27/87-6/5/87	58.12
11	6/22/87-7/16/87	127.50

Small dosimetry capsules were included with each experiment. Each capsule contained wires of 0.1% Co-Al, Ni, Fe, Ti, and 80% Mn-Cu. Each wire was gamma counted at Argonne and activation rates were computed considering the irradiation histories and gamma absorption. The results are listed in Table I.

Neutron energy spectral adjustments were then made for each irradiation using the STAY'SL computer code starting with a previously-measured spectrum. [2] The resultant fluxes and fluences are listed in Tables II - III. As can be seen in the Tables, the activities and fluxes for all three runs are in agreement within a few percent. These results also agree with the previous run numbers 1-4, also with helium cooling.

Damage calculations were performed for each run using the SPECTER computer code[4] and the results are listed in Table IV.

FUTURE WORK

Additional experiments are in progress in the Omega West Reactor. In particular, experiments are planned with water cooling in order to confirm the spectral differences between water and helium.

REFERENCES

1. L. R. Greenwood, Damage Analysis and Fundamental Studies quarterly Progress Report, DOE/ER-0046/25, pp. 5-7 (May 1986).

2. L. R. Greenwood, Damage Analysis and Fundamental Studies Quarterly Progress Report, DOE/ER-0046/4, pp. 15-20 (Feb. 1981).

3. L. R. Greenwood, Fusion Reactor Materials Semi-Annual Progress Report, DOE/ER-0313/2, pp. 34-37 (Sept. 1987).

4. L. R. Greenwood and R. K. Smither, SPECTER: Radiation Damage Calculations for Materials Irradiations, ANL/FPP-TM197, January 1985.

Table I

Activation Rates Measured in the Omega West Reactor
(activities are in atom/atom-sec, ± 2%, at 8 MW)

Reaction	Run 9	Run 10	Run 11
$^{58}Fe(n,\gamma)^{59}Fe$ ($x10^{-11}$)	6.44	6.35	5.98
$^{59}Co(n,\gamma)^{60}Co$ ($x10^{-9}$)	2.16	2.05	2.08
$^{54}Fe(n,p)^{54}Mn$ ($x10^{-12}$)	2.74	2.81	2.75
$^{58}Ni(n,p)^{58}Co$ ($x10^{-12}$)	3.61	3.63	3.40
$^{46}Ti(n,p)^{46}Sc$ ($x10^{-13}$)	3.73	3.77	3.60
$^{55}Mn(n,2n)^{54}Mn$ ($x10^{-15}$)	8.42	8.46	8.27

Table II

Neutron Fluxes for Omega West Reactor
(Flux $x10^{13}$ n/cm^2-s at 8 MW, ± 10%)

Energy, MeV	Run 9	Run 10	Run 11
Thermal (<.5eV)	7.28	6.94	6.92
0.5eV - 0.1 MeV	4.74	4.58	4.80
>0.1	5.45	5.49	5.43
>1	2.68	2.72	2.67
Total	17.47	17.01	17.15

Table III

Neutron Fluences for Omega West Reactor
(Fluence $x10^{18}$ n/cm^2, ± 10%)

Energy, MeV	Run 9	Run 10	Run 11
Thermal (<.5eV)	3.40	14.50	31.75
0.5eV-0.1MeV	2.22	9.57	22.04
>0.1	2.55	11.47	24.92
>1	1.25	5.69	12.24
Total	8.16	35.55	78.72

Table IV

Damage Parameters for Omega West Reactor
(dpa $x10^{-3}$, He in appb)

Element	Run 9		Run 10		Run 11	
	dpa	He	dpa	He	dpa	He
Al	3.27	1.07	14.72	4.83	31.98	10.49
Ti	1.97	0.99	8.88	4.45	19.29	9.67
V	2.23	0.04	10.03	0.17	21.80	0.36
Cr	2.01	0.28	9.04	1.27	19.65	2.75
Fe	1.78	0.49	8.00	2.21	17.38	4.80
Ni	1.89	7.57	8.50	34.04	18.47	73.96
cu	1.72	0.41	7.76	1.85	16.85	4.01
Nb	1.74	0.09	7.82	0.42	16.98	0.91

3. MATERIALS ENGINEERING AND DESIGN REQUIREMENTS

MATERIALS HANDBOOK FOR FUSION ENERGY SYSTEMS – J. W. Davis (McDonnell Douglas Astronautics Company – St. Louis)

OBJECTIVE

To provide a consistent and authoritative source of material property data for use by the fusion community in concept evaluation, design, and performance/verification studies of the various fusion energy systems. A second objective is the early identification of areas in the materials data base where insufficient information or voids exist.

SUMMARY

The effort during this reporting period has focussed on two areas: (1) publication of data pages, and (2) automation of the data pages. The data pages contained new engineering information on lithium and stainless steel along with additional Supporting Documentation pages on annealed and cold worked stainless steel. These pages were distributed in May. In the area of automation, work is proceeding on schedule toward the formation of an electronic materials data base for the MFE computer network.

PROGRESS AND STATUS

During the last reporting period. work focussed on developing and publishing data sheets for both Volume 1 (Engineering Data) and Volume 2 (Supporting Documentation). The data page for Volume 1 consisted of new data on the specific heat, electrical resistivity, and enthalpy of lithium and the physical and mechanical properties of 316 stainless steel at cryogenic temperatures. The Volume 2 data pages included the information needed to develop the data pages mentioned above. along with additional supporting documentation data pages on 316 stainless and electrical insulators, which were previously published in Volume 1. Work is in progress to publish information on the 21-b-9 steel, for use as magnet case and on preparing data sheets on vanadium for use in high heat flux components.

In addition to these activities, work is also in progress on developing an electronic version of the handbook. The first step in this direction was taken two years ago, when a special computer code was developed to assist in the publication of the approved data pages. Over the past two years as more data pages were developed using this program, the resident files essentially became a defacto data base. Therefore the next logical step is to modify this data bank into an electronic version of the Handbook. With an electronic handbook, the user is assured of an up-to-date version of the data page each time he/she accesses the file. This has historically been a weakness in all handbooks, since it is incumbent upon the user to take the time to incorporate the latest revisions into their book. While many of the users make a conscientious effort to do this, there are instances when they do not receive all of the data Pages in their update. To make sure that all of the handbooks are up to date. a summary listing of the data pages contained in the handbook is usually distributed on an annual basis. This forces the user to check every page in their handbook to make sure that they have the latest revision. The difficulty in developing an electronic handbook is the need to have both graphics and text in the files and to create a macro server system that is user friendly to the extent that it can assist the user in material selection and material comparisons. The work during this period was directed toward locating an existing data base program, resident within the MFE computer system, and to evaluate that program to determine if it fits the requirements of the handbook. At the present time, it appears that such a program is available and we are currently evaluating it. At the same time, we are developing a server program to overlay on this program which will direct the user to the appropriate files through a series of questions using menus.

FUTURE WORK

During the next reporting period, work will continue on the development of vanadium data pages and on an electronic handbook. We are targeting a demonstration of an embryonic of an electronic handbook for the fourth quarter of 1988.

4. FUNDAMENTAL MECHANICAL BEHAVIOR

No contributions received this period.

5. RADIATION EFFECTS: MECHANISTIC STUDIES, THEORY AND *MODELING*

IRRADIATION CREEP MECHANISMS: AN EXPERIMENTAL PERSPECTIVE - F. A. Garner and D. S. Gelles (Pacific Northwest Laboratory)

OBJECTIVE

The object of this effort is to determine the mechanisms involved in radiation-induced deformation oi structural materials and to apply these insights for extrapolation of available fast reactor data to fusion-relevant conditions.

SUMMARY

An extensive review was conducted of a variety of radiation-induced microstructural data, searching for microstructural records of various irradiation creep mechanisms. It was found that the stress-affected evolution of dislocation microstructure during irradiation is considerably more complex than envisioned in most theoretical modelling studies. particularly in the types of interactive feedback mechanisms operating. Reasonably conclusive evidence was found for a SIPA-type mechanism (stress-induced preferential absorption) operating on both Frank loops and network dislocations. Stress-induced preferential loop nucleation (SIPN) processes may also participate but are thought to be overshadowed by the stronger action of SIPA-type processes operating on Frank interstitial loops. It was not possible to discern from microstructural evidence between second-order SIPA and first-order SIPA mechanisms. the latter arising from anisotropic diffusion. Evidence was presented. however. that validates the operation of stress-induced preferential unfaulting of Frank loops and stress-induced growth of previously stressed material following removal of applied stress. Dislocation glide mechanisms are also participating but the rate appears to be controlled by SIPA-type climb processes. Applied stresses were shown to generate very anisotropic distributions of Burgers vector in the irradiation-induced microstructure.

PROGRESS AND STATUS

Introduction

The confident design of nuclear power plants requires knowledge of the strains that develop in structural components during their service in radiation environments. While fully empirical equations can be developed from dimensional changes observed in reactor experiments, extrapolation to higher levels of radiation exposure or different service environments is facilitated by knowledge of the microscopic physical processes involved in producing macroscopic strains. A number of processes which contribute to macroscopic strain have been identified. although not all occur in a given material or in a given set of irradiation conditions. These are void swelling. irradiation growth. irradiation creep. thermal creep, recovery of deformation-induced microporosity. and volume changes associated with various phase transformations or segregation phenanena. Many of these processes are interactive and each responds differently to applied stress. radiation environment and material variables such as dislocation density or texture. While sane of these processes are volume conservative. others are not. Those involving volume changes can lead to either isotropic or anisotropic distribution of strain.

The first part of this paper demonstrates that conventional measurements of strain and volume change cannot completely separate the individual contributions of each of the superimposed processes. This limits our ability not only to extrapolate empirical correlations of macroscopic strain but also limits the identification of the major microscopic processes and their relative contributions to total deformation. It will be shown that currently used correlations for irradiation creep of austenitic alloys by necessity include several non-creep components of strain.

While radiation-induced void growth and phase transformations leave an integrated record of their behavior both in the bulk density and the microstructure of a metal. irradiation creep and growth were originally thought to leave no comparable microstructural record. However. over the last decade it has been shown by many investigators that records of the stress state are indeed imprinted in the mtcrostructure by creep and growth processes. Therefore. another approach to guide correlation development is to search for microstructural evidence that discriminates not only between the various strain contributions but also between the different physical models advanced to describe a given strain contribution.

The second part of this paper reviews the relevant published microstructural data and presents sane previously unpublished data and analyses. The data fall into three major categories. These are the surface topography of ion-irradiated metals. dynamic observations of microstructural components during electron irradiation of thin film specimens. and finally the post-irradiation observation of stressed bulk specimens irradiated with either fast neutrons or high energy ions.

This paper focuses primarily on face-centered cubic metals and alloys. It will not address in detail the many proposed models of irradiation creep and their theoretical description. For this purpose. the reader is referred to two recent and extensive reviews. The first by Matthews and Finnis[1] concentrates

on the models themselves and the second by Hall[2] focuses more on the evolution of dislocation microstructure. Additional information is supplied by Henager and Simonen[3] and also by Coghlan.[4] The latter paper focuses primarily on a review of recent irradiation creep results while the former focuses on mechanisms of creep most likely to occur at low damage exposures.

Macroscopic measurements of neutron-induced creep and or with their interpretation

The literature contains many papers which address the study of irradiation creep using both neutron and charged particle irradiation. Reference 5, for instance. shows that neutron-induced creep may be studied using stress relaxation methods. bent beam techniq es, pressurized tubes. or constant load approaches involving tensile specimens or helical springs.! For the purpose of this paper, we shall focus on data derived from pressurized tubes. which represent the source of most recently produced creep data from neutron environments. The biaxial stress state found in the wall of a thin-walled pressurized tube causes creep deformation that expands the diameter of the tube at the expense of a thinner wall. Thus the length of the tube is not altered by creep. In theory, therefore. one could assess the swelling component of strain by measuring changes in the length of the tube. In practice. however, such measurements are generally not made for a variety of reasons. Only nondestructive measurements of tube diameter changes and destructive post-irradiation measurements of density change are performed to assess swelling-induced strain.

There are a number of strain components that contribute to each type of experimental measurement. These varied contributions cannot always be separated from each other. If microscopy is employed to measure swelling the only major strain detected is that due to void formation. a process known to be completely isotropic in its distribution of strain. When one measures swelling in alloys of engineering relevance by immersion density techniques. however, not only is the void volume measured but also the texture-dependent and often anisotropic contributions that arise from recovery of deformation-induced microporosity and volume changes associated with various phase transformations.[6,7] The latter range in magnitude from hundredths of a percent to several volume percent and can be either dilational or contractional in nature. Finally. the use of post-irradiation dimensional change measurements can identify only the net presence of anisotropy but cannot discriminate between the relative contributions of each strain component.

When irradiated specimens evolve under stress, other strain contributions occur. Creep strains develop even in the absence of Irradiation. but the phase instabilities mentioqed earlier are often sensitive to both applied stresses and radiation in their rate of development. Thus a portion of the volume changes related to phase transformations appear to be a component of both irradiation and thermal creep. Under irradiation, however, both creep and phase stability are altered. and due to the influence of stress the onset of swelling can also be accelerated.[8,9] Thus. a typical pressurized tube used to measure irradiation creep develops strains that are a complex function of radiation-modified creep, swelling. recovery and phase changes. all of which are potentially stress-sensitive. but each in a different manner.

Another problem arises from the difficulty in extrapolating these strains to higher fluence. different stress levels and other displacement rates. Due to the constraints associated with limited reactor space. funding. time. and engineering practicality. it is usually impossible to irradiate sufficient specimens of different types at any one set of irradiation conditions in order to isolate and identify all of the various interactive strain components. For instance. one cannot obtain a stress-affected swelling measurement without sacrificing a creep tube. thereby rendering it unavailable for continued creep measurements. The general practice is therefore to measure only the diameter change of an unstressed tube and thereby only the stress-free component of swelling. This unavoidably includes the stress-affected swelling component as part of the creep strain and introduces two sorts of errors which affect the validity of creep correlations for extrapolation beyond exposures at which the data were developed. First, the stress-affected swelling and phase change components are included as creep contributions but they saturate after some exposure. while that due to true irradiation creep does not. Second. all components of swelling are thought to be isotropically distributed whereas creep is inherently an anisotropic process. Therefore. the distribution of some portion of the swelling strains between the three coordinates will be incorrectly included in the creep correlation.

One consequence of the foregoing is that pressurized tube data on alloys of engineering relevance cannot be used to discriminate between the various proposed creep mechanisms. particularly at relatively low irradiation exposures where many of the proposed non-creep mechanisms would be expected to dominate the strain measurement. In turn, this guarantees that design correlations for irradiation creep will be largely empirical. although they can range from very complex[10] to very simple[11,12] In nature.

The simplest empirical irradiation creep correlations focus primarily on the acceleration of irradiation creep that coincides with the onset of swelling[11-15] while many of the creep models focus on microstructural scenarios that do not involve void swelling. In the following sections. we will focus on the earliest stages of microstructural evolution in relatively simple metals and proceed toward both later stages of evolution and more complex alloys.

Types of microstructural evidence

The stresses that drive irradiation creep processes can arise from a variety of sources. In addition to applied stresses. creep can be activated by stresses arising from temperature differences. differential swelling. constraints placed in the path of swelling-induced deformation and even lattice parameter changes associated with precipitation and segregation. While stresses arising from such sources cannot always be quantified. they can be used to study facets of irradiation creep behavior. In the following sections. we will first examine the influence of swelling-generated stress on the surface topography and underlying microstructure of ion-irradiated materials. We will then review the results of experiments involving dynamic observation of electron-irradiated thin foils. both with and without applied stresses. Finally. we will cover the results of post-irradiation examination of bulk specimens irradiated with either neutrons or high energy ions.

Surface topography of ion-irradiated materials

When materials are bombarded with gas atoms at relatively low irradiation temperatures where irradiation creep cannot easily operate. stresses exceeding the yield strength can be generated below the surface leading to pitting,[16] blistering[16,17] or crazing[18] of the surface. The first two of these phenomena have been shown to be dependent on the orientation presented by the material to the foil surface. often varying from grain to grain. Wolfer and Garner[19] showed that orientation-dependent lateral stresses which develop in response to bubble-induced swelling are responsible for much of this variation. Whereas Evans[20] reached th conclusion that the gas pressure in the bubbles was the prime initiator of blister formation. Wolfer" later showed that both gas pressure and lateral stresses played significant roles in blister formation, with the latter controlling the orientation dependence.

At temperatures where irradiation creep operates easily, the lateral stresses that arise from self-ion induced swelling (gas-free voids) are lower but sufficient in themselves to cause significant alteration of the bombarded surface. Johnston and coworkers demonstrated that one consequence of ion-induced swelling was an elevation of the specimen surface as shown in Figure 1[22]. They derived an empirical correlation relating swelling in the peak displacement region to the step height generated at the boundary between irradiated and unirradiated regions. This correlation stated that each 60 A of step height implied 1% swelling in the peak displacement region.

Fig. 1. Surface of a duplex alloy, Uranus 50, bombarded with 10^{17} Ni+ ions/cm^2 at 625 °C. The austenite grains have swollen and risen above the adjacent low-swelling ferrite grains. No lateral expansion of the austinite grains has occurred. reflecting the unidirectional nature of the swelling.[22]

Garner. Wire and Gilbert[23] later showed that the step height conversion factor was dependent on the target material and ion energy but most importantly. represented a plastic flow in which the total volume change was accommodated solely by movement of mass perpendicular to the specimen surface. (Primak[18] had independently reached the same conclusion with respect to crazing in gas ion irradiation of quartz and vitreous silica.) The redirection of two-thirds of the mass flow towards the specimen surface implies that ion-induced swelling experiments should more correctly be characterized as ion-induced creep experiments.

The surface topography of ion-irradiated materials at swelling-relevant tmperatures thus contains an integrated record of the dependence on crystalline geometry of various irradiation creep mechanisms. driven by an anisotropic compressive stress state determined only by the ratio of the local swelling rate and the creep compliance.[23] This latter quantity depends not only on the orientation of the grain with respect to the surface but changes as the underlying microstructure passes through various evolutionary regimes. The internal stress in the swelling layer is thus limited to levels below the yield stress. as evidenced by an inability to explain the experimental observations in terms of the orientation dependence of yielding and also by an absence of microstructure typical of abrupt yielding.

As shown in Figure 2, Johnston and coworkers observed that ion-induced step heights often varied from grain-to-grain and that twinned regions within a grain could exhibit either lower or higher step heights than the grain in which they are located. implying a dependence of swelling on grain orientation.[24] Chang. Bajaj and Diamond[25] noted that grains with orientations closest to the major poles ([111],[001] and [011]) exhibited smaller step heights than did grains oriented around minor axes ([113],[123] and [223]).

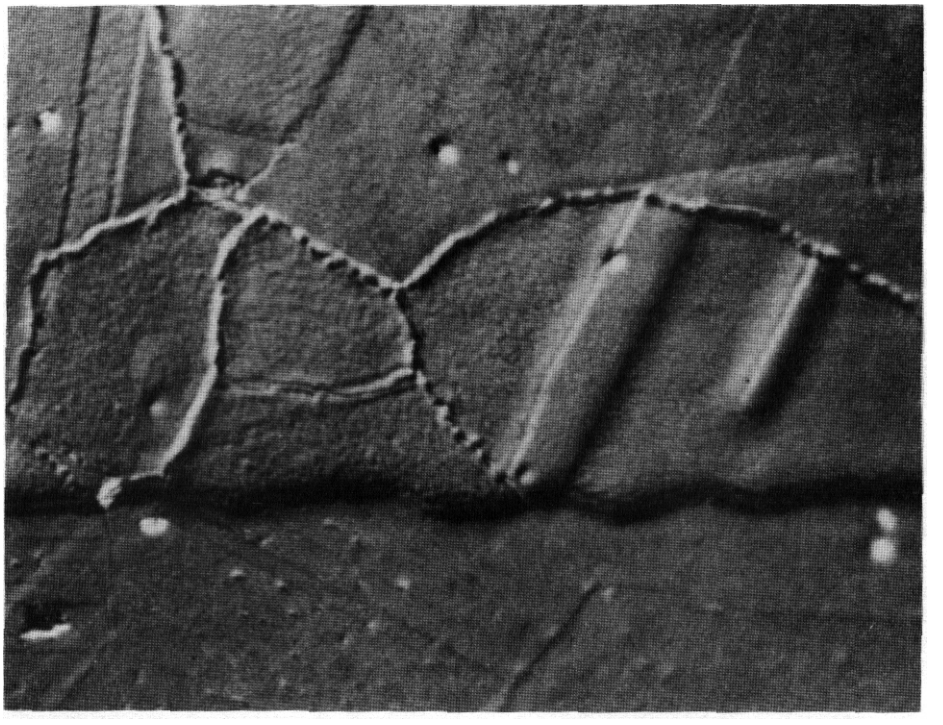

Fig. 2. Surface detail on annealed 304 specimen bombarded with $7X10^{16}$ Ni^{+} ions/cm^2 at 660°C.[24] Two twins on the right are elevated above the grain. and twin at upper left is slightly depressed. The large horizontal step in the foreground represents the boundary between exposed and shielded areas at the mask edge.

Wolfer and Garner calculated the response of various creep microstructures and creep mechanisms as a function of grain orientation to the stress state found in ion bombarded foils.[19] It was found that the largest levels of stress arose in microstructures having the least degree of freedom, i.e., those composed only of Frank loops. For foil normals lying parallel to sane low index directions, the SIPA (Stress Induced Preferential Absorption of interstitials) mechanism of creep could not operate. Wolfer and Garner concluded that the orientation-dependent differences in step height arose only in the incubation period of swelling and represented a temporary difficulty in movement of mass by the SIPA mechanism for loop-dominated microstructures with unfavorable orientations. Once microstructures composed of free dislocations developed. the effects of swelling-generated stresses and crystal orientation were predicted to diminish strongly.

One conclusion drawn from these various ion bombardment studies is that one might expect an anisotropy in the distribution of dislocation Burgers vectors to result from or cause the unidirectional movement of mass toward the surface. To the knowledge of the authors of this paper. however. no studies of this possibility have ever been conducted for ion-irradiated metals. As will be shown later. such anisotropfes are observed in other types of studies.

The studies in References 19 and 23 also foreshadowed the later finding that creep and swelling would always co-evolve at rates which were commensurate, each accelerating at the same time. avoiding the generation of large levels of swelling-induced internal stresses.

Electron irradiation in the absence of applied stress

Buckley and Manthorpe[26] demonstrated that observations of dislocation behavior relevant to the study of irradiation creep could be made using thin foils without applied stress. They noted that dislocation movements were of two distinct types: spasmodic. large amplitude jerks which frequently alternated in direction, and relatively slow but progressive unidirectional drifts. The former have the characteristics of dislocation glide and the latter were presumed to represent dislocation climb originating from the preferential absorption of interstitial atoms. They also noted that dislocation fluxes measured during irradiation increased rapidly with temperature above 300°C coincident with the onset of void swelling. In addition. they found that the initially isotropic dislocation climb fluxes later became heavily biased toward those dislocations which moved mass toward the specimen surface. This was described as a consequence of biaxial restraining stresses which developed at the perimeter of the irradiated region. causing irradiation creep toward specimen surfaces.

Irradiation creep represents only a stress-induced modification of the point defect capture efficiencies of various microstructural sinks. but the stress-free capture efficiencies are also the subject of theoretical investigation.[1,2,27] Charged particle irradiations conducted without applied stress are sanetimes used to derive consistent sets of material parameters, including the bias factors of various microstructural sinks toward net capture of interstitials.[28-30] One such electron study concluded that voids also exhibit a preference for interstitial absorption,[30] and a similar conclusion was reached in an ion irradiation study.[31] This conclusion is particularly relevant to the observation that both irradiation creep rates and dislocation fluxes accelerate with the onset of void swelling.

Studies utilizing charged particle irradiation to obtain stress-free capture efficiencies require that the impact of variables atypical of the neutron environment be factored into the analysis.[32-35] Particularly relevant are recent findings that radiation-induced segregation at foil surfaces induces a bias against the absorption of vacancies at the foil surface,[34] that segregation at void surfaces changes their capture efficiencies for both vacancies and interstitials,[37] and that the typically higher displacement rates of charged particle irradiations significantly alters the bias of both voids and dislocations.[38,39]

Previously unpublished results of electron irradiation studies

The successful description of irradiation creep phenanena requires not only the identification of the mechanisms involved. but also a description of the identity and density of the microstructural canponents on which the mechanisms operate. The discontinuous nature of microstructural data extracted from neutron irradiation experiments requires that sane details of canponent evolution in response to environmental variables and fluence be examined using simulation studies of a continuous nature. Comparison of data derived from neutron and electron irradiation experiments[32,35,36] has not only demonstrated the validity of simulations applied to this objective. but has also led to an improved understanding of the factors which control the development of various kinds of dislocation loops and their relative contribution to irradiation creep deformation.

The analysis and experiments described in this section were initiated to resolve two ananalies discussed in an earlier paper.[36] These concerned the growth behavior of several kinds of irradiation-produced dislocation loops. First. whereas neutron-produced loops usually possess relatively regular boundaries, electron-produced loops often possess quite irregular or crenulated boundaries. implying that electron simulations are not relevant to neutron experience. Second. as shown in Figure 3a, measurement of growth rates of loop area in electron irradiations showed that the Frank interstitial loops grew at rates substantially larger than those of diamond prismatic loops which co-existed in the same volume and were subjected to the same local environment. This latter observation appears to be in conflict with predictions based on the preferential interstitial capture or bias theory[40] that forms the basis of the SIA creep theory,[41] and therefore casts doubt on the validity of such theories.

Origin of irregular growth behavior

There are a number of observations that can be made from Figure 3b that illuminate the possible origin of irregular loop growth. First, both the Frank interstitial and diamond prismatic loops exhibit irregular growth behavior. although each does so in a different manner. The prismatic loops located just below the letter A in Figure 3b are attempting to retain the expected diamond shape but develop additional facets as the irradiation proceeds. Apparently the loops are encountering obstacles in the loop plane that restrict further growth. The resulting irregularities are retained at higher fluence. The nature of the obstacles is not revealed in these micrographs. being invisible under these diffraction conditions.

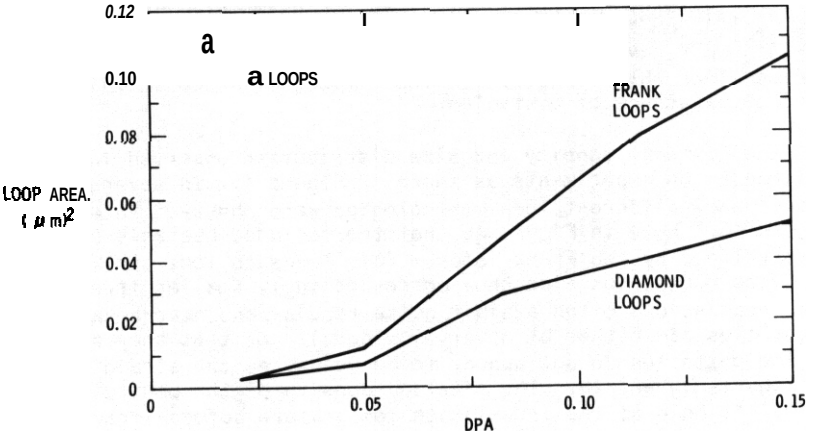

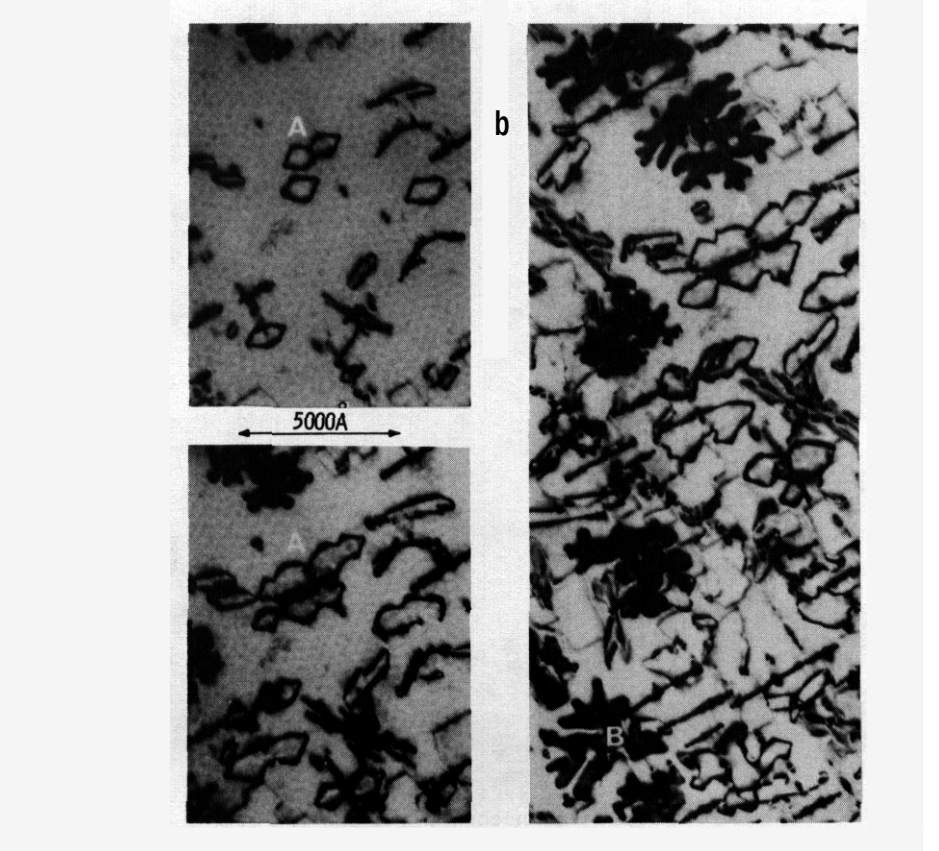

Fig. 3. (a) Relative growth rates of Frank interstitial and prismatic dislocation loops during 1.0 MeV electron irradiation of annealed 316 stainless steel at 500°C and $3X10^{-5}$ dpa/sec, (b) loop growth sequence.

The Frank faulted loops also appear to be encountering the same or similar obstacles. This praess gives rise to highly irregular boundaries, which are not constrained to develop the straight line segments characteristic of prismatic loops. Since the faulted loop boundaries are not governed as strongly by minimum line length considerations, the Frank loops are able to envelop and aclude the obstacles. Although no contrast is associated with the obstacle under the imaging conditions used. an estimate of the obstacle size (or its sphere of Influence) can be obtained from the acluded area.

Many of the faulted loops shown in Figure 3b contain small non-faulted areas surrounded by faulted regions. These occluded non-faulted areas correspond to nodes observed at lower fluence. The loop marked B in the right-hand micrograph of Figure 3b contains an obstacle that is just about to be

enveloped. The intersected cross sections of the obstacles are roughly circular. and therefore the obstacles are probably roughly spherical. The Frank loop just above the letter A in Figure 3b has 25 nodes and inclusions in a circular area of approximately 4000 A diameter. This corresponds to a planar obstacle density of about 2×10^{16} cm^{-2}, with diameters of 30 A. The volumetric obstacle density is therefore on the order of 10^{15} cm^{-3}. Many of the loops viewed edge-onward appear to exhibit contrast indicative of small obstacles along their length, but the limited evidence in this micrograph is not considered conclusive proof of existence of obstacles.

It should be noted that the obstacle density and size distribution observed in this study are not always observed in other irradiation experiments as shown in Figure 4. In several nominally identical irradiations on similar specimens, different loop morphologies were observed in exploratory irradiations conducted at approximately 500°C. Note In Figure 4b that the occluded obstacle sizes are much smaller. and therefore more easily enveloped by the Frank loops. This leads to less striking irregularities in loop shape. The prismatic loop boundaries also show correspondingly smaller irregularities. The loops in other nominally similar irradiations often exhibit quite regular and near-hexagonal shapes. From this it is inferred that the obstacles are either at a very low density or that they are too small to impede the growth of the loops. The obstacles do not appear to be voids. as the strain contrast of small voids can be easily observed in Figures 3b and 4a. The size and density of the obstacles appears to be related to the time at which the foil is held at the irradiation temperature before irradiation commences.

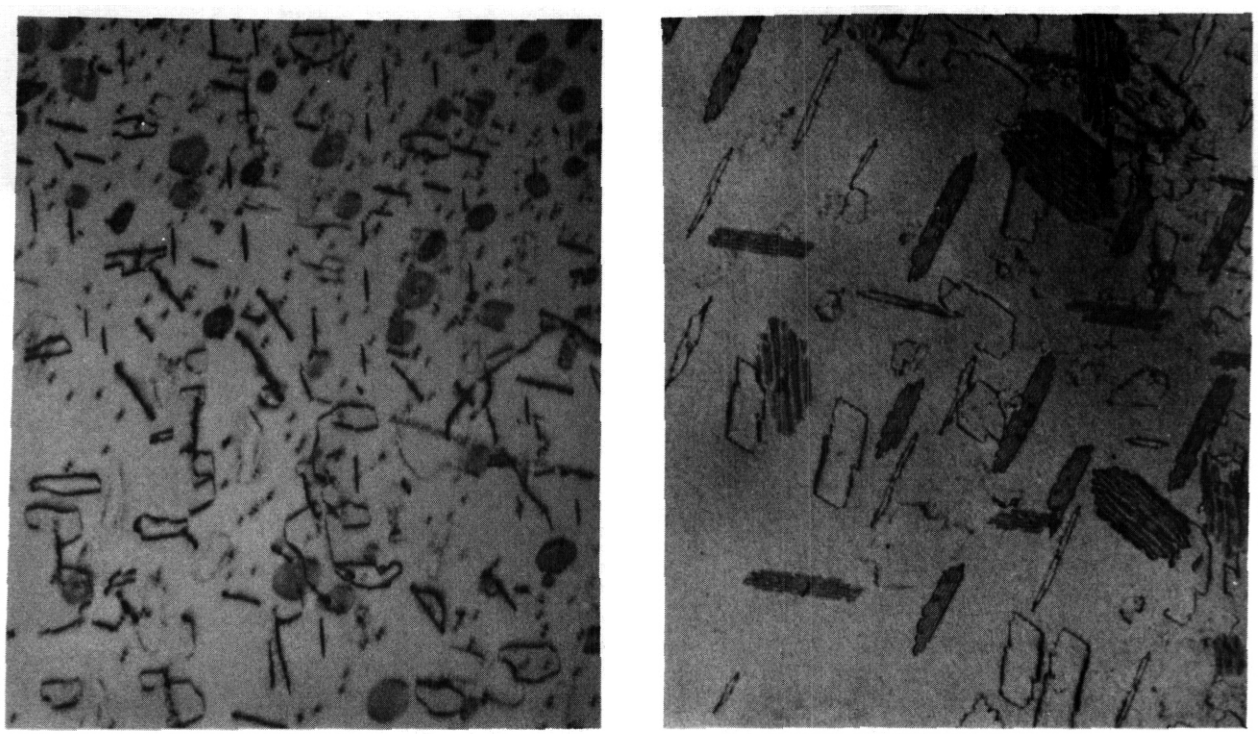

Fig. 4. Loop microstructure developed in two nuninally similar electron irradiatlon experiments conducted on annealed 316 stainless steel. Irradiation conditions are the same as that of Figure 3, except for the time at which the foils were held at temperature prior to irradiation.

Other experiments have observed irregular loop growth in austenitic steels irradiated with electrons[42-43] and ions.[44] In the latter study, it was shown that the degree of irregularity was affected by the displacement rate increases associated with pulsed irradiation. Several of these studies attributed the irregularity to arise from loop intersection with precipitates.[42,44]

Estimation of relative growth rates for r

According to Laidler and coworkers,[35] the prismatic loops shown in Figure 3b lie on {112} planes with Burgers vector b = 1/2 <110>, and the faulted interstitial loops lie on {111} planes with b = 1/3 <111>. Another loop orientation that will be considered is that of diamond-shaped loops with the 1/2 <011> Burgers vector lying on {012} planes. These latter loops have been observed in many fcc metals Including stainless steel.[45]

An earlier discussion[35] stated that a Frank loop should grow slower than a diamond loop. since the former required the creation of a faulted region. This expectation is incorrect however. The stacking fault energy is electronic in nature and arises from the disruption of the periodicity of the electron potential. Although the stacking fault energy contributes to the activation barrier for nucleation. all first-nearest-neighbor atomic relationships are preserved and therefore there are no elastic distortions associated with the stacking fault. The bias for growth arises from the elastic interaction of point defects with the strain field of the dislocation. which in turn is related to the magnitude and orientation of the Burgers and normal vectors of the loop.

Although the stacking fault energy does not contribute to the bias of the dislocation loop line. it affects the local equilibrium concentration of vacancies in the vicinity of the loop. and thus the vacancy emission rate from the loop. This is because an increase in the loop area increases the stacking fault energy. This term becomes important only at high temperature or low irradiation damage rate.

Wolfer and Ashkin[40] showed that the interstitial capture efficiency of infinitesimal loops is given by

$$Z = 1 + A_1 (\bar{n} \cdot \bar{b})^2 + A_2 [b^2 + 1/3(\bar{n} \cdot \bar{b})^2] \qquad [1]$$

where $\bar{n}$ is the loop normal vector. and A_1 and A_2 are coefficients that depend on the loop radius, temperature, and point defect parameters such as relaxation volume and elastic polarizability.[40]

Since the A_1 and A_2 parameters are independent of loop identity, the relative growth rates of infinitesimal loops can be determined by computing the terms containing $\bar{b}$ and $\bar{n}$. Note that the second term in Equation [1] is the largest contributor to the bias factor.[40] The vector terms and growth rate for each loop are shown in Table 1. The calculation of relative growth rate assumed the vacancy capture efficiency to be 1.0.

TABLE 1
CALCULATION OF LOOP BIAS FACTORS

	Frank Loop	Diamond on {012}	Diamond on {112}
$\bar{b}$	$\frac{a}{3}$ [111]	$\frac{a}{2}$ C011	$\frac{a}{2}$ C011
$\bar{n}$	$\frac{1}{\sqrt{3}}$ C111	$\frac{1}{\sqrt{5}}$ [012]	$\frac{1}{\sqrt{6}}$ [112]
b^2	$\frac{a^2}{3}$	$\frac{a^2}{2}$	$\frac{a^2}{2}$
$(\bar{n}\cdot\bar{b})^2$	$\frac{a^2}{3}$	$\frac{9\,a^2}{20}$	$\frac{3\,a^2}{8}$
$b^2 + 1/3(\bar{n}\cdot\bar{b})^2$	$\frac{4\,a^2}{9}$	$\frac{13\,a^2}{20}$	$\frac{5\,a^2}{8}$
Relative growth rate based on second term	0.68	1.00	0.96

Therefore, for very small sizes the diamond loop (on either plane) should grow faster than the faulted loop. There are several problems with this analysis. however. The treatment used in the development of Equation [1] is applicable to very small loops only and involves a spatial integration of point defect fluxes around the loop, which at large distances appears to be a point sink. Equation [1] breaks down when the loop radius is larger than approximately 100 A.[40] The relative relationship of loop growth rates should be preserved at larger sizes. however. It was also implicitly assumed that the loops have circular boundaries. an assumption that is obviously inconsistent with the experimental observations. As shown below. the A_1 and A_2 coefficients are written in terms of absorption per loop area although the absorption of point defects occurs along the loop perimeter.

$$A_1 = -\frac{1}{21}\left(\frac{1+\nu}{1-\nu}\right)^2 \frac{aG}{1024\,kT}\frac{1}{R^2}, \qquad [2]$$

$$A_2 = \left(\frac{3}{32(1-\nu)}\right)^2 \left\{\frac{3}{7}\left[\frac{2}{7}(1-2\nu)\frac{wK}{kT}\right]^2 + \frac{73}{1155}(1-2\nu)^2\frac{ak}{kT} - 0.004606\frac{aG}{kT}\right\}\frac{1}{R^2}, \qquad [3]$$

where R is the loop radius. ν is Poisson's ratio, α^G and α^k are elastic polarizabilities. K is the bulk modulus, w is the misfit volume. k is the Boltzmann constant and T is the absolute temperature.

If the line length per unit area for the faulted loop is substantially greater than that of the prismatic loops. a 68% relative bias per unit area could easily lead to a larger growth rate for the faulted loop. The experimentally determined growth rate for faulted loops is roughly twice that of prismatic loops as shown in Figure 3a. If the relative growth rates shown in Table 1 were applicable at all loop sizes, this would require a ratio of approximately 29 in the line length per unit area for the two types of loops. This is in reasonable agreement with the irradiation series shown in Figure 3b.

It Is important to question whether the phenomenon discussed above for electron irradiation at high displacement rates is relevant to reactor irradiations conducted at lower displacement rates. It is traditional to invoke "temperature shifts" when comparing irradiations at different displacement rates[32] and thus one would expect rate-related irregularities in loop shape to persist until higher temperatures in charged particle irradiations. In general the loops observed in neutron-irradiated material are more regular in appearance for temperatures on the order of 450 to 550°C.[46] As shown in Figure 5, however, irregular loops have been observed at relatively low neutron exposures and relatively low temperatures.[36,47] Kawanishi and Ishino showed that loops in neutron-irradiated Fe-16Ni-15Cr were very regular in the absence of other solutes. but became very irregular when carbide forming elements were added.[47] It appears therefore that the irregular growth habit of faulted loops is a phenomenon relevant to both the neutron and electron environments in the low temperature portion of the swelling regime. The swelling phenomenon is known to be dependent on the displacement rate. however. and it appears that the crenulated loop phenomenon may be similarly sensitive. A model is required which allows crenulated Frank loop growth to occur provided the displacement rate is sufficiently high. the temperature is sufficiently low an4 only for certain combinations of obstacle size and density.

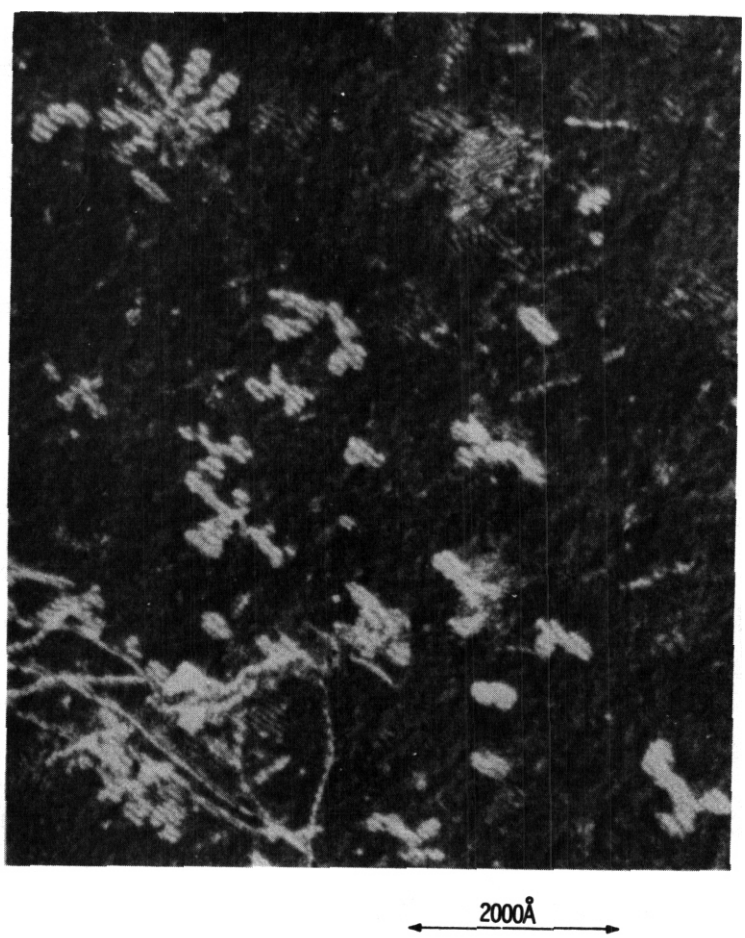

Fig. 5. Dark Field Micrograph Showing Irregular Shaped Frank Interstitial Loops observed in 304 stainless steel irradiated at 370°C to 2 dpa.[36]

Growth of irregular loops

Consider a curved segment or "finger" of a Frank interstitial loop existing at constant tenperature. The further growth of the segment is opposed by thermodynamic driving forces which tend to reduce the dislocation line length. These forces increase with increasing temperature and induce a net flow of vacancies between line segments of different vacancy chemical potential.

At the tip of a finger, the equilibrium vacancy concentration is given by

$$C_v(\text{tip}) = C_v^{eq} \exp[-\frac{\lambda\Omega}{kT}], \qquad [4]$$

providing we ignore the contribution of the stacking fault energy since it is small compared to that of the line tension.

The line tension[48] λ is

$$\lambda = \frac{Gb}{4\pi(1-\nu)r}(\ln\frac{r}{b} - 0.59), \qquad [5]$$

where r is the radius of curvature. G is the shear modulus, ν is Poisson's ratio. k is the Boltzmann constant. T is the temperature and Ω the atomic volume. (A core radius has been selected equal to the Burgers vector b.) C_v(tip) is seen to be lower than the bulk equilibrium vacancy concentration C_v^{eq}. Along the concave portions, i.e., at the nodes. the vacancy concentration would be

$$C_v(\text{node}) = C_v^{eq} \exp[+\frac{\lambda\Omega}{kT}], \qquad 161$$

providing that no obstacles were there. The presence of an obstacle will modify C_v(node), but the nature of the modification is unknown.

The vacancy concentration at the straight section, C_v(straight), also differs from C_v^{eq} due to the interaction with the adjacent straight section. The two straight sections form a dipole. and if their separation distance h is small compared to the dimension of the loop. then

$$C_v(\text{straight}) = C_v^{eq} \exp[F/kT], \qquad [7]$$

where the climb force is given by

$$F = \frac{Gb\Omega}{4\pi(1-\nu)h}. \qquad [8]$$

Note that C_v(straight) > C_v^{eq} > C_v(tip)... so that the difference $\Delta C_v = C_v(\text{straight}) - C_v(\text{tip})$ will cause a net flow of vacancies from the straight sections to the tips of the fingers. If this occurs. the obstacle will be occluded in the process.

The flow of vacancies takes place probably by pipe diffusion with a migration coefficient D_v^{pipe} so that the vacancy current j_v from node to tip is given by

$$j_v^{pipe} = \frac{b^2}{L} D_v^{pipe} \Delta C_v, \qquad [9]$$

where L is the length of the finger.

The radiation-induced current j of atoms (interstitials minus vacancies) to the tip is

$$j \simeq 2\pi r \left[Z_i(r)\, D_i C_i - Z_v(r)\, D_v C_v\right]. \qquad [10]$$

where Z_i and Z_v are the interstitial and vacancy capture efficiencies and D_i and D_v are the diffusion coefficients. The growth rate of the finger's length can be approximated by

$$\frac{dL}{dt} = \frac{b^2}{2r}\,(j - j_v^{pipe}). \qquad [11]$$

The curvature at the tip depends on the finger length L and the average separation distance ℓ of obstacles. If a simple sinusoidal model is used for the crenulated shape of the loop one finds that

$$r \simeq \frac{2}{L}\left(\frac{\ell}{2\pi}\right)^2. \qquad [12]$$

Using equations [9], [11] and [12], one obtains

$$\frac{dL}{dt} = \pi b^2\left[Z_i D_i C_i - Z_v D_v C_v - 2\,\frac{b^2}{\ell^2}\, D_v^{pipe}\, \Delta C_v\right]. \qquad [13]$$

The evaluation of equation [13] for $\frac{dL}{dt} > 0$ yields the conditions under which finger growth will proceed for a given obstacle separation distance. Crenulated growth thus occurs when

$$Z_i D_i C_i - Z_v D_v C_v > 2\pi\,\frac{b^2}{\ell^2}\, D_v^{pipe}\, \Delta C_v. \qquad [14]$$

Note that small obstacle spacings and high temperatures (expressed through the temperature dependencies of D_v^{pipe} and ΔC_v) tend to increase the right hand side of the inequality in equation [14]. This provides the explanation of the high temperature cut-off of finger growth at any given displacement rate. Above the cut-off temperature the loop will not propagate a finger at that obstacle density and displacement rate. The loop will grow in another direction until it is completely constrained by obstacles and ceases to grow. In practice this seldom happens because the obstacle's diameter must be smaller than the separation distance between obstacles. At some high density the precipitate would become small enough and cease to function as an obstacle or even as an identifiable second phase.

The displacement rate-related temperature shift observed in the cut-off of crenulation during isothermal irradiations at higher temperatures arises not only from the known temperature shift of loop nucleation with increasing displacement rate but also from the increase in the left hand side of inequality [14] with increasing displacement rate.

In the foregoing discussion the possible dependence of precipitate density and mean size on temperature and displacement rate was ignored. Precipitates usually increase in size and decrease in density with increasing temperature. The possible details of this dependence are different for each alloy and add additional complexity to the description of the cut-off phenanenon.

Note that the foregoing analysis does not apply to prismatic loops. however. which respond to obstacles in a quite different manner.

Experimental test of some features of the model

The dependence of crenulated loop growth on displacement rate cannot be easily determined without simultaneously changing the effective temperature due to the temperature shift phenomenon involved in loop nucleation. However. if loops are nucleated and grown to reasonable sizes at one temperature. and the temperature raised thereafter. the effect of temperature on crenulations developed at the lower temperature can be studied. Therefore. two exploratory irradiation experiments were conducted to observe Frank interstitial loop behavior before and after a temperature change. Both irradiations were conducted on a single specinen of 20%cold worked AISI 316 stainless steel which had been annealed for one hour at

1200°C prior to irradiation. The central displacement rate was ~1.0 dpa/hr and the beam-induced temperature rise in the irradiated area was calculated to be small (≤5°C).[49] The measurement of projected loop areas and perimeters was performed using a Quantimet 720 Image Analyzing Computer.

In the first irradiation one area of the specimen was irradiated for a total of ten minutes at 500°C, and micrographs were taken intermittently. After cooling the specimen to 150°C a stereo pair was taken of the bombarded region. The temperature was then raised to 600°C and the specimen was irradiated for a total of six minutes. At 500°C the Frank loops developed the irregular shapes commonly observed at this temperature and displacement rate as shown in Figure 6(a,b). These irregular shapes were observed at relatively small loop sizes (~30 nm in diameter) after four minutes of irradiation. Larger loops viewed edgewise appeared to be associated with many small (≤10 nm) diffraction contrast features thought to arise from the presence of small precipitates. The irregularities of Frank loops were initially retained upon unfaulting and subsequent formation of prismatic loops, but these new loops developed segment lengths within several minutes which were straight rather than curved.

When the irradiation was resumed with the temperature raised to 600°C the Frank loops quickly lost their irregular perimeters as shown in Figure 6(c,d). Within two minutes (≤0.03 dpa) all loops evolved into more compact shapes with sides composed of relatively straight line segments. Many developed the hexagonal shape characteristic of interstitial loops in fcc metals.

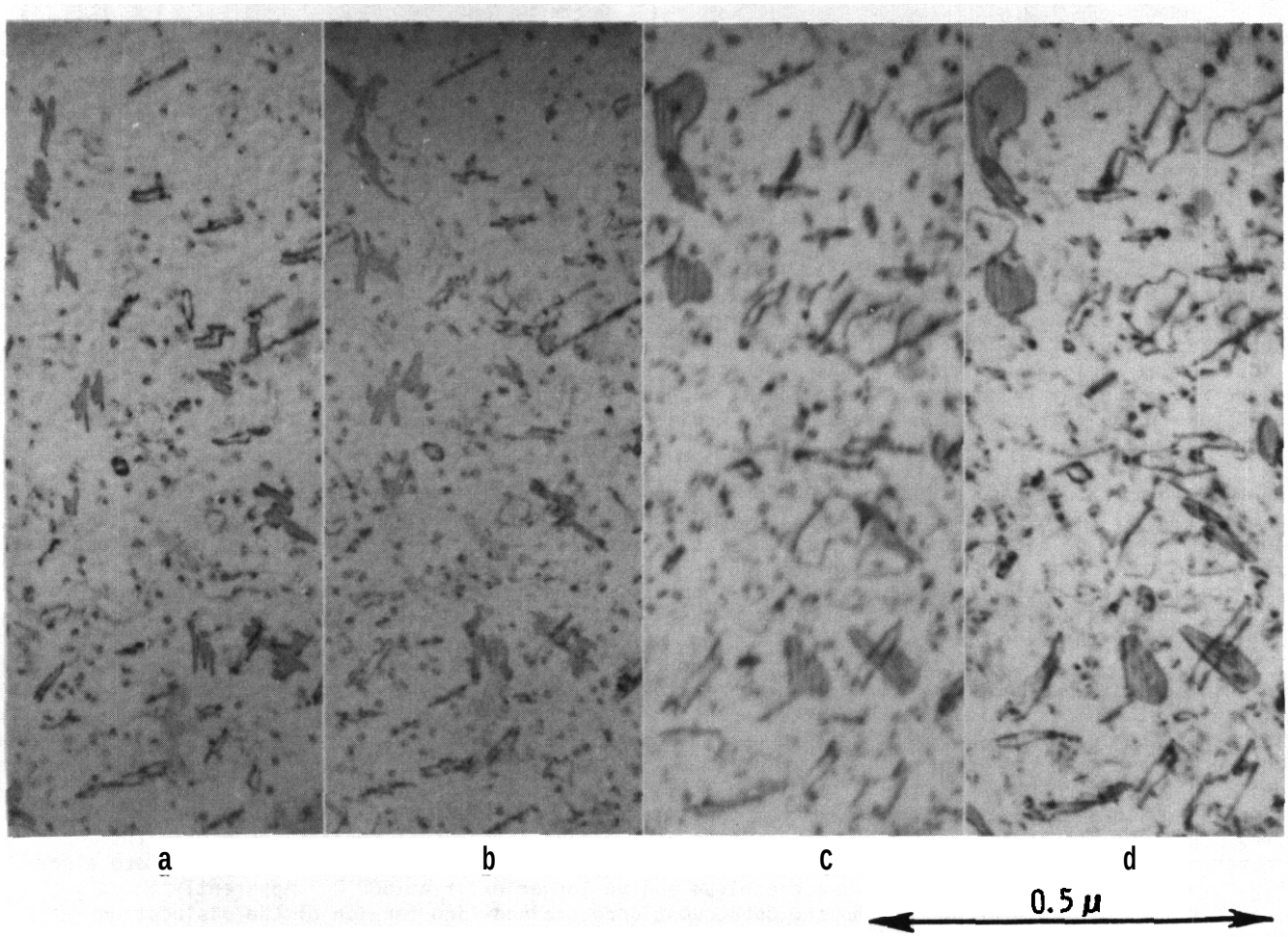

Fig. 6. Change in Frank interstitial loop growth behavior in 316 stainless steel during electron irradiation at 500°C (a,b) followed by further irradiation at 600°C (c,d).

In the second experiment. irradiation proceeded at 500°C on a new area for 15 minutes prior to the first observation. The central region of the irradiated area contained highly crenulated Frank loops which grew to span the entire foil thickness. At an elapsed time of 25 minutes the temperature was increased to 600°C and the irradiation was resumed. Unfortunately, all loops in the central area unfaulted quickly (≤ one minute). The irradiation was continued. however. in the hope that the desired Information could be obtained from loops on the periphery of the irradiated area. This effort was

rewarded in that a number of loops survived and one such loop was favorably oriented for photography. It was found to be visible in all micrographs taken in the interval of 15 to 35 minutes. Figure 7 illustrates the general behavior of this loop. The loop is inclined ~35° to the foil plane and lies near the upper surface of the foil.

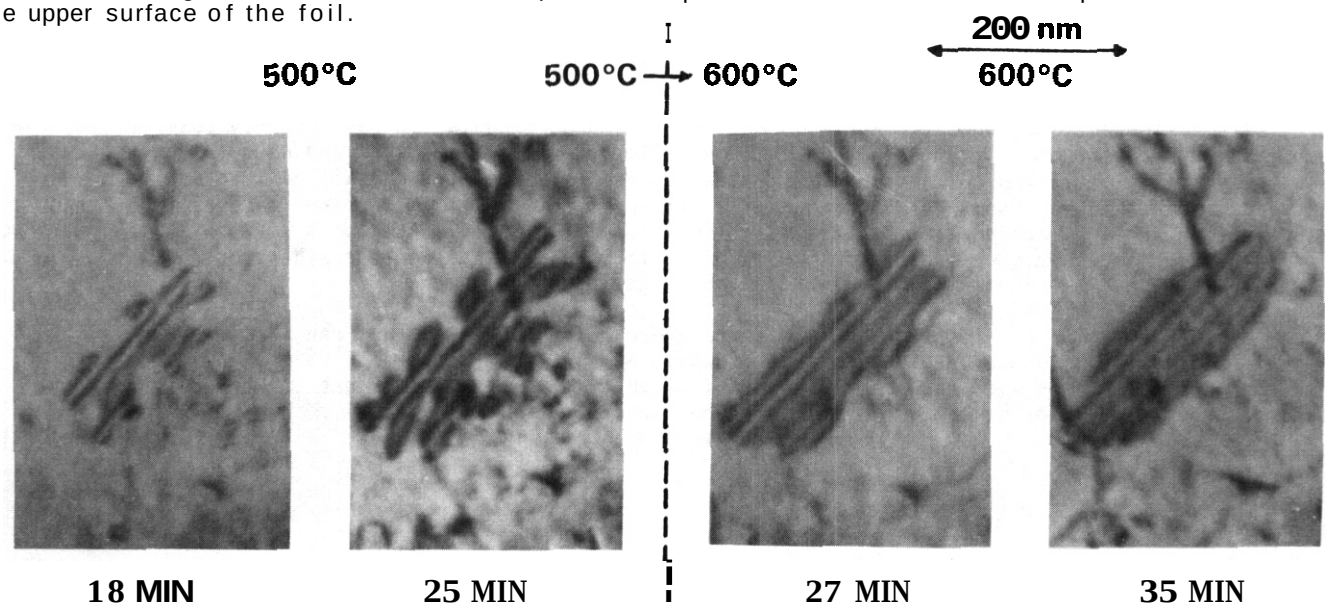

Fig. 7. Influence of a temperature increase on the growth behavior of Frank interstitial loops in 316 stainless steel. At 600°C, the precipitates at the base of the nodes dissolve. The loop decreases its perimeter at constant loop area and exhibits a lower growth rate thereafter.

When first observed the loop had already begun to develop a crenulated boundary. which became increasingly irregular thereafter. After the temperature was increased. the loop quickly developed a more compact shape. As shown in Figure 8a, this transformation occurred largely due to the retraction of the extended fingers into the body of the loop. It is important to note that the more compact loop does not include any occluded obstacles. This suggests that the obstacles have dissolved. The history of the loop perimeter was fairly complex. The perimeter appeared to grow linearly with time for the first 18 minutes. providing that the loop was assumed to nucleate at the beginning of the experiment. The growth rate of the perimeter increased to a new rate after 18 minutes.

When the temperature was increased to 600°C the loop suffered a 42% reduction in perimeter within the next two minutes. followed by a more gradual decline over the next 6-1/2 minutes. The perimeter was just beginnlng to increase again when the experiment was terminated. Contrary to expectations the shrinkage of perimeter was accomplished without unfaulting or loss of loop area. At 500°C the loop grew in area at a rate proportional to time squared. While the loop was shrinking in perimeter at 600°C it grew in area at a slower rate as shown in Figure 8b, reflecting its smaller perimeter and perhaps sane influence of the higher temperature.

In this second experiment the micrographs were also examined for evidence of the presence of precipitates at 500°C and their subsequent dissolution at 600°C. Although the precipitates are not visible when the loop is in full contrast there are sane contrast features suggestive of precipitates which are visible when the loop is viewed on edge. Figure 9a demonstrates that when another loop is imaged almost out of contrast. small precipitates can be seen at the base of the lobes. Stereographic examination of these precipitates confirm that they lie across the plane of the loop. When viewed in stereo. the loops appear to enclose the precipitate at a radius larger than that of the precipitate, indicating that the sphere of influence is larger than the physical size of the precipitate. Note also in Figure 9b that these precipitates have dissolved and no longer exist at 600°C. Apparently these precipitates are unstable at 600°C, and the subsequent unrestrained line tension of the dislocation provides a driving force for reduction In loop perimeter.

The studies presented in this section confirm the contention that electron-produced dislocation microstructures can be used to describe the dynamic behavior expected in neutron irradiatlon studies. but also reinforce the necessity of factoring displacement rate effects into the analysis.

Electron irradiation in the presence of applied stress

It is possible to apply loads to thin areas of metal specimens during irradlation with electrons, but it is difficult to determine the actual stress level in the area under observation. Buckley and Manthorpe[50] irradlated Al-Si alloys in a hlgh voltage electron microscope and were able to calculate the

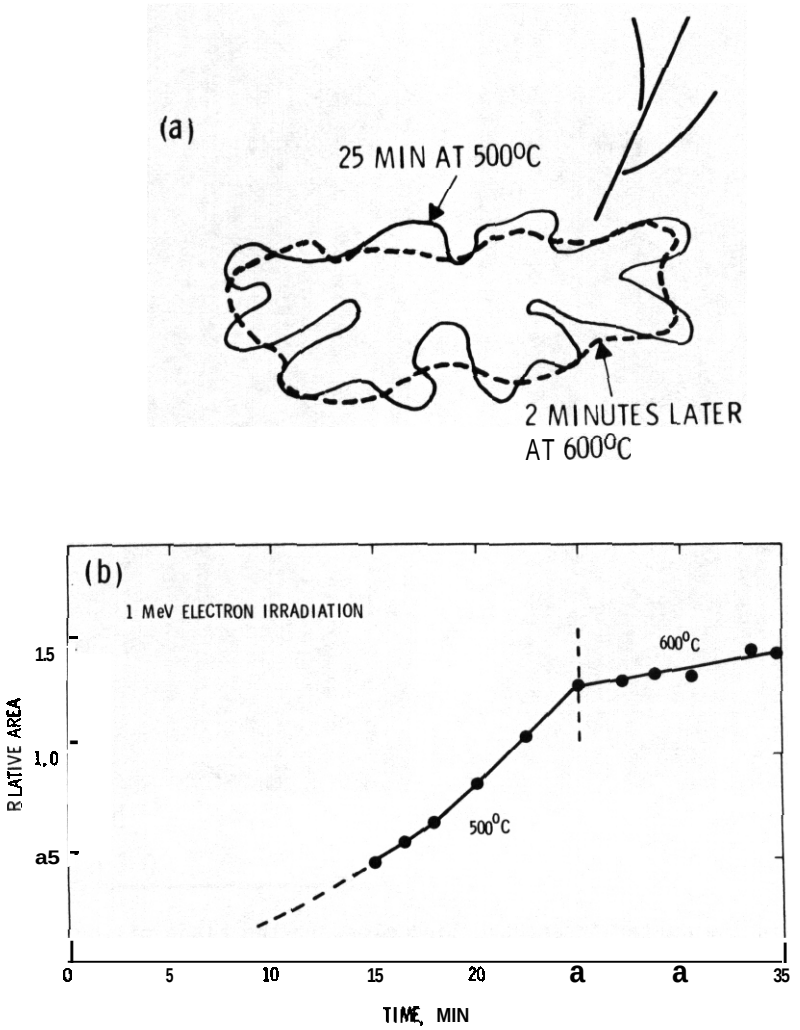

Fig. 8. (a) Superimposed outlines of loop perimeter, showing that nettransport of vacancies from loop nodes to loop fingertips causes a retraction of the fingers into the body of the loop. (b) Reduction in growth rate coincident with the reduced perimeter.

local stress on network dislocations by measuring the bowing of dislocation segments. The dislocations were found not to dwell in a unique and invariant stress field. but were observed to be subjected to elastic strain field perturbations emanating from the continually altering spatial distribution of neighboring dislocations. The local stress on individual dislocations often changed sign and sanetimes changed in strength by orders of magnltude. Theoretical models of creep do not in general include the possibility of strongly varying local stresses.

In most studies, however. the magnitude of the mechanically applied stresses in thln foils were not specifled[51-53] or were estimated (for suitable specimen geometries) by dividing the applied load by the measured cross sectional area.[54-58] Stresses may also be induced by other factors such as oxide formation[59] or surface image forces.[51]

In all cases where stress was applied to a wide variety of fcc metals during electron irradiation. the total number of loops was observed to increase, with those loops whose plane normal vector made the smallest angle with the stress direction, having the highest planar density. For those studies where the loop size was reported. it was obvious that the Increase In loop density was realized by a reduction in average loop *sire.* Several authors[51-54] also reported that the rate of loop disappearance by unfaulting events correlated with the resolved normal stress as well, such that loops favorably oriented for nucleation were also destroyed at accelerated rates. Jitsukawa[57] however. related the probability of Frank loop unfaulting In irradiated pure nickel to the resolved shear stress along <112> directions. which served to initiate the reaction producing a perfect dislocation loop.

$$\bar{a}/3\ (111) + \bar{a}/6\ [121] + \bar{a}/6\ [112] = \bar{a}/2\ [011]$$

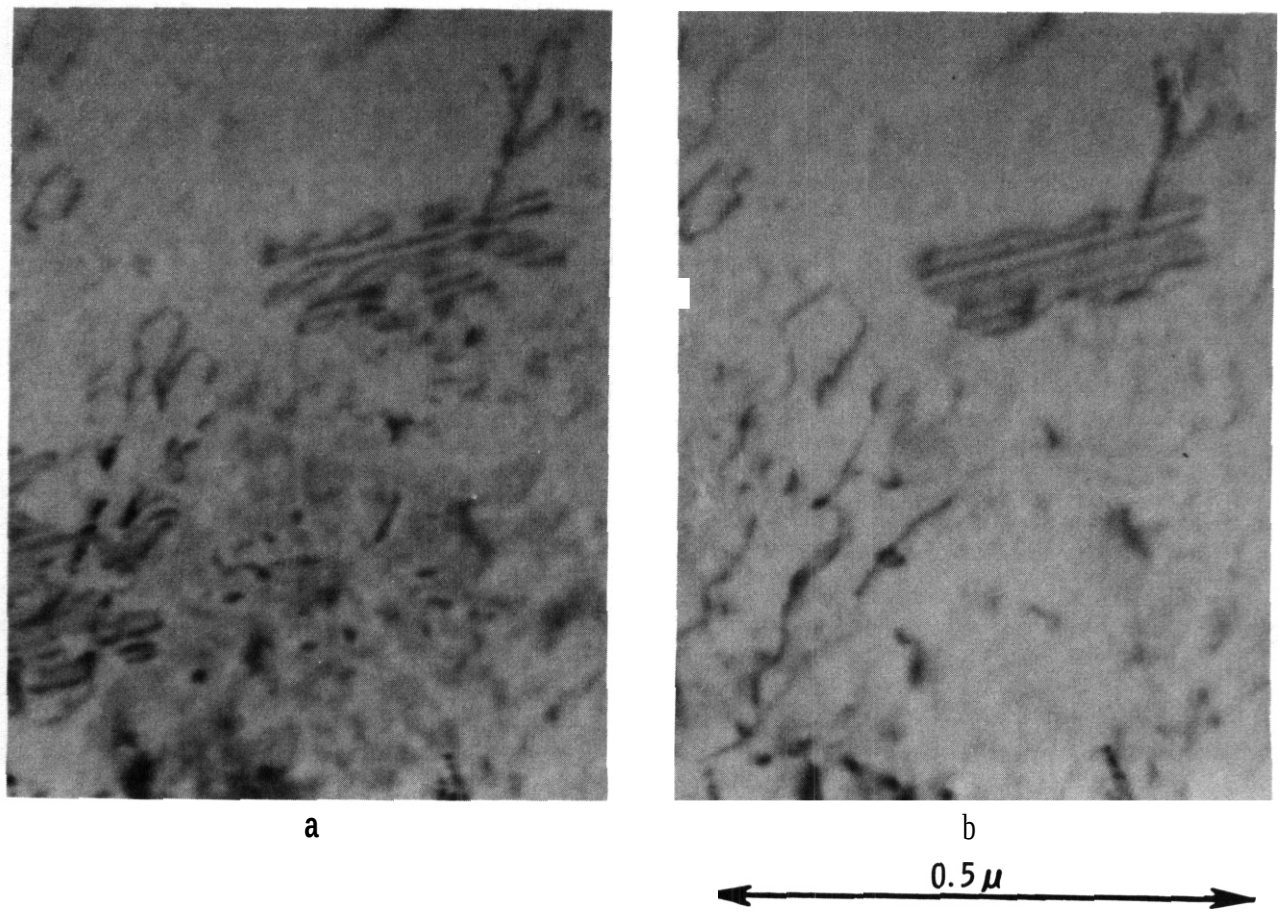

Fig. 9. (a) The large loop in the center foreground lies close to the plane of the micrograph and is almost out of contrast. Small precipitates are visible at the base of each note. (b) At 600°C the precipitates have dissolved and the loop has unfaulted.

Another feature of Jitsukawa's work was the observation that the growth rate of unfaulted perfect loops was larger than that of Frank loops. This observation is not inconsistent with the results of the previous section. In pure nickel precipitation does not occur and Frank loops do not develop the crenulated shape that produced the faster growth seen in 316 stainless steel.[35,36] More recent research by S. Jitsukawa. Y. Katano and K. Shiraishi is now available for quotation in advance of publication and shows that the average growth rate of loops is indeed enhanced by increases in the resolved normal stress on the loop plane. as shown in Figure 10.

It is not yet clear whether the perfect dislocation loops form only by unfaultlng of Frank loops. If this is indeed so, much unfaulting has to occur at very small and unresolvable sizes in order to explain the mixed loop populations shown in Figure 3b. Hishinuma and co-workers[43] note that under some conditions, these loops appear not to be formed by unfaulting but by "direct agglomeration of interstitials". The authors of this paper are not aware of supporting evidence for this proposal. Unpublished data by Jitsukawa. Katano and Shiraishi suggest that diamond-shaped perfect loops originate from Frank loops, rotatlng when they are small in size. All of the studies cited above agree that the rate of unfaulting is tied to the buildup of network dislocation density. however.

The results of both stressed and unstressed studies confirm the contention that loops are nucleated continuously during irradiation. although the rate of nucleation decreases as the overall microstructural density increases. The lifetime of an individual loop also decreases as the probability for interaction increases.

Irradiation With Other Charged Particles

Indirect evidence of stress-induced anisotropic loop distribution has been found using fission fragment irradiation of molybdenum single crystal wafers[60-62] and also using single crystal whiskers of copper[63] and tungsten.[64] Additional indirect evidence has also been presented for helium-bombarded nickel foils.[65]

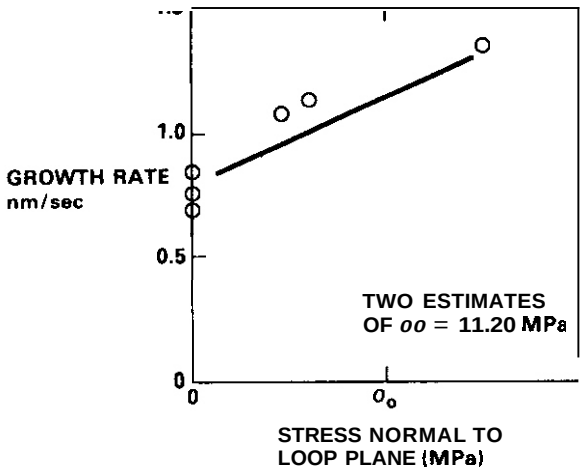

Fig. 10. Measurements of growth rate of Frank faulted interstitial loops in electron-irradiated nickel as a function of resolved normal stress on the loop plane. The lower estimate of σ_0 was derived from the specimen geometry and the applied load while the higher estimate utilized a relationship between applied stress and line tension of a perfect loop. (Data supplied in advance of publication by S. Jitsukawa, Y. Katano and K. Shiraishi).

The most convincing direct evidence using charged particles other than electrons was provided by Atkins and McElroy[66]. They used 3.5 MeV protons to irradiate relatively thick (~25 m) foils of Ni-2.5%Si at 623K in both the stress-free and stressed (50 MPa tensile) condition. Thus the effect of surfaces was minimized and the stress state was well characterized. Two grains in the unstressed specimen were analyzed and contained dislocation loops of which 98% or more were of Frank interstitial type. The remainder were small <110> unfaulted loops. It was found that in the absence of applied stress the planar loop diameters and densities were independent of orientation. It was realized. however. that beam-induced temperature variations over the gage length of the specimen precluded a direct comparison of the stressed and unstressed specimens. since it could not be guaranteed that they were at the same temperature.

The effect of applied stress on loop sire and planar density was therefore assessed by comparing the data from seven adjacent. randomly oriented grains. one of which had almost equal resolved normal stresses on each of the four closed-packed planes. While this grain had essentially identical loop densities and sizes on all four planes. there was a good correlation between loop density and resolved normal shear stress in the other seven grains. The applied stress had influenced the partitioning of loops but did not influence the total loop density or loop size. Relatively large <110> unfaulted loops were found at 5-10% of the density exhibited by Frank loops and sane small voids were also observed. The accumulated strain was four times larger than that attributed to the Franks loops. indicating a substantial contribution to the total strain from the unfaulted loops. There may also have been sane influence of silicon segregation on loops during irradiation but this possibility was not addressed by Atkins and McElroy.

It is important to note that the total loop density and area were insensitive to orientation. indicating that the conservation of interstitials was also unaffected. We cannot, however. draw the conclusion that the total number of loops had increased with stress at the expense of the loop size, since we cannot make a comparison between the stressed and unstressed specimens. A trade-off of this sort was observed in the electron irradiations discussed in the previous section.

Another ion experiment provided the insight that glide processes could daninate the strain observed during irradiation of relatively soft metals. but the rate of strain was controlled by climb over irradiation-induced clusters and loops. Michel, Hendrick and Pieper[67] irradiated cold-worked nickel with 22 MeV deuterons at 224°C and were able to relate the observed transient creep rates to the time-dependent densities of defect clusters, loops and network dislocations.

Neutron Irradiation Experiments

In bulk materials irradiated in fast reactors. it is relatively easy to design creep microstructure experiments in which there are essentially no effects of surface or chemical environment and no measurable gradients in temperature, displacement rate or stress within the volume to be observed by microscopy. The data presented in this section were derived from pressurized tube irradiations in which a biaxial stress state existed (hoop stress = 2 x axial stress). Most of these experiments involve more

complex engineering-relevant microstructures than are used in typical charged particle irradiation studies. It is also not possible to gather continuous data; each specimen represents only a snapshot of the irradiation response. with little information on the previous history of the evolution. On the other hand, it is possible in such experiments to reach the higher displacement levels relevant to engineering concerns.

Okamoto and Harkness[68] performed the first experiment of this type using a creep tube constructed from annealed 316 stainless steel with a relatively high hoop stress of 30 Ksi (206 MPa). At 2.4 X 10^{21} n cm^{-2} (E>0.1MeV) or 1.2 dpa at 380°C they found variations in planer density that varied as much as 30% from the average density. Unfortunately. a stress-free specimen was not available for comparison and it was not possible to relate the planar loop distributions in the stressed specimen to details of the stress state. In agreement with the results of Atkins and McElroy[66] the loops on each close-packed plane exhibited similar size distributions. The loops had not yet experienced significant interactions. Voids were observed in the examined volume but the swelling was not calculated.

Brager. Garner and their coworkers[69-72] conducted a similar series of studies on annealed 316 stainless steel Irradiated to -10 dpa at 500°C in a fast reactor, but they preserved a record of the relation between the stress state and the microstructure. In the first subset of these experiments they examined a stress-free tube irradiated to 10 dpa with another irradiated at 66 MPa. The latter stress level is rather small and is thought to be barely sufficient to overcome the early internal stresses generated by carbide formation.[6] Significant levels of loop interaction had occurred in both specimens toward the end of the irradiation. as evidenced by the presence of a network dislocation density of -0.7 X 10^{10} cm^{-2} and a related reduction of loop density on one plane in each specimen. The mean loop size increased at the higher stress level. indicating an accelerated rate of loop growth. The total loop density of the two specimens was comparable but there was a tendency toward increased loop density on planes with higher resolved normal stress levels. It was also proposed that the maximum loop size was dictated by the probability of loop interaction with other loops and free dislocations.

Brager and Garner also irradiated to 13.5 dpa two other annealed specimens at hoop stress levels of 130 and 163 MPa. These exhibited a clear increase in total loop density with applied stress as well as a correlation between planar loop densities and resolved normal stress (See Figure 11). The network dislocation density was several times larger than those observed at 0 and 66 MPa and there were indications of an increased level of loop and dislocation interaction. The loop size distribution in these higher stress specimens also appeared to be dictated by the probability of loop intersection with other dislocation components.

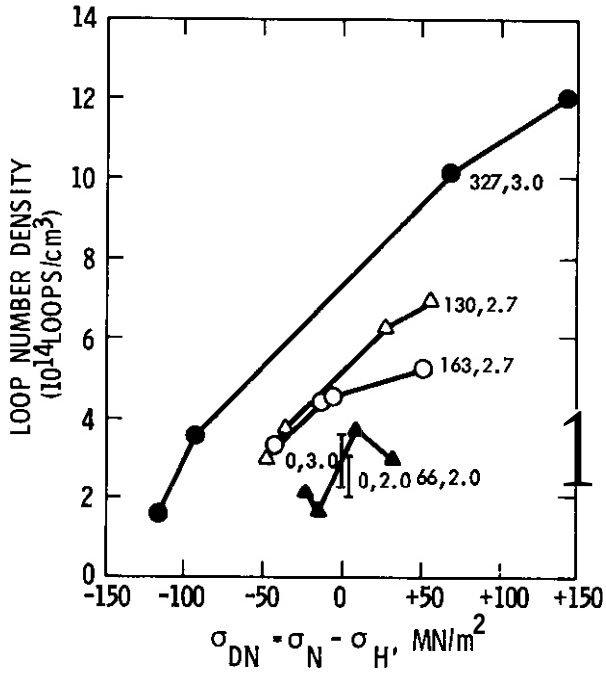

Fig. 11. The dependence of planar loop densities observed in 316 stainless steel irradiated in a fast reactor at 500°C.[70] The stresses (MPa) and neutron fluences (10^{22} n cm^{-2} (E>0.1 MeV)) are shown for each specimen. The data at 3.0 X 10^{22} n cm^{-2} are for 20% cold-worked tubes; all other data are for annealed tubes. The parameter σ_{DN} is defined as the resolved normal stress σ_N on the loop plane minus the hydrostatic stress σ_H. For this specimen geanetry σ_H is one-half of the hoop stress.

In the same irradiation series. Brager and Garner also examined 20% cold-worked 316 irradiated to ~15 dpa at 0 and 321 MPa, the latter stress level comparable to that employed by Okamoto and Harkness. (See Figure 11 for a compilation of data from both annealed and cold-worked specimens.) In this case interaction of Frank Loops with pre-existing dislocations was guaranteed at all stages of the evolution. The mean loop size did not change significantly with stress but the total number density increased, implying that stress increased the number of interstitials available for formation of loops. This is not a violation of the law of conservation of mass but is a reflection of the fact that interstitials were "borrowed" from the less competitive (lower bias) network dislocations. The amount of borrowed interstitials lost by the network is not reflected in the micrograph used to analyze the microstructure, since a micrograph tells us only where a dislocation resides at the moment the "snapshot" is taken. It does not tell us from where a given dislocation has migrated or the strain produced as a result of the migration.

If the borrowing or competition proposal has any merit. we should expect ths amount of borrowing to increase with both stress and the network dislocation density. As shown in Figure 12, the favored growth of dislocation loops over climb of network dislocations indeed increases as predicted.

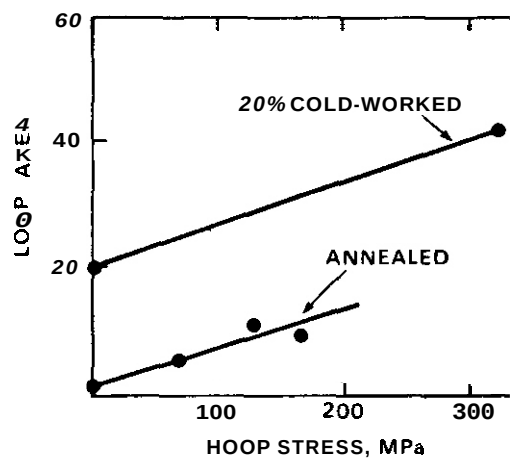

Fig. 12. Total loop area observed in several stainless steel specimens irradiated at 500°C in fast reactor to 10-15 dpa.

At this high stress level the applied stress dominated over the internal stresses and there was a clear correlation between planar loop densities and the resolved normal stress. The loops on the most densely populated plane were six times that of the lowest density plane. The size distribution was completely dictated by the probability of loop interaction with the dislocation and loop network. This latter conclusion implies that loops are forming throughout the irradiation; otherwise one would expect all loops to have been destroyed relatively early by interaction events. especially in cold-worked materials. Another related conclusion is that loops must grow rather quickly to sizes that are subject to a high probability of intsraction.

An important additional insight from this and other studies was that the saturation level of network dislocations at sufficiently high exposure was independent of the starting dislocation density and stress level.[72] This conclusion has since been expanded to specify that the saturation density is relatively independent of other variables such as irradiation temperature. displacement rate and helium level.[73-75] Models describing this process require the continuous nucleation of Frank loops.[74,75]

In a separate set of similar experiments. D. S. Gelles examined the microstructure of creep tubes constructed of Nimonic PE16 and Inconel 706 and irradiated at 0 and 176 MPa to 10 dpa at 550°C.[71,76-79] These are much more complex precipitation-strengthened alloys which are known to invclve radiation-induced segregation, causing formation of γ' phase on both dislocations and loops. These alloys are also known to slowly suffer relatively large precipitation-induced changes in density during irradiation unless they are sufficiently aged prior to insertion in reactor.

In the one case where such aging was not conducted. no correlation between Frank loop density and resolved normal stress was found, reflecting the presence of large internal stresses during the irradiation. In the other alloys. there was a clear correlation between planar densities and resclved normal stress. When stress was absent. there was no orientation dependence of these densities. With the exception of a few small areas in the process of extensive unfaulting, network dislocations existed at very low densities in these specimens.

Within the accuracy of the measurements, the total number of loops in areas without significant interaction increased with stress and the size decreased correspondingly. with the loop area remaining constant. The increase of loops on favored planes was realized at the expense of loops on unfavorably oriented planes. such that they were depressed in density below that of the stress-free specimen. This is different from the case of 316 stainless steel where all close-packed planes can increase in loop density by borrowing interstitials from network dislocations.

Gelles. Garner and Adams[79] introduced one particularly significant finding not realized in previous studies. They showed that the anisotropy induced in the Frank loop population by stress is not only propagated into the network dislocation density but is accentuated at each stage of the evolution. They demonstrated that the first and last of the three evolutionary stages were dominated by the SIPA mechanism of irradiation creep, one involving Frank loops and one involving network dislocations. In agreement with the electron studies of Caillard and coworkers[51-53], the second stage (unfaulting) was found not to be isotropically distributed between the three possible 1/2 <110> dislocation Burger vectors that can originate from a 113 [111] loop. Even more importantly. Gelles[77] showed that subsequent interactions between network dislocations and Frank loops must obey certain crystallographic constraints that are atypical of autocatalytic unfaulting. The consequences of these constraints on irradiation creep are quite significant. First. a given Frank loop can be unfaulted by only half of the possible perfect dislocations and any two dislocation vectors can unfault all loops. Second. the interaction proceeds in a manner that produces more line length of the impinging network dislocation as shown in Figures 13 and 14. Thus. the first loop that unfaults tends to produce a slowly evolving cascade of unfaulting events producing dislocations all of the same type. In effect. the applied stress produces a highly anisotropic dislocation microstructure uniquely suited to move mass in the direction consistent with relaxation of the applied stress. Gelles demonstrated that the resulting anisotropies in dislocation density of Nimonic PE16 could range from ~10 to ~40, when comparing the densities of the highest and lowest populated Burgers vectors.[76] Unpublished studies by Gelles of annealed 316 stainless steel irradiated at 650° to 40 dpa found variations in density on the order of 4 to 5.

This highly anisotropic network has another consequence. however. in that it is uniquely suited to unfault the very loops from which it is born. Thus, one would expect at very high exposure that the most favorably oriented loops would be destroyed at higher rates. balancing sanewhat their higher production rate. This situation would tend to suppress the microstructural record expressed in the loop population as it could be captured in a micrograph.[79]

$$\frac{a}{2}[\bar{1}\bar{1}0] + \frac{a}{3}[111] = \frac{a}{6}[\bar{1}\bar{1}2]$$

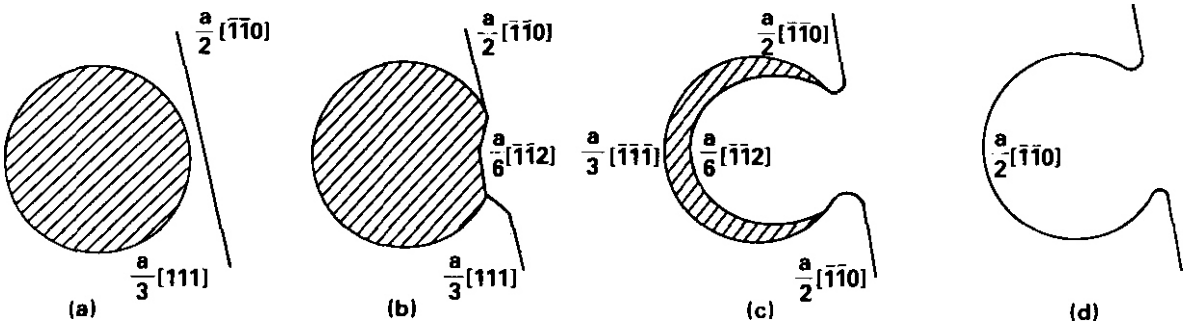

$$\frac{a}{6}[\bar{1}\bar{1}2] + \frac{a}{3}[\bar{1}\bar{1}\bar{1}] = \frac{a}{2}|\bar{1}\bar{1}0|$$

Fig. 13. The Frank loop unfaulting mechanism proposed by Gelles.[77]

Gelles. Garner and Brager demonstrated this possibility by examining the microstructure of stress-free and stressed (207 MPa) specimens of 20% cold-worked 316 stainless steel at 475°C and 46 dpa.[71] In another unpublished study. Gelles examined annealed 316 stainless steel irradiated to 40 dpa at 450°C in both the stress-free and 138 MPa hoop stress conditions. In both of these studies. it was found that the microstructural record of the stress state was visible but reduced in strength at this high fluence level. It was also concluded that loop nucleation continues at high fluence levels although the total loop density declines by a factor of two to three compared to that observed at lower exposures. Another complication in interpreting these two studies was that each involved significant levels of void swelling. The swelling was clearly enhanced by stress and was heterogeniously distributed. This suggests that the stress state included large contributions arising from incompatability strains.

Fig. 14. Micrograph showing three Frank interstitial loops designated by letters A, B, C in neutron-irradiated Nimonlc PE16 being unfaulted by perfect dislocations. Voids are also visible.

It is important to note that the creep processes involving loops are probably not suppressed at high fluence; only our ability to capture a record of the competing processes is impaired since micrographs do not indicate the speed of migration or the lifetime of individual dislocation components. We also cannot measure in a micrograph the time-dependent components of the stress state arising from internal sources.

Another particularly significant conclusion was advanced by Gelles,[76] who noted that the perfect dislocation network in Nimonic PE16 was pure edge in character. but lay on (001) planes. probably as a consequence of their γ' coating. Therefore. dislocation glide on (111) planes is negligible and SIPA creep must be the controlling creep mechanism.

One further consequence of network anisotropy would be the influence exerted on further irradiation-induced strain if the stress was to be removed. Figure 15 shows that 316 stainless creep tubes irradiated first under stress and then without stress tend to "coast" in the direction required by the anisotropy. The ensuing strain is not due to creep since the stress has been removed and is not due to swelling. since it was confirmed by density change measurements that swelling had not yet started. In effect. this is a form of radiation growth and will continue until a dislocation microstructure evolves that is compatible with the new stress state. Since the anisotropy of loops and dislocations is expected to increase monotonically with stress, it is not surprising that growth is also observed to increase with stress level.

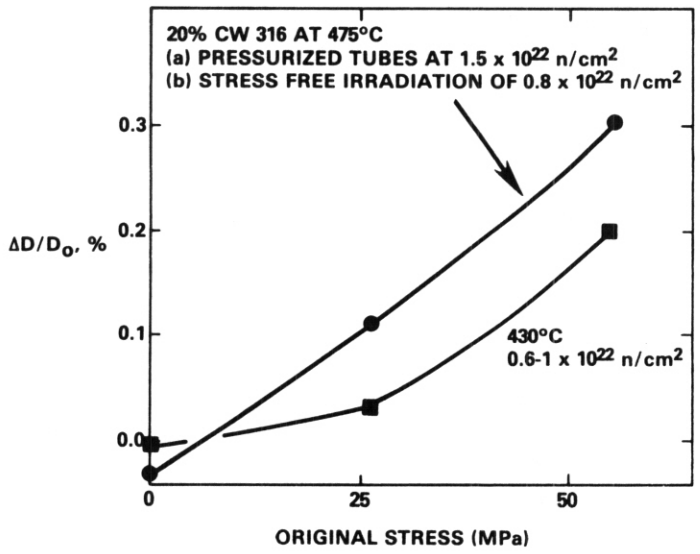

Fig. 15. Continued dimensional strain of two groups of 20% cold-worked 316 pressurized tubes after depressurization and reirradiation. Each group was first irradiated to a given fluence of either 0.6-1 or 1.5 x 10^{22} n cm^{-2} (E>0.1 MeV), then depressurized and reirradiated for another 0.8 x 10^{22} n cm^{-2}. The resultant radiation-induced growth was observed at both 430 and 475°C.

Discussion

There is no doubt at this point that stress indeed imprints records of its presence on the microstructure of irradiated metals. These records are sometimes transient in nature and cannot always be captured in micrographs. For instance, it is impossible to capture glide events in a micrograph or events in which rates of growth, intersection or migration are important. One must use dynamic observations for situations of this type.

If we put together the evidence from the various types of experimental studies it is possible to construct a rather detailed scenario describing the stress-affected and very dynamic microstructural evolution of irradiated metals and then use this scenario for theoretical modeling studies of irradiation creep. This evolution is considerably more complicated than envisioned in most theoretical studies, however. The complexity is largely associated with the transient nature of individual components and the interactive nature of all components. Such interactions not only participate positively in the evolution (i.e., network formation) but also lead to negative feedback effects (loss of loop record at high exposures). The interactions are related not only to direct physical impingement of components, however. To this point, we have considered loop nucleation to respond to applied stresses only. In reality continued nucleation of all but the first loops takes place in the presence of an environment of pre-existing loops, dislocations and other components. The strain field perturbations of these are superimposed on the applied stress field and exert feedback onto further nucleation and growth. Adams has also shown that additional feedback processes exist when one considers the incompatibility strains that develop in polycrystalline materials as a result of loop formation.[80] It should also be recognized that SIPA creep processes operate by borrowing interstitials from less competitive or unfavorably oriented dislocation components. In a highly anisotropic microstructure there are very few unfavorably oriented dislocations and loops from which to borrow. This must exert some feedback on the creep process.

For these reasons, the easiest microstructural records to interpret necessarily involve the simplest microstructures, those produced mostly at low irradiation exposures. Records developed in more complex microstructures are also useful, but one must avoid the tendency to make simplistic statements about microstructures containing complex and interactive components. One cannot say, for instance, that the SIPA mechanism would promote an increase in mean loop size and the absence of such an increase precludes the action of SIPA, particularly if unfaulting and other interactive effects of the types demonstrated in this paper are involved.

To this point. we have not mentioned any observations of vacancy loops although their presence is Often postulated in various irradiation creep models.[1,2] In fact, these are not usually observed in stainless steels at swelling-relevant temperatures. Wolfer and Si-Ahmed[81] have shown that there exists a bias difference between an interstitial and vacancy-type loop such that both can coexist. providing no other abundant sink exists whose capture ratio Z_i/Z_v is less than that of a vacancy loop. Such conditions are expected to occur in metals with very low densitfes of network dislocations and prior to the onset of void nucleation. Recalling the microstructures presented in this paper, it is not surprising that vacancy loops were absent. Reference 81 contains a list of studies where such restrictive microstruc- tural conditions were met and vacancy loops were observed, however.

At first glance. the strong response of Frank loops to applied stress appears to support a creep mechanism involving stress-induced loop alignment or stress-induced changes in loop nucleation rates via a decrease in the activation barrier.[60-64,82-87] This mechanism is sanetimes designated as stress-induced preferential nucleation (SIPN). A number of researchers have explained their data based on such models.[56,60-64,66,69]

Garner. Wolfer and Brager[70] showed. however, that no real nucleation barrier exists beyond the di-interstitial stage. The binding energy of the di-interstitial Is thought to be on the order of 1 eV, and there is a correspondingly low probability of spontaneous dissociation. To meet this objection. Wolfer[91] developed a revised model which considered the stress-induced rotation of the tri-interstitial clusters which serve as embryonic loops. He showed, however. that under the most optimum conditions, this effect was insufficient in itself to explain the data of Okamoto and Harkness[68] or that of Brager. Garner and Guthrie.[69]

Garner and coworkers[70,88] as well as Wolfer[73] noted that a SIPA-type (Stress-Induced Preferential Absorption) mechanism was capable of describing the large response of planar loop densities to resolved stress. The enhanced growth rate of loops on favored planes was visualized to enable such loops to spend less time at very small sizes where random fluctuations in vacancy arrival rate might lead to their destruction. In effect, the SIPA mechanism enhanced the survivability of loops on favorably oriented planes. As shown in Figure 11, the loop bias can be related to the SIPA-relevant parameter σ_{DN}, the normal component of the deviatoric stress tensor for the plane of interest. This parameter is defined as $\sigma_{DN} = \sigma_N - \sigma_H$ where σ_N is the normal stress on the plane and σ_H is the hydrostatic stress. Since the latter is independent of the identity or orientation of the plane, the correlation between planar loop density and normal stress is preserved, but σ_{DN} can be negative for unfavorably oriented planes. This causes a depression of loop density cn unfavorably oriented planes relative to that of favorably oriented planes.

One frequently overlooked aspect of this model is that the relative enhancement or suppression of growth rates was shown to peak as a function of loop radius and approaches zero at larger loop sizes.[70] This means that favorably oriented loops will reach a size where stress no longer affects their growth. allowing unfavorably oriented loops to eventually approach the same size. When added to the various feedback and interaction mechanisms discussed earlier. this may explain the sometimes observed independence of loop size on planar orientation, the absence of which is often used to dismiss the SIPA mechanism in preference to the SIPN mechanism.

The most convincing direct evidence for the SIPA mechanism is the data shown in Figure 10 where the growth rate of loops was found to increase with resolved normal stress. The data in Figures 11 and 12 are also highly supportive of the proposal that SIPA influences strongly the growth rata of Frank loops. These data and the other data noted above do not preclude the operation of the SIPN mechanism, however. The strongest conclusion that can be made is that the effect of SIPA on loops is probably more important than that of SIPN.

One of the major problems with earlier SIPA models was that they were not large enough when coupled with observed microstructural densities to account for nmasured macroscopic strain rates without invoking other creep mechanisms such as glide. Part of this problem was resolved when it was realized that an applied stress could modify the point-defect diffusion in the crystal, particularly the anisotropy.[89-95] This leads to several SIPA-type effects. which are caused by the stress-induced amisotropy of the point-defect diffusivity.[91] The most important of these is a first order effect due to elastodiffusion, an external stress-induced global anisotropy of the diffusivity, as compared to the others which are second order in nature. and which are due to the local anisotropy involving the dislocation-strain field. Woo[91-92] has provided an excellent description of the possible mechanisms capable of producing a SIPA-type effect, including the elastodiffusion SIPA or first order SIPA. sometimes designated as SIPA-AD where AD refers to anisotropic diffusion.

The data presented in this paper cannot be used to distinguish between the different possible SIPA mechanisms, but the authors of a recent study involving the analysis of macroscopic creep s rains have invoked the elasto-diffusion SIPA-AD mechanism as being consistent with their observations.[56]

It is felt that reasonably strong microstructural evidence has been presented In this paper to support the operation of some SIPA-type mechanism not only for loops but also for dislocation segments. It is considered particularly significant that models used to describe the maintenance of network dislocations

at saturation invoke a SIPA-type process operating on loops to continuously generate the new and anisotropic line length. It is thought that these dislocations could then migrate with SIPA-type processes controlling the role played by glide mechanism.

It also appears that stress-assisted preferential unfaulting mechanisms are certainly operating at the same time. In addition. it has been demonstrated clearly that one consequence of anisotropic microstructures is that stress-induced "growth" can occur when the stress is removed. SIPA-induced growth (SIG) was predicted and analyzed in a theoretical paper by Woo."

Sometimes the anisotropy of dislocation microstructure induced by applied stress must first overcome a pre-existing anisotropy of another type. Bates. Cummings and Gilbert[98] showed that radiation-induced growth occurred in 316 stainless steel tubes in the absence of stress. The dislocation and grain texture developed during tube production was such that the fractional length change was greater than one-third of the fractional volume change, which in turn was always greater than the fractional diameter change. indicating radiation-induced growth in the axial direction of the tube. Growth was found to increase with increasing radiation exposure and to be much more pronounced in the 20% cold-worked condition compared to that of the annealed condition. Even more importantly, the axial growth at a given set of irradiation conditions declined as the applied stress level increased, indicating that the stress-induced anisotropy was supplanting the anisotropy introduced in the tube forming process.

Two other creep-related observations resist easy description, however. First. although evidence was presented for enhanced dislocation fluxes occurring coincident with the onset of void swelling. the microstructural mechanism is not completely obvious.

There are several types of models based on the I-creep model of Gittus[99] that predict a creep rate component proportional to the swelling rate. All of these models envision voids to serve as repositories for vacancies, producing an excess flux of interstitials to dislocations. The most relevant of these models use the climb rate produced by SIPA processes[67,97,100-102] to control the rate of glide.

If we use the best current value of creep compliance of austenitic steels in the absence of stress ($B_o \approx 10^{-6}$ MPa^{-1} dpa^{-1}) and the contribution due to swelling-enhanced creep DS, where $D \approx 10^{-2}$ MPa[14,15] and the steady-state swelling rate S_{max} = 1%/dpa[103], we calculate that the dislocation flux associated with steady-state swelling must be two orders of magnitude larger than that preceding the onset of swelling. Perhaps this very large enhancement represents primarily the difference in mobility between loop-dominated and fully anisotropic dislocation network microstructures in annealed steels. However, the difference seems to be too large when comparing the creep of cold-worked materials before and after the onset of swelling.

Perhaps some portion of the cause of swelling- hanced creep lies in segregation-related arguments involving either the alteration of sink strengths?' or changes in matrix composition.[103,104] Garner and Wolfer have advanced a model which attempts to explain how the network and loop densities can be relatively insensitive to irradiation-induced changes in matrix chemistry while the creep rate can be changed substantially via changes in vacancy diffusivity.[105] It appears that the creep record as captured in a snapshot micrograph is selective in the variables to which it responds. primarily because it cannot measure dislocation and loop fluxes.

The second observation for which there is no current explanation is the apparent disappearance of irradiation creep at temperatures above ~500'C when void swelling approaches ~10%.[106-108] The leading candidate mechanism is thought to involve the generation of highly anisotropic dislocation and loop microstructure, but more research is necessary to confirm such a proposal.

CONCLUSIONS

It has been shown that both internally-generated and applied stresses indeed imprint on radiation-induced microstructures a record of their presence as well as a record of the operation of a variety of proposed irradiation creep mechanisms. Interpretation of these records is complicated by the complexity of the microstructural response, particularly in its interactive and feedback aspects. In particular, the SPA-type mechanism has been shown to leave the strongest record. and when acting with other mechanisms to produce a microstructure that is highly anisotropic in its distribution of Burgers vectors.

ACKNOWLEDGEMENTS

The assistance of W. G. Wolfer in describing crenulated loop growth is gratefully acknowledged. H. R. Brager and J. J. Laidler also supplied several micrographs of crenulated loops. S. Jitsukawa. Y. Katano 2nd K. Shiraishi kindly provided the results of their electron irradiation experiments in advance of publication. C. H. Woo provided a carefcl review of the paper and provided suggestions that led to several significant improvements.

FUTURE WORK

This first stage effort on microscopic data is complete. The next stage involves the collection and analysis of macroscopic creep data for both ferritic and austenitic steels that may be employed in fusion devices.

REFERENCES

1. J. R. Matthews and M. W. Finnis. Proceedings of International Workshop on Mechanisms of Irradiation Creep and Growth, Eds. C. H. Woo and R. J. McElroy (Hecla Island. Manitoba. Canada. June 22-25, 1987) to be published in J. Nucl. Mater., also Harwell Report TP 1238, July 1987, United Kingdom.

2. B. O. Hall, "Dislocations in Solids," Ed. F.R.N. Nabarro (Elsevier Science Publishers, B. V.. 1986) pp. 237-294.

3. C. H. Henager, Jr. and E. P. Simonen, "Effects of Radiation on Materials," Twelfth International Symposium. ASTM STP 870, Eds. F. A. Garner and J. S. Perrin. (American Society for Testing and Materials, Philadelphia. PA, 1985) pp. 75-97.

4. W. A. Coghlan. International Metals Reviews, 31 (1986) 245-257.

5. "Proceedings of the International Conference on Fundamental Mechanisms of Radiation Induced Creep and Growth." Chalk River. May 8-10, 1979, Eds. G. J. C. Carpenter. C. E. Coleman and S. R. MacEwen (North-Holland Publishing Co., Amsterdam, 1980).

6. F. A. Garner. W. V. Cummings, J. F. Bates and E. R. Gilbert. Hanford Engineering Development Laboratory Report HEOL-TME 78-9, Richland, WA, June 1978.

7. R. J. Puigh. A. J. Lovell and F. A. Garner, J. Nucl. Mater., 122 and 123 (1984) 242-245.

8. F. A. Garner. E. R. Gilbert and D. L. Porter. "Effects of Radiation on Materials." Tenth Conference, ASTM STP 725, Eds. D. Kramer. H. R. Brager and J. S. Perrin (American Society For Testing and Materials. Philadelphia. PA, 1981) pp. 680-697.

9. O. L. Porter. M. L. Takata and E. L. Wood, J. Nucl. Mater., 116 (1983) 272-276.

10. R. J. Puigh. E. R. Gilbert and B. A. Chin. "Effects of Radiation on Materials." Proceedings Eleventh International Symposium. ASTM STP 782, Eds. H. R. Brager and J. S. Perrin (American Society For Testing and Materials. Philadelphia. PA. 1982) pp. 108-121.

11. R. W. Clark. A. S. Kumar and F. A Garner. J. Nucl. Mater., 155-156 (1988), in press.

12. F. A. Garner and O. L. Porter. J. Nucl. Mater., 155-156 (1988), in press.

13. J. P. Foster. W. G. Wolfer. A. Biancheria and A. Boltax. "Proceedings Conference on Irradiation Embrittlement and Creep in Fuel Cladding and Core Components," (British Nuclear Energy Society. London, 1972) pp. 273-281.

14. K. Ehrlich, J. Nucl. Mater., 100 (1981) 149.

15. J. L. Boutard, Y. Carteret. R. Cauvin. Y. Guerin and A. Maillard, "Proceedings Conference on Oimensional Stability and Mechanical Behavior of Irradiated Metals and Alloys," Brighton, England (British Nuclear Energy Society, 1983) Vol. I pp. 109-112.

16. L. H. Milacek and R. D. Daniels. J. Appl. Phys., 39 (1968) 5714.

17. S. K. Das and M. Kaminsky. Review Article "Radiation Effects on Solid Surfaces." Ed. M. Kaminsky. Advan. Chem. Ser.. Vol. 158 (American Chemical Society, Washington. 1976) Ch. 5.

18. W. Primak, J. Appl. Phys., 35 (1964) 1342-1347.

19. W. G. Wolfer and F. A. Garner. J. Nucl. Mater., 85 & 86 (1979) 583-589.

20. J. H. Evans, J. Nucl. Mater., 76 & 77 (1978) 228-234.

21. W. G. Wolfer. J. Nucl. Mater., 93 & 94 (1980) 713-720.

22. W. G. Johnston. J. H. Rosolowski. A. M. Turkalo and T. Lauritzen, J. Nucl. Mater., 46 (1973) 273-278.

23. F. A. Garner. G. L. Wire and E. R. Gilbert. "Radiation Effects and Tritium Technology for Fusion Reactors." **CONF-750989** (Gatlinburg. TN 1975) Vol. 1, pp. 474-490.

24. W. G. Johnston. J. H. Rosolowski, A. M. Turkalo and K. D. Challenger, Scripta Met. 6 (1972) pp. 999-1006.

25. A. L. Chang, R. Bajaj and S. Diamond, "Advanced Techniques for Characterizing Microstructures," Eds. F. W. Wiffen and J. A. Spitznagel, (The Metallurgical Society of AIME, Warrendale, PA, 1982) pp. 147-155.

26. S. N. Buckley and S. A. Manthorpe, J. Nucl. Mater., 65 (1977) 295-301.

27. F. A. Nichols and Y. Y. Liu. "Radiation-Induced Changes in Microstructure." 13th International Symposium (Part 1), ASTM STP 955, Eds. F. A. Garner, N. H. Packan and A. S. Kumar (American Society for Testing and Materials, Philadelphia, PA, 1987) pp. 414-431.

28. S. N. Buckley. R. Bullough and M. R. Hayns. J. Nucl. Mater., 89 (1980) 283-295.

29. M. H. Yoo and J. O. Stiegler. Phil. Mag., 36 (1977) 1305-1315.

30. B. Cochrane, S. B. Fisher, K. B. Miller and P. J. Goodhew, J. Nucl. Mat., 120 (1984) 79-87.

31. J. Tenbrink. R. P. Wahi and H. Wollenberger. J. Nucl. Mater., 155-156 (1988), in press.

32. F. A. Garner and J. J. Laidler, "Proceedings Workshop on Correlation of Neutron and Charged Particle Damage," CONF-760673 (Oak Ridge National Laboratory, Oak Ridge, TN, June 8-10, 1976) pp. 177-240.

33. F. A. Garner. J. Nucl. Mater., 117 (1983) 177-197.

34. A. D. Marwick, J. Nucl. Mater., 135 (1985) 68-76.

35. J. J. Laidler. F. A. Garner and L. E. Thomas. "Radiation Damage in Metals." Eds. N. L. Peterson and S. D. Harkness (American Society For Metals. Metals Park, OH. 1975) pp. 194-226.

36. F. A. Garner. R. W. Powell. S. Diamond. T. Lauritzen, A. F. Rowcliffe, J. A. Sprague and D. Keefer. "Radiation Effects in Breeder Reactor Structural Materials." Eds. M. L. Bleiberg and J. W. Bennett (The Metallurgical Society of AIME, New York. 1977) pp. 543-569.

37. W. G. Wolfer, F. A. Garner and L. E. Thomas in Reference 10. pp. 1023-1041; also J. Nucl. Mater., 114 (1983) 292-304.

38. R. Bullough and N. M. Ghoniem. J. Nucl. Mater., 127 (1985) 47-55.

39. H. Rauh and R. Bullough, Harwell Report TP 1085, also Phil. Mag., 52 (1985) 383.

40. W. G. Wolfer and M. Ashkin, J. Appl. Phys., 46 (1975) 547.

41. W. G. Wolfer. M. Ashkin and A. Boltax. "Properties of Reactor Structural Alloys After Neutron or Particle Irradiation." ASTM STP 570, Eds. C. J. Baroch and F. R. Shober, (American Society for Testing and Materials, Philadelphia. PA, 1975) pp. 233-258.

42. T. M. Williams. J. Nucl. Mater., 79 (1979) 28-42.

43. A. Hishinuma. Y. Katano, K. Fukaya and K. Shiraishi. J. Nuc. Sci. Tech., 13 (1976) 656-662.

44. E. H. Lee. N. H. Packan. M. B. Lewis and L. K. Mansur. Nucl. Inst. Meth. Phys. Res., B16 (1986) 251-259.

45. B. Hudson and M. J. Makin, Phil. Mag., 11 (1965) 423.

46. H. R. Brager. J. L. Straalsund. J. J. Holmes and J. F. Bates. Met. Trans., 2 (1971) 1893.

47. H. Kawanishi and S. Ishino. J. Nucl. Mater., 155-156 (1988), in press.

48. J. P. Hirth and J. Lothe, "Theory of Dislocations," (McGraw-Hill Publ. Co., New York, 1968) p. 150.

49. F. A. Garner. L. E. Thomas and D. S. Gelles. "Experimental Methods for Charged Particle Irradiations." CONF-750947, (Gatlinburg. TN, September 30, 1975), pp. 51-81.

50. S. N. Buckley and S. A. Manthorpe. "Proceedings Conference on Irradiation Embrittlement and Creep in Fuel Cladding and Core Components," (British Nuclear Energy Society, London, 1972) pp. 253-258.

51. O. Caillard. J. L. Martin and B. Jouffrey. Acta Met., 28 (1980) 1059-1067.

52. O. Caillard and J. L. Martin. J. Micros. Spectr. Electron., 6 (1981) 361-370.

53. J. L. Martin. Rad. Eff., 101 (1986) 199-200.

54. T. Tabata, Y. Nakajima, T. Kida and H. Fujita. "Proceedings Fifth International Conference on High Voltage Electron Microscopy," (Japanese Society of Electron Microscopy. Kyoto. 1977) pp. 519-527.

55. A. Sato, C. Ikeda, S. Nakamura. M. Suzuki and T. Mori, Scripta Met., 20 (1986) 1119-1124.

56. M. Suzuki. "Radiation Damage of Stainless Steels Under Stress." Masters Thesis. Tokyo Institute of Technology, 1988: in Japanese.

57. S. Jitsukawa. Y. Katano and K. Shiraishi, J. Nucl. Sci. Tech., 21 (1984) 671-677.

58. N. Igata, Y. Kohno and J. Nishimura. J. Nucl. Mater., 141-143 (1986) 790-793.

59. M. Griffiths. M. H. Loretto and R. E. Smallman. Phil. Mag., A49 (1984) 613-624, also J. Nucl. Mater., 115 (1983) 313-322.

60. J. Leteurtre. J. L. Pouchou and L. Zuppiroli, Phil. Mag., 27 (1973) 1323-1334.

61. L. Zuppiroli. J. L. Pouchou. A. Francois, J. Leteurtre and Y. Quere, Phil. Mag., 35 (1977) 853-870.

62. L. Zuppiroli, Atomic Energy Commission of France Report CEA-R-4873. 1977: in French.

63. J. Y. Bounaud and J. Leteurtre, "Fundamental Aspects of Radiation Damage in Metals." CONF-751006-P2 (Gatlinburg, TN, 1975) pp. 790-796.

64. J. Ponsoye. Rad. Eff., Q (1971) 13-26.

65. Yu. N Sokursky and L. N. Protsenko. J. Br. Nucl. Energy Soc., 14 (1975) 137-143.

66. T. Atkins and R. J. McElroy. in Reference 27, pp. 447-465.

67. O. J. Michel. P. L. Hendrick and A. G. Pieper, J. Nucl. Mater., 75 (1978) 1-6.

68. P. R. Okamoto and S. O. Harkness. J. Nucl. Mater., 48 (1973) 204-206.

69. H. R. Brager. F. A. Garner and G. L. Guthrie, J. Nucl. Mater., 66 (1977) 301-321.

70. F. A. Garner. W. G. Wolfer and H. R. Brager, "Effects of Radiation on Structural Materials." ASTM STP 683, Eds. J. A. Sprague and D. Kramer (American Society For Testing and Materials. Philadelphia. PA, 1979) pp. 160-183.

71. O. S. Gelles. F. A. Garner and H. R. Brager. in Reference 8, pp. 735-753.

72. H. R. Brager. F. A. Garner. E. R. Gilbert. J. E. Flinn and W. G. Wolfer. in Reference 36, pp. 727-755.

73. W. G. Wolfer. J. Nucl. Mater., 90 (1980) 175-192.

74. F. A. Garner and W. G. Wolfer. in Reference 10. pp. 1073-1087 and in expanded form in University of Wisconsin (Madison) Fusion Report UWFDM-484, September 1982

75. W. G. Wolfer and B. B. Glasgow. Acta Met., 33 (1985) 1997-2004.

76. O. S. Gelles in Reference 3, pp. 98-112.

77. O. S. Gelles. "Dislocation Modelling of Physical Systems," Eds. M. F. Ashby, R. Bullough. C. S. Hartley and J. P. Hirth (Pergammon Press. New York. 1980) pp. 158-162.

78. D. S. Gelles in Reference 8, pp. 562-582.

79. O. S. Gelles. F. A. Garner and B. L. Adams. "Damage Analysis and Fundamental Studies Quarterly Progress Report." DOE/ER-0046/11 (U. S. Department of Energy. Washington. DC, November. 1982) pp. 81-100.

80. B. L. Adams. J. Nucl. Mater., 115 (1983) 49-55.

81. W. G. Wolfer and A. Si-Ahmed, Phys. Lett., 76A (1980) 341-343.

82. R. V. Hesketh. Phil. Mag., Z (1962) 1417; J. Nucl. Mater., 35 (1970) 250.

83. H. Wiedersich and J. L. Katz, Adv. Colloid and Interface Sci., 10 (1979) 33.

84. W. G. Wolfer, J. P. Foster and F. A. Garner, Nucl. Tech., 16 (1972) 55-63.

85. A. D. Brailsford and R. Bullough. Phil. Mag., 27 (1973) 49.

86. G. W. Lewthwaite. J. Nucl. Mater., 46 (1973) 324.

87. K. Herschbach and W. Schneider. J. Nucl. Mater., 51 (1974) 215.

88. F. A. Garner and W. G. Wolfer. Trans. Am. Nucl. Soc., 28 (1978) 144-145.

89. E. J. Savino. Phil. Mag., 36 (1977) 323.

90. Z. K. Saralidze. Sov. Phys. Solid State, 20 (1978) 1568.

91. C. H. Woo. J. Nucl. Mater., 120 (1984) 55.

92. C. H. Woo, "Proceedings of International Workshop on Mechanisms of Irradiation Creep and Growth." Eds. C. H. Woo and R. J. McElroy (Hecla Island. Manitoba. Canada. June 22-25. 1987) to be published In J. Nucl. Mater.

93. C. H. Woo. in Reference 27, pp. 70-89.

94. B. C. Skinner and C. H. Woo, Phys. Rev., 30 (1984) 3084-3097.

95. E. J. Savino and C. N. Tomé, J. Nucl. Mater., 108 and 109 (1982) 405.

96. C. Wassilew. K. Ehrlich and H. J. Bergmann. "Influence of Radiation on Material Properties (Part II)," ASTM STP 956, Eds. F. A. Garner, C. H. Henager, Jr. and N. Igata (American Society for Testing and Materials. Philadelphia. PA, 1987) pp. 30-53.

97. C. H. Woo. Phil. Mag., 42 (1980) 551-558.

98. J. F. Bates, W. V. Cummings and E. R. Gilbert. J. Nucl. Mater., 99 (1981) 75-84.

99. J. H. Gittus. Phil. Mag., 25 (1972) 345.

100. L. K. Mansur. Phil. Mag., 39 (1979) 497.

101. C. H. Woo in Reference 70, pp. 640-655.

102. L. K. Mansur and W. A. Coghlan. In Reference 15, Volume 2, pp. 65-69.

103. F. A. Garner. J. Nucl. Mater., 122 and 123 (1984) 459-471.

104. F. A. Garner and W. G. Wolfer. J. Nucl. Mater., 122 and 123 (1984) 201-206.

105. F. A. Garner and W. G. Wolfer. in Reference 79. pp. 101-112.

106. F. A. Garner. D. L. Porter and B. J. Makenas. J. Nucl. Mater., 148 (1987) 279-287.

107. D. L. Porter and F. A. Garner in Reference 96, pp. 11-21.

108. D. L. Porter and F. A. Garner. in Reference 92.

DETAILED DERIVATION OF STOCHASTIC THEORY OF DIFFUSIONAL PLANAR ATOMIC CLUSTERING – N. M. Ghoniem (University of California, Los Angeles)

OBJECTIVE

The objective of this work is to develop a general stochastic theory for agglomeration of interstitial loop in irradiated materials, and to apply this theory to the determination of the loop bias factor.

SUMMARY

Atomic clustering into circular planar disks is an important process responsible for interstitial loop formation in the bulk of irradiated materials, and the evolution of atomic planes during thin film growth. In this report, we develop a general stochastic theory for the formstion of planar atomic clusters by atomic diffusion. Equation. for the rates of change of atomic species, and for the nucleation rate of atomic clusters are simultaneously solved with appropriate equations for the average size and various momenta of the distribution function. An application of the theory is given by comparing the results of calculations with experimental data on interstitial loop formation in ion-irradiated nickel.

PROGRESS AND STATUS

1. Introduction and background

Atomic clustering in solids which are in nou-equilibrium thermodynamic conditions have been described by rate equations, in analogy to formulations used in chemical kinetics, as far back as the early 1950s. The work of Damask and Dienes' is an example of early theoretical models of atomic clustering. Their approach, which is an extension of Chandrasekhar's theory of colloid coagulation,[1] has been successful in explaining various aspects of defect annealing. Theoretical efforts have then been concerned with either the nucleation phase of clustering,[3–5] or the growth regime.[6–9] Only recently have theories been advanced to treat nucleation and growth of atomic clusters ea inseparable parts of an evolution process.

Early efforts in this area have investigated atomic clustering processes using systems of non-linear ordinary differential equations. These systems represent consenation equations of hierarchies of atomic clusters of increasing size.[10–17] Theoretical implications of system boundedness, global conservation, and boundary and initial conditions were largely unexplored. Solution of the ensuing system of clustering equations is analytically not possible, and mathematical and numerical approximations are therefore necessary. For example, grouping methods, where a group of equations are assigned the same reaction rate, have been introduced by Kiritani[13] and Hayns.[14] Solution of a large system with global atomic conservation to determine the necessary number of equations has been developed by Ghoniem.[''] It is shown in this work that additional equations must be included as function of time, and that the number of equations for an accurate solution can be prohibitively large. In the study of multistate kinetic transitions, the hierarchy of master equations (or rate equations) can be transformed to an equivalent parabolic partial-differential equation.[''] The resulting continuum equation is of the Fokker-Planck (F-P) type, and it describes a process of particle diffusion in a general drift field. This approach was used to model vacancy and interstitial atom clustering by Sprague, Russell and Choi,[20] Wolfer, Mansur and Sprague,[21] and also by Hall.[22] The mathematical properties of the continuum equation have led to some controversy over the validity of the representation for small-size clusters. The truncation of the Taylor series at the second derivative may be invalid for $\Delta z/z \simeq 0(1)$ and $\Delta K/K \simeq O(1)$, where z is the cluster size and K is a generic rate constant. Therefore, a hybrid method was successfully developed by Ghoniem and Sharafat.[23] In this method, the details of small-size clustering are conserved by rate equations, and the behavior of large-size clusters is described by the F-P equation. The hybrid method was also discussed for helium effects on nucleation by Trinkaus and Ullmaier.[24]

Approximate solutions for the distribution function of a kinetic system, obtained by replacing the master equation by a parabolic partial-differential equation in the distribution function itself, is rooted in statistical physics. Rayleigh,[25] and somewhat later Einstein,[''] were the first to use this technique. The procedure wea then developed in greater generality by Fokker[''] and Planck.[28]

Problems with the mathematical approximation to the discrete master equation are well known in the statistical mechanics literature.[29–33] Kramers[29] and Moyal[30] observed that it would be wrong to assume that a valid next approximation to the F-P equation can be formed by truncating the higher order terms in the Taylor series expansion. Van Kampen[31] and Gurol[''] have studied the problem of correcting the F-P approximation using the system size-expansion method. The second approximation in the expansion yields the F-P equation, while successive corrections add to the coefficients in the F-P equation in addition to adding higher derivative terms. The F-P equation becomes an exact equivalent to the master equation only if the transition probabilities are Gaussian.[33]

The approach followed thus far for analyzing microstructure evolution is based on a deterministic causal description provided by rate theory conservation equations. However the existence of a large number of interacting entities, on the order of 10^{30} atoms in a typical engineering solid, implies that the degrees of freedom of the system are much larger than what can be representad by rate equations. Such a situation naturally leads to fluctuations around a reference

state. The existence of these fluctuations can be important in two respects. First, fluctuations around a critical state can determine the extent of nucleation of embryonic dusters. Second, as the clustering system evolves, Euctuations determine the dispersion or spread around the average state.

Recent efforts by Gurol,[34] Clement and Wood,[34] Trinkaus,[35] and by Kitajima and co-workers[36–39] have considered an interpretation to atomic clustering within the framework of statistical mechanics. In this regard, the conventional rate equations describing concentrations of various cluster sizes are replaced by probability density equations. Invoking the assumptions of a Markovian-Gaussian process for the transition probabilities, it can he shown that the F-P equation is a valid representation of the probability density function. Kitajima[38] has in fact used this procedure, which was established within the past 20 years for other problems involving fluctuations.[19,33] In this report, we develop and solve equations representing the evdution of the probability density of planar atomic clusters. We consider atomic agglomeration in two-dimensional (ZD) planar disks as a result of single-atom diffusional transport. Once agglomeration starts, the atomic cluster is considered to be immobile. The description is an extension of the author's earlier hybrid method,[23] where discrete master equations can accurately describe the transient nudeation process, and an F-P equation is used to represent larger sires. Instead of the conventional Taylor series expansion,[34] we present a description of Euctuations within the framework of statistical mechanics.[19,39] In this approach, it is possible to include the collisional and diffusional effects of cascades. Chou and Ghoniem[40,41] have studied both effects using the Monte Carlo (MC) method, and reasonable estimates of the influence of cascade-induced Euctuations are calculated. Section 2 is devoted to development of master and F-P equations describing system evdution. This is followed in Sec. 3 by a derivation of a coupled set of equations for the moments of the system distribution function. The method is then applied in Sec. 4 to the results of experiments on the evdution of interstitial loop during irradiation with heavy ions. Limitations of the method are finally discussed in Sec. 5.

2. Nucleation and Fokker-Planck equations

We focus here on the development of interstitial loop for several reasons. (1) Nucleation of loop is a very fast process and the critical cluster size is on the order of two to three interstitial atoms;[34] (2) A 1-D F-P equation is sufficient for the description of evolution, which allows for tractable presentations of analytical solutions; (3) Well quantified experimental measurements exist[34] where the present theory can he used to test the effects of various approximations.

The evolution of interstitial atom clusters starts with conventional rate equations for the conservation of radiation-produced point defects: vacancies and interstitial atom. The concentrations of vacancies, C_v, and interstitials, C_i, are given by.[34]

$$\frac{dC_v}{dt} = \epsilon P - \alpha C_v C_i - \lambda_v C_v \quad , \tag{1}$$

$$\frac{dC_i}{dt} = \epsilon P + K_v(2) C_v C_{2i} + 2\delta C_{2i} - K_i(1) C_i^2 - \alpha C_v C_i - K_i(2) C_i C_{2i} - \lambda_i C_i \quad , \tag{2}$$

where P is the production rate of point defects, ϵ is the fraction of point defects surviving instantaneous recombination within the cascade, α is their subsequent mutual recombination rate, $K_a^b(x)$ is a general reaction rate between a mobile specie (a) and an immobile specie (b) containing x atoms, and 6 is the di-interstitial dissociation rate. The parameters λ_i and λ_v represent effectiveloss rates to homogenous microstructural sinks, and are given by:

$$\lambda_v = \left[\sum_j D_v k_{v,j}^2 + \sum_{x=x^*}^{X} K_v(x)\, C_\ell(x) \right] \quad , \tag{3}$$

and

$$\lambda_i = \left[\sum_j D_i k_{i,j}^2 + \sum_{x=x^*}^{X} K_i(x)\, C_\ell(x) \right] \quad , \tag{4}$$

where $D_{v,i}$ are diffusion coefficients, $k_{i,j}^2$ are sink strength of type j as in conventional rate theory,[1] and $C_\ell(x)$ is the concentration of interstitial loop containing x atoms. The first summation is over all sink types and the second is carried over the loop distribution function up to a maximum size X. Details of expressions for the various reaction rates have been previously reported,[10–14,17] and will not he repeated here. It is to be noted here that trapping of self-interstitial atoms can he readily included by a modification of the interstitial diffusion coefficient,[34,35] where a trap binding energy is introduced.

The formation of di-interstitial atomic dusters can also be adequately described by the homogeneous rate theory,[34] which results in the follwing equation:

$$\frac{dC_{2i}}{dt} = K_i(1) C_i^2 - K_i(2) C_i C_{2i} - \delta C_{2i} - \lambda_{2i} C_{2i} - 2K_{2i}(2) C_{2i}^2 \quad , \tag{5}$$

where the di-interstitial cluster was also assumed to be mobile. The absorption rate constant at sinks, λ_{2i}, is given by an exprewion similar to Eq. (4).

The clustering of large-size interstitial loops can, in principle, be described by an expanded net of master equations. However, it was shown previously by several authors[13-18] that if the di-interstitial binding energy is large (≥ 1 eV), the backward reaction rates become very small. We will use this idea to simplify the clustering problem by single atomic step. First Eq. (5) is written as:

$$\frac{dC_{2i}}{dt} = J_1 - J_2 \quad , \tag{6}$$

where J_1 is a current representing the net rate of transformation of single interstitial atoms to a di-interstitial cluster, and J_2 is for the net rate of transformation to tri- or tetra-clusters, i.e.,

$$J_1 = K_i(1)C_i^2 - \delta C_{2i} - \lambda_{2i}C_{2i} \quad , \tag{7}$$

and

$$J_2 = K_i(2)C_iC_{2i} + 2\,K_{2i}(2)C_{2i}^2 \tag{8}$$

The rate constants 6 and λ_{2i} are not strongly dependent on x, and Eq. (6) can be replaced by an equivalent equation describing di-atomic cluster nucleation:

$$\frac{\partial C^*}{\partial t} \simeq \frac{\partial}{\partial x} J^* \tag{9}$$

In Eq. (9), the concentration of critical nuclei $C^* = C_{2i}$, and the nucleation current J^* is approximated by J_2. The equation provides a simple means for calculating the nucleation current, which, in turn, supplies one of the necessary boundary conditions for the F-P equation, representing the size distribution of planar atomic dusters.

For sizes above the di-interstitial critical nucleus size (i.e., $x \geq 3$), the master equation describing the rate of change of the concentration, $C(x)$, or equivalently the probability denaity, is given by[17]

$$\frac{\partial C(x)}{\partial t} - (\alpha C_i + \gamma)\,K(x-1)\,C(x-1) + \beta C_v K(x+1)\,C(x+1) - (\alpha C_i + \gamma + \beta C_v)\,K(x)\,C(x) \quad , \tag{10}$$

where the reaction rate has now been separated into a time-dependent component and a *size* dependent component. αC_i represents the rate of interstitial atom impingement while $K(x-1)$ is the corresponding combinatorial factor that is size dependent. γ is the vacancy thermal emission rate, which is nearly independent of x for $x \geq 3$, and βC_v is the rate of vacancy impingement. Following the conventional methods,[17-18] we expand the cluster concentration, C, and the combinatorial numbers, K, around x, and truncate the Taylor aeries after second order. This results in the familiar F-P equation:

$$\frac{\partial C}{\partial t} + \vec{\nabla} \cdot \vec{J} = 0 \quad , \tag{11}$$

where the operator $\vec{\nabla} = \partial/\partial x$, in this case, and current $\vec{J}$ is given by the 1-D component:

$$\vec{J} = J_x = \mathcal{F}C - \frac{\partial}{\partial x}(DC) \quad , \tag{12}$$

where the drift coefficient $\mathcal{F}$, and the dispersion coefficient D can be expressed as:

$$\mathcal{F} = g_1\,K(x) \quad , \tag{13}$$

and

$$\mathrm{D} = D_o = g_2\,K(x) \quad , \tag{14}$$

and g_1 and g_2 are mainly functions of the temperature and displacement rate, given by

$$g_1 = \frac{4}{3}\left(\frac{3}{\pi}\right)^{1/4}(\alpha Z C_i + \gamma - \beta C_v) \quad , \tag{15}$$

$$g_2 = \frac{2}{3}\left(\frac{3}{\pi}\right)^{1/4}(\alpha Z C_i + \gamma + \beta C_v) \quad , \tag{16}$$

and Z is a constant bias factor for dislocation Imp, ensuring that $g_1 \geq 0$ at quasi-steady state, and $K(x)$ is a size-dependent combinatorial factor.[17] Equations (13) and (14) are based on mixed diffusion/surface reaction controlled kinetics, where the combinatorial number, $K(x)$, is proportional to the number of atom around the Imp perimeter ($x^{1/2}$), and a size-dependent function (see Ref. 17).

The previously outlined approach for the derivation of the F-P equation is based upon the master equation for single-step transitions. However, the effects of large scale transitions of a more general stochastic nature can be described by the methods of statistical mechanics, with the Smoluchowsky-Chapman-Kolmogorov (SCK) equation for a Markovian process as a starting point,[33,38] i.e.,

$$C(x,t) = \int C(x_o,0)\,\psi(x,t;\,x_o,0)\,dx_o \quad , \tag{17}$$

where the transition probabilities, ψ in this case, need not be exactly known. An integro-differential equation can be formulated for ψ, from which various moments are calculated. The FP equation [Eq. (11)] is shown[19,33,37] to be an

approximation to the SCK equation [Eq. (17)]. The drift and dispersion functions can be defined in a more general sense as[19]

$$\mathcal{F}_j(x) = \frac{<\Delta x(x)>}{\Delta t_j} \quad , \tag{18}$$

and

$$D_j(x) = \frac{\langle(\Delta x(x))^2\rangle - [<\Delta x(x)>]^2}{2\Delta t_j} \tag{19}$$

where the interval Atj is a characteristic correlation time for a statistically independent stochastic process, j. The notation, $< >$, is used to indicate time-averaging of a size fluctuation, Δx, over a time interval Δt_j.

There are three different stochastic processes that influence the evolution of interstitial loop: single atomic transitions, transitions caused by the diffusion of defects contained in a cascade, and transitions caused by direct cascade collisions. The overall drift and diffusion coefficients can be expressed as the sum of the respective values of the statistically independent processes. Using the subscript s for the first process, cd for the second, and cc for the third, we have

$$\mathcal{F} = \mathcal{F}_s + \mathcal{F}_{cd} + \mathcal{F}_{cc} \simeq \mathcal{F}_s \quad , \tag{20}$$

and

$$D = D_s + D_{cd} + D_{cc} \tag{21}$$

The expressions for single-step transitions are already given in Eqs. (13) and (14), while those for cascade collisions D_{cc} and diffusion D_{cd} can be estimated in a manner similar to the work of Kitajima.[36,38] We now proceed to describe our application of the moments method to the solution of the general F-P equation for loop evolution.

3. Moments method for the solution of the Fokker-Planck equation

The moments method has been successfully used for the approximate determination of distribution functions, when described by partial or integro-differential equations, as in the work of Sigmund[43] and in that of Clement and Wood." Equations (11) and (12) can be put in the form

$$\frac{\partial C}{\partial t} = -\frac{\partial}{\partial x}(\mathcal{F}C) + \frac{\partial^2}{\partial x^2}(DC) \tag{22}$$

The zeroth moment of Eq. (22) gives

$$\frac{dN}{dt} = J^* \quad , \tag{23}$$

where $N = \int_{x^*}^{\infty} C\,dx$, and is readily obtained by the direct integration of Eq. (23). N is the total density of atomic clusters, regardless of their size. The upper bound has been approximated as ∞ for mathematical simplicity. Solution to the second-order parabolic partial differential Eq. (22) is possible, provided the following boundary and initial conditions are satisfied:

$$\left.\begin{array}{lcll} C(\infty, t) & = & 0 & \\ C(x^*, t) & = & C_{2i}(t) \equiv C^*, & or \\ J(x^*, t) & = & J^* & , \text{ and} \\ C(x, 0) & = & 0 & , \quad x > x^* \end{array}\right] \quad . \tag{24}$$

The average size, $<x>$, is obtained as follows: $<x> N = \int_{x^*}^{\infty} x\,C\,dx$. Taking time derivatives, we obtain:

$$\frac{\partial}{\partial t}[<x> N] = \int \frac{\partial}{\partial t}(x\,C)\,dx = \int x\,\frac{\partial C}{\partial t}\,dx = \int -x\,dJ \quad , \tag{25}$$

where $\partial x/\partial t = 0$, because x and t are independent variables of the dependent variable C.

Now, performing further differentiation of Eq. (25), we obtain:

$$N\frac{\partial}{\partial t}<x> + <x> J^* = [x\,J]_{\infty}^{*} + \int_{x^*}^{\infty} J\,dx \quad ,$$

or

$$\frac{\partial}{\partial t}<x> = \frac{J^*}{N}[x^* - <x>] + \frac{1}{N}\int_{x^*}^{\infty} J\,dx \tag{26}$$

Substituting for J in Eq. (26), we obtain

$$\frac{\partial}{\partial t}<x> = \frac{J^*}{N}[x^* - <x>] + \frac{1}{N}\left[\int_{x^*}^{\infty}(\mathcal{F}C - \frac{\partial}{\partial x}DC)\,dx\right]$$

The last equation yields:

$$\frac{\partial}{\partial t}<x> = \frac{J^*}{N}(x^* - <x>) + <\mathcal{F}> - \frac{1}{N}[DC]_{x^*}^{\infty} \quad ,$$

where $<\mathcal{F}>$ is the average value of the drift function, $\mathcal{F}$, over the size distribution function C. Finally the equation for the average size, $<x>$, is given by:

$$\frac{d}{dt}<x> = <\mathcal{F}(x)> - (<x> - x^*)\frac{d}{dt}\ln N + \frac{D'C'}{N} \tag{27}$$

The second and third terms of Eq. (27) give the effects of nucleation on the average size. Here the symbol < > is used for averages mer the distribution function, i.e., $\langle \eta(x) \rangle = \int_0^\infty \eta(x)\, C(x)\, dx$, and $\eta(x)$ is any arbitrary function of x.

Let us define the rth moment, M_r as follows:

$M_r = \langle (x - \langle x \rangle)^r \rangle$, and $\langle (x - \langle x \rangle)^r \rangle \int_{x^*}^\infty C(x,t)\, dx = \int_{x^*}^\infty (x - \langle x \rangle)^r\, C(x,t)\, dx$,

or

$$M_r N = \int_{x^*}^\infty (x - \langle x \rangle)^r\, C(x,t)\, dx \quad . \tag{28}$$

Taking the time derivatives of both sides of Eq. (28) and using the initial and boundary conditions, we obtain:

$$\frac{\partial}{\partial t}(M_r N) = \int_{x^*}^\infty \frac{\partial}{\partial t}(x - \langle x \rangle)^r\, C\, dx \quad , \tag{29}$$

or

$$M_r \frac{\partial N}{\partial t} + N \frac{\partial M_r}{\partial t} = \int_{x^*}^\infty \left[(x - \langle x \rangle)^r \frac{\partial C}{\partial t} + C\, r (x - \langle x \rangle)^{r-1} \left(- \frac{\partial \langle x \rangle}{\partial t} \right) \right] dx$$

$$= - \int_{x^*}^\infty (x - \langle x \rangle)^r\, dJ - r \frac{\partial \langle x \rangle}{\partial t} \langle (x - \langle x \rangle)^{r-1} \rangle N \quad . \tag{30}$$

Using the symbols, ., for time derivatives, and, ′, for derivatives with respect to x, we get

$$M_r \dot{N} + N \dot{M}_r + r \langle \dot{x} \rangle M_{r-1} N = - \int_{x^*}^\infty (x - \langle x \rangle)^r d \left[\mathcal{F} C - (\mathcal{D} C)' \right]$$

$$= - \left[(x - \langle x \rangle)^r \mathcal{F} C \right]_{x^*}^\infty + \int_{x^*}^\infty \mathcal{F} C\, r (x - \langle x \rangle)^{r-1}\, dx + \left[(x - \langle x \rangle)^r (\mathcal{D} C)' \right]_{x^*}^\infty - \int_{x^*}^\infty (\mathcal{D} C)' r (x - \langle x \rangle)^{r-1}\, dx$$

$$= (x^* - \langle x \rangle)^r J^* + r N \langle \mathcal{F} (x - \langle x \rangle)^{r-1} \rangle - \int_{x^*}^m r (x - \langle x \rangle)^{r-1} d(\mathcal{D} C)$$

$$= (x^* - \langle x \rangle)^r J^* + r N \langle \mathcal{F} (x - \langle x \rangle)^{r-1} \rangle - r \left[(x - \langle x \rangle)^{r-1} \mathcal{D} C \right]_{x^*}^\infty + r(r-1) \int_{x^*}^\infty \mathcal{D} (x - \langle x \rangle)^{r-2}\, C\, dx$$

$$= (x^* - \langle x \rangle)^r J^* + r \left[(x^* - \langle x \rangle)^{r-1} \mathcal{D}^* C^* \right] + r N \langle \mathcal{F} (x - \langle x \rangle)^{r-1} \rangle + r(r-1) N \langle \mathcal{D} (x - \langle x \rangle)^{r-2} \rangle \quad . \tag{31}$$

Therefore,

$$\langle \dot{M}_r \rangle = r \langle \mathcal{F} (x - \langle x \rangle)^{r-1} \rangle + r(r-1) \langle \mathcal{D} (x - \langle x \rangle)^{r-2} \rangle$$

$$+ r \frac{\mathcal{D}^* C^*}{N} (x^* - \langle x \rangle)^{r-1} + \frac{\partial}{\partial t} (\ell n\, N) \left[(x^* - \langle x \rangle)^r - M_r \right] - r M_{r-1} \langle \dot{x} \rangle \quad . \tag{32}$$

Substituting for $\langle \dot{x} \rangle$, we get:

$$\langle \dot{M}_r \rangle = r \left[\langle \mathcal{F} (x - \langle x \rangle)^{r-1} \rangle - M_{r-1} \langle \mathcal{F} \rangle \right] + r \frac{\mathcal{D}^* C^*}{N} \left[(x^* - \langle x \rangle)^{r-1} - M_{r-1} \right]$$

$$+ \frac{\partial}{\partial t} (\ell n\, N) \left[(x^* - \langle x \rangle)^r - M_r - r M_{r-1} (x^* - \langle x \rangle) \right] + r(r-1) \langle \mathcal{D} (x - \langle x \rangle)^{r-2} \rangle \quad . \tag{33}$$

Now let us define the nudeation functions, ξ_r, the distortion functions, Φ_r, and the dispersion functions, Ψ_r, as:

$$\xi_1 = \frac{\mathcal{D}^* C^*}{N} - (\langle x \rangle - x^*) \frac{\partial}{\partial t} (\ell n\, N) \quad ,$$

$$\xi_r = r \frac{\mathcal{D}^* C^*}{N} \left[(x^* - \langle x \rangle)^{r-1} - M_{r-1} \right] + \frac{\partial}{\partial t} (\ell n\, N) \left[(x^* - \langle x \rangle)^r - M_r - r M_{r-1} (x^* - \langle x \rangle) \right] \quad ,$$

$$\Phi_r = r \left[\langle \mathcal{F} (x - \langle x \rangle)^{r-1} \rangle - M_{r-1} \langle \mathcal{F} \rangle \right] \quad ,$$

$$\Psi_r = r(r-1) \langle \mathcal{D} (x - \langle x \rangle)^{r-2} \rangle \tag{34}$$

The complete system of moment equations can now be described as:

$$\left.\begin{aligned} \frac{d}{dt}\langle x\rangle &= \langle \mathcal{F}\rangle + \xi_1 \ , \\ \frac{d}{dt}\langle M_r\rangle &= \Psi_r + \Phi_r + \xi_r \ , \quad r = 2,3, \ldots \infty \end{aligned}\right\} \tag{35}$$

Since the distribution function is not known *a priori*, averaging of functions can only be made in an approximate way. For an arbitrary function of x, the average value over the distribution function is given by:

$$\left.\begin{aligned} \langle \eta(x)\rangle &= \frac{1}{N}\int_{x^*}^{\infty} \eta C\, dx = \frac{1}{N}\int_{x^*}^{\infty}\left[\eta(\langle x\rangle) + \frac{(x-\langle x\rangle)}{1!}\eta'(\langle x\rangle)\right. \\ &\quad \left. + \frac{(x-\langle x\rangle)^2}{2!}\eta''(\langle x\rangle) + \ldots\right] C\, dx \\ \langle \eta(x)\rangle &= \eta(\langle x\rangle) + \sum_{k=2}^{\infty}\frac{M_k}{k!}\frac{d^k\eta(\langle x\rangle)}{dx^k} \end{aligned}\right\} \tag{36}$$

The dispersion function, Ψ_r, is given by averaging the product of the diffusion coefficient and the quantity $(x-\langle x\rangle)^{r-2}$ over the distributim function. Thus

$$\Psi_r = r(r-1)\left\{D(\langle x\rangle - \langle x\rangle)^{r-2} + \sum_{k=2}^{\infty}\frac{M_k}{k!}\frac{d^k}{dx^k}\left[D(x-\langle x\rangle)^{r-2}\right]\Big|_{\langle x\rangle}\right\} \tag{37}$$

The function D, takes different forms, depending on the value of r. For $r = 2$, we obtain

$$\Psi_2 = 2\left\langle D(x-\langle x\rangle)^0\right\rangle = 2\langle D\rangle = 2\left[D(\langle x\rangle) + \sum_{k=2}^{\infty}\frac{M_k}{k!}\frac{d^kD}{dx^k}\Big|_{\langle x\rangle}\right] \tag{38}$$

Now, since $D = g_2 K(x) x^{1/2}$, we obtain for $K(x) = 1$:

$$\Psi_2 = 2\left[D + \frac{g_2}{2}\sum_{k=2}^{\infty}\frac{M_k}{k!}(-1)^{k-1}\frac{1\times 3\times 5\ldots\times(2k-3)}{2^{k-1}}\langle x\rangle^{-(2k-1)/2}\right] \ . \tag{39}$$

The aeries is convergent for large x. An approximation to Ψ_2 can be obtained by truncating the series at its lowest limit, i.e., $k = 2$:

$$\Psi_2 \approx 2\left\{D(\langle x\rangle) + \frac{g_2}{2}(-1)\frac{M_2}{2}\langle x\rangle^{-3/2}\right\} = 2g_2\langle x\rangle^{1/2}\left[1 - \left(\frac{\sqrt{M_2}}{2\langle x\rangle}\right)^2\right] \ . \tag{40}$$

The distortion function, ϕ_r, is given by

$$\begin{aligned} \phi_r &= r\left\{\mathcal{F}(\langle x\rangle)(\langle x\rangle - \langle x\rangle)^{r-1} + \sum_{k=2}^{\infty}\frac{M_k}{k!}\frac{d^k}{dx^k}\left[\mathcal{F}(x-\langle x\rangle)^{r-1}\right]\Big|_{\langle x\rangle} - M_{r-1}\langle \mathcal{F}\rangle\right. \\ &= r\left\{\delta(r-1)\mathcal{F}(\langle x\rangle) + \sum_{k=2}^{\infty}\frac{M_k}{k!}\frac{d^k}{dx^k}\left[\mathcal{F}(x-\langle x\rangle)^{r-1}\right]\Big|_{\langle x\rangle}\right. \\ &\quad \left.\left. - M_{r-1}\left[\mathcal{F}(\langle x\rangle) + \sum_{k=2}^{\infty}\frac{M_k}{k!}\frac{d^k}{dx^k}(\mathcal{F})\Big|_{\langle x\rangle}\right]\right\} \ . \end{aligned} \tag{41}$$

Similar to the dispersion function, for r = 2, we obtain $\phi_2 = 2[\langle \mathcal{F}(x-\langle x\rangle)\rangle - M_1\langle \mathcal{F}\rangle]$, but $M_1 = \langle x - \langle x\rangle\rangle = 0$ and

$$\langle \mathcal{F}(x\langle x\rangle)\rangle = \mathcal{F}(x-\langle x\rangle)|_{\langle x\rangle} + \sum_{k=2}^{\infty}\frac{M_k}{k!}\frac{d^k}{dx^k}[\mathcal{F}(x-\langle x\rangle)] \tag{42}$$

As an approximation, we truncate the series at $k = 2$ to obtain

$$\phi_2 \approx \frac{M_2}{2}[\mathcal{F} + (x-\langle x\rangle)\mathcal{F}']' = \frac{M_2}{2}[2\mathcal{F}' + (x-\langle x\rangle)\mathcal{F}''] = 2M_2\mathcal{F}' = g_1 M_2\langle x\rangle^{-3/2} \ . \tag{43}$$

Now, let $\lambda \equiv [(M_2)^{1/2}/2\langle x\rangle]^2$.

Approximate equations for the average value of x and the second moment are given by

$$\frac{d\langle x\rangle}{dt} \approx \xi_1 + g_1\langle x\rangle^{1/2}\left(1-\frac{\lambda}{2}\right) \quad , \tag{44}$$

and

$$\frac{dM_2}{dt} \approx \xi_2 + 2g_2\langle x\rangle^{1/2}\left[1-\lambda\left(1-\frac{2g_1}{g_2}\right)\right] \quad . \tag{45}$$

Integration of the set of Eq. (29) can, in principle, describe the distribution function by defining any desired number of moments. Representation of the distribution function from the knowledge of the various moments is not unique, however. To accomplish this task, we will use the cummulant functions, κ_n, where $\kappa_1 = \langle x\rangle$, $\kappa_2 = M_2$, $\kappa_3 = M_3$, $\kappa_4 = M_4 - 3M_2^2$, ... ; the coefficientsof skewness and excess, $G_1 = \kappa_3/\kappa_2^{3/2}$, $G_2 = \kappa_4/\kappa_2^2$, ... ; and the normal or Gaussian function $Z(\xi) = (1/\sqrt{2\pi})e^{-\xi^2/2}$ and $\xi = [(x - \langle x\rangle)/\sqrt{M_2}]$.

The distribution function, $C(x,t)$, can now be found as:[45]

$$\begin{aligned} C(x,t) \;=\; N\Bigg\{ & Z(y) - \left[\frac{G_1}{6}Z^{(3)}(y)\right] + \left[\frac{G_2}{24}Z^{(4)}(y) + \frac{G_1^2}{72}Z^{(6)}(y)\right] \\ & - \left[\frac{G_3}{120}Z^{(5)}(y) + \frac{G_1G_2}{144}Z^{(7)}(y) + \frac{G_1^3}{1296}Z^{(9)}(y)\right] \\ & + \left[\frac{G_4}{720}Z^{(6)}(y) + \frac{G_1^2}{1152}Z^{(8)}(y) + \frac{G_1G_2}{720}Z^{(8)}(y)\right. \\ & \left. + \frac{G_1^2G_2}{1728}Z^{(10)}(y) + \frac{G_1^3}{31104}Z^{(12)}(y)\right] + \ldots\Bigg\} \quad . \end{aligned} \tag{46}$$

Equation (32) can be simplified, knowing that the normal function, Z, satisfies the differential equation $Z^{(m+2)}(y) + yZ^{(m+1)}(y) + (m+1)Z^{(m)}(y) = 0$, and hence the recurrence relation, $Z^{(m)}(y) = (-1)^m H(y,m)Z(y)$, holds. The function $H(y,m)$ are the Hermite Polynomials: $H_1(y) = -y$, $H_2(y) = y^2 - 1$, $H_3(y) = -y^3 + 3y$.

Following Kendall and Stuart,[45] one can derive relationshipe between the cummulants and moments. When the transformation,

$$z = y\sqrt{M_2} + \langle x\rangle \quad , \tag{47}$$

is substituted into Eq. (32), and the cummulants replaced by moments, we finally arrive at an approximation to the distribution function

$$C(x,t) \simeq \frac{N}{\sqrt{2\pi M_2}}\exp\left(-\frac{y^2}{2}\right)\left[1 + \frac{M^3}{6M_2^{3/2}}H_3(y) + \frac{1}{24}\left(\frac{M_4}{M_2^2} - 3\right)H_4(y) + \frac{M_3^2}{72M_2^3}H_6(y) + \ldots\right] \quad . \tag{48}$$

4. Numerical results for a simplified example

The method presented in the previous section is a formal procedure which should be tested for convergence and accuracy for specific applications. However, we will not attempt this in the present report. Rather, an illustrative example of interstitial loop evolution will he given in this section where comparison with experiments are made. It is instructive to show that, even though several complicating features are neglected, the solution gives qualitative agreements with experiments. It is to he nokd that current transmission electron microcope (TEM) techniques are still too crude to accurately describe fine features of microstructure evolution, and hence a simple description may be desirable.

Hall and Potter[15] performed ion-irradiation experiments on Ni, Ni-Si, and Ni-Aℓ alloys. A series of experiments on Ni-4 at % Si were carried out, where 3.0 MeV Ni^{58+} ions were used to bombard samples at 465°C. Their ion flux was 2.3 x 10^{11} cm^{-2} s^{-1}, which corresponded to a peak displacement damage rate of 3 x 10^{-4} dpa/s. A summary of their experimental observations is given in Table I.

Table I. Experimental observation of the Hall-Potter experiments [15] at 465°C.

Dose (dpa)	Total Loop Density ($loop/m^3$)	Avg Loop Diam (nm)
0.11	4.84 x 10^{20}	11.5
0.35	4.97 x 10^{20}	30.2
0.67	4.87 x 10^{20}	34.1

A aeries of calculations were performed using Eqs. (1)–(5) for the concentrations of vacancies, self-interstitial atoms, and di-interstitials, respectively. Equation (23) was simultaneously integrated for the total loop density, and Eqs. (30)

and (31) for the average loop size and the second moment of the distribution function. A trapping model was adopted for interstitial atom migration, where the effective migration energy, E_i^{m*}, is written as $E_i^{m*} = E_i^m + E_i^t$, where E_i^m h the interstitial migration energy without trap and E_i^t is the binding energy of self-interstitials to atomic-size trap. A standard set of defect parameters has been used throughout the calculations. Only three parameten were treated as free variables, and thoee are the trapping energy (E_i^t), the di-interstitial binding energy (E_{2i}^B), and the interstitial loop bias factor (Z_i^ℓ). The remainder of the parameten were treated as standard values commonly used in the Literature

Defect Parameter	Value	Defect Parameter	Value
Vacancy migration energy, E_v^m	1.28 eV	Dislocation interstitial bias factor, Z_i	1.01
vacancy formation energy, E_v^f	1.8 eV	Interstitial migration energy, E_i^m	2.20 eV
Cascade defect survival efficiency, ε	0.3	Di-interstitial migration energy,	0.80 eV
Interstitial atom vibration frequency, ν_i	$10^{13} s^{-1}$	Trapping energy for self-interstitials, E_i^t	0.35 eV
Vacancy vibration frequency, ν_v	$5 \times 10^{13} s^{-1}$	Di-interstitid binding energy, E_{2i}^b	1.19eV
Initial dislocation density, ρ	$5 \times 10^{14} m^{-2}$	Loop interstitial bias factor, Z_i^ℓ	2.0

To compare with experimental data, the loop size distribution must be described as a function of the loop diameter, D, rather than its size x. Conservation of probability gives $C(x,t)\,dx = C(D,t)\,dD$. Hence $C(D,t) = C(x,t)\,(dx/dD)$, since, for a circular atomic dhk in an FCC material

$$\pi \frac{D^2}{4} \frac{a_0}{\sqrt{3}} = x \frac{a_0^3}{4}$$

where a_0 in the interatomic spacing. Thus: $D = Kx^{1/2}$, where $K = 3^{1/4}/\sqrt{\pi}\, a_0$. The distribution function, C(D,t), is now given by $C(D,t) = (2/K)\, x^{1/2} C(x,t)$. It is to be noted that the transformation from a number of atoms, x, to a circular dink with diameter, D, introduces another distortion to the distribution function.

The temporal dependencies of point–defect concentrations (C_v and C_i), the di-interstitial concentration (C_{2i}), the nudeation current (J^*), and the density of critical dusters (C') are shown in Fig. 1. It in observed that quasi-static conditions are achieved within a short irradiation time (on the order of 0.001 dpa). Thin in in accordance with earlier calculations (e.g., Ref. 17). The bulk of interstitial Imp nudeation is achieved within this transient dose. Further irradiation results in a small amount of nudeation and in substantial development of the loop size distribution. This observation will be useful in further simplificationsof the problem.

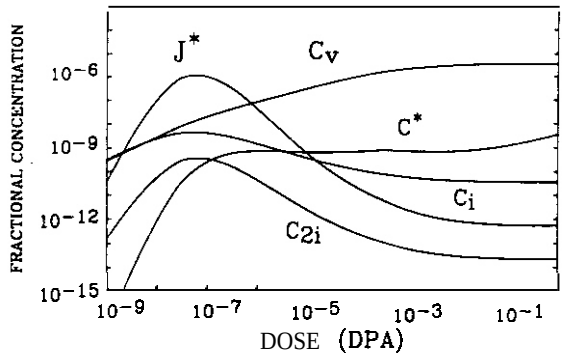

Fig. 1. Time dependence of vacancy (C_v), intentitid (C_i), di-interstitial (C_{2i}), and critical nucleus (C') concentrations. Also shown is the nucleation current [$J^*(at/at/s)$].

The effects of parametric variations in Z_i^I, E_i^{mI}, and E_{2i}^b on the average size of dislocation loop and on the total loop density is shown in Figs. 2 through 7. An increase in the loop bias factor, Z_i^I, results in an increase in the average loop diameter, as shown in Fig. 2. On the contrary, the loop density is not sensitive to the factor as indicated in Fig. 3. This is fortunate since measurements of the loop density can he used to determine defect parameters other than the bias factor. The effectsof the di-interstitial binding energy on the average loop diameter is shown in Fig. 4, while the corresponding effect on the total density is shown in Fig. 5. An increase in the E_{2i}^b will dramatically increase the loop density and reduce the average diameter. The value of 1.19 eV is shown to result in reasonable correlation with experimental data, and is also consistent with our previous conclusions.[37] The effective interstitial migration energy shows an opposite dramatic influence on both the average diameter (Fig. 6) and the total density (Fig. 7). The interstitial atom migration energy and the di-interstitial binding energy determine the probability of loop nucleation, and atomic conservation dictates the average loop size.

The distribution function of interstitial loop at 0.2 dpa, 1.0dpa and 1.8 dpa is shown in Fig. 8. In this calculation, only the effects of single-step transitions on the stochastic dispersion coefficient, D, are included. Comparison with the experimental data of Hall and Potter[38] shows that this may be an underestimation of the magnitude of stochastic fluctuations and that collision cascade effects must be included.

In the following, we apply a simple model for calculating the effects of collision cascades on the diffusioncoefficient, and hence on the size distributim. Kitajima[39] calculated the effects of cascade collisions and cascade-induced point-defect fluctuations on the dispersion coefficient, D. Cascade-induced point–defect fluctuations, and cascade re-solution were calculated by Chou and Ghoniem in a series of papers.[40,41,46] Because of its simplicity, we apply Kitajima's model, where the cascade-induced dispersion coefficient, $D_{cd}+D_{cc}$, is taken as a multiple of the single-step transition dispersion coefficient. Figure 9 shows that the effects of cascades are significant on the dispersion of the loop distribution function.

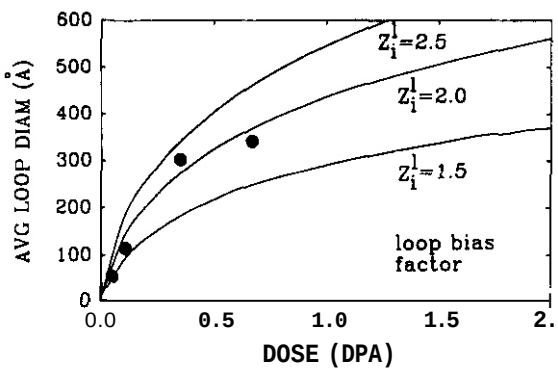

Fig. 2. Effect of interstitial loop bias factor (Z_i^I) on the average loop diameter (– ≡ theory, • ≡ experiment).

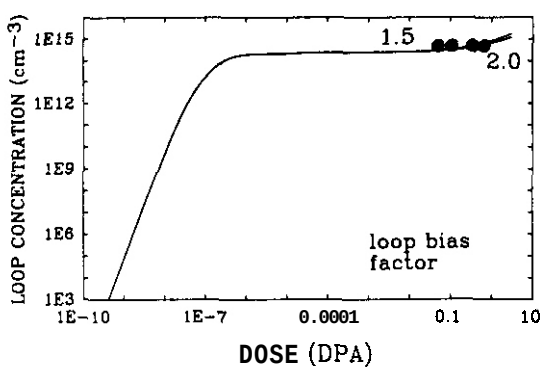

Fig. 3. Effect of the loop bias factor (Z_i^I) on the total loop concentration (– ≡ theory, • ≡ experiment).

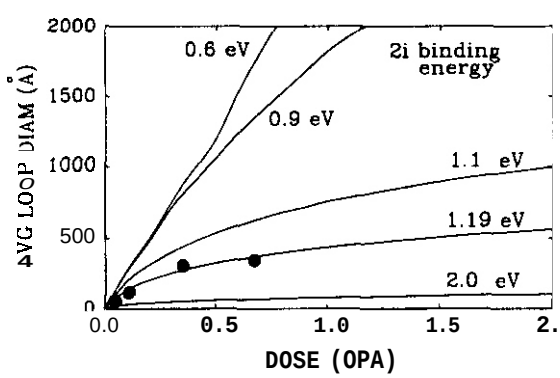

Fig. 4. Effect of di-interstitial binding energy on the average loop diameter (– ≡ theory, • ≡ experiment).

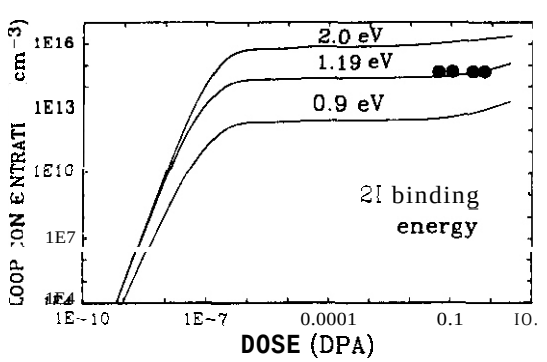

Fig. 5. Effect of di-interstitial binding energy on the total loop concentration (– ≡ theory, • ≡ experiment).

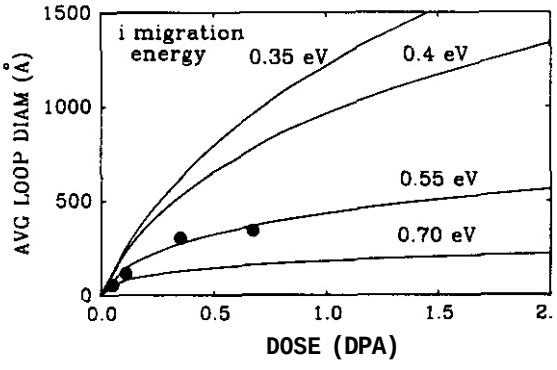

Fig. 6. Effect of the effective interstitial migration energy on the average loop diameter (– ≡ theory, • ≡ experiment).

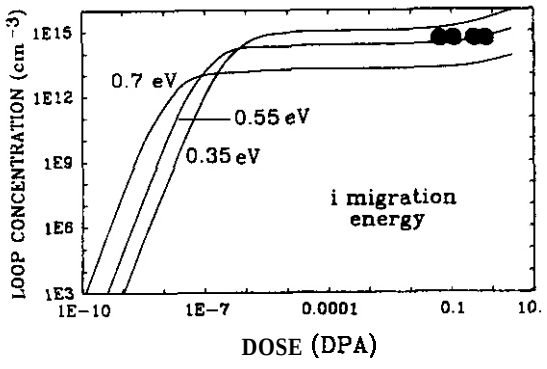

Fig. 7. Effect of the effective interstitial migration energy on the total loop density concentration (– ≡ theory, • ≡ experiment).

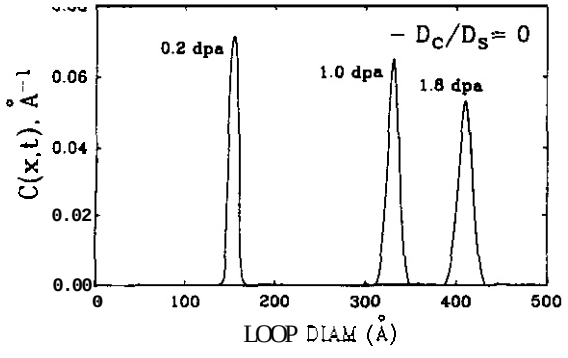

Fig. 8. Distribution function of interstitial loop at various displacement damage doses.

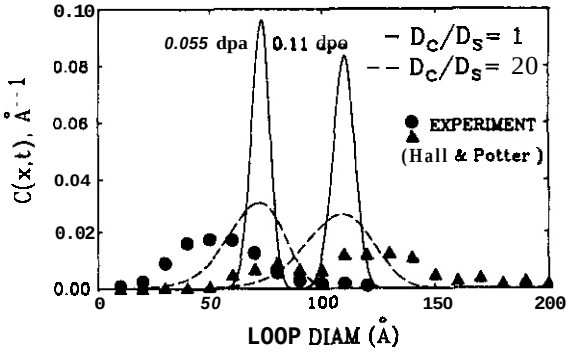

Fig. 9. Effects of cascades on the dispemion of the interstitial loop distribution function (– ≡ theory, • ≡ experiment).

5. Conclusions

The nucleation phase of interstitial loops is shown to be very fast, and the transient period for loop formation is over after about 0.001 dpa. The effects of three point-defect parameters on loop density and average size is studied by comparing theoretical calculations to experiments. An increase in the loop bias factor, Z_i^l, is found to increase the average loop size but has a very small effect on the total loop density. An increase in the di-interstitial binding energy, E_{2i}^b, increases the loop density and reduces the average diameter in a significant way. For nickel, a value of E_{2i}^b = 1.19 eV reproduces available experimental data. The value of the effective self-interstitial migration energy has a dramatic effect on the total loop density and the loop average size. A value of $E_i^{me} = 0.55$ eV shows consistency with experimental data. This is an indication that interstitial migration is hindered by atomic traps.

The distribution function of interstitial loop, when displayed as a function of the loop diameter, is non-Gaussian. The deviation from Gaussian behavior is caused by several factors. First, the continuous nucleation of small-size Imp introduces a component of small-size loop. Second, if the dispersion and drift functions are size dependent, higher order additional terms are introduced as corrections to the Gaussian distribution function. Third, the assumption that the stochastic process of atomic additions to a cluster results in an instantaneous circular disk results in a transformation of the stochastic process from sire space to diameter space. This transformation introduces another distortion to the distribution function.

Atomic agglomeration in interstitial loop under irradiation is affected by collision cascades. Comparisons of theoretical calculations and experiments indicate that the stochastic fluctuations in loop sizes caused by the net absorption of single interstitial atom are not adequate to explain the wide dispersion in the distribution function. To be consistent with experimental observations additional fluctuations because of cascades must be included.

Acknowledgment

This work was supported by the U.S. Department of Energy, Office of Fusion Energy, Grant # DE-FG03-84ER52110, with UCLA.

References

[1] A.C. Damask and G. Dienes, Phya. Rev. 120, 99(1960).
[2] S. Chandrasekhar, Rev. Mod. Phys. 15, 1(1943).
[3] J.L. Kat. and H. Wiedersich, J. Chm. Phys. 55, 753(1971).
[4] K.C. Russell, Acta Metall. 19, 753(1971).
[5] J.J. Burton, Scripta Metall. 5, 449(1971).
[6] R. Bullough and R.C. Perrin, in Proceeding. *of the Symposium* on *Radiation* Damage in Reactor *Materials*, Vol. II (IAEA, Vienna, 1889) p. 233.
[7] A.D. Brailsford and R. Bullough, J. Nud. Mater. 44, 121(1972).
[8] L.K. Mansur, Nucl. Technol. 40, 5(1978).
[9] N.M. Ghoniem and G.L. Kulcinski, Radiat. Effects 39(1), 47(1978).
[10] B.L. Eyre and R. Bullough, J. Nucl. Mater. 26, 249(1968).
[11] R. Sizmann, J. Nucl. Mater. 69 *k* 70, 386(1978).
[12] L.M. Brown, A. Kelly and R.M. Mayer, Phil—. Mag. 19, 721(1969).
[13] M. Kiritani, J. Phys. Soc. Jpn, 35, 95(1973).
[14] M.R. Hayns, J. Nucl. Mater. 56, 267(1975).
[15] B.O. Hall and D.I. Potter, in *Proceedings of the 9th International Symposium* on *Effects of Radiation* on *Structural Materials*, ASTM-STP-683 (ASTM, Richland, WA, 1978) p. 789.
[16] Koiwa, J. Phys. Soc. Jpn, 37, 1532(1974).
[17] N.M. Ghoniem and D.D. Cho, Phys. Status Solidi A 54, 1971 (1979).
[18] N.M. Ghoniem, J. Nucl. Mater. 89, 359(1980).
[19] G. Nicolis and I. Prigogine, *Self-Organization* in Non-Equilibrium *Systems* (Wiley, New York, 1977) p. 243.
[20] J.A. Sprague, K.C. Russell, and Y.H. Choi, in Proceeding, *of* the Conference on *Fundamental Aspects of* Radiation *Damage* in *Metals*, M.T. Robinson and F.W. Young, Eds., CONF-751006-P2 (NTIS, Springfield, VA, 1975) p. 1181.
[21] W.G. Wolfer, L.K. Mansur and J.A. Sprague, in *Proceedings of International* Conference on Radiation *Effects* in Breeder Reactor *Structural Materials*, *M.* Bleiberg and J.W. Bennet, Eds. (AIME, Scottsdale, AZ, 1977), p. 841.
[22] B.O. Hall, J. Nucl. Mater. 91, 63(1980).
[23] N.M. Ghoniem and S. Sharafat, J. Nud. Mater. 92 (121), (1980).
[24] H. Trinkaus and H. Ullmaier, Philos. Mag. A 39, 563(1979).
[25] Lord Rayleigh, Philos. Mag. 32, 424(1891).
[26] A. Einstein, Ann. Phys. 19, 371(1905).
[27] A.D. Fokker, Ann. Phys. 43, 810(1914).
[28] M. Planck, Sitzber. Preuss. Akad. Wissensch., 324(1917).
[29] H.A. Kramers, Physica (Utrecht) 7, 284(1940).
[30] J.E. Moyal, J. R. Stat. Soc. B 2, 150(1949).
[31] N.G. Van Kampen, Can. J. Phys. 39, 551(1961).
[32] H. Gurol, Trans. Am. Nucl. Soc. 27, 264(1977).
[33] I. Oppenheim, K.E. Schuler and G.H. Weis, Adv. Mol. Relaxation Processes, 1, 13(1967-68).
[34] C.F. Clement and M.H. Woad, J. Nucl. Mater. 89, 1(1980).
[35] H. Trinkaus, Phys. Rev. B 27, (12) 7372(1983).
[36] K. Kitajima, N. Yoshida and E. Kuramoto, J. Nucl. Mater. 103 & 104, 1355(1981).
[37] K. Kitajima, E. Kuramoto and N. Yoshida, J. Nucl. Mater. 108 & 109, 267(1982).
[38] K. Kitajima, J. Nud. Mater. 133 *k* 134, 64(1985).
[39] K. Kitajima, Y. Akashi and E. Kuramoto, J. Nucl. Mater. 133 *k* 134, 486(1985).
[40] P. Chou and N. Ghoniem, J. Nud. Mater. 117, 55(1983).
[41] P. Chou and N. Ghoniem, J. Nucl. Mater. 137, 63(1985).
[42] W. Schilling and K. Schroeder, in *Consultant Symposium* on the *Physics of Irradiation Produced Voids*, R.S. Nelson, Ed., AERE Harwell Report, AERE-R7934 (1975) p. 212.
[43] P. Sigmund, Phys. Rev. 184, 383(1969).
[44] C.F. Clement and M.H. Wood, Proc. R. Soc. London, Ser. A 368, 521(1979).
[45] M.G. Kendall and A. Stuart, *The* Advanced Theory *of Statistics* (3rd edition), Vol. I, Ch. 3, (Charles Griffith & Co., London, 1969) p. 73.
[46] P. Chou and N.M. Ghoniem, Nucl. Instrum. Methods in Phys. Res. B 23, (1987)175.

FUTURE WORK

Higher order moments will be evaluated for the loop distribution function in order to ascertain the validity of finite moments representation.

THE INFLUENCE OF NICKEL CONTENT ON THE SWELLING OF Fe-Cr-Mn-Ni ALLOYS

F. A. Garner (Pacific Northwest Laboratory) and H. Takahashi (University of Hokkaido)

OBJECTIVE

The object of this effort is to determine the nature of the driving forces which tend to destabilize the austenite and to promote changes in dimensions in the Fe-Cr-Mn austenitic alloy system during irradiation.

SUMMARY

The density changes measured in three separate series of Fe-Cr-Mn-Ni austenitic alloys irradiated in FFTF-MOTA Cycle 1D indicates that nickel additions do not decrease swelling as had been anticipated. These data are contrary to the behavior observed in electron irradiation of one of these three alloy series.

PROGRESS AND STATUS

Introduction

The irradiation-induced swelling and phase stability of simple Fe-Cr-Mn austenitic alloys has been reported in earlier publications.[1-4] In general. it has been shown that the swelling of these alloys is less sensitive to composition than are comparable Fe-Cr-Ni alloys. It was also shown that a greater degree of phase instability exists in the Fe-Cr-Mn system. The differences in these two facets of alloy behavior are thought to arise partially from the different influence of nickel and manganese on vacancy diffusion and also from their different impact on austenite stabilization. In particular. it was shown that relatively slow-diffusing nickel segregates at sinks while faster-diffusing manganese migrates away from microstructural sinks. The out-migration of manganese leads to nucleation of ferritic phases while nickel segregation keeps the various microstructural sinks safely within the austenite regime.

Nickel additions are known to delay void nucleation in the Fe-Cr-Ni system[5] and, as shown in Figure 1, electron irradiation studies of Fe-17Cr-19Mn-XNi alloys have shown a similar behavior.' In order to study the interactive effects of nickel and manganese, three sets of Fe-Cr-Mn-Ni austenitic alloys were irradiated in FFTF-MOTA. The motivation for studying these alloy systems was not only to see if nickel additions reduce swelling but also to ascertain whether the simultaneous segregation of nickel and the out-migration of manganese at sinks would balance and thereby promote an increased level of phase stability.

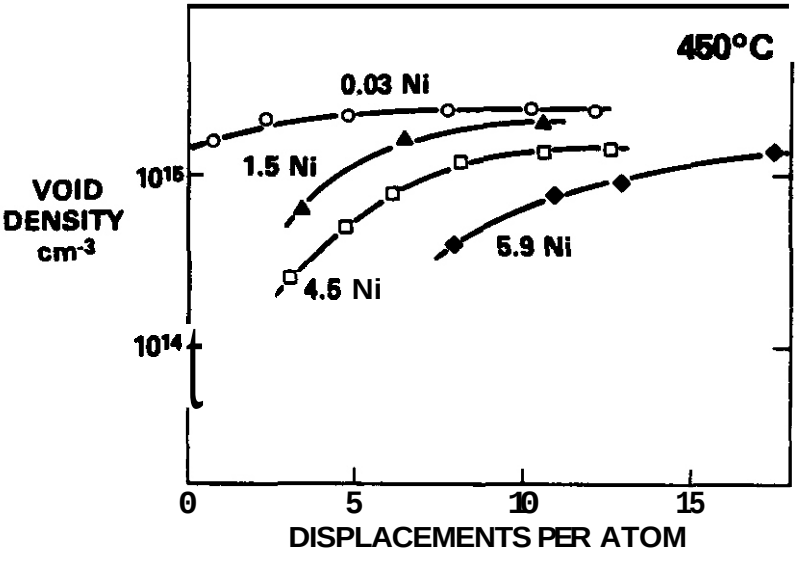

Fig. 1. Effect of nickel level on void nucleation in 1.3 MeV electron irradiatlon of Fe-17Cr-19Mn-XNi alloy series at 450°C. The primary effect of nickel is to delay void nucleation and extend the transient regime of swelling.

Experimental Details

The first set of alloys is identical to those irradiated earlier with electrons,[6] being Fe-17Cr-19Mn-XNi with 0.5Si, 0.02P, 0.10C and 0.16N. These alloys contained relatively low nickel levels (≤5.9 wt%) and were irradiated in the annealed condition (1030°C for 0.5hr. and air cooled).

The second and third sets contained larger levels of nickel and were simple quaternary alloys based on Fe-15Cr-15Mn-XNi and Fe-30Mn-10Cr-XNi. These alloys were also irradiated in the annealed condition. The compositions of all three alloy series are shown in Table 1.

Table 1. Composition of Alloys (Wt%)

Series 1*

Fe-16.83Cr-19.49Mn-0.03Ni-0.54Si-0.10C-0.020P-0.162N

Fe-16.59Cr-18.87Mn-1.47Ni-0.55Si-0.10C-0.019P-0.164N

Fe-16.95Cr-19.08Mn-5.90Ni-0.52Si-0.10C-0.022P-0.099N

Series 2**

Fe-15Cr-15Mn

Fe-15Cr-15Mn-5Ni

Fe-15Cr-15Mn-10Ni

Fe-15Cr-15Mn-ENi

Series 3**

Fe-10Cr-30Mn

Fe-10Cr-30Mn-5Ni

Fe-10Cr-30Mn-10Ni

Fe-10Cr-30Mn-15Ni

* All with 0.006S, 0.05-0.07Cu and 0.01-0.03Mo
** Nominal Canposition

All alloys were prepared in the form of microscopy disks 3mm in diameter by 0.25mm thick and irradiated in static sodium in MOTA 10 of the Fast Flux Test Facility (FFTF) at ~$3X10^{-6}$ dpa sec^{-1} using the Materials Open Test Assembly (MOTA) which nominally controls the temperature to ±5°C. There was one abnormal temperature event of approximately one hour duration during the MOTA 10 irradiation. the details of which are shown in Table 2. The range of neutron spectra over this assembly produces approximately 5 dpa for each $1.0X10^{22}$ ncm^{-2} (E>0.1 MeV); the estimated dpa levels reached are also included in Table 2. The bulk swelling levels were measured using an immersion density technique which is accurate to 0.15% change In density.

Table 2. Temperature and Fluence Histories for MOTA ID

Nominal Temperature (°C)	Displacement Exposure (dpa)	Off-Normal Events*
420	a	None
470	17	657°C for 70 Min.
550	20	749°C for 50 Min.
650	18	928°C for 50 Min.

• These events occurred at displacmnt levels which were -53% of the total exposures quoted above.

Results and Discussion

The swelling (calculated from density change) measured in these three alloy series is shown in Figures 2 and 3. Contrary to our expectations. the effect of nickel additions is not to delay swelling but to increase it initially. While further nickel increases were sometimes found to decrease swelling. it was only at relatively high nickel levels. These results may not actually be In conflict with the data shown in Figure 1, however. Note that the electron irradiation experiment was conducted at 450°C and at a displacement rate of $2X10^{-3}$ dpa/sec. One assumes that a "temperature shift" arising from differences in displacement rate is necessary to correlate the neutron and electron irradiation data. these two experimnts may not have been operating at comparable temperatures.

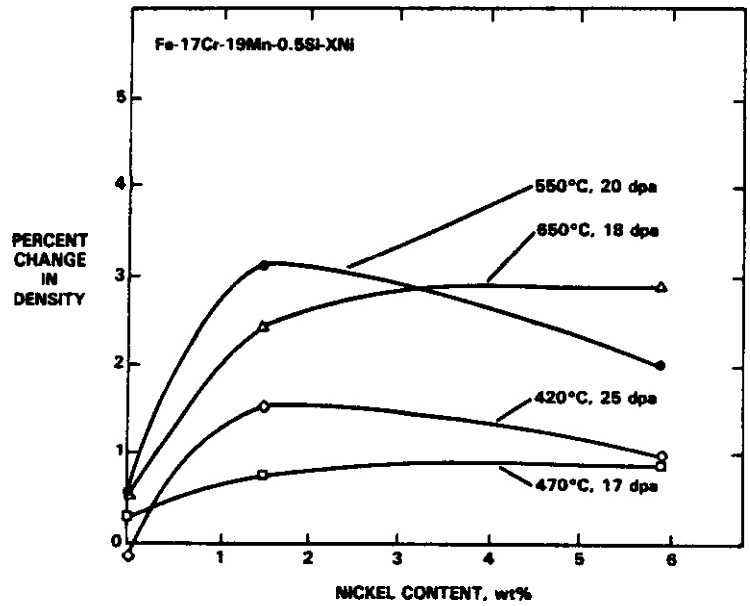

Fig. 2. Neutron-induced swelling of Fe-17Cr-19Mn-XNi alloy series irradiated in FFTF-WTA.

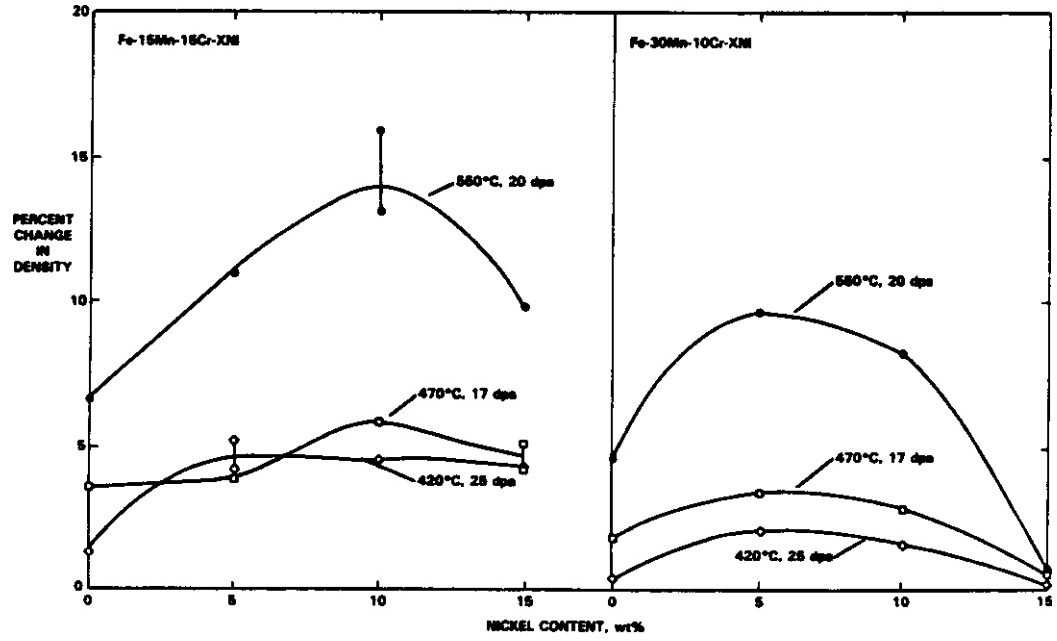

Fig. 3. Neutron-induced swelling in Fe-15Mn-15Cr-XNi and Fe-30Mn-10Cr-XNi alloy series irradiated in FFTF-WTA.

The lower swelling of the first alloy series compared to that of the second and third series is thought to reflect primarily the presence of silicon and other solutes.

The lack of agreement of these data with our expectation derived from electron irradiation studies signals that once again this alloy system is different from that of the simple Fe-Cr-Ni system and requires further study prior to development of a low-activation alloy based on the Fe-Cr-Mn austenitic system. While nickel per se must be reduced or removed to meet current low-activation guidelines. the interplay between nickel and manganese may teach us much about the nature of the driving forces tending to destabilize the Fe-Cr-Mn alloy system during irradiation.

The impact of the one hour temperature increase experienced halfway through this experiment is not thought to have affected these results very much. First. the trends observed with nickel content were the same for all four irradiation temperatures. even though the over-temperature event did not affect the 420°C capsule. Second. the over-temperature event also occured to other subcapsules which experienced irradiation in MOTAs 1B, 1C and 1D. When data on Fe-Cr-Mn alloys from those capsules were plotted, there were no discontinuities observed.[4] Third, the trends with nickel and chromium content observed in series 2 and 3 are consistent with those observed in Fe-Cr-Mn alloys at 16 dpa without an over-temperature event. probably reflecting the fact that the temperature-sensitive void nucleation stage occurs very early in these simple alloys.[1]

FUTURE WORK

These specimens will be shipped to Japan for microscopy examination.

REFERENCES

1. F. A. Garner. H. R. Brager. D. S. Gelles and J. M. McCarthy. J. Nucl. Mat., 148 (1987) 294-301.

2. F. A. Garner, F. Abe and T. Noda, J. Nucl Mat., 154-156 (1988), in press.

3. J. M. McCarthy and F. A. Garner. J. Nucl. Mat., 154-156 (1988), in press.

4. F. A. Garner and H. R. Brager. pp. 195-206 in "Radiation-Induced Changes in Microstructure," 13th International Symposium, ASTM STP 955, F. A. Garner, N. H. Packan and A. S. Kumar. Eds., American Society for Testing and Materials. Philadelphia. 1987.

5. F. A. Garner and A. S. Kumar, pp. 289-314 in Reference 4.

6. H. Takahashi. T. Takeyama, K. Tanikawa and R. Miura, J. Nucl. Mat., 133-134 (1985) 566570.

6. DEVELOPMENT OF STRUCTURAL ALLOYS

6.1 Ferritic Stainless Steels

EFFECTS OF IRRADIATION ON LOW ACTIVATION FERRITIC ALLOYS, A REVIEW - D. S. GELLES (PACIFIC NORTHWEST LABORATORY)

OBJECTIVE

The objective of this work is to determine the applicability of low activation ferritic alloys as fusion reactor structural materials. The manuscript was prepared for the Symposium - Reduced Activation Alloys for Fusion Service.

SUMMARY

A broad range of ferritic alloys is possible which satisfy the low activation requirement for near-surface burial of fusion reactor materials after decommissioning. Low activation bainitic alloys in the Fe-2Cr canposition range, martensitic alloys in the Fe-7 to 9Cr range and stabilized martensitic alloys in the Fe-12Cr range have been successfully fabricated and are undergoing testing as demonstrated by efforts in Europe, Japan and the United States. However, it is found that irradiation significantly degrades the properties of bainitic and stabilized martensitic alloys. Bainitic alloys containing vanadium develop severe hardening due to irradiation-induced prscipitation at tmperatures below 450°C and extreme softening due to carbide coarsening at temperatures above 500°C. Stabilized martensitic alloys which rely on manganese additions to provide a fully martensitic microstructure are embrittled at grain boundaries following irradiation leading to severe degradation of impact properties. The most promising composition regime appears to be the Fe-7 to 9 Cr range with tungsten additfons in the 2% range where high temperature mechanical properties and microstructural stability are retained and impact properties are relatively unaffected by irradiation.

PROGRESS AND STATUS

Introduction

The effort to develop special low activation ferritic or martensitic steels for fusion reactor applications is international. Laboratories in Japan, Britain and the U.S. are each designing. fabricating and testing alloys which would increase the acceptability of fusion power by decreasing the quantity of highly activated material. A call for development of such alloys originated with the US Department of Energy (DOE) Panel on Low Activation Materials for Fusion Applications.[1] The panel noted that "lower activation materials for fusion reactors are technically possible. may be important to the public acceptance of fusion energy, and should be a main goal of the fusion program." for low activation. only minor changes in canposition appear to be required. The element additions which must be carefully controlled are Cu, Ni. Mo, Nb and N, with Nb representing the most severe restriction.[2-5] Alternately. isotopic tailoring could in principle, Provide equivalent performance. For example. HT-9, a 12 Cr martensitic steel under study for fusion applications. could be made acceptable if Mo additions could be isotopically tailored.[6]

The alloy compositions being considered for low activation ferritic or martensitic steels are based on two commercially important alloy classes: 2 1/4 Cr steels and the super 9 to 12 Cr steels. The former is. in fact, a bainitic class and the latter a martensitic class. Both of these steels contain Mo at levels of about 1%. Therefore. design of low activation alternatives requires substitution for Mo. W and V are leading candidates, with consideration given for using Ta as a substitute for Nb. In order to obtain a fully martensitic 12 Cr steel without additions of Ni, austenite stabilizing additions must be included. Mn and C have thus far been considered. Therefore, three classes of low activation ferritic/martensitic alloys are possible: la, chranium bainitic alloys, 7 to 9 Cr martensitic alloys and 12 Cr stabilized martensitic alloys. The alloy compositions which have been considered are given in Table 1, and. for canparison. examples of similar cmercial alloys are given in Table 2. The alloys in Table 1 have been grouped by canposition in order to emphasize the similarities between the approaches taken at different laboratories. Examination of Table 1 shows that the 7 to 9 Cr alloy class and the 12 Cr alloy class are about equal in size and the smallest group is the 2 Cr range. In each class, each of the alloying approaches have been tried: W substituted for Mo. V substituted for Mo and small additions of Ta substituted for Nb (except that Ta additions have not been added in the 2 Cr alloy class). However, in many cases, the higher Cr alloys were found to be duplex martensitic/delta ferritic and. therefore, further changes in composition specification were needed.

The effect of fast neutron irradiation on microstructure and properties has been examined for each of the alloy classes with V additions. for the two high chranium classes with W additions, and, to a certain

Table 1. Compositions of Lon Activation Alloys (in weight percent)

Alloy	Cr	W	V	C	Si	Mn	Ta	B	N	P	S	Ref
2Cr-2W	2.06	1.96	--	0.10	0.29	0.50			.001	<.002	.004	7
2CrV	2.36	--	0.25	0.11	0.17	0.40						8
2Cr-1WV	2.30	0.93	0.25	0.10	0.13	0.34						
2Cr-2W	2.48	1.99	0.01	0.11	0.15	0.39						
2Cr-2WV	2.42	1.98	0.24	0.11	0.20	0.42						
L1 2CrV	2.32	<.01	0.50	0.09	0.08	<.01			.004	<.005	.003	8
L2 2Cr-1V	2.82	<.01	1.01	0.09	0.08	<.01			.003		.002	
L3 2Cr-1VMn	2.46	--	1.50	0.11	0.30	0.30			.015	<.005	.015	
5Cr-2W	4.84	1.98	--	0.10	0.30	0.50			.002	<.002	.004	7
5Cr-2WV	5.00	2.07	0.25	0.13	0.25	0.47						8
F-82	7.52	2.2	0.19	0.10	0.17	0.49	--	.0035	.002	.003	.002	9
F-82H	7.65	2.0	0.18	0.09	0.09	0.49	0.04	.0034	.002	.005	.001	
9Cr-2W	8.92	1.92	--	0.10	0.28	0.48			.002	<.002	.003	7
9Cr	8.96	--	--	0.10	0.30	0.49			.001	"	.003	
9Cr-1W	9.01	0.99	--	0.10	0.29	0.48			.002	"	.004	
9Cr-2W	8.92	1.92	--	0.10	0.28	0.48			.002		.003	
9Cr-4W	9.09	3.93	--	0.10	0.29	0.50			.002		.002	
9Cr-.25V	8.82	--	0.26	0.13	0.30	0.46			.019		.002	
9Cr-.5V	8.86	--	0.53	0.11	0.29	0.48			.020	"	.003	
9Cr-1V	8.72	--	1.03	0.12	0.31	0.51			.018		.003	
9Cr-2WV	8.73	2.09	0.24	0.12	0.25	0.51						8
9Cr-2WVTa	8.72	2.09	0.23	0.10	0.23	0.43	0.075					
GA3X nom.	9	2.5	0.3	0.15	--	--					--	8
melt	7.5	1.95	0.02	0.17		.002					.005	
GA3X	9.00	2.0	0.30	0.15	0.06	0.04			0.002	.001	.001	10
GA5X	8.92	2.1	0.30	0.15	0.05	0.04			"	"	.002	
LA12	9.1	0.68	0.24	0.16								11
LA13	9.2	2.90	0.25	0.17								
LA13	9.22	2.90	0.25	0.17	0.42	0.74	--		.059			12
LA13Ta	9.0	2.96	0.25	0.18	0.04	0.70	0.11		.045			
LA12	9.1	0.68	0.24	0.16	0.37	0.79	--		.06			
LA12Ta	9.8	0.85	0.27	0.16	0.03	0.80	0.10		.042			
LA12TaLN	9.1	0.77	0.25	0.17	0.02	0.74	0.10		.004			
LA12LC	9.0	0.76	0.38	0.09	0.03	1.01	--		.033			
LA12TaLC	8.9	0.76	0.39	0.09	0.03	1.01	0.09		.019			
L4 9CrV	9.13	0.01	0.52	0.10	0.09	0.02			.003	<.005	.003	8
L6 9Cr-1V	9.14	0.02	1.23	0.20	0.09	1.08			.003	"	.003	
L5 9CrV	9.02	0.01	0.51	0.10	0.09	2.68			.003	"	.003	
L7 9CrlWV	8.82	0.89	0.27	0.10	0.10	2.44			.002		.004	
LA2	11.4	<.02	0.26	0.16								11
LA3	11.5	0.24	0.25	0.16								
LA4	10.9	0.65	0.25	0.17								
LA5	10.9	1.12	0.24	0.16								
LA6	11.7	1.95	0.24	0.15								
LA7	11.2	3.04	0.23	0.17								
LA8	11.1	0.66	0.46	0.16								
LA9	11.7	0.77	0.80	0.15								
LA10	11.4	0.70	0.25	0.16				0.0083				
LA11	11.2	0.69	0.25	0.16					0.103			
LA14	11.4	2.94	0.25	0.17			0.19		0.04			
LA7	11.3	2.94	0.25	0.17	0.26	0.76	--		.059			12
LA7Ta	11.4	2.90	0.25	0.15	0.07							
LA7TaLN	11.1	2.95	0.24	0.18	0.04	0.70	0.10		.005			

Table 1 (Cont'd)

Alloy	Cr	W	V	C	Si	Mn	Ta	B	N	P	S	Ref
L8 12CrlV	12.19	<.01	1.05	0.09	0.10	6.47			.003	<.005	.005	8
L9 12CrlWV	11.81	*0.89*	0.28	**0.10**	0.11	6.47			.003	"	.005	
12CrlWVTa	11.96	*0.82*	0.23	0.09	0.10	6.56	0.14		.008	<.005	.004	13
12CrlWVTa	11.95	**0.80**	0.25	0.10	0.09	6.45	0.20		.003	<.005	.006	
12CrlVWTa	11.80	0.22	0.97	0.10	0.10	7.84	*0.23*		.005	<.005	.006	
12Cr-2WV	11.49	2.12	**0.23**	0.10	0.24	0.46						8
12Cr2WV3Mn	11.23	1.79	0.21	0.08	0.23	2.76						14
12Cr2WV6Mn	10.86	1.97	0.21	0.08	**0.20**	5.57						
1Cr2WV	11.52	1.83	0.22	0.17	0.20	0.40						
GA4X nom.	11	2.5	0.3	0.15								8
melt	10.2	1.1	**0.2**	0.01	--	.011					<.003	
GA4X	11.0	**2.0**	0.30	0.14	0.05	0.04			,002	.001	.001	10
GA6X	11.1	2.1	0.30	0.15	0.07	0.04			"	"	.002	
12Cr-2W	11.56	1.96	--	0.10	**0.32**	0.49			.001	<.002	.003	7
15Cr-2W	14.72	1.94	--	0.11	0.30	0.49			.001	"	.003	

nom. - nominal canposition
melt - actual melt canposition

Table *2*. Examples of Commercial Alloy Compositions Similar to Low Activation Ferritic Alloys.

	Composition (weight percent)										
Alloy	Cr	Mo	C	Mn	Ni	V	Si	Nb	W	e	S
2 Cr-1Mo	2.25	1.0	0.09	0.45	--	<.03	0.20	--	--	<.015	<.015
T91	8.43	**0.89**	0.09	0.37	0.11	0.24	0.16	0.08	--	.011	.004
FV 448	11.3	0.66	0.15	--	0.75	0.25			<0.02		
HT-9	11.80	1.02	**0.21**	0.50	0.58	**0.32**	0.22	--	0.50	.007	.003

extent. for the 12 Cr manganese stabilized steels with Ta additions. The purpose of this paper is to Summarize the similarities and differences of alloy response to neutron irradiation in order to provide a basis for selecting the optimum low activation ferritic alloy canposition for fusion reactor applications.

Summary of Results

Studies of the effect of irradiation on low activation ferritic alloys have included uniaxial tensile tests following irradiation to fluences as high as 45 dpa,[15,16] Charpy impact tests following irradiation at 365 C to 15 dpa[17] and microstructural examinations following irradiation to 45 dpa.[15,16,18] These results can now be augmented with preliminary observations by the author of microstructural response following irradiation to 115 dpa. The alloys examined included *2* Cr steels with V additions (L1, L2 and L3 in table 1), 7 to 9 Cr steels with V or W additions (L4 to L7, GA3X and GA4X in table 1) and 12 Cr steels. stabilized with Mn and with V or W additions (L8 and L9 in Table 1). All data were obtained from specimens irradiated in the Fast Flux Test Facility (FFTF), Richland, Washington. which is a liquid metal test reactor equipped with a fully instrumented Materials Open Test Assembly (MOTA). Although the transmutation reactions that would be produced by high energy neutrons in a fusion reactor environment are absent, MOTA irradiations should provide useful data on relative phase stability and swelling sensitivity.

The results shaing the effect of irradiation on tensile properties a5 a function of dose at 420 and 585°C are sumnarized in Figure 1. Specimens were a miniature sheet geanetry: 2.5 *cm* overall length. 0.15 an wide. 0.075 an thick and with a gauge section of 0.75 *cm*. At 420°C, specimens were tested following

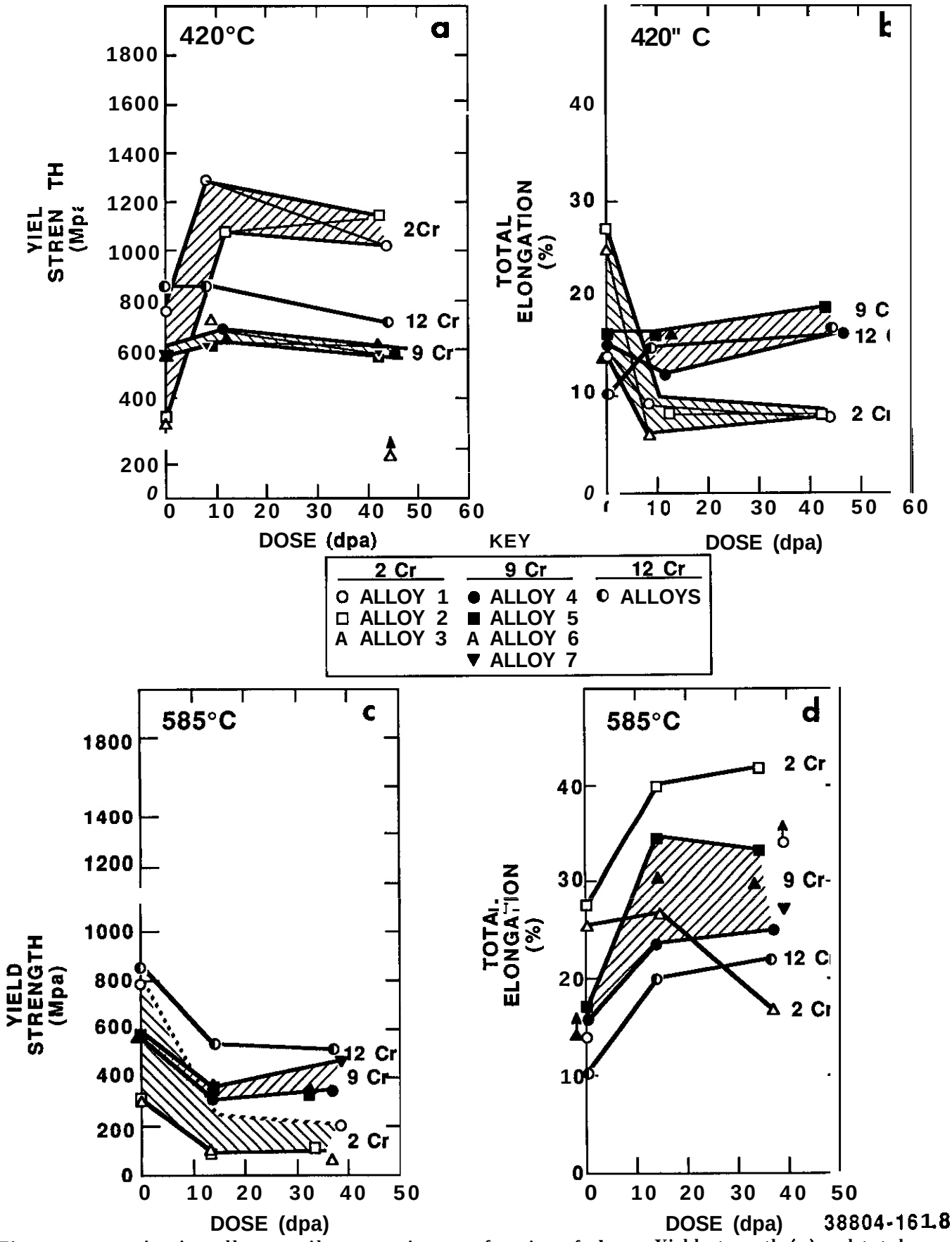

Fig. 1. Low activation alloy tensile properties as a function of dose. Yield strength (a) and total elongation (b) following irradiation at 420°C and yield strength (c) and total elongation (d) following irradiation at 585°C are shown.

irradiation to 10 and 40 dpa. The results showed three distinctly different responses in the three alloy classes. The low chromium bainitic alloys exhibited large increases in yield strength and corresponding decreases in elongation following irradiation to 10 dpa. Irradiation to higher dose produced moderate softening. In canparison. the 9 and 12 Cr steels showed only minor changes in strength and elongation as a function of dose. However. the 12 Cr steels provided higher inherent strength. After irradiation at 585 C, all alloys became weaker and gave increased elongation. However, the 2 Cr steels all showed the weakest response, with saturation in properties by 13 dpa. The 9 Cr steels gave intermediate yield strength values. The evidence of minor increases in strength in 9 Cr alloys following the decreases observed at 13 dpa are probably misleading because alloy 7 was not tested at 13 dpa. The 12 Cr steel was the strongest. but underwent decreases in strength similar to the 9 Cr response. However. in the case of alloy 7, Fe-9Cr-1W, the strength at 38 dpa was similar to that of the 12 Cr steel. Therefore, 9 Cr steels can be designed to provide high temperature strength similar to those of 12 Cr steels but 12 Cr steels appear to have the best tensile properties.

The effect of irradiation on OBTT Charpy response is summarized in Figure 2 and in Table 3. Figure 2 shows Charpy impact curves for one third size precracked miniature Charpy specimens before and after irradiation to 10 dpa at 365°C. The data are arranged according to Cr content; the 2 Cr steel in Figure 2a, the 7 to 9 Cr steels in Figure 2b and the 12 Cr steels in Figure 2c. From Figure 2, it is apparent that the 7 to 9 Cr steels are better behaved than the 2 or 12 Cr steels. The shift in ductile-to-brittle transition temperature (DBTT) due to irradiation is much smaller and the initial upper shelf energies (USE) are generally higher. Therefore, the larger decrease observed in USE due to irradiation for 9 Cr steels is of little consequence. The shift in DBTT for the 12 Cr stabilized steels is much larger. and. for the 2 Cr steel. the DBTT following irradiation was above the capability of the test apparatus. The tabulation of results in Table 3 demonstrates that the 7 to 9 Cr steels gave shifts in DBTT due to irradiation of 20 to 60°C whereas 12 Cr stabilized steels gave shifts on the order of 200°C (and the 2 Cr steel shift could not be measured). In all cases where results were obtained, the decrease in USE was of little concern. Therefore. based on DBTT response, the 7 to 9 Cr alloy class is superior.

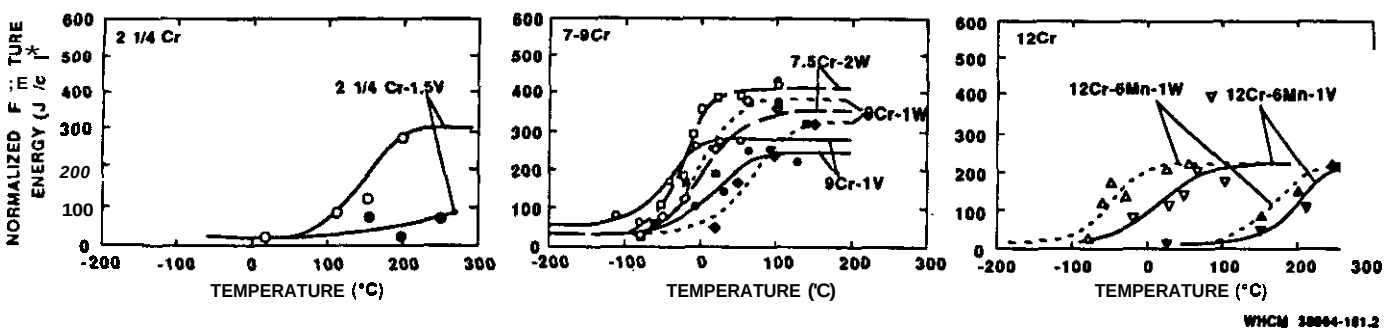

Fig. 2. Normalized fracture energy as a function of test temperature for one-third size precracked Charpy specimens of (a) 2-1/4 Cr steel. (b) 7 to 9 Cr steels and (c) Mn stabilized 12 Cr steels. In each case. the behavior following irradiation to 10 dpa at 365°C (closed symbols) can be canpared with the control behavior (open symbols).

Fractographic examinations have been performed on several of the specimens for which results are shown in Figure 2. The examinations revealed that. in several cases. the brittle fracture mode changed from transgranulzr cleavage to intergranular cleavage as a result of irradiation. However. ductile failure remained transgranular. This is shown in Figure 3 which provides canparison of unirradiated and irradiated specimen fracture surfaces adjacent to the fatigue precrack for test temperatures near the DBTT. In each case, the precrack was on the left, but the brittle fracture surface fills most of the fractograph. Figure 3a compares unirradiated and irradiated 2Cr-1.5V and shows that brittle fracture appearance is unaffected by irradiation. Figure 3b, c and d provide similar canparison of 7Cr-2W, 9Cr-1V and 9Cr-1WV. For the 7 Cr alloy, brittle fracture in both unirradiated and irradiated specimens is by transgranular cleavage, whereas in the 9 Cr alloys, the fracture mode changes from predominantly brittle transgranular cleavage in unirradiated specimens to predaninantly intergranular cleavage following irradiation. Therefore, although the Charpy response in the 9 Cr alloys was not greatly affected by irradiation, a change in fracture mode did occur. indicating that irradiation weakened grain boundary cohesion in canparison with the grain interiors. Figures 3e and f provide similar comparisons for 12Cr-6Mn-1V and 12Cr-6Mn-1WV steels respectively. In both cases, brittle failure is largely by trans-granular cleavage for unirradiated Specimens but is due to cleavage at grain boundaries following irradiation. However, the observation that no change in fracture mode occurs for the 7Cr-2W alloy indicates that excess tungsten is probably not responsible. A more likely explanation is that manganese additions are responsible, as has been shown in a similar alloy series.[19]

Microstructural examinations have been performed on low activation ferritic alloys following irradiation at test temperatures fran 365 to 600°C and to doses as high as 115 dpa. The specimen matrix consisted of alloys L1 to L9 irradiated at ~420°C to 9.8, 43 and 114 dpa, at 420°C to 14 dpa and 600 C to 34 dpa[15,16] and of alloys GA3X and GA4X following irradiation at 365 C to 11 dpa, at 426 C to 33 dpa, to 520°C to 34 dpa. and to 600°C to 34 dpa.[18] Examinations have shown that low activation ferritic alloys are affected by radiation over the full range of temperatures examined. Following irradiation at 365 and

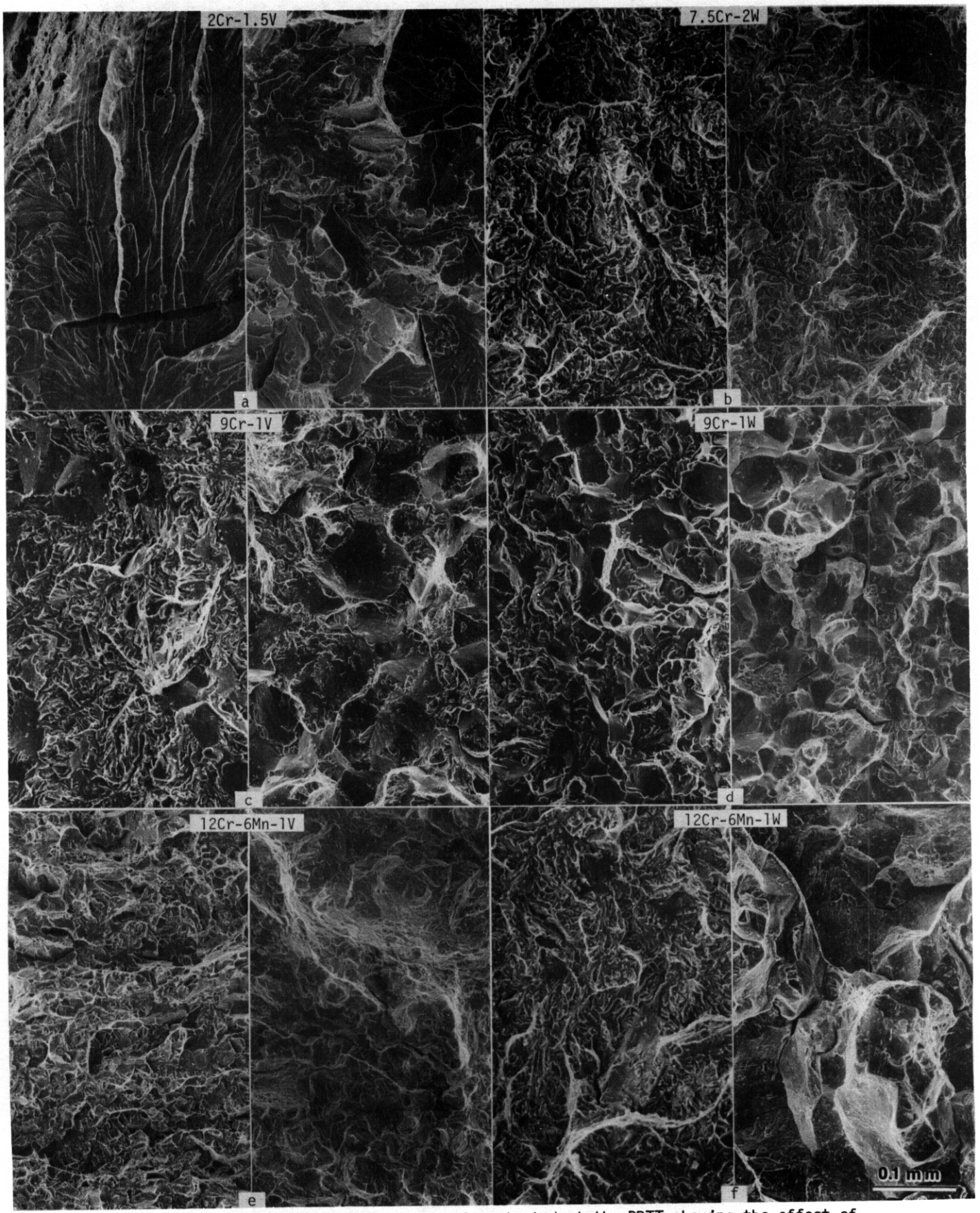

Fig. 3. Fracture surfaces of selected charpy specimen tested at the DBTT showing the effect of irradiation to 10 dpa at 365 ℃ (on right) for a) 2Cr-1.5V steel L3, b) 7.5Cr-2W steel GA3X, c) 9Cr-1V steel L5, d) 9Cr-1W steel L7, and e) 12Cr-6Mn-1V steel L8 and f) 12Cr-6Mn-1WV steel L9.

Table 3. Summary of DBTT Behavior in Low Activation Ferritic Alloys Following Irradiation at 365°C to 10 dpa[17].

Alloy	Code	Control DBTT (°C)	Irrad. DBTT (°C)	Shift in DBTT (°C)	Control USE (J/cm^2)	Irrad. USE (J/cm^2)	Change in USE (J/cm^2)
2Cr-1.5V	L3	169	>250	na	308	na	na
7.5Cr-2W	GA3X	-24	0	24	405	345	-60
9Cr-1V	L5	-44	18	62	280	239	-40
9Cr-1W	L7	12	44	32	370	330	-40
12Cr-6Mn-1V	L8	10	200	190	201	201	0
12Cr-6Mn-1W	L9	-52	165	217	219	219	0

na : not available

420 C, dislocation evolution and precipitate development were found and several examples of irradiation induced void swelling were identified. Following irradiation at 520°C, effects of irradiation were not as apparent, but examples of void swelling and precipitate coarsening could be identified. Finally, following irradiation at 600°C, coarsening of both precipitate and martensite lath structures could be demonstrated.

The microstructural development at 365 and 420°C varied as a function of composition. Most notable was fine M_7C_3-type second phase precipitate development and void formation in 2Cr-V alloys, void formation in 7 to 9 Cr alloys and α' precipitate development, intermetallic precipitation and carbide coarsening in 12 Cr alloys.

Examination of 2Cr alloys following irradiation at 420°C showed extensive precipitation of rod shaped particles on the order of 25 nm long and 3 nm in diameter, and a<100> perfect dislocation loop formation (approximately 40 nm in diameter) even at doses as low as 10 dpa.[15] The precipitate was found to contain equal proportions of V and Cr and modest amounts of Fe,[16] but the crystal structure has not yet been determined. These microstructural changes were undoubtedly responsible for the large yield strength increases observed in the alloy class following irradiation at 420°C. Figure 4 has been prepared to show the precipitation and void swelling response in this alloy class following irradiation to 115 dpa. The microstructures are shown in void contrast as a function of V content. Swelling response is found to be very sensitive to the amount of V present; for levels of 0.5 and 1.0%, negligible swelling is found, but for 1.5% V, extensive swelling developed. Void formation was noted at fluences as low as 10 dpa in the 1.5 V alloy.[15] Therefore, void swelling resistance is imparted by additions of 0.5 to 1.0% V, probably

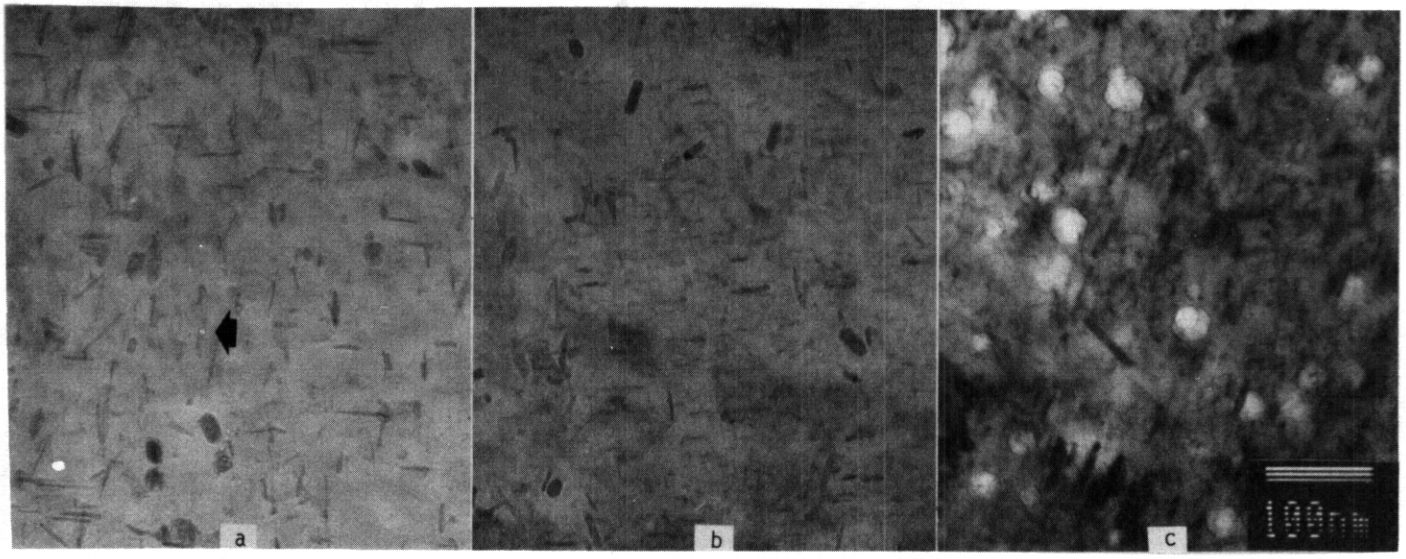

Fig. 4. Comparison of precipitate and void structures as a function of V content for specimens irradiated at 420°C to 115 dpa a) 2Cr-0.5V alloy L1, b) 2Cr-1V alloy L2 and c) 2Cr-1.5V alloy L3. The imaging conditions used in c) do not show the precipitate particles clearly

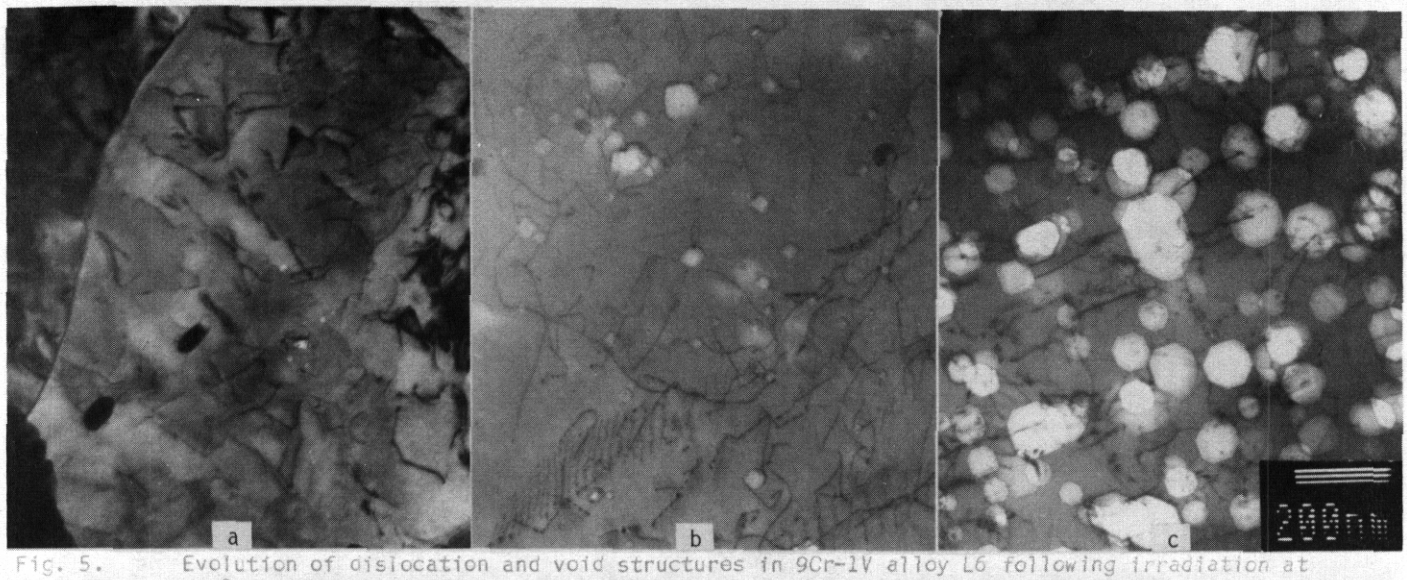

Fig. 5. Evolution of dislocation and void structures in 9Cr-1V alloy L6 following irradiation at 420°C to a) 10 dpa, b) 43 dpa and c) 114 dpa.

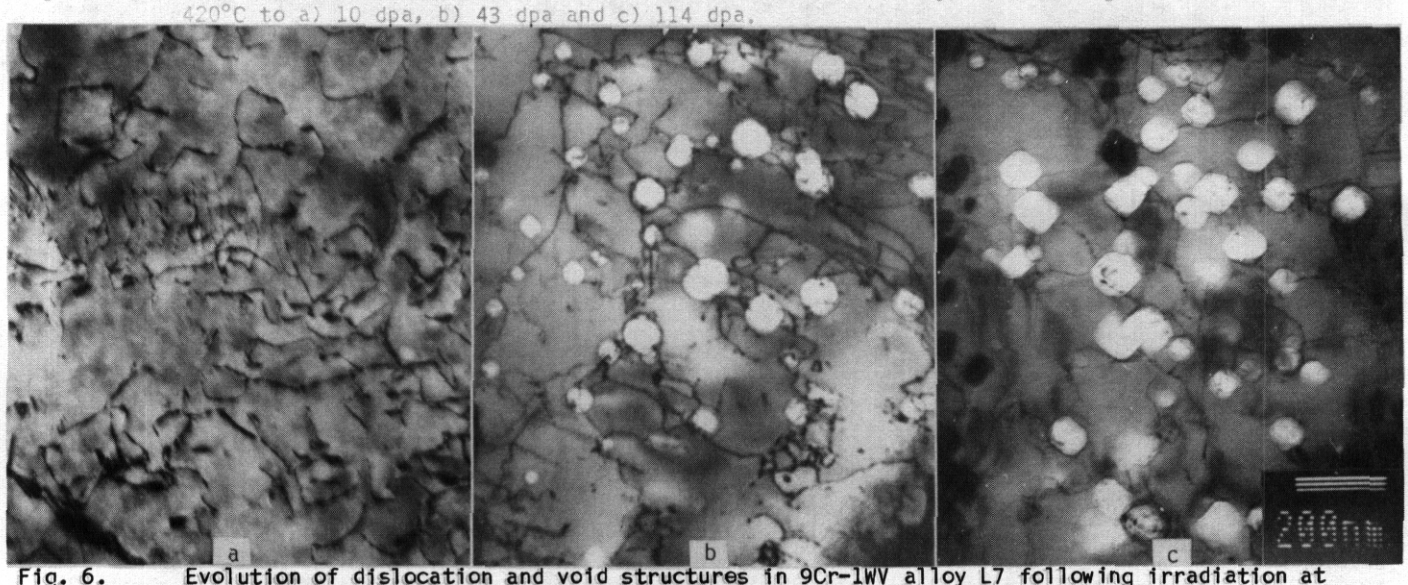

Fig. 6. Evolution of dislocation and void structures in 9Cr-1WV alloy L7 following irradiation at 420°C to a) 10 dpa, b) 43 dpa and c) 114 dpa.

Twelve Cr alloys were found to represent an intermediate case. Void swelling was found to develop after 40 dpa, and after 115 dpa swelling was extensive in the 12Cr-1V alloy L8, but still in the incubation stage in the 12Cr-1WV alloy L9. The precipitate structure included a fine distribution of equiaxed particles on the order 10 nm in diameter which were nonuniformly distributed from one martensite lath to the next. The precipitate was present after 15 dpa and remained stable with only minor coarsening to higher dose. It has been identified as Cr rich α' based on dark field imaging characteristics and similarities with behavior in other 12Cr steels.[21] Examples of these microstructures are provided in Figure 8 showing precipitate, void and dislocation structures within laths following irradiation to 43 dpa at 420°C. For example. Figure 8a shows the equiaxed precipitate nonuniformly

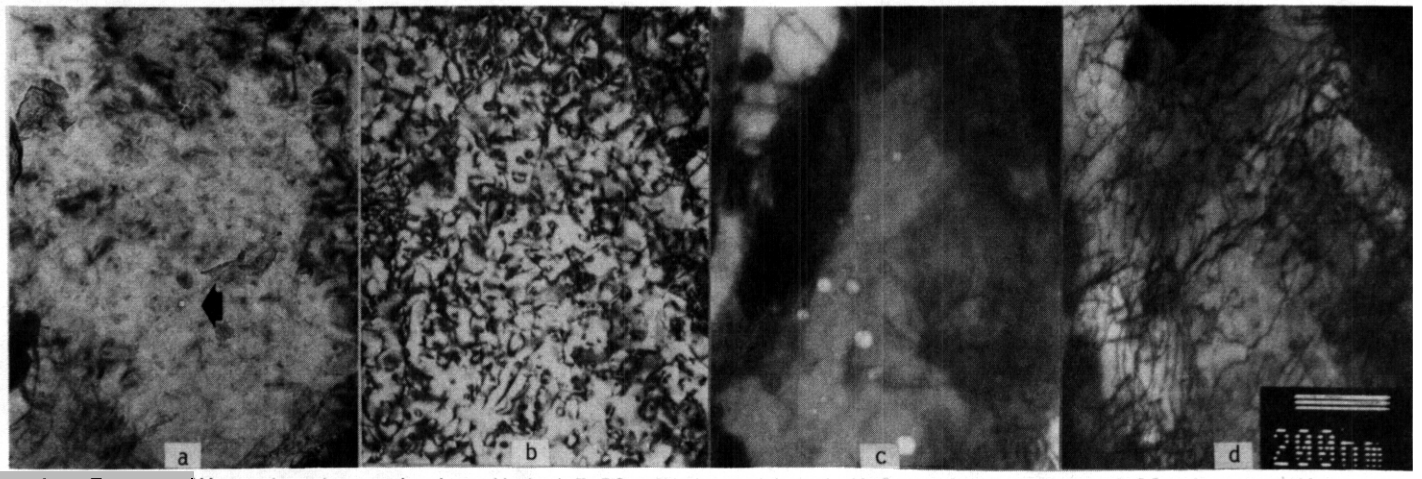

Fig. 7. Microstructures in irradiated 7.5Cr-2W in void and dislocation contrast following irradiation at 365°C to 11 dpa, a) and b), and following irradiation at 420°C to 34 dpa, c) and d).

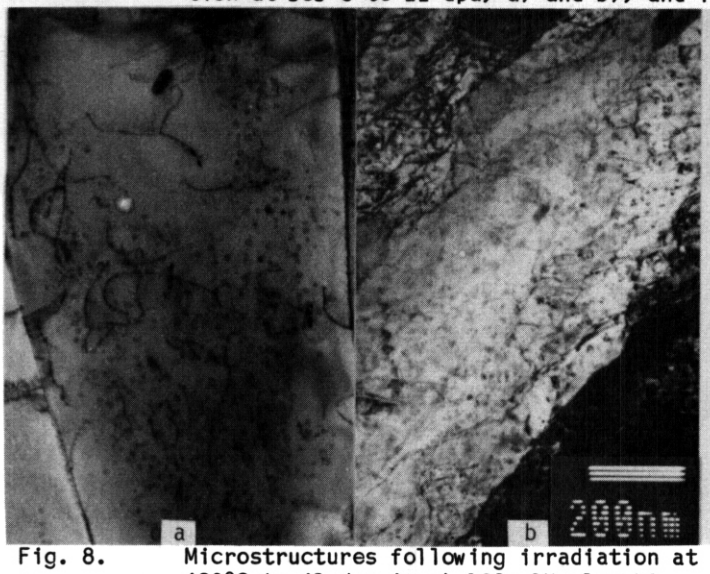

Fig. 8. Microstructures following irradiation at 420°C to 43 dpa in a) 12Cr-1V aloy L8 and in b) 12Cr-1WV alloy L9.

Fig. 9. Stacking fault features in 12Cr-1WV alloy L9 following irradiation at 600°C to 34 dpa in a) bright field contrast and b) matrix dark field contrast.

the distribution of particles is different in neighboring laths. Dislocation evolution has developed a network structure and in each micrograph one void can be identified. More difficult to identify was change to the lath boundary carbide distributions.

Fol1wing irradiation at 520°C, the alloys were found to be relatively unaffected by irradiation. No void swelling was observed in bainite or martensite and only a few examples of irradlation induced dislocation loops were found. The exception was in the case of GA4X, a 10Cr-1W alloy with negligible carbon and. therefore, containing mainly delta ferrite. where void and dislocation evolution was found near grain boundaries and where voids were generally elongated and associated with precipitate particles. In general, the carbide structure was similar to the pre-irradiation structure. However. canpositional analysis of extracted particles revealed unexpected phases and carbide compositions. The 2Cr-0.5V alloy developed a dominant precipitate phase equally rich in Fe and Cr with minor additions of V. Also. 9 and 12 Cr alloys containing W were found to have developed $M_{23}C_6$ compositions with W levels in the range 10 to 20 percent. The observation of void formation in GA4X indicates that W additions can enhance void swelling behavior.

All alloy microstructures were altered considerably due to irradiation at 600°C. The major effect was rearrangement of martensite lath boundaries into more equiaxed subgrain structures with concurrent carbide and subgrain coarsening. This coarsening was undoubtedly responsible for observed losses in strength. However, alloys containing high Mn had developed fault structures often in regions containing carbides. These structures were more prevalent in 12Cr-1WV. Examples of the faults are shown in Figure

9 with a region compared in bright field and matrix dark field contrast. A reasonable explanation is that the faults are stacking faults in austenite and. therefore, austenite is forming during Irradiation at 600°C. This explanation indicates that Mn additions on the order of 6 percent have the added disadvantage of lowering the A_{c1} temperature (the temperature at which one gets austenite on heating1 to below 600°C.

Discussion

Although only a small fraction of the alloy compositions listed In Table 1 has been tested or examined following fast neutron irradiation. sufficient information has been obtained to provide reasonable predictions of performance for each of the alloy classes. The important results obtained can be summarized as follows. The 2Cr-1V alloy class is inherently susceptible to precipitation hardening following irradiation at 420°C and to excessive softening following irradiation at 585°C. Based on observed behavior in 2 Cr-1Mo,[22,23] it can be anticipated that similar precipitation hardening will occur in 2Cr-1W alloy systems as well. Experiments are In progress to verify this point.[8] Therefore. although 2Cr-1W may provide better high temperature strength. it is not likely that sufficient improvements in performance will be obtained to make the 2Cr alloy class viable for fusion reactor applications.

The 12 Cr alloys which are stabilized with additions of Mn can also be eliminated as potential low activation fusion alloys. Although tensile properties are generally better than those in lower Cr alloys. impact properties are sufficiently degraded following irradiation to cause concern. formation of austenite and Intermetallic chi phase in such alloys[19], and reduced weldability. Also,[24] indicate that Mn additions to 12 Cr steels do not provide a viable canposition range for low activation steels. Insufficient information is available to provide prediction of behavior for 12 Cr alloys stabilized with carbon. Carbon levels on the order of 0.2 percent are possible, giving good tensile and high temperature properties, Impact properties following irradiation are of most concern. Tests are being initiated on a good heat of GA4X, 11Cr-2.5WV with 0.15C, but it will be several years before results are available.

The 7 to 9 Cr alloys appear most promising for low activation fusion reactor applications. The alloys have good tensile and impact properties, both prior to and following irradiation. good resistance to phase instability during Irradiation and Sufficient high temperature strength. They are expected to be sufficiently corrosion resistant. The major detriment to their use is void swelling. However, dimensional changes due to irradiation induced swelling in ferritic alloys are expected to remain small because swelling rates are so low,[25] and, therefore. swelling resistance is not expected to be a major consideration for these alloys. Comparisons between V and W alloying additions indicate that higher W levels are superior. In fact, results to date Indicate that W levels on the order of 2 percent work very effectively. Concerns about phase instability. such as Fe–Cr–W chi phase formation. have proven to be groundless, at least to doses on the order of 30 dpa.[18] Therefore. the most promising composition developed to date appears to be 7 to 9Cr-2WV.

CONCLUSIONS

A broad range of low activation ferritic alloys are possible. Low activation bainitic alloys In the Fe–Xr composition range. martensitic alloys in the Fe-7 to 9Cr range and stabilized martensitic alloys in the Fe-12Cr range have been successfully fabricated and are undergoing testing on an international level. Hwever, it is found that irradiation significantly degrades the properties of bainitic and stabilized martensitic alloys. Bainitic alloys containing vanadium develop severe hardening due to Irradiation induced precipitation at temperatures below 450°C and extreme softening due to carbide coarsening at temperatures above 500°C. Stabilized martensitic alloys which rely on manganese additions to provide a fully martensitic microstructure are embrittled at grain boundarles following irradiation leading to severe degradation of impact properties. The most promising composition regime appears to be the Fe-7 to 9 Cr range with tungsten additions in the 2%range where high temperature mechanical properties and microstructural stability are retained and impact properties are relatively unaffected by irradiation. The higher void swelling behavior observed In these alloys is not expected to be a major problem.

FUTURE WORK

Reports describing microstructural development at 115 dpa in greater detail and tensile behavior at 75 dpa will follow.

REFERENCES

1. Report of the DOE Panel on Low Activation Materials for Fusion Applications, R.W. Conn, Panel Chairman. UCLA/PPG-728, June 1983.

2. D.G. Doran, A.F. Rowcliffe and F.M. Mann. J. Nucl. Matls., Vol. 141-143, 1986, 1074.

3. O.N. Jarvis. Low-Activity Materials Reuse and Disposal, AERE - R 10860, July 1983.

4. C. Ponti. Fusion Tech., Vol. 13. 1988, 157.

5. G.J. Butterworth and L. Giancarli, J. Nucl. Matls., ICFRM-3 Conference Proceedings. to be published.

6. J.D. Gordon, J.J. Thomson and S.N. Suchard. Isotopically Tailored HT-9 Steel for Radioactive Waste , TRW-FRE-001, December 1983.

7. T. Noda, F. Abe, H. Araki and M Okada, J. Nucl. Matls., Vol. 141-143, 1986, 1102.

8. R.L. Klueh, D.S. Gelles and T.A. Lechtenberg, J. Nucl. Matls., Vol. 141-143, 1986, 1081.

9. M. Tamura, H. Hayakawa. M. Tanimura, A. Hishinuma, T. Kondo. J. Nucl. Matls., Vol. 141-143, 1986, 1067.

10. Letter; C-Y. Hsu to D.S. Gelles, September 29, 1987 providing compositions of alloys manufactured by Mitsubishi Corporation, Japan.

11. D. Dulieu. K.W. Tupholme and G.J. Butterworth, J. Nucl. Matls., Vol. 141-143, 1986, 1097.

12. K.W. Tupholme, D. Dulieu and G.J. Butterworth, J. Nucl. Matls., ICFRM-3 Conference Proceedings, to be published.

13. M.L. Hamilton and D.S. Gelles, to be presented at the Symposium - Reduced Activation Alloys for Fusion Service, PNL SA 15421A.

14. R.L. Klueh. in Alloy Development for Irradiation Performance Semiannual Progress report for the Period ending September 30, 1985, DOE/ER-0045/15, 117.

15. D.S. Gelles and M.L. Hamilton, J. Nucl. Matls., Vol. 148, 1987. pp. 272-278; for an expanded version see in Alloy Development for Irradiation Performance Semiannual Progress report for the Period ending September 30, 1984, DOE/ER-0045/13, 128.

16. D.S. Gelles and M.L. Hamilton. in Alloy Development for Irradiation Perf - Semiannual Progress report for the Period ending March 31, 1986, DOE/ER-0045/16, 131.

17. N.S. Cannon, W.L. Hu and O.S. Gelles. in Fusion Reactor Materials Semiannual Progress Report for the Period Ending March 31, 1987. DOE/ER-0313/2, 119.

18. D.S. Gelles, C-Y. Hsu and T.A. Lechtenberg, J. Nucl. Matls., ICFRM-3 Conference Proceedings, to be published; for an expanded version see in Fusion Reactor Materials Semiannual Progress Report for the Period Ending September 30, 1987. DOE/ER-0313/3, 150.

19. D.S. Gelles and W.L. Hu, in Fusion Reactor Materials Semiannual Progress Report for the Period Ending September 30, 1986, DOE/ER-0313/1, 251.

20. H.R. Brager and F.A. Garner, in Effects of Radiation on Structural Materials, ASTM STP 683, J.A. Sprague and D. Kramer. eds, ASTM, 1979. 207.

21. D.S. Gelles and L.E. Thomas, in Topical Conference on Ferritic Alloys for Use in Nuclear Energy Technologies, J.W. Davis and D.J. Michel. Eds.. AIME, Warrendale, PA.. 1984, 559.

22. D.S. Gelles, W.J. Mills and L.A. James. in Alloy Development for Irradiation Performance Semiannual Progress report for the Period ending March 31, 1981, DOE/ER-0045/6, 165.

23. D.S. Gelles. in Radiation-Induced Changes in Microstructure: 13th International Symposium (Part I), ASTM STP 955, F.A. Garner, N.H. Packan and A.S. Kumar, Eds., ASTM, Philadelphia. PA., 560.

24. H.T. Lin and B.A. Chin, in Fusion Reactor Materials Semiannual Progress Report for the Period Ending March 31, 1987, DOE/ER-0313/2, 135.

25. D.S. Gelles and R.L.Ermi, in Alloy Development for Irradiation Performance Semiannual Progress report for the Period ending September 30, 1983, DOE/ER-0045/11, 103.

THE DEVELOPMENT OF FERRITIC STEELS FOR FAST INDUCED-RADIOACTIVITY DECAY -- R. L. Klueh, D. J. Alexander, and W. R. Corwin (Oak Ridge National Laboratory)

OBJECTIVE

Induced radioactivity in the first-wall and blanket-structure materials will make these components highly radioactive after their service lifetime, leading to difficult radioactive waste-management problems. One way to minimize the disposal problem is to use structural materials in which radioactive isotopes induced by irradiation decay quickly to levels that allow simplified disposal techniques. We are assessing the feasibility of developing such ferritic steels.

SUMMARY

Charpy impact tests were made on eight heats of normalized-and-tempered chromium-tungsten steel that contained various levels of chromium, tungsten, vanadium, and tantalum. The impact behavior of several of these steels was found to compare favorably with the properties of analogous chromium-molybdenum steels that are presently being considered as candidate structural materials for fusion-reactor applications.

PROGRESS AND STATUS

Introduction

We have continued the studies to characterize eight heats of ferritic steel designed for fast induced-radioactivity decay (FIRD).[1-5] These steels were patterned on the chromium-molybdenum steels that are of interest for fusion-reactor applications -- namely, 2¼Cr-1Mo, 9Cr-1MoVNb, and 12Cr-1MoVW steels. The major changes for the chromium-molybdenum steels involve the replacement of molybdenum by tungsten, the use of vanadium in a 2¼% Cr steel, and the replacement of niobium in the 9% Cr steel by tantalum. (Although tantalum can be used in a FIRD steel, the decay of its transmutation products immediately after irradiation in a fast- or mixed-spectrum reactor makes such a steel difficult to study. Therefore, few, if any, irradiated transmission electron microscopy studies will be performed on steels containing tantalum.)

We previously presented preliminary microstructural[5] and tensile data[2,4] on these steels. In this report, the impact behavior as determined from Charpy impact tests will be presented.

Experimental procedure

The nominal compositions of the major elements for the eight heats of steel under study are given in Table 1. Detailed chemical compositions have been presented previously,[3] as well as details on the preparation of the heats.[3]

Table 1. Proposed nominal compositions for fast induced-radioactivity decay steel development program

Alloy	Nominal Chemical Composition[a] (wt %)				
	Cr	W	V	Ta	C
2¼CrV	2.25		0.25		0.1
2¼Cr-1WV	2.25	1	0.25		0.1
2¼Cr-2W	2.25	2			0.1
2¼Cr-2WV	2.25	2	0.25		0.1
5Cr-2WV	5	2	0.25		0.1
9Cr-2WV	9	2	0.25		0.1
9Cr-2WVTa	9	2	0.25	0.12	0.1
12Cr-2VW	12	2	0.25		0.1

[a]Balance iron.

Tests were made on normalized-and-tempered steel. The 2.25Cr-2W steel was normalized by annealing 1 h at 900°C and air cooling. The other seven heats were annealed 1 h at 1050°C and air cooled; the higher temperature was used for these steels to assure that any vanadium carbide present was dissolved during the austenitization. Two tempering treatments were tested: 1 h at 700°C and 1 h at 750°C (the only exception to these tempering temperatures was for the 2¼Cr-1WV steel, which was tempered 1 h at 725°C and 1 h at 750°C).

Impact specimens were made from normalized-and-tempered 15.9-mm-thick plate. Specimens were made in accordance with ASTM specification E 23 with dimensions of 10 by 10 by 55 mm; specimens contained a 2-mm-deep, 45-deg V-notch with a 0.25-mm-root radius. All specimens were taken along the rolling direction with the notch running transverse to the rolling direction (L-T orientation).

Each individual Charpy data set was fitted to a hyperbolic tangent function for obtaining the transition temperature and upper-shelf energy.

Results

A summary of the data is given in Table 2, where the ductile-brittle transition temperature (OBTT) and the upper-shelf energy (USE) are given for each steel. The OBTT values given in the table were determined at 41 and 68 J levels; lateral expansion measurements were also made.

Table 2 Impact properties of FIRD steels

Steel	Tempering Temperature[b] (°C)	Impact Properties[a] TT_{41J} (°C)	TT_{68J} (°C)	TT_{LE} (°C)	USE (J)
2¼CrV	700	85	86	85	240
	750	66	69	70	318
2¼Cr-1WV	725	52	53	52	220
	750	8	23	38	340
2¼Cr-2W	700	24	24	12	260
	750	-41	-30	-31	324
2¼Cr-2WV	700	85	110	112	131
	750	31	31	31	265
5Cr-2WV	700	−61	−46	-46	219
	750	−97	−76	−83	259
9Cr-2WV	700	7	26	33	157
	750	−69	−48	−42	217
9Cr-2WVTa	700	−47	−24	−20	181
	750	−95	−78	−82	258
9Cr-1MoVNb	700	56	68	68	161
	750	27	41	41	199
12Cr-1MoVW	700	33	68	64	99
	750	4	29	26	115
12Cr-2WV	700	11	20	19	168
	750	−13	−2	−24	193

[a] TT_{41J} is 41-5 (30 ft-lb) transition temperature; TT_{68J} is 68-J (50 ft-lb) transition temperature; TT_{LE} is lateral expansion transition temperature as determined by 0.889-mm expansion; USE is upper-shelf energy.

[b] All steels were tempered 1 h; before tempering all but the 2¼Cr-2W were normalized at 1050°C; the 2¼Cr-2W was normalized at 900°C.

Impact curves are shown in Fig. 1 for the 2¼ Cr steels tempered at 750°C. The 2¼Cr-2W steel had the lowest OBTT and highest USE. For the vanadium-containing 2¼ Cr steels, the steel without tungsten had the highest OBTT, followed by 2¼Cr-1WV and 2¼Cr-2WV steels, which were similar. Data scatter was quite large for the 2¼Cr-1WV steel, and the one high point well removed from the trend of the other data points caused this curve fit to have a lower DBTT than would have been the case if this point had not been included. When tempered at 700°C (Table 2), the 2¼Cr-2W steel again had the best combination of DBTT and USE. The 2¼Cr-2WV steel had the worst properties for these tempering conditions. However, the DBTT values of all four steels were considerably above those obtained after tempering at 750°C.

In Fig. 2. impact curves for the high-chromium steels tempered at 750°C are shown. All of the steels had OBTT values well below room temperature; the 5Cr-2WV and 9Cr-2WVTa had properties that were superior to those of the 9Cr-2WV and 12Cr-2WV steels, although the latter steels had excellent properties after the 750°C temper. After tempering at 700°C, the relative behavior of the different steels remained the same (Table 2), but the OBTT was higher and the USE lower than after tempering at 750°C.

For comparison, Charpy impact tests were conducted on the 9Cr-1MoVNb and 12Cr-1MoVW steels (Table 2). Full-size Charpy specimens were machined from 15.9-mm-thick plates that had been austenitized 1 h at 1050°C, air cooled and tempered 1 h at 700°C and 1 h at 750°C — the identical heat treatments used for the impact specimens of the experimental steels. A tempered martensite microstructure resulted for both of the Cr-Mo steels after such heat treatments.

A comparison of the properties for the Cr-Mo steels and the high-chromium Cr-W steels indicated that the Cr-W steel values were better than those for Cr-Mo steels (Table 2). In Fig. 3, a comparison is shown after the 750°C temper for the two Cr-Mo steels and their Cr-W analogs -- the 9Cr-2WVTa and 12Cr-2WV steels. The 9Cr-2WVTa had the best properties, but the 12Cr-2WV steel also had better properties than those of the 9Cr-1MoVNb and 12Cr-1MoVW steels.

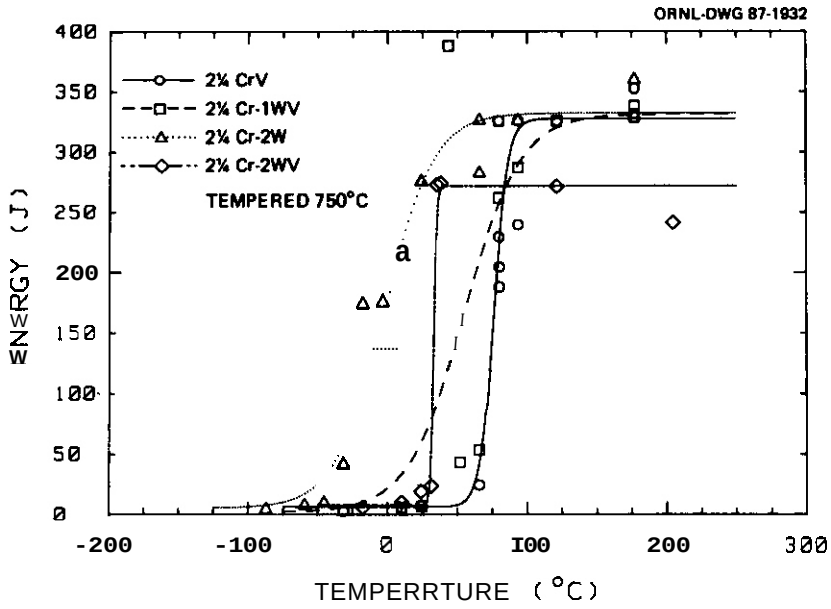

Fig. 1. The Charpy V-notch impact curves for 2¼CrV, 2¼Cr-1WV, 2¼Cr-2W, and 2¼Cr-2WV steels; all steels were tempered 1 h at 750°C.

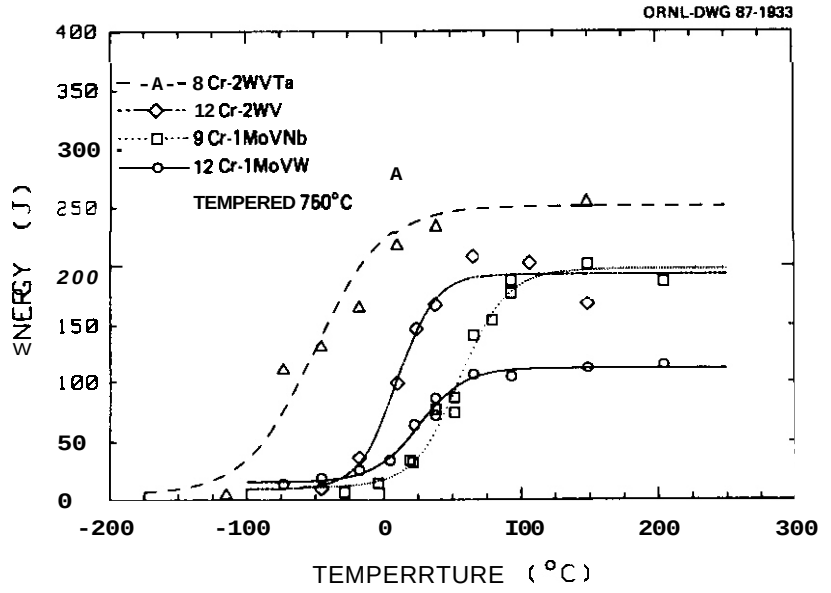

Fig. 2. The Charpy V-notch impact curves for 5Cr-2WV, 9Cr-2WV, 9Cr-2WVTa, and 12Cr-2WV steels; all steels were tempered 1 h at 750°C.

Discussion

Normalized-and-tempered microstructures of the eight steels tested in this study have been discussed.[1,5] The 2¼CrV alloy had 30 to 35% tempered bainite, with the remainder being polygonal or proeutectoid ferrite. For the composition with 1%W -- the 2¼Cr-1WV steel -- the microstructure contained ~55% tempered bainite and 45% ferrite. Less polygonal ferrite was observed in the 2¼Cr-2W and 2¼Cr-2WV steels: the 2¼Cr-2W steel was essentially 100% bainite and the 2¼Cr-2WV steel contained 15 to 20% polygonal ferrite.'

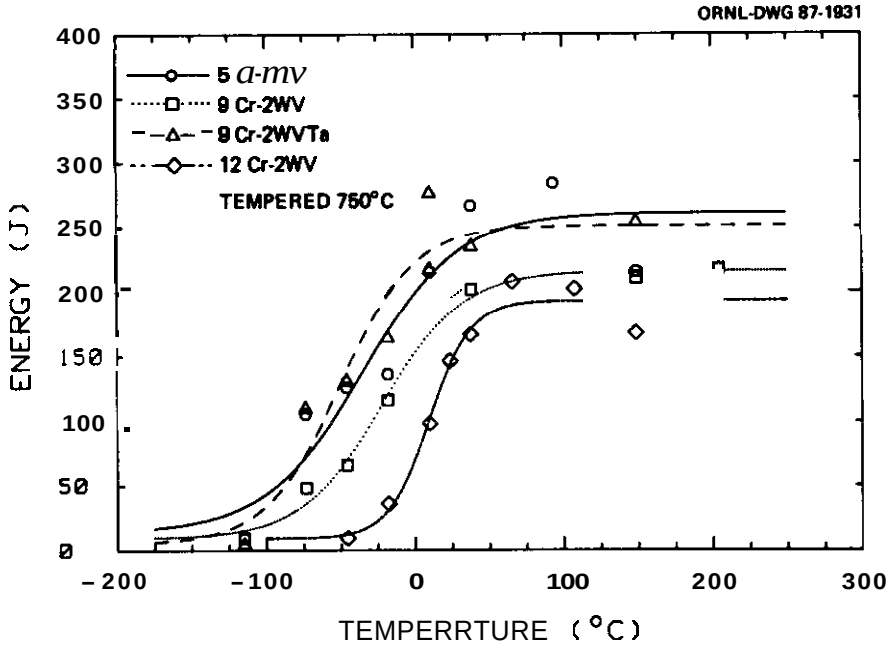

Fig. 3 A comparison of the Charpy V-notch impact curves for 9Cr-2WVTa and 12Cr-2WV steels with the curves for 9Cr-1MoVNb and 12Cr-1MoVW steels; all steels were tempered 1 h at 750°C.

The 5Cr-2WV, 9Cr-2WV, and 9Cr-2WVTa steels were 100% tempered martensite.[1] However, the 12Cr-2WV steel contained approximately 25% delta-ferrite, with the balance being martensite. The only major difference in the martensite of these four steels was that the 9Cr-2WVTa had a much finer prior austenite grain size than the other three steels.' The microstructures of the 9Cr-1MoVNb and 12Cr-1MoVW steels to which the Cr-W steels were compared were 100% tempered martensite after normalizing and tempering.'

For fusion-reactor applications, the impact properties are expected to be crucial. When irradiated by neutrons, the OBTT of the 12Cr-1MoVW steel can increase by over 200°C.[6,7] Therefore, it is desirable that any steel used for such applications have as low a DBTT as possible.

When the results for the Cr-W steels were compared against the results for 9Cr-1MoVNb and 12Cr-1MoVW steels for similar heat treatments (Table 2), the properties of the 5Cr-2WV, 9Cr-2WV, 9Cr-2WVTa, and 12Cr-2WV steels Were superior to those for 9Cr-1MoVNb and 12Cr-1MoVW steels. However, the results in Table 2 for the Cr-Mo steels are not for these steels heat treated to obtain optimum impact properties. A OBTT of -50°C and a USE of 255 J were obtained for this heat of 9Cr-1MoVNb steel when it was austenitized 1 h at 1038°C and tempered for 1 h at 760°C.[7] For the same heat of 12Cr-1MoVW steel austenitized 1 h at 1050°C and tempered 2.5 h at 780°C. a DBTT of -2.4°C and a USE of 115 J were obtained,[8] which is similar to the values obtained for the 12Cr-2WV steel in the present work, even though the 12Cr-2WV steel contained 25% delta ferrite. For other heats of 12Cr-1MoVW steel, somewhat better values were obtained.[8] It should be noted. however, that heat-treatment variations for the Cr-W steels could also lead to an improvement of the properties of these steels.

Investigators have concluded that small amounts of delta-ferrite[9,10] and such ferrite accompanied by carbides at the ferrite-martensite boundaries[10] cause an increase in the DBTT and a decrease in the USE in 12Cr-1MoVW steel. An increase in the DBTT of about 25°C was observed for 1% delta-ferrite[9] and an increase of 30 to 50°C was observed when about 5% delta ferrite was present in the microstructure.[10] Although the impact properties of the 12Cr-2WV steel containing 25% delta-ferrite were not as good as those of the 5 Cr and 9 Cr steels that Were entirely martensitic (Fig. 2), they were superior to the Cr-Mo steels heat treated similarly (Fig. 3). When the results for the 12Cr-2WV steel are compared with those for the 12Cr-1MoVW, the indication is that it must be more than the delta-ferrite in the 12Cr-1MoVW steel that causes the deterioration in properties. This conclusion is supported by impact data on 9Cr-1MoVNb that contained about 20% delta-ferrite,[11-13] which also had superior properties to those of 12Cr-1MoVW steel. Those results[11-13] plus those of the present study indicate that the inferior properties of the 12Cr-1MoVW steel are not caused by the delta-ferrite, but may be due to the higher-carbon content of the 12Cr-1MoVW steel (the 12Cr-1MoVW steel contains 0.2% C against –0.1% C for the 12Cr-2WV steel). Carbon is known to adversely affect impact properties.[14] The higher carbon content has been found to result in large amounts of precipitate,[15] which could degrade the impact properties.

It appears that the use of a duplex structure of martensite and delta ferrite should not be ruled out on the basis of impact properties. However. the 12Cr-2WV steel must be ruled out at present because its strength was not as good as the strength of the 9 Cr steels and the 2¼Cr-2WV steel.[2,4]

Although these steels are still at an early stage of development, the impact properties of the 2¼Cr-2WV steel were somewhat disappointing, in view of the excellent tensile properties of this steel.[2,4] Yield stress and ultimate tensile strength values for this steel were as good or better than those for 9Cr-2WV and 9Cr-2WVTa steel and approached the values for 9Cr-1MoVNb and 12Cr-1MoVW steel.[2,4] A mixed structure of tempered bainite and polygonal ferrite -- the microstructure of the 2¼Cr-2WV steel -- is known to result in inferior impact behavior compared to a steel with a microstructure made up of a single constituent.[16] This may explain why the 2¼Cr-2W steel had the best impact behavior of the 2Y4 Cr steels (Table 2 and Fig. 3).

The observation that the impact behavior of a bainitic steel is superior to one containing polygonal ferrite means that it should be possible to improve the impact properties of the 2¼Cr-2WV steel by heat treatment and by increasing the hardenability. By proper alloying, the hardenability of the steel can be increased and the ferrite eliminated. Finally, the type of bainite that forms can also affect the impact properties;" the type of bainite, in turn, depends on the hardenability.

Summary and conclusions

By eliminating molybdenum and niobium from steels used for fusion reactor structural components, induced radioactivity will decay faster, which will allow simpler radioactive waste-disposal techniques for these reactor components when they are discarded after service. Such fast induced-radioactivity decay (FIRD) ferritic steels are being developed. The steels are patterned on the conventional ferritic steels being considered as candidates for fusion-reactor applications -- 2¼Cr-1Mo, 9Cr-1MoVNb, and 12Cr-1MoVW steels. In these steels, tungsten was used as a replacement for molybdenum, and tantalum was substituted for niobium.

To determine the effect of Cr, W, V, and Ta, eight heats of steel were obtained. Alloys containing 2% W (an atom-for-atom replacement of molybdenum in the Cr-Mo steels) and 0.25% V were produced for chromium levels of 2¼, 5, 9, and 12% (designated 2¼Cr-2WV, 5Cr-2WV, 9Cr-2WV, and 12Cr-2WV). A 9Cr-2WV steel with 0.07% Ta (9Cr-2WVTa) and 2¼ Cr steels with 0.25% V and 0 and 1%W (2¼CrV, and 2¼Cr-1WV) and with 2% W and no vanadium (2¼Cr-2W) were also produced. Carbon was maintained at 0.1% for all of the steels.

Impact properties of the 5Cr-2WV, 9Cr-2WV, 9Cr-2WVTa, and 12Cr-2WV steels were superior to those for 9Cr-1MoVNb and 12Cr-1MoVW steels when all steels were given similar heat treatments. The excellent impact properties of the 12Cr-2WV steel occurred despite the 25% delta-ferrite in the microstructure. Impact properties of the 2¼Cr-2WV steel, which had excellent tensile properties relative to the other Cr-W steels, were inferior to those of the high-chromium (5-12% Cr) steels. This was attributed to microstructure, and the development of a low-chromium FIRD steel with good strength and impact behavior should be possible with further alloying and proper heat treatment.

REFERENCES

1. R. L. Klueh, "The Development of Ferritic Steels for Fast Induced-Radioactivity Decay," pp. 117-123 in ADIP Semiannu. Prog. Rep., Sept. 30, 1985, DOE/ER-0045/15, U.S. DOE, Office of Fusion Energy.

2. R. L. Klueh, "The Development of Ferritic Steels for Fast Induced-Radioactivity Decay," pp. 109-113 in ADIP Semiannu. Prog. Rep., Mar. 31, 1986, DOE/ER-0045/16, U.S. DOE, Office of Fusion Energy.

3. R. L. Klueh and J. M. Vitek, "The Development of Ferritic Steels for Fast Induced-Radioactivity Decay," pp. 156-157 in ADIP Semiannu. Prog. Rep., Sept. 30, 1984, DOE/ER-0045/12, U.S. DOE, Office of Fusion Energy.

4. R. L. Klueh, "The Development of Ferritic Steels for Fast Induced-Radioactivity Decay," pp. 162-169 in Fusion Reactor Materials Semiannu. Prog. Rep., Mar. 31, 1987, DOE/ER-0313/2, U.S. DOE, Office of Fusion Energy.

5. R. L. Klueh and P. J. Maziasz, "The Development of Ferritic Steels for Fast Induced-Radioactivity Decay," pp. 161–169 in Fusion Reactor Materials Semiannu. Prog. Rep., Sept. 30, 1987, DOE/ER-0313/3, U.S. DOE, Office of Fusion Energy.

6. F. A. Smidt, Jr., J. R. Hawthorne, and V. Provenzano, "Fracture Resistance of HT-9 After Irradiation at Elevated Temperature," pp. 269-264 in Effects of Radiation on Materials, ASTM STP *125*, D. Kramer, H. R. Brager, and J. S. Perrin, Eds., American Society for Testing and Materials, Philadelphia, 1981.

7. J. M Vitek, W. R. Corwin, R. L. Klueh, and J. R. Hawthorne. "On the Saturation of the DBTT Shift of Irradiated 12Cr-1MoVW With Increasing Fluence." J. Nucl. Mater. 141-143, 948-953 (1986).

8. W. R. Corwin and A. M. Hougland, "Effect of Specimen Size and Material Condition on the Charpy Impact Properties of 9Cr-1Mo-V-Nb Steel," pp. 325-338 in The Use of Small Scale Specimens for Testing Irradiated Material, ASTM STP 888, W. R. Corwin and G. E. Lucas, tds., herican Society for Testing and Materials, Philadel'phia, 1986.

9. K. Anderko, K. Oavid, W. Ohly, M Schirra, and C. Wassilew, "Optimization Work on Niobium Stabilized 12% CrMoVNb Martensitic Steels for Breeder and Fusion Reactor Applications," pp. 299-306 in Ferritic Alloys for Use in Nuclear Energy Technologies, The Metallurgical Society of AIME, Warrendale, Pa., 1984.

10. B. A Chin and R. C. Wilcox. "The Effect of Heat Treatment on the Impact Properties of a 12Cr-1Mo-V-W Steel. pp. 347-356 in Ferritic Alloys for Use in Nuclear Energy Technologies, The Metallurgical Society of AIME, Warrendale, Pa, 1984.

11. Y. Hosoi, N Wade, T. Urita, M Tannino. and H Komatsu. "Change in Microstructure and Toughness of Ferritic-Martensitic Stainless Steels Ouring Long-Term Aging," J. Nucl. Mater. 133 8 134, 337-342 (1984).

12. Y. Hosoi, N. Wade, S. Kunimitsu, and T. Urita, "Precipitation Behavior of Laves Phase and Its Effect on Toughness of 9Cr-2Mo Ferritic-Martensitic Steel," J. Nucl. Mater. 141-143, 461-465 (1986).

13. N Igata, "Ferritic/Martensitic Dual-Phase Steel as Fusion Reactor Materials," J. Nucl. Mater. 1338134, 141-148 (1985)

14. F. B. Pickering, Physical Metallurgy and the Design of Steels, Applied Science Publishers, Ltd., London, 1978.

15. J. M Vitek and R. L. Klueh, "Precipitation Reactions During the Heat Treatment of Ferritic Steels," Metall. Trans. 14A, 1047-1055 (1983).

16. O. A. Canonico, private communication, 1987

17. R. L. Klueh, "Bainite in Cr-Mo Steels," pp. 601-606 in Martensitic Transformations (COMAT), Japan Institute of Metals, Sendai, Japan, 1987.

FRACTOGRAPHIC EXAMINATION OF LOW ACTIVATION FERRITIC ALLOY CHARPY IMPACT SPECIMENS - D. S. Gelles (Pacific Northwest Laboratory) and N. S. Cannon (Westinghouse Hanford Company)

OBJECTIVE

The objective of this work is to determine the applicability of low activation ferritic alloys as fusion reactor structural materials.

SUMMARY

Miniature charpy specimens of six low activation ferritic alloys have been fractographically examined in order determine the effect of irradiation on impact fracture behavior. A change in brittle fracture mode due to irradiation was found for four of the six alloys. The fracture mode changed from transgranular cleavage to intergranular failure at prior austenite boundaries. The cause is ascribed to Mn additions in the alloys. Examinations also indicated that for the 9Cr-1W alloy. the DBTT as measured by absorbed energy measurements does not agree with an explanation based on fracture appearance. The cause is not yet understood.

PROGRESS AND STATUS

Introduction

A series of one-third size low activation ferritic alloy Charpy impact specimens has been tested following irradiation to 10 dpa at 365°C and compared to unirradiated specimens.[1] The results showed that alloys of composition Fe-2Cr-1.5V, Fe-12Cr-6Mn-1V and Fe-12Cr-6Mn-1W develop unacceptably large shifts in ductile to brittle transition temperature (DBTT) due to irradiation, Fe-9Cr-1V develops a small shift and Fe-9Cr-1W and Fe-7.5Cr-2W develop negligible shifts. There was little effect on upper shelf energy (USE) in all cases. These results are shown in Figure 1 which compares behavior as a function of alloy Cr content. Open data points represent results for unirradiated specimens and filled in data point show results for irradiated specimens. From Figure 1, it can be shown that the 2 Cr-1.5V alloy had a high OBTT prior to irradiation, and, following irradiation, the DBTT was shifted beyond the limits of the testing capability. The 12Cr alloys both showed adequate behavior in unirradiated specimens but large shifts in OBTT were found due to irradiation. The most promising response was found in the 7 to 9 Cr alloy class where unirradiated specimens gave adequate behavior prior to irradiation and very small shifts following irradiation. This class also provided the highest USE response.

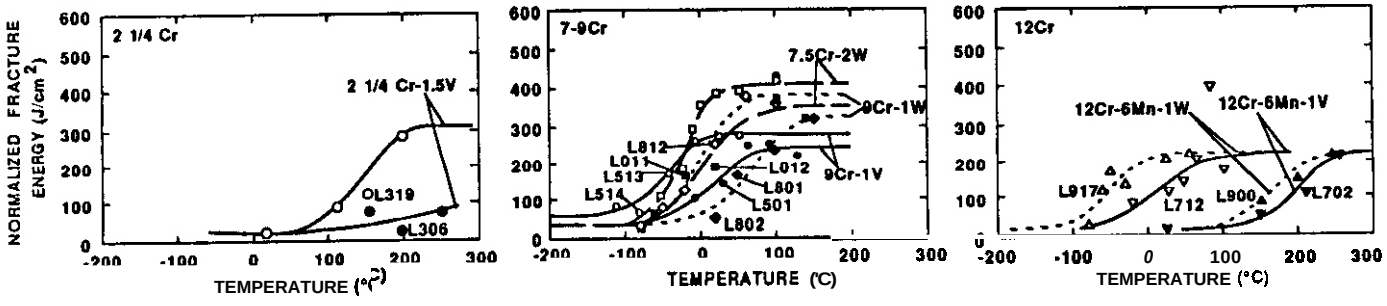

Figure 1. Normalized fracture energy as a function of test temperature for Charpy specimens of a) 2 Cr steel, b) 7 to 9 Cr steels and c) Mn stabilized 12 Cr steels including unirradiated specimens (open points) and specimens irradiated at 365°C to 10 dpa (closed points). Specimens selected for fractographic examination are labelled with specimen identification codes.

The purpose of the present effort is to provide further insight into the Charpy impact response of irradiated low activation ferritic alloys by examining the fracture surfaces of selected specimens. This examination is one of a series intended to identify changes in fracture behavior due to irradiation.[2-4]

Experimental Procedures

Specimens selected for fractographic examination are listed in Table 1 with Charpy test conditions and measured normalized fracture energy. In general. the specimens which were selected had been tested at approximately the transition temperature so that both ductile and brittle fracture behavior could be examined at the same time. Four exceptions were specimens L306, L012, L514 and L802 which were tested at

temperatures corresponding to energy absorption typical of the lower shelf. The specimens that were selected are identified in Figure 1 by specimen identification number. Experimental procedures were identical to those used previously.

Table 1. Charpy specimens of low activation ferritic alloys selected for fractographic examination.

Alloy	I.D.	Irrad. Temp. (°C)	Dose (dpa)	Test Temp. (°C)	Normalized Fracture Energy (J/cm^2)
2Cr-1V	L319	---	--	150	124
	L306	365	11.3	200	36
7.5Cr-2W	L022	---	--	-50	106
	L011	365	10.5	-20	161
	L012	365	10.5	21	191
9Cr-1V	L514	---	--	-80	64.5
	L513	---	--	-40	169
	L501	365	12.0	22	142
9Cr-1W	L814	---	--	-20	125
	L812	---	--	20	262
	L802	365	12.0	21	46
	L801	365	12.0	50	163
12Cr-6Mn-1V	L712	---	--	25	118
	L702	365	12.0	210	111
12Cr-6Mn-1W	L917	---	--	-60	110
	L900	365	12.0	150	83.1

Results

Stereo fractographs of each of the specimens which were examined are displayed in Figures 2 to 17. In each case, the fracture surface created during the Charpy test is shown with the adjacent fatigue precrack surface on the left so that crack propagation can be envisioned as going from left to right. In general. a specimen which is tested at the DBTT will show a brittle region adjacent to the fatigue surface which covers about half the fractured ligament and the remainder will be ductile. Figure a) in each case shows the whole of the fractured ligament at low magnification and b) provides an example at higher magnification of an area in the center of the specimen immediately adjacent to the fatigue surface. The reader is encouraged to vier these fractographs with a stereoscopic aid in order to fully appreciate changes in fracture appearance.

Specimens of 2Cr-1.5V were found to be quite coarse grained. with ductile failure by dimple rupture and brittle failure by transgranular cleavage fracture. Brittle fracture appearance was unaffected by irradiation. The unirradlated specimen shown in Figure 2 is unusual due to the fact that the brittle region is not centered. A very large grain on the lower left. and adjacent grains have been cleaved but except for one cleavage failure towards the upper center, the remainder of the specimen failed in a ductile fashion. Such behavior is more typical of weld metal response where inhomogeneities and internal stresses are large. These specimens were found to be very difficult to fatigue precrack. probably because inhomogeneities were present. The fracture appearance shown in Figure 3 of an irradiated specimen tested at 200°C is typical of a specimen that has failed on the lower shelf. As a result. ductile failure is limited to regions near specimen surfaces. and the region adjacent to the fatigue surface (figure 3b) shows negligible plastic deformation. Therefore, the interpretation of a DBTT well above 250 C for the irradiated condition of 2Cr-1.5V is confined.

Specimens of 7.5Cr-2W gave the response expected of martensitic stees. Figure 4. showing an unirradlated specimen rested at -50°C and Figures 5 and 6, showing irradiated specimens tested at -20 and 21 C, indicate fracture is extremely well behaved. The prior austenite grain size is fine, on the order of 0.1 mm (100 m) but brittle failure is predaninantly by transgranular cleavage (and ductile shear along connecting prior austenite grain boundaries.) Ductile failure is by uniform dimple rupture.

Specimens of 9Cr-1V show sanewhat different response. The prior austenite grain size is a little larger. on the order of 0.15 to *0.2* mm, and failure is well behaved with little evidence for inhomogeneities. However. brittle failure in the unirradiated condition reveals a tendency for failure at prior austenite grain boundaries. Both tests on the lower shelf (Figure 7b) and at the DBTT (Figure

8b) show relatively smooth darker surfaces without river pattern steps (due to martensite lath structure). These darker features are examples of grain boundary cleavage. Up to 20 percent of brittle failure in both specimens appears to be due to grain boundary cleavage. Similar features have been noted previously in HT-9 specimens.[3] Following irradiation, brittle failure in 9Cr-1V shifts almst canpletely to grain boundary cleavage whereas ductile failure is uniformly dimple rupture. The ductile and brittle regions are easily differentiated in Figure 9a) showing an Irradiated specimen of 9Cr-1V tested at the DBTT, but Figure 9b) reveals martensite lath packet structure on only about 20 percent of the brittle fracture surface. Therefore. a change in fracture mechanism has occurred but only a minor increase in DBTT results.

Specimens of 9Cr-1W provided several surprises (Figures 10-13). Specimens selected to show behavior at the DBTT. both unirradiated and irradiated, were found to be entirely ductile with no evidence of cleavage fracture. Figure 11 of an unirradiated specimen tested at 20°C and Figure 13 of an irradiated specimen tested at 50 C show specimens that have failed entirely by dimple rupture. In both cases, the normalized fracture energy is considerably lower than the USE value and the test temperature is very close to the DBTT. The unirradiated specimen tested at -20°C that is shown in Figure 10 and the irradiated specimen in Figure 12 that was tested at 21 C were selected to be close to the lower shelf. However. inspection of Figures 10 and 12 shows fracture appearance with more dimple rupture than cleavage representing a test temperature at or above the DBTT based on a fracture appearance criterion. It must therefore be assumed that either sanethng unusual happens during plastic deformation as a function of temperature in this canposition range or that the USE is actually lower than that measured. The brittle fracture appearance of the unirradiated 9Cr-1W shows a tendency for failure at prior austenite grain boundaries. and similar features can be identified on the fatigue precrack. However, the daninate brittle fracture made is transgranular cleavage. The brittle fracture appearance of the irradiated specimen tested at 21°C was found to be very similar to the 9Cr-1V case: almost totally brittle fracture at prior austenite boundaries. In fact, the fracture surface in Figure 12b) shows more extensive grain boundary failure than does Figure 9b). Wedge cracks extending into the surface are clearly visible. as if grains are about to be pulled out. As it is unlikely that brittle failure was at prior austenite boundaries in the unirradiated condition. a change in fracture mode due to irradiation has probably occurred. Therefore. irradiation has apparently changed the brittle fracture mode in 9Cr-1W as well.

The 12Cr alloys behaved similarly. As shown in Figures 14 and 16, the unirradiated conditions of 12Cr-6Mn-1V and 12Cr-6Mn-1W tested at the DBTT failed by transgranular cleavage in the brittle mode and by dimple rupture in the ductile mode. Failure is well behaved in the V alloy shown in Figure 14, despite the fact that this alloy contains 5 percent delta ferrite.[5] However. for each alloy. a change in failure mode occurred as a result of irradiation so that brittle failure was by failure at prior austenite boundaries. Figure 15 is not easy to interpret because the high test temperature has resulted in oxidation of the surface, but examples of wedge cracking are clearly indicated in both Figures 15b) and 17b), and. in fact. failure is by grain boundary failure in the brittle region. Therefore, as with the 9 Cr alloys. a change in brittle fracture mode has occurred in the 12Cr alloys as a result of irradiation.

Rockwell hardness measurements were made on selected specimens in order to prwide further basis for explanation of observed behavior. It may be noted that tensile data is available for these alloys following irradiation at 420°C,[5,6] but no tensile measurements were made on specimens irradiated at 365 C. The results of hardness measurements are given in Table 2. Comparison of the results in Table 2 provides the unexpected conclusion that irradiation has not produced large changes in hardness. Significant changes were only noted in 2Cr-1V, where hardness rose fran 15.8 to 27.3. and 2.7Cr-2W, where hardness measured fran 19.2 to 24.6. In all other cases, hardness Increased less than 3 points. Table 2 also provides estimates for tensile strength based on carbon and alloy steels (fran the SAE Handbook). The hardness increase for 2Cr-1V corresponds to a tensile strength increase fran 700 to 900 MPa or 302. (Reference 5 indicates an increase fran approximately 400 MPa or 125% increase.) Therefore. the changes in Charpy impact behavior for 2Cr-1V can be ascribed to irradiation induced hardening but changes in behavior for the 12Cr alloys must be ascribed to other causes such as segregation.

Discussion

Fractographic examination of low activation charpy impact specimens has provided two observations which affect interpretation of the impact property data: 1) Fracture surfaces of alloy 9Cr-1W specimens which were tested at the DBTT were found to have failed only by ductile dimple rupture whereas partial failure by brittle fracture was expected. 2) A change in brittle fracture mode fran transgranular cleavage to brittle failure at prior austenite grain boundaries was observed in four of the six steels studied. The purpose of this section will be to enlarge on these observation,

Observation of only ductile dimple rupture on fracture surfaces of Charpy specimens tested at the DBTT is very unusual. The present series of examinations provides four examples to show that it does occur in a 9Cr-1W alloy, and includes both unirradiated and irradiated specimen conditions. Given the number of corroborating observations. the possibility of specimen misidentity or mixup can probably be ruled out. Unfortunately. a straightforward explanation for the behavior is not apparent. Specimens L814 and L802, which were tested at temperatures corresponding to lower shelf behavior did show brittle fracture and therefore the cause of the DBTT in this material is normal: a shift fran a ductile to a brittle fracture

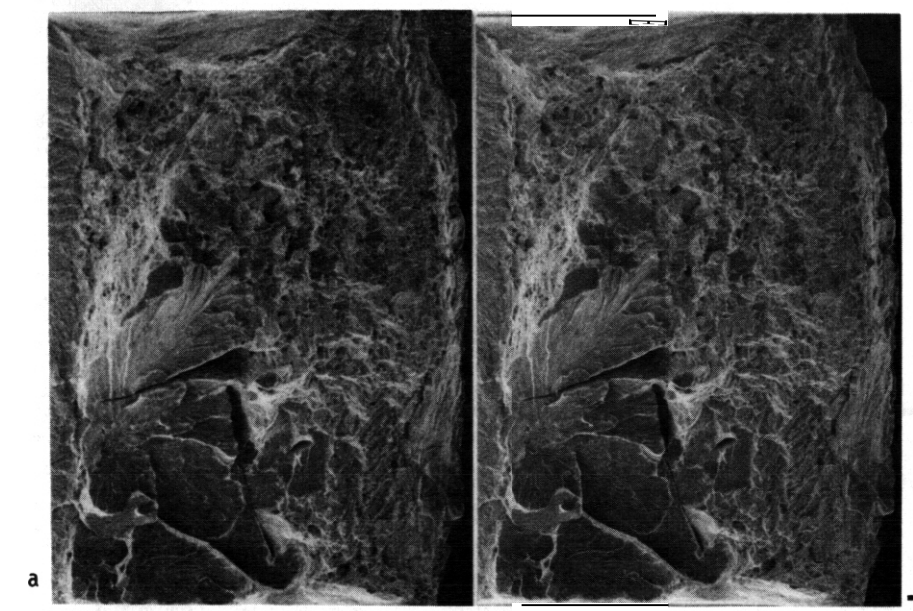

Figure 2. Fractographs of 2Cr-1.5V alloy specimen L319 following testing at 150°C at a) low magnification and b) intermediate magnification.

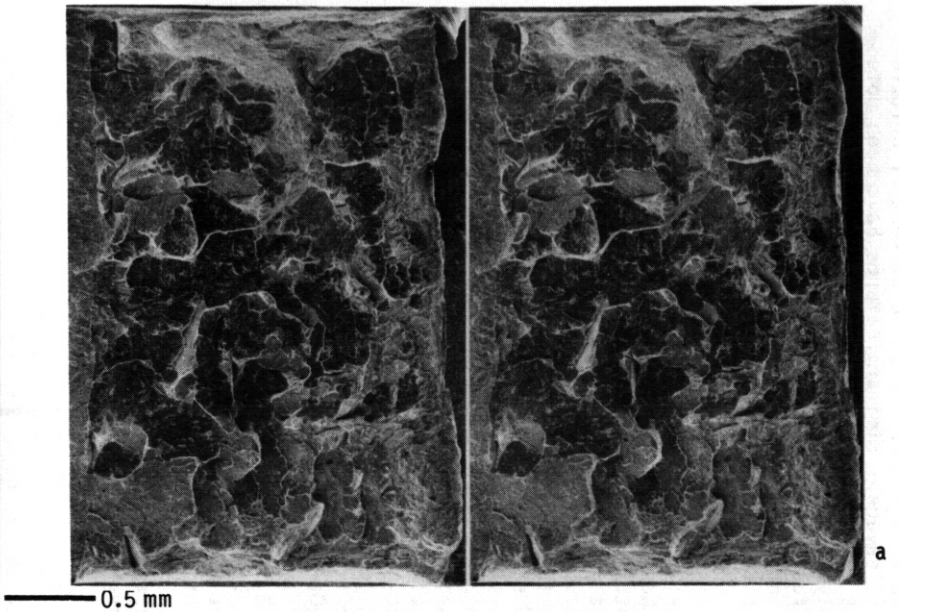

Figure 3. Fractographs of 2Cr-1.5V alloy specimen L306 following irradiation and testing at 200°C at a) low and b) intermediate magnification.

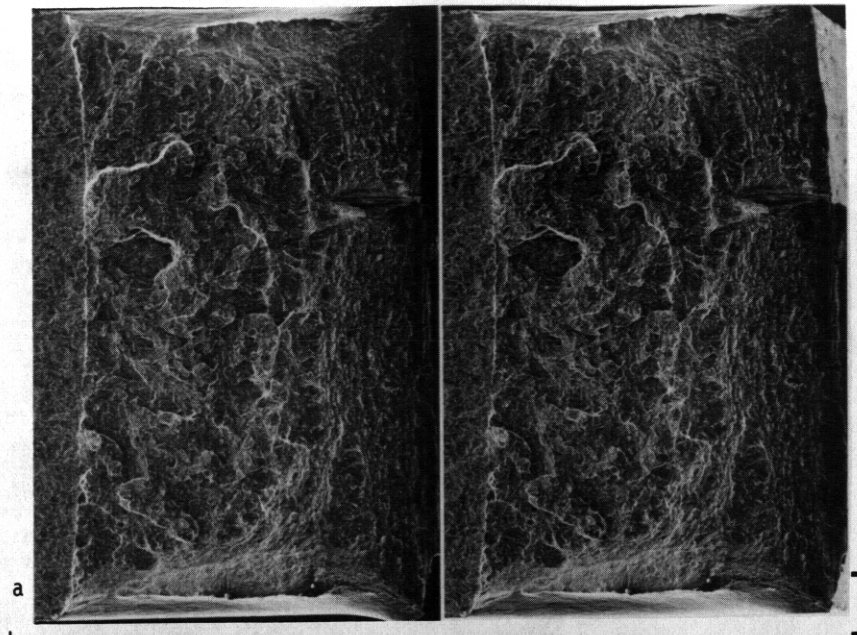

Figure 4. Fractographs of 7.5Cr-2W alloy specimen LO22 following testing at -50°C at a) low and b) intermediate magnification.

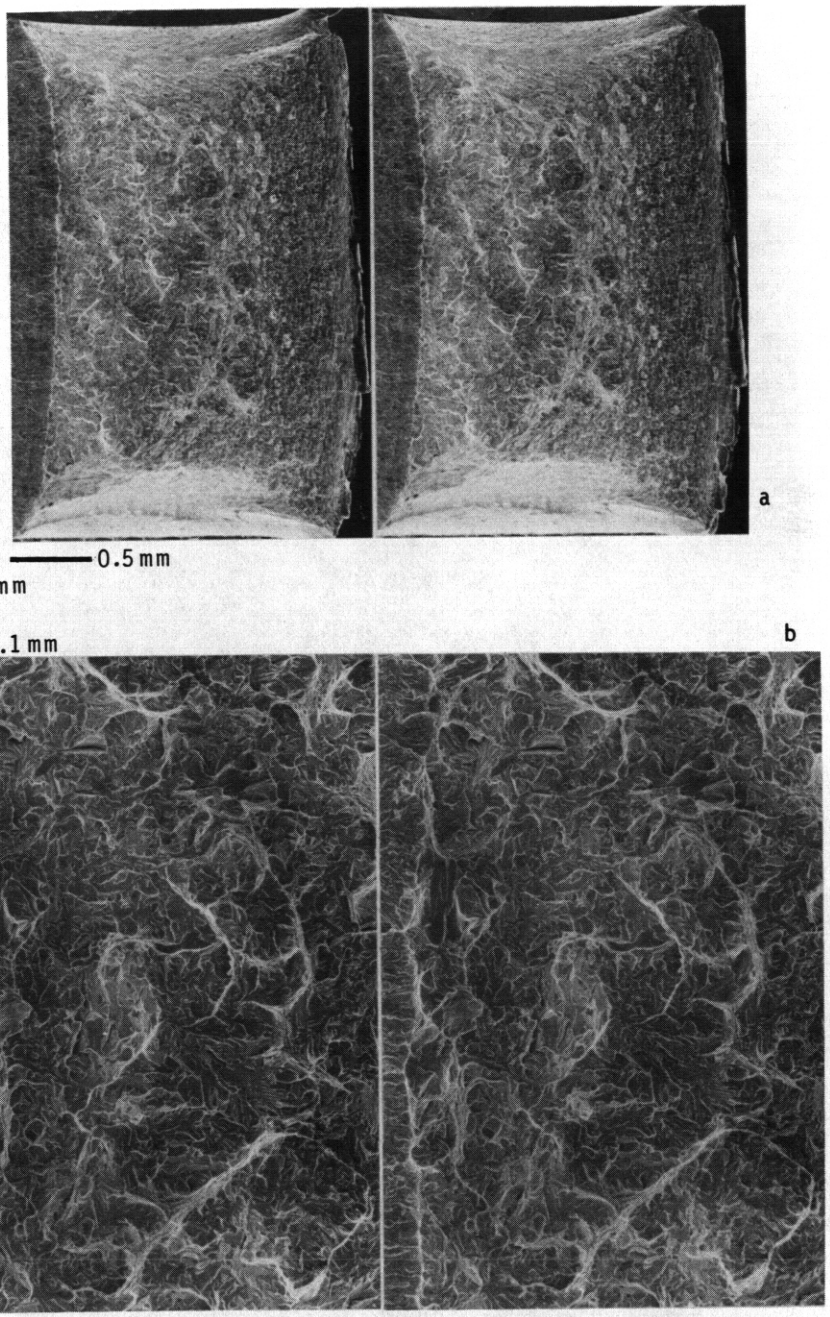

Figure 5. Fractographs of 7.5Cr-2W alloy specimen LO11 following irradiation and testing at -20°C at a) low and b) intermediate magnification.

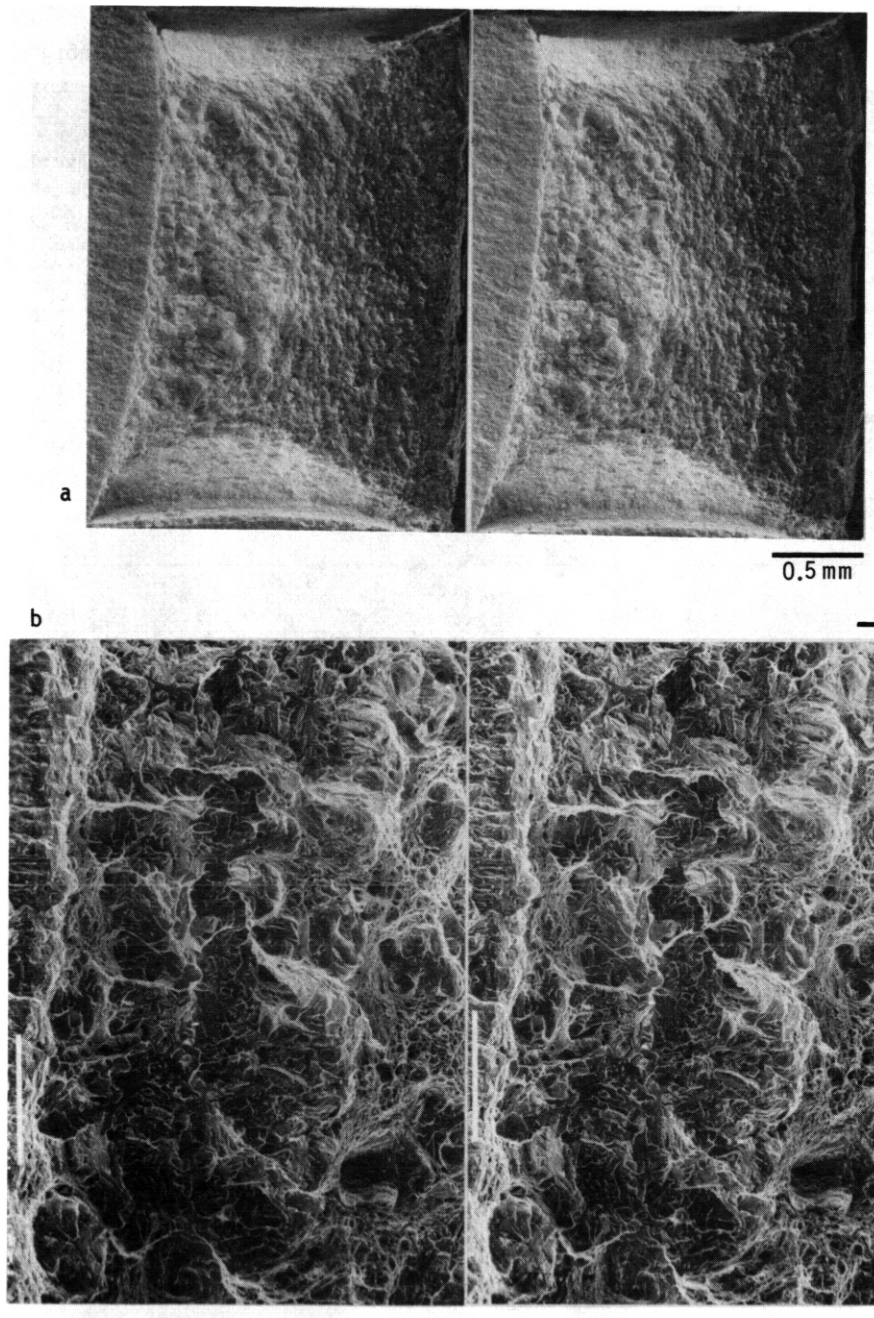

Figure 6. Fractographs of 7.5Cr-2W alloy specimen L012 following irradiation and testing at 21°C at a) low and b) intermediate magnification.

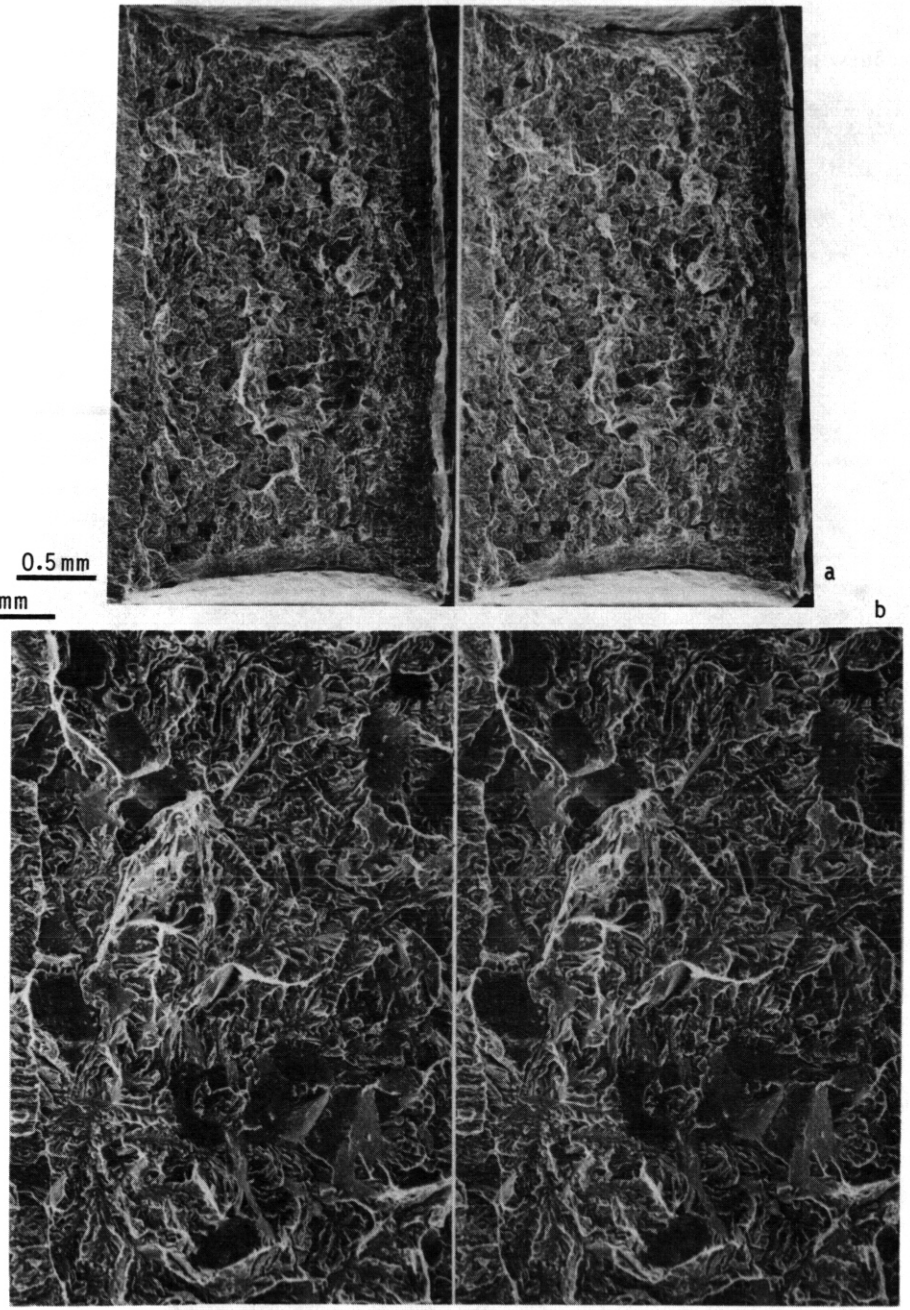

Figure 7 Fractographs of 9Cr-1V alloy specimen L514 following testing at -80°C at a) low magnification and b) intermediate magnification.

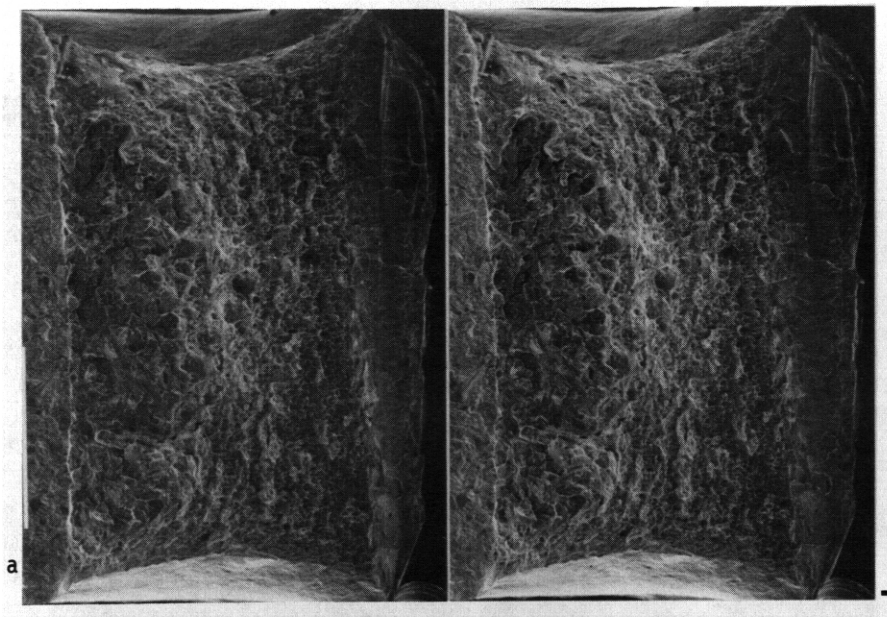

Figure 8. Fractographs of 9Cr-1V alloy specimen L513 following testing at -40°C at a) low and b) intermediate magnification.

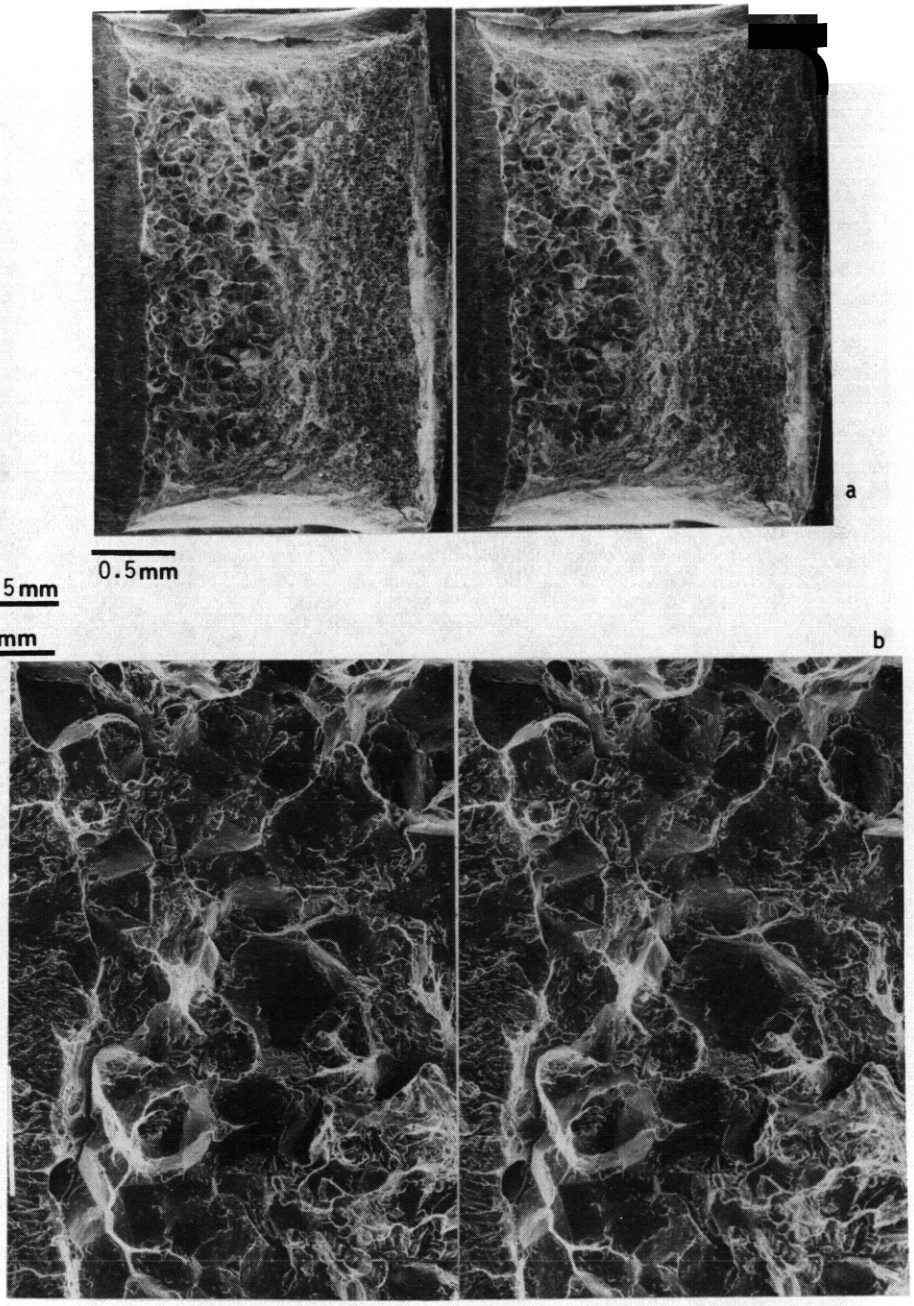

Figure 9. Fractographs of 9Cr-1V alloy specimen L501 following irradiation and testing at 22°C at a) low magnification and b) intermediate magnification.

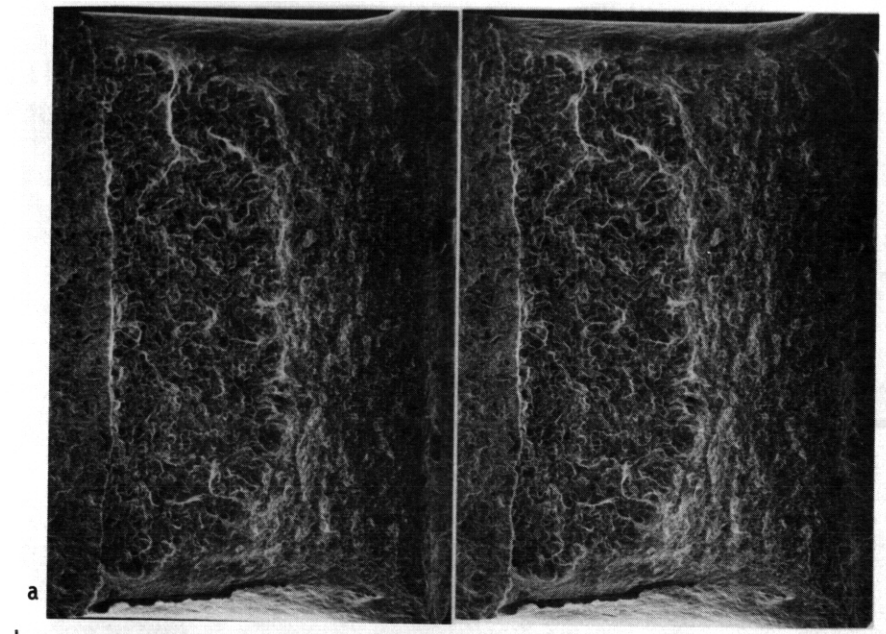

Figure 10. Fractographs of 9Cr-1W alloy specimen L814 following testing at -20°C at a) low and b) intermediate magnification.

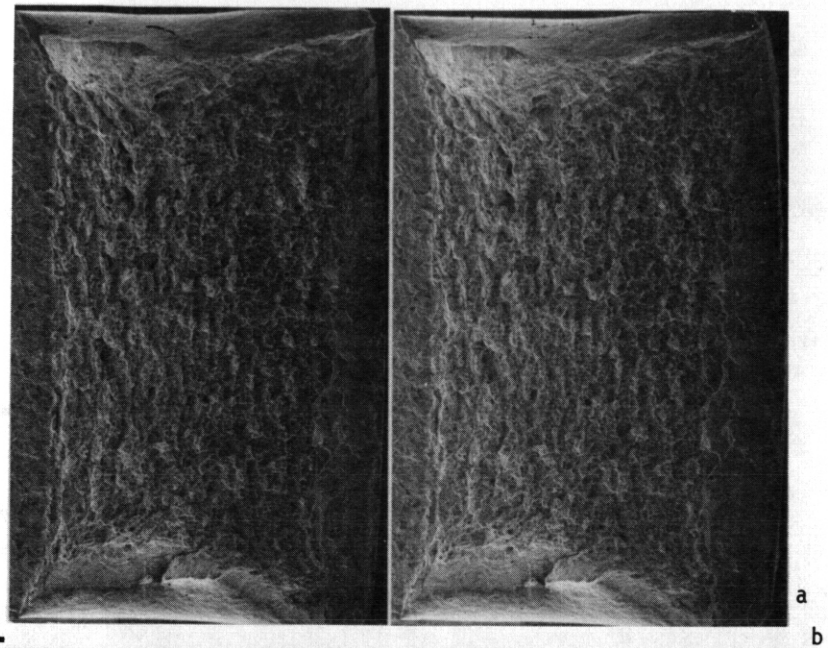

Figure 11. Fractographs of 9Cr-1W alloy specimen L812 following testing at 20°C at a) low and b) intermediate magnification.

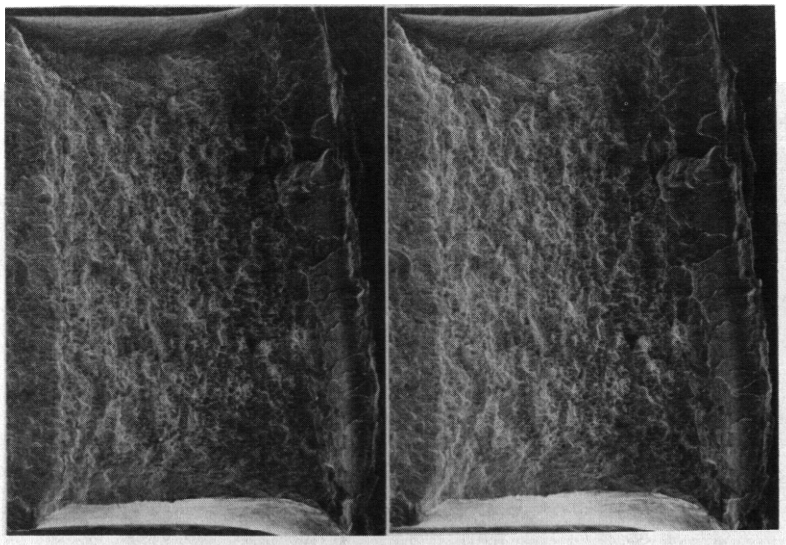

Figure 12. Fractographs of 9Cr-1W alloy specimen L802 following irradiation and testing at 21°C at a) low magnification and b) intermediate magnification.

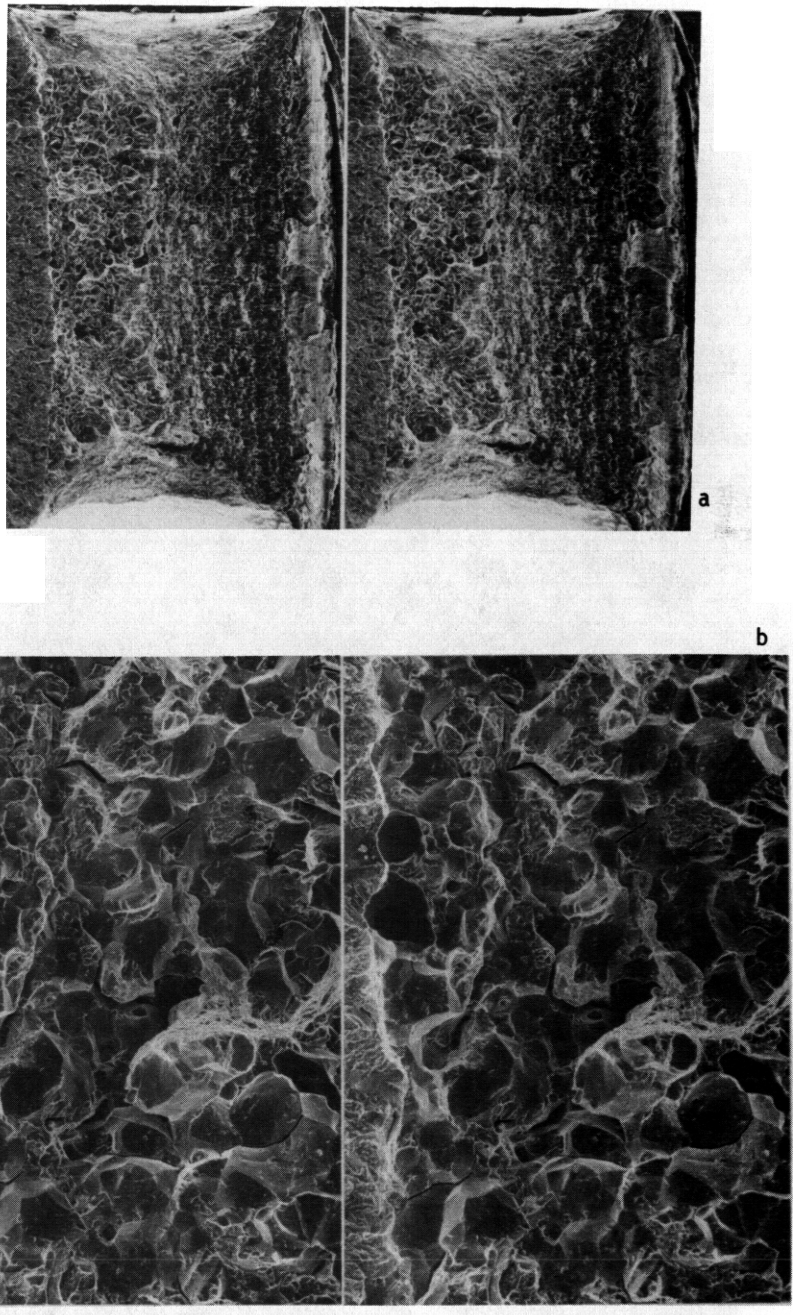

Figure 13. Fractographs of 9Cr-1W alloy specimen L801 following irradiation and testing at 50°C at a) low and b) intermediate magnification.

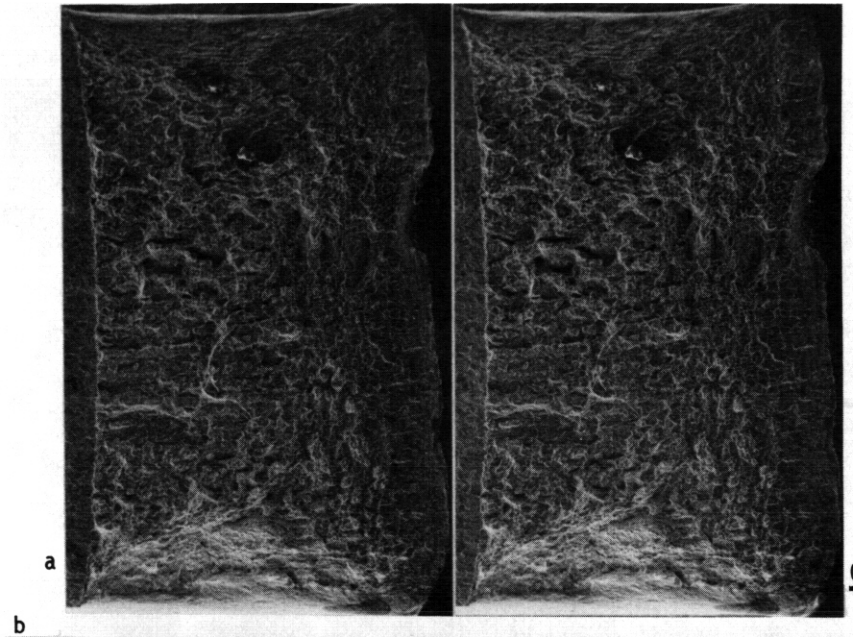

Figure 14. Fractographs of 12Cr-6Mn-1V alloy specimen L712 following testing at 25°C at a) low magnification and b) intermediate magnification.

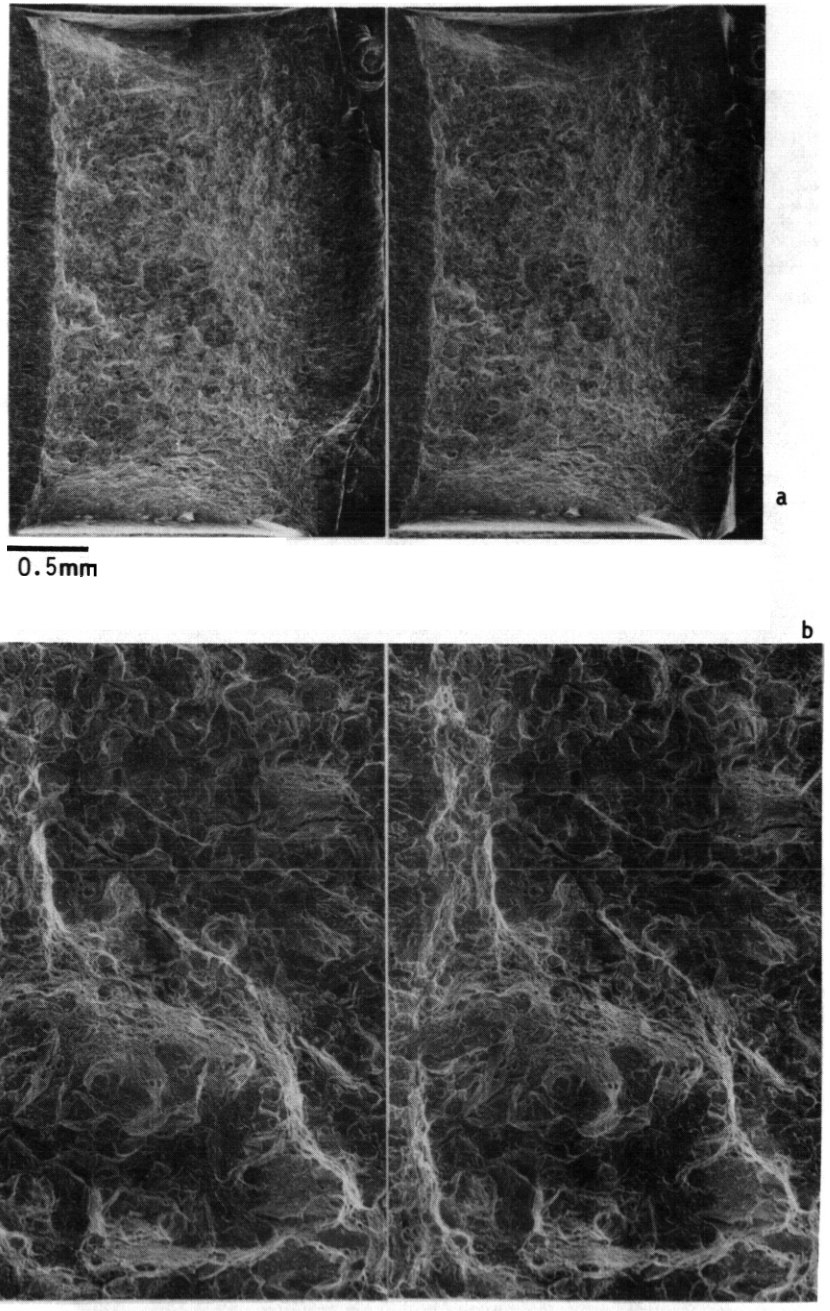

Figure 15. Fractographs of 12Cr-6Mn-1V alloy specimen L702 following irradiation and testing at 210°C at a) low and b) intermediate magnification.

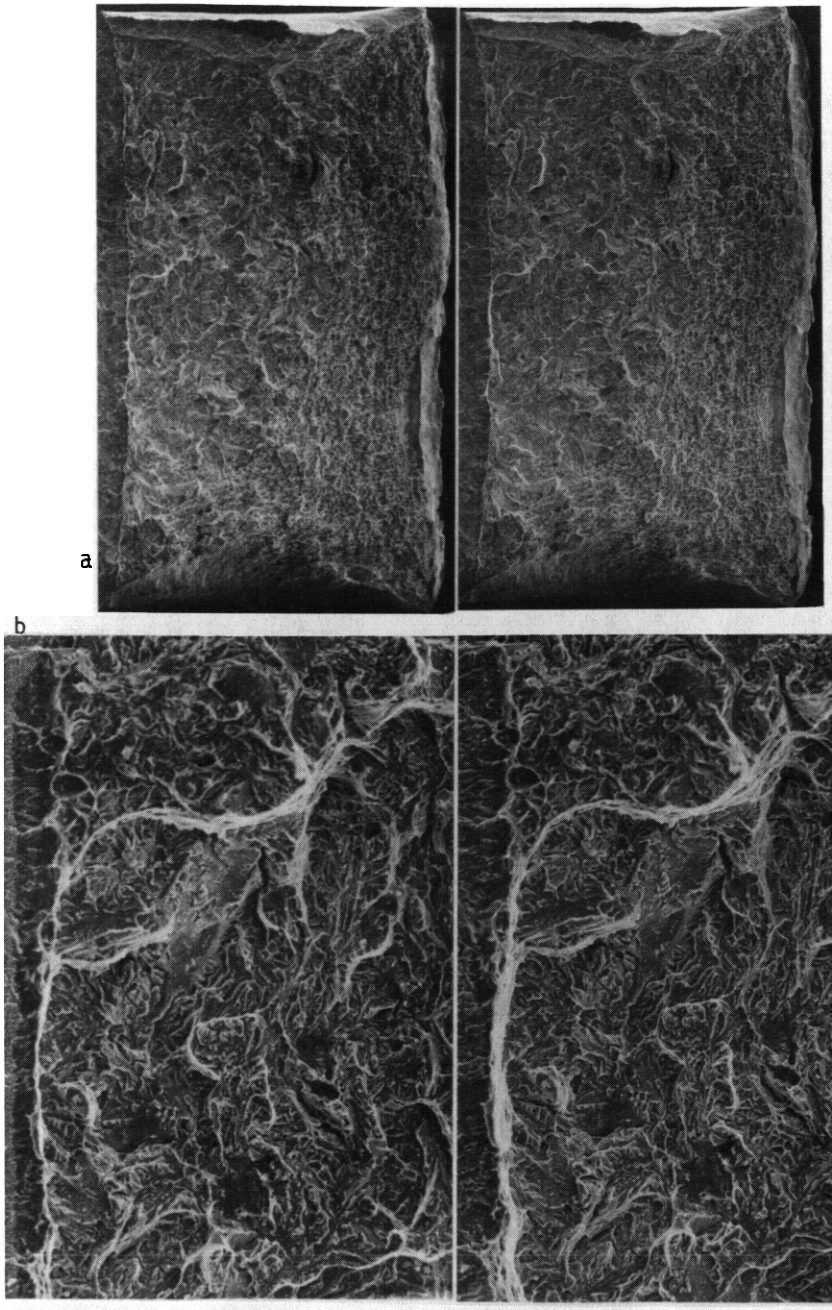

Figure 16. Fractographs of 12Cr-6Mn-1W alloy specimen L917 following testing at -60°C at a) low magnification and b) intermediate magnification.

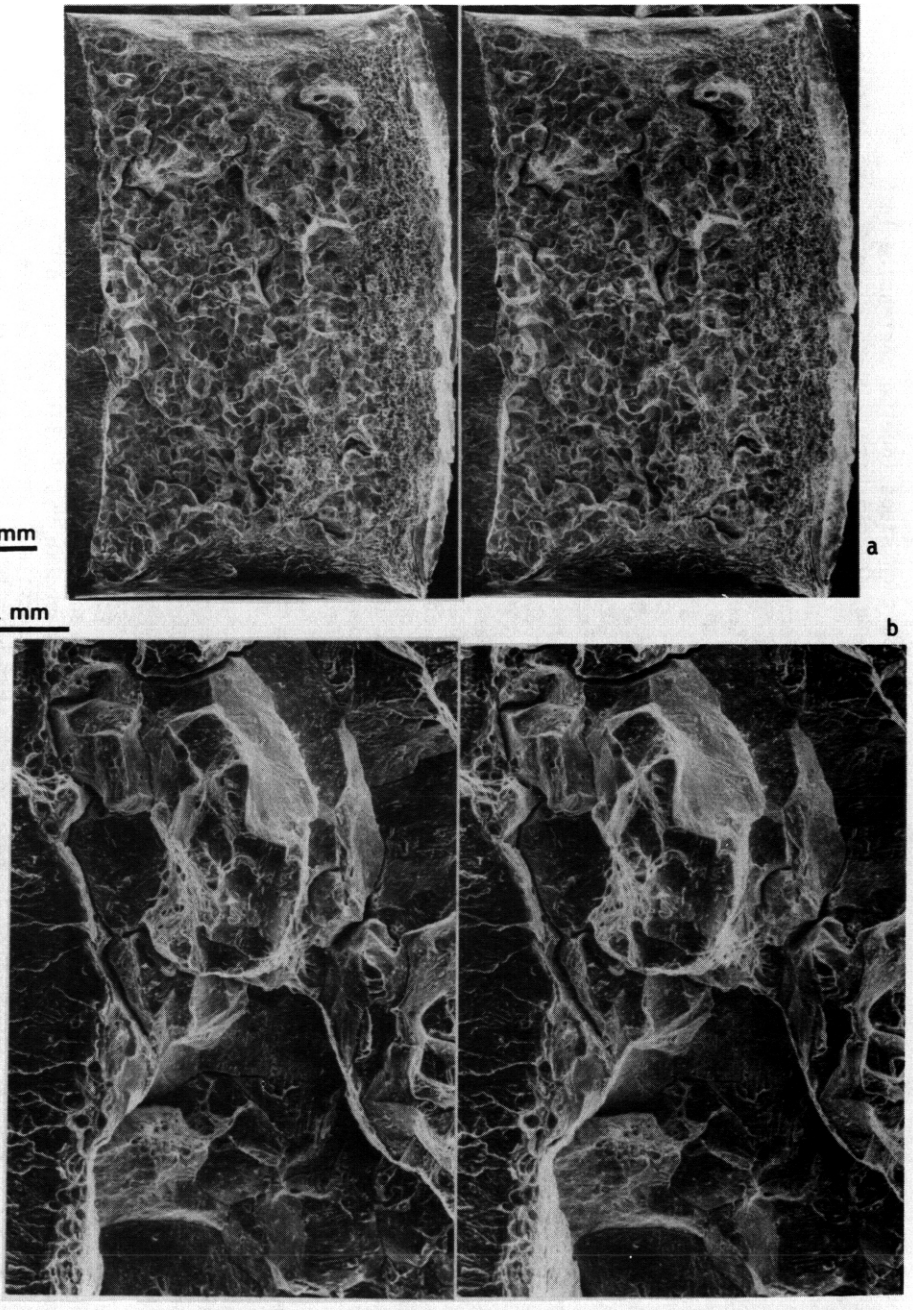

Figure 17. Fractographs of 12Cr-6Mn-1W alloy specimen L900 following irradiation and testing at 150°C at a) low and b) intermediate magnification.

8b) show relatively smooth darker surfaces without river pattern steps (due to martensite lath structure). These darker features are examples of grain boundary cleavage. Up to 20 percent of brittle failure in both specimens appears to be due to grain boundary cleavage. Similar features have been noted previously in HT-9 specimens.[3] Following irradiation. brittle failure In 9Cr-1V shifts almost canpletely to grain boundary cleavage whereas ductile failure is uniformly dimple rupture. The ductile and brittle regions are easily differentiated in Figure 9a) showing an irradiated specimen of 9Cr-1V tested at the DBTT, but Figure 9b) reveals martensite lath packet structure on only about 20 percent of the brittle fracture surface. Therefore. a change in fracture mechanism has occurred but only a minor increase in DBTT results.

Specimens of 9Cr-1W provided several surprises (Figures 10-13). Specimens selected to show behavior at the DBTT. both unirradiated and irradiated, were found to be entirely ductile with no evidence of cleavage fracture. Figure 11 of an unirradiated specimen tested at 20% and Figure 13 of an irradiated specimen tested at 50T show specimens that have failed entirely by dimple rupture. In both cases, the normalized fracture energy is considerably lower than the USE value and the test temperature is very close to the DBTT. The unirradiated specimen tested at -20T that is shown in Figure 10 and the irradiated specimen in Figure 12 that was tested at 21% were selected to be close to the lower shelf. However. inspection of Figures 10 and 12 shows fracture appearance with more dimple rupture than cleavage representing a test temperature at or above the DBTT based on a fracture appearance criterion. It must therefore be assumed that either something unusual happens during plastic deformation as a function of temperature in this canposition range or that the USE is actually lower than that measured. The brittle fracture appearance of the unirradiated 9Cr-1W shows a tendency for failure at prior austenite grain boundaries, and similar features can be identified on the fatigue precrack. However. the daninate brittle fracture made is transgranular cleavage. The brittle fracture appearance of the irradiated specimen tested at 21% was found to be very similar to the 9Cr-1V case: almst totally brittle fracture at prior austenite boundaries. In fact, the fracture surface in Figure 12b) shws more extensive grain boundary failure than does Figure 9b). Wedge cracks extending into the surface are clearly visible. as if grains are about to be pulled out. As it is unlikely that brittle failure was at prior austenite boundaries in the unirradiated condition, a change in fracture mode due to irradiation has probably occurred. Therefore. Irradiation has apparently changed the brittle fracture mode in 9Cr-1W as well.

The 12Cr alloys behaved similarly. As shown in Figures 14 and 16, the unirradiated conditions of 12Cr-6Mn-1V and 12Cr-6Mn-1W tested at the DBTT failed by transgranular cleavage in the brittle mode and by dimple rupture in the ductile mode. Failure is well behaved in the V alloy shown in Figure 14, despite the fact that this alloy contains 5 percent delta ferrite.[5] However, for each alloy. a change in failure mode occurred as a result of irradiation so that brittle failure was by failure at prior austenite boundaries. Figure 15 is not easy to interpret because the high test temperature has resulted in oxidation of the surface, but examples of wedge cracking are clearly indicated in both Figures 15b) and 17b), and, in fact, failure is by grain boundary failure in the brittle region. Therefore. as with the 9 Cr alloys. a change in brittle fracture mode has occurred in the 12Cr alloys as a result or irradiation.

Rockwell hardness measurements were made on selected specimens in order to provide further basis for explanation of observed behavior. It may be noted that tensile data is available for these alloys following irradiation at 420°C,[5,6] but no tensile measurements were made on specimens irradiated at 365 C. The results of hardness measurements are given in Table 2. Canparison of the results in Table 2 provides the unexpected conclusion that irradiation has not produced large changes in hardness. Significant changes were only noted in 2Cr-1V, where hardness rose from 15.8 to 27.3. and 2.7Cr-2W, where hardness measured from 19.2 to 24.6. In all other cases, hardness increased less than 3 points. Table 2 also provides estimates for tensile strength based on carbon and alloy steels (from the SAE Handbook). The hardness increase for 2Cr-1V corresponds to a tensile strength increase from 700 to 900 MPa or 30%. (Reference 5 indicates an increase from approximately 400 MPa or 125% increase.) Therefore, the changes in Charpy impact behavior for 2Cr-1V can be ascribed to irradiation induced hardening but changes in behavior for the 12Cr alloys must be ascribed to other causes such as segregation.

Discussion

Fractographic examination of low activation charpy impact specimens has provided two observations which affect interpretation of the impact property data: 1) Fracture surfaces of alloy 9Cr-1W specimens which were tested at the DBTT were found to have failed only by ductile dimple rupture whereas partial failure by brittle fracture was expected. 2) A change in brittle fracture mode from transgranular cleavage to brittle failure at prior austenite grain boundaries was observed in four of the six steels studied. The purpose of this section will be to enlarge on these observation.

Observation of only ductile dimple rupture on fracture surfaces of Charpy specimens tested at the DBTT is very unusual. The present series of examinations provides four examples to show that it does occur in a 9Cr-1W alloy, and includes both unirradiated and irradiated specimen conditions. Given the number of corroborating observations. the possibility of specimen misidentity or mixup can probably be ruled out. Unfortunately. a straightforward explanation for the behavior is not apparent. Specimens L814 and L802, which were tested at temperatures corresponding to lower shelf behavior did show brittle fracture and therefore the cause of the DBTT in this material is normal: a shift from a ductile to a brittle fracture

mode with decreasing temperature. However. that specimen also showed that, using a definition of DBTT based on fracture appearance, the DBTT would be lower. The most likely explanation for such a disparity is that large changes in plasticity occur as a function of test temperature during upper shelf testing. But the cause for such a phenanenon during impact loading is not yet understood.

Four of the six alloys tested were found to undergo a change in brittle fracture mode fran transgranular cleavage to intergranular fracture at prior austenite boundaries. Because one of the exceptions was the alloy containing 2 percent W, it is unlikely that the behavior is due to excessive V and W in the 9 to 12 Cr composition range. A more likely cause is the presence of Mn. It has been shown that Mn additions promote shifts in DBTT following irradiation.[2,7] In that study. Mn additions were made to 12Cr-1Mo alloys in order to reduce the necessary Ni and C contents for a fully martensitic structure. Charpy specimens were irradiated at 365 C to 5 and 11 dpa and it was found that large shifts in DBTT resulted which were in proportion to the amount of Mn present. For the alloy containing 3.3 Mn, the shift was 130 C and for the alloy containing 6.6 Mn, the shift was 220°C. Also. a change in brittle fracture mode was found following irradiation fran transgranular cleavage to intergranular failure at prior austenite boundaries. The present results on 12 Cr alloys provide similar results (except that the shifts in DBTT are not as large). This suggests that the 9Cr-1W alloy. which contains 2.44 percent Mn, and the 9Cr-1V alloy. which contains 1.1 percent Mn, are being affected *by* Mn additions in a similar way. Note that the 7.5Cr-2W alloy contains no intentional additions of Mn. Therefore. these results provide confirmation that Mn additions to steels are detrimental for their effect on temper embrittlement,[8] at least for irradiation environments. even though the additions of Si. P and S are kept low.

CONCLUSIONS

A series of low activation miniature Charpy specimens have been examined by scanning electron microscopy in order to provide further understanding of the irradiation embrittlement process. It was found that irradiation resulted in a change in brittle fracture mode for four of the six alloys examined: 9Cr-1V, 9Cr-1W, 12Cr-1V and 12Cr-1W. The cause of the change is ascribed to Mn additions in the alloys. The examinations also indicated that the DBTT of the 9Cr-1W may be lower than experimentally measured based on a fracture appearance criterion for DBTT. The cause for this discrepancy has not been determined.

FUTURE WORK

This effect will be continued when specimens irradiated to higher fluence are available.

REFERENCES

1. N.S. Cannon. W.L. Hu and O.S. Gelles. DOE/ER-0313/2, 119.

2. O.S. Gelles and W.L. Hu, DOE/ER-0313/1, 251.

3. O.S. Gelles and W.L. Hu, Alloy Development for Irradiation Performance Semiannual Progress report for the Period ending March 31, 1985. DOE/ER-0045/14, 137.

4. O.S. Gelles. W.L. Hu, F.H. Huang and G.O. Johnson, Alloy Development for Irradiation Performance Semiannual Progress report for the Period ending September 30, 1983, DOE/ER-0045/11, 115.

5. D.S. Gelles and M.L. Hamilton. Alloy Development for Irradiation Performance Semiannual Progress report for the Period ending September 30, 1984, DOE/ER-0045/13, 128.

6. O. S. Gelles and M L. Hamilton, IBID, DOE/ER-0045/16,131.

7. W.L. Hu and O.S. Gelles. Alloy Development for Irradiation Performance Semiannual Progress report for the Period ending March 31, 1986, DOE/ER-0045/16, 140.

8. J. Yu and C.J. McMahon, Jr., Met. Trans. A, 11A (1980) 291.

IMPACT BEHAVIOR OF 9-Cr AND 12-Cr FERRITIC STEELS AFTER LOW-TEMPERATURE IRRADIATION — R. L. Klueh, J. M. Vitek, W. R. Corwin, and D. J. Alexander (Oak Ridge National Laboratory)

OBJECTIVE

The objective of this work is to determine the effect of irradiation on the impact behavior of 9Cr-1MoVNb and 12Cr-1MoVW steels. By irradiating these steels and these steels with 1 and 2% Ni in mixed-spectrum reactors, we are attempting to study the simultaneous effect of displacement damage and transmutation helium on the impact properties.

SUMMARY

Miniature Charpy impact specimens of 9Cr-1MoVNb and 12Cr-1MoVW steels and these steels with 1 and 2% Ni were irradiated in the High-Flux Isotope Reactor (HFIR) at 50°C to displacement damage levels of up to 9 dpa. Nickel was added to study the effect of transmutation helium. Irradiation caused an increase in the ductile-brittle transition temperature (DBTT). The 9Cr-1MoVNb steels, with and without nickel, showed a larger shift than the 12Cr-1MoVW steels, with and without nickel. Under certain conditions, the DBTT of the nickel-doped steels showed a larger shift than that of the undoped steels. The results were interpreted to mean that helium affected the DBTT in the same way as the displacement damage.

PROGRESS AND STATUS

Introduction

A steel in a fusion reactor first wall will experience displacement damage from the high-energy neutrons from the fusion reaction. Displacement damage can lead to changes in the impact behavior as measured by Charpy impact tests.[1-5] In addition to displacement damage, large amounts of transmutation helium will also form in the first-wall material of a fusion reactor. To study the effect of simultaneously produced displacement damage and transmutation helium, nickel has been added to the 9-Cr and 12-Cr steels.[6] When these nickel-doped steels are irradiated in a mixed-spectrum reactor, such as the HFIR. displacement damage is produced by the fast neutrons in the spectrum, and helium is produced by a two-step transmutation reaction of ^{58}Ni with the thermal neutrons in the spectrum. One objective of this work was the determination of the effect of helium on the impact properties.

Experimental Procedure

Electroslag-remelted heats of standard 9Cr-1MoVNb (0.1% Ni) and 12Cr-1MoVW (0.5% Ni) steels were prepared. These compositions with 1 and 2% Ni, designated 9Cr-1MoVNb-2Ni, 12Cr-1MoVW-1Ni, and 12Cr-1MoVW-2Ni, were also prepared. Specimens were obtained from normalized-and-tempered 5.35-mm-thick plates. The 9-Cr steels were annealed 0.5 h at 1040°C and the 12-Cr steels 0.5 h at 1050°C, after which they were air cooled. The 9Cr-1MoVNb steel was tempered 1 h at 760°C; the 12Cr-1MoVW and 12Cr-1MoVW-1Ni steels were tempered 2.5 h at 780°C. The 9Cr-1MoVNb-2Ni and 12Cr-1MoVW-2Ni steels were tempered 5 h at 700°C. Tempered martensite microstructures were obtained by such heat treatments. Details on chemical composition, heat treatment, and microstructure have been published.[6]

Miniature Charpy V-notch (C_v) specimens were machined from the heat-treated plate in the longitudinal (LT) orientation. The subsize specimens measured 5 by 5 by 25.4 mm and contained a 0.76-mm-deep 30° V notch with a 0.05- to -0.08-mm-root radius. In the irradiated conditions, such miniature specimens show impact behavior similar to that found in full-sized C_v specimens.[7,8]

The specimens were irradiated in three capsules in HFIR at the reactor-coolant temperature of ~50°C as follows: Specimens in the capsule designated HFIR-CTR-T3 were irradiated in the peripheral target region of the reactor to displacement-damage levels of 5.7 to 9.1 dpa. Capsules designated HFIR-CTR-RB1 and HFIR-CTR-RB2 were irradiated in the beryllium-reflector region to displacement-damage levels of 2.7 to 4.5 dpa and 4.3 to 9.2 dpa, respectively. The displacement-damage levels and helium concentrations of the specimens depended on the position of the specimen in the capsule; the helium concentration also depended on the amount of nickel in the material.

Tests were carried out in a pendulum-type impact machine specially modified to accommodate the subsize specimens. Detailed information on the test equipment has been published.8 To obtain the DBTT and upper-shelf energy (USE), impact energy-temperature curves were generated by fitting the data with a hyperbolic tangent function. Because of the limited number of specimens available, the USE could not always be determined accurately. The DBTT was chosen at a fixed energy level of 9.2 J, which is analogous to the frequently used criterion of 68 J in a full-size specimen.

Results

The results are given in Table 1. There are difficulties with these types of tests. First, reactor space limitations restrict the number of specimens that can be irradiated per capsule. For RB1, there were six specimens for each of the two 9-Cr steels, four for 12Cr-1MoVW, five for 12Cr-1MoVW-1Ni, and only three for 12Cr-1MoVW2-Ni. In RB2, only four specimens were irradiated for each material except 9Cr-1MoVNb-2Ni, for which there were only two specimens. No data are given for 9Cr-1MoVNb-2Ni irradiated in RB2. The T3 capsule contained more specimens (seven or eight for each steel) but for only two steels: 12Cr-1MoVW and 12Cr-1MoVW-2Ni. A second problem with these types of irradiation experiments results from the variation in flux along the length of the capsule. This variation leads to different fluences for the different specimens of the same steel. Therefore, specimens with different displacement-damage levels and helium concentrations were used to produce a given Charpy impact curve.

Table 1. Charpy Impact Properties of Unirradiated and Irradiated Cr-No Steels

Steel	Experiment	Irradiation Effects		DBTT[a] (°C)	ΔDBTT (°C)	USE (J)
		dpa	(appm He)			
9Cr-1MoVNb	C[b]	Unirradiated		-40		26
	RB1	2.7–3.4	2.5–3	62	102	20
	RB2	4.4–5.8	4–6	70	110	17
9Cr-1MoVNb-2Ni	C	Unirradiated		-90		24
	RB1	2.8–3.4	35–43	53	143	11
12Cr-1MoVW	C	Unirradiated		–35		26
	RB1	4.3	15	-33	2	20
	RB2	7.2–9.2	30–39	–2	31	25
	T3	6.C–9.0	11–17	3	36	24
12Cr-1MoVW-1Ni	C	Unirradiated		-37		23
	RB1	3.9	26	30	67	20
	RB2	8.4	66	37	74	23
12Cr-1MoVW-2Ni	C	Unirradiated		–25		17
	RB1	4.0–4.5	50–55	31	62	11
	RB2	6.1–7.4	93–114	66	91	13
	T3	5.7–9.1	36–58	51	76	15

[a]Measured at 9.2 J. [b]Unirradiated control specimens.

The variations in displacement-damage level and helium concentration for each set of specimens are given in Table 1. Note that, although the 12Cr-1MoVW and 12Cr-1MoVW-2Ni steel specimens irradiated in RB2 had displacement damage levels similar to those irradiated in T3. these specimens contained more helium than those irradiated in RB2. This was caused by a higher thermal flux in the reflector region of the reactor where the RB2 capsules were located in the reactor. Transmutation helium is generated from nickel by thermal neutrons.

Table 1 gives the DBTT as measured at the 9.2 J level, the DBTT shift, (ΔDBTT), and the USE. The USE of the 9Cr-1MoVNb steel was lower than normally observed for this steel. This was previously discussed and attributed to an under-temper condition.[5] Note that the data obtained in the T3 and RB2 experiments on the 12Cr-1MoVW and 12Cr-1MoVW-2Ni steels are in good agreement. This adds confidence to the results obtained from sets of specimens with only 3 or 4 specimens, because 7 and 8 specimens were irradiated and tested for the two materials in the T3 experiment while only four specimens of each were irradiated and tested in the RB2 experiment.

Discussion

Previous work has shown that the nickel additions have no significant effect on the microstructures and the precipitates that form in the 9Cr-1MoVNb and 12Cr-1MoVW steels.[9] The differences in the Charpy behavior of the unirradiated nickel-doped and undoped steels were previously discussed.' A tempering treatment of 700°C was used for the steels containing 2% Ni because nickel lowers the A_{c_1} temperature. Although the 760 and 700°C tempering temperatures for the 9Cr-1MoVNb and 9Cr-1MoVNb-2Ni steels, respectively, resulted in somewhat similar hardnesses, the strength of the 9Cr-1MoVNb was less than that for 9Cr-1MoVNb-2Ni.[6] Generally, the steel tempered to the lowest strength is expected to have the lowest DBTT. just the opposite to what was observed (Table 1).

There are indications that nickel decreases the DBTT and the USE in pearlitic steels.[10] Chromium, molybdenum, and tungsten have the opposite effect. Assuming the same effect occurs in a martensitic structure, these alloying effects would explain the observations on the 9-Cr steels. Such large effects were not observed for the 12-Cr steel.

As expected, the results on the irradiated specimens showed that neutron irradiation caused an increase in OBTT. A relatively large decrease in USE accompanied the increase in DBTT for the 9-Cr steels

but the 12-Cr steels showed relatively small changes in USE. The decrease in USE for the 9Cr-1MoVNb was progressively larger with increasing displacement-damage level. The 9Cr-1MoVNb-2Ni steel also showed a large decrease in USE following irradiation.

The results indicate a difference between the 9-Cr and 12-Cr steels. For the 9Cr-1MoVNb steel, there was a large increase in DBTT after irradiation to 2.3 to 3.4 dpa, with essentially no change for the higher dpa (4.3-5.7 dpa). The shift in DBTT for the 12-Cr steels was substantially lower: after ~4 dpa, only a small increase occurred. However, this curve was obtained with only four specimens, and one of the data points did not follow the expected sequence. (Note in Table 1 that this Charpy curve was the only one that had a large decrease in the USE, which could be a further indication that this curve is inaccurate.) Because of the displacement of this one point, the OBTT calculated by the curve-fitting procedure is probably inaccurate, and the USE is higher than that given in Table 1. However, there was good agreement in the results for the 12Cr-1MoVW steel specimens irradiated to ~9 dpa in RB2 and T3. These curves showed a ΔDBTT of 31 and 36°C, respectively, with little change in USE. Thus, the increase in DBTT for the 9Cr-1MoVNb steel (102–110°C) was nearly three times that for the 12Cr-1MoVW steel (31–36°C).

Gelles et al.[11,12] tested pre-cracked Charpy specimens of 9Cr-1MoVNb and 12Cr-1MoVW that were irradiated in the RB1 and RB2 capsules. Although different heats of steel, slightly different heat treatments, and different orientations were irradiated, similar changes in OBTT were obtained: The OBTT of the 9Cr-1MoVNb and 12Cr-1MoVW steels increased 90 and 30°C, respectively,[11] in RB1, and 130 and 62°C, respectively,[12] in RB2.

The majority of the previous results was for specimens irradiated at elevated temperatures.[1-5] Irradiation of 12Cr-1MoVW steel in EBR-II to displacement-damage levels of *26* dpa (little helium) at 390°C gave rise to an increase in DBTT of 144°C,[3] a considerably larger increase than observed for irradiation at 50°C. Similarly, specimens irradiated 4 to 9 dpa in HFIR at 300 and 400°C had ΔDBTTs of 164 and 217°C, respectively.[4] As the irradiation temperature was increased above 400°C, ΔDBTT decreased; it was 50°C at 550°C.[3,5]

All of the data are shown in Fig. 1(a), which is updated from when it was previously presented.[4] The figure indicates that the increase in DBTT for 12Cr-1MoVW steel goes through a maximum around 400°C. This is in contrast with the data for the 9Cr-1MoVNb steel [Fig. 1(b)]. After irradiation at 390°C in EBR-II, the AOBTT for 9Cr-1MoVNb is only about 50°C,[3] compared with 90 to 110°C after the 50°C irradiation; after irradiation at 450°C and above, no change in OBTT was observed.' Thus, the ADBTT-temperature curve for the 9Cr-1MoVNb steel shows decreases as the temperature increases from 50 to 400°C, after which it drops rapidly to zero.

The behavior observed for the 9Cr-1MoVNb steel is the expected behavior. An increase in DBTT is expected to result from the hardening caused by the displacement damage, and as the temperature is increased, some of the hardening is offset by recovery effects. Gelles et al. found black-dot damage in both the 9Cr-1MoVNb and 12Cr-1MoVW steels irradiated at 50°C, with no apparent difference between the two steels.[11] In tensile tests after irradiation at 50°C, similar amounts of hardening were observed for 9Cr-1MoVNb and 12Cr-1MoVW steels.[13] With an increase in the irradiation temperature, defects and some of the dislocations of the structure can anneal out, although some additional hardening can occur because of irradiation-induced precipitation.[9,14] Tensile tests on 9Cr-1MoVNb and 12Cr-1MoVW steels have shown that the strength was increased by irradiation at 400°C, but the strength increase was less than that after irradiation at 50°C.[15,16] After irradiation at 450°C and above, there was little change in strength compared to the unirradiated steel. These tensile results show a change in properties with irradiation temperature similar to that observed for the impact properties of the 9Cr-1MoVNb steel [Fig. 1(b)].

The previous results give no reason to expect a difference in behavior between 9Cr-1MoVNb and 12Cr-1MoVW. However, some significant differences have been observed in the precipitation in the 12Cr-1MoVW and 9Cr-1MoVNb during irradiation.[9] Maziasz et al.[9] observed that, after irradiation in HFIR at 300 to 500°C, some of the $M_{23}C_6$ in the as-tempered microstructure of the 9Cr-1MoVNb steel had dissolved and the subgrain structure had coarsened. This contrasted with the $M_{23}C_6$ and subgrain structure in the 12Cr-1MoVW steel, which remained stable. Irradiation of the 9Cr-1MoVNb steel at 300 to 500°C also caused a dissolution of some of the finer MC particles and a coarsening of the larger particles. Some coarsening of MC also occurred in the 12Cr-1MoVW steel, but large amounts of irradiation-produced M_6C also formed.

The observed changes in the microstructure of the 9Cr-1MoVNb steel between 300 and 500°C could affect the DBTT. The coarsening of the subgrain structure should lower the DBTT. Thus, as the irradiation temperature increases, these recovery effects offset some of the hardening caused by the displacement damage. For the 12Cr-1MoVW steel, no softening due to subgrain coarsening occurs and the hardening effect due to irradiation-produced M_6C is superimposed on the production of displacement damage. Another way of looking at these results is that the 9Cr-1MoVNb steel behaves as expected, assuming that radiation hardening causes the DBTT shift. If the precipitation reactions did not occur in the 12Cr-1MoVW steel and it behaved as expected, the DBTT shift for this steel would be less than that for 9Cr-1MoVNb at all temperatures. However, the curve in Fig. 1(a) for the 12Cr-1MoVW steel consists of the expected curve [similar to Fig. 1(b), but with a lower shift at 50°C] with the effect of precipitation superimposed on it.

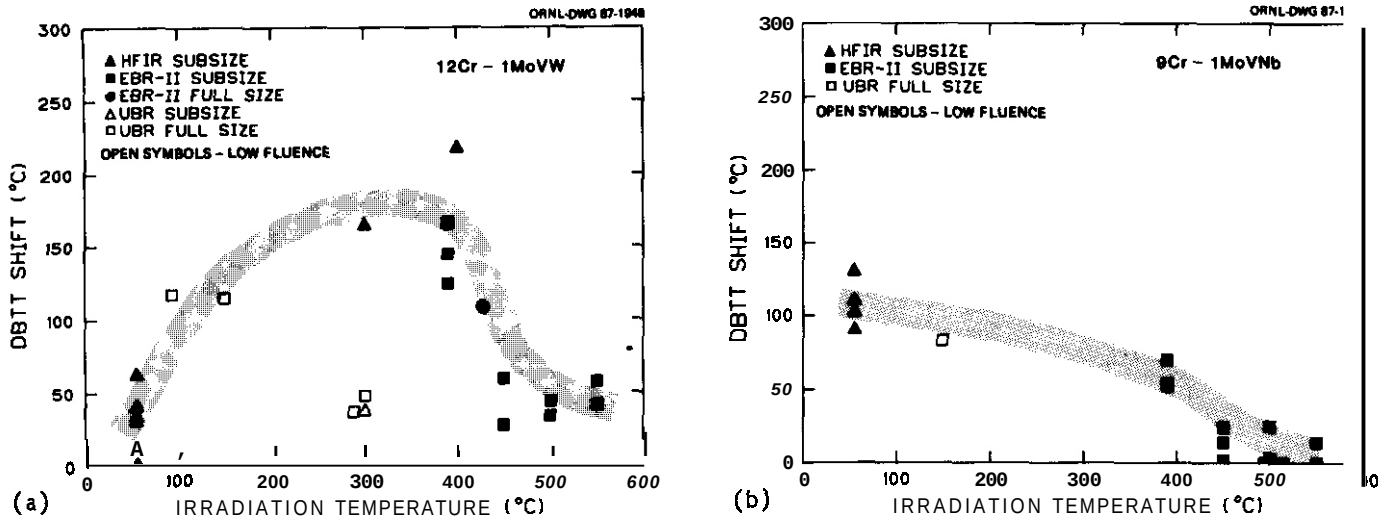

Fig. 1. Increase in DBTT as a function of irradiation temperature for (a) 12Cr-1MoVW and (b) 9Cr-1MoVNb steel.

Helium appears to affect the impact properties. This is most clearly shown by the results for the nickel-doped and undoped 12-Cr steels (Table 1). The small amounts of data make definite conclusions difficult. However, for a given dpa (and helium concentration) the AOBTT values increase as the helium concentration (nickel concentration) is increased. Also, the differences in the results for the tests for experiments RB2 and T3 for the 12Cr-1MoVW-2Ni are noteworthy. The ADBTT for the tests from RB2 was 91°C and from T3 was 76°C. Both sets of specimens were irradiated to similar displacement-damage levels, but the specimens in T3 contained 36 to 58 appm He, while those from RB2 contained 93 to 114 appm. Furthermore, the ADBTT for the 12Cr-1MoVW-2Ni irradiated in T3 was similar to that for the 12Cr-1MoVW-1Ni irradiated in RB2. Similar displacement-damage levels and helium concentrations were achieved for both materials under these test conditions.

An interpretation of the difference in the results for the 9Cr-1MoVNb and 9Cr-1MoVNb-2Ni steels is difficult because of the different heat treatments used for these two steels. The 9Cr-1MoVNb-2Ni has a much lower DBTT prior to irradiation than the 9Cr-1MoVNb. Nevertheless, the 9Cr-1MoVNb-2Ni steel shows a larger shift in OBTT, which may be attributable to helium.

Because of the low irradiation temperatures, the mechanism by which helium affects the properties would be expected to be caused by helium in solution. The possibiltty of a saturation of ADBTT due to displacement-damage effects has been discussed.[4,12] The present results indicate a helium effect is superimposed on the displacement-damage effect. Although the helium effect would also be expected to saturate, a much larger ΔDBTT might be expected than the 144 to 166°C shift observed for 12Cr-1MoVW steel irradiated at 390°C in EBR-II.[3,5] More tests of the type discussed in this report will be required to determine the maximum effect.

SUMMARY AND CONCLUSIONS

Charpy impact specimens of standard 9Cr-1MoVNb and 12Cr-1MoVW steels and these steels doped with up to 2% Ni were irradiated at 50°C in HFIR to displacement-damage levels of up to 9 dpa. Because of the nickel present in the steels, irradiation in HFIR produced up to 115 appm He.

Irradiation caused an increase in the DBTT of all steels. The increase was larger for the 9-Cr steels than the 12-Cr steels. The results from these and other studies indicate that the change in ΔDBTT with temperature for the 12Cr-1MoVW has a peak at ~400°C and decreases at higher or lower temperatures. The ΔDBTT for 9Cr-1MoVNb decreases gradually as the irradiation temperature increases from 50 to 400°C, after which it quickly decreases to zero. The data indicate that helium caused an increase in the DBTT of the 9-Cr and 12-Cr steels in addition to that caused by displacement damage.

REFERENCES

1. F. A. Smidt, Jr., J. R. Hawthorne, and V. Provenzano, p. 269 in Effects of Radiation on Materials, STP 725, ed. D. Kramer, H. R. Brager, and J. S. Perrin. American Society for Testing and Materials, Philadelphia. 1981.

2. J. R. Hawthorne, J. R. Reed, and J. A. Sprague, p. 580 in Effects of Radiation on Materials: Twelfth Inter. Sym.., STP 870, ed. F. A. Garner and J. S. Perrin, American Society for Testing and Materials, Philadelphia. 1985.

3. W. L. Hu, p. 106 in ADIP Semiannu. Prog. Rep. Sept. 30, 1984, DOE/ER-0045/13, U.S. DOE, Office of Fusion Energy.

4. J. M. Vitek. W. R. Corwin, R. L. Klueh, and J. R. Hawthorne, J. Nucl. Mater. 141-143 (1986) 948.

5. W. R. Corwin, J. M. Vitek, and R. L. Klueh, J. Nucl. Mater. 147 (1987) 312.

6. R. L. Klueh, J. M. Vitek. and M. L. Grossbeck, p. 648 in Effects of Irradiation on Materials: Eleventh Conference, ASTM STP 782, ed. H. R. Brager and J. S. Perrin, American Society for Testing and Materials, Philadelphia, 1982.

7. W. R. Corwin, R. L. Klueh, and J. M. Vitek, J. Nucl. Mater. 122&123 (1984) 343.

8. W. R. Corwin and A. M. Hougland, p. 325 in The Use of hall-Scale Specimens for Testin Irradiated Material, ed. W. R. Corwin and G. E. Lucas, American Society for Testing and Materia s, Philadelphia, 1986.

9. P. J. Maziasz, R. L. Klueh and J. M. Vitek. J. Nucl. Mater. 141&143 (1986) 929.

10. J. A. Rinebolt and W. J. Harris, Jr., Met. Trans. 43 (1951) 1175.

11. D. S. Gelles, W. L. Hu, F. W. Huang, and G. D. Johnson, p. 115 in ADIP Semiannu. Prog. Rep. Sept. 30, 1983, DOE/ER-0045/11, U.S. DOE, Office of Fusion Energy.

12. D. S. Gelles, J. Nucl. Mater. 149 (1987) 192.

13. R. L. Klueh and J. M. Vitek, p. 615 in Ferritic Alloys for Use in Nuclear Energy Technologies, ed. J. W. Davis and D. J. Michel, The Metallurgical Society of AIME, Warrendale, Pennsylvania, 1984.

14. D. S. Gelles and L. E. Thomas. p. 343 in ADIP Semiannu. Prog. Rep. Mar. 31, 1982, DOE/ER-0045/8, U.S. DOE, Office of Fusion Energy.

15. R. L. Klueh and J. M. Vitek, J. Nucl. Mater. 132 (1985) 27.

16. R. L. Klueh and J. M. Vitek, J. Nucl. Mater. 137 (1985) 44.

FRACTOGRAPHIC EXAMINATION OF CHARPY IMPACT SPECIMENS FROM THE HFIR-MFE-RB2 TEST - D.S. Gelles and W.L. Hu* (Pacific Northwest Laboratory and *formerly Westinghouse Hanford Company)

OBJECTIVE

The objective of this work is to determine the effect of low temperature irradiation in HFIR on the properties of ferritic stainless steels in order to determine the applicability of these alloys as first wall materials.

SUMMARY

Selected fracture surfaces of miniature Charpy specimens of HT-9 in base metal, weld metal and heat affected zone (HAZ) metal conditions, and 9Cr-1Mo in base metal and weld metal conditions have been examined by scanning electron microscopy following irradiation in HFIR-MFE-RB2 at 55°C to 10 dpa. Hardness measurements have also been made. Comparison of results with results on specimens irradiated to low dose demonstrates only minor changes in fracture behavior, but continued increases in hardness due to irradiation. Therefore, the mechanism controlling the degradation of impact properties does not affect the fracture path but does affect strength. A mechanism is proposed to explain the behavior based on microchemical segregation of carbide forming elements.

PROGRESS AND STATUS

Introduction

Two experiments have now been performed to determine the effect of irradiation at low temperature on Charpy impact properties of martensitic steels.[1,2] Both experiments demonstrated that shifts in ductile to brittle transition temperature (DBTT) resulted when HT-9 and 9Cr-1Mo were irradiated at 50°C to doses on the order of 5 and 10 dpa. The results of those tests are shown in Figures 1 and 2. Figure 1, taken from reference 1, provides a comparison from the first experiment of the effect of 55 C irradiation in the High Flux Isotope Reactor (HFIR) on various conditions of HT-9 and 9Cr-1Mo for two dose levels.' Charpy impact energy is plotted as a function of specimen test temperature in order to determine the DBTT, and arrows connect the corresponding curves at 5 and 10 dpa In order to emphasize the effect of increased dose on behavior. The shifts for 9Cr-1Mo were unexpectedly larger than those for HT-9. Tests on specimens irradiated at higher temperatures give larger shifts in DBTT for HT-9, and the DBTT for 9Cr-1Mo is lower than that for HT-9 prior to irradiation.

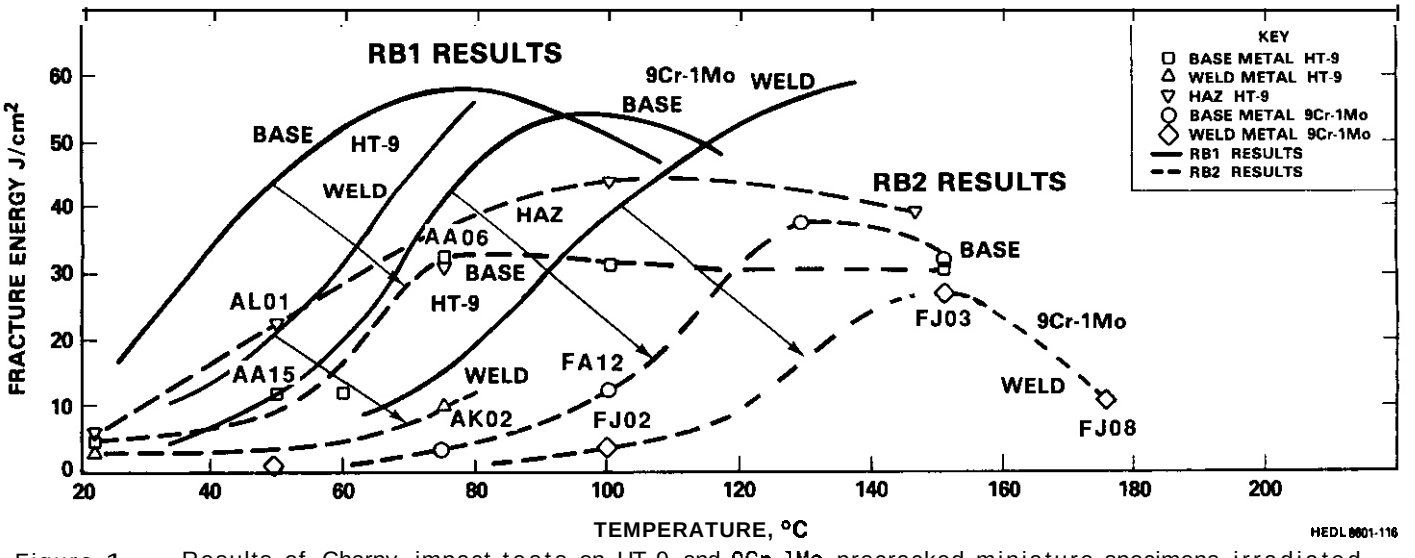

Figure 1. Results of Charpy impact tests on HT-9 and 9Cr-1Mo precracked miniature specimens irradiated in the RB2 Test in comparison with results fran the RB1 test showing normalized fracture energy as a function of test temperature. Specimens selected for fractographic examination are designated by specimen identification code.

The second experiment examined the effect of 50°C irradiation in HFIR as a function of alloy canposition in order to assess the effect of He/dpa ratio on deformation behavior. Figure 2 gives the results of DBTT shift for both experiments as a function of dose. The data base includes several alloying variations in order to evaluate the effect of nickel content and the resultant effect of He/dpa on behavior,[2] and therefore the nickel content for each curve is included. Figure 2 can be used to

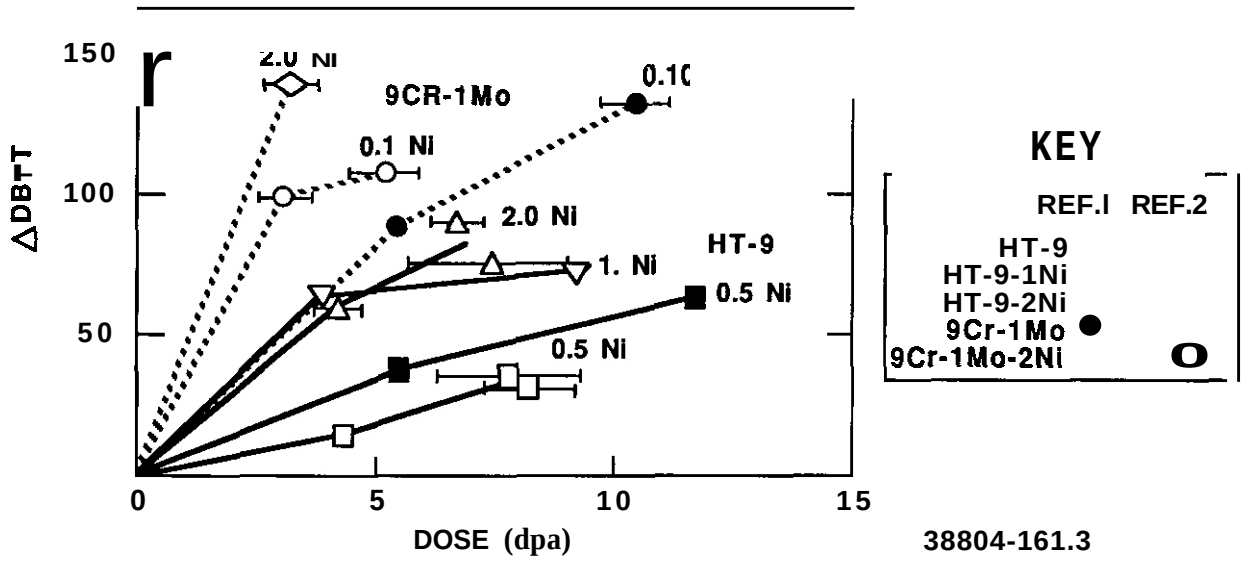

Figure 2. Shift in DBTT as a function of dose for miniature Charpy specimens of martensitic steels irradiated in HFIR at 55°C. Closed symbols are fran reference 1 and open symbols are fran reference 2.

demonstrate that nickel additions increased the observed shifts in OBTT for 9Cr-1Mo and for HT-9. However, the unexpected differences between 9Cr-1Mo and HT-9 could not be attributed to a nickel or helium effect since HT-9 contains significantly more nickel than does 9Cr-1Mo; sane other factor was more important. Furthermore. with incr asing dose. DBTT generally increased. exhibiting unsaturated behavior at 10 dpa in the first experiment.' but suggesting saturation in two of the four relevant examples fran the second experiment (9Cr-1Mo-0.1Ni and HT-9-1Ni).[2] However, taken as a whole. the data base indicates that saturation should not be expected before a dose of 20 dpa. Explanations given for the observed behavior were speculative. In one case, the differences in behavior between the two alloys were attributed to either a segregation phenanenon or behavior where radiation damage to carbides affects crack nucleation response.[1] In the other case, differences were ascribed to unusually high radiation resistance in the HT-9 to precipitation which resulted in reduced irradiation hardening. Therefore. 9Cr-1Mo behaved normally but HT-9 gave unexpectedly small shifts in DBTT.[2]

The purpose of the present effort is to continue the study of effects of irradiation at low tmperatures by examining the fracture surfaces of selected specimens fran reference 1 in order to provide further insights in the processes controlling behavior. Fractography on specimens irradiated to 5 dpa has been reported previously,[3] and the present work examines similar specimens irradiated to 10 dpa. Fractographs in both this and the previous work are presented as stereo pairs and the reader is strongly encouraged to view them stereoscopically in order to fully appreciate the fracture response.

Experimental procedures

Specimens selected for fractographic examination are listed in Table 1 along with test conditions and results. These specimens are also identified in Figure 1 by identification code. In general. the specimens were selected to show behavior at the DBTT so that brittle behavior, ductile behavior and the

Table 1. Specimens selected for fractographic examination fran the HFIR-MFE-RB2 irradiation test.

Material	Specimen	Fluence (dpa)	Test Temp. (°C)	P_{max} (kn)	E_{total} (J)	E_{total} (J/cm²)
HT-9 Base Metal	AA15	11.6	50	1.90	1.41	11.9
	AA06	11.6	75	1.85	3.94	34.3
HT-9 Weld Metal	AK02	11.4	75	1.59	1.31	11.0
HT-9 HAZ	ALOI	10.5	50	1.13	2.48	20.8
9Cr-1Mo Base Metal	FA12	9.7	100	1.18	1.31	11.3
9Cr-1Mo Weld Metal	FJ02	10.4	100	1.22	0.51	4.4
	FJ03	9.7	150	1.64	3.49	29.7
	FJ08	9.7	175	1.25	1.38	11.5

transition fran brittle to ductile behavior could be examined in one specimen. However, in the case of 9Cr-1Mo weld metal. two specimens tested on the upper shelf, FJ03 and FJOB. were examined in order to provide explanation of the large differences in fracture energy between them. Also. a Specimen of HT-9 base metal. AA06, was examined in order to compare ductile behavior on the upper self with specimen AA02[1] to explain the large decrease in fracture energy as a function of dose. The fracture surface of one half of each specimen was sliced off using a slow speed saw in order to reduce the specimen volume and thereby minimize radiation levels. and examinations were performed on a JEM 35C scanning electron microscope using standard procedures.[3] The tilt angle between specimen settings for stereo fractographs is routinely 8.0° .

Results

The fracture surfaces of specimens selected for examination are shown in Figures 3 to 10. In each case, both a low magnification example. sharing the whole of the fractured ligament, and an intermediate magnification example, showing the center of the specimen adjacent to the fatigue precracked surface, are provided as stereographic pairs. The fatigue precrack surface appears on the left so that crack propagation can be envisioned proceeding fran left to right.

Figure 3 shows the fracture surface of the HT-9 base metal specimen identified as AA15 which was tested at 50 C following irradiation to 12 dpa with absorbed energy corresponding to about one third of the upper shelf value. Both the low magnification example shown in Figure 3a and the higher magnification example shown in Figure 3b are for a fully ductile fracture behavior which failed by dimple rupture. No evidence for brittle fracture was identified. This can *be* demonstrated by canparison with Figure 4 which provides the fracture surface of HT-9 base metal specimen AA06, tested at 75 C following irradiation to 12 dpa with absorbed energy corresponding to upper shelf behavior. The silver paint used to attach specimen AA06 to the holder has crept onto the fracture surface at top and bottan obscuring the fracture appearance, but the region shaing in the center of figure 4a is representative of the fracture behavior. The fracture surface is ductile with an unusual step about one third of the way across the fractured ligament. Of particular note is the similarity between Figures 3b and 4b which shows that in both cases. failure is clearly by dimple rupture after a large initial stretch zone was formed. but much of the failure surface is steeply inclined. indicative of failure by shear. Canparison with Figure 7.6.7 in reference 3, of the fracture surface for specimen AA02 tested near the upper shelf following irradiation to a lower dose. shows similar features. However. the dimple size is coarser for the lower dose condition, on the order of 25 to 50 um for AA02 and 10 to 25 µm for AA06.

Therefore, the fracture appearance of specimen AA15 is not typical of HT-9 near the DBTT. Specimen AA01, described in Figure 1.6.6 of reference 3 and corresponding to the same condition but at a lower dose of 5 dpa, showed behavior more typical of a specimen tested at the DBTT except that the stretch zone was larger and the brittle region accounted for more than half the surface area of the fractured ligament. indicative of fracture somewhat above the DBTT. As the fracture surface shown in Figure 3 is so different. it is assumed that a specimen mix up has occurred.

Figure 5 shows the fracture surface of HT-9 weld metal specimen AK02 irradiated to 11 dpa and tested at 75 C, with absorbed energy corresponding to behavior near the lower shelf. Figure Sa shows two distinct fracture modes typical of a specimen tested near the DBTT. a brittle mode on the left and adjacent to the fatigue precrack which is plateau-like with flat planar surfaces and vertical connecting surfaces. and a ductile mode which is less planar and shows more gradual changes in surface relief. The brittle region accounts for over about two thirds of the surface area of the fractured ligament. Therefore, although insufficient specimens were available to define upper shelf behavior for this condition. the shift in DBTT indicated for HT-9 weld metal in Figure 1 is reasonable. The fracture surface shown in Figure 5b at higher magnification is typical of brittle transgranular fracture and the stretch zone between the precrack and the brittle region is small. Small flecks of contamination on the surface should be ignored. Canparison of Figure 5 with that for AK03, Figure 7.6.10 in reference 3, is not very fruitful because AK03 only showed ductile behavior. However. the ductile dimple sire and surface features are very similar.

Figure 6 provides fractography for HT-9 HAZ specimen AL01 which was irradiated to 11 dpa and tested at 50°C, corresponding to behavior at the DBTT. Figure 6a shows fracture appearance typical of a specimen test just below the DBTT, with brittle failure by transgranular cleavage and ductile failure by fine dimple rupture and shear failure, similar to that shown in Figure 4. However. towards the top and bottom of the fractograph, the dimple rupture is much coarser. more representative of the behavior found on specimen AA02 in reference 3. Further inspection of Figure 4a provides indications of the same behavior in Specimen AA06. Therefore. it can be concluded that fracture appearance is similar for base metal and HAZ metal even though Charpy response is different. Figure 6b shows the fracture appearance at higher magnification. At first examination, the surface looks typical of transgranular cleavage fracture. with featherlike striations indicating the martensite lath structure. However, on closer examination, the following can be noted. The stretch zone is unusual for brittle fracture. forming a narrow rib of ductile material. without a clear transition to brittle fracture. There are unusual deep pits, particularly noticeable in the lower right area. which appear to represent dimple rupture in very localized regions. Finally. the characteristic feather-like striations are really not present as striations; rather. they appear almost like dimple rupture cups. All of these features may be the result

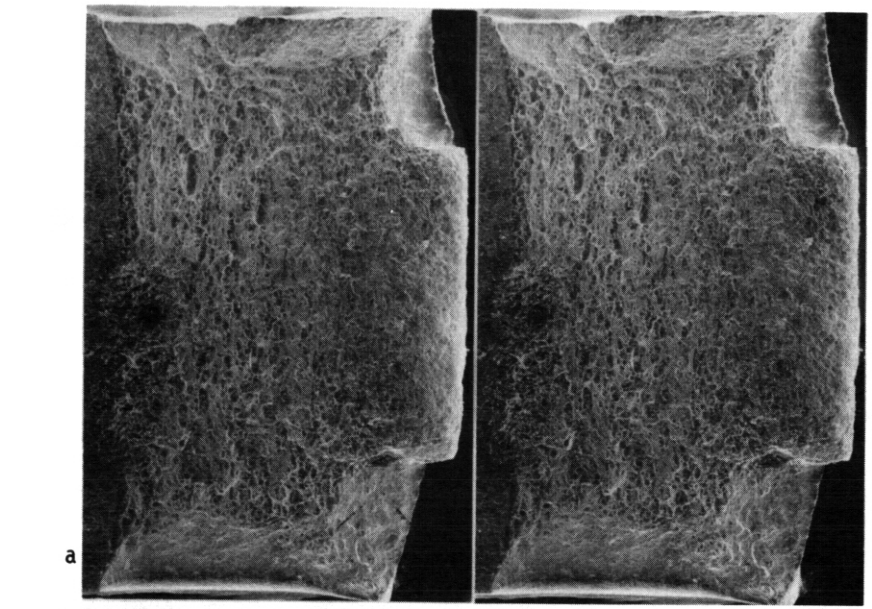

Figure 3. Fractographs of HT-9 base metal specimen AA15 following irradiation to 12 dpa and testing at 50°C at a) low magnification and b) intermediate magnification.

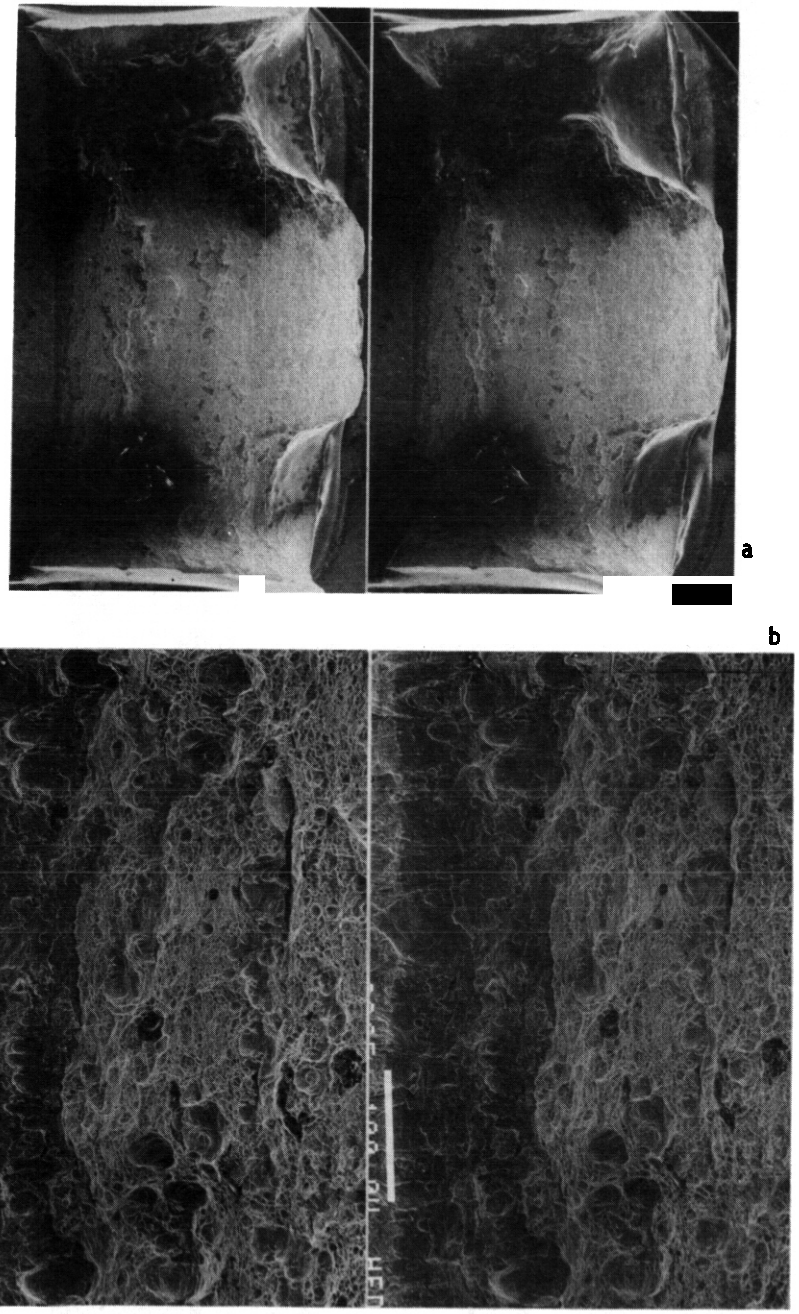

Figure 4. Fractographs of HT-9 base metal specimen AA06 following irradiation to 12 dpa and testing at 75°C at a) low magnification and b) intermediate magnification.

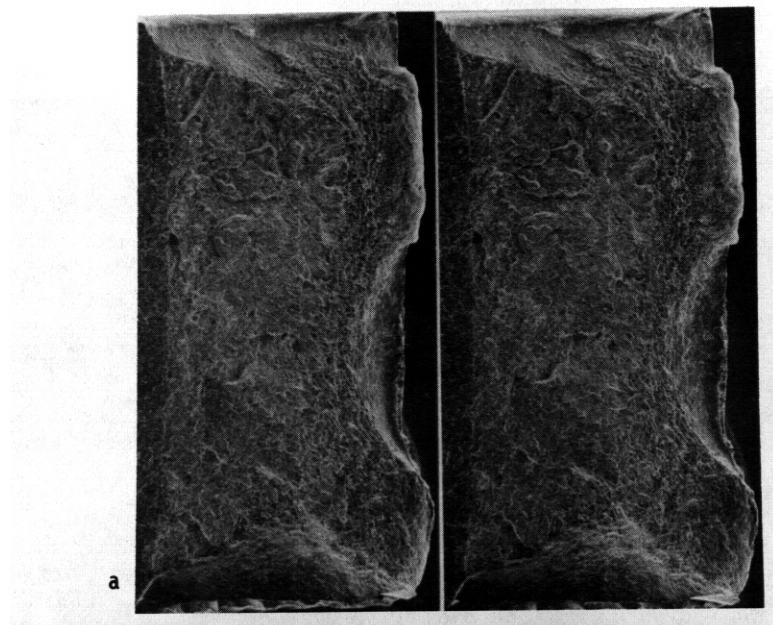

Figure 5. Fractographs of HT-9 weld metal specimen AKO2 following irradiation to 11 dpa and testing at 75°C at a) low magnification and b) intermediate magnification.

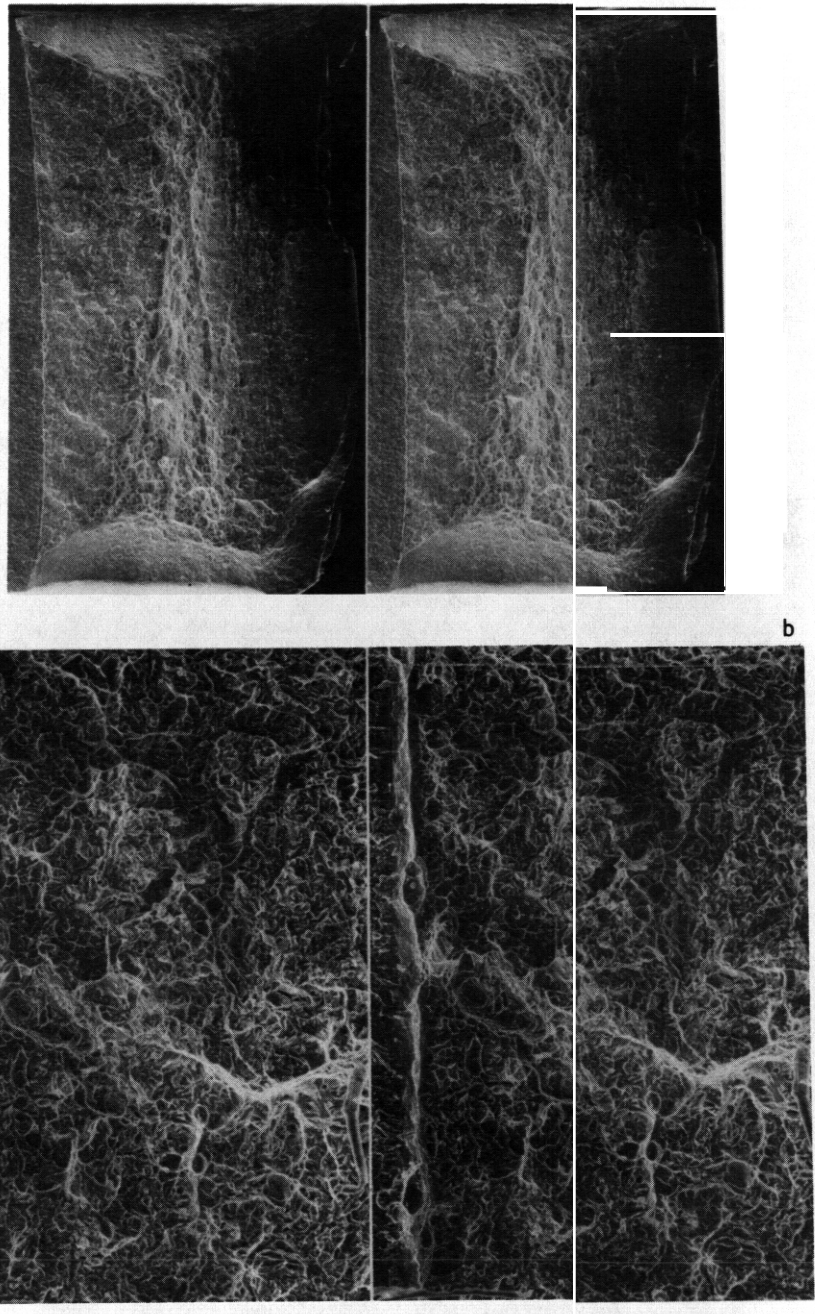

Figure 6. Fractographs of HT-9 HAZ metal specimen ALO1 following irradiation to 11 dpa and testing at 50°C at a) low magnification and b) intermediate magnification.

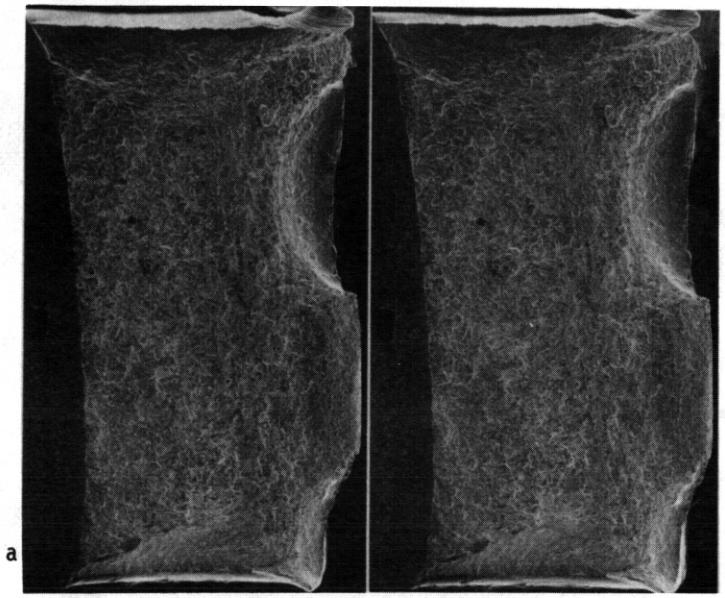

Figure 7. Fractographs of 9Cr-1Mo base metal specimen FA12 following irradiation to 10 dpa and testing at 100°C at a) low magnification and b) intermediate magnification.

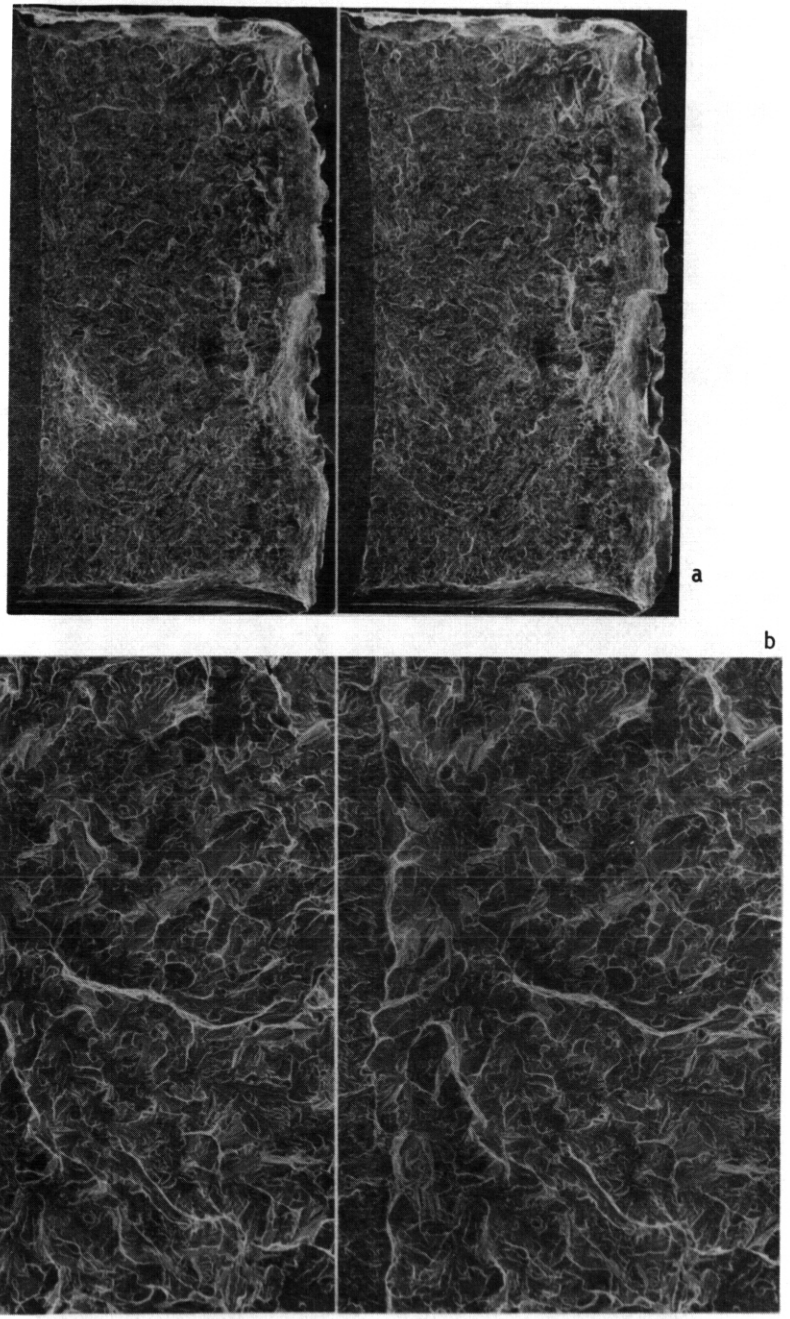

Figure 8. Fractographs of 9Cr-1Mo weld metal specimen FJ02 following irradiation to 10 dpa and testing at 100°C at a) low magnification and b) intermediate magnification.

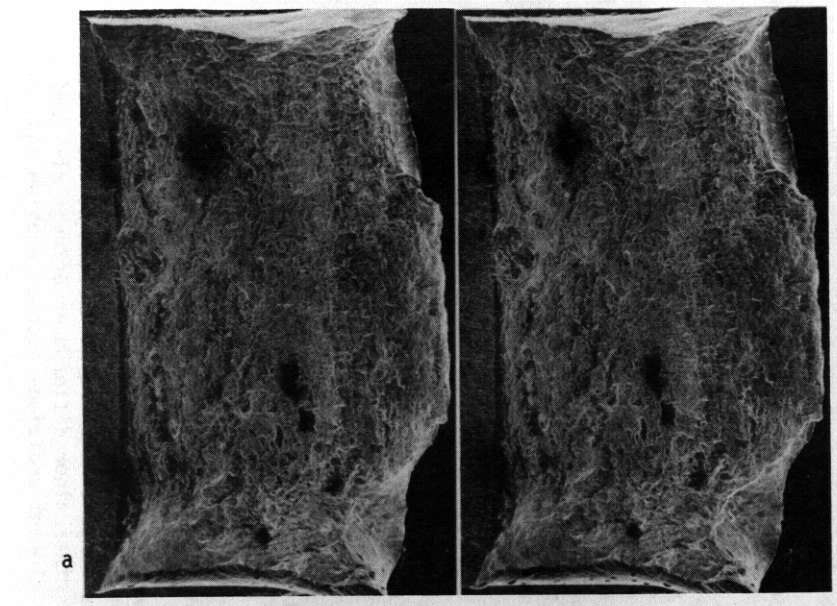

Figure 9. Fractographs of 9Cr-1Mo weld metal specimen FJ03 following irradiation to 10 dpa and testing at 150°C at a) low magnification and b) intermediate magnification.

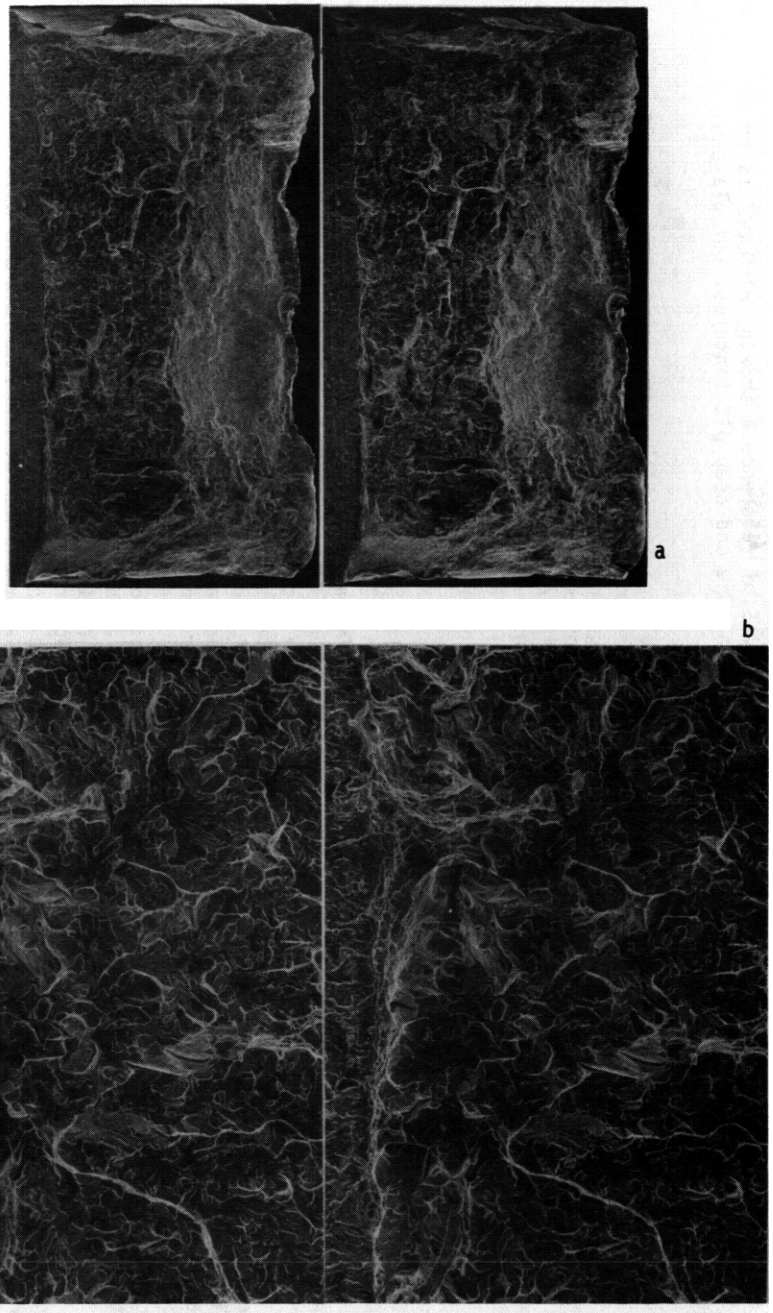

Figure 10. Fractographs of 9Cr-1Mo weld metal specimen FJ08 following irradiation to 10 dpa and testing at 175°C at a) low magnification and b) intermediate magnification.

of an over-aged carbide structure. Figures 7.2.14 and 7.2.15 of reference 4 showing HT-9 H N response following irradiation at 550 and 390°C show similar stretch zone and deep pit features. but plateau structure and feather-like striations are more apparent.

Figure 7 shows the fracture surface of 9Cr-1Mo base metal specimen FA12 which was tested at 100°C corresponding to behavior at the DBTT. The fracture appearance as shown at low magnification in Figure 7a is typical of a specimen tested at the DBTT, with transgranular brittle cleavage and ductile dimple rupture. Brittle cleavage extends half way across the fractured 1igament. At higher magnification. Figure 7b, the fracture surface also appears typical of brittle fracture. Comparison with specimen FA17 irradiated to half the dose and shown in Figure 7.6.8 of reference 3 gave very similar features (although the contrast was quite different.) Therefore, no change in fracture mode can be identified to explain the large shift in DBTT which was observed with increasing dose.

Figures 8, 9 and 10 show 9Cr-1Mo weld metal specimens FJ02, FJ03 and FJ08 which had been tested at 100, 150 and 175°C, respectively. Based on energy absorbtion, FJ02 was expected to display lower shelf behavior and FJ03 and FJ08 upper shelf behavior. FJ03 and FJ08 were examined because FJ08 gave an impact energy of approximately one third that of FJ03 but it was tested at a higher tfmperature. Figure 8a shows behavior typical of lower shelf response, with approximately 90 percent of the 1igament length having failed by transgranular brittle cleavage. Figure 8b shows that fracture surface in the brittle region is typical of lower shelf fracture in martensitic steels. Comparison with specimen FJ05, irradiated to laver dose with DBTT response and shwn in Figure 7.6.11 of reference 3, showed no significant differences in behavior. Differences in contrast accentuated the lath feather-like appearance at laver dose. but fracture appearance was otherwise similar.

Specimen FJ03 shown in Figure 9 gave upper shelf response for the most part but one small region was found to be brittle. That region can be seen in Figure 9a as an unusual feature toward the upper center of the specimen and adjacent to the precrack. The brittle region is shown at higher magnification in Figure 9b, and appears as flat transgranular brittle cleavage regions centered around a deep fissure and surrounded by steep large stretch zones and adjacent dimple rupture. Therefore. limited cleavage fracture occurred in the vicinity of the feature causing the deep fissure, but cleavage was halted for sane reason and ductile failure propagated from the cleavage crack. The fracture appearance of FJ03 is typical of a material tested just below the temperature required for upper shelf behavior.

Specimen FJ08 was found to be very different. As shwn in Figure 10a, failure occurred as if the specimen had been tested at the DBTT, with half the specimen failing by transgranular brittle cleavage and the remainder by ductile dimple rupture. The brittle fracture shown in Figure 10b is similar to that shown in Figure 8. Therefore the impact energy measure for this specimen was typical of response at the DBTT and not on the upper shelf. An error in test temperature may be at fault. but it is possible that large variations in material response occur in 9Cr-1Mo weld metal.

Rockwell C hardness measurements were made on specimens representing each of the irradiated conditions examined. The results are as follws. HT-9 base metal specimen AM6 gave 34.3 ± 0.95 R_C, HT-9 weld metal specimen AK02 gave 33.7 ± 0.7 R_C, HT-9 HAZ specimen AL01 gave 30.2 ± 0.5 R_C, 9Cr-1Mo base metal specimen FA07 (irradiated to 9.7 dpa and tested at 150 C) gave 26.3 ± 1.5 R_C and 9Cr-1Mo weld metal specimen FJ08 gave 27.3 ± 0.5 R_C. These values indicate that the improved impact properties observed in HT-9 HAZ in comparison with other HT-9 conditions is a result of lower irradiation hardening because AL01 gave the lowest hardness values. Also, when these values are compared with measurements at lower fluence (29.5 ± 0.5 R_C for HT-9 base metal and 24.7 ± 0.4 R_C for 9Cr-1Mo base metal at 5.5 to 5.6 dpa),[3] the further shift in DBTT due to irradiation can be correlated with a further increase in irradiation hardening of 5 R_C points for HT-9 and 1.5 points R_C for 9 Cr-1Mo. However, the increases in DBTT due to irradiation are not directly proportional to the hardness increases.

Discussion

The present fractographic results on specimens irradiated at 55° C in the HFIR RB2 test are very similar to those obtained on specimens irradiated in the RB1 irradiation at 55°C to lower dose.[1] Although degradation in impact properties and hardness increases continued with increasing dose, the fracture mode did not change. As a consequence, explanations for the continued degradation must be based on microstructural changes which did not influence the mechanism of fracture. Given the fact that HT-9 shws greater continued increases in hardening with increasing dose. the argument that HT-9 shows unusually low hardening can be ruled out. However, the present results do not provide the basis for a mechanism to explain the degradation of impact fracture properties.

But the information contained in Figure 2 does provide a further basis for explaining the observed behavior. It is apparent that the shift in DBTT as a function of nickel increases for each alloy base. However. the differences between HT-9 with 1 percent nickel and 2 percent nickel are probably small and nickel cannot be responsible for differences between the response of HT-9 and 9Cr-1Mo because HT-9 contains more nickel but is less affected by irradiation at low temperature. As nickel is not the overriding factor in controlling properties. it is likely that other minor differences between HT-9 and 9Cr-1Mo are responsible. These differences are probably minor element additions such as niobium and

vanadium. Therefore, a mechanism similar to the one used to explain irradiated pressure vessel steel behavior may be pertinent. If segregation of copper in pressure vessel steels can control behavior, then additions of niobium and nickel may have the same effect for the same reason in 9 to 12Cr steels. Copper is known to form very small copper-rich regions which act as hardening centers. The copper precipitates can form rapidly. Nickel additions have been shown to promote G phase in 12Cr steels at 420°C.[5] Therefore. a driving force exists for nickel-rich precipitation at lower temperatures. (Nickel additions beyond a certain limit may not increase hardening further. The behavior shown in Figure 2 suggests that one percent may be the limit, since increasing from 1 to 2 percent in HT-9 produces no increment in DBTT.)

A mechanism based on microchemical segregation of niobium and nickel. much the same way copper segregates in irradiated pressure vessel steels. does agree with observed impact behavior following HFIR irradiation as a function of heat treatment. HT-9 in the HAZ condition has effectively undergone an over-tempering treatment following a normal temper. Presumably. this has resulted in further carbide precipitation. thereby removing elements from solid solution which would promote irradiation hardening. The likely candidates include niobium. vanadium, chromium and molybdenum. Therefore. less of these' elements would be available in HAZ metal for the formation of .hardening centers during 55 C irradiation and the resulting shift in DBTT would be reduced.

As the effect of irradiation on mechanical properties is large at low temperatures and as the change in behavior has not been measured at saturation levels, it is evident that further tests are needed. If HFIR continues to be unavailable for testing over the next few years, the US fusion materials program will have to look elsewhere for an appropriate test facility.

CONCLUSIONS

Fractographic examination of miniature Charpy specimens of HT-9 in base metal. weld metal and heat affected zone (HAZ) metal conditions. and 9Cr-1Mo in base metal and weld metal conditions which had been irradiated in HFIR-MFE-RB2 at 55°C to 10 dpa reveals only minor effects of continued irradiation on fracture. Canparison of results with results on specimens irradiated to a lower dose level also demonstrates only minor changes in fracture behavior. Therefore. the mechanism controlling the degradation of impact properties does not affect the fracture path and is probably microchemical in nature.

FUTURE WORK

This work should be continued by determining the dose needed for saturation of properties during low temperature irradiation.

REFERENCES

1. W.L. Hu and D.S. Gelles. DOE/ER-0313/2, 115.

2. R.L. Klueh. J.M. Vitek. W.R. Corwin and D.J. Alexander. "Impact Behavior of 9-Cr and 12-Cr Ferritic Steels after Low-Temperature Irradiation", to be published in the proceedings of ICFRM-3, J. Nucl. Matls.

3. D.S. Gelles. W.L. Hu, F.H. Huang and G.D. Johnson, DOE/ER-0045/11, 115.

4. D.S. Gelles and W.L. Hu, DOE/ER-0045/9, 178.

5. D.S. Gelles and L.E. Thomas, in Proceedinos of Topical Conference on Ferritic Allovs for use in Nuclear Enerav Technologies, J.W. Davis and D.J. Michel, Eds. (AIME. Warrendale, PA, 1984), p. 559.

MICROSTRUCTURAL DEVELOPMENT OF 10Cr–2Mo FERRITIC STEEL IRRADIATED IN HFIR AT 500°C TO 34 dpa — M. Suzuki (Japan Atomic Energy Research Institute, assigned to ORNL), P. J. Maziasz (Oak Ridge National Laboratory), S. Hamada, and A. Hishinuma (Japan Atomic Energy Research Institute)

OBJECTIVE

The objective of this study is to determine the microstructural development of Japanese 10Cr–2Mo ferritic steel irradiated at 500°C to 34 dpa in HFIR.

SUMMARY

Microstructural development was studied in 10Cr–2Mo ferritic steel containing 1 wt % Ni which was irradiated to 34 dpa at 500°C in HFIR. The results showed considerable evolution of the precipitates, but no significant void development was observed. The a- and x-phases were identified as radiation-induced precipitates in this steel.

PROGRESS AND STATUS

Experimental procedures

The material used in the present irradiation experiment was dual-phase 10Cr–2Mo ferritic steel. The chemical composition and heat-treatment condition (normalizing and tempering) for this steel are given in Table 1. Normalizing was done at 1050°C for 0.5 h, and then tempering was conducted at 775°C for 1 h. The as-tempered condition was found to have a mixed structure consisting of tempered martensite/laths and 6-ferrite. The material was irradiated in HFIR at 500°C to 34 dpa and to an estimated helium content of about 150 appm. For comparison, this material was also thermally aged at 500 and 600°C for up to 5000 h. Microstructural observations Were conducted using a JEM2000FX analytical electron microscope (AEM) equipped with X-ray energy dispersive spectroscopy (XEOS). Precipitates were analyzed after being extracted onto carbon replica films. This extraction technique was quite necessary in the present study for two reasons. First, the irradiated material was very radioactive. which made XEDS analysis using thin films almost impossible. Secondly, electron diffraction analysis was difficult even for unirradiated material because the precipitates were very small and the matrix was ferromagnetic.

Table 1. Chemical composition (wt %) and heat treatment of the material used[a]

Alloy	Content, wt %													
	C	Si	Mn	P	S	Ni	Cr	Mo	Cu	Nb	V	W	Co	N
10Cr–2Mo	0.056	0.74	0.60	0.016	0.0059	0.99	9.76	2.41	0.02	0.06	0.12	0.01	0.016	0.0067

[a]Heat treatment — normalizing 1050°C, 0.5 h. Tempering — 775°C, 1 h.
Microstructure — tempered lath martensite plus δ-ferrite.

Results and discussion

As-tempered and thermally aged material. — Microstructures of the as-tempered 10Cr-2Mo ferritic steel are shown in Fig. 1. Figure 1(a) shows the mixed structure of 6-ferrite and tempered martensite laths. Figure 1(b,c) show the δ-ferrite region and a region of martensite/laths, respectively. Precipitates are seen mostly along boundaries between lath martensite and 6-ferrite regions, although small amounts of precipitates were also found at lath interfaces or on the interior of the δ-ferrite grains.

After thermal aging at 500°C for 5000 h. the as-tempered microstructure generally did not change. However, small precipitates began to form in the δ-ferrite interior or in tempered lath martensite regions (see Fig. 2). Changes were obvious after aging at 600°C, as shown in Fig. 3 after aging for 3000 h. Coarse precipitates appeared within 6-ferrite grains and along the boundaries between the martensite lath regions and 6-ferrite.

A typical example of the precipitate distribution observed on the carbon extraction replica is shown in Fig. 4. Figure 4 (a,b) shows the δ-ferrite region and tempered lath martensite regions, respectively. By comparison with in-foil microstructure, it was apparent that the carbon replica process adequately reproduced the precipitate distribution found in the original material. The precipitate phases observed in the

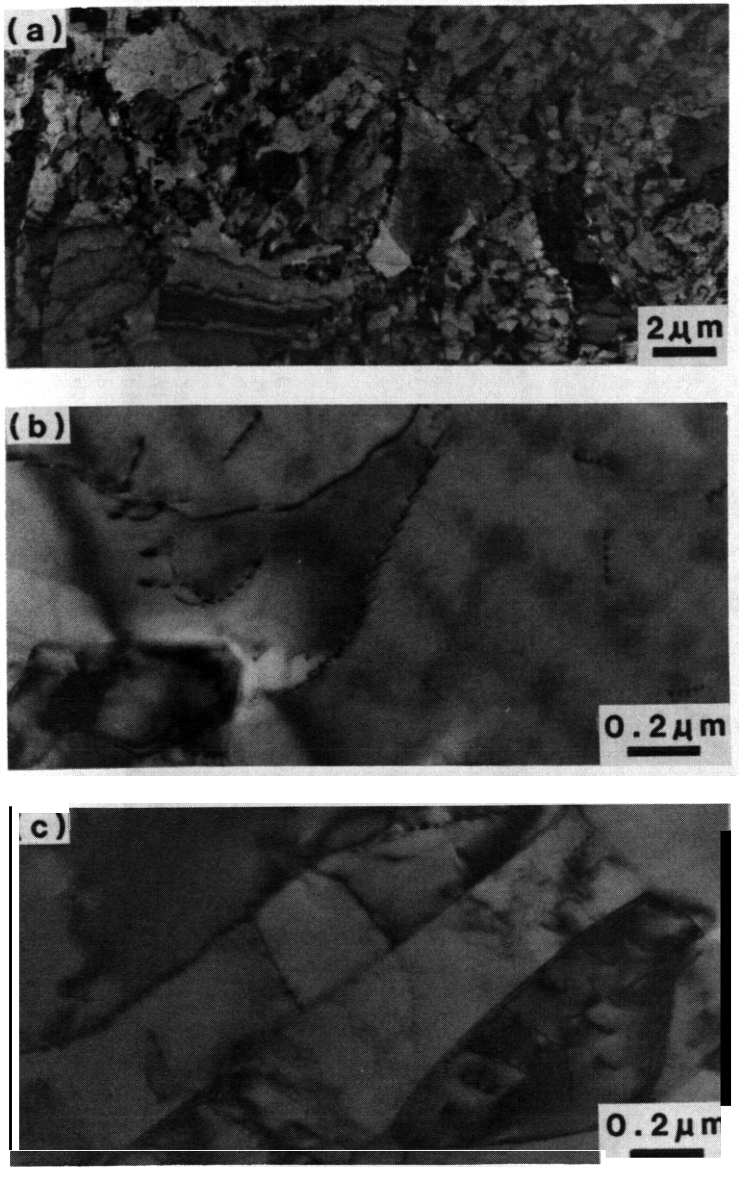

Fig. 1. As-tempered microstructures of 10Cr-2Mo steel (a) Lower magnification view showing the mixed structure comprised of tempered lath martensite and δ-ferrite and higher magnification views of (b) δ-ferrite and (c) tempered lath martensite regions.

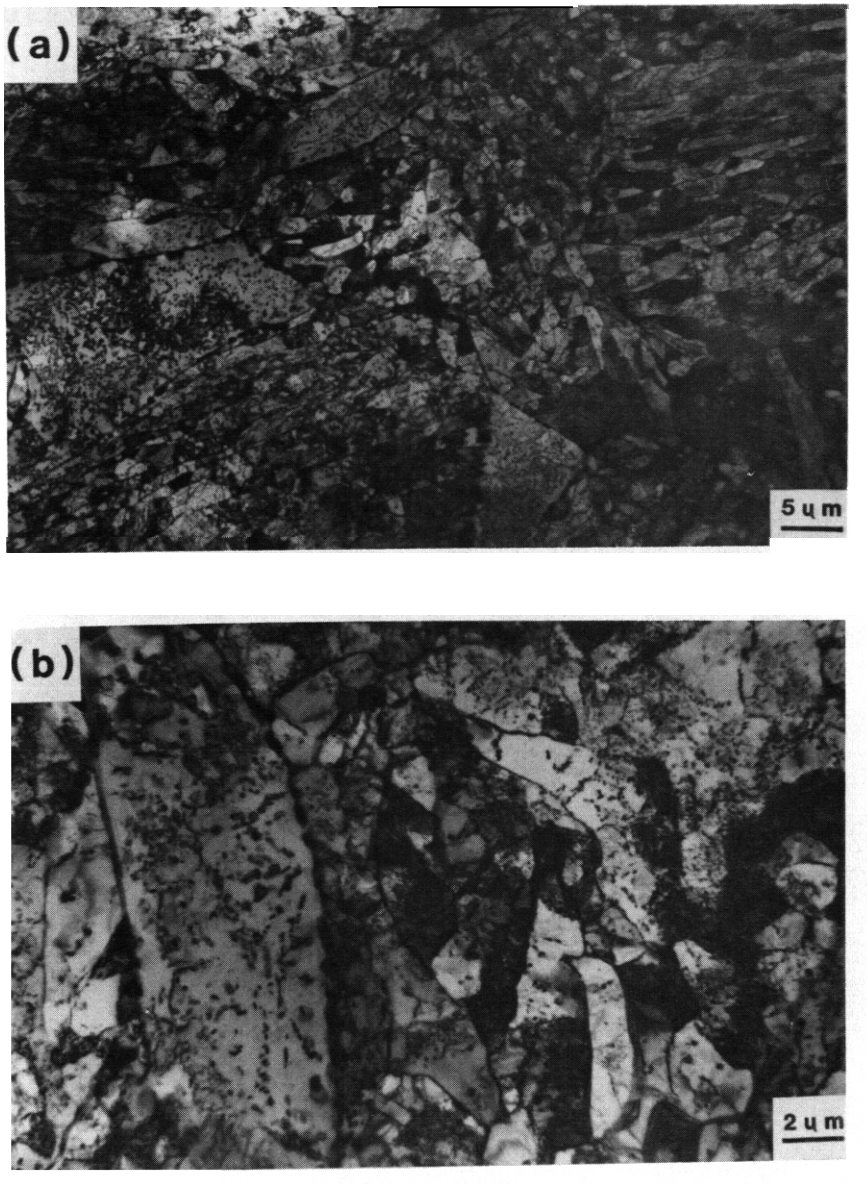

Fig. 2. Microstructures of 10Cr-2Mo steel after aging at 500°C for 5000 h at (a) lower and (b) higher magnifications.

ORNL-Photo 2936-88

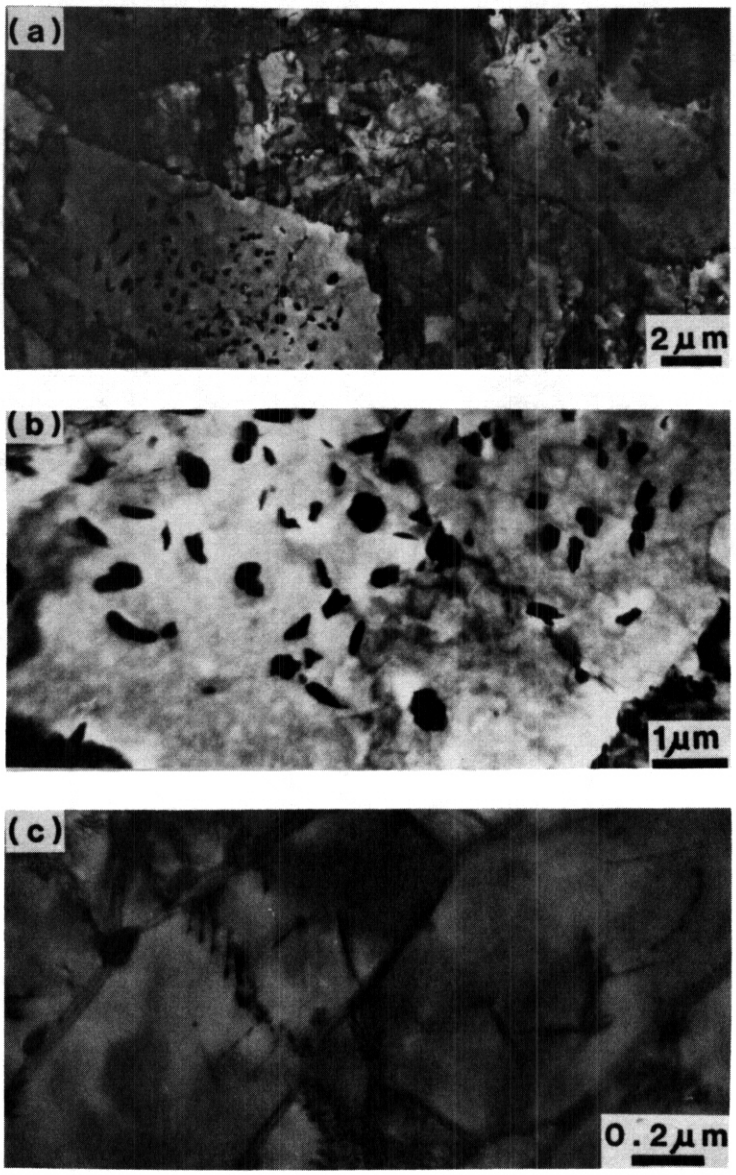

Fig. 3. Microstructures of 10Cr-2Mo steel after aging at 600°C for 3000 h. (a) Lower magnification and then higher magnifications of (b) δ-ferrite, and (c) tempered lath martensite regions.

as-tempered material were mainly M_6C and $M_{23}C_6$. Typical particles observed on the replica are shown in Fig. 5 with their XEDS spectra. In addition to these precipitates, fine niobium-rich MC precipitates (NbC) were also detected (Fig. 6).

After aging at 600°C for 3000 h, many Laves phase particles were observed not only at grain boundaries, but also within δ-ferrite grains themselves. A typical example is shown in Fig. 7. The volume fraction of $M_{23}C_6$ in the aged samples was much less relative to the as-tempered material. This was confirmed by broad-beam spectra, which measure the average together with many particles over a wider region. These results suggest a general trend of precipitate evolution by thermal aging as follows:

(As tempered)	↔	(Aged at 600°C for 3000 h)
M_6C		M_6C
$M_{23}C_6$		Laves phase
NbC		$M_{23}C_6$
		NbC

ORNL-Photo 2937-88

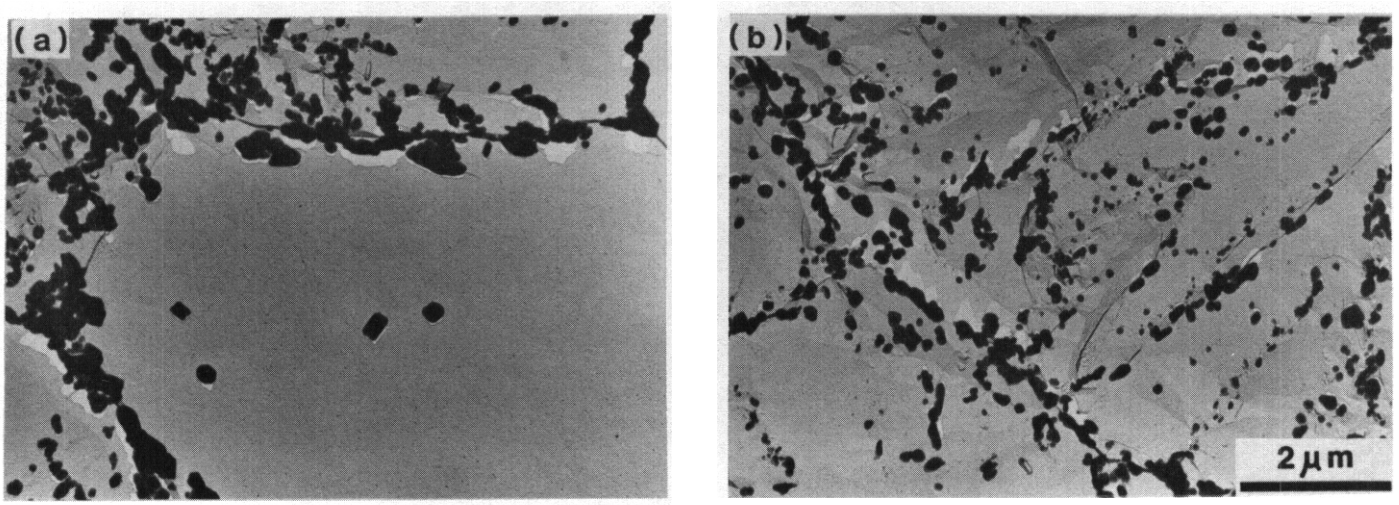

Fig. 4. Replica microstructures of the as-tempered 10Cr-2Mo steel. (a) δ-ferrite region; (b) lath structure region.

ORNL-Photo 2938-88

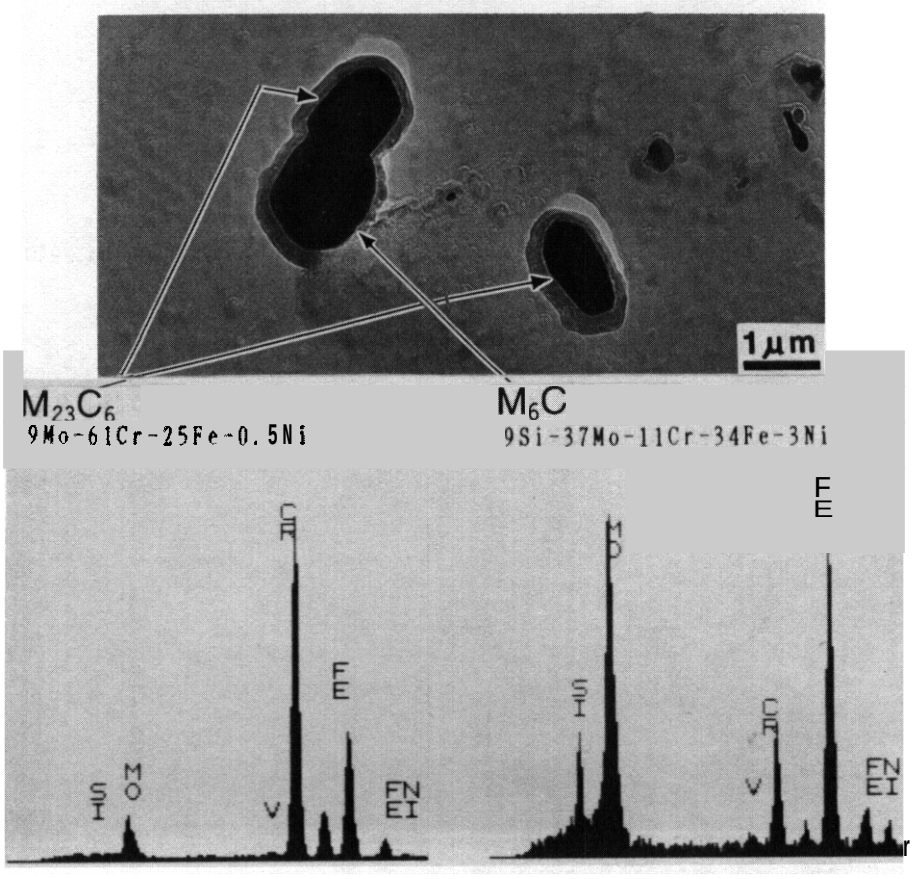

Fig. 5. Replica microstructure of the as-tempered 10Cr-2Mo steel and XEDS spectra, from particles of $M_{23}C_6$ and M_6C, as indicated.

ORNL-Photo 2939-88

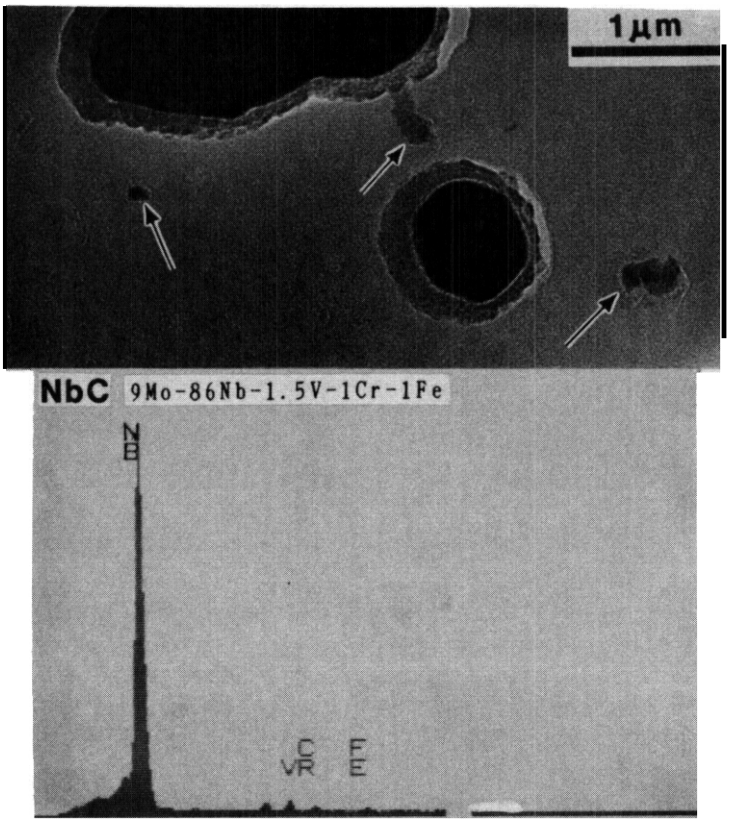

Fig. 6. Replica microstructure of the as-tempered 10Cr-2Mo steel showing NbC and its corresponding spectrum.

ORNL-Photo 2940-88

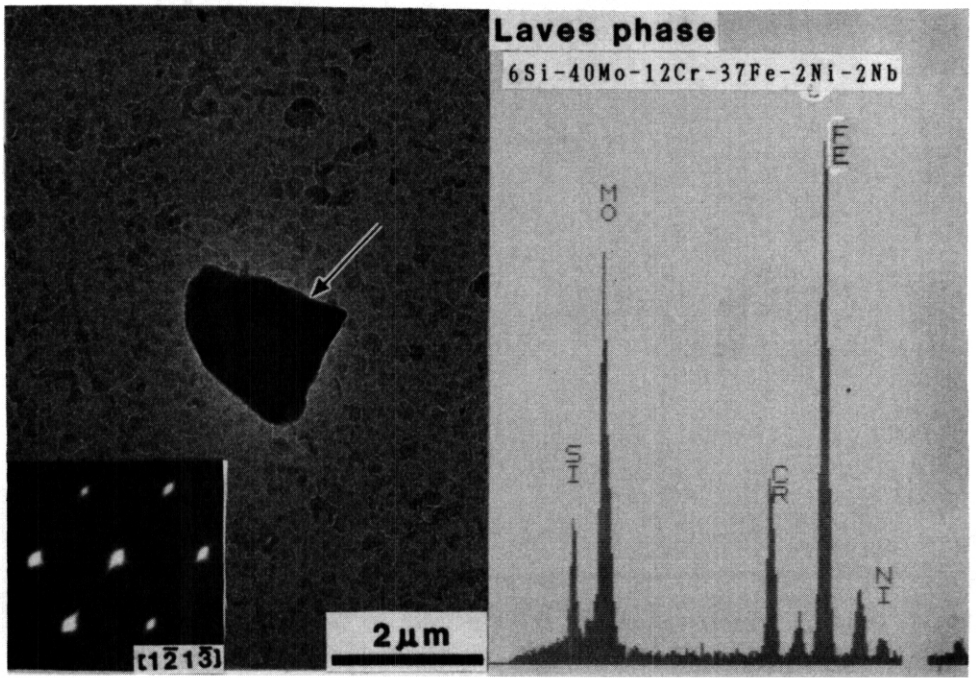

Fig. 7. Replica microstructure of 10Cr-2Mo steel aged at 600°C for 3000 h showing Laves phase and its corresponding XEDS spectrum.

Irradiated material – Figure 8 shws the microstructure of the material after irradiation at 500°C to 34 dpa. Many fine precipitates were observed throughout the material. Except for a denuded zone about 300 nm wide along the lath interface. very coarse precipitates were seen to form uniformly within the lath structure. Figure 8(d) shows the cavity microstructure observed in a 6-ferrite grain interior. Many very fine cavities. about 5 nm in diameter, could be seen. However, very few such cavities were observed in the lath regions. Judging from these observations. swelling was about 0.25% or less.

ORNL-Photo 2941-88

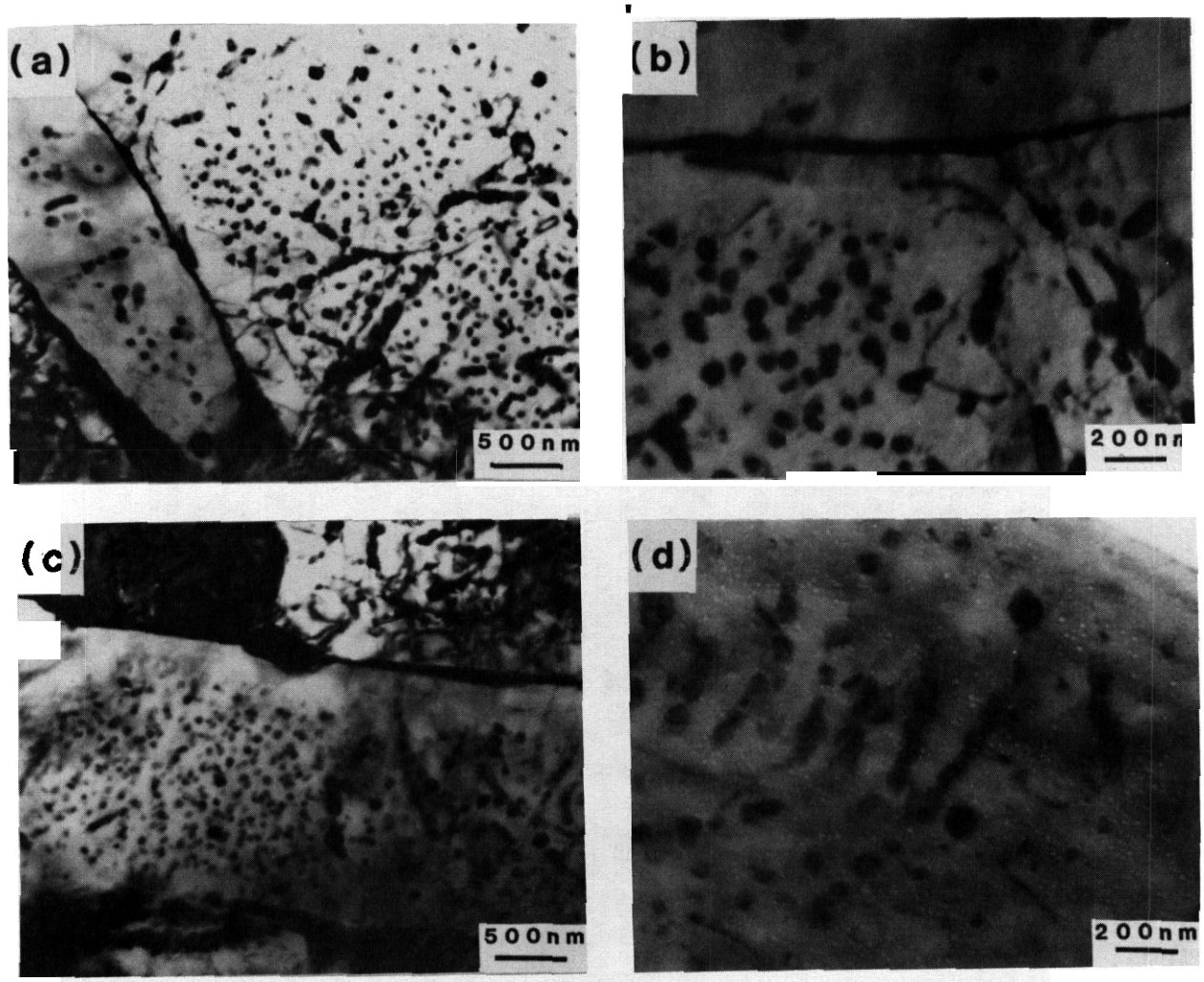

Fig. 8. Microstructures of 10Cr-2Mo steel after irradiation at 500°C to 34 dpa in HFIR, showing (a,c) many of radiation-produced precipitates both in δ-ferrite and lath regions and (d) cavity microstructure in the δ-ferrite region.

Analysis of the replica revealed two kinds of radiation-produced precipitates. One is a-phase and another is x-phase. The σ-phase had either a globular- or rod-type rmrphology, and contained voids inside the particle (Fig. 9). The x-phase had a similar morphology (Fig. 10). The chemical composition of the two phases were also similar, but x-phase contained more iron and less molybdenum than o-phase. Nearly all the fine precipitates observed in thin foils appeared to be either a-phase or x-phase. Most of the larger precipitates were identified as M_6C. These M_6C precipitates were suspected to have formed prior to irradiation because their chemical composition is so close to that of the same phase in the irradiated material. NO $M_{23}C_6$ was detected in the irradiated materials. Dissolution of the $M_{23}C_6$ may well be related to the development of the s- and x-phases. NbC could also be detected after irradiation. Precipitate evolution during HFIR irradiation at 500°C could be summarized as follows:

(As tempered)	↔	(Irradiated at 500°C to 34 dpa)
M_6C		M_6C
$M_{23}C_6$ → dissolve		
		σ-phase (radiation produced)
		χ-phase (radiation produced)
NbC	→	NbC

In contrast to the development of Laves phase during thermal aging, σ- and x-phases became the dominant precipitates produced in 10Cr-2Mo by neutron irradiation at 500°C in HFIR.

ORNL-Photo 2942-88

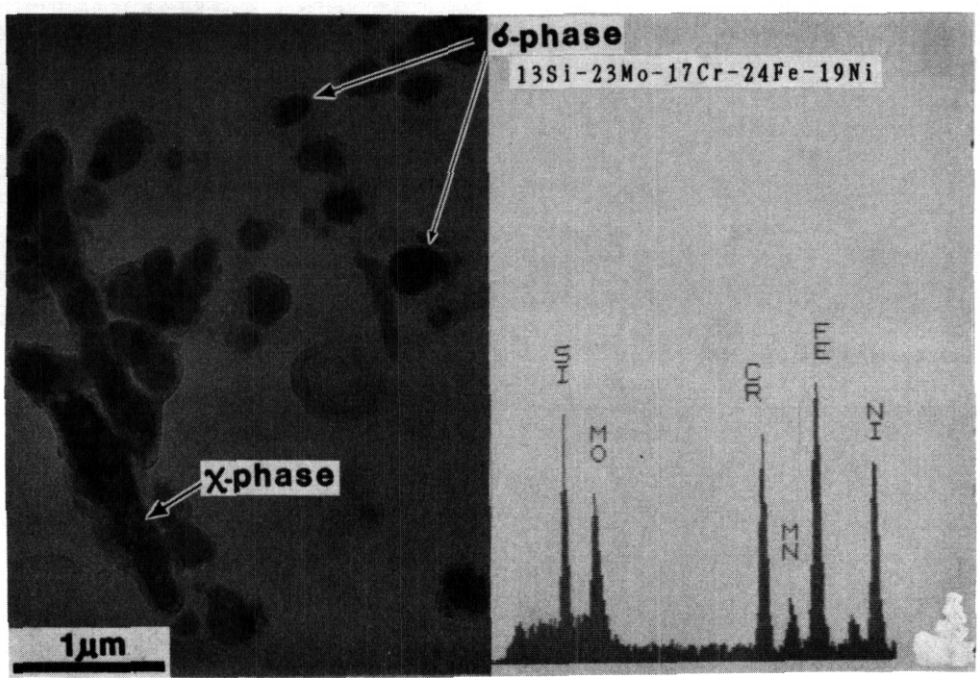

Fig. 9. Replica microstructure of 10Cr-2Mo steel irradiated at 500°C to 34 dpa in HFIR showing a-phase and its corresponding XEDS spectrum.

CONCLUSIONS

The 10Cr-2Mo ferritic steel was thermally aged at 500 and 600°C as well as irradiated at 500°C to 34 dpa in HFIR. Observations revealed the following:

1. Radiation-induced microstructural changes included the formation of many fine bubbles (–5 nm), and many fine precipitates. Dislocation loops were not observed.

2. Laves phase formed in addition to the as-tempered $M_{23}C_6$, M_6C, and NbC during thermal aging at temperatures from 500 to 600°C. By contrast, abundant σ- and χ-phases formed during HFIR irradiation. and as-tempered $M_{23}C_6$ appeared to have dissolved during irradiation.

3 The nonuniformity in the radiation-induced microstructure could be related to the nonuniform (dual phase) as-tempered structure. Many more fine cavities (most of them stable, subcritical bubbles) were found in the 6-ferrite region than in the tempered martensite lath regions. Fine radiation-produced precipitates of χ- and o-phases were also found in both regions, but the lath regions had less because a precipitate-denuded zone was formed along the lath subgrain boundaries. While as-tempered NbC and M_6C survived during HFIR irradiation at 500°C, the as-tempered $M_{23}C_6$ dissolved during Irradiation.

ORNL-Photo 2943-88

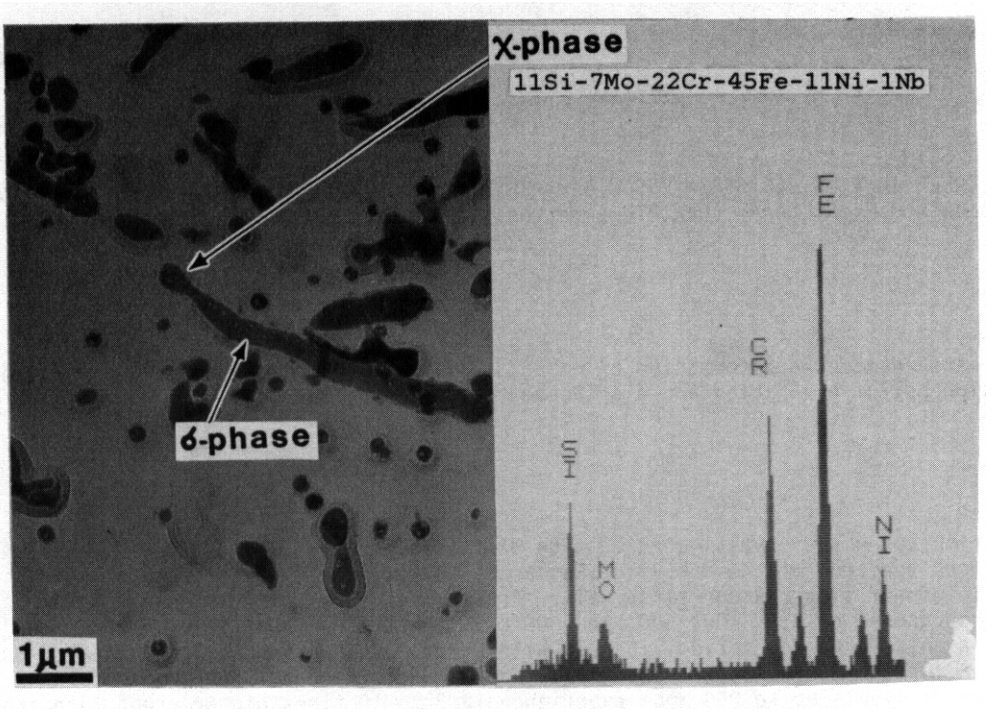

Fig. 10. Replica microstructures of the as-tempered 10Cr-2Mo steel irradiated at 500°C to 34 dpa in HFIR showing %-phase and it's corresponding XEOS spectrum.

FUTURE WORK

Further work will be extended to 10Cr-2Mo steel irradiated at different temperatures and/or to higher dose.

6.2 Austenitic Stainless Steels

IRRADIATION CREEP IN TYPE 316 STAINLESS STEEL AND U.S.-PCA WITH FUSION REACTOR He:dpa LEVELS

M. L. Grossbeck and J. A. Horak (Oak Ridge National Laboratory)

OBJECTIVE

To evaluate in-reactor deformation of candidate first-wall materials under irradiation conditions which simulate fusion helium generation and displacement rates.

SUMMARY

Irradiation creep was investigated in type 316 stainless steel (316 SS) and U.S. Fusion Program PCA using a tailored spectrum of the Oak Ridge Research Reactor (ORR), in order to achieve a He:dpa value characteristic of a fusion reactor first wall. Pressurized tubes with stresses of 20 to 470 MPa were irradiated at temperatures of 330. 400, 500, and 600°C. It was found that irradiation creep was independent of temperature in this range and varied linearly with stress at low stresses, but the stress exponent increased to 1.3 and 1.8 for 316 SS and PCA. respectively, at higher stresses. Specimens of PCA irradiated in the ORR and having helium levels up to 200 appm experienced a 3 to 10 times higher creep rate than similar specimens irradiated in the Fast Flux Test Facility (FFTF) and having helium levels below 20 appm. The higher creep rates are attributed to either a lower flux or the presence of helium. A mechanism involving interstitial helium-enhanced climb is proposed.

The enhanced creep rates observed in the presence of helium might serve to relieve swelling stresses in a fusion reactor first wall, and hence, must be considered in reactor design.

PROGRESS AND STATUS

Introduction

Irradiation creep is important in structures under irradiation. Stresses introduced by swelling are often relieved by irradiation creep; however. an imbalance of the two processes can lead to phenomena such as fuel pin bowing in fission reactors. In fusion reactors, irradiation creep will be important in determining deformation of the first wall and blanket structures in response to swelling stresses as well as thermal and primary load stresses. In a fusion reactor, irradiation creep will take place in the presence of high levels of helium, the effect of which is unknown. Irradiation creep has been studied in fast reactors, where the helium production rate is very low, as well as in mixed-spectrum reactors where the helium production rate is very high. However, irradiation creep has not previously been studied under conditions where the fusion reactor level of helium per atomic displacement (He:dpa) is achieved. The present experiment achieved this goal by tailoring the neutron spectrum of the ORR. In order to establish the effect of helium, the creep rates observed in the spectrally tailored experiment will be compared with creep results Dbtained from irradiating the same heat of PCA in the FFTF.

Experimental procedures

In order to achieve the fusion reactor He:dpa level of about 12 appm/dpa for 316 SS, the ORR irradiation vehicle was provided with a removable core piece. The irradiation began with water surrounding the irradiation capsule in order to rapidly burn in ^{59}Ni with the resulting high thermal flux. After 6.5 dpa, an aluminum core piece replaced the water, and after a total of 8.5 dpa, hafnium replaced the aluminum. With this progression, a He:dpa ratio of 12 was achieved after about 6 dpa, and this ratio remained for the duration of the irradiation.

The specimens consisted of pressurized tubes 25.4 mm in length and 4.57 mm in diameter. The tubes were pressurized with helium to effective stress levels' of 20 to 470 MPa depending upon irradiation temperature. The alloys studied were 316 SS (HT X15893) of composition, in weight percent except where noted, as follows: 4* appm B, 0.06 C, 0.3 Co, 17.4 Cr, 0.3 Cu, 1.7 Mn 2.1 Mo, 0.06 N, <0.05 Nb. 12.4 Ni, 0.037 P, 0.18 S, 0.67 Si, 0.01 Ta. <0.05 Ti, bal Fe, and PCA (HT K-280) of composition: 0.05 C, 14.0 Cr, 1.8 Mn, 2.3 Mo, 0.01 Nb. 16.3 Ni. 0.01 P, 0.44 Si, 0.24 Ti, bal Fe. The specimens were fabricated from drawn tubing with residual cold-work levels of 20 and 25% for the 316 SS and PCA. respectively. Four irradiation temperatures were

investigated: 330, 400, 500, and 600°C. Temperature control was achieved by immersing the specimens in NaK surrounded by a gas gap. Based upon the temperature of the thermocouples in the specimen chambers, the composition of the gas in the control gap was varied from pure helium to pure argon to control temperature. The specimens were removed from the reactor for examination at damage levels of 5 and 12 dpa and helium levels of 44 and 160 appm for 316 SS and 56 and 200 appm for PCA.

The tubes were profiled with a non-contacting laser micrometer system with a precision of ±250 nm. Although the complete tube profiles were used to evaluate the specimens, the average diameter of the central three-fifths of each tube was used in the analysis of the data. Swelling measured by immersion density on unpressurized tubes was subtracted from the creep data.

Results and Analysis

The effective creep strain as a function of effective stress is shown for both 316 SS and PCA in Figs. 1 and 2, respectively. For stresses below about 350 MPa, both alloys exhibit a nearly linear dependence of creep strain on stress with the stress exponents having an average value of 0.96 for each alloy when averaged over the four temperatures. At higher stress levels the curves become non-linear, with the stress exponent for 316 SS becoming 1.3 and the stress exponent for PCA becoming 1.8. The slope appears to be still increasing at the highest stress levels investigated. Data from tubes that appear to have failed were not considered.

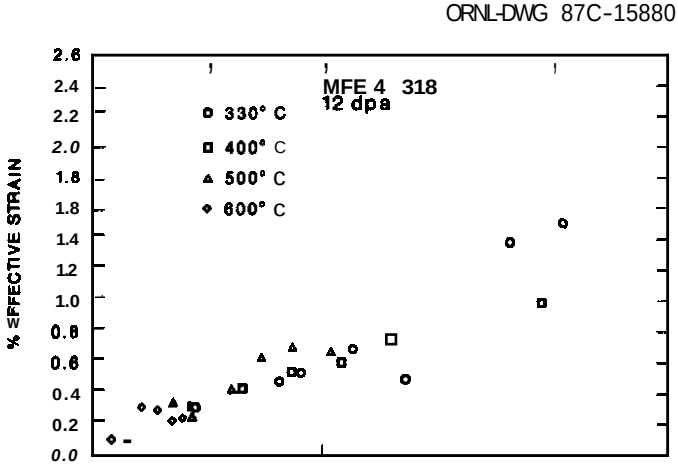

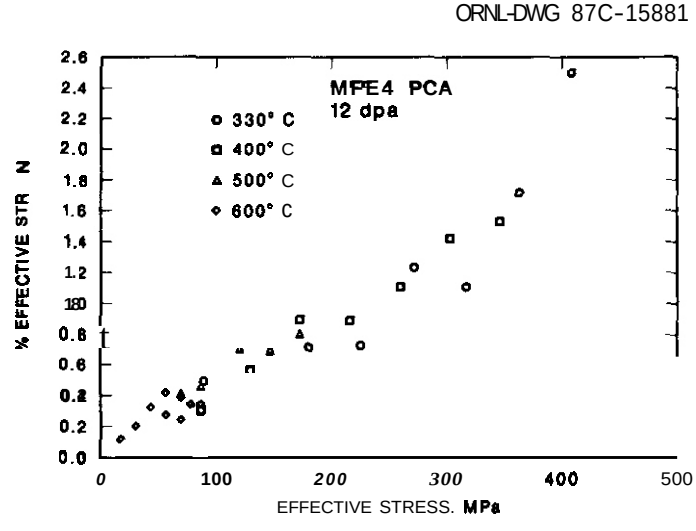

Fig. 2. Effective irradiation creep strain for U.S. Fusion Program PCA irradiated in the ORR spectrally tailored experiment (MFE-4).

In order to evaluate the effect of helium on irradiation creep, the data in the present study were compared with data from Puigh[2] on pressurized tubes of the same heat of PCA irradiated in the FFTF. Because of the hard spectrum of this reactor, the helium production rate is only 0.28 appm/dpa (ref. 3).

The ratio of creep strain to stress is plotted as a function of dpa in Fig. 3 for the present study in the ORR as well as for the FFTF at 400°C. It is apparent that the creep rate is higher for the material irradiated in the ORR. The same behavior is observed at 500°C (Fig. 4) and 600°C (Fig. 5). although scatter in the data makes the comparison less clear at the highest temperature.

Discussion

The linear stress dependence exhibited by the data in Figs. 1 and 2 at low stresses is the commonly observed behavior especially at low stresses.[4,5] It is the result characteristic of the stress-induced preferential absorption (SIPA) mechanism of irradiation creep.[6] An increasing stress exponent at higher stresses has also been previously observed.[2,7,8] Hudson and Nelson attribute this behavior to thermal creep at 500°C and Wassilew attributes this behavior to a transition from the SIPA mechanism to a climb-enabled glide mechanism.[7,8] The climb-enabled glide mechanism proposed by Mansur[9] predicts a quadratic dependence on stress. The present data show a stress exponent of 1.3 for 316 SS and 1.8 for PCA at 330°C. If this higher exponent results from a transition in mechanism, the fact that it is lower than two could result from the fact that the transition is not yet complete at the stress levels investigated. It is also possible that both mechanisms operate throughout the entire range of stress, but the quadratic dependence becomes

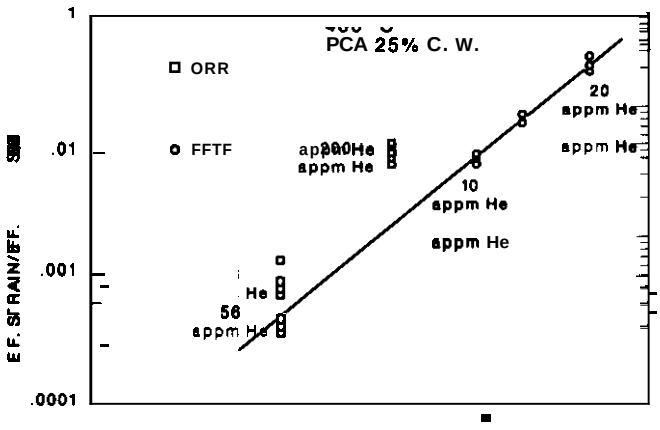

Fig. 3. Effective strain per unit effective stress as a function of dpa for U.S. Fusion Program PCA irradiated in the ORR spectrally tailored experiment and in the FFTF at 400°C.

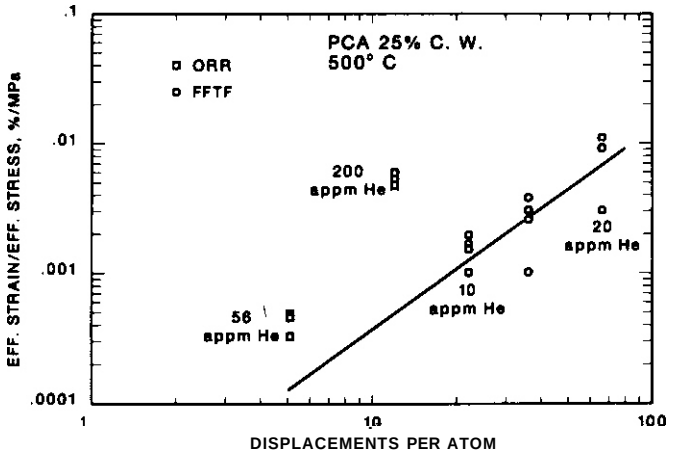

Fig. 4. Effective Strain per unit effective stress as a function of dpa for U.S. Fusion Program PCA irradiated in the ORR spectrally tailored experiment and in the FFTF at 500°C.

transition to quadratic stress behavior the significantly lower stresses used for were probably below the transition stresses, this phenomenon was not observed in the present investigation. However, such behavior might be expected since increased thermal activation of pinned dislocations associated with higher temperatures could result in glide at lower stresses.

The higher creep rates of ORR-irradiated material compared with FFTF-irradiated material shown in Figs. 3 through 5 will now be considered. Since the PCA specimens used in Puigh's work were fabricated from the same tubing used in the present investigation, the difference in creep rate can result only from differences in the irradiation environment. Four possibilities are apparent: the fluence level, the flux level. the energy spectrum. and the presence of helium. As seen from the plot; of Figs. 3 through 5, especially at 400°C, the FFTF data are well described by the straiaht-line least-squares fit shown, and the extrapolation in dpa to the data from this study is not a large one. The difference in the fluxes deserves careful consideration. In specimens irradiated in the Dounreay Fast Reactor, Lewthwaite and Mosedale observed an increase in creep rate per dpa with decreasing flux.[10] Straalsund observed no effect in austenitic stainless steels irradiated in the EBR-II. McElroy et al.,[11] on the basis of fast reactor data, concluded that there is an increase in creep rate with increasing flux but that the effect is small; Mosedale and Lewthwaite observed a similar trend in annealed material.[12] Wassilew also observed an increased creep rate at higher flux levels.[8] Since a higher flux results in a higher defect recombination rate, theory predicts that the irradiation creep rate per unit fluence should decrease with increasing flux, provided that the microstructure shows no dependence on flux. Clearly, the effect of flux on irradiation creep is not yet resolved. Thermal neutrons have been shown to be more effective in producing defects than fast neutrons.[13] This effect could result in a higher level of irradiation creep; however, the increment of irradiation creep would be expected to diminish as the spectrum was hardened during the course of the irradiation in the ORR. The opposite was observed.

The remaining possibility for the observed increase in creep rate in the present experiment is the effect of helium. The helium production rates for the ORR spectrally tailored experiment and the FFTF differ by a factor of about 60, and the creep rates are increased by a factor of 3 to 10. The mechanism by which the helium might increase the creep rate is not determined as yet. One possibility is that helium affects the microstructural sink strengths, which in turn affect the fates of point defects resulting in altered creep rates.[9] Another possibility that is proposed depends more directly on the presence of helium. It is known that helium exists in the lattice both as an interstitial and as a substitutional solute[14] as well as being trapped in clusters and cavities. It is suggested that a portion of the helium produced by the irradiation will contribute to the interstitial population which should contribute to dislocation climb and thus to irradiation creep. In this process the helium atoms that diffuse to the dislocations as interstitials. producing a net climb of the dislocation, then occupy lattice sites in the same manner as self-interstitials. In the presence of a stress, climb of the dislocation might be sufficiently rapid to prevent the agglomeration of enough helium to form bubbles along the dislocation.

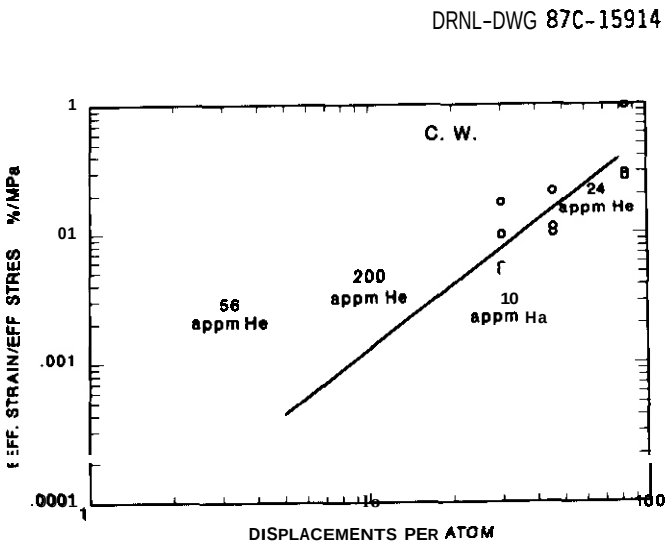

Fig. 5. Effective strain per unit effective stress as a function of dpa for U.S. Fusion Program PCA irradiated in the ORR.

The question that must now be addressed is whether the number of interstitial helium atoms is significant compared to the population of self-interstitials. The fraction of the helium concentration that will reside in interstitial sites can be estimated. To do this, a method used by Mansur et al.[15] will be followed. The rate equation for the production and loss of helium interstitials can be written as:

$$\tau_s^{-1} C_s + G'\Omega C_s + R_r C_i C_s - K_{He} C_v C_{He} = 0 \quad .$$

(1) (2) (3) (4)

Term (1) is the production rate of interstitial helium by thermal release of substitutional helium; term (2) is the displacement rate of substitutional helium; term (3) is the rate of exchange of self-interstitials and substitutional helium, producing a helium interstitial; term (4) is the loss rate of interstitial helium converted to substitutional helium through capture by vacancies. The loss to sinks, such as dislocations and grain boundaries, is neglected. All terms are per unit volume. The necessary expressions are interpreted as follows:

$\tau_s = \nu^{-1} \exp[(E^b_{He-v} + E^m_{He})/kT]$ is the mean residence time of helium in a vacancy before thermal release, ν is the attempt frequency which will be taken to be b^2/D^0_{He} where b is the Burgers vector and D^0_{He} is the coefficient in the diffusitivity of substitutional helium. E^b_{He-v} is the binding energy between a substitutional helium atom and a vacancy and E^m_{He} is the energy of migration of helium. G' is the generation rate of interstitial helium by direct displacement per unit concentration of substitutional helium. The symbol $R_r = 4\pi r_r D_i$ is the coefficient of replacement where a self-interstitial dislodges a substitutional helium atom; r_r is the radius of the replacement volume. $K_{He} = 4\pi r_{He-v} (D_{He} + D_v)$ is the capture coefficient of a vacancy for an interstitial helium atom; r_{He-v} is the radius of the capture volume. C_s is the concentration of substitutional He, Ci is the concentration of self-interstitials, C_v is the concentration of vacancies, and C_{He} is the concentration of interstitial helium. What was felt to be reasonable values for the above parameters were used in the calculation; the values appear in Table 1. The result is that the ratio C_{He}/C_s ranges from 10^{-8} to 10^{-5} over the range of 300 to 600°C. If a helium concentration of 100 appm were in substitutional sites, the interstitial helium concentration then is in the range of 10^{-12} to 10^{-9} atom fraction. This is to be compared with the self-interstitial population for which 10^{-12} is a representative value. Therefore, the calculation shows that the generated helium can make a significant contribution to the total interstitial population so that the mechanism is considered a plausible one. Considering the very large uncertainties involved in this calculation, it is considered only an attempt to determine if the suggested mechanism is possible.

CONCLUSIONS

1. Irradiation creep in the range of 330 to 600°C is independent of temperature in the presence of fusion reactor-like helium generation rates in the austenitic steels studied.

2. Irradiation creep strain is linear in stress at low stresses but increases with a stress exponent approaching two at high stresses. This was most apparent in PCA but was observed only at 330°C due to the limited range of stress at the higher temperatures.

3. The irradiation creep rate is three to ten times higher for the high-helium ORR irradiation, where the He:dpa value is about 12, compared with FFTF irradiation, where the He:dpa value is only 0.28 appm/dpa.

Values	Reference
	16
r_{He-v} = 5 Å	
$D_v = 1.4 \times 10^{-2} \exp(-1.38\ eV/kT)$	16
$D_{He} = D_H(Ni) = 48 \times 10^{-3} \exp(-0.41\ eV/kT)$	17
$G' = 2.7 \times 10^{-7}/cm^{-3}\ s^{-1}$	(ORR experimental data)
$C_v = 10^{-6}$ atom fraction	
$C_i = C_v \frac{D_v}{D_i}$	

4. The higher creep rate is believed to result from either the lower flux in the ORR experiment or from the higher level of helium.

5. A mechanism of helium-assisted climb is proposed to account for the increase in creep rate due to helium.

FUTURE WORK

Irradiation creep work will be extended in two ways: to lower temperatures and to additional alloys. The experiments ORR-MFE-6J and -7J will cover temperatures of 60. 200, 330. and 400°C. In addition, both austenitic and ferritic alloys will be investigated.

REFERENCES

1. E. R. Gilbert and L. D. Blackburn, Trans. ASME, J. Eng. Mat. & Tech. (April 1977) 168.
2. R. J. Puigh, J. Nucl. Mater. 141-143 (1986) 954.
3. R. L. Simons, p. 12 in Damage Analysis and Fundamental Studies Quarterly Progress Report, DOE/ER-0046/19 (July–Sept. 1984), USDOE, Office of Fusion Energy.
4. J. L. Straalsund, p. 191 in Radiation Effects in Breeder Reactor Structural Materials, M.L. Bleiberg and J. W. Bennett, ed., The Metallurgical Society of AIME, New York, 1977.
5. L. C. Walters, G. L. McVay, and G. D. Hudman, ibid. p. 277.
6. W. G. Wolfer and M. Ashkin, J. Appl. Phys. 47 (No. 3) (1976) 791.
7. J. A. Hudson and R. S. Nelson, J. Nucl. Mater. 65 (1977) 279.
8. C. Wassilew, "Analysis of the In-Reactor Creep and Creep-Rupture Life Behaviour of Stabilized Stainless Steels and the Ni-Base Alloy Hastelloy X, Primarbericht, KFZ, Karlsruhe, February 1987.
9. L.K. Mansur, Phil. Mag. A 39 (1979) 497.
10. G. W. Lewthwaite and D. Mosedale, J. Nucl. Mater. 90 (1980) 205.
11. W. N. McElroy, R. E. Dahl, Jr., and E.R. Gilbert, Nucl. Eng. & Design 14 (1970) 319.
12. D. Mosedale and G. W. Lewthwaite, p. 169 in Creep Strength in Steel and High-Temperature Alloys, proceedings of a conference held at the University of Sheffield, 20-22 Sept. 1972, The Metals Society.
13. J. A. Horak and T. H. Blewitt, Nucl. Tech. 27 (1975) 416.
14. W. Schilling, p. 303 in: Proc. of Yamada Conf. 5 on Point Defects and Defect Interactions in Metals (University of Tokyo Press, 1982).
15. L. K. Mansur, E. H. Lee, P. J. Maziasz, and A. F. Rowcliffe, J. Nucl. Mater. 141-143 (1986) 633.
16. L. K. Mansur and M. H. Yoo, J. Nucl. Mater. 74 (1978) 228.
17. J. K. Tien, p. 309 in Effect of Hydrogen on Behavior of Materials, A. W. Thompson and I. M. Bernstein, ed., The Metallurgical Society of AIME, New York, 1975.

IRRADIATION CREEP AND EMBRITTLEMENT BEHAVIOR OF AISI 316 STAINLESS STEEL AT VERY HIGH NEUTRON FLUENCES

D. L. Porter (Argonne National Laboratory)
F. A. Garner (Pacific Northwest Laboratory)

OBJECTIVE

The object of this effort is to determine the mechanisms by which the microstructural evolution of irradiated austenitic alloys respond to differences in composition or radiation variables.

SUMMARY

The irradiation-induced creep and swelling of AISI 316 stainless steel have been investigated at two temperatures (400 and 550°C) to very high neutron fluences. It is shown that creep and swelling can be considered as interactive phenomena with several stages of creep related to the total amount of accumulated swelling. The final stage involves the apparent cessation of creep and has been observed only at the higher irradiation temperature. The development of a coincident and severe ex-reactor embrittlement problem after irradiation at 400°C appears also to be separately related to the development of substantial swelling. This latter phenomenon was not observed at 550°C. The mechanisms thought to be possibly responsible for each of these two phenomena are discussed in detail.

PROGRESS AND STATUS

Introduction

In earlier reports, it was shown that at 550°C the neutron-induced creep rate of AISI 316 stainless steel unexpectedly begins to decline at high fluence and eventually disappear.[1,2] This phenomenon appears to be related only to the presence of significant levels of void swelling (5 to 10%), which in turn is determined by the starting thermomechanical condition of the alloy and the accumulated neutron fluence. One consequence of this phenomenon is that the total diametral growth rate of internally pressurized capsules cannot exceed ~0.33%/dpa, the rate dictated by steady-state swelling alone.

It was initially thought that there might be a second creep-related consequence in response to the accumulated void volume. Significant changes in fracture mode were also found to occur in this steel coincident with 5 to 10% swelling, although these observations were made on steel specimens irradiated at lower temperatures (in the range of 370 to 430°C) and tested out of reactor.[1,3] It was speculated that a possible connection existed between the two phenomena, in which the reduced creep rate was somehow related to the strong reduction in tearing modulus observed in ex-reactor tensile tests.

In order to test this supposition, a series of creep capsules irradiated at ~400°C were examined. The first results were reported elsewhere' but the capsules did not exhibit a reduction in creep rate similar to that observed at 550°C. The 400°C capsules were irradiated to higher displacement levels than those at 550°C (–130 versus 80 dpa) and were maintained at a larger range of hoop stress levels (343 versus 206 MPa). Note that 400 and 550°C are the temperatures at the axial center of the capsules. There are small gradients in temperature along the tubes but the data in this report were extracted only fran the centerline position.

This paper reports the results of continued investigation of the 400 and 550°C creep experiments, concentrating on the possible relationship between the changes in fracture mode and the disappearance of creep with increasing swelling.

Experimental Details

The steel employed was the V87210 reference heat of AISI 316 used in the U.S. Breeder Reactor Program. Its composition in wt% was Fe-13.57 Ni-16.36 Cr-2.88 Mo-1.42 Mn-0.47 Si-0.07 C-0.02 P-0.01 S with <0.005 B. This steel was irradiated in five metallurgical conditions: solution annealed, 10% cold-worked, 20% cold-worked, 20% cold-worked followed by aging for 24 hours at 482°C (designated Heat Treat C), and Heat Treat C followed by another aging for 216 hours at 704°C to cause extensive carbide precipitation. This latter heat treatment is hereafter designated as Heat Treat O but is often called the Garafalo treatment. All conditions were prepared using vendor-produced 20% cold-worked steel as the starting condition. Thus, the 10% cold-worked condition was prepared by working the annealed condition prepared in the laboratory from the 20% cold-worked condition.

The two sets (400 and 550°C) of helium-pressurized creep capsules have been described in detail elsewhere.[5,6] In brief, all capsules were 1.02 m long with an outer diameter of 0.584 cm and a wall thickness of 0.038 cm. Whereas the 400°C capsules were pressurized to hoop stress levels ranging from 0 to 343 MPa (50 ksi) along their length, only the top 0.28 m length of the 550°C capsules was pressurized to yield hoop stress levels varying from 0 to 207 MPa (0 to 30 ksi). A typical 550°C capsule is shown in Figure 1. The

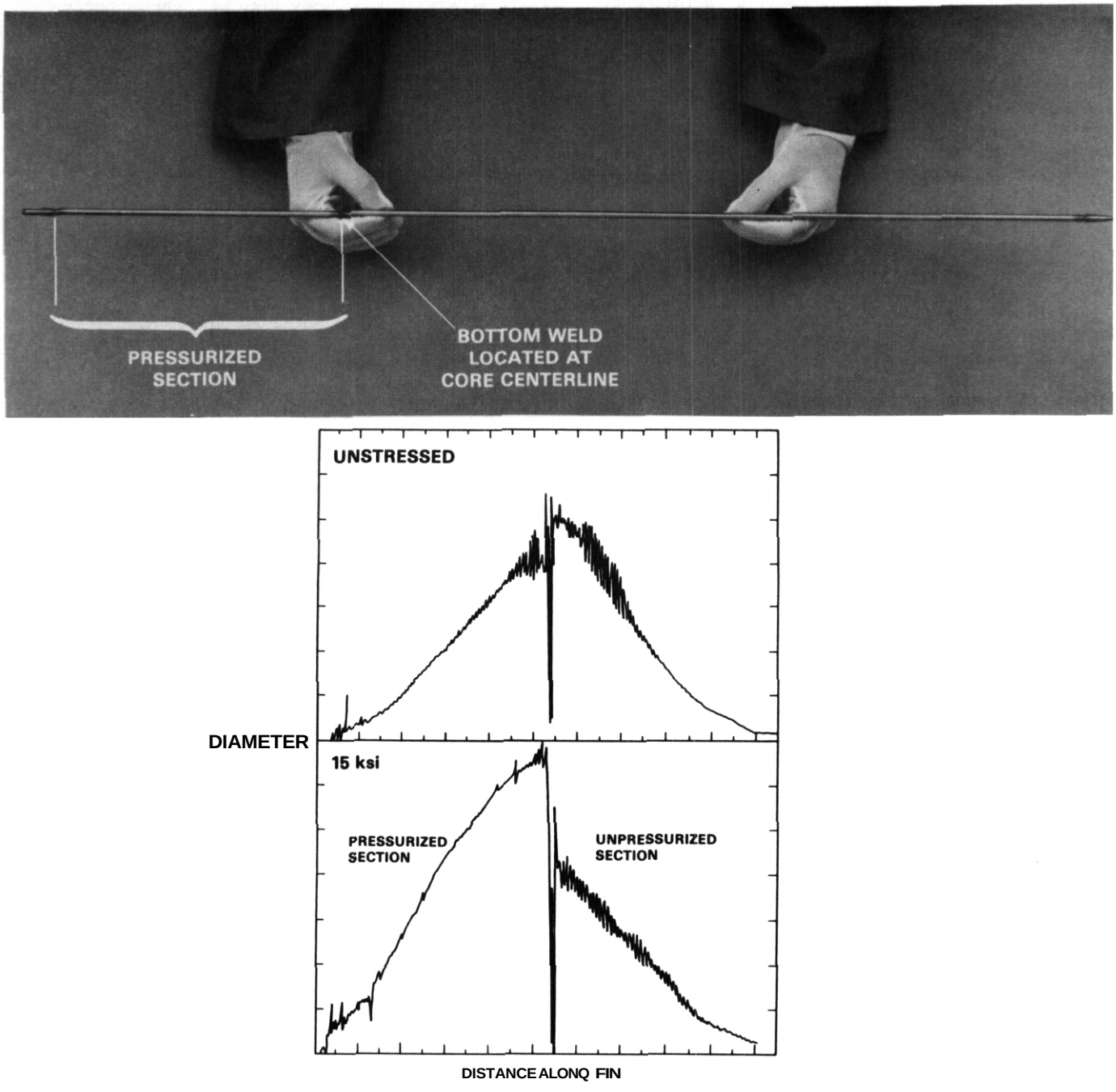

Fig. 1. Picture of a 550°C Irradiation Creep Capsule and Typical Profilometer Traces of Irradiated Capsules. The 400°C capsules are pressurized along their entire length.

pressurized portion of the 550°C capsule was welded to the lower portion of the capsule which contained a tantalum rod whose nuclear heating raised the temperature of the reactor sodium as it flowed upward. The 400°C capsules also contained a loosely fitting stainless steel rod in the bottom 0.71 m The purpose of this rod was to reduce the pressure pulse associated with gas release that would accompany a sudden pin failure. The tantalum rod in the 550°C capsule also served this same purpose.

The irradiations proceeded in two 37-pin subassemblies in Row 7 of the Experimental Breeder Reactor EBR-II in Idaho Falls, Idaho. Approximately 5 dpa (±10%) are produced in the core of this reactor for each 10×10^{22} n/cm2 (E>0.1 MeV). The dpa (displacements per atom) levels cited for each datum are derived by incorporating the position dependence of the neutron energy spectra. Most capsules were irradiated at constant stress and temperature but some were deliberately subjected to abrupt changes in stress level and/or temperature. Inadvertent changes in stress level also occurred when some capsules failed during irradiation. Capsules which experienced such changes are covered in more detail elsewhere.'

The capsules were cycled in and out of reactor for interim examination and measurement. Some of these were measured as many as twenty-two times, averaging between examinations approximately 6 dpa at the core centerline position. Diameter measurements were made with a contact profilometer on a spiral trace along the entire length of the capsule after each irradiation period. Examples of typical traces are shown in Figure 1. Some capsules had obviously failed during a given irradiation period and most of these were withdrawn. Those that did not fail and a few of those that did fail were returned for reirradiation until a decision was made to terminate the irradiation of that particular capsule. At that point, the unfailed capsules were punctured and the gas volume measured to confirm that the design stress level had been maintained throughout the irradiation.

Some capsules, particularly those that were initially in the annealed condition at 550°C, were found not to have gas pressure at the end of the experiment and thus to have failed at an indeterminate time by some not quite obvious mode, such as pin-hole failure.' It is postulated that this occurred as a consequence of the design pressure (which is reached only in reactor) exceeding the yield stress of the softer annealed material at 550°C, causing the end-cap weld to fail at the beginning of the irradiation. Since the stress history of these capsules was unknown, these pins were not used in the analysis of irradiation creep.

Some capsules were sectioned into 1 in. axial increments and immersion density measurements were performed to determine the amount of stress-affected swelling.

Results: 400°C Capsules

When the 400°C capsules were removed for the last time from the hexagonal duct that encases them during irradiation, it became obvious that they would have to be handled with care. One of the capsules failed in a very brittle manner while being pulled out of the duct assembly. As shown in Figure 2, another capsule broke into three pieces while being clamped into a vise for cutting of density sections. In each case, the capsules which failed were at 400°C and were constructed from the higher swelling Heat Treat D material at a hoop stress of 276 MPa (40 ksi). Each failed in the region near the core center position at dose levels of ~130 dpa with a local swelling level of ~14%. The failure mode appears to be identical to that reported in References 1 and 3.

No similar embrittlement problems were observed for capsules irradiated at 400°C in more swelling-resistant thermomechanical conditions or for capsules irradiated in any condition at 550°C, even though the latter accumulated swelling levels ranging from 9 to 20%.

The two capsules that failed upon removal not only exhibited the largest levels of swelling at 400°C but also the largest levels of irradiation creep. As demonstrated in Figure 3, one carefully handled capsule of Heat Treat D at 400°C and 276 MPa was found to have a total diameter change of 20%, with roughly 15% due to irradiation creep. Using a procedure described in detail elsewhere,[4] the instantaneous creep coefficient can be calculated from diameter measurements of both stressed and unstressed capsules, assuming that swelling at 400°C is not very sensitive to stress. Based on other results this assumption appears to be reasonable.[4,8] The stress-free swelling rate of this steel at 400°C was found to range from 0.05 to 0.11% per dpa, depending on the thermomechanical starting condition and the environmental history.[4]

Figure 4 shows that the instantaneous creep coefficient for the Heat Treat D condition at 400°C and 276 MPa is relatively large at first and increases steadily with fluence, possibly saturating somewhere between 20 and 30 x 10^{-30} $cm^2/n \cdot psi$. Figure 5 shows that the 20% cold-worked condition both creeps and swells at 400°C at slower rates than does Heat Treat D. Note in Figure 6 that the instantaneous creep coefficient of 20% cold-worked steel is independent of stress level and also appears to saturate in magnitude at higher exposure.

Results: 550°C Capsules

The swelling of the five metallurgical conditions of this steel in general has been found at 550°C to be Heat Treat D >annealed> 20% cold-worked, Heat Treat C >10% cold-worked.[5,6] The lesser swelling of the 10% cold-worked condition probably reflects the different annealing conditions it received in the laboratory compared to that of the mill-prepared 20% cold-worked condition. Normally, the swelling decreases as the cold-work level increases, providing that the intermediate annealing conditions between cold-work passes does not change. The onset of swelling for AISI 316 is known to be sensitive to many production variables including the rate of feed of the tube through the annealing furnace.[9] Laboratory anneals are in general conducted for times that exceed the residence time of mill-prepared steels.

Since the creep rate is generally thought to increase as swelling accumulates, one would expect that the total deformation would exhibit the same dependence on starting condition as seen in the swelling behavior. Figure 7 shows that the total deformation behavior of a typical series of 550°C capsules follows the trends observed in the swelling behavior of earlier studies.

Figure 8 shows the total diametral strains measured at the position of maximum displacement rate for three high fluence capsules in the Heat Treat D condition. Note that while the transient regime of diametral deformation decreases in duration with increasing stress, the post-transient deformation rate does not

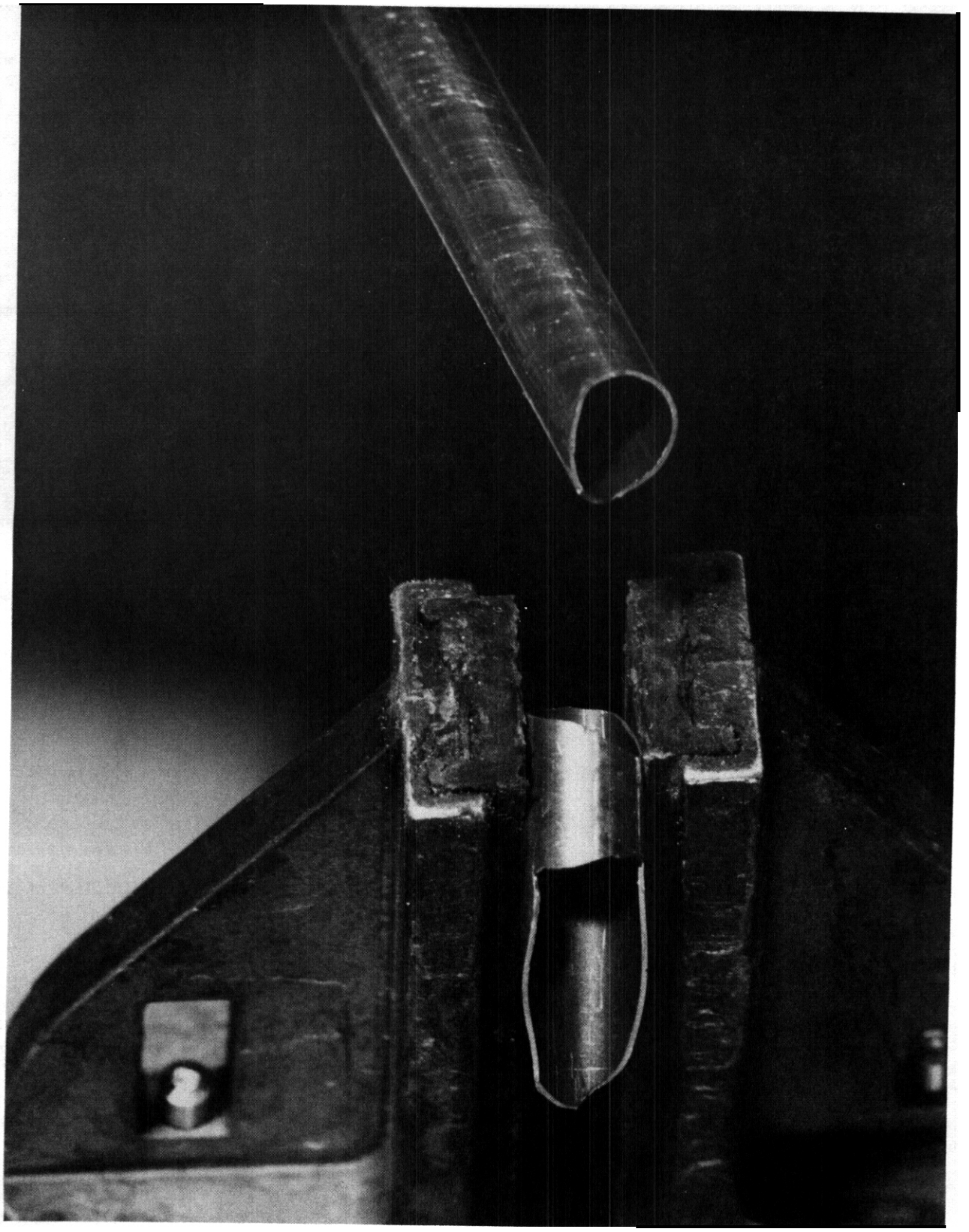

Fig. 2. Failure During Mounting of Severely Ernbrittled AISI 316 Capsule in the Heat Treat D Condition after Irradiation to 130 dpa at 400°C and a Hoop Stress of 276 MPa (40 ksi).

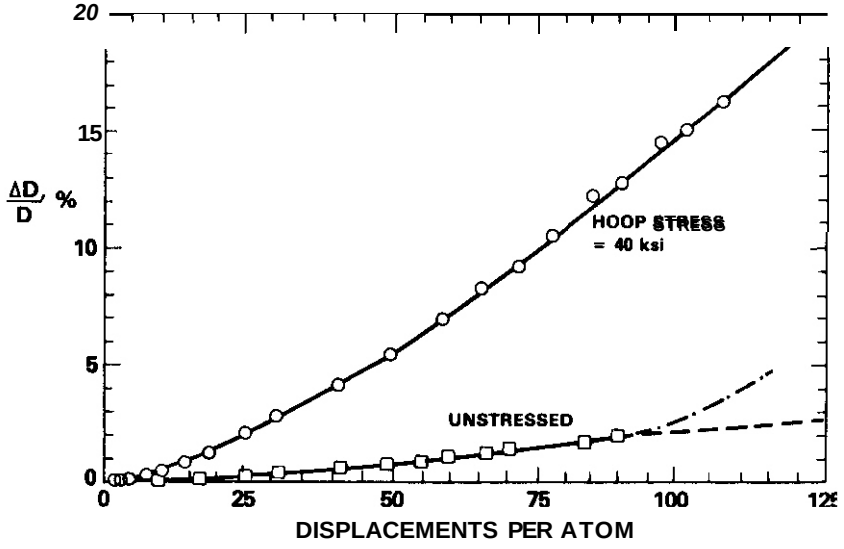

Fig. 3. Irradiation Creep and Swelling-Induced Strain at 400°C for the Heat Treat D Condition in the Unstressed and Stressed Capsules.

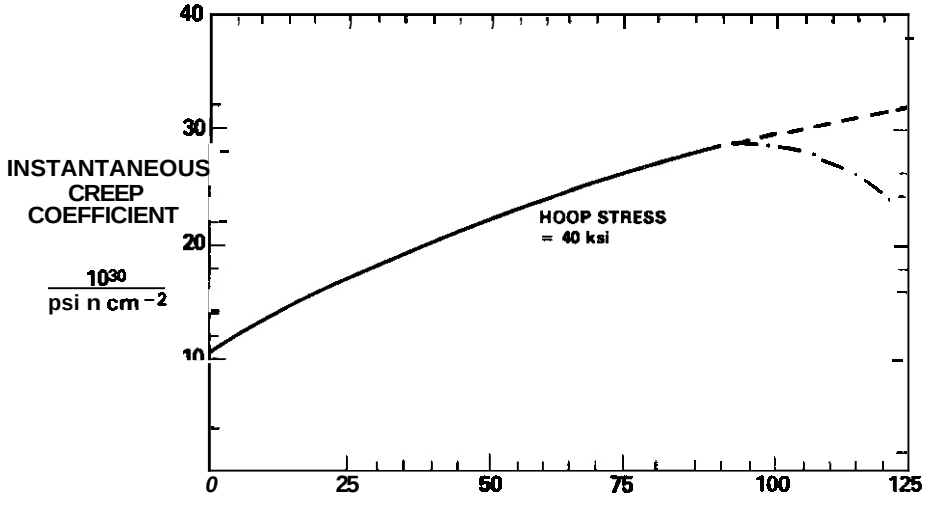

Fig. 4. Instantaneous Creep Coefficient of Heat Treat D at 400°C Derived from Data in Figure 3

appear to change. Even more significantly, the total deformation rate does not exceed the value of 0.33%/dpa expected from steady-state swelling alone. (Similar behavior was also observed at 550°C in the 10% and 20% cold-worked conditions.[2,7] It appears that the well-known linear stress dependence of the irradiation creep rate has disappeared somewhere between hoop stress levels of 0 and 103 MPa (15 ksi). Based on the current conception of irradiation creep where the largest component of the creep rate is thought to be proportional to the swelling rate' one would expect at 200 MPa to reach and maintain a creep rate at high fluence that approaches a value comparable to the swelling-induced deformation rate. Figure 9 shows that the instantaneous creep coefficient of Heat Treat D at 206 MPa (30 ksi) peaks between 20 and 30 x 10^{-30} $cm^2/n \cdot psi$, however, and then falls toward zero thereafter.

Discussion

The data presented in this and earlier reports suggest that both the ex-reactor embrittlement observed at room temperature (for material irradiated at −400°C) and the late-term disappearance of irradiation Creep at 550°C arise independently as consequences of large levels of swelling. These two phenomena do not appear to be directly related and each occurs at different temperatures in this study. The severe low temperature embrittlement at 400°C has been ascribed to the compound action of a strongly radiation-hardened matrix and the late-term segregation of nickel to void surfaces.3 The strong dependence of stacking fault energy on

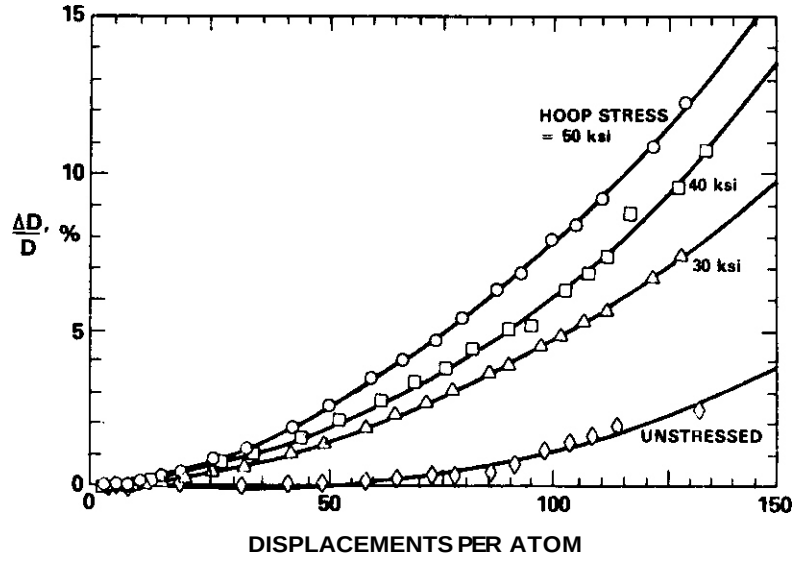

Fig. 5. Irradiation Creep and Swelling-Induced Strain at 400°C of the 20% Cold-Worked Condition in Unstressed and Stressed Capsules. The stress levels were 206, 276, and 343 MPa (30,40,50 ksi)

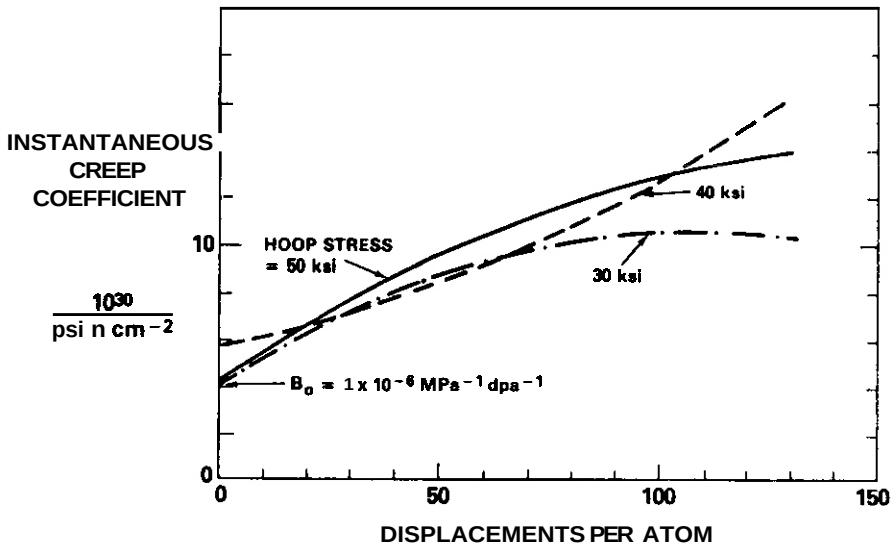

Fig. 6. Instantaneous Creep Coefficients at 400°C of 20% Cold-Worked AISI 316 Derived from Data in Figure 5

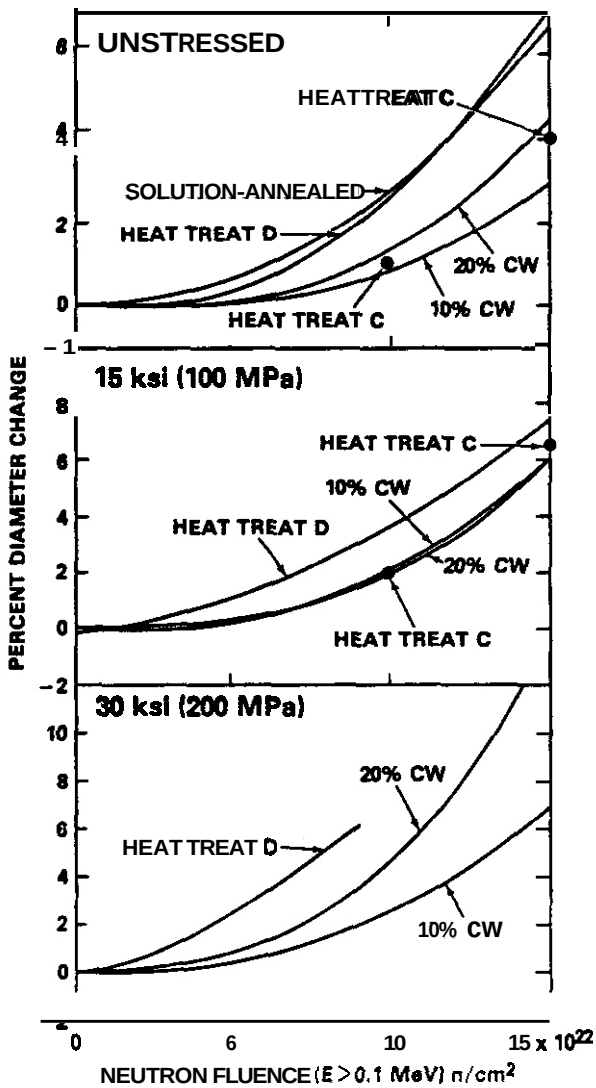

Fig. 7. Typical Deformation Behavior at Core Centerline of 550°C Creep Capsules with Different Stress Levels and Starting Metallurgical Conditions.

nickel and chromium content and particularly on deformation temperature combine to promote extensive stress-induced formation of ϵ-martensite in the nickel-depleted matrix, leading to a very brittle ex-reactor fracture mode characterized as quasi-cleavage. The absence of severe embrittlement in the 550°C capsules probably reflects several aspects of the much lower densities of microstructural components induced by radiation at 550°C compared to those produced at 400°C. First, the radiation-induced hardening is *much* lower at 550°C and second, the surface area of the voids is much lower for a given level of swelling.[10] This would tend to reduce the total amount of nickel removal from the matrix and may help to account for the absence of severe embrittlement at 550°C.

In this study, only Heat Treat D capsules were observed to fail and embrittlement tests were not conducted on other thermomechanical conditions. Earlier studies have shown that embrittlement is independent of starting condition, however, and depends primarily on the swelling level.[3]

Prior to discussing the disappearance of creep at 550°C and its maintenance at 400°C, one must first be convinced that the observation of creep disappearance is not an artifact of the test procedure. The gas pressure and volume are always determined at the end of each capsule's life and thus creep disappearance cannot be ascribed to loss of gas pressure. The gas pressure does drop as the capsule diameter increases in response to irradiation creep. It is very easy to show, however, that the stress in the wall stays the same, since the diameter change is compensated by a thinning of the capsule wall. While the biaxial stress state of pressurized capsules do not cause the capsule to increase in length as a result of creep, the capsule does increase in all three important dimensions (length. diameter, and wall thickness) in response to swelling. It is a simple calculation to show that the hoop stress will decrease with swelling in the following manner.

$$\sigma_{HOOP} = \sigma^{0}_{HOOP}/(1 + \bar{S})$$

where $\bar{S}$ is the average swelling over the entire length of the capsule. Due to the long length of these capsules $\bar{S}$ is relatively small even for large values of maximum swelling. Thus, the drop in creep rate cannot be ascribed solely to the effect of swelling and creep on capsule dimensions.

If we search for microstructural origins of creep disappearance, there are a number of mechanism which come to mind. First, it has been proposed by Jung and Ansari that irradiation creep is correlated to the yield strength of a metal although "this correlation must for the present be considered entirely empirical."[11] The increase in yield strength due to radiation-induced microstructural components has been determined previously[10] and the hardening associated with swelling is insufficient to account for the near cessation of creep observed in this experiment at 550°C. Even more importantly, the yield strength of irradiated AISI 316 is much higher at 400°C than at 550°C,[10] but it is at the higher temperature that creep disappears.

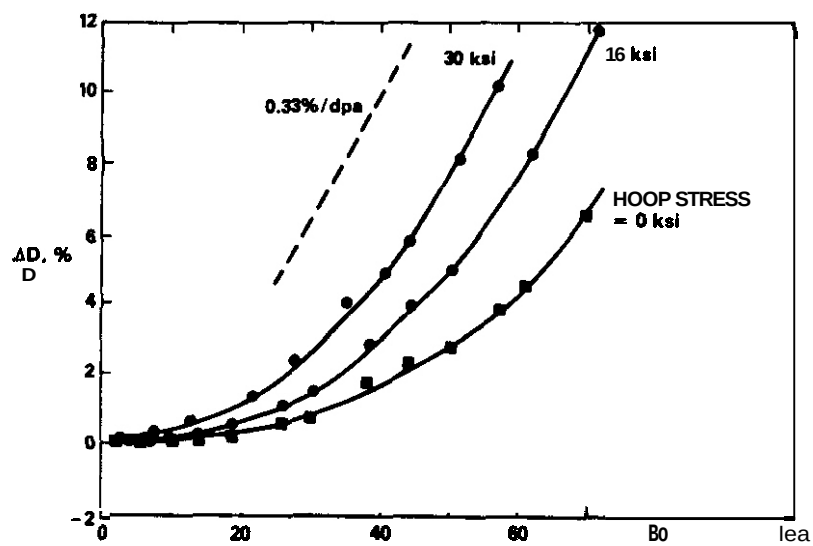

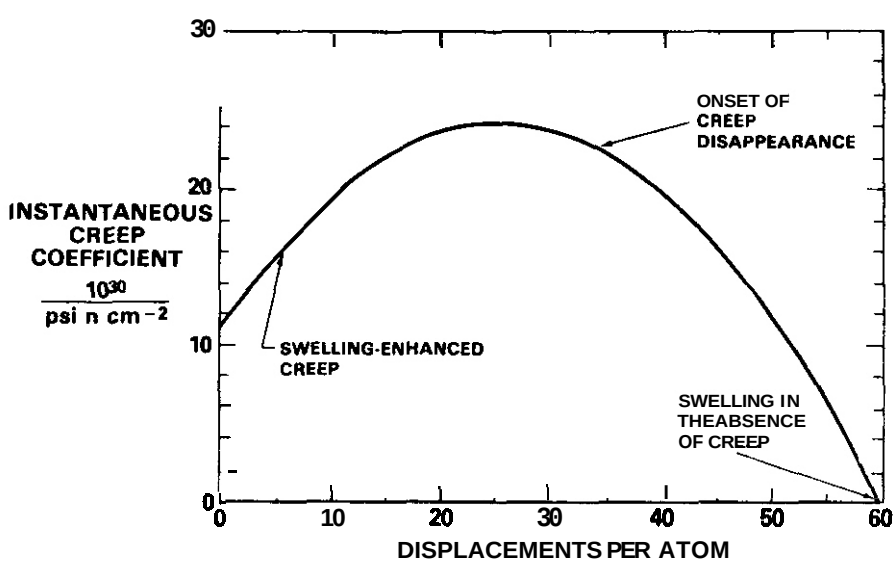

Fig. 9. Instantaneous Creep Coefficient of Heat Treat D at 550°C and 206 MPa (30 ksi) Derived from Data in Figure 8

Creep and swelling in various models have been assumed to be proportional to some function of the shear modulus, as discussed elsewhere.[12] There are void-induced changes in the basic properties of metals such as thermal conductivity and elastic properties. The latter include the shear, bulk, and Young's moduli, as well as Poisson's ratio. The origin and magnitude of these changes have been described by a number of researchers.[13-17] The various moduli are predicted to drop initially with swelling at a rate of 1 to 2 percent per percent of swelling but Poisson's ratio changes at a much lower rate. Marlowe and Appleby measured Young's modulus to increase initially in annealed steel as the dislocation density increased and then to decline at a rate of 1.6 to 2.7% for each percent of swelling.[17] Straalsund and Day determined that the shear, Young's and bulk moduli declined at a rate of 2.3, 2.4, and 2.6 percent per percent of swelling.[18] Poisson's ratio was also found to decrease at a rate of 0.23 percent per percent of swelling. None of these changes are sufficient in themselves to account for the disappearance of creep.

There are other types of direct-coupling mechanisms whereby swelling might affect creep and lead to its eventual disappearance. First of all, at large levels of swelling, the overwhelming majority of dislocations terminate on void surfaces, a situation in which the climb rate of dislocations can be strongly affected by pipe diffusion into the voids. This might change the net bias of the dislocation network. Second, the glide distance will be decreased as the voids become the dominant obstacle. This would make dislocation climb over void obstacles the dominant creep mechanism and reduce the amount of glide-type creep that can occur for a given level of irradiation.

Third, if the creep process is now restricted primarily to irradiation-induced climb of dislocations, one can envision a situation in which the stress-induced absorption (SIPA) creep mechanism[19] may no longer operate effectively. This mechanism requires that the climb of dislocations lying on some planes be enhanced by the applied stress state, while other less favorably oriented dislocations are inhibited in their climb rate. In short, this mechanism requires that dislocations be on different planes and have different Burgers vectors. Gelles and coworkers have recently shown that large levels of applied stress lead to a strong anisotropy of dislocations such that unfavorably oriented dislocations exist at substantially reduced densities, while favorably oriented dislocations are strongly increased in density.[20,21] Similar stress-induced anisotropies have been observed in the Frank loop population.[22,23] Hence, the SIPA creep mechanism may not function very effectively after the applied stress state has substantially altered the dislocation and loop microstructure.

The foregoing discussion on stress-induced anisotropy of dislocations and loops is based on anisotropies which were observed to develop prior to the onset of substantial levels of swelling. There are no data to show how such anisotropies are affected by the dominating presence of voids, which will exert their own bias contribution.[24] Perhaps even more importantly, the presence of high levels of large voids will distort the local stress state experienced by dislocations. This latter consideration has not been addressed theoretically and may have a large impact on irradiation creep.

Another possible influence of voids lies in their ability to segregate nickel at their surfaces, previously discussed as a contributing cause of the severe embrittlement phenomenon. This will change the stacking fault energy from one location to another, with possible effects on formation and separation of partial dislocations. The segregation of nickel will also change the bias contributions arising from the voids themselves.[25]

None of the above cited mechanisms offer in themselves an obvious explanation as to why creep disappears at 550°C but not at 400°C. Perhaps the cessation of creep may only be coincident with large levels of swelling but not directly related to void growth. As an example of another possible mechanism, it was shown in an earlier paper that the formation of intermetallic phases at higher irradiation temperatures affects the thermal creep rate.[26] These phases do not form at 400°C.

While most of the mechanisms cited above could act to decrease the rate of irradiation creep, no one of them appears to be sufficient in itself to cause the total elimination of creep. Perhaps the net effect of all these mechanisms is somehow compounded to induce the phenomenon of creep disappearance. Since the diametral creep rate saturates at approximately one-third of 1%/dpa, the latter being the steady-state swelling rate,[27] this implies that stress-affected swelling itself is isotropic. These swelling-induced increases in volume obviously require dislocation motion but the apparent disappearance of creep implies either a greatly reduced mobility of dislocations, or at least a reduction in their ability to sense and react to the stress state. This apparent paradox awaits the acquisition of more data before it can be resolved. It is difficult to imagine, however, how the applied and swelling-generated stresses are being relieved on a microscopic level when the macroscopic creep rate seems to have disappeared.

There is another conclusion of relevance to the subject of swelling-creep interactions. Current design practice is to use creep and swelling predictive correlations arising from separate data bases. Creep data are generated at much larger than anticipated stress levels in order to maximize the level of creep and facilitate its measurement while swelling equations are often derived from irradiation of stress-free specimens. The predictions of such creep and swelling correlations are combined under the implicit assumption that creep and swelling strains are independent and additive even though creep seems to be related to swelling in its early stages. The phenomenon of creep disappearance casts the unqualified use of this assumption into doubt.

It has been proposed that the creep rate $\dot{\varepsilon}$ at any relevant temperature is linearly dependent on stress a and related to the swelling rate $\dot{S}$ by the following relation.[27-30]

$$\frac{\dot{\varepsilon}}{\sigma} = B_o + D_o \dot{S}.$$

The creep compliance B_o has been shown to be independent of temperature and approximately equal to 1×10^{-6} MPa^{-1} dpa^{-1} for a wide range of austenitic steels.[29,30] The swelling-enhanced creep coefficient D_o is likewise thought to be relatively constant at $\sim 10^{-2}$ MPa^{-1} over a wide range of steels and temperatures.[29]

Using the insight gained in an earlier study[4] of stress-independent swelling at 400°C to analyze the data in Figure 3, the values of B_o and D_o can be calculated. Note in Figure 4 that the instantaneous creep coefficient ($B_o + D_o \dot{S}$) is independent of stress level as predicted and appears to saturate at higher exposures. At zero dpa and therefore zero swelling rate, B_o is indeed $\sim 1 \times 10^{-6}$ MPa^{-1} dpa^{-1}. Assuming a swelling rate of ~0.04%/dpa and using the 40 ksi curve at 130 dpa, D_o is calculated to be -0.6×10^{-2} MPa^{-1}. The estimates of both B_o and D_o thus appear to be in good agreement with the anticipated values.

CONCLUSIONS

The creep rate of AISI 316 induced by neutron radiation appears to be influenced by the onset of swelling, first increasing in direct proportion to the swelling rate and sometimes decreasing and even ceasing as voids become the dominant feature of the microstructure. The nature of the interactions between creep and swelling appear to be independent of temperature in the early stages of swelling but dependent on temperature in the later stages.

The emergence of a severe embrittlement phenomenon associated with swelling likewise appears to be strongly dependent on temperature but is not thought to be directly related to the disappearance of creep. While the microstructural origins of the mbrittlement phenomenon appear to be relatively simple and clear, the possible causes of the cessation of creep are many and it may be their aggregate operation that is the origin of the ohenomenon.

FUTURE WORK

This effort will continue, focussing on microscopic examination of the fracture surfaces of the AISI 316 tubes irradiated at 400°C.

REFERENCES

1. F. A. Garner, H. R. Brager, M. L. Hamilton, R. A. Dodd and D. L. Porter, Radiation Effects, Vol. 101, pp. 37-53, (1987).

2. F. A. Garner, D. L. Porter and B. J. Makenas, Journal of Nuclear Materials, Vol. 148, pp. 279-287, (1987).

3. M. L. Hamilton, F. H. Huang, F. A. Garner and W.J.S. Yang, In Influence of Radiation on Material Properties, ASTM STP 956, F. A. Garner, C. H. Henager, Jr. and N. Igata, eds., American Society for Testing and Materials, Philadelphia, Pennsylvania, pp. 245-270 (1987).

4. F. A. Garner and D. L. Porter, Journal of Nuclear Materials, Vols. 154-156, (1988) in press.

5. L. C. Walters, G. L. McVay and G. D. Hudman, In Radiation Effects in Breeder Reactor Structural Materials, M. L. Bleiberg and J. W. Bennett, eds., The Metallurgical Society, New York, pp. 277-294, (1977).

6. G. L. McVay, R. E. Einziger, G. L. Hofman and L. C. Walters. Journal of Nuclear Materials, Vol. 78, pp. 201-209, (1978).

7. D. L. Porter, and F. A Garner, ibid ref. 3, pp. 11-21.

8. F. A. Garner, E. R. Gilbert and D. L. Porter, In Effects of Radiation on Materials: Tenth Conference, ASTM STP 725, D. Kramer, H. R. Brager and J. S. Perrin, eds., American Society for Testing and Materials, Philadelphia, Pennsylvania, pp. 680-697.

9. F. A. Garner, In Optimizing Materials for Nuclear Applications, F. A. Garner, D. S. Gelles and F. W. Wiffen, eds., The Metallurgical Society, New York, pp. 191-207, (1977).

10. F. A. Garner, M. L. Hamilton, N. F. Panayotou and G. D. Johnson, Journal of Nuclear Materials, Vols. 103 and 104, pp. 803-808, (1981).

11. P. Jung and M. I. Ansari, Journal of Nuclear Materials, Vol. 138, pp. 40-45, (1986).

12. J. F. Bates, Journal of Nuclear Materials, Vol. 87, pp. 409-415, (1979).

13. Z. Hashin and S. Strikman, Journal of Mechanical Physics of Solids, Vol. 11, pp.127-140, (1963).

14. Z. Hashin, 1962, Journal of Applied Mechanics, Vol. 29E, p. 143.

15. H-S. Chen and A. Acrivos, International Journal of Solid Structures, Vol. 14, p. 349, (1978).

16. G. Ondracek, Materials Chemistry and Physics, Vol. 15, pp. 281-313, (1986).

17. M. Marlowe and W. K. Appleby, Transactions of the American Nuclear Society, Vol. 16, p. 95, (1973).

18. J. L. Straalsund and C. K. Day, Nuclear Technology, Vol. 20, p. 27, (1973).

19. W. G. Wolfer, Journal of Nuclear Materials, Vol. 90, p. 175, (1980).

20. O. S. Gelles, In Effects of Radiation on Materials: Twelfth International Symposium, ASTM STP 870, F. A. Garner and J. S. Perrin, eds., American Society for Testing and Materials, Philadelphia, Pennsylvania, pp. 98-112, (1985).

21. D. S. Gelles, F. A. Garner and 8. L. Adams, In Damage Analysis and Fundamental Studies Quarterly Progress Report, DOE/ER-0046/11, pp. 81-100, (1982).

22. H. R. Brager, F. A. Garner and G. L. Guthrie, Journal of Nuclear Materials, Vol. 66, pp. 301-321, (1977).

23. O. S. Gelles, F. A. Garner and H. R. Brager, ibid. ref. 8, pp. 735-753.

24. W. G. Wolfer, Journal of Nuclear Materials, Vols. 122 and 123, pp. 367-378, (1984).

25. W. G. Wolfer, F. A. Garner and L. E. Thomas, In Effects of Radiation on Materials: Eleventh International Symposium, ASTM STP 782, H. R. Brager and J. S. Perrin, eds., American Society for Testing and Materials, Philadelphia, Pennsylvania, pp. 1023-1041, (1982).

26. R. J. Puigh, A, J. Lovell and F. A. Garner, Journal of Nuclear Materials, Vols. 122 and 123, pp. 242-245, (1984).

27. F. A. Garner, Journal of Nuclear Materials, Vols. 122 and 123, pp. 459-471, (1984).

28. J. P. Foster, W. G. Wolfer, A. Biancheria and A. Boltax, In Proceedings BNES Conference on Irradiation Embrittlement and Creep in Fuel Cladding and Core Components, London, England, p. 273, (1972).

29. K. Ehrlich, Journal of Nuclear Materials, pp. 100:149, (1981).

30. J. L. Boutard, Y. Carteret, R. Cauvin, Y. Guerin and A. Maillard, In Proceedings BNES Conference on Oimensional Stability and Mechanical Behavior of Irradiated Metals and Alloys, Brighton, England. Vol. 1, p. 109, (1983).

SWELLING AND PHASE STABILITY OF COMMERCIAL Fe-Cr-Mn ALLOYS IRRADIATED IN FFTF-MOTA

J. M McCarthy and F. A. Garner (Pacific Northwest Laboratory)

OBJECTIVE

The object of this effort is to determine the suitability of Fe-Cr-Mn base alloys for fusion reactor service.

SUMMARY

Five canmercial alloys based on the Fe-Cr-Mn alloy system have been irradiated in FFTF-MOTA at 420, 520 and 600°C to exposures ranging as high as 60 to 75 dpa. Sane alloys were irradiated in two or three thermal-mechanical starting conditions. Density measurements have been performed on all combinations of alloy. thermal-mechanical treatment and irradiation condition. Microscopy on three of the five alloys has been cmpleted, concentrating only on the highest exposure level at each temperature.

Compared to the simple Fe-Cr-Mn ternary alloys. the cmercial alloys tended *to* develop less a- and ε-martensite and a-ferrite but higher levels of $M_{23}C_6$ and σ.

PROGRESS AND STATUS

Introduction

In previous reports, the swelling and phase stability of simple Fe-Mn and Fe-Cr-Mn alloys were explored after irradiation in FFTF-MOTA to various neutron exposure levels.[1-5] Swelling data derived frcm density change measurements were also reported for five commercial Fe-Cr-Mn base alloys irradiated to exposures of 9 dpa at 420°C, and 14 dpa at both 520 and 600°C.[1-3] The composition and thermal mechanical starting conditions of these alloys are shown in Tables I and 11.

Swelling data are now available for these alloys for three exposure levels at each temperature of 420. 520 and 600°C. Microscopy is also in progress on specimens irradiated at the highest exposure levels which range fran 60 to 75 dpa. At this time microscopy on 18/18 Plus. Nitronic 32 and NMF3 is complete and examination of AMCR is in progress.

The details of the experimental procedure are the same as those of the earlier studies and are set forth in Reference 2. The alloys are being examined in both the unirradiated and irradiated conditions.

Results of Swelling Measurements

The swelling observed in these alloys is shown in Figures 1-4. All alloys were observed to exhibit void swelling to one degree or another, with NMF3 having the least amount.

Results of Phase Stability Studies

Alloy 18/18 Plus

As shown in Figure 5, this alloy in the 20% cold-worked condition exhibits a high density of dislocations and twins in a matrix of Y. After irradiation to 75 dpa at 420°C, $M_{23}C_6$ precipitated hanogeneously as cubes within undeformed portions of the matrix and heterogeneously on twin boundaries and high angle grain boundaries. as shown in Figures 6a and 6b. The cold-worked and aged condition retained a high density of dislocations and twins and developed the same precipitate structure but it also exhibited recrystallization at some grain boundaries. The recrystallized grains were found to be a-ferrite with widths on the order of 200 nm.

At 520°C and 75 dpa the heterogeneous precipitates were larger than that observed at 420°C but the hanogeneous precipitation was approximately the same (see Figure 71. In the cold-worked and aged condition the heterogeneous precipitates were larger and arranged in planes along twin boundaries. It also appeared that they formed at the expense of a reduced homogeneous population in the matrix. as shown in Figure 8.

After irradiation at 600°C to 60 dpa, the cold-worked material contained $M_{23}C$ within the grains and σ along grain boundaries (see Figure 9). In contrast, the cold-worked and aged material did not contain intragranular $M_{23}C_6$ and the a precipitates were more equiaxed in nature, showing a preference for grain boundary triple points as nucleation sites, as shown in Figure 10. The canposition of the intergranular $M_{23}C_6$ at 600°C in the cold-worked and aged material was in weight % 78Cr-3Mn-17Fe-2Mo. The intergranular σ in the same specimen had a composition in weight % of 58.5Cr-40Fe-1.5Mo.

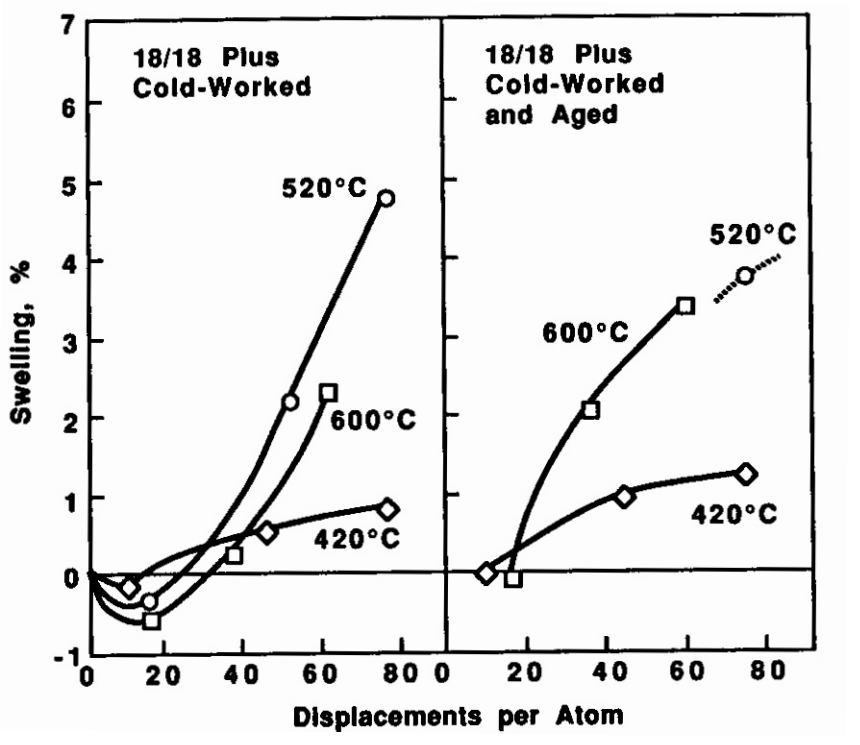

Fig. 1. Swelling observed in alloy 18/18 Plus in the cold-worked and cold-worked and aged conditions.

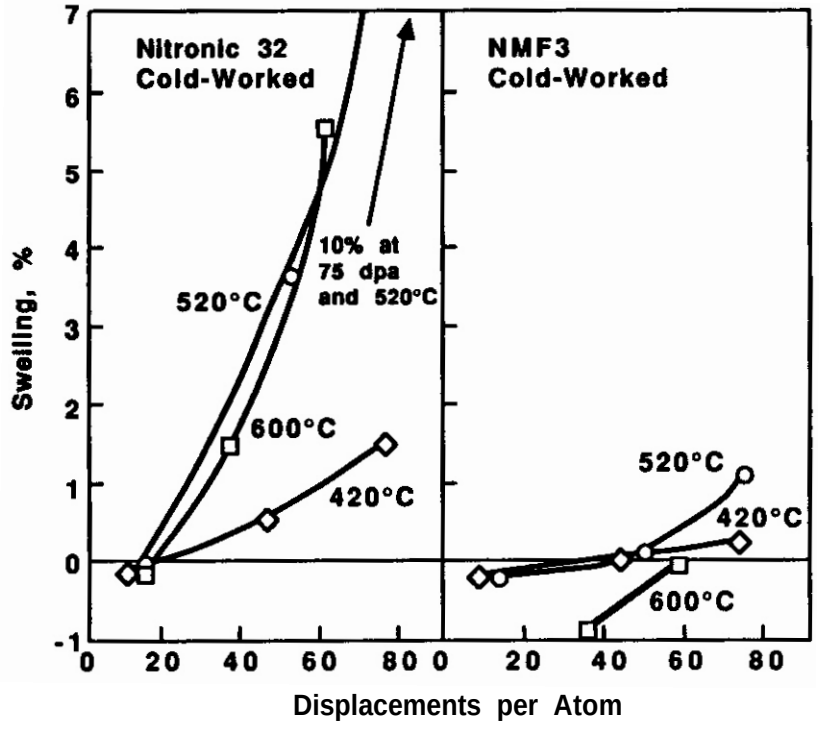

Fig. 2. Swelling observed in alloys Nitronic 32 and NMF3, both in the cold-worked condition.

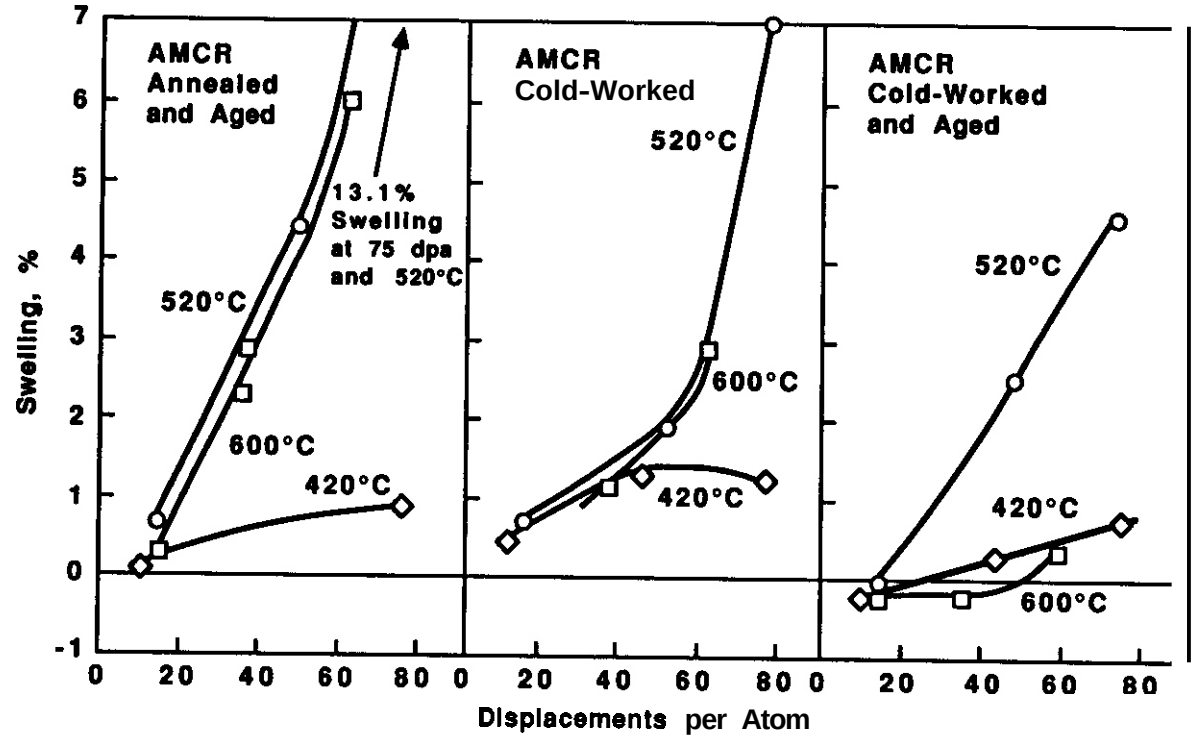

Fig. 3. Swelling observed in alloy AMCR in three thermal–mechanical conditions.

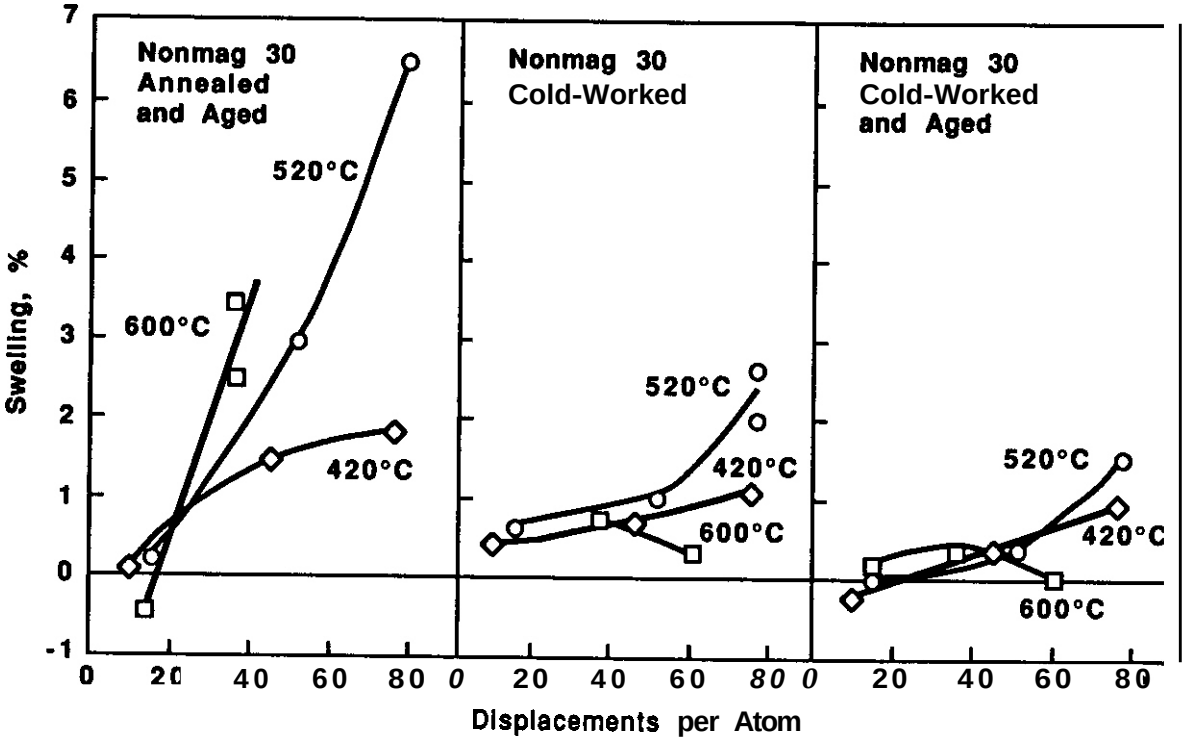

Fig. 4. Swelling observed in alloy NONMAG 30 in three thermal–mechanical conditions.

Table I. Composition of Commercial Fe-Cr-Mn Austenitic Alloys

Designation	Vendor	Composition wt%
Nitronic Alloy 32	ARMCO	18Cr-12Mn-1.5Ni-0.6Si-0.2Cu-0.2Mo-0.4N-0.1C-0.02P
18/18 Plus	CARTECH	18Cr-18Mn-0.5Ni-0.6Si-1.0Cu-1.1Mo-0.4N-0.1C-0.02P
AMCR 0033	CREUSOT-MARREL	10Cr-18Mn-0.7Ni-0.6Si-0.06N-0.2C
NMF3	CREUSOT-MARREL	4Cr-19Mn-0.2Ni-0.7Si-0.09N-0.02P-0.6C
NONMAG 30	KOBE	2Cr-14Mn-2.0Ni-0.3Si-0.02N-0.02P-0.6C

Table II. Thermal-Mechanical Starting Conditions

Description	Conditions
Nitronic Alloy 32	CW
18/18 Plus	CW, CWA
AMCR 0033	CW, CWA, SAA
NMF3	CW
NONMAG 30	CW, CWA, SAA

Note: CW = 1030°C/0.5 h/air cool + 20% cold-work. CWA = cold-worked condition + 650°C/ h/air cool. SAA = 1030°C/1 h/air cool + 760°C/2 h/air cool.

Alloy Nitronic 32

As shown in Figure 11. this alloy in the cold-worked and unirradiated condition exists primarily as Yand contains a high density of twins and dislocations. There is. however. a small volume fraction of ε-martensite as evidenced by weak diffraction spots showing $\langle 0001\rangle_\varepsilon \| \langle 111\rangle_\gamma$ in an area containing stacking faults (Figure 12).

At an irradiation temperature of 420°C there was sane heterogeneous precipitation of $M_{23}C_6$ in the Y matrix but only on twin boundaries. At 520°C, there was heterogeneous precipitation of $M_{23}C_6$ but there was still no hanogeneous precipitation within the matrix. Decreasing the Mn content and increasing the Ni content appears to strongly suppress $M_{23}C_6$ carbide precipitation. At 600°C σ phase was observed along grain boundaries and at triple points with some intragranular precipitation (Figure 13).

Alloy NMF3

Cold-worked NMF3 prior to irradiation exhibited a high dislocation density with twins in a γ matrix. There were also thin c-martensite plates within the Y (as shown in Figure 14) and occasionally there were grains canposed solely of ε-martensite.

Following irradiation at 420°C, there was precipitation on the twin boundaries as well as the ε/γ boundaries. These boundaries were attacked preferentially during electropolishing, as shown in Figure 15, presumably due to canpositional changes induced by irradiation. Sane of the precipitates on these boundaries were identified to be M C6 and were on the order of 60 nm in size. Hanogeneous precipitation of $M_{23}C_6$ also Occurred within the "" matrix (Figure 16). A second unknown type of precipitate of composition 65Mn-20Fe-15Cr was also found in an extraction replica. Analysis is underway to identify this precipitate. shown in Figure 17. There was no evidence of c-martensite formation.

At 520°C the most striking feature of the microstructure was the extensive decanposition of the Y/Y grain boundaries into wide belts of mixed a ferrite grains. $M_{23}C_6$ and retained austenite. as shown in Figures 18-20. The grains themselves were Y with homogeneous precipitation of $M_{23}C_6$.

At 600°C decanposition at grain boundaries was not observed but the microstructure was quite different from that observed in the other two alloys in that no σ was observed. Also. as shown in Figures 21 and 22, large (~1μm wide) 6-martensite plates have formed and within these plates large $M_{23}C_6$ rods have precipitated. The remainder of the γ matrix contained a low density of large voids (sane of which were elongated). as well as stacking faults and twins. There were also large (300-500 nm) $M_{23}C_6$ precipitates found at grain boundaries (Figure 23).

Discussion

With the exception of the lower swelling alloy NMF3, there are not large differences in swelling behavior for alloys with the same thermal-mechanical condition. In assessing the effect of composition and thermal-mechanical condition on swelling, it is instructive to make a canparison between the commercial alloys and the simple alloys described in References 1-5. This exercise is canpllcated by the fact that the simple alloys with two exceptions (Fe-15Cr-15Mn and Fe-30Mn)[5] were irradiated only in the annealed condition and most of the cmercial alloys were irradiated only in the cold-worked or cold-worked and aged conditions. We can only make valid comparisons for similar solute levels, however. providing the thermal-mechanical condition is the same.

Cold-worked 18/18 Plus begins to swell a little later than does cold-worked Nitronic 32. The major difference between these two alloys is the higher manganese level of 18/18 Plus. A similar trend with manganese was observed in the simple Fe-Cr-Mn alloys.[3,5] The swelling of cold-worked AMCR and cold-worked 18/18 Plus is roughly the same. The major difference between these two alloys is the laer chranium level. The swelling of simple ternary alloys was found earlier to be quite insensitive to chranium level.

Other comparisons become a bit more precarious due to substantial variations in more than one element. A comparison between NMF_3 and MONMAG 30 spans significant differences in Cr, Mn, Ni, Si and N. The effect of nickel content on swelling of Fe-Cr-Mn-Ni alloys has recently been shown to be sanewhat complex.[6] The relatively long incubation period of all the commercial alloys canpared to those of the solute-free ternary alloys is thought to reflect pr m rily the addition of silicon, an element known to have a large influence on delaying void nucleation.

Several other features of the swelling data deserve notice. First, cold-working delays swelling in AMCR and the effect of aging is variable. both in agreement with the data of Reference 5. Second. the swelling at 520 and 600°C is usually of the same magnitude in each alloy while that of 420°C is usually significantly lower. The same trends were observed in the simple solute-free ternary alloys. Finally. the swelling data at relatively low neutron fluence frequently exhibit negative values or can be extrapolated to positive nonzero intercepts at 0 dpa, both of which indicate the presence of phase-related changes in alloy density.

The phase stability of the simple Fe–Cr–Mn alloy system during neutron irradiation has been studied previously[3,4] and the phase stability during neutron irradiation of. more complicated alloys has also been reported.[9,10] Additional studies have been conducted on the phase stability of various Fe-Cr-Mn steels during cold–work and/or thermal aging.[5,11–15]

In the absence of solutes Fe–Cr–Mn alloys in the annealed condition are known to be susceptible to the sequential embrittling martensite transformations $\gamma_{fcc} \rightarrow \varepsilon_{hcp} \rightarrow \alpha_{bcc}$,[15] a process hich can be altered sanewhat by irradiation due to the operation of the inverse Kirkendall effect.' Also observed was the tendency during irradiation to form ferrite phases and the intermetallic chi phase. The embrittling o was not observed in annealed alloys in either the unirradiated or irradiated conditions[4] but did form in cold–worked solute–modified alloys during thermal aging.[5]

While σ formation during thermal aging is known to be accelerated by molybdenum and silicon additions, it is also strongly enhanced by cold-working.[5,12,15] Garner, Abe and Noda have advanced a mechanism for o formation that centers on the very high diffusivities encountered on moving grain boundaries during recrystallization.

In the current study, the following general features were observed. First, the commercial alloys are much more stable against martensite and ferrite formation than the unstabilized ternary alloys. This is of course the rationale for adding austenite stabilizing elements such as N, C and Ni. Following irradiation ε-martensite was observed only in NMF3, the alloy with the lowest level of chranium. With a reduction in ε-martensite formation. there are fewer nucleation sites for a–martensite formation. a–ferrite was observed only in 18/18 Plus irradiated at 420°C. (Schlle and coworkers at the Joint Research Center in Ispra, Italy in a private communication have stated that their studies show the tendency toward a–ferrite formation becomes much stronger at 400°C than at 600°C). Since chi phase was observed in the earlier studies to form ina–ferrite and a–martensite. it is also not surprising that chi phase was not observed in this study.

Second, the formation of chromium-rich $M_{23}C_6$, a direct consequence of carbon addition, increased with temperature and fell as the chranium level fell. NMF3 has a very low level of chranium (4%) and therefore formed the least amount of $M_{23}C_6$, even though it has the highest level of carbon (0.6%).

Finally. the low level of chranium in NMF3 precludes the formation of the chranium–rich a. The formation of σ requires high temperatures and recrystallization which explains why o was observed in cold–worked and cold–worked and aged 18/18 Plus and Nitronic steels but only at 600°C. Formation of σ can occur even in the absence of radiation for the range of manganese levels studied here.[5,12]

Several phases that were not observed should be mentioned. First. Cr_2N was not observed, although it has been reported to develop in long' duration creep specimens constructed from AMCR alloy.[13] Second, no radiation–induced nickel–rich phases such as γ' or G phase were found. reflecting the low level of nickel in these alloys. It is these phases that are known to control much of the swelling behavior of Fe–Cr–Ni steels.[7,8]

Conclusions

While the phase stability of AMCR has not yet been investigated, the swelling resistance and phase stability of the cmercial alloys with reasonable (≥10%) chranium levels is superior to that of simple ternary Fe–Cr–Mn alloys. 'This offers promise that a suitable Fe–Cr–Mn alloy can be developed for fusion service. Care must be taken, however, to ensure that three embrittling phases, ε-martensite, a–martensite and a–ferrite, not be replaced by other potentially deleterious phases such as carbides and othat show a preference for nucleating at grain boundaries where they can initiate intergranular failure.

Future Work

This effort will continue, concentrating on the phase stability of irradiated AMCR steel and the thermal stability of all steels in this experiment.

REFERENCES

1. H. R. Brager. F. A. Garner, O. S. Gelles and M. L. Hamilton, J. Nucl. Mater. 133 and 134 (1985) 907.

2. F. A. Garner and H. R. Brager. in: Radiation–Induced Changes in Microstructure, ASTM STP 955, Eds. F. A. Garner. N. H. Packen and A. S. Kumar (American Society for Testing and Materials. Philadelphia, PA, 1985) p. 195.

3. F. A. Garner, H. R. Brager, D. S. Gelles and J. M. McCarthy. J. Nucl. Mater. 148 (1987) 294.

4. J. M McCarthy and F. A. Garner, J. Nucl. Mater., 154-156 (1988) in press.

5. F. A. Garner. F. Abe and T. Noda, J. Nucl. Mater., 154–156 (1988) in press.

6. F. A. Garner and H. Takahashl. this report.

7. F. A. Garner and W. G. Wolfer. J. Nucl. Mater., 102 (1981) 143; J. Nucl. Mater., 122 and 123 (1984) 201–206.

8. B. Esmailzadeh, A. Kumar and F. A. Garner, J. Nucl. Mater.. 133 and 134 (1985) 590–593.

9. D. S. Gelles and F. A Garner, J. Nucl. Mater., 133 and 134 (1985) 521–524.

10. P. J. Maziasz and M. L. Grossbeck, in: Alloy Development for Irradiation Performance Semiannual Progress Report. DOE/ER-0045/14 (1985). pp. 49–51.

11. P. J. Maziasz and R. L. Kleuh, in: Alloy Development for Irradiation Performance, DOE/ER-0045/15 (1986) pp. 54-60.

12. Y. Okazaki. M. Mochizuki, K. Miyahara and Y. Hosoi. "σ-Phase Formation In High Mn–Cr–Fe Alloys". to be presented at the 14th International Symposium on Effects of Radiation on Materials. Andover, MA, June 27, 1988.

13. E. Ruedl, R. Matera and G. Valdré, J. Nucl. Mater.. 151 (1988) 238–244.

14. A. H. Bott, F. B. Pickering and G. J. Butterworth. J. Nucl. Mater.. 141–143 (1986) 294.

15. Y. Tomota, M. Strum and J. W. Morris, Jr., Met. Trans. 17A (1986) 537.

Fig. 5. Bright field TEM image of unirradiated cold-worked 18/18 Plus.

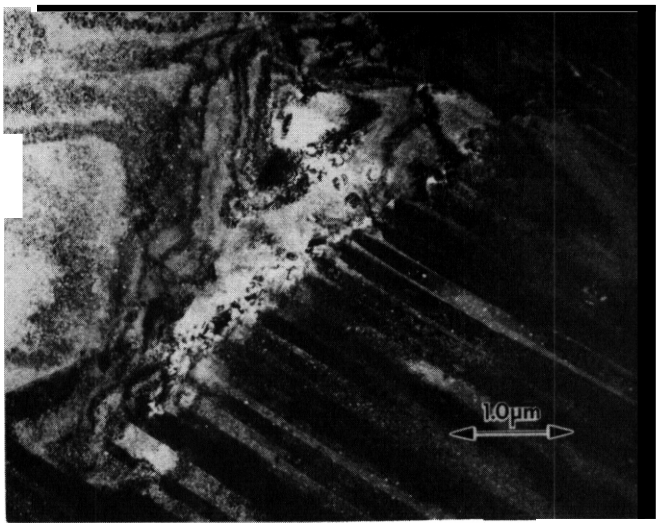

Fig. 6a. Bright field TEM image of cold-worked 18/18 Plus irradiated at 420°C.

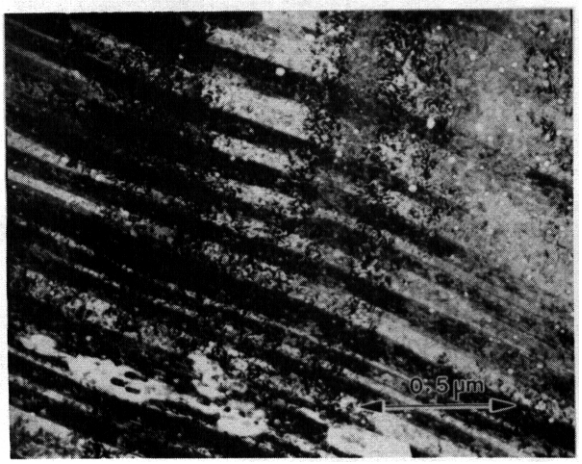

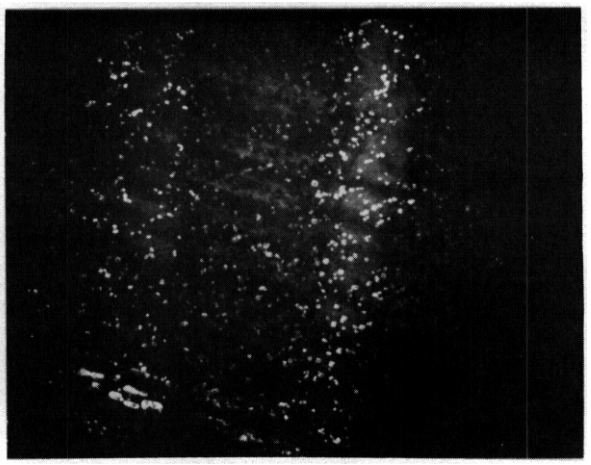

Fig. 6b. Bright field and dark field TEM images of γ matrix showing homogeneous and heterogeneous precipitation of $M_{23}C_6$ in 18/18 Plus irradiated at 420°C.

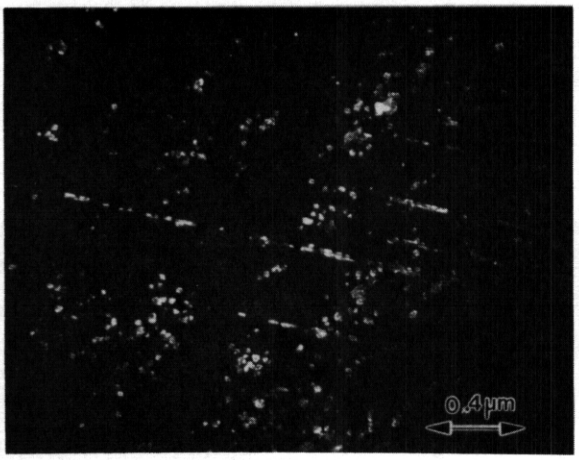

Fig. 7. Dark field TEM image of $M_{23}C_6$ in cold-worked 18/18 Plus irradiated at 520°C to 75 dpa.

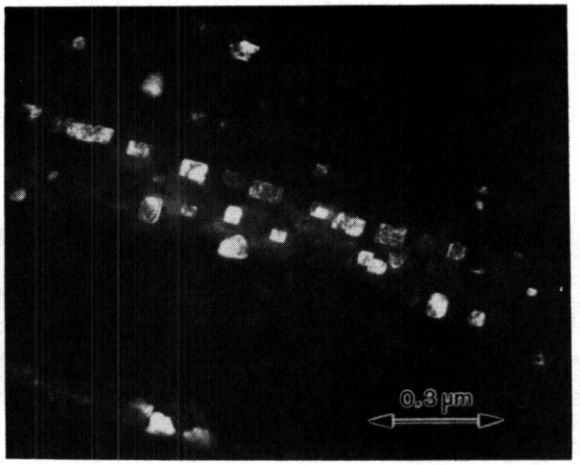

Fig. 8. Dark field TEM image of $M_{23}C_6$ in cold-worked and aged 18/18 Plus irradiated at 520°C.

Fig. 9a. Bright field TEM image of small rectangular precipitates along a grain boundary and within the grain in cold-worked 18/18 Plus irradiated at 600°C to 60 dpa.

Fig. 9b. Bright field image of σ coating a grain boundary with some $M_{23}C_6$ within the grain in cold-worked 18/18 Plus irradiated at 600°C to 60 dpa.

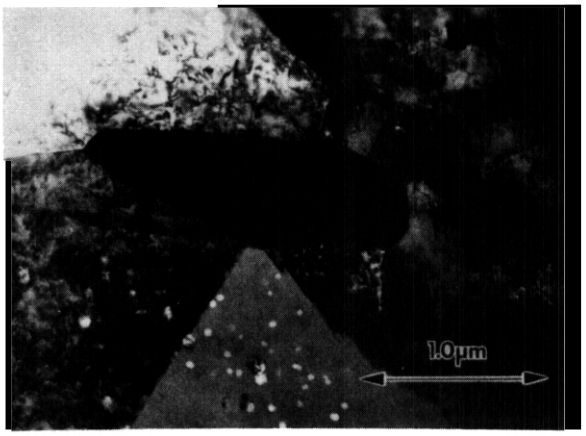

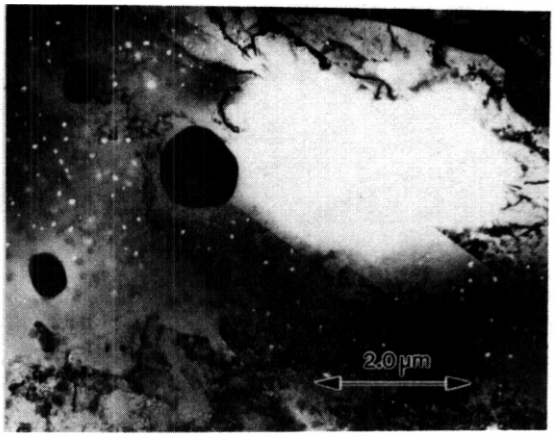

Fig. 10. Bright field images of intergranular and Intragranular σ precipitates in cold-worked and aged 18/18 Plus that was irradiated at 600°C to 60 dpa.

Fig. 11. Bright field image of unirradiated cold-worked Nitronic Alloy 32.

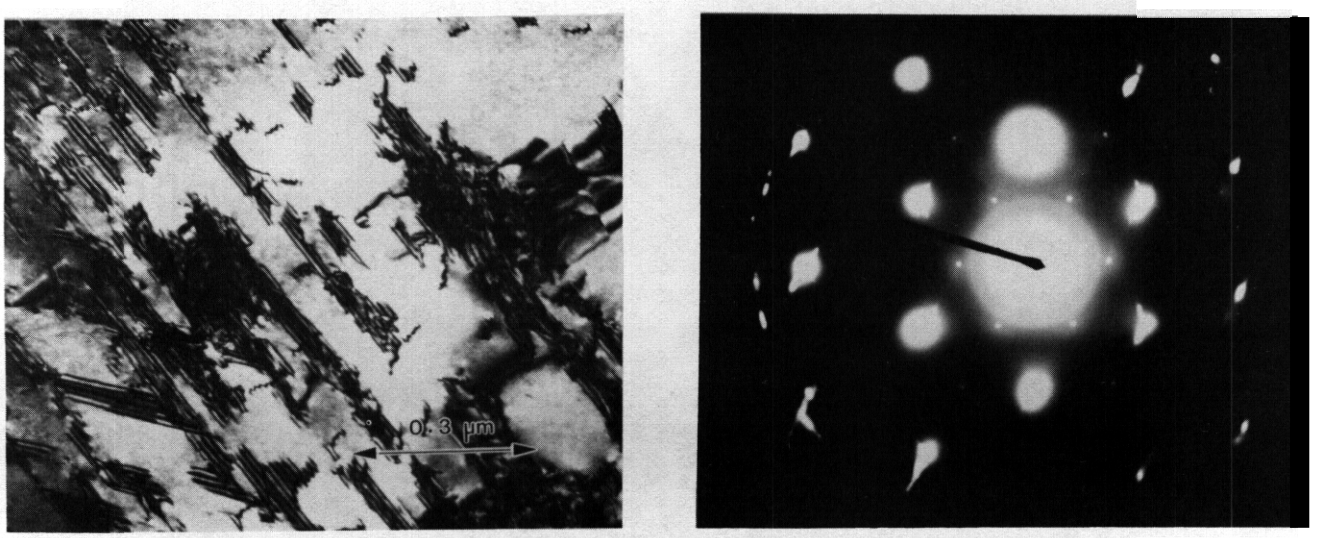

Fig. 12. Bright field image of a region in Nitronic Alloy 32 with stacking faults and a diffraction pattern from that area showing $\langle 0001\rangle_{\varepsilon} \| \langle 111\rangle_{\gamma}$.

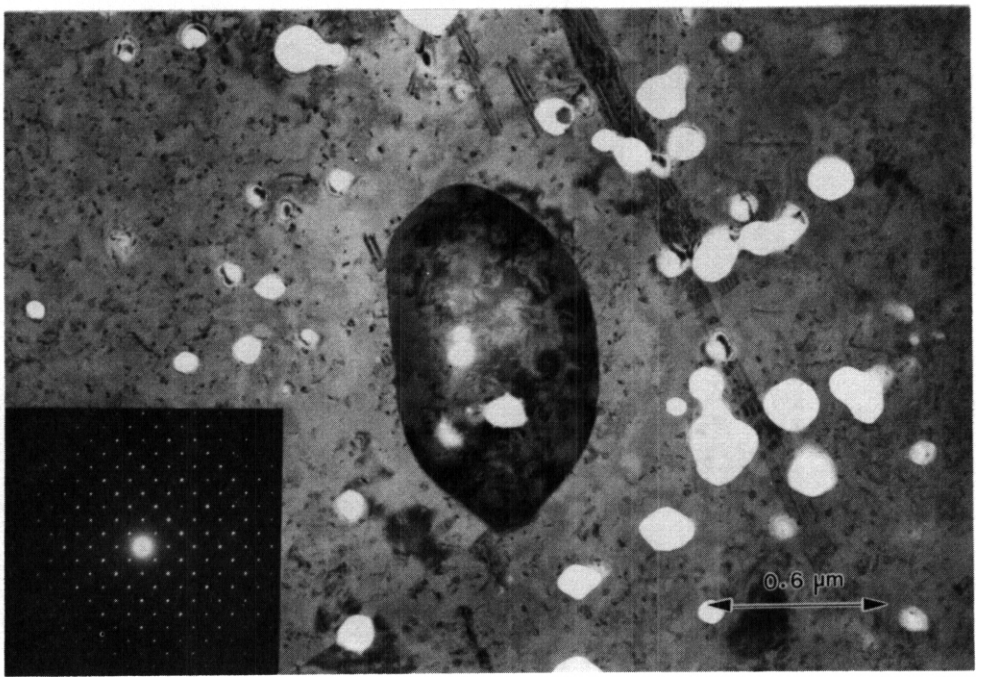

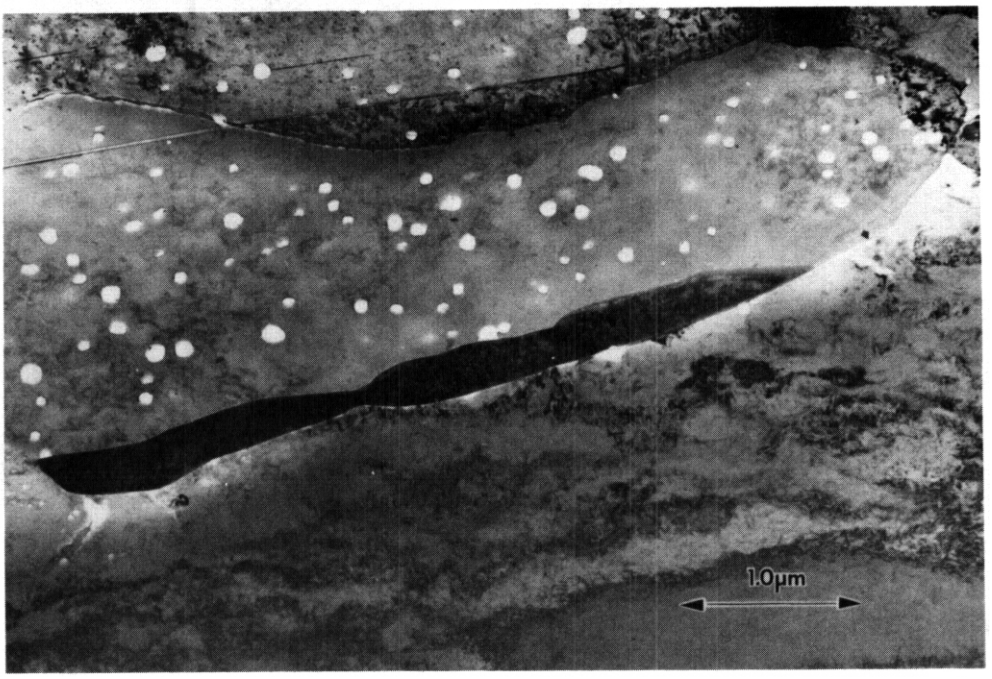

Fig. 13. Bright field images of Intragranular and intergranular σ In cold-worked NItronIc Alloy 32 irradiated at 600°C to 60 dpa.

Fig. 14a. Bright field image of unirradiated cold-worked NMF3 showing twins and a high dislocation density.

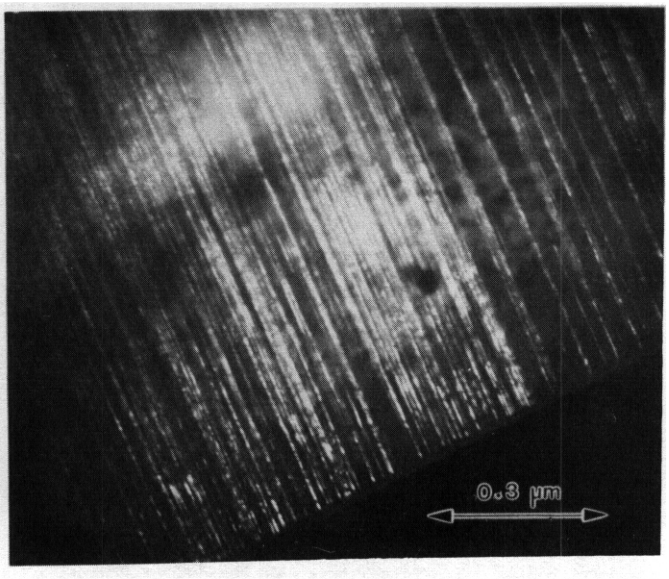

Fig. 14b. Dark field image of (martensite in unirradlated cold-worked NMF3.

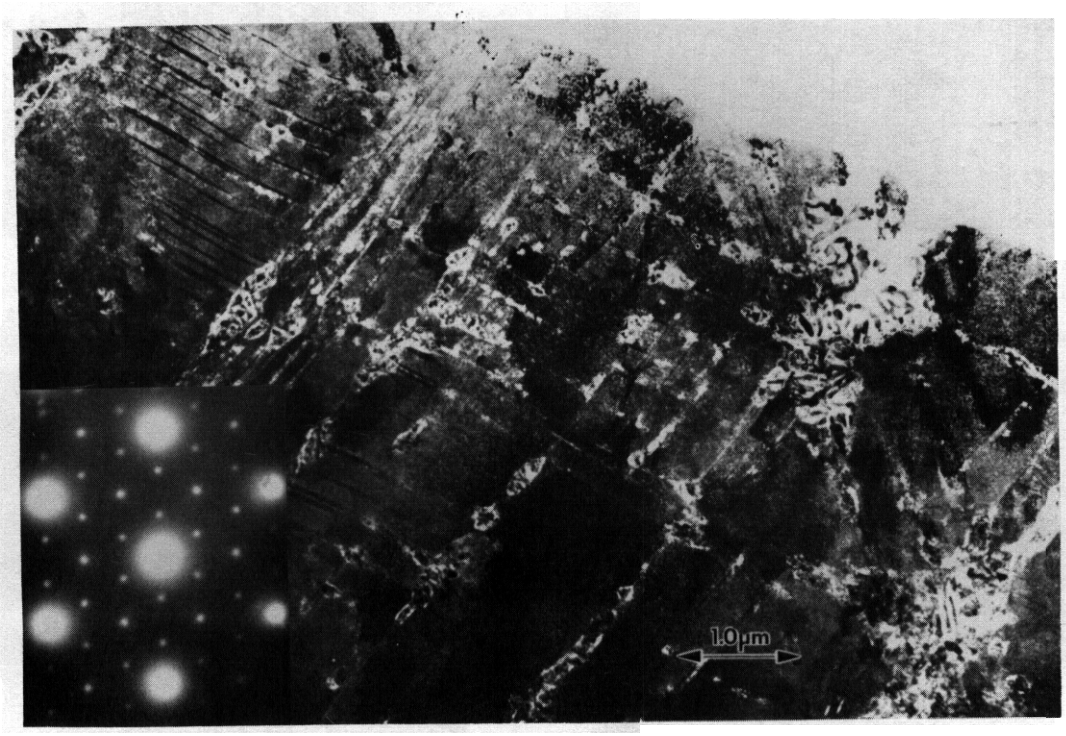

Fig. 15. Bright field image of cold-worked NMF3 irradiated at 420°C with inset diffraction pattern showing $\langle 111 \rangle_{M_{23}C_6} \| \langle 111 \rangle_{\gamma}$.

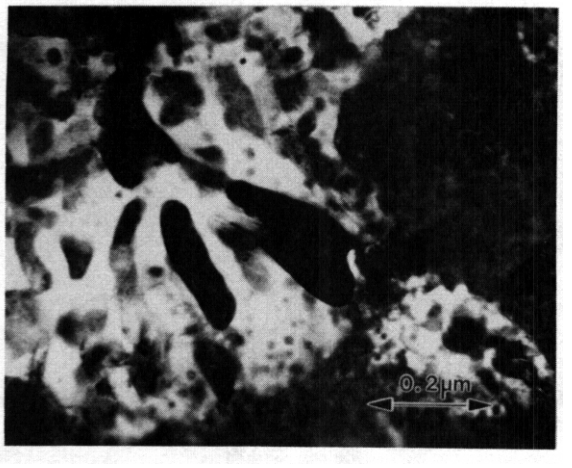

Fig. 16. Bright field image of unknown precipitate, having a canposition in weight % of 65Mn-20Fe-15Cr at a twin boundary in NMF3 irradiated at 420°C to 15 dpa.

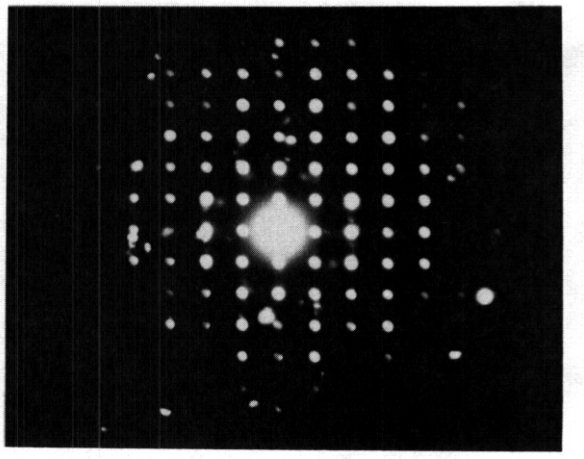

Fig. 17. Low index microdiffraction pattern frcm the unknown precipitate in Fig. 16.

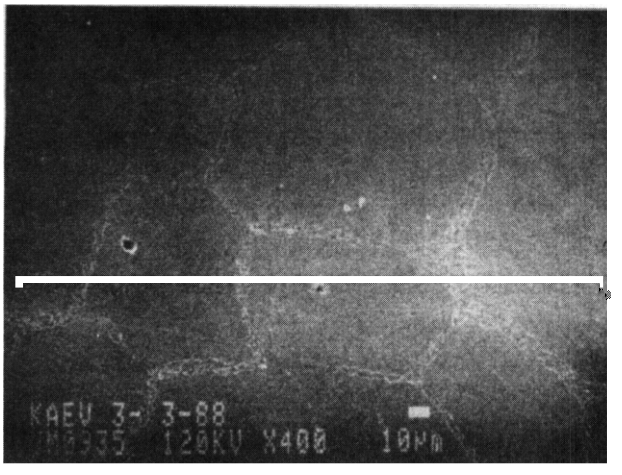

Fig. 18. SEM micrograph of the surface of an electrc-polished NMF3 specimen irradiated at 520°C to 75 dpa showing highly decomposed Y/Y grain boundaries,

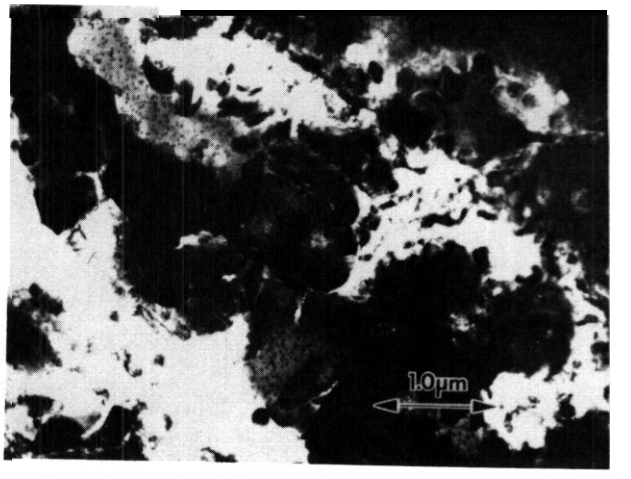

Fig. 19. Bright field E M image of a decanposed grain boundary in NMF3 irradiated at 520°C to 75 dpa.

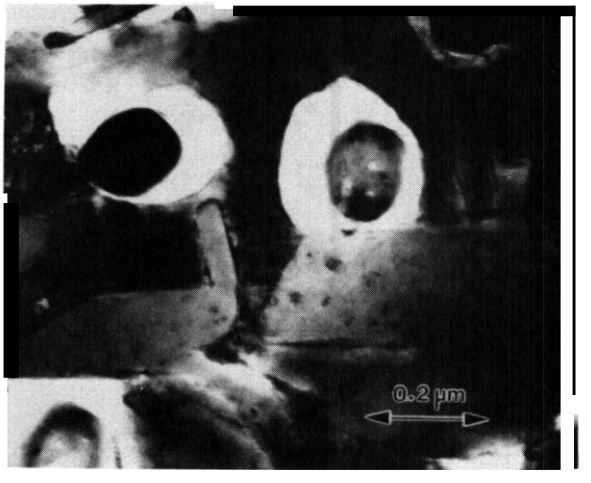

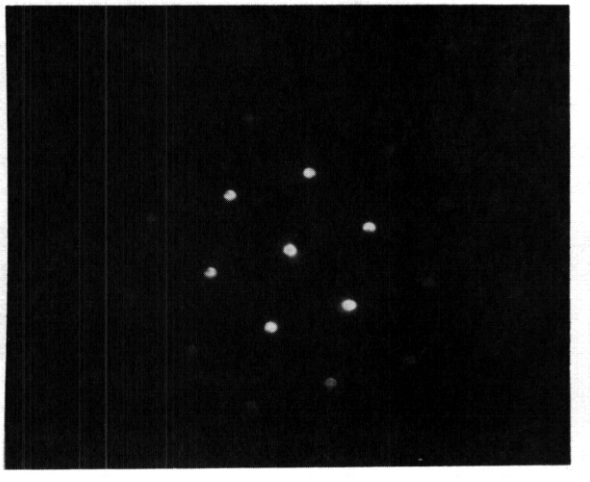

Fig. 20. Bright field EM image of a decanposed grain boundary at higher magnification shaing faceted α grains and a microdiffraction pattern fran one of the α grains at a <111> zone axis.

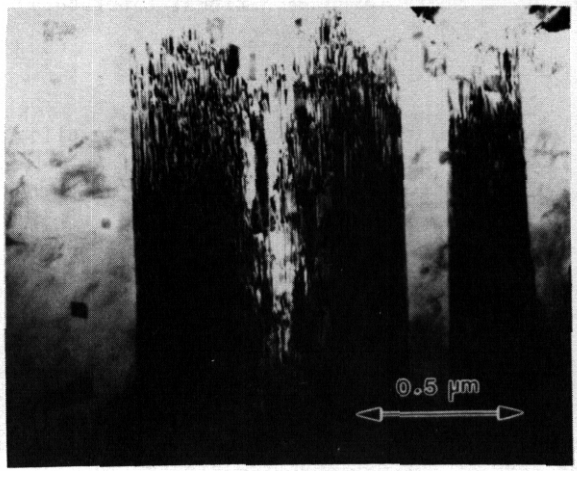

Fig. 21. Bright field image of E-martensite plates in NMF3 irradiated at 600°C to 60 dpa.

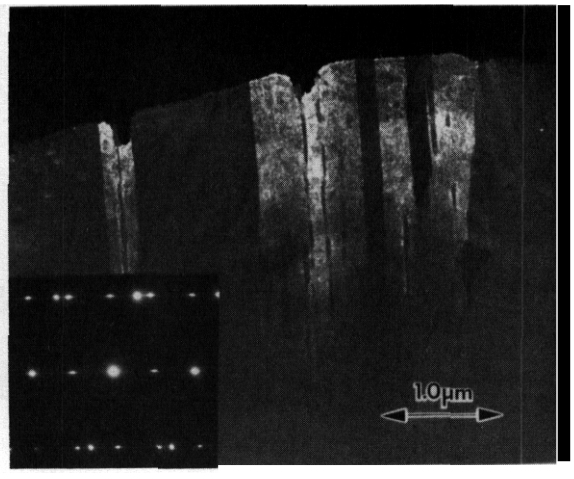

Fig. 22. Dark field TEM image of E-martensite plates with inset diffraction pattern showing $\langle 1\bar{2}10\rangle_\varepsilon \parallel \langle 110\rangle_\gamma$.

Fig. 23a. Bright field TEM image of $M_{23}C_6$ at grain boundaries, large voids (same elongated) and stacking faults within γ grains in NMF3 irradiated at 600°C to 60 dpa.

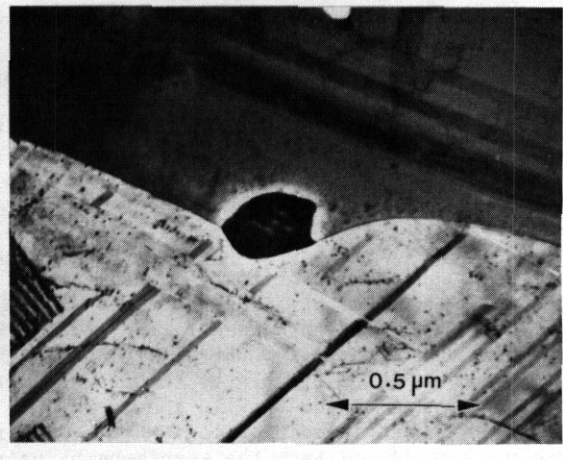

Fig. 23b. Intergranular $M_{23}C_6$ in cold-worked NMF3 irradiated at 600°C to 60 dpa at higher magnification.

6.3 Vanadlu Alloys

HYDROGEN CONCENTRATION DISTRIBUTION IN VANADIUM-BASE ALLOYS AFTER SURPACE PREPARATION AND EXPOSURE TO LIQUID LITHIUM

B. A Loomis, A B Hull, Q K Chopra, and D. L. Smith (Argonne National Laboratory)

OBJECTIVE

The objective of this research is to provide guidance on the applicability of vanadium-base alloys for structural components in a fusion reactor.

SUMMARY

The A concentration distributions in near-surface layers of V-15Cr-5Ti and V-3Ti-0.5Si alloy specimens were determined by uae of a chemical dissolution technique together with a determination of the hydrogen partial pressure on heating the specimens. These results contribute to an understanding for the exceptional resistance to hydrogen embrittlement of the V-3Ti-0.5Si alloy in comparison to the V-15Cr-5Ti alloy. Also, the H concentration distributions in the V-15Cr-5Ti and V-3Ti-0.5Si alloys were determined after immersion in liquid lithium at 500°C for 20-25 h. The H concentration in the V-15Cr-5Ti alloy decreased from an initial level of 0.19 at. % to 0.002 at. % and the H concentration in the V-3Ti-0.5Si alloy decreased from 0.31 at. % to 0.034 at. % after the lithium exposure. These results suggest that the greater loss of ductility exhibited by the V-15Cr-5Ti alloy, in comparison to the V-3Ti-1Si and V-20Ti alloys, on neutron irradiation is not attributable to an increased H concentration. Significant amounts of H were evolved from corrosion products formed on the surface of the V-3Ti-0.5Si alloy during the lithium exposure. The V-3Ti-0.5Si alloy has a twofold greater propensity for H uptake than the V-15Cr-5Ti alloy.

PROGRESS AND STATUS

Introduction

The temperature dependence of the tensile properties of the V-15Cr-5Ti, V-15Ti-7.5Cr, V-20Ti, V-12Cr-5Ti, V-10Cr-5Ti, V-10Cr-10Ti, V-3Ti-0.1Si, and V-3Ti-0.5Si alloys has been determined for temperatures ranging from 25 to 700°C.[1,2] The ductile-brittle transition temperature (DBTT), which was determined from these tensile test results, was less than 25°C for the V-15Ti-7.5Cr, V-20Ti, V-3Ti-0.1Si, and V-3Ti-0.5Si alloys. The DBTT for the V-10Cr-5Ti, V-12Cr-5Ti, V-10Cr-10Ti, and V-15Cr-5Ti alloys was also less than 25°C if these alloys were annealed to reduce the hydrogen concentration prior to the tensile test. If these latter alloys were not annealed prior to the tensile test, the DBTT ranged from 40°C to 90°C. Therefore, a Cr/Ti concentration ratio of 1.0-3.0 in these V-Cr,Ti,Si alloys resulted in greater susceptibility to hydrogen embrittlement. Subsequent analyses of the hydrogen concentration in the V-15Cr-5Ti and V-3Ti-0.5Si alloys revealed that the alloys contained 0.17 at. % and 0.33 at. % hydrogen, respectively, if they were not annealed prior to the tensile test.[3] Since the solubility of hydrogen in these alloys at 25°C was expected to be >1.5 at. %,[4,5] not only was it difficult to explain the embrittlement of either of the alloys by the low hydrogen concentration, but it was especially difficult to explain the absence of hydrogen embrittlement for the V-3Ti-0.5Si alloy containing twice the hydrogen concentration of the V-15Cr-5Ti alloy. These results aeemed explicable by the presence of an extremely non-uniform hydrogen concentration in the near-surface layers of the tensile specimens. We have used a chemical dissolution technique to determine the hydrogen concentration profile in the near-surface layers of V-15Cr-5Ti and V-3Ti-0.5Si alloy specimens. Hydrogen was introduced into the specimens by using the same surface finishing schedule that resulted in embrittlement of the V-15Cr-5Ti alloy but not the V-3Ti-0.5Si alloy tensile specimens. The results are presented in this report.

The tensile properties for the V-15Cr-5Ti, V-20Ti, and V-3Ti-1Si alloys have also been reported for specimens after neutron irradiation to 24-40 atom displacements per atom (dpa) at 400-700°C in the PPTF and EBR-II reactors.[6,7] These tensile test results purportedly show that the V-15Cr-5Ti alloy is more susceptible to irradiation hardening and embrittlement than the V-20Ti and V-3Ti-1Si alloys. The greater susceptibility of the V-15Cr-5Ti alloy to irradiation embrittlement in comparison to the V-20Ti and V-3Ti-1Si alloys is not dissimilar to the greater susceptibility of the V-15Cr-5Ti alloy to hydrogen embrittlement in comparison to the V-20Ti and V-3Ti-0.5Si alloys. The neutron-irradiated tensile specimens were irradiated in a liquid lithium or sodium environment and subsequently retrieved from these media by dissolution of the lithium or sodium in liquid NH_3 and/or in an ethyl-methyl alcohol mixture. Therefore, the potential existed for the introduction of hydrogen into the specimens and for contribution to the embrittlement of the alloys. In this report, we also present the results of a determination of the hydrogen concentration distribution in the V-15Cr-5Ti and V-3Ti-0.5Si alloys after exposure to liquid lithium at 500°C and after alternative lithium dissolution procedures to retrieve the alloys from the aolid lithium.

Materials and procedures

Specimens with approximate dimensions Of 1.9 x 1.0 cm x 0.09 cm were obtained from 50% cold-worked sheet of the V-15Cr-5Ti and the V-3Ti-0.5Si allays. Chemical analyses of the materials, which were performed by the Analytical Department of the Teledyne Wah Chang Albany Company, are presented in Table 1 Hydrogen was introduced into these specimens by rigorous adherence to a surface finishing (SF) schedule.

Table 1. Alloy compositions

Nominal Composition	concentration (wt %)		Concentration (ppm)					
	Cr	Ti	O	N	C	Si	H	S
V-15Cr-5Ti	13.5	5.2	1190	*360*	500	390	<5	*<30*
V-3Ti-0.5Si	-	3.1	580	190	*140*	5400	<5	90

This schedule consisted of removal of a 25±2-µm-thick surface layer from each of the 1.9 x 1.0-cm surfaces by use of a Whirlimet machine and *30*-, 12-, 9-, and 3-um-diameter alumina-coated papers in succession with water coolant. This SF schedule resulted in the introduction of 0.195 and 0.308 at. % H into the V-15Cr-5Ti and V-3Ti-0.5Si alloy specimens, respectively (each specimen had a total surface area of ~3.80 cm^2). In Some instances this SF schedule was preceded by an anneal of the specimen at 1125°C for one hour in an ion-pumped vacuum system with a typical pressure of 8×10^{-9} mm Hg. The initial anneal did not change the quantity of H that was introduced by the SF procedure. *Also,* in some instances, the SF schedule for a specimen was followed by polishing for *30* or 60 min with a vibratory machine and 0.05-um-diameter alumina particles suspended in ethylene glycol.

Alloy specimens with an identical SF schedule or no SF, i.e., in the as-received (AR) condition, were sectioned by chemical dissolution of specimen near-surface layers for layer thicknesses ranging from 4 to 153 µm. In the case of the V-15Cr-5Ti alloy, the chemical dissolution was accomplished by immersion of a specimen in a solution consisting of 25 vol. % H_2SO_4, 25% HF, *25%* H_2O, and 1% HNO_3 at 5-10°C. The chemical dissolution for the V-3Ti-0.5Si alloy was accomplished by immersion of a specimen in a solution of 95% HNO_3 and 5% HF at 5-10°C.

The number of hydrogen atoms introduced into the specimens by a surface preparation procedure, the intrinsic hydrogen concentration in the specimens, and the hydrogen concentration in sectioned specimens were determined from the partial pressure of hydrogen (P_H) that was evolved on heating a specimen at a rate of 15°C/min from 25°C to 1000°C. The P_H was determined by use of a quadrupole, partial-pressure, residual gas analyzer (RGA) mounted in an ion-pumped vacuum system. The temperature of *a* specimen during heating was determined by use of a recording infrared pyrometer. Integration of the area under the P_H versus temperature curve with the aid of a computer, and hydrogen concentration data obtained by use of the inert gas fusion (IGF) technique for specimens with an identical SF schedule, provided a reference calibration for the P_H versus T curves obtained for sectioned specimens.

Three important assumptions were necessary for the interpretation of the experimental results. (I) The alloy specimens that were analyzed for their hydrogen concentration by the IGF technique were heated to 2600°C. It is assumed for the purpose of this report that significant hydrogen evolution from an alloy does not occur on heating above 1000°C. *(2)* It is assumed that the specimens prepared for sectioning contained nearly identical concentrations of hydrogen before sectioning. The experimental data show that the concentrations may differ by 0.01-0.02 at. %. (3) Since the specimens did not have exactly the same total surface area, the data were normalized to a surface area of 3.80 cm^2 using a direct proportionality.

For a determination of lithium exposure effects an the H distribution in vanadium-base alloys, V-15Cr-5Ti and V-3Ti-0.5Si alloy specimens were either (a) contained in open-top 304 stainless steel capsules, which were then filled with lithium and suspended in flowing lithium (1 L/min) at 500°C for *20* h, or (b) immersed directly in the flowing lithium for 25 h. The lithium contained 0.07 at. % H. For a determination of the effect of dissolution of the lithium in the capsules on the H concentration distribution in the V-15Cr-5Ti alloy, the lithium-filled capsules containing alloy specimens were immersed either in liquid NH_3 or in an alcohol mixture containing *50%* ethyl alcohol and 50% methyl alcohol chilled to 5-10°C. After dissolution of the lithium, the specimens were successively immersed in the alcohol mixture and in water. In the case of the specimens that were immersed directly in the flowing lithium, the lithium was removed from the specimens by immersion in liquid NH_3 and by subsequent successive immersions in the alcohol mixture and water.

Experimental results

General P_H versus T curve. The general temperature dependence for the evolution of H from the specimens considered in this report is shown in Fig. 1. The contribution of adsorbed H to the total H

evolved during heating was relatively insignificant, and the adsorbed H was removed from the chamber with such rapidity that it was impossible to reliably determine P_H values. Therefore. the contribution of this source of H (I, Fig. 1) was not included in the integration of the P_H versus T curve. Hydrogen evolution from oxides, carbides, and nitrides on the surface of a specimen occurred in the temperature range of 200 to 300°C. The evolution of H from the V-15Cr-5Ti and V-3Ti-0.5Si specimens that received a surface finish commenced at 325°C and continued to 1000°C with the peak evolution occurring at 450±50°C. However, approximately 95% of the total evolved H was released in the temperature range of 325 to 600°C. In the case of the as-received specimens that did not receive a surface finish. the temperature for peak evolution of H from the V-3Ti-0.5Si alloy was 600°C, whereas the temperature for peak H evolution from the V-15Cr-5Ti alloy was 675°C.

Reference P_H versus T curves. The reference P_H versus T curves for the V-15Cr-5Ti and V-3Ti-0.5Si alloys are shown in Figs. 2 and 3, respectively. The integrated area under the P_H versus T curve for H evolution from the V-15Cr-5Ti alloy was 141.36 x 10^{-6} mm·°C. The concentration of H in a specimen with the "identical" treatment was determined by IGF to be 0.18 at. %. The integrated area for H evolution from the V-3Ti-0.5Si alloy was 257.65 x 10^{-6} mm·°C. The concentration of H in a specimen with the "identical" treatment was determined by IGF to be 0.33 at. %. Therefore, we obtain

$$785 \times 10^{-6} \text{ mm·°C/at. \% H} \qquad \text{(V-15Cr-5Ti)}$$

and

$$777 \times 10^{-6} \text{ mm·°C/at. \% H} \qquad \text{(V-3Ti-0.5Si).}$$

It should be noted in Figs. 2 and 3 that the V-15Cr-5Ti and V-3Ti-0.5Si specimens were prepared by the "identical" procedure. Nevertheless, the H concentration in the V-3Ti-0.5Si alloy specimen was approximately twice the H concentration in the V-15Cr-5Ti alloy. The twofold greater propensity for H retention in the V-3Ti-0.5Si alloy in comparison to the V-15Cr-5Ti alloy was noted repeatedly in this study.

The "blank" reference P_H versus T curves far the V-15Cr-5Ti and V-3Ti-0.5Si alloy specimens are also shown in Figs. 2 and 3, respectively. With the aid of the computer, these curves were subtracted from all the P_H versus T curves subsequently presented in this report. This subtraction was made in order to provide for some consideration of adsorbed H and H desorbed from the wall of the vacuum system. The H concentration in the V-15Cr-5Ti alloy specimen was determined to be 0.02 at. % by IGF analysis and 0.011 at. % by RGA analysis (using the conversion factor from above). The H concentration in the V-3Ti-0.5Si alloy specimen was determined to be 0.02 at. % by IGF analysis and 0.009 at. % by RGA analysis. The relative H concentrations obtained by RGA analysis for the V-15Cr-5Ti and the V-3Ti-0.5Si alloys are believed to be more precise than the concentrations obtained by IGF analysis because of an acknowledged uncertainty in the IGF analyses for H concentrations of <0.025 at. %.

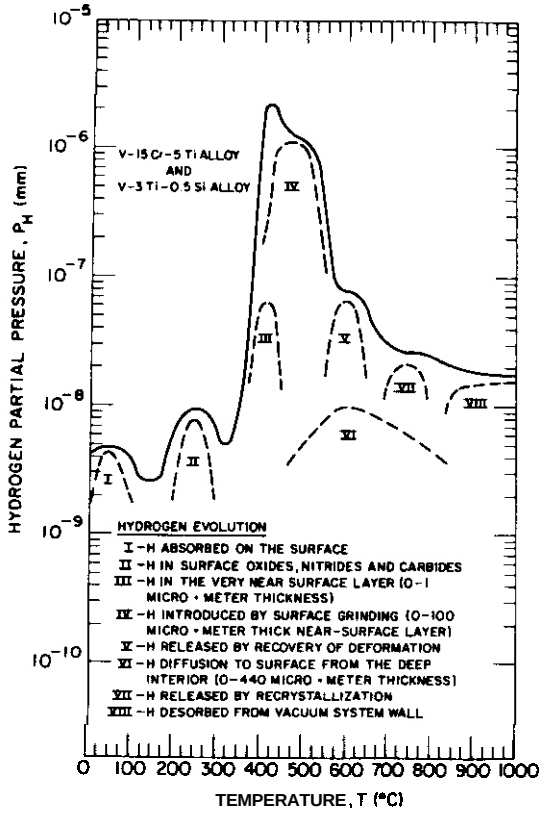

Fig. 1. General temperature dependence of P_H.

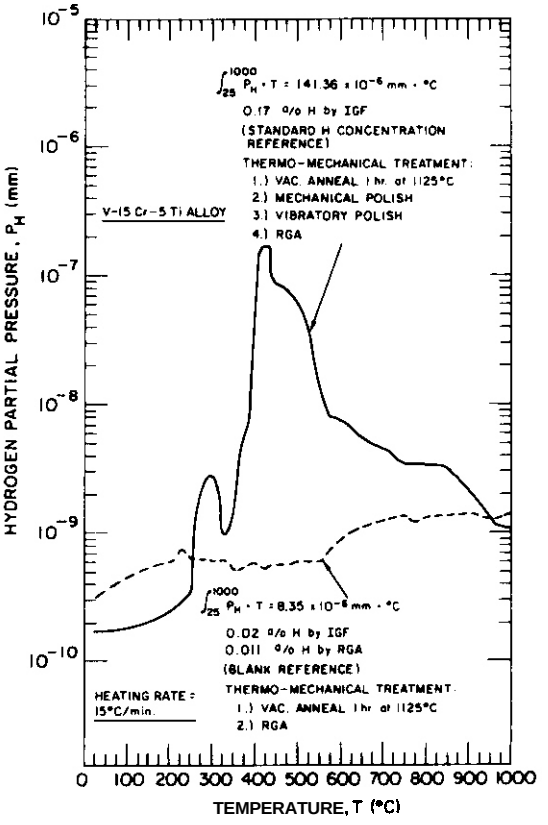

Fig. 2. Reference P_H versus T for the V-15Cr-5Ti alloy.

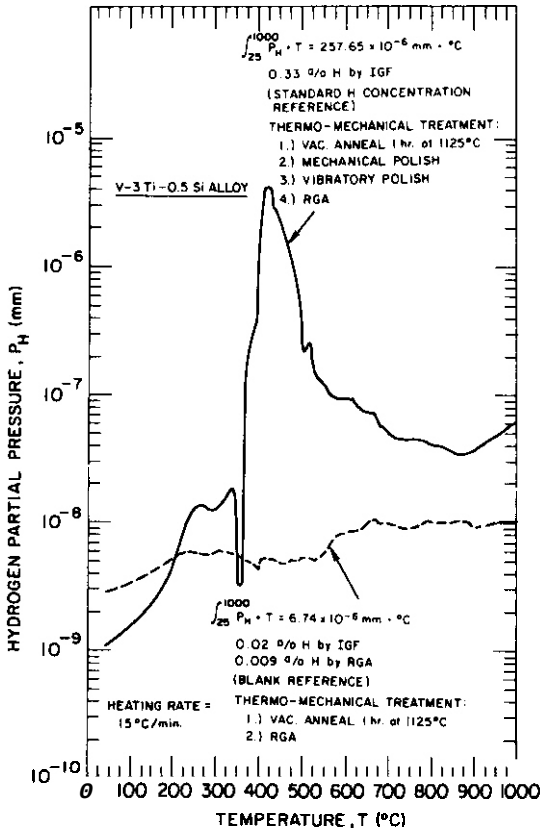

Fig. 3. Reference P_H versus T for the V-3Ti-0.5Si alloy.

Introduction of H during sectioning. Interpretation of the experimental sectioning results required that a minimal amount of H be either introduced into or removed from the specimens during sectioning. The H concentration profiles that were obtained on sectioning the as-received V-15Cr-5Ti and V-3Ti-0.5Si specimens to a depth of 150 μm are shown in Fig. 4. In the case of the **V-15Cr-5Ti** alloy (Fig. 4a), there was evidence for the introduction of 0.025 at. % H after sectioning to a depth of **152** μm. In the case of the **V-3Ti-0.5Si** allay (Fig. **4b),** there was no evidence for the introduction of H by the dissolution process. In fact, the dissolution process may have caused a small (0.01 at. %) reduction of the H concentration. These H concentration changes were considered to ***be*** acceptable relative to the concentration of H (0.2–0.3 at. %) introduced during the SF procedure. Moreover, these minor H Concentration changes may be intrinsic to these as-received vanadium-base **alloys.**

H concentration profile after sectioning. The integrated **area** derived from the P_H versus T curves, the H concentration remaining in a sectioned specimen, and the H concentration in the sectioned layers of the V-15Cr-5Ti end **V-3Ti-0.5Si** specimens are listed **in** Table **2.** The temperature dependence **of the** P_H **f**or the **AR,** AR and surface finished, and the **AR,** surface finished, and sectioned V-15Cr-5Ti and **V-3Ti-0.5Si** specimens is shown in Figs. 5 and ***6***, respectively. For the purpose of clarity, P_H data for specimens sectioned to only two depths, ~5 and ~150 **μm,** are presented in Figs. 5 and ***6***.

The near-surface H concentration profiles that were derived from the P_H versus T curves for the surface-finished V-15Cr-5Ti and V-3Ti-0.5Si alloy specimens are shown in Fig. 7. The concentration profiles in Fig. 7 **were** obtained by plotting the H concentration that was determined for each layer thickness (Table **2**) at the midpoint of the layer thickness. The average H concentration in the 4.7-um-thick near-surface layer of the V-3Ti-0.5Si alloy was 11.33 at. %, even though the bulk H concentration **was** only **0.31** at. %. However, the H concentration in the 5.9-μm-thick near-surface layer of the V-15Cr-5Ti alloy was only **1.55** at. %, with a bulk H concentration of 0.20 at. %. The relatively high H concentrations in the 0-5 μm near-surface region decreased in bath alloys to 0.4-0.5 at. % at the 31 μm depth. The experimental results suggest a further increase of the H Concentration at depths ranging from 31 μm to 50 μm, with an eventual decrease of the average H **concentration** to 0.15 at. % for the V-15Cr-5Ti alloy and 0.18 at. % for the V-3Ti-0.5Si alloy at the ***150-440*** **μm** depth.

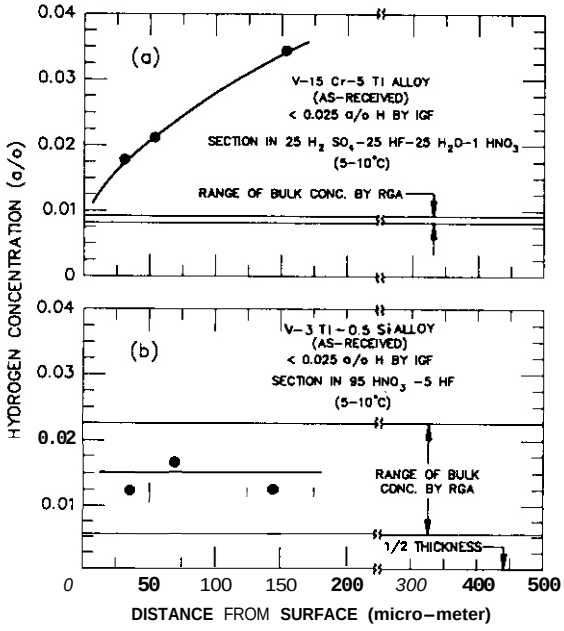

Fig. 4. Introduction of H during sectioning of (a) V-15Cr-5Ti and (b) V-3Ti-0.5Si alloys.

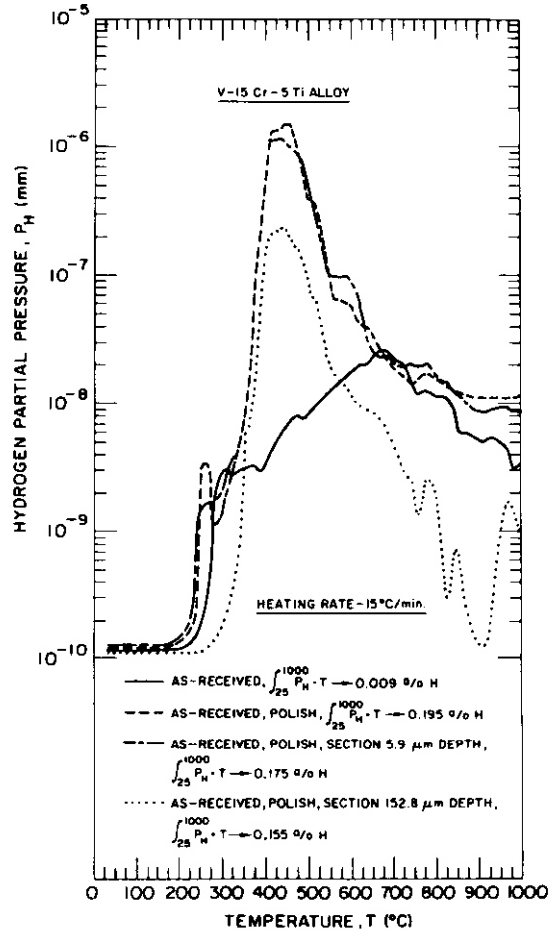

Fig. 5. P_H versus T for sectioned V-15Cr-5Ti alloys.

Table 2 Hydrogen concentration in V-15Cr-5Ti and V-3Ti-0.5Si alloys

Allay	Normalized P_H vs. T (10^6 mm·°C)	H Concentration (at. %)	Layer Thickness (μm)	Layer H Concentration (at. %)
V-15Cr-5Ti	149.90	0.195	-	-
	133.25	0.175	5.9	1.55
	123.69	0.162	16.1	0.94
	121.91	0.160	31.4	0.56
	143.39	0.188	67.2	0.14
	121.60	0.159	100.4	0.23
	118.03	0.155	152.8	0.19
V-3Ti-0.5Si	239.38	0.308	-	-
	147.56	0.189	4.7	11.33
	137.84	0.177	8.0	6.74
	144.90	0.186	15.7	3.38
	223.72	0.288	31.3	0.42
	237.04	0.305	61.1	0.17
	150.61	0.194	101.2	0.59
	142.68	0.184	149.9	0.45

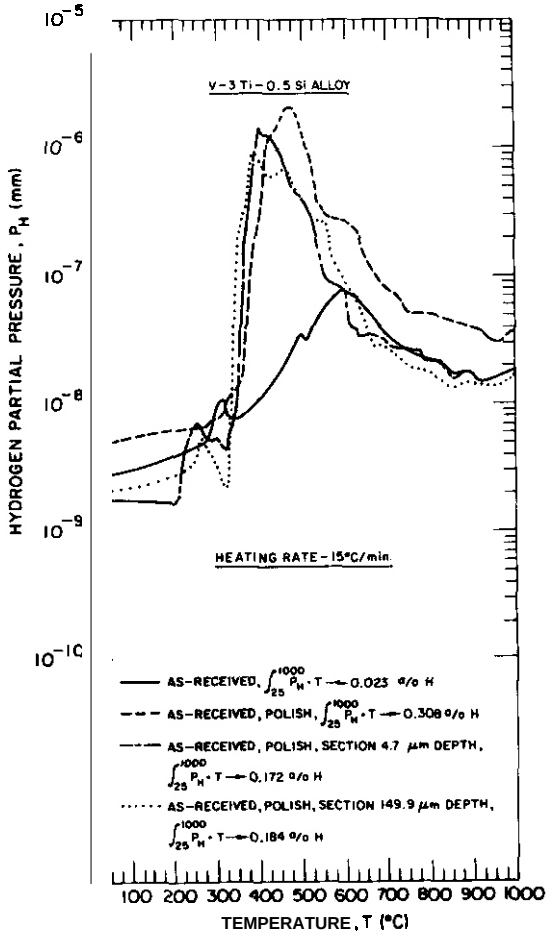

Fig. 6. P_H versus T for sectioned V-3Ti-0.5Si alloys.

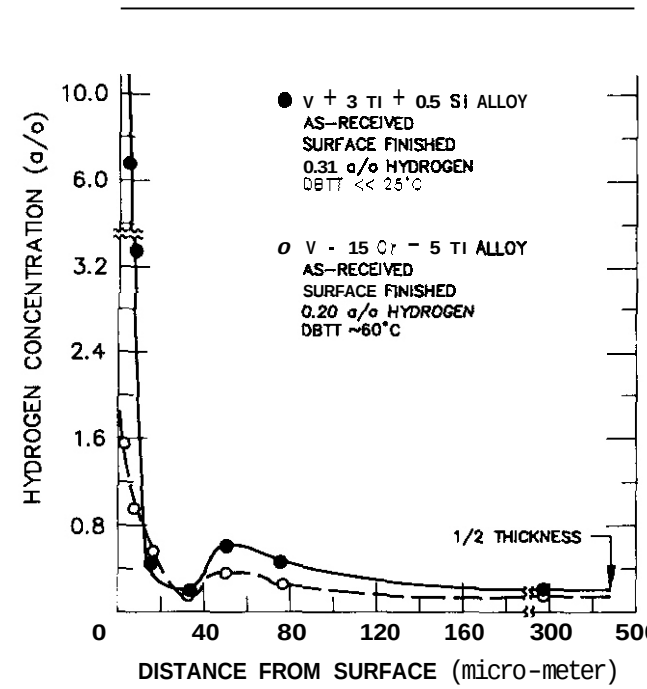

Fig. 7. H concentration profile in surface-finished V-15Cr-5Ti and V-3Ti-0.5Si alloy specimens.

Effect of alloy immersion in lithium an the H distribution. The H concentrations in the V-15Cr-5Ti and V-3Ti-0.5Si alloy specimens after either direct immersion in liquid lithium at 500°C for 25 h or retrieval from lithium-filled capsules that were immersed in the liquid lithium far 20 h are listed in Table 3. The V-15Cr-5Ti alloy specimens that were placed in the lithium-filled capsules initially contained 0.011 at. % H. The H Concentration in these specimens decreased to 0.004 at. % after dissolution of the lithium in the capsule in liquid NH_3 and to 0.009 at. % after dissolution of the lithium in the capsule in ethyl-methyl alcohol.

The dependence of P_H on T for the V-15Cr-5Ti and V-3Ti-0.5Si alloy specimens after direct immersion in liquid lithium (500°C) for 25 h is shown in Figs. 8 and 9, respectively. The H concentration in the V-15Cr-5Ti alloy decreased from 0.195 at. % to 0.002 at. % during this relatively short exposure even *though* the lithium contained 0.07 at. % H. The H concentration in the V-3Ti-0.5Si alloy decreased from 0.308 at. % to 0.034 at. %. In the case of the V-3Ti-0.5Si alloy, a corrosion product film was clearly discernible on the specimen surfaces, and the H associated with this corrosion product accounted for 21% of the total evolved H (100-300°C). For comparison, a corrosion product film was not observed on the V-15Cr-5Ti specimen and the H evolved in the temperature range of 100-300°C accounted for <0.01% of the total evolved H.

Discussion

The DBTT for the V-3Ti-0.5Si alloy containing 0.33 at. % H has been reported to be much less than 25°C, whereas the DBTT for the V-15Cr-5Ti alloy containing 0.17 at.% H has been reported to be 60°C.[1,2] Likewise, it has been reported that the DBTT for a V-10Ti alloy containing 0.33 at. % H is substantially lower than the DBTT for a V-10Cr alloy containing 0.18 at. % H.[8,9]

The present experimental results show that V-3Ti-0.5Si allay specimens containing 0.31 at. % H introduced by surface finishing can have 11 at. % H in the very-near-surface layer. Also, the present experimental results show that V-15Cr-5Ti alloy specimens containing 0.20 at. % H introduced by surface finishing can have 1.55 at. % H in the very-near-surface layer. The solubility of H in vanadium at 25°C has been reported to be 2.4 at. %.[4] Titanium has been reported to increase the solubility of H in vanadium, whereas chromium may decrease or not affect the solubility of H in vanadium.[1] Also, it has been reported

Table 3. Hydrogen concentration in V-15Cr-5Ti and V-3Ti-0.5Si alloys after immersion in lithium

Alloy	Treatment	Integrated P_H vs. T (10^{-6} mm·°C)	H Concentration (at. %)
V-15Cr-5Ti	Annealed	8.51	0.011
	Li-filled capsule (NH_3 dissolution)	2.60	0.004
	Li-filled capsule (alcohol dissolution)	6.85	0.009
	AR, surface finished	149.90	0.195
	AR, surface finished (25 h in Li)	1.06	0.002
V-3Ti-0.5Si	AR, surface finished	239.38	0.308
	AR, surface finished (25 h in Li)	26.01	0.034

that the diffusion coefficient for H in vanadium is decreased by the addition of TI solute whereas Cr solute has no effect on the H diffusion coefficient.[5] It has been postulated that the presence of existing hydrides and/or stress-induced hydride formation have a major role in the embrittlement of vanadium alloys.[10] However, on the basis of an extensive investigation of H embrittlement in V-Cr and V-Ti alloys, Owen et al. have recently advanced the idea that hydrides have no major role in the embrittlement of V-Cr alloys and H embrittlement of these alloys is due to H in solution.[8] We have not completed the microstructural observations on the alloy specimens considered in this study. The observations that have been made thus far by optical microscopy at 25°C show that the near-surface layers of the V-3Ti-0.5Si alloy specimens (DBTT of <<25°C) as well as the V-15Cr-5Ti alloy specimens (DBTT of 40-90°C) are replete with hydride precipitates. These preliminary observations by optical microscopy suggest that hydrogen in solution has the major role in the embrittlement of vanadium alloys whereas the hydrides in thermal equilibrium with hydrogen in solution have a lesser role.

The H concentrations that were determined to be present in the V-15Cr-5Ti and V-3Ti-0.5Si alloys after either direct immersion in liquid lithium or containment in lithium-filled capsules show that, unless the lithium has H concentrations greatly in excess of 0.07 at. %, it is unlikely that H contributes to the irradiation hardening and embrittlement of vanadium-base alloys.

An unexpected result from these studies was the observation of significant H evolution from the corrosion product layer formed on the surface of the vanadium alloys exposed to liquid lithium. Also, these results show that the V-3Ti-0.5Si alloy has a twofold greater propensity for uptake of H than the V-15Cr-5Ti alloy.

CONCLUSIONS

1. Grinding, polishing, and machining of vanadium alloys with or without water or organic cooling-lubrication media can result in the introduction of significant concentrations of H into the near-surface layers.

2. Hydrides are visible in the near-surface layers of surface-finished specimens of the V-3Ti-0.5Si and V-15Cr-5Ti alloys.

3. If vanadium alloys are neutron irradiated in lithium-filled capsules and the H concentration in the lithium is not greatly in excess of 0.07 at. %, then H will not contribute to the hardening and embrittlement.

4. The corrosion-product layer formed on the surface of vanadium alloys exposed to liquid lithium can retain significant amounts of H.

5. The V-3Ti-0.5Si alloy has a twofold greater propensity for uptake of H than the V-15Cr-5Ti alloy.

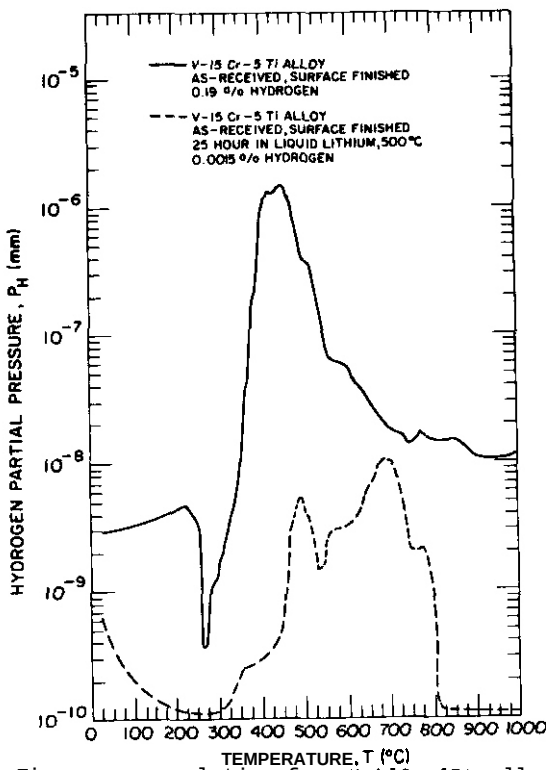

Fig. 8. H evolution from V-15Cr-5Ti alloy specimen after exposure to liquid lithium at 500°C far 25 h.

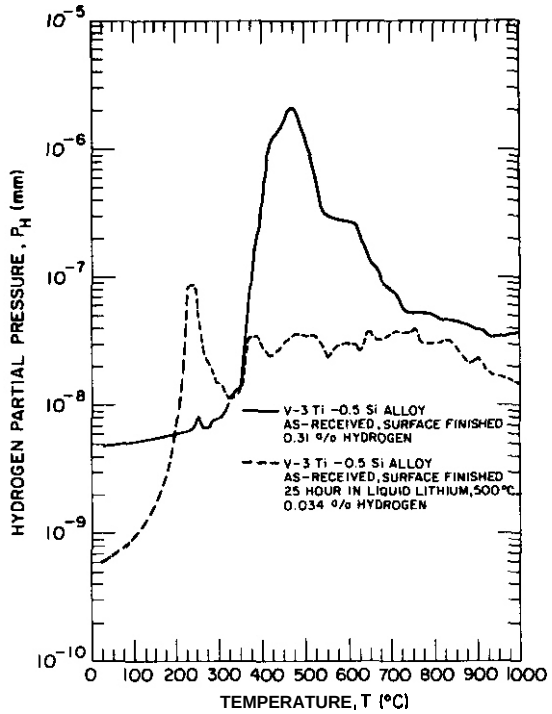

Fig. 9. H evolution from V-3Ti-0.5Si alloy specimen after exposure to liquid lithium at 500°C for 25 h.

FUTURE WORK

Additional work on the subject of this report is not contemplated at this time.

REFERENCES

1. B. A. Loomis, R. H. Lee, D. L. Smith, and J. R. Peterson, "Strength, Ductility, and Ductile-Brittle Transition Temperature for MFR Candidate Vanadium Alloys," Proceedings of the Third International Conference on Fusion Reactor Materials. Karlsruhe, Federal Republic of Germany. October 4-8, 1987, to be published in J. Nucl. Mater.

2. B. A. Loomis, unpublished results for the V-10Cr-10Ti and V-3Ti-0.5Si alloys.

3. B. A. Loomis, unpublished results of H analyses.

4. D. G. Westlake, "A Resistometric Study of Phase Equilibria at Low Temperatures in the Vanadium-Hydrogen System," Trans. Met. Soc. AIME 239, 1341-1344 (1967).

5. S. Tanaka and H. Kimura, "Solubility and Diffusivity of Hydrogen in Vanadium and Its Alloys Around Room Temperature," Trans. Jpn. Inst. Met., 20, 647-658 (1979).

6. D. N. Braski, "The Effect of Neutron Irradiation on Vanadium Alloys," J. Nucl. Mater. 141-143, 1125-1131 (1986).

7. M. L. Grossbeck and J. A. Horak, "Tensile Properties of V-15Cr-5Ti Following Neutron Irradiation and Helium Implantation," Radiat. Eff. 101, 169-171 (1986).

8. C. V. Owen, W. A. Spitzig, and O. Buck, "Effects of Hydrogen on Low Temperature Hardening and Embrittlement of V-Cr Alloys," Metall. Trans. 18A, 1593-1601 (1987).

9. W. A. Spitzig, C. V. Owen, T. J. Rowland, and O. Buck, "Hydrogen-Induced Strengthening in V-Ti Alloys," J. Less-Common Met. 115, 45-56 (1986).

10. D. G. Westlake. "A Generalized Model for Hydrogen Embrittlement," Trans. Am. Soc. Met. 62, 1000-1006 (1969).

THE MICROSTRUCTURE OF SEVERAL VANADIUM ALLOYS AFTER IRRADIATION IN FFTF AT 420°C TO 82 dpa — D. N. Braski (Oak Ridge National Laboratory)

OBJECTIVE

The goal of this research is to investigate the effects of neutron irradiation and helium generation on the microstructure of vanadium alloys.

SUMMARY

The damage produced by neutron irradiation in the microstructures of the four vanadium alloys was qualitatively the same. Except for V–20Ti, no new precipitate phases were observed after irradiation. Fine, rod-shaped particles were found surrounding the pre-existing titanium carbonitrides in V–20Ti. The V–15Cr–5Ti and Vanstar-7 alloys exhibited very low swelling, while V–3Ti–1Si and V–20Ti displayed slightly higher values (i.e., >0.1%). The swelling in V–3Ti–1Si increased with increasing helium content because the helium boosted cavity nucleation with only a slight loss in average cavity size.

PROGRESS AND STATUS

Experimental

The source. chemistry, and final heat treatment for each vanadium allay are given in Table 1. Miniature tensile specimens (SS-3) were machined from 0.76-mm-thick sheet of V–15Cr–5Ti and Vanstar-?, and from 0.51-mm-thick sheet of V–3Ti–1Si. Disks, 3 mm in diameter, were punched from 0.25-mm-thick sheets of all four vanadium alloys and used for transmission electron microscopy (TEM).

Table 1. Vanadium alloy data

Alloy	Heat	Composition, wt %								Final Heat Treatment
		Cr	Ti	Fe	Zr	Si	C	O	N	
V–15Cr–5Ti[a]	CAM-834-3	14.5	6.2				0.032	0.031	0.046	1 h at 1200°C
Vanstar-7[a]	CAM-837-7	9.7		3.4	1.3		0.064	0.028	0.052	1 h at 1350°C
V–3Ti–1Si	11153		3.4	0.04		1.28	0.045	0.091	0.026	1 h at 1050°C
V–20Ti	CAM-832		20.3				0.020	0.039	0.044	1 h at 1100°C

[a]Source: Westinghouse Electric Corporation. [b]Source: KFK, Karlsruhe, West Germany (Dr. D. Kaletta).

Selected disks and tensile specimens were doped with 3He using a modified "tritium trick" technique.' In this procedure, the specimens were held under a tritium pressure of 53 kPa (400 torr) at 400°C while the decay process took place. The levels of 3He ranged from 23 to 480 appm. Several V–15Cr–5Ti and V–3Ti–1Si disks were injected with 3He at 420°C, using an accelerator, in order to compare the resultant helium bubble distributions and subsequent swelling with those in the ^{3}He-doped specimens. The ^{4}He levels were either 10 or 100 appm.

Before irradiation, tensile specimens and disks Were sealed (by welding) in 9.5-mm-OD × 8.3-mm-ID × 38.1-mm-long TZM subcapsules containing ^{7}Li. During the irradiation at elevated temperatures. the lithium protected the vanadium alloys from picking up interstitial contaminants such as C, N. and O. Additional specimens were encapsulated and used as thermally aged control specimens. This encapsulation work was provided by the Westinghouse Hanford Corp.[2] The subcapsules were irradiated in the FFTF, Materials Open Test Assembly (MOTA) experiment at 420, 520, and 600°C to a fluence of approximately 1.4×10^{23} n/m^2, which produced a damage level of about 82 dpa in the vanadium alloys. Unfortunately, the subcapsules at 520 and 600°C experienced temperature excursions above the desired temperatures during the irradiation. Due to the uncertainties in interpretation resulting from these excursions, these specimens were not examined.

Following the irradiation, the subcapsules irradiated at 420°C Were cut open and the ^{7}Li was dissolved using liquid ammonia. The specimens were further cleaned in successive baths consisting of: a mixture of ethyl alcohol and water (1:1, by volume), water, and ethyl alcohol. Irradiated TEM disks were dual jet-polished at −30°C in a solution of 12.5 vol % conc. H_2SO_4 in methanol. Cavity swelling was determined for the polished foils by measuring and counting the cavities observed in TEM micrographs with a Zeiss particle size

analyzer. Foil thickness was measured using stereo techniques. A final value for cavity swelling $(\Delta V/V_0)$ was calculated as:

$$\Delta V/V_0 = \Delta V/V_f - \Delta V ,$$

where ΔV is the total cavity volume, V_0 is the original metal volume. and V_f is the final volume of the foil.

Results

1. Damage Structure

The damage structures of the three alloys and also V–20Ti were generally similar. A typical example of such a structure is shown in Fig. 1 for the Vanstar-7 after 82 dpa. The damage structure is a complicated mixture of small dislocation loops and dislocation segments. No attempt was made in this experiment to quantify either the nature or numbers of the various defects. Qualitatively. it can be seen that the defect density is high, which would be expected in light of the substantial yield strength increase observed for that alloy.

ORNL-Photo 1414-88

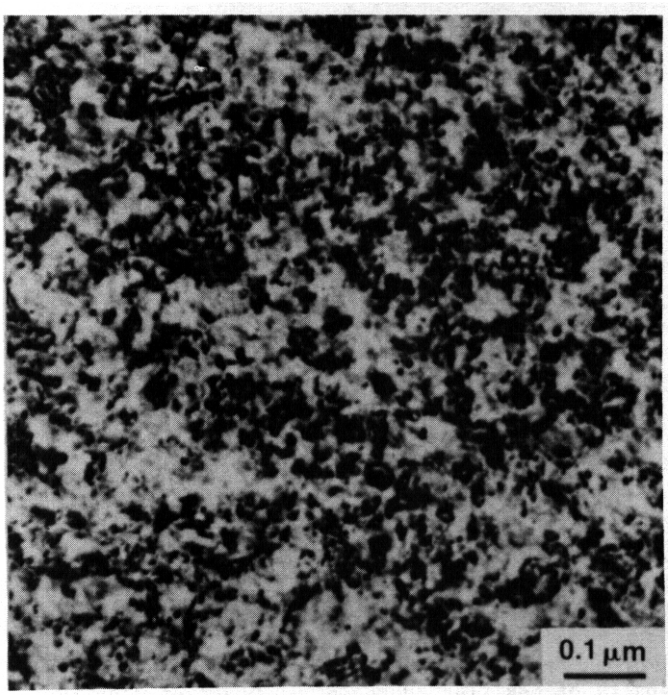

Fig. 1. Irradiation-produced defects in Vanstar-7 after 82 dpa at 420°C. The specimen contained no preimplanted helium.

2. Helium Bubbles

Once an alloy containing helium is irradiated, the primary locations where helium bubbles may be observed are the grain boundaries or particle/matrix interfaces. The bubbles in the matrix absorb vacancies and become cavities. Micrographs of grain boundary bubbles in V–15Cr–5Ti, after helium doping and then after irradiation, are shown in Fig. 2 After the tritium trick is performed, a network of approximately 5-nm-diam bubbles can be found on the grain boundaries [Fig. 2(a)] and carbide particle surfaces. After neutron irradiation to 82 dpa, the networks were somewhat more diffuse [Fig. 2(b)], but the bubbles were still about the same size. Therefore, it appears that the helium distribution in the grain boundaries has not changed markedly during the irradiation at 420°C.

3. Radiation-Induced Precipitation

No obvious radiation-induced Precipitate phases were observed in V–15Cr–5Ti, Vanstar-7, or V–3Ti–1Si. Disk-shaped precipitates have been observed by Loomis and Kestel[3] in ion-irradiated V–15Cr–5Ti from 550 to 750°C, but the precipitate size decreased with temperature and the particles were only 2 nm in diameter at 550°C. Therefore, if the same phase is forming in that alloy under neutron irradiation, it may be too small to resolve by TEM, especially with the existing damage structure in the background. A fine, rod-shaped precipitate phase, that tended to concentrate around existing titanium carbonitride particles,[4] was observed in the matrices of V–20Ti. However. examination of the thermally aged control specimens is needed to determine if the phase is thermally- or radiation-induced.

4. Swelling

Cavities formed in the grain matrices of a number of vanadium alloys and caused swelling. The results of the swelling measurements are presented in Table 2. Without any implanted helium, the V–15Cr–5Ti exhibited zero swelling after the irradiation to 82 dpa. Even with 300 appm ^{3}He (tritium trick), or 10 and 100 appm ^{4}He (accelerator-injected). swelling was less than 0.01%. Therefore, V–15Cr–5Ti should be considered a very low-swelling alloy. The Vanstar-7 alloy was also very low swelling, both with and without implanted helium. By canparison, both the V–3Ti–1Si and V–20Ti displayed swelling values >0.1%, but were still quite low compared to many austenitic stainless steels.[5]

ORNL-Photo 1415-88

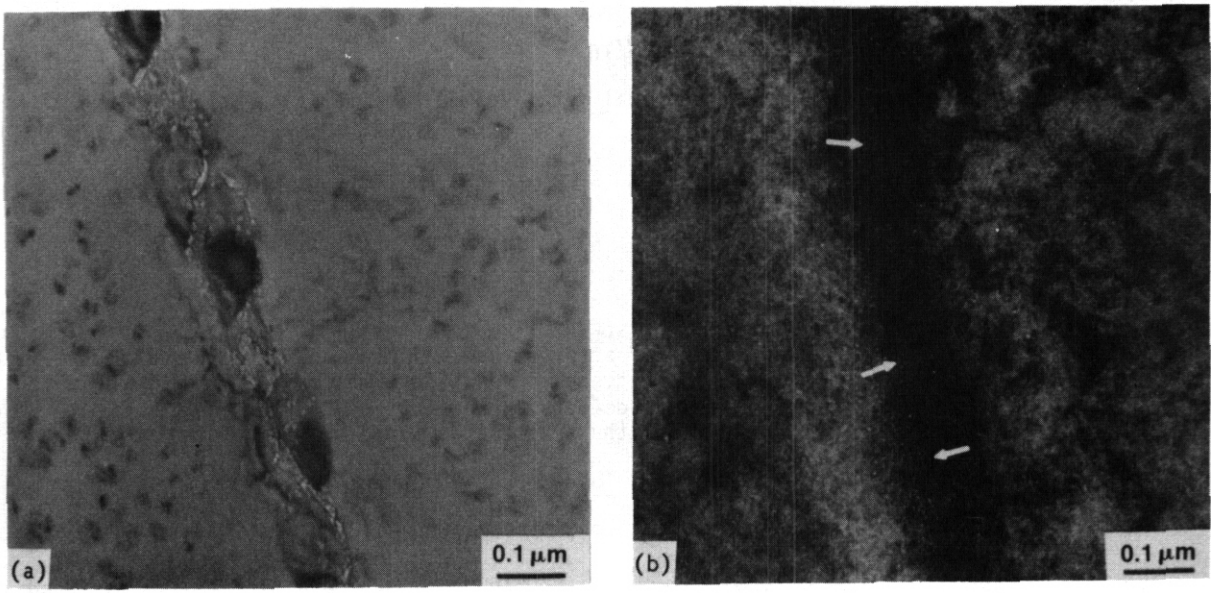

Fig. 2 Grain boundary helium bubbles in V–15Cr–5Ti (300 appm level): (a) Before irradiation. and (b) after irradiation to 82 dpa in FFTF.

Table 2. Cavity swelling of vanadium alloys irradiated in FFTF to E2 dpa at 420°C

Alloy	Specimen No.	Level, appm ^{3}He	Level, appm ^{4}He	Swelling (%) $\frac{\Delta V}{V - \Delta V}$
V–15Cr–5Ti	RA49	0		0
V–15Cr–5Ti	RA31	300		(0.01
V–15Cr–5Ti	A1		10	<0.01
V–15Cr–5Ti	A7		100	t0.01
Vanstar-7	QA99	0		(0.01
Vanstar-7	QA70	150		10.01
V–3Ti–1Si	H4		100	0.332
V–3Ti–1Si	E0	0		0.257
V–3Ti–1Si	61	23		0.568
V–3Ti–1Si	46	135		0.768
V–3Ti–1Si	24	480		1.130
V–20Ti	WA00	0		0.955

The swelling in V–3Ti–1Si was observed to increase with helium content. as listed in Table 2 and shown in the micrographs in Fig. 3. The micrographs were taken of specimens having 0, 23, 135. and 480 appm of implanted ^{3}He. It is clear that swelling increased with increasing helium level. The actual swelling values for these same four specimens are plotted as a function of helium level in Fig. 4(a). At first, swelling increases rapidly, but then tends to saturate as the helium level increases to 480 appm. Note also that a specimen implanted with ^{4}He has less swelling than would be expected for one with a similar level of ^{3}He implanted using the tritium trick. However. since the value for this one specimen is within the expected scatter and the accelerator-injected helium levels were not confirmed by analysis, one hesitates to make any distinction between swelling in ^{3}He- and ^{4}He-implanted specimens. The average cavity diameters and cavity number densities are shown as a function of helium level for the same V–3Ti–1Si specimens in Fig. 4(b). In going from 0 to 480 appm ^{3}He, the average cavity diameter for the four specimens drops from only about 16.5 to 12 nm, but the number density of cavities Increases an order of magnitude. Therefore, increasing the helium level appears to increase the nucleation of cavities in this alloy while slightly decreasing their average size.

Let us now compare the irradiated microstructures in vanadium alloy specimens that have the helium implanted by two different techniques (Fig. 5). A specimen of V–3Ti–1Si doped with 135 appm ^{3}He at 400°C [Fig. 5(a)] is contrasted with one injected with 100 appm ^{4}He at 420°C [Fig. 5(b)]. Both specimens have a higher concentration of cavities near their respective grain boundarles, but the ^{3}He-doped specimen has substantially more cavities throughout the microstructure and, consequently, higher swelling.

ORNL-Photo 1416-88

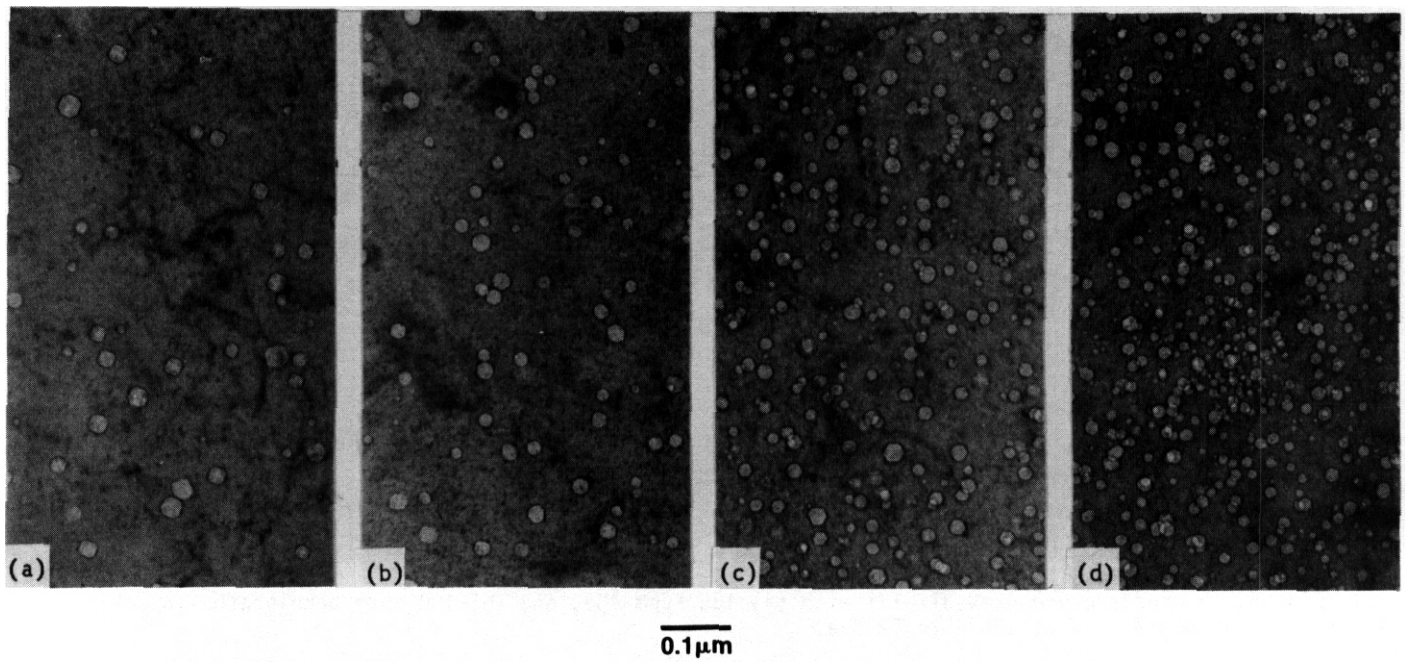

Fig. 3. Matrix cavities in V–3Ti–1Si with (a) 0, (b) 23. (c) 135, and (d) 480 appm of preimplanted ^{3}He, after irradiation in FFTF at 420°C to 82 dpa.

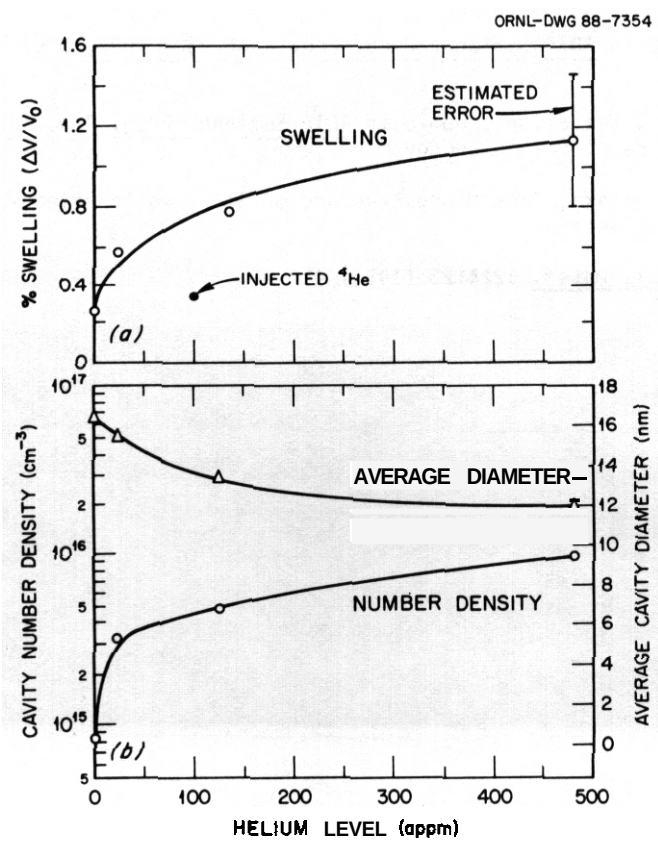

Fig. 4. (a) Cavity swelling, and (b) average cavity diameter and cavity number density, in V-3Ti-IS1 irradiated to 82 dpa in FFTF, as a function of the preimplanted helium level.

ORNL-Photo 1417-88

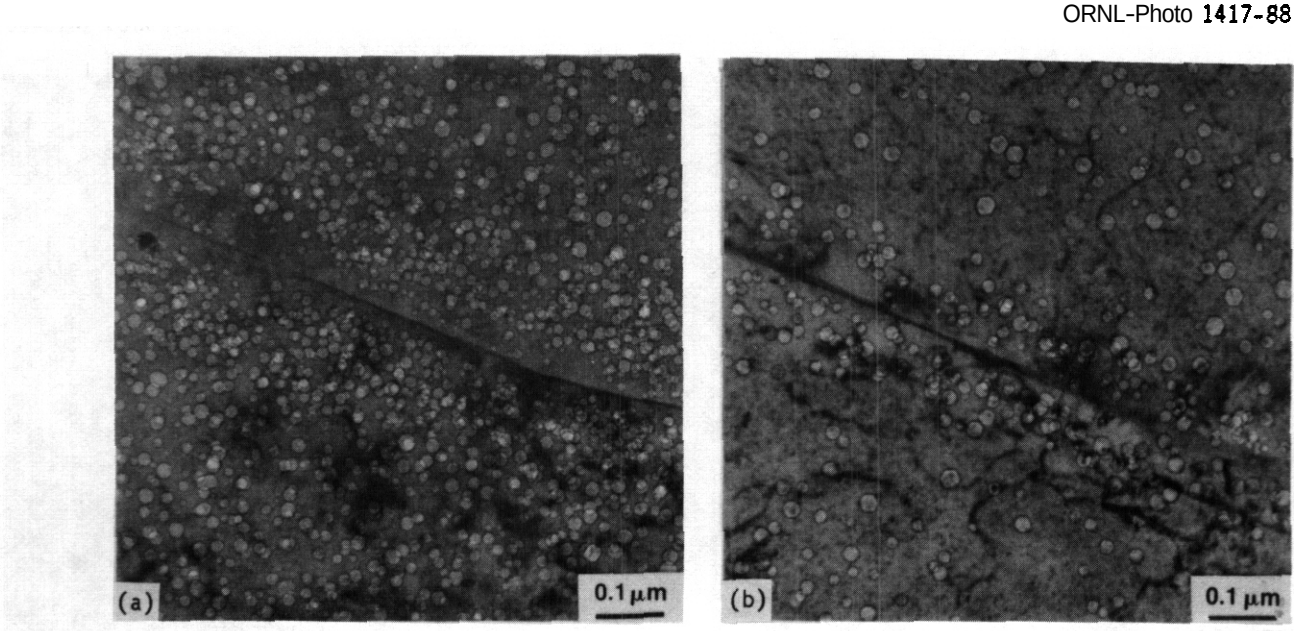

Fig. 5 Microstructure of V–3Ti–1Si with (a) 135 appm ^{3}He, and (b) 100 appm accelerator-injected ^{4}He, after irradiation in FFTF at 420°C to 82 dpa.

REFERENCES

1. D. N. Braski and D. W. Ramey, pp. 1211–24 in Effects of Radiation on Materials: Twelfth Inter. Symp., ASTM STP 870, F. A. Garner and J. S. Perrin, Eds., American Society for Testing and Materials, Philadelphia.

2. A. M. Ermi, pp. 21–40 in ADIP Semiann. Prog. Rep. Sept. 30, 1984, DOE/ER-0045/13, U.S. DOE, Office of Fusion Energy.

3. B. A. Loomis and B. J. Kestel, pp. 65-70 in ADIP Semiann. Prog. Rep. March 31, 1986. DOE/ER-0045/16, U.S. DOE, Office of Fusion Energy.

4. T. Schober and D. N. Braski, "The Microstructure of Selected Annealed Vanadium-Base Alloys." to be submitted to Metallurgical Transactions.

5. P. J. Maziasz, J. Nucl. Mater. 12211123 (1984) 472–86.

6.4 Copper Alloys

ANALYSIS OF COPPER AND COPPER ALLOYS AFTER LOW-LEVEL TRITIUM CHARGING — S. J. Zinkle (Oak Ridge National Laboratory)

OBJECTIVE

The objective of this study is to determine the influence of very low levels of helium on the mechanical properties and microstructure of copper and two copper alloys.

SUMMARY

Copper and the copper alloys Cu-Zr and Cu-Cr-Zr-Mg were implanted with ~50 appb He using the tritium trick. The measured helium concentration was an order-of-magnitude higher than that expected from calculations based on the established solubility of tritium in copper. A comparison with specimens annealed in hydrogen showed that 50 appb He does not have an appreciable effect on the tensile properties of any of the tested materials.

PROGRESS AND STATUS

Introduction

The effects of helium on the mechanical properties of copper are not well established. Vela and Russell[1] found that 500 appm He had little effect unless the copper containing the helium was annealed above 800°C. Carpenter and Nicholson[2] observed substantial embrittlement at test temperatures above 400°C for helium concentrations of ~300 appm, and no observable effects for 25 appm He. On the other hand, Goods[3] has recently observed a dramatic decrease in the room temperature ductility of copper that contained 2 appm He following long-term annealing at 200°C. El-Shanshoury et al.[4] found that the total elongation in copper decreased from 45 to 10% following a 0.1 dpa neutron irradiation at 100°C that generated 5 appm He. One of the goals of the present investigation is to determine whether very low levels of helium (<0.1 appm) have any significant effect on the mechanical properties of copper.

Experimental procedures

The materials for this investigation consisted of 250-μm foils of copper and two commercial copper alloys, AMZIRC and AMAX-MZC. AMZIRC contains 0.15% Zr while MZC contains 0.04% Mg, 0.15% Zr, and 0.8% Cr. The alloys were tested in both the cold-worked-and-aged (CWA) condition and the solution-annealed-and-aged (SAA) condition. Details of the heat treatment and physical properties of these alloys have been reported elsewhere.[5] A chemical analysis of the copper used in this study by Combustion Engineering did not detect any metallic impurities with concentrations >10 ppm. However, the copper did contain 21 ppm (85 appm) of oxygen, so it cannot be classified as "oxygen-free." The chemical analysis also detected 3 ppm N, 11 ppm S, and 36 ppm C. The copper foil was cold rolled to produce a 50% reduction in thickness (from 600 to 300 μm) and then recrystallized by annealing in helium for 10 min at 450°C.

TEM disks and tensile specimens (SS-2 geometry[6]) were punched from the foils, wrapped in tantalum foil, and placed in the Oak Ridge high-pressure tritium facility.[7] The samples were baked out at 700°C for 24 h under vacuum, and then they were annealed at 400°C in tritium at 53 kPa (400 torr) for 792 h. The specimens were outgassed following the charging by annealing for 43 h at 700°C in vacuum. The measured surface activity of the foils remained very high after conventional surface cleaning techniques were performed, indicating that a significant amount of tritium was still trapped near the specimen surface. A light polish with 600-grit sandpaper was successful in lowering the surface activity to safe levels. Additional foils of the copper and copper alloys were annealed in hydrogen at 400°C for 792 h in order to separate helium effects from hydrogen effects. These control specimens were not given the 700°C annealing treatment before or after charging.

The ^{3}He concentration in the tritium-charged specimens was measured by Dr. Brian Oliver of Rockwell International using a vacuum fusion technique. Duplicate tensile specimens were tested in air at room temperature using a crosshead speed of 0.5 mm/min (strain rate ~7×10^{-4}/s). Tensile specimens were also tested in vacuum at 400°C. TEM specimens were jet electropolished in a solution of 33% HNO_3/67% CH_3OH at −20°C.

Results

The tritium trick produces low levels of helium in copper alloys due to the low solubility of hydrogen in copper. The solubility of tritium in copper at a pressure of 400 torr and a temperature of 400°C is ~0.8 appm according to the data reviewed in refs. 8 and 9. The solubility of hydrogen is much higher for the solute elements that are present in the copper alloys of this study. However, the low solute concentration in the alloys offsets the higher solubility, so that the net effect is small. For example, the addition of 0.8% Cr to copper in the form of chromium precipitates (aged MZC alloy) should increase the hydrogen solubility from 0.8 to 0.9 appm. The measured 3He concentrations for the tritium-doped specimens are given in Table 1. It can be seen that the alloys (particularly MZC) contain a higher helium concentration than the pure copper specimen. An even more significant result is the magnitude of the helium concentrations. The expected helium level in copper, calculated from the solubility data and the tritium charging time of 792 h, is only 4 atomic parts per billion (appb). The measured value is about an order-of-magnitude higher than the calculated number.

Table 1. Measured helium concentrations (appb) in tritium-doped copper and copper alloys

Copper	AMZIRC (SAA)	AMZIRC (CWA)	MZC (SAA)	MZC (CWA)
33.0 ± 0.8	48.2 ± 1.5	48.0 ± 0.2	94.6 ± 1.3	73.1 ± 0.1

The room-temperature tensile properties of the copper and copper alloys after the tritium and hydrogen charging are given in Table 2. The corresponding tensile properties measured at 400°C are given in Table 3. There was no strong effect of the tritium doping on the tensile properties. The pure copper showed a slight increase in yield strength and a slight decrease in elongation. The tensile properties of the alloys were influenced more by thermal annealing effects than by helium effects. The tritium specimens were softer and more ductile than the hydrogen control specimens due to the additional annealing at 700°C that they experienced. The annealing caused precipitate overaging and recrystallization. The measured ductility was generally lower at 400°C than at room temperature. This may be an artifact of the thin tensile specimen geometry.

The microstructure of the pure copper specimens consisted of large grains that contained a very low density of cavities ($<10^{17}/m^3$). These cavities were present in both the tritium- and hydrogen-charged specimens and may be due to water vapor associated with the excess oxygen in the copper matrix. There was no significant amount of observable cavitation in the copper alloys. The cold-worked-and-aged MZC specimens did not recrystallize during the hydrogen anneal treatment.

Table 2. Room-temperature tensile properties of copper and copper alloys after charging at 400°C with tritium or hydrogen

		Copper	AMZIRC (SAA)	AMZIRC (CWA)	MZC (SAA)	MZC (CWA)
Strength, MPa						
Yield	T_2	80	60	90	80	90
	H_2	40	150	130	240	390
Ultimate	T_2	200	230	270	310	290
	H_2	250	280	340	410	480
Elongation, %						
Uniform	T_2	23	26	30	25	28
	H_2	30	15	25	16	11
Total	T_2	28	29	37	31	34
	H_2	33	17	29	19	14

Discussion

The helium concentrations measured in copper and the copper alloy following tritium charging suggest that the tritium solubility in copper at 400°C is much higher than expected from solubility data in the literature. There are several possible explanations for this observation. First, there is evidence that the solubility of hydrogen in copper and nickel can be increased by a factor of 2 or more for polycrystalline or cold-worked specimens as compared to single crystals.[10,11] Second, there is strong evidence that oxygen-contaminated surface layers will produce enhanced hydrogen solubilities at low temperatures.[11] The observations in the present study tend to support this conclusion — a large enhancement in the tritium concentration was found near the specimen surface as determined from surface activity measurements. Third, it has been established that Arrhenius plots of hydrogen solubility versus reciprocal temperature for nickel exhibit curvature due to the temperature dependence of the relevant thermodynamic functions.[12] This leads to a large (one order-of-magnitude) enhancement in the hydrogen solubility at low temperatures compared with values obtained by extrapolation from high temperatures. However, the solubility of hydrogen in copper has been measured at temperatures of 400°C and below.[8,9,13] There is no evidence in the literature for an enhanced solubility of hydrogen in copper at low temperatures. Finally, Caskey et al.[13] have found that the amount of absorbed tritium in copper correlates with the oxygen content in the metal. Their results suggest that an oxygen content of 20 wt ppm can lead to an order-of-magnitude increase in the amount of absorbed tritium compared to oxygen-free copper. This would explain the anomalous results

for copper. A different mechanism would have to be invoked to explain the high helium levels in the copper alloys since they were fabricated using oxygen-free (<3 ppm) copper. Researchers from Sandia National Laboratory (Livermore) have recently observed anomalously high helium concentrations in pure copper specimens that were charged with tritium, in agreement with the findings of the present study.[14] In summary. we are not aware of any model in the literature that satisfactorily explains the high helium levels observed in both the tritium-charged copper and copper alloys.

Table 3. Elevated-temperature (400°C) tensile properties of copper and copper alloys after charging at 400°C with tritium or hydrogen

		Copper	AMZIRC (SAA)	AMZIRC (CWA)	MZC (SAA)	MZC (CWA)
Strength, MPa						
Yield	T_2	70	64	74	90	90
	H_2	66	90	100	170	180
Ultimate	T_2	120	150	200	200	200
	H_2	150	190	210	290	290
Elongation, %						
Uniform	T_2	19	20	35	18	27
	H_2	22	9	24	11	11
Total	T_2	21	24	39	26	31
	H_2	26	12	29	13	15

CONCLUSIONS

The tritium trick has been applied to copper and two commercial copper alloys in order to study helium effects at low concentrations. Tritium charging at 400°C resulted in an order-of-magnitude higher concentration of helium than that expected from hydroaen isotooe solubility data. The cause of this solubility enhancement is unknown, although it may be related to (surface) oxide-tritium interactions.

Helium concentrations in copper of ~50 appb have no significant effect on the tensile properties measured at 22 or 400°C.

ACKNOWLEDGMENTS

The author gratefully acknowledges the assistance of D. N. Braski, L. T. Gibson, N H Rouse, and E. L. Ryan during this investigation.

REFERENCES

1. P. Vela and B. Russell, J. Nucl. Mater. 19 (1966) 3126.

2. G.J.C. Carpenter and R. B. Nicholson, p. 383 in Radiation Damage in Reactor Materials (IAEA, Vienna 1969), Vol. 2; also AECL-3331 (April 1969).

3. S. H. Goods, Scripta Met. 20 (1986) 565.

4. I. A. El-Shanshoury et al., J. Nucl. Mater. 29 (1969) 161.

5. S. J. Zinkle, D. H. Plantz. A. E. Bair, R. A. Oodd, and G. L. Kulcinski, J. Nucl. Mater. 1338134 (1985) 685; also see S. J. Zinkle et al., OAFS Quart. Prog. Rep., DOE/ER-0046/20 (February 1985), p. 85.

6. R. L. Klueh, p. 53 in ADIP Semiann. Prog. Rep. Sept. 30, 1984, DOE/ER-0045/13, U.S.DOE Office of Fusion Energy.

7. D. N. Braski and D. W. Ramey, p. 1211 in Effects of Radiation on Materials: 12th Inter. Symp., ASTM STP 870, ed., F. A. Garner and J. S. Perrin (ASTM 1985).

8. W. DUrrschnabel and H. Vosskühler, p. 657 in Gase and Kohlenstoff in Metallen, ed., E. From and E. Gebhardt (Berlin: Springer, 1976).

9. S. A. Stewart, Review of Hydrogen Isotope Permeability Through Materials, UCRL-53441 (August 1983).

10. W. Eichenauer et al., Z. Metallkd. 56 (1965) 287 and 55 (1964) 217.

11. K. Kiuchi and R. B. McLellan, J. Less-Common Metals 95 (1983) 283.

12. R. B. McLellan and P. L. Sutter, Acta Met. 32 (1984) 2233.

13. G. R. Caskey, Jr., et al., Corrosion 32 (1976) 370.

14. Personal communication from Dr. B. M. Oliver to S. J. Zinkle (1986).

6.5 Environmental Effects on Structural Alloys

CORROSION IN LIQUID METAL ENVIRONMENTS: SUSCEPTIBILITY OF Fe_3Al EXPOSED IN A LITHIUM THERMAL CONVECTION LOOP AND MECHANISMS OF IRREGULAR ATTACK BY LITHIUM AND LEAD-LITHIUM - P. F. Tortorelli (Oak Ridge National Laboratory)

OBJECTIVE

The purpose of this work is to characterize the corrosion of candidate or model fusion materials by slowly flowing lithium and Pb-17 at. % Li in the presence of a temperature gradient. Dissolution and deposition rates are measured as a function of alloy composition, exposure time, temperature, and additions to the liquid metals. These measurements are combined with microstructural analyses of the specimen surfaces to establish mechanisms and rate-controlling processes for the corrosion and mass transfer reactions, determine the suitability of particular materials for service in specific liquid metal environments, and provide input into fusion materials development.

SUMMARY

Despite its attractiveness as a low activation material, Fe_3Al was found to have relatively poor corrosion resistance in molten lithium at 500°C. The corrosion of another ordered metallic alloy, Fe-Ni-V, by lithium at 600°C was found to be a two-stage process involving preferential depletion of nickel and nitriding and/or carburizing of vanadium. Results from percolation theory showed that a reactive path model could not explain the Irregular attack induced by preferential depletion in a lead-lithium environment; a model based on surface destabilization appeared to be more appropriate.

PROGRESS AND STATUS

Iron aluminides

The recent development of iron aluminides[1] offers an attractive combination of high-temperature strength and low-residual activation for fusion applications. However, information about the resistance of such materials to radiation damage and corrosion is necessary before evaluation of its potential as a fusion material can be made.

While pure iron is not severely corroded by lithium, aluminum readily dissolves. However, previous work[2] has shown that exposure of stainless steel to lithium containing aluminum leads to the development of a stable aluminum-containing surface on the steel that effectively inhibits corrosion, We have now exposed Fe_3Al to thermally convective lithium over an extended exposure period to qualitatively assess its corrosion resistance. Figure 1 shows weight loss data as a function of time for Fe-28Al-4Cr (at. %) exposed at 500°C in a lithium thermal convection loop (constructed of type 316 stainless steel). The measured weight losses and steady state rate (3.4 $mg/m^2 \cdot h$) are not particularly low for a 500°C exposure to nonisothermal lithium; they are greater than what is expected for type 316 stainless steel at this temperatures and are about the same as measured for Fe-12Cr1MoVW steel at 600°C.[4] Examination of the surface exposed at 500°C for 5691 h revealed surface roughening and some porosity (Fig. 2). Energy dispersive X-ray analysis of this surface showed significant depletion of aluminum: the average aluminum surface concentration was only 15 at. %. The preferential dissolution of this element must have contributed greatly to the total measured weight loss. This dissolution is driven not only by the relatively high solubility of aluminum in lithium, but also by dissimilar metal mass transfer between the small amount of Fe_3Al and the loop wall material. In view of this, the amount of aluminum loss was probably greater than what would be measured in Fe_3Al lithium systems.

Evaluation of penetration models

It has been shown previously that molten lead-lithium is quite aggressive towards ferrous alloys, particularly in the presence of a thermal gradient.[5-7] With austenitic steels, exposure to Pb-17 at. $ Li causes deep irregular attack as a result of penetration by the liquid metal, which appeared to be related to the selective dissolution of one or more elements.[5] Based on a model of Harrison and Wagner,[8] it was suggested that the observed morphological changes could be explained by surface destabilization (extreme surface roughening) induced by this preferential dissolution (principally of nickel).[5] However, recently, a percolation model has been successfully applied to the case of selective dissolution in aqueous environments[9] and it is also appropriate to consider this type of approach to the corrosive attack of type 316 stainless steel by lead-lithium. A simple alternative model based on such would be localized penetration along highly reactive paths, if they exist in the lattice. The probability of the existence of a significant number of such paths is a direct function of the concentration of the reactive element and can

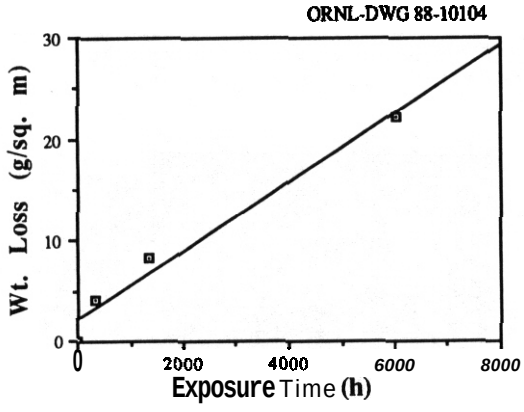

Fig. 1. Weight loss versus time for ordered Fe-28Al-4Cr (at. %) exposed to thermally convective lithium at 500°C.

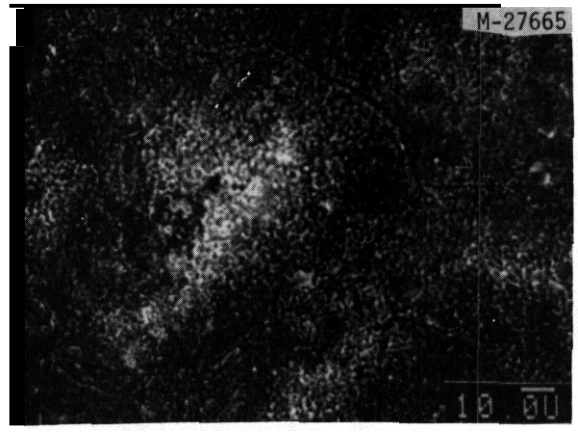

Fig. 2. Scanning electron micrograph of ordered Fe-28Al-4Cr (at. %) exposed to thermally convective lithium at 500°C for 5691 h.

be derived using the formalism of percolation theory.[10] For infinite connected paths, the concentration at which selective dissolution can occur is directly related to the percolation threshold, which is slightly less than 20 at. % for the fcc lattice. If, for the sake of simplicity, we assume that, based on solubilities in the lead-lithium, the starting material is composed of a very reactive component (Ni) and a rather inert one (Fe-Cr), extended penetrations would be expected for a minimum concentration of about 20 at. % Ni due to the existence of connected nickel atoms. which are quickly dissolved and transported into the liquid. Penetrative attack is actually observed at nickel concentrations much less than this limit (approximately 11 at. %). Indeed. a simple one-dimensional calculation shows that, at this concentration, the probability of finding a penetration depth on the order of even just a few microns was zero. Therefore, it is apparent that, while there are experimental indications that the attack is related to the selective dissolution of nickel, there is not a sufficient nickel concentration to geometrically explain the corrosion-induced morphology. In view of this finding and other observations (for example, the effect of cold work),[11] the surface destabilization model seems to be the most appropriate explanation for the observed attack of Fe-Ni-Cr alloys exposed to molten lead-lithium.

Austenitic stainless steel also corrodes nonuniformly when exposed to thermally convective lithium, albeit the resulting corrosion zone is somewhat different in morphology than what is observed for lead-lithium. A qualitative assessment of the growth of this zone as a function of tine showed that the kinetics were not consistent with the surface destabilization model. This does not necessarily mean that surface destabilization is not the cause of the observed corrosion morphology; in lithium, other reactions besides the dissolution of nickel and other elements (for example, formation of chromium-containing products) can strongly influence the overall corrosion process[4,12] and can thus complicate an analytical evaluation of the penetration kinetics.

Other examples of irregular corrosion in a liquid metal environment were found when Fe-Co-V and Fe-Ni-V ordered alloys were exposed in lithium thermal convection loops.[13] When originally reported, it was thought that redeposition of dissolved species played an important role in the formation of the observed "porous" layers. However, further analysis and recent reports on the corrosion of vanadium by lithium[14-16] have shown that. in the case of the Fe-Ni-V alloy, corrosive attack could best be described by a two-stage process involving surface destabilization and subsequent corrosion (nitriding and/or carburizing) of the vanadium. As described previously,[13] after extended exposure to molten lithium at 600°C, the Fe-Ni-V alloy was severely corroded (see Fig. 3). Two distinct corrosion zones can be observed: a very porous or open outer layer and a more compact, but still somewhat porous, inner zone next to the unaffected matrix. Analysis of the two zones by energy dispersive X-ray analysis showed that the outer one is primarily composed of iron, while the inner layer contains iron and vanadium (see Table 1). Nickel was extensively depleted in both layers, while the composition of the matrix matched that of the starting material (Fe-32Ni-22V-0.4Ti, wt %). The iron/vanadium ratio of the inner layer was the same as that in the underlying matrix: it corresponds to what is calculated from the depletion in nickel to 1 wt %. It therefore appears that the inner zone forms strictly by preferential dissolution of nickel. The resulting porous layer is thus related to this selective depletion and could well be due to surface destabilization, as discussed above. At the start of the exposure, the structure of the Fe-Ni-V was that of gamma prime (ordered fcc). The depletion of nickel resulted in a composition of the inner layer (Table 1) that is within the two-phase alpha-Fe + sigma (FeV) field of the Fe-V system.[17] These two phases can be seen in the inner layer of the polished cross sections shown in Fig. 3. The FeV phase can provide sufficient vanadium to react with nitrogen and/or carbon in lithium to form nitrides or carbides. These somewhat brittle products can then be removed by flow turbulence or during the sample removal and cleaning process.[15] The removal of the vanadium product would explain the almost pure iron layer observed on these specimens and the enlarged porosity in the outer layers (see Fig. 3 and Table 1). A calculation based on the Fe-V phase diagram17 and the lever rule showed that if all of the vanadium of the sigma phase was reacted and lost (but none of the vanadium in solution in alpha-Fe was affected), the resulting vanadium concentration of the outer layer would be about 9 wt %, which is consistent with the measured value (see Table 1) given the relative simplicity of the assumptions.

In view of the above observations, it is apparent that the corrosion of the ordered Fe-Ni-V alloy is a unique two-stage process that involves (1) the preferential depletion of nickel with surface destabilization and (2) the conversion of sigma to Iron and vanadium nitride and/or carbide. The relative rates of the two prlnclpal reactions are such that a corrosion zone wlth two distinct layers can be observed.

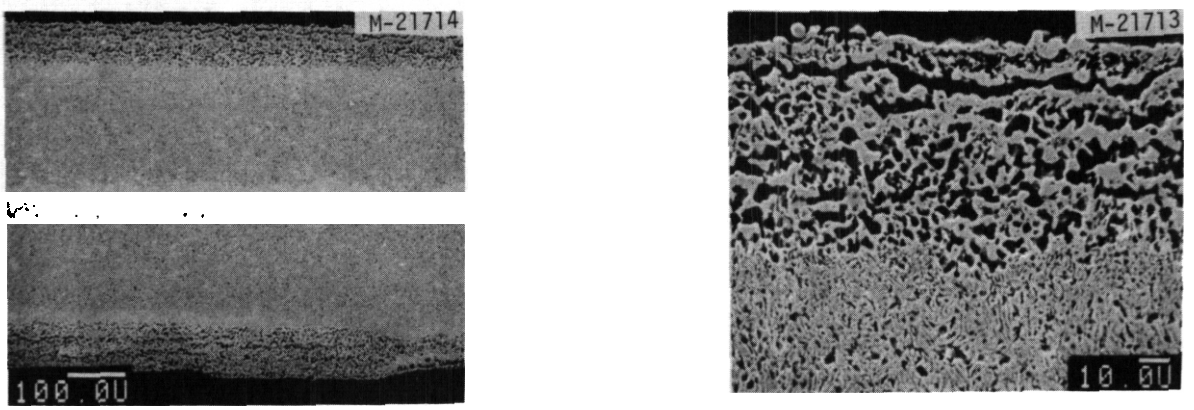

Fig. 3. Scanning electron micrographs of polished cross sections of ordered Fe-32Ni-22V-0.4Ti (wt %) exposed to thermally convective lithium at 600°C for 7495 h.

Table 1. Compositional analysis of LRO-35 specimens exposed to thermally convective lithium at 600°C for 2512 and 7495 h

Analyzed area	Exposure tlme (h)	Concentration (wt %)[a]			
		Fe	Ni	V	Ti
Outer corrosion zone	2512	92	1	6	1
Outer corrosion zone	7495	93	1	4	1
Inner corrosion zone	2512	73	1	25	1
Inner corrosion zone	7495	67	1	30	0.5
Matrix	2512	46	31	22	0.5
Matrix	7495	46	31	22	0.5

[a]Averaged measurements based on standardless analysis using ZAF-corrected energy dispersive X-ray spectral data.

CONCLUSIONS

1. Fe_3Al does not have good corrosion resistance to thermally convective lithium at 500°C.

2. In Pb-17 at. % Li, the nickel concentration of type 316 stainless steel is not sufflclent to produce the irregular attack ("porosity") by a reactive path mchanism. A surface destablllzation model appeared to be the most appropriate model for the observed corrosion process.

3. Because of the complications caused by surface product reactions. the surface destablllzation model alone does not adequately describe the penetration kinetics for type 316 stainless steel exposed to molten lithium.

4. The corroslon of the ordered Fe-NI-V alloy by nonlsothermal lithium is a unique two-stage process that Involves (a) the preferential depletion of nickel wlth surface destablllization and (b) the conversion of sigma to Iron and vanadium nitrides andlor carbides.

FUTURE WORK

Over the next six months, liquid metal corrosion studies will Include exposure of low-activation austenitic and ferritic steels and corrosion inhibltlon experiments In thermally convective Pb-17 at. % Li,

analysis of mass transfer in this environment, and preliminary evaluation of a "corrosion-optimized" ferritic (7Cr) steel exposed in a lithium thermal-convection loop. Experiments to study the aqueous corrosion of developmental low-activation austenitic alloys will be initiated.

REFERENCES

1. C. G. McKamey et al., *Evaluation of Mechanical and Metallurgical Properties of Fe_3Al-Based Aluminides*, ORNL/TM-10125, September 1986.

2. P. F. Tortorelli et al.. "Corrosion Inhibition in Systems of Lithium with Nickel-Bearing Alloys," pp. 1610–13 in *Pmceedings Eighth Symposium on Engineering Problems of Fusion Research,* IEEE Publication No. 79CH1441-5 NPS, 1979.

3. P. F. Tortorelli and J. H. DeVan, "Mass Transfer Kinetics in Lithium-Stainless Steel Systems," pp. 81-88 in *Pmceedings Third International Conference on Liquid Metal Engineering and Technology,* Vol. 3, The British Nuclear Energy Society, 1985.

4. P. F. Tortorelli, "Corrosion of Ferritic Steels by Molten Lithium: Influence of Competing Thermal Gradient Mass Transfer and Surface Product Reactions," *J. Nucl. Mater.* 154-156 (1988), to be published.

5. P. F. Tortorelli and J. H. DeVan, "Corrosion of Ferrous Alloys Exposed to Thermally-Convective Pb-17 at. % Li," *J. Nucl. Mater.* 141-143, 592–98 (1986).

6. O. K. Chopra and D. L. Smith, "Compatibility of Ferrous Alloys in a Forced Circulation Pb-17Li System," *J. Nucl. Mater.* 141-143, 566–70 (1986).

7. H. U. Borgstedt, G. Drechsler, G. Frees, and Z. Peric, "Corrosion Testing of Steel X 18 CrMoVNb 12 (1.4914) in a Pb-17 Li Pumped Loop," *J. Nucl. Mater.* 154-156 (1988), to be published.

8. J. D. Harrison and C. Wagner, "The Attack of Solids by Liquid Metals and Salt Melts," *Acta Metall.* 7, 722–35 (1959).

9. K. Sieradzki et al., "The Relationship Between Dealloying and Transgranular Stress-Corrosion Cracking of Cu-Zn and Cu-Al Alloys," *J. Electrochem. Soc.* 134, 1635–39 (1987).

10. D. Stauffer, *Introduction to Percolation Theory,* Taylor and Francis, London, 1985.

11. P. F. Tortorelli, "Thermal Gradient Mass Transfer in Ferrous Alloy Pb-17 at. % Li Systems," pp. 279–87 in *Fusion* Reactor *Materials Semiannual Pmgress Report March 31, 1387,* DOE/ER-0313/2, U.S. DOE, Office of Fusion Energy, September 1987.

12. G. E. Bell, P. F. Tortorelli, and M. A. Abdou, "Corrosion and Mass Transfer in Lithium 12Cr-1MoVW Steel Systems," pp. 260–63 in *Fusion Reactor Materials Semiannual Progress Report September 30, 1987,* DOE/ER-0313/3, U.S. DOE, Office of Fusion Energy, April 1988.

13. P. F. Tortorelli, J. H. DeVan, and C. T. Liu, "Corrosion of Low Activation Austenitic Steels and Ordered Alloys in Thermally Convective Lithium," pp. 180–87 in *ADIP Semiannual Pmgress Report September 30, 1985,* DOE/ER-0045/15, U.S. DOE, Office of Fusion Energy, February 1986.

14. P. Hubberstey and P. G. Roberts, "Corrosion Chemistry of Vanadium in Liquid Lithium Containing Dissolved Nitrogen," *J. Nucl. Mater.* 154-156 (1988), to be published.

15. O. K. Chopra and D. L. Smith, "Corrosion Behavior of Vanadium Alloys in Flowing Lithium," *J. Nucl. Mater.* 154-156 (1988), to be published.

16. H. U. Borgstedt, M. Grundmann, J. Konys, and Z. Peric, "A Vanadium Alloy for the Application in a Liquid Metal Blanket of a Fusion Reactor," *J. Nucl.* Mater. 154-156 (1988), to be published.

17. W. G. Moffatt, *The Handbook* of *Binary Phase Diagrams,* Vol. 3, General Electric Co., 1981.

CORROSION AND MASS TRANSFER IN LITHIUM 12Cr-1MoVW STEEL SYSTEMS - G. E. Bell (University of California, Los Angeles), P. F. Tortorelli (Oak Ridge National Laboratory), and M. A. Abdou (University of California, Los Angeles)

OBJECTIVE

The objective of this research is to provide experimental data for development of, and comparison with, an analytical model of the mass transport of 12Cr-1MoVW steel in the presence of thermally convective lithium. Measurements of chemical and metallurgical changes are used to understand mechanisms and kinetics of the relevant reactions.

SUMMARY

A corrosion and mass transport study utilizing two lithium/12Cr-1MoVW steel thermal convection loops was completed after 3040 and 2510 h at maximum temperatures of 505 and 655°C, respectively. Mass transfer was not a simple function of temperature and elemental solubility and temperature gradient played an important role. At temperatures above 580°C, mass transfer was dominated by temperature gradient while, between 450 and 580°C, it appeared to be controlled by surface reactions involving nitrogen, lithium, and chromium and surface carbides. The corrosion rates from this work were significantly lower than those adopted in recent blanket studies.

PROGRESS AND STATUS

As reported previously,[1] a corrosion and mass transfer study was undertaken using thermal convection loops (TCLs) of a modified ORNL design. The two TCLs operated at maximum temperatures (T_{max}) of 505 and 655°C, with temperature differentials of approximately 150 and 140°C, respectively. Experimental exposures were completed after 3040 h of specimen exposure in the T_{max} = 505°C TCL and after 2510 h in the higher temperature loop. Weight change data as a function of specimen position and temperature for selected specimens from the two loops are shown in Figs. 1 and 2. As noted from data at shorter times,[2] weight changes in the T_{max} = 655°C loop were more than an order of magnitude larger than those in the T_{max} = 505°C TCL. Weight loss occurred in most specimens from the T_{max} = 505°C loop. However, specimens in its heated leg with temperatures greater than approximately 450°C showed significant weight gains despite being at the highest temperature loop positions. Weight loss did not monotonically increase with temperature and mass transfer from the heated leg to the cooled leg was not apparent from the weight change data. In the higher temperature loop, weight losses and gains occurred in both the heated and cooled legs. Weight losses were recorded for specimens above 580°C and weight gains were measured below this temperature.

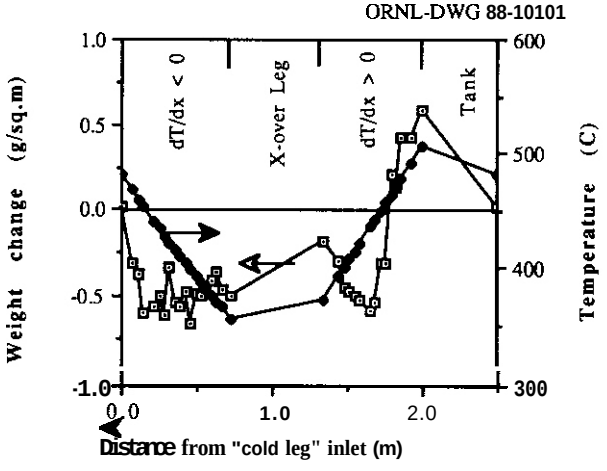

Fig. 1. Weight change and temperature profile for T_{max} = 505°C 12Cr-1MoVW steel-lithium loop, Reynolds number = 1400, 3040 h of exposure.

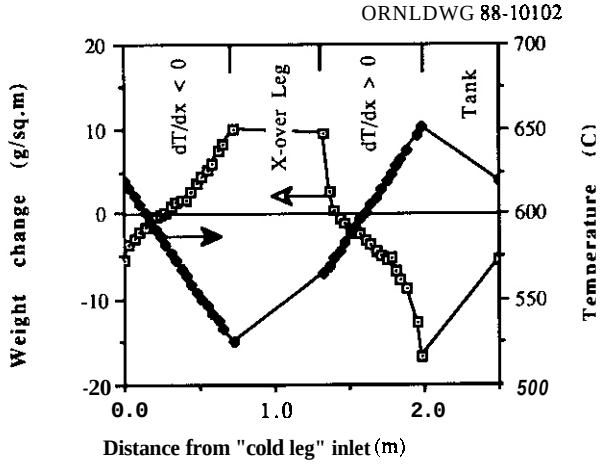

Fig. 2. Weight change and temperature profile for T_{max} = 655°C 12Cr-1MoVW steel-lithium loop, Reynolds number = 1600, 2510 h of exposure.

In chromium-containing steels, increased weight losses with increasing nitrogen in lithium have been related to the formation of a ternary lithium-chromium-nitride compound on the steel.[3-5] The reaction is given in Eq. (1).

$$Li_3N + 1/5\ Cr \rightarrow 1/5\ Li_9CrN_5 + 6/5\ Li \quad . \qquad (1)$$

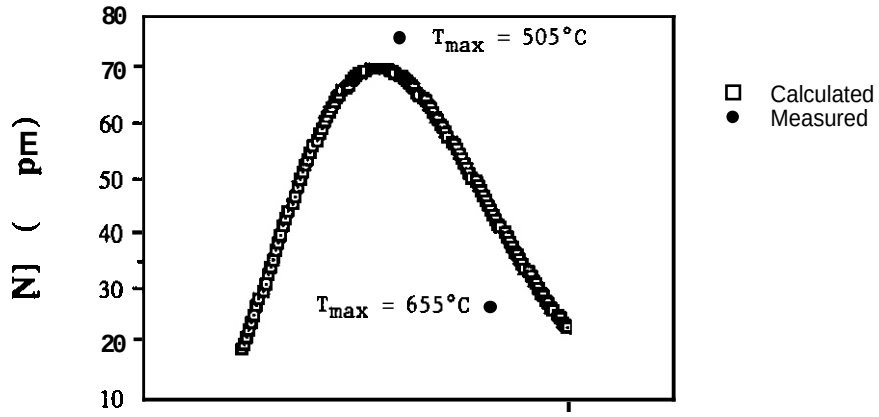

In view of the above discussion, the small weight losses below 450°C were probably due to formation of an adherent, protective film of Li_9CrN_5 (ref. 4) during loop operation and the subsequent removal of the film by specimen cleaning. This would explain the near uniform weight losses between 360 and 450°C. While solubility-driven thermal gradient mass transfer did not appear to be significant in the lower temperature TCL, at higher temperatures (above 580°C), many of the observations are characteristic of such behavior. This would indicate that the Li_9CrN_5 has finite solubility in lithium or is less adherent in this temperature range. Alternatively, nitrogen at the levels found at the higher temperatures no longer may control the corrosion process. Similar changes in behavior as a function of T_{max} have been observed in earlier TCL experiments with 12Cr-1MoVW characterized by lower lithium temperature, mass flow rate, and Reynold's number.[8,9] The magnitude of the weight changes in this investigation was consistent with previous investigations at lower temperatures.[8-11] However, mass transfer rates and weight changes were between a factor of 4 or 5 lower than were estimated in certain design studies.[12]

Surface analyses of exposed specimens revealed additional information about features like those reported previously:[2] "pebble-like" structures on all underlying surfaces and nodules at intermediate temperatures. Energy dispersive X-ray (EDX) analysis of the pebbled specimen surfaces showed depletion in chromium to between 4 and 10 wt % from the starting 11.9 wt %. As described earlier,[2] the nodules were composed of chromium and iron (rich in chromium with respect to the original composition) and further EOX analyses have now shown that the ratio of chromium to iron increased with increasing temperature. Furthermore, X-ray diffraction patterns of specimen surfaces heavily populated with such nodules clearly showed the presence of $M_{23}C_6$. Surface chromium contents were highest at intermediate temperatures where the $M_{23}C_6$ nodules were found. It is not clear whether the observations of chromium depletion, surface "pebbling," and $M_{23}C_6$ nodule formation were related. However, surface chromium content decreased with increasing pebble size and temperature.

The $M_{23}C_6$ nodules were only present at temperatures between 450 and 570°C, and growth of these carbide nodules were the cause of the net weight gains in the hottest portion of the T_{max} = 505°C TCL. The nodules appeared first and disappeared last at the grain boundaries of the specimens, where carbides on the steel surface served as nucleation sites for subsequent growth. Qualitatively, more nodules were present on the specimens from the T_{max} = 655°C TCL than on those from the lower temperature loop; this was probably due to more chromium and carbon available from dissolution and decarburization processes, which readily occurred at the higher temperatures. The chromium-to-iron ratios of the surface $M_{23}C_6$ nodules were consistent with those found in 12Cr-1MoVW steel.[13] The identification of these nodules as carbides and the similarity of such features to those observed in independent loop experiments[8-11] emphasizes the importance of chromium and carbon reactions and subsequent transport (possibly via ternary nitride corrosion product and $M_{23}C_6$ nodule formation) in the temperature range of interest for ferrous alloy-lithium systems, as has been suggested previously.[4,9]

As discussed elsewhere,[2,14] the formation of $M_{23}C_6$ deposits may be related to surface products from reactions with nitrogen and pre-existing carbides, particularly at the grain boundaries, on the steel surface. The temperatures (450 to 570°C) at which the nodules occur are near the 520°C (sigma-phase) solidus phase boundary[15] and the theoretical maximum of the equilibrium nitrogen in lithium [Eq. (1)], as indicated by Fig. 3. The presence of lithium and/or a lithium-nitrogen-chromium corrosion product may affect the kinetics of the carbide phase formation and growth. In particular, a change in chromium solubility at the 520°C solidus may decrease chromium activity on the steel surface. However, regardless of the mechanism by which such nodules form, it is apparent that the formation of the surface nodules and other surface reactions must be considered in any mass transfer model of Li-Fe-Cr(-Ni,Mn) systems and, specifically, in the design of heat transport systems utilizing Fe-Cr alloys with lithium.

CONCLUSIONS

1. Analyses of results from two lithium thermal convection loop experiments operated at maximum temperatures of 505 and 655°C for 3040 and 2510 h. respectivelv. showed that mass transfer in lithium-12Cr-1MoVW steel systems was not a simple function of temperature and elemental solubility. Temperature gradient played an important role.

2. At temperatures above 580°C. mass transfer was dominated by temperature gradient while, between 450 and 580°C, it appeared to be controlled by reactions involving nitrogen, lithium, chromium, and surface carbides.

3. Thermodynamic calculations showed that the measured nitrogen concentrations of the lithium in the two loops were determined by equilibrium with a Li_9CrN_5 product.

4. In the intermediate temperature range, large $M_{23}C_6$ surface nodules were identified. The formation of these carbides strongly influenced the measured weight change profiles around the loops.

5. The corrosion rates from this work were significantly lower than those adopted in recent blanket studies.

REFERENCES

1. G. E. Bell, M. A. Abdou, and P. F. Tortorelli, "Thermal Convection Loop Studies in Support of Mass Transport Modeling of Lithium/12Cr-1MoVW Steel Systems," pp. 275-78 in *Fusion Reactor Materials Semiannual Pmgrees Report March 31, 1987,* DOE/ER-0313/2, U.S. DOE, Office of Fusion Energy, Oak Ridge National Laboratory, Oak Ridge, Tenn., September 1987.

2. G. E. Bell, P. F. Tortorelli, and M. A. Abdou, "Corrosion and Mass Transfer in Lithium 12Cr-1MoVW Steel Systems," pp. 260–63 in *Fusion Reactor Materials Semiannual Pmgress Report September 30, 1987,* DOE/ER-0313/3, U.S. DOE, Office of Fusion Energy, April 1988.

3. E. E. Hoffman, ***Cormswn*** of ***Materials by Lithium at*** *Elevated Temperatures,* ORNL-2924 (1960).

4. M. G. Barker et al., "The Interaction of Chromium With Nitrogen Dissolved in Liquid Lithium," *J. Nucl. Mater.* 114, 143–49 (1983).

5. W. F. Callaway, "The Reaction of Chromium with Lithium Nitride in Liquid Lithium," pp. 18-18–26 in ***Pmc. 2nd Intern.*** Conf. *on Liquid* ***Metal Technology in Energy*** *Production,* CONF-800401-P2, U.S. DOE, 1980.

6. R. J. Pulham and W.R. Watson, "Corrosion of 316 Steel by Lithium-Lead Alloys under Nitrogen," in ***14th*** *Symposium* on *Fusion* ***Nuclear Technology*** *Abstracts,* ***September 8–12, 1986,*** Avignon, France, 1987.

7. K. Natesan, "Influence of Nonmetallic Elements on the Compatibility of Structural Materials with Liquid Alkali Metals," *J. Nucl. Mater.* 115, 251–62 (1983).

8. P. F. Tortorelli and J. H. DeVan, "Corrosion of an Fe-12Cr-1MoVW Steel in Thermally Convective Lithium," pp. 215–21 in *Pmc. Topical Conf.* on *Ferritic Alloys for Use in Nuclear Energy Applications*, AIME, 1984.

9. P. F. Tortorelli, "Corrosion of Ferritic Steels by Molten Lithium: Influence of Competing Thermal Gradient Mass Transfer and Surface Product Reactions," *J. Nucl. Mater.* 154-156 (1988), to be published.

10. O. K. Chopra and D. L. Smith, "Influence of Temperature and Lithium Purity on Corrosion of Ferrous Alloys in a Flowing Lithium Environment," *J. Nuct. Mater.* 141-143, 584–91 (1986).

11. O. K. Chopra and D. L. Smith, "Compatibility of Ferritic Steels in Forced Circulation Lithium and Pb-17Li Systems," *J. Nucl.* Mater. 154-156 (1988), to be published.

12. D. L. Smith et al., *Blanket Comparison and Selection Study-Fiml* Report, ANL/FPP-84-1, Argonne National Laboratory, September 1984.

13. J. M. Vitek and R. L. Klueh, "Precipitation Reactions During the Heat Treatment of Ferritic Steels," *Metall. Tmne.* 14A, 1047–55 (June 1983).

14. G. E. Bell, "Thermal Convection Loop Experiments and Modeling of Mass Transport and Deposition in Lithium/HT9 Systems," Ph.D. dissertation, University of California, Los Angeles, 1988.

15. R. P. Elliot, *Constitution of Binary Atloyw*, First Supplement, McGraw-Hill Book Company, Inc., New York, 1965.

ASSESSMENT OF STRESS-CORROSION CRACKING FOR NEAR-TERM FUSION REACTORS -- R.H. Jones (Pacific Northwest Laboratory[a])

OBJECTIVE

The objective of this evaluation was to identify and assess the potential for stress-corrosion cracking (SCC) in near-term, water-cooled fusion reactors. Identification of critical issues, evaluation of the relevant stress-corrosion data base and recommendations on materials selection was also an objective of this study.

SUMMARY

Water-cooled, near-term fusion reactors will operate under conditions at which SCC is possible; however, control of material purity and fabrication procedures can reduce the probability of crack initiation and growth. Some of the critical issues identified in this evaluation are: 1) will irradiation-assisted stress-corrosion cracking (IASCC) occur at temperatures lower than 100°C, and if so, is the neutron fluence threshold equal to or less than near-term reactor fluences? 2) will aqueous-salt solutions cause SCC? and 3) will radiolysis accelerate SCC in clean water or aqueous-salt coolants?

PROGRESS AND STATUS

Background

Irradiation-assisted SCC is a concern for several in-core components in light-water reactor (LWR) systems. Components at risk include 1) upper guide structures, 2) control blade sheaths, 3) fuel bundle handles in boiling-water reactor (BWR) systems, and 4) bolts and control rod guide tubes in pressurized-water reactor (PWR) systems. The exact mechanism is not clearly understood but is thought to include both an alteration of the aqueous environment by the in-core γ radiation and an alteration of the material microstructure by the in-core neutron flux. Recent tests using samples taken from 304 SS components in BWR systems have shown an increasing susceptibility to IASCC after irradiation at 288°C to a fluence of approximately 5 x 10^{20} n/cm² (E > 1 MV). Clarke, Hale, and Siesler (1) recently found that the presence of γ radiation results in a shift in the electrochemical potential to more positive values in BWR environments and that this shift increases susceptibility to IASCC. The energy introduced by the γ radiation results in the generation of species that would not be possible under other conditions. These species (peroxides, etc.) act to increase the aggressiveness of the environment.

At a recent workshop co-sponsored by the Division of Materials Sciences of the U.S. Department of Energy (DOE) and the Electric Power Research Institute (EPRI), Jones and Simonen (2) sumnarized the key radiation damage issues in IASCC as follows:

- What is the dominant SCC mechanism and what is the role of:
  - P, S, and Si segregation
  - film rupture process
  - stress dependence
  - hydrogen or anodic dissolution?
- What is the role of hardening and embrittlement?
- How is the crack tip strain and stress distribution affected by radiation?
  - Radiation hardening could cause localized flow/corrosion/channel fracture.

Some additional metallurgical factors, beyond those listed previously, were discussed at the DOE/EPRI workshop on IASCC (3). These factors included:

- early stages of carbide precipitation
- grain boundary structure
- radiation damage denuded zone
- grain boundary stress from segregation.

The possible contribution of these factors to IASCC are unknown, as little research has been conducted on metallurgical effects aside from impurity segregation.

Fujita et al. (2) evaluated the SCC behavior of 304 SS in high-temperature water (250°C) during a gamma ray radiation of 4.5 x 10^{4} rad/h. They found that the fracture strain at strain rate of 5 x 10^{-7} to 5 x 10^{-6} s^{-1} was unaffected in water with less than 20 ppb oxygen but was decreased about 50% in water with

(a) Operated for the U.S. Department of Energy by Battelle Memorial Institute under Contract DE-AC06-76RLO 1830.

8 ppm oxygen. Fujita et al. (4) suggested that the increased hydrogen concentration in the water from radiolysis caused the breakdown of the passive film and thereby caused intergranular stress-corrosion cracking (IGSCC) of sensitized material. Kuribayashi and Okabayashi (5) also observed increased IGSCC of 304 SS from radiation in oxygenated high-purity water and in a boiling 12% NaCl solution with a pH of 3. In the low pH experiment, Kuribayashi and Okabayashi (5) concluded that the gamma radiation caused a radiolytic reaction of Fe^{2+} + $Fe3^{+}$ and that the strong oxidizing ferric ions accelerated the corrosion rate and hence affected the IGSCC.

Chemical processes at the tip of a stress-corrosion crack could be strongly influenced by irradiation. Irradiation-induced solute segregation of impurities. such as phosphorus, and depletion of chromium near grain boundaries have been measured in irradiation experiments. These segregation processes have also been related to embrittlement and sensitization in SCC tests in the absence of irradiation. Interactions between irradiation, corrosion, and segregation have not been studied. Elemental hydrogen is also known to affect cracking, especially in high-strength steel. The distribution of hydrogen in an irradiated alloy is not expected to be the same as in an unirradiated alloy because of interactions of hydrogen with irradiation defects.

Mechanical processes at the tip of a stress-corrosion crack are also expected to be strongly influenced by irradiation. Irradiation creep can enhance stress relaxation at the crack tip and hence can reduce the driving force for crack extension in a constant deflection loading mode. Conversely, an enhanced crack tip strain rate may accelerate the stress-corrosion crack growth rate. Experiments have indicated that irradiation fluxes and material stresses cause significant enhancement in stress relaxation. Stress relaxation caused by irradiation has not been examined relative to the crack tip constraints. In addition, post-irradiation plastic deformation is observed to be affected by irradiation histories. Inhomogeneous shear affects passive film rupture in unirradiated metals. In irradiated metals, localized shear is strongly affected by irradiation microstructures and, hence, is expected to contribute to irradiation effects on SCC.

Of these processes, hydrogen embrittlement to ferritic steels is of concern because it appears that radiation will increase the yield strength, induce impurity segregation to grain boundaries, and enhance hydrogen absorption. The effects of radiation-induced precipitation and helium embrittlement are unknown but should not be ignored; irradiation-enhanced corrosion will affect stress-corrosion, but the effect should be small. It was estimated by Jones and Wolfer (6) that radiation induced grain boundary segregation of phosphorus in 316 SS could increase the stress-corrosion crack growth rate by a factor of 8. Recently, Jones (7,8) estimated the effect of irradiation creep on the stress corrosion crack growth rate. This evaluation examined only the relationship between creep rate, crack growth rate (which was dependent on the crack tip strain rate as proposed by Ford), and stress. It did not consider the possibility of stress relaxation at the crack tip. The conclusion of this assessment was that irradiation creep could increase the crack growth rate 1000 times at a stress of 10 MPa and 4 times at 100 MPa, but the effect diminished at higher stresses.

Stress-Corrosion Cracking Issues

Temperature Dependence

The effect of water coolant temperature on SCC and IASCC is a key factor in assessing the potential for SCC and IASCC in near-term fusion reactor concepts. Water coolant temperatures as high as 250°C have been proposed for the European ITER while proposed coolant temperatures are lower than 100°C. 150°C and 120°C for the U.S., Japanese, and USSR designs, respectively. There is ample evidence that SCC and IASCC occurs with austenitic stainless steels at 288°C based on LWR experience. Oxygen and other impurities are known to exacerbate SCC of sensitized stainless steels in water, while localized corrosion from crevices and galvanic corrosion from dissimilar metal couples are factors in crack initiation. Cold work introduced during fabrication by bending, grinding for weld preparation, and welding also accelerate SCC. Cyclic stresses and transient water chemistry conditions from startup/shutdown cycles also contribute to SCC in LWRs.

Many SCC and IASCC processes are thermally activated such that the SCC and IASCC subcritical crack growth rate decreases with decreasing temperature (9), Figure 1. Such a temperature dependence has been noted for austenitic stainless steels for a constant

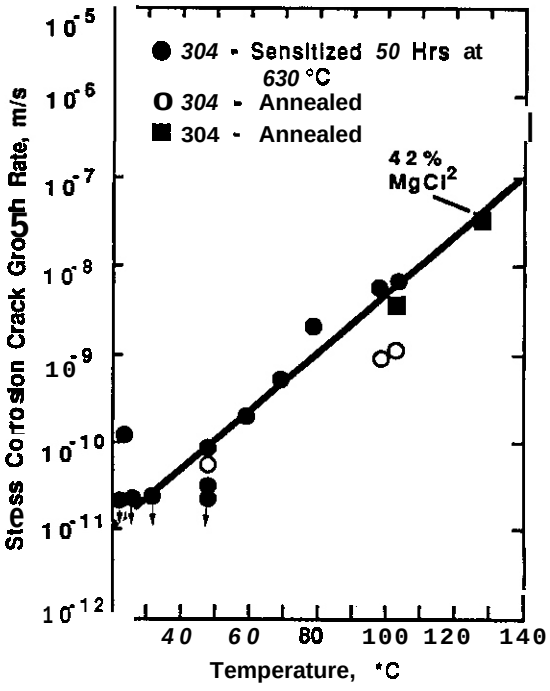

Fig. 1. Effect of temperature on stress corrosion of austenitic stainless steels in 22 pct NaCL aerated. CCB specimens, K = 40 to 50 MPa$\sqrt{m}$. (Ref. 9)

water chemistry, material and stress condition. However, the effect of water chemistry is sufficiently dominant that crack velocities (10^{-6} cm/s) approaching those at 300°C have been obtained at 40°C in water with additions of 10 ppm of Cl^- and F^- (10). Therefore, control of water chemistry and material sensitization will be necessary to ensure that SCC does not occur in near-term fusion reactors operating at temperatures lower than 100°C.

As indicated in the background section, the specific cause(s) of IASCC have not been determined. It is clear that some radiation damage process must precede the onset of crack growth and that at 288°C this threshold occurs at around 10^{21} n/cm² (~1 dpa). However, at lower temperatures it is expected that this damage threshold may be substantially higher since solid-state diffusional processes are involved. An exception to this might be a process involving a combined effect of radiation hardening and hydrogen-induced subcritical crack growth which could occur at 25°C.

There is considerable evidence that radiation enhanced impurity segregation is one of the primary factors involved in IASCC. Evidence for segregation of impurities such as P, Si, and S include heavy ion irradiation studies by Brimhall et al. (11), electron irradiation studies by Fukuya et al. (12) and in-reactor IASCC studies by Garzarolli et al. (13) showing improved performance for high-purity alloys. In unirradiated 316 SS, Andresen and Briant (14) found that an intergranular SCC mode was favored by S segregation in 288°C water but that the crack velocity was unaffected by impurity segregation. Phosphorus and N segregation did not affect the fracture mode or crack velocity. These results suggest that some other radiation damage process besides segregation may be necessary for IASCC to occur. Radiation hardening or other microstructural changes may be involved.

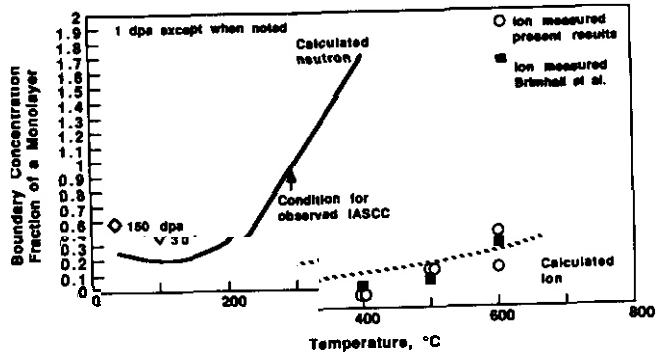

Fig. 2. Calculated phosphorus segregation versus temperature (15).

Radiation-enhanced segregation of P and Si has been observed in 304 SS irradiated with neutrons to a fluence of 9×10^{20} n/cm² at 300°C (15). This observation is the lowest temperature at which radiation-enhanced impurity segregation has been measured since the heavy ion and electron irradiation studies were conducted at temperatures of 400°C and above. In an effort to evaluate the temperature dependence of radiation-enhanced impurity segregation, Simonen and Jones (16) calculated solute segregation kinetics using a non-equilibrium model by Lam et al. (17). The results of this calculation are shown in Figure 2 with surface impurity concentration versus irradiation temperature for different displacement rates. The data for a displacement rate of 5×10^{-4} dpa/s corresponds to the heavy ion irradiation data of Brimhall et al. (11) and the model was calibrated to this data. The parameters chosen to fit the model to experimental data were found to be physically realistic, so it was concluded that the model was a reasonable representation of the physical processes occurring during irradiation. At displacement rates more consistent with in-reactor conditions or structural materials in a near-term fusion reactor, the impurity segregation after 1 dpa exceeds that observed with heavy ion irradiations. Also, segregation decreases rapidly with temperature down to about 200°C but reaches a minimum at 100°C with measurable segregation predicted at a temperature of 50°C. This low-temperature segregation occurs because of the mobility of interstitials at low temperature. Therefore, these calculations predict that radiation-induced solute segregation may occur at temperatures well below 100°C so that if impurity segregation is a primary factor in IASCC, it could occur at temperatures below 100°C. The threshold fluence for IASCC at low temperatures will obviously be greater than at 300°C and based on the calculated impurity segregation at 300°C this threshold would exceed 30 dpa at 100°C.

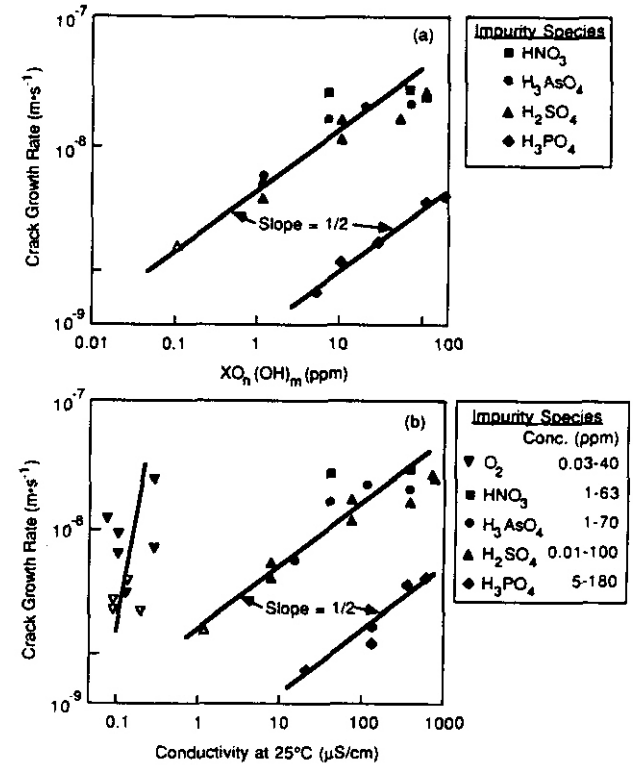

Fig. 3. Crack growth rate versus oxyacid concentration and conductivity for sensitized 304 SS at 288°C (18).

Stress-Corrosion Cracking in Aqueous-Salt Coolants

Concentrated lithium salt solutions are being considered as coolants for near-term fusion reactors. The data base for SCC of austenitic stainless steels in concentrated salt solutions is very sparse with the exception of $MgCl_2$. Both intergranular and transgranular SCC can occur in boiling (155°C) $MgCl_2$; however, the propensity for cracking is related to the concentration of Cl^-, which destroys the passive film-forming capacity of austenitic stainless steels. There is no evidence that concentrated $LiNO_3$ solutions affect passivity of stainless steels, although there have been few studies. Shack et al. (18) have evaluated the effect of the concentration of several oxyacids on the SCC of sensitized 304 SS with the results shown in Figure 3. Several of the oxyacids had identical effects as a function of concentration while H_3PO_4 had the least effect. Shack et al. (18) concluded that the oxyacid effect was due primarily to the change in solution conductivity and the resulting change in metal ion transport within the crack tip and not to a change in the pH accompanying the addition of the oxyacid. A crack velocity exceeding 10^{-6} cm/s was observed for a nitrate concentration of 100 ppm which if extrapolated to a 1% (10,000 ppm) salt solution would predict a crack growth rate of 10^{-5} cm/s. At this crack velocity, a stress-corrosion crack will propagate through a 1-mm-thick wall in 3 h.

There are several significant differences between the results of Shack et al. (18) and the conditions that are likely to exist in an ITER type reactor. First, their material was sensitized while ITER material will not be sensitized if low-carbon austenitic stainless steel and proper welding procedures are used. Other differences include the temperature of 288°C, the low pH, and the type of stainless steel, 304 SS versus 316 SS. Since the data base for assessing the effect of concentrated lithium salt solutions on SCC of 316 SS or PCA is essentially non-existent, it will be necessary to obtain this data for the relevant fusion reactor conditions.

Effects of Radiolysis

There are a number of processes by which radiolysis can affect the water chemistry and electrochemical potential of a material. Of particular interest to an ITER type reactor is the effect of radiolysis of "pure" water and aqueous-salt coolants on SCC. A stress-corrosion cracking study by Fujita et al. (4) indicated that the strain to failure of sensitized 304 SS in water at 250°C with 8 ppm oxygen decreased from 15% to 10% in the presence of gamma radiation. This difference suggests an increase in the crack growth rate of about 50%, which is a relatively small effect. Again, this is for sensitized material and an elevated temperature so the conditions are not the same as expected in an ITER type fusion reactor.

Changes in the nitrite to nitrate ratio can occur as a result of radiolysis. An example of a 3-fold increase in this ratio for a ground water was observed at a flux of 10^4 rad/h by Van Konynenburg (19), although for most of the ground waters and a high purity water evaluated the nitrite to nitrate ratio remained constant. At a gamma-flux of 2 x 10^5 rad/h the nitrite to nitrate ratio remained fairly constant at about 1. Van Konynenburg explained these differences as being due to the catalytic activity of the rock and crushed glass included in the water during irradiation. The case for high purity water probably relates best to the ITER fusion reactor environment, which suggests no change in the nitrite to nitrate ratio with time in either the low-flux or higher-flux (2 x 10^5 rad/h) experiments. The obvious concern for the ITER reactor environment is whether other substances will be immersed in the coolant with catalytic activity which will raise the nitrite to nitrate ratio. Corrosion and stress-corrosion experiments of fusion reactor materials in the aqueous-salt coolant and a gamma-flux is necessary to properly evaluate the ITER-relevant conditions.

Radiation Hardening Effects

Jacobs et al. (20) have measured the tensile properties of 304 SS, 304L, 316, and 316NG following irradiation at 288°C. After irradiation to a fluence of 2.5 x 10^{21} n/cm²; exceeds the neutron fluence threshold for IASCC, the total elongations were 11.2, 7.3, 16.7 and 20.5% for the 304, 304L, 316, and 316NG, respectively and the reductions of area were 32.3, 35.7, 47.9 and 40.3% for the same steels, respectively. The yield strengths had increased to about 650 MPa. All steels showed significant IASCC in post-irradiation constant extension rate tests in 288°C water, with the 304L steel showing evidence of IASCC at a fluence of 8.3 x 10^{20} n/cm²; IASCC was not apparent in the other steels until a fluence of 2.1 x 10^{21} n/cm². The total elongation and reduction of area for the 304L steel was 20 and 47.3%. respectively, at this fluence; thus the toughness was greater than the other steels at the onset of IASCC. Therefore, IASCC does not appear to be directly related to a decrease in toughness. Significant differences in the radiation hardening and toughness of stainless steels irradiated at 100 and 300°C are not expected although for 316SS irradiated to low fluence in R-NS II, Heinisch et al. (21) observed a factor of five difference in the yield strength increase at 90°C relative to 290°C. A separate evaluation of radiation hardening and embrittlement is not necessary to assess IASCC for ITER design considerations if post-irradiation stress-corrosion tests are conducted.

Material Recommendations

Based on our present understanding of SCC and IASCC of austenitic stainless steels in aqueous environments, it is possible to make the following recommendations regarding the selection and fabrication of com-

ponents for an ITER type reactor:

1. Use a low-carbon grade austenitic stainless steel, certify material chemistry prior to fabrication.
2. Use proper weld procedures as determined by the LWR industry.
3. Specify a steel with the lowest possible P, S, and Si impurity concentrations.
4. Maintain strict water chemistry control for oxygen, chlorides, sulfur compounds, etc.
5. Transient conditions (temperatures, stresses, water chemistry) exacerbate SCC; devise startuplshutdown procedures that minimize these effects (input from those in the LWR industry would be very useful to help define these procedures).
6. Eliminate the presence of crevices and galvanic couples.
7. Minimize surface damage caused by grinding and pitting during material cleaning and cold work and residual stress caused by fabrication processes such as welding.

FUTURE DIRECTION

Continued evaluation of critical issues in the SCC and IASCC of fusion reactor materials is planned, as are stress-corrosion tests in water and aqueous-salt coolants and a gama-flux of 10^5 rad/h.

REFERENCES

1. W. L. Clarke. D. A. Hale. and M. Siesler. "Effect of Gamma Radiation on SCC Testing of Irradiated Stainless Steel in High iemperature Water," in Proceedings of Second International-Symposium on Environmental Degradation of Materials in Nuclear Power Systems - Water Reactors, Monterey, California, Sept. 9-12, 1985.
2. R. H. Jones and E. P. Simonen., "Effect of Irradiation on Materials Properties and Stress Corrosion Cracking Susceptibility," DOE/EPRI Workshop on Irradiation Assisted Stress Corrosion Cracking, Charlotte, North Carolina, June 1986.
3. DOE/EPRI Workshop on Irradiation Assisted Stress Corrosion Crackinu.. eds. D. Keefer and R. L. Jones, Charlotte, North' Carolina, June 1986.
4. N. Fujita, M. Akiyama, and T. Tamura, Corrosion 37(6), p. 335 (1981).
5. M. Kuribayashi and H. Okabayashi, J. Jpn. Inst. Metals 46, p. 170 (1982).
6. R. H. Jones and W. G. Wolfer, "Modeling Crack Growth Processes in Fusion Reactor Materials," J. Nucl. Matls. 1221123, pp. 379-390 (1984).
7. R. H. Jones, "Some Considerations of Radiation Effects on Stress Corrosion Cracking of Fusion Reactor Materials," Damage Analysis and Fundamental Studies Quarterly Report, April-June 1984, p. 61, DOE/ER-0046/18.
8. R. H. Jones, "Some Radiation Damage-Stress Corrosion Synergisms in Stress Corrosion," in Proceedings of Second International Symposium on Environmental Degradation of Materials in Nuclear Power Systems - Water Reactors, Monterey, California, Sept. 9-12, 1985.
9. M. O. Speidel, Metall. Trans. A, 12A, p. 779 (1981).
10. S. M. Bruemer and A. B. Johnson, Jr., in Proceedings of the International Symposium on Environmental Degradation of Materials in Nuclear Power Systems - Water Reactors, Myrtle Beach, South Carolina, August 1983, p. 571.
11. J. L. Brimhall, D. R. Baer, and R. H. Jones, "Radiation Induced Phosphorus Segregation in Austenitic and Ferritic Alloys," in Proceedings of the Third Fusion Reactor Materials Meeting, eds. J. B. Whitley, K. L. Wilson and F. W. Clinard. J. Nucl. Matl. 122. p. 196 (1984).
12. K. Fukuya, S. Nakahigashi and M. Terasawa, Scripta Metall. 19, pp. 959-962, (1985).
13. F. Garzarolli, D. Alter, and P. Dewes, Proceedings of the Second Internal Symposium on Environmental Degradation of Materials in Nuclear Power Systems - Water Reactors, Monterey, p. 131, (1985).
14. P. L. Andresen and C. L. Briant, Third International Conference on Environmental Degradation of Materials in the Nuclear Power Industry - Water Reactors, Traverse City, Michigan, September 1987.
15. K. Fukuya, S. Nakahigashi, and M. Terasawa, ibid.
16. E. P. Simonen and R. H. Jones, ibid.
17. N. Q. Lam, P. R. Okamoto, H. Wiedersich and A. Taylor, "Radiation-Induced Solute Segregation and Precipitation in Alloys," Metall. Trans. 9A, pp. 1707-1714, (1978).
18. W. J. Shack, T. F. Kassner, P. S. Maiya, J. Y. Park, and W. E. Ruther, "Environmentally Assisted Cracking in Light Water Reactors: Semiannual Report," April-September 1985, NUREG/CR-4667, Vol. I.
19. R. A. Van Konynenburg, "Radiation Chemical Effects in Experiments to Study the Reaction of Glass in an Environment of Gama-Irradiated Air, Groundwater and Tuff," May 2, 1986, UCRL-53719.
20. A. J. Jacobs, G. P. Wojadlo, K. Nakata, Y. Yoshida and I. Masaoka, Proceedings of the Third International Conference on Environmental Degradation of Materials in Nuclear Power Industry - Water Reactors, Traverse City, Michigan, September 1987.
21. H. L. Heinisch, S. D. Atkin and C. Martinez, J. Nucl. Matl. 141/143, pp. 807-815 (1986).

CORROSION AND COMPATIBILITY STUDIES IN FLOWING LITHIUM ENVIRONMENTS -

O. K. Chopra, A B. Hull. and D. L. Smith (Argonne National Laboratory)

OBJECTIVE

The objective of this program is to investigate the influence of a flowing lithium environment on the corrosion behavior and mechanical properties of structural alloys under conditions of interest for fusion reactors. Corrosion rates are determined by measuring weight change and depth of penetration of internal corrosion as a function of time, temperature, and liquid metal purity. These measurements, coupled with metallographic evaluation of the alloy surface, are used to establish the mechanism and rate-controlling processes of the corrosion reactions. Studies of the long-term environmental effects on mechanical properties focus on nonmetallic element transfer and surface reactions.

SUMMARY

A new experimental facility has been constructed for investigating the corrosion/mass transferldeposition mechanisms that are anticipated when liquid lithium is used as a tritium breeding material for fusion reactors.

PROGRESS AND STATUS

Introduction

To date, studies on the corrosion behavior of structural materials in liquid lithium systems have focused on effects of time, temperature, and liquid metal purity.[1-3] The results indicate that mass transfer and deposition most likely will determine the maximum operating temperature of liquid lithium blanket systems. Available data are insufficient to quantify the influence of additional system parameters on corrosion. These additional parameters include flow velocity, system temperature gradient (ΔT), magnetic field, bimetallic system effects, and surface area/temperature profile. Previous studies[4,5] that examined velocity effects in a forced circulation loop were conducted on Type 316 SS in austenitic stainless steel loops. Corrosion data indicate that chemical interactions between allo elements and nitrogen in lithium play a dominant role in the dissolution behavior of austenitic steels.' Consequently, the velocity effect data obtained for austenitic stainless steels may not be representative of other structural materials. Also information on the effects of AT on corrosion of structural materials is very limited. Additional work is needed to clearly establish the relative effects of system parameters on corrosion/mass transfer in lithium blanket structures.

This report describes a new experimental facility for investigating the corrosionlmass transferldeposition mechanisms at characteristic velocities and system temperatures and for quantifying the influence of the system parameters mentioned above.

Experimental capability of the new test facility

The new Argonne Lithium Corrosion Experiment (ALICE), which is constructed of ferriticlmartensitic steel (Fe-9Cr-1Mo, ASTM P9 A355), simulates conditions projected for a liquid metal heat transport system. ALICE can be used to assess various containment materials in terms of their corrosion rates, mass transfer, and material deposition all as functions of time, temperature, velocity, AT, and lithium purity conditions. Candidate containment materials to be investigated include vanadiun alloys and ferritic steels.

The capabilities of the existing ANL fatigue and failure testing loop (FFTL-3) for corrosion studies in lithium and lithium/lead environments are limited to low velocities (Table 1), at which circulation provides only for impurity control of the liquid metal. The new test facility provides experimental capability for investigating velocity effects on the corrosionlmass transferldeposition processes in liquid metal systems.

The new test facility consists of two counterflow primary loops (Fig, 1). In Loop 1, lithium is circulated from the supply vessel to the inner specimen chambers of the two annular test sections (A and B) and back to the supply vessel. In test section A, lithium is heated to the maximum loop operating temperature; in test section B, it is cooled. Loop 2 includes the supply vessel, the outer chambers of the two annular test sections, and a low-velocity, isothermal test section. The lithium supply to the isothermal test section is through a heat exchanger which can be used to change the maximum temperature of test sections A and B. A secondary loop, or lithium purification loop, consists of the supply vessel, a counterflow heat exchanger exiting from the supply vessel to reduce the lithium temperature, and a cold trap. The primary loops each utilize two induction pumps in series to provide the desired high velocities. A single pump is provided for the secondary loop. The details regarding the design calculations and strategies are presented elsewhere.

Table 1. Comparison of New Test Facility with Existing ANL FFTL-3 LOOP

Parameter	ALICE	FFTL-3
Structural material	Fe-9Cr-1Mo (ASTM-P9 A355) Ferritic	Type 304 SS (austenitic)
Total Volume of lithium (ℓ)	26	20
Primary loop	forced circulation, two counterflow loops	forced circulation, single loop
Estimated lithium velocity (cm/s)	1 - 60	- 1
Secondary loop	cold trap	cold trap and magnetic trap
Experimental capabilities	corrosion/mass transfer/ deposition	corrosion/mechanical testing
Specimen exposure locations	two test sections with AT dynamic and an isothermal test section	two isothermal test sections
Test section length (m)	1.3	0.15
Maximum temperature (°C)	550	550
Minimum temperature (°C)	210 (cold trap)	210 (cold trap)

The elemental composition of the Fe-9Cr-1Mo stock (rod, plate, and pipe sections), determined by spectrochemical analyses and confirmed by microprobe analyses at ANL is presented in Table 2. In two cases, it was necessary to substitute alternate structural alloys. Since ferromagnetic materials cannot be used in the electromagnetic pumps and in the magnetic flowmeters. AISI Type 304 steel was used in these sections. Also, a commerical ferritic/martensitic steel (Type 4-3: Fe-12Cr) was used for the heat exchanger in the secondary loop. In both cases, the alternate materials are located in the low-temperature regions of the system.

The welds of Fe-9Cr-1Mo were produced with the gas tungsten-arc (GTA) process with filler inaterial of the same composition (AWS classification ER505). All welds were subjected to postweld heat treatment (PWHT) at 732°C for 1/2 to 1 h and then air cooled. After PWHT and cooling, the quality of welding was confirmed by dye penetrant testing, helium leak testing of major welded components (vessels. heat exchanoers. cold traps), and nondestrictive radiography. In several cases, repiacement'welds were required to obtain satisfactory quality assurance.

This state-of-the-art test facility will provide lithium test flow velocities to 0.6 m/s, temperatures to 550°C, and system ΔTs up to 150°C. The major nonmetallic impurities, N, C, and H are controlled and monitored by different techniques. A hydrogen meter is installed in the isothermal test vessel. Hydrogen is monitored by equilibrating yttrium samples in lithium and using the reported data[8] on the distribution coefficient of hydrogen between yttrium and lithium. Nitrogen is controlled by hot gettering with Ti foils immersed in the Li stream to form a surface nitride and also by dissolved getters such as calcium metal.

There is a strong indication[9] that the cold trap assists in the control of carbon below the upper concentration limits imposed by temperature-dependent solubility constraints. In the cold trap region, the two additional valves (Fig. 1) are included for installation of a magnetic trap or a lithium sampling apparatus.

Loop operation

ALICE will be operated over a range of temperatures and lithium flow rates. The absolute and differential temperatures and flow velocities in the loop (Fig. 1) can be adjusted by varying the heat input on the supply vessel and the two test sections. and by adjusting the flow in the different loops with the five induction pumps. A comparison between the design parameters of the new system and the existing FFTL-3 loop is given in Table 1.

ARGONNE LITHIUM CORROSION EXPERIMENT (ALICE)

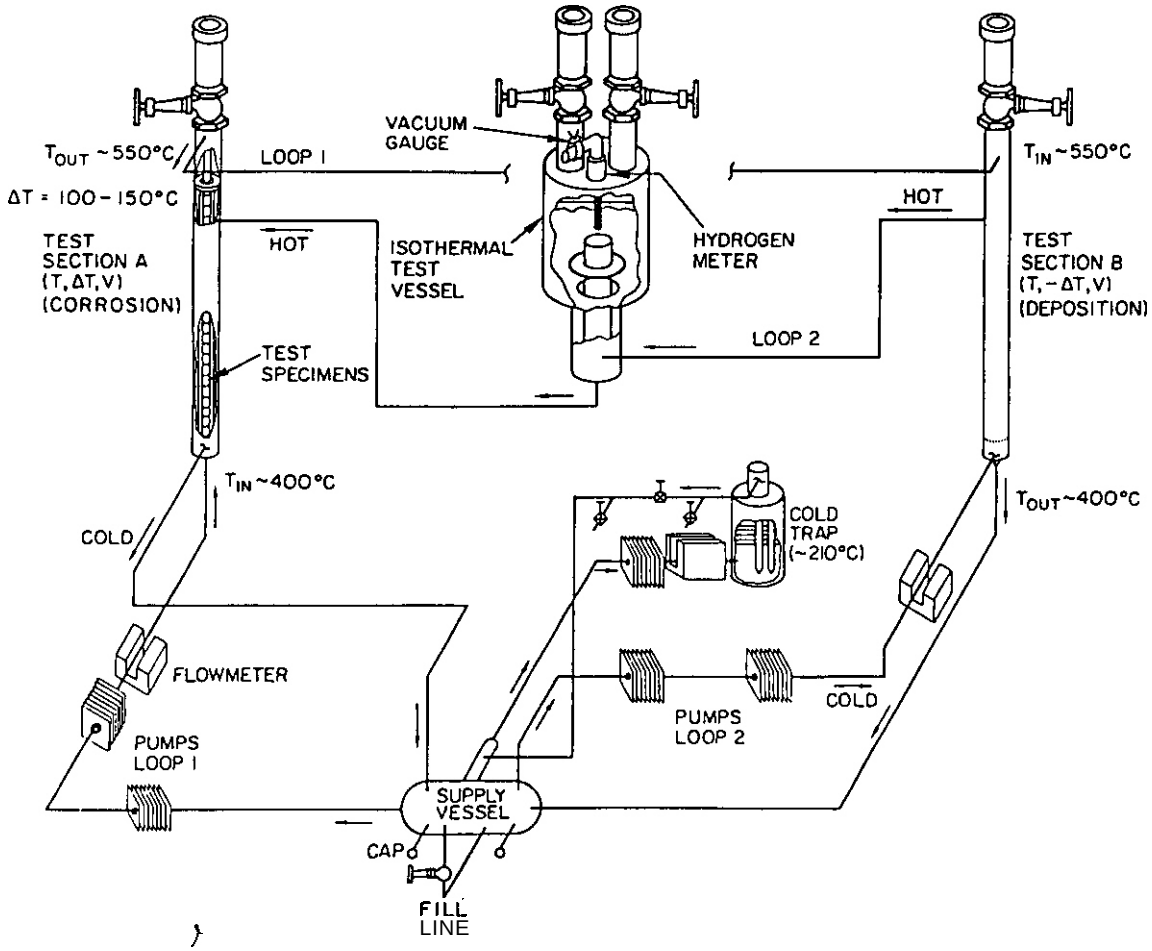

Fig. 1. Isometric view of the forced-circulation Li loop ALICE.

Four specimen sample ports are present in the facility: two in the isothermal test vessel and one in each of the two test sections. Every sample port has a double valve arrangement to isolate the lithium-argon atmosphere from the environment.

The material samples to be immersed in the lithium are contained in a specimen holder. Threaded retraction rods allow insertion and removal of the specimens and sheath tubes. The cylindrically shaped test specimens are stacked in a vertical column (Fig. 1) to create a continuous tube. Lithium flow velocities are maximized by flow through the annulus between the test specimens and the inner chamber of test sections A and B.

During long-term corrosion experiments, chemical and metallurgical changes in the test specimens are evaluated by optical and scanning electron microscopy and by weight loss measurements. The specimens are weighed and evaluated at well-defined inte als, and the corrosion rate constants and mechanisms are analyzed by means of the XLRATE algorithm.[**] The chemical purity of the lithium is also evaluated as a function of time by means of other chemical algorithms.[11]

CONCLUSIONS

A new lithium corrosion/mass transfer test facility, which is constructed of ferritic/martensitic steel (Fe-9Cr-1Mo), simulates conditions projected for a liquid metal heat transport system. The test facility provides test velocities to 0.5 m/s, temperatures to 550°C, and system ΔTs up to 150°C. The corrosion test

Table 2. Elemental Composition (wt%) of Structural Materials Used in the Fabrication of New Test Facility

ELEMENT	Structural Material: 0.38" OD Tube	0.75' OD Test Section Interior	1.25" OD HEX Interior on Isothermal Test Vessel	3" OD Supply Vessel	8" OD Static Test Vessel
C	0.16	0.16	0.10	0.14	0.12
Mn	0.58	0.47	0.54	0.42	0.32
Si	0.45	0.30 (0.27)	0.22 (0.87)	0.23 (0.74)	0.33
P	0.024	0.29	0.29	0.024	0.21
S	0.015	0.32	0.016	0.019	0.28
Ni	0.18	0.16	0.18	0.24 (0.28)	0.22 (0.27)
Cr	8.41	8.13 (8.79)	8.35 (8.28)	8.35 (8.63)	8.23 (8.72)
Mo	0.98	0.82 (0.76)	0.96 (1.08)	0.93 (1.16)	0.94 (0.81)
N	0.0421	0.0337	0.0264	0.0269	0.0399
Fe	88.74	89.49 (88.18)	89.26 (87.76)	89.01 (87.30)	89.54 (89.03)

*Determined by spectrochemical analyses, and confirmed by microprobe analyses (values in parentheses).

region simulates a fusion reactor blanket region with a low inlet temperature and a higher ($\Delta T \sim 150°C$) outlet temperature. Test specimens in the deposition region provide a measure of the deposition processes that occur in a heat exchanger as the liquid metal is cooled ($\Delta T \sim 150°C$). In addition to temperature and flow control, tne facility provides for control and monitoring of impurities in the liquid.

FUTURE WORK

Shakedown tests will be conducted to establish liquid metal purity and the loop operating conditions, eg., velocity and test section AT. The concentrations of nonmetallic impurity elements will be monitored and minimized.

REFERENCES

[1] O. K. Chopra, O. L. Smith, P. F. Tortorelli, J. H. DeVan, and D. K. Sze, Fusion Technol. 8(1985) 1956.

[2] O. K. Chopra and P. F. Tortorelli. J. Nucl. Mater. 122&123(1984) 1201.

C31 P. F. Tortorelli and O. K. Chopra, J. Nucl. Mater. 103&104(1981) 621.

C41 D. G. Bauer, W. E. Stewart, I. N. Sviatoslavsky, and D. K. Sze, Proc. 2nd Int. Conf. Liquid Metal Technology in Energy Production, Richland, Washington. April 20-24, 1980. CONF-800401-P2, pp. 13-73. J. M. Kahlke, ed., U. S. Department of Energy (1980).

[5] G. A. Whitlow, W. L. Wilson, W. E. Ray, and M. G. Down, J. Nucl. Mater. 85&86(1979) 283.

[6] O. K. Chopra and D. L. Smith, J. Nucl. Mater. 141-143(1986) 584.

C71 D. L. Smith, O. K. Chopra, and A. B. Hull, Proc. Int. Symp. on Fusion Nuclear Technology, Tokyo, Japan, April 10-15, 1988.

[8] D. L. Smith, R. H. Lee, and R. M. Yonco. Proc. 2nd Int. Conf. Liquid Metal Technology in Energy Production, Richland, WA, April 20-24, 1980, CONF-800401-P2, p. 2, U. S. Department of Energy (1980).

[9] R. M. Yonco and M. I. Homa. J. Nucl. Mater. 138(1986) 117.

[10] A. B. Hull and J. R. Hull, Water Resour. Res. 23(1987) 707.

[11] A. 8. Hull, PhD Dissertation, Northwestern University, Evanston, IL, (1987) p. 240.

7. SOLID BREEDING MATERIALS

MECHANICAL PROPERTIES OF SOLID BREEDER MATERIALS - C. Y. Chu,* R. B. Poeppel, J. P. Singh, and K. C. Goretta
(Argonne National Laboratory)

OBJECTIVE

The objectives of this program are to characterize the room-temperature mechanical properties and high-temperature creep properties of selected lithium ceramics.

SUMMARY

Room temperature strength, fracture toughness. Young's modulus, and thermal-shock resistance were determined for 68 to 98% dense lithium orthosilicate (Li_4SiO_4) specimens. In the low-density regime, both strength and fracture toughness were controlled by the density of the specimen. At high density, the strength depends on grain size. Young's modulus values ranged from 30 to 103 GPa for densities ranging from 68 to 98% TD. A critical quenching temperature difference in the range of 150 to 170°C was observed in thermal-shock tests of bar speciimens. Steady-state creep tests indicated that 90% dense Li_4SiO_4 fractures at $T \leq 800$°C before reaching steady state and deforms plastically at above 900°C. At 900°C, it is more creep-resistant than Li_2O, about equal to Li_2ZrO_3, and less creep-resistant than $LiAlO_2$ and Li_2SiO_3.

PROGRESS AND STATUS

Introduction

Lithium-bearing ceramics are being considered as blanket materials for the breeding of tritium in fusion power reactors. Lithium orthosilicate (Li_4SiO_4) is a potential breeder material because of its high lithium content and high stability relative to other lithium-containing ceramics. Room temperature strength and toughness and high-temperature creep resistance are important properties relative to installation and operation of breeder blankets, and are therefore essential for designing an efficient blanket.

Experimental procedures

Li_4SiO_4 powder was synthesized by the solid-state reaction of lithium oxide with amorphous silica, and sintered at between 900 and 1000°C to obtain rectangular bars (49 x 6 x 3 mm) and cylindrical pellets (D = 3.6 mm, L = 5.0 mm) for mechanical tests. The sintering schedule, sintered density, grain size, and elastic modulus for five batches of Li_4SiO_4 are listed in Table 1.

Table 1. Sintering schedule, sintered densities, average grain size, and elastic modulus for five batches of Li_4SiO_4

Batch	Sintering Temp. (°C)[a]	Hold Time (h)	Density (% TD)[b]	Average Grain Size (μm)	Elastic Nodulus (GPa)
B1	900	0	68	4	38.2
B2	950	0	77	5	57. I
B3	1000	0.15	93	10	103.2
B4	1000	4	98	25	82.8
B5	1000	8	96	50	94.9

[a]Heating rate was 100°C/h.
[b]Theoretical density of Li_4SiO_4 was taken to be 2.39 g/cm^3.

As-sintered rectangular bars with various densities and grain sizes were subjected to flexural strength and fracture toughness tests. Flexural strength was measured in the four-point bending mode with an Instron testing machine. The support span was 44 mm, the loading span was 22 mm, and the crosshead speed was 1.21 mm/min. Fracture toughness was measured by the single-edge notched beam (SENB) technique with a notch width of 0.6 mm. The specimens were ground to a surface finish of 6000 grit. Elastic modulus was determined by ultrasonic velocity measurement. Thermal-shock resistance was determined by measuring the flexural

*Work performed in partial fulfillment of requirements for M.S. degree, Illinois Institute of Technology, Chicago, IL 60616.

strength of 49 x 6 x 3-mm specimens before and after quenching from various high temperatures into silicone oil at room temperature.

High-temperature constant-strain-rate (CSR) tests were performed in a 99.9% argon gas atmosphere in direct compression with an Instron Model 1125 universal testing machine. 90% dense cylindrical pellets were heated to temperatures ranging from 750 to 1025°C (0.67 to 0.86 T_m, where T_m is the melting temperature in Kelvin) and subjected to strain rates ranging from 5×10^{-6} to 2×10^{-3} s^{-1}. After the CSR test. specimens were weighed and their dimensions measured immediately upon removal from the apparatus in order to determine whether the density changed during testing.

Results and discussion

Figure 1 shows the flexural strength, and Fig. 2 the fracture toughness, of Li_4SiO_4 as a function of density and grain size. In the low-density (up to 90% TD) regime, the strength and toughness of Li_4SiO_4 are primarily controlled by the density of the specimen. The flexural strength was observed to increase from 33 to 58 MPa as the density increased from 68 to 90% TD. The corresponding increase in fracture toughness was observed to be from 0.6 to 1.1 $MPa\sqrt{m}$. For high-density specimens (>90% TD), the strength decreases with increasing grain size. The critical stress intensity factor K_{IC} for an SENB specimen can be related to the critical applied stress σ_c by $K_{IC} = \sigma_c(a)^{1/2}Y(a/W)$, where Y is a dimensionless constant which depends on the geometry of the loading and the crack configuration, a denotes notch depth, and W denotes sample width for a four-point bend specimen. It was observed that the strength could be correlated to fracture toughness by using the above equation far specimens with densities of up to 93% TD. This suggests that the critical flaw size does not change with density in the range from 68 to 93% TD (grain size from 4 to 10 μm). The Young's modulus of Li_4SiO_4 ranged from 38.2 to 103.2 GPa for densities between 68 and 93% TO and, as expected, decreased with increasing porosity for specimens in the range from 68 to 93% TD.

The results of thermal-shock experiments, shown in Fig. 3, indicate that the strength of the material is not degraded for values of quenching temperature difference (AT) up to 150°C. At a critical value ΔT_c = 150 to 170°C, the strength decreased sharply from 85 MPa to a value of 10 MPa, after which it remained constant with further AT increase (up to 300°C). This strength behavior as a function of AT is consistent with the prediction of the fractural-mechanical theory for thermal shock developed by Hasselman.

In high-temperature steady-state creep tests, 90% dense specimens fractured at 800°C and below before reaching steady state. For tests above 900°C in which fracturing did not occur, a clear eteady-state Stress σ_s was established. It was found that no appreciable grain growth or densification occurred during deformation. For polycrystalline materials, the steady-state strain rate for a given temperature is usually proportional to σ^n, where n is a characteristic exponent corresponding to the dominant creep mechanism. The stress exponent n can be obtained by plotting ln (strain rate) vs ln σ_s and was determined to be 3.6 at temperatures above 950°C, and to increase with decreasing temperature. This phenomenon may be a consequence of the transition from extrinsic to intrinsic control of deformation. The steady-state flow stress measured at 900°C for Li_4SiO_4 can be compared with those of other lithium-containing ceramics which are being considered for fusion blankets. As shown in Fig. 4, for a temperature of 900°C, 90% dense Li_4SiO_4 is more resistant to plastic flow than is Li_2O, about equal to Li_2ZrO_3, and less resistant than $LiAlO_2$ and Li_2SiO_3. (The value of flow stress for $LiAlO_2$ is interpolated from data at 800 and 1000°C.)

CONCLUSIONS

1. In the low-density regime, both the flexural strength and toughness of Li_4SiO_4 were controlled by the density of the specimen. The strength and fracture toughness increased from 33 to 58 MPa and 0.6 to 1.1 $MPa\sqrt{m}$, respectively, as the density increased from 68 to 93% TD.

2. The thermal-shock experiment indicated a critical quenching temperature difference in the range of 150 to 170°C.

3. At temperatures of 800°C and lower, Li_4SiO_4 fractured without exhibiting appreciable plasticity when deformed at slow strain rates.

4. Steady-state creep tests suggested that the deformation of 90% dense Li_4SiO_4 is controlled by dislocation climb at 900°C. At this temperature, Li_4SiO_4 is more resistant to plastic flow than Li_2O, about equal to Li_2ZrO_3, and less resistant than $LiAlO_2$ and Li_2SiO_3. For temperatures below 950°C, the stress exponent n increases with decreasing temperature. This may be a consequence of transition from extrinsic to intrinsic control of deformation.

FUTURE WORK

No more experimental work will be done on this project. The completed work will be the subject of four conference presentations.

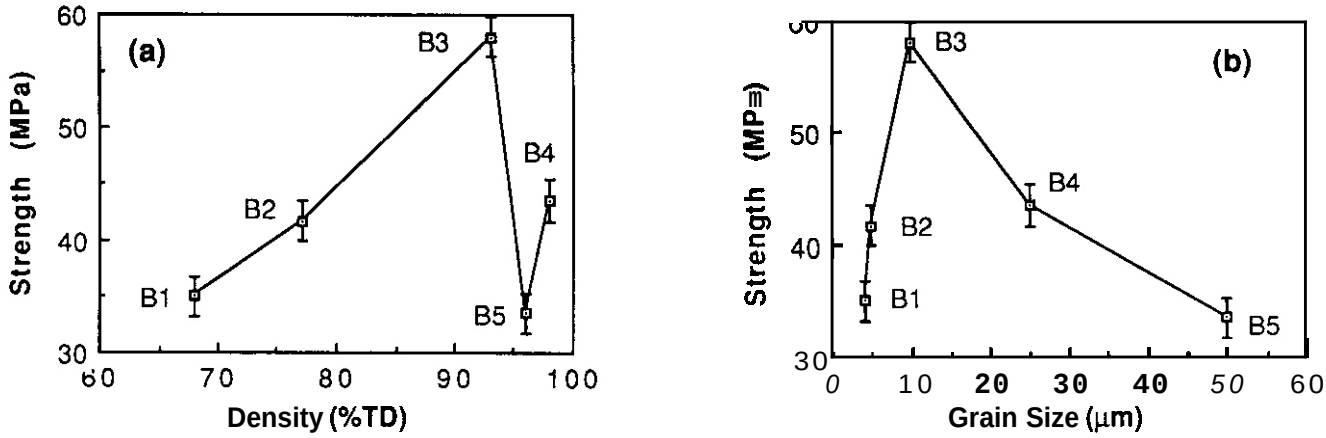

Fig. 1 Flexural strength as a function of (a) density and (b) grain size.

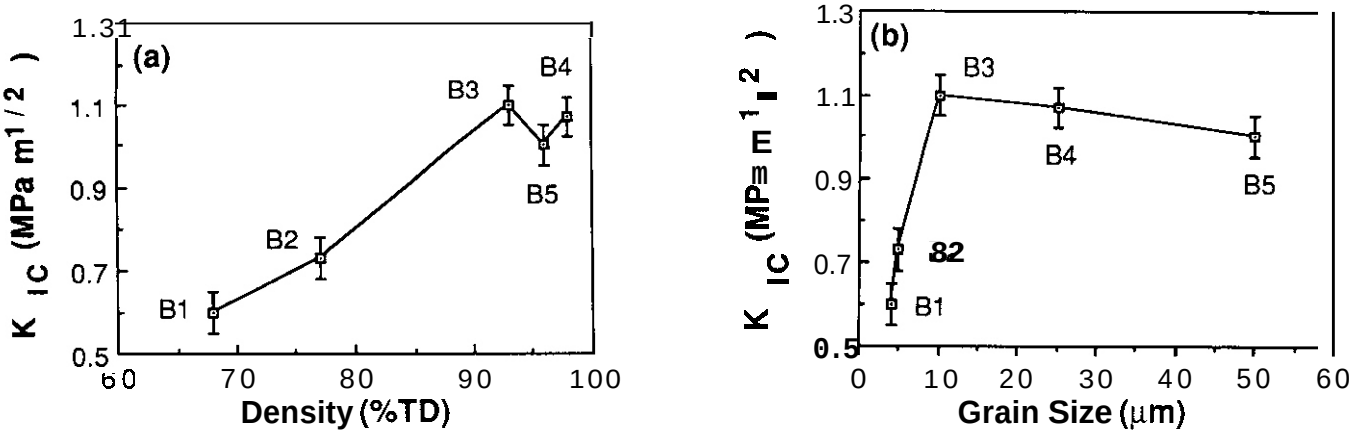

Fig. 2. Fracture toughness as a function of (a) density and (b) grain size.

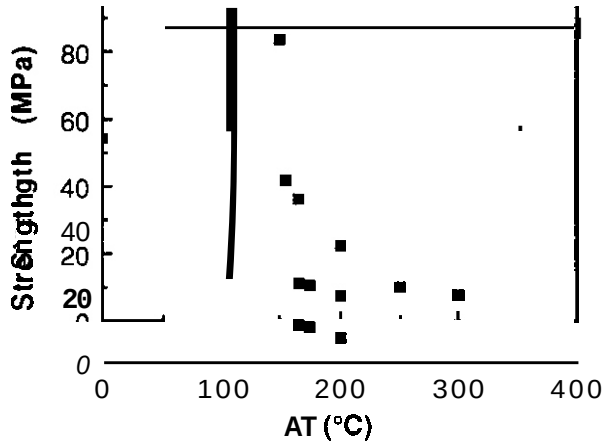

Fig. 3. Fracture strength as a function of temperature difference.

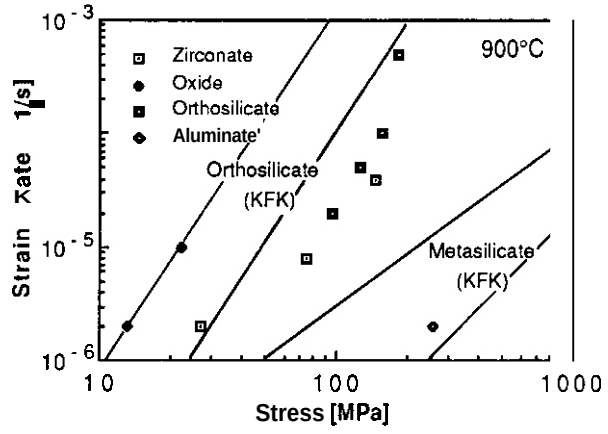

Fig. 4. Comparison of the steady-state stress vs strain rate behavior of Li-containing ceramics.

REFERENCES

1. C. Y. Chu, K. Bär, J. P. Singh. R. B. Poeppel, and M. C. Billone, "Relationship Between Fabrication Parameters and Structural Characteristics of Sintered Lithium Orthosolicate," presented at the International Symposium on Fusion Nuclear Technology, Tokyo, Japan, April 10-15, 1988; paper to be published in Proceedings.

2. K. Bär, C. Y. Chu, J. P. Singh, K. C. Goretta, J. L. Routbort, M. C. Billone, and R. B. Poeppel, "Mechanical Properties and Deformation of Polycrystalline Lithium Orthosilicate," ibid.

3. C. Y. Chu, K. Bär, J. P. Singh, and R. B. Poeppel, "Preparation and Fabrication of Lithium Orthosolicate Powder and Pellets," presented at the 90th Annual Meeting of the American Ceramic Society, Nuclear Division, Cincinnati, Ohio, May 1-5, 1988.

4. K. Bär, C. Y. Chu, J. P. Singh, K. C. Goretta, J. L. Routbort, and R. B. Poeppel, "Mechanical Properties of Polycrystalline Lithium Orthosilicate," ibid.

ADSORPTION, DISSOLUTION, AND DESORPTION CHARACTERISTICS OF THE $LiAlO_2$-H_2O SYSTEM

Albert K. Fischer and Carl E. Johnson (Argonne National Laboratory)

INTRODUCTION

Adsorption of H_2O, dissolution of OH^-, and rates of evolution of $H_2O(g)$ are being measured for the $LiAlO_2$-$H_2O(g)$ system to provide thermodynamic and kinetic data for these processes for $LiAlO_2$, a candidate for a tritium breeder in fusion reactors. Such data relate to the issues of tritium retention and release, and, hence, to concerns about tritium inventory in ceramic tritium breeder materials. The information will enable (1) conparison of candidate breeder materials, (2) calculation of operating conditions, and (3) elucidation of the principles underlying the behavior of tritium in breeder materials.

The most recent corrections have been applied to the isotherms for H_2O adsorption and OH^- solubility on and in $LiAlO_2$ for the temperatures of 400, 500, and 600°C. For adsorption, these corrections are for the dissolution process that proceeds simultaneously with adsorption. For solubility, the corrections are for residual hydroxide corresponding to baseline conditions. The observed higher degree of adsorption at 500°C compared with that at 400°C is to be understood as reflecting two chemisorption processes with different activation energies. An atomistic basis for the distinction is given. Solubility decreases with rising temperature.

RESULTS AND DISCUSSION

Adsorption measurements are made by the frontal analysis technique of gas chromatography and solubility data are provided by measurement of the uptake of $H_2O(g)$ after the adsorption is finished. The technique has been described in earlier reports.

Until now. the working assumption in the analysis of the adsorption-dissolution curves has followed the common dictum that the adsorption process is considerably more rapid than the dissolution process. As a result, only a negligible contribution was expected from dissolution to the apparent quantity of adsorbed $H_2O(g)$. The observed sharpness of the breakthrough points has tended to support this view. Despite this for high temperature systems such as those being studied, in which diffusion can become more rapid, it was considered worth testing the assumption. One way would be to repeat the measurements with a sample of different surface to volume ratio. However, in addition to such a course being expensive in terms of effort, there would arise questions of accurate reproduction of all other factors that might be influential: for example, more material of different particle size from the same batch is not available.

Another way to utilize the kinetic information contained in the existing data to assess the diffusional contribution. A procedure to do this was devised. It involves fitting an equation to the dissolution curve over the time interval immediately after adsorption and at least equal in length to the adsorption time. The resulting expression for the dissolution rate is then used to calculate the amount of dissolution occurring during the adsorption period. In effect, the procedure is to back-extrapolate the dissolution to the time of sample injection. In order to apply this procedure, it is necessary to supply a correction for the point-by-point readings of the water analyzer. These corrections are for the response curve of the water analyzer in the "step-up" mode of a measurement. The necessary data were gathered and this was done for the various flow rates used in the measurements. An initial spot-check of the runs showed that the dissolution correction was indeed significant. Therefore, each one of the previously reported runs was reanalyzed according to this approach. The effect of the correction is to diminish the previously stated degree of adsorption and to increase the previously stated solubilities.

New data for the adsorption and solubility isothenns for 600°C (873 K) are included in the analysis together with the earlier data for 400°C (673 K) and 500°C (773 K). From the raw data, before refining the data analysis in the manner described above, it appeared that the degree of adsorption at 600°C is less than at the two lower temperatures. This trend is not surprising, but there remained the earlier counter-intuitive finding that adsorption at 500°C was apparently greater than at 400°C. Additional experimental evidence was sought in this period to resolve this point. Two additional measurements of adsorption at 400°C and at 500°C were made at closely similar partial pressures of $H_2O(g)$ and in pairs closely spaced in time (within a day). The results reinforced the earlier conclusion about greater adsorption at 500°C than at 400°C. The new data and the earlier data were pooled. The rationale for the apparently inverted relationship between the 400 and 500°C isotherms is well understood and is developed below.

Figure 1 shows the adsorption isotherms for 400, 500, and 600°C after the data points were corrected for dissolution. For clarity of the relationships of the isotherms to each other, they are coplotted without data points. The curves report the fraction of the surface, θ, covered by OH^- as a function of partial pressure of $H_2O(g)$, P_{H2O}. The isotherms are of the Freundlich type, as reported earlier. The 400°C and the 600°C isotherms are nearly parallel, with the respective regression equations being:

$$\log\theta = (0.593 \pm 0.141) + (0.517 \pm 0.182)\log(p_{H_2O})$$

and

$$\log\theta = (0.376 \pm 0.113) + (0.593 \pm 0.157)\log(p_{H_2O})$$

The 500°C isotherm is:

$$\log\theta = (0.055 \pm 0.018) + (0.359 \pm 0.024)\log(p_{H_2O})$$

The apparently anomalous observation of higher adsorption at a higher temperature is a fairly comn finding and was explained by Taylor in 1931 (H. S. Taylor, J. Am. Chem. Soc., 53(1931) 578). It had been observed that for some systems, experimentally measured adsorption isobars followed a course like ABCD in Fig. 2. The explanation follows from the existence of two separate adsorption processes which, if they could be separated, would follow the isobars ABE and FCD. The isobar FCD reflects a process with a relatively high activation energy compared to that of process ABE which could be unactivated. Starting from A, the system shows the expected decline in the amount adsorbed as temperature rises. The temperature is too low for process FCD to be appreciably activated and it therefore essentially does not function. At B, the temperature has risen enough so that sufficient activation energy is supplied to the process represented by the FCD isobar for that process to start contributing to the total amount adsorbed. A region of increasing adsorption with rising temperature has been entered. This second process becomes increasingly dominant as its rate rises with rising temperature until the system is described essentially by it alone. Then, adsorption again declines with increasing temperature in the expected way. A closely relevant example of increasing adsorption with rising temperature is the report by Gruber (J. Phys. Chem., 66(1962) 48) on the adsorption of H_2 on η-Al_2O_3: the amount adsorbed increased by a factor of three from 300 to 500°C. This is an issue that will become more relevant in the forthcoming measurements of H_2O adsorption in the presence of H_2.

In the present case, adsorption of $H_2O(g)$ on $LiAlO_2$ is viewed as involving two kinds of chemisorption. An atomic basis for such a distinction could be that one kind of chemisorption involves lithium ions and adjacent oxides, and the other kind involves aluminum ions and adjacent oxides. Slopes of approximately 0.5 observed for the 400 and 600°C isotherms are supportive of dissociative chemisorption, in which one molecule of H_2O forms two adjacent OH- groups. The observed lower value of slope for the 500°C curve is expected if additive effects from an additional process are involved. Evidence consistent with two surface processes in the evolution of water vapor from $LiAlO_2$ was reported earlier. During heatup after a run, the water evolution curve showed a double peak and was interpreted as showing that different kinds of sites were involved. Because more than one isotherm for a given process is needed if one is to calculate heats of adsorption, and the present situation provides only one isotherm for each process, conclusions on heats of adsorption must await measurements of additional isotherms.

Corrected isotherms for hydroxide solubility in $LiAlO_2$ are presented in Fig. 3 for 400, 500, and 600°C. In addition to the corrections originating in the dissolution occurring during adsorption, discussed above, there is also a correction for residual hydroxide that was discussed in earlier reports. This correction accounts for the hydroxide in equilibrium with the water content of the gas phase under baseline conditions. Applying this correction requires, at this time, an assumption about the solubility of $LiAl_5O_8$ in $LiAlO_2$. It is assumed that for the small amounts $LiAl_5O_8$ at issue here, the $LiAl_5O_8$ is a solute in $LiAlO_2$ rather than a separate phase. With this assumption, the expected slope is 0.4 in a plot of $\log(x_{OH^-})$ vs $\log(p_{H_2O})$.

Therefore, corrections for residual OH- were made for each of the data points to give slopes of 0.4. (If $LiAl_5O_8$ were a separate phase, a slope of 0.5 would be appropriate.) The regression equations for OH- solubility at 400, 500, and 600°C, respectively, are:

$$\log(x_{OH^-}) = (-2.420 \pm 0.054) + (0.401 \pm 0.057)\log(p_{H_2O})$$

$$\log(x_{OH^-}) = (-2.664 \pm 0.128) + (0.402 \pm 0.109)\log(p_{H_2O})$$

$$\log(x_{OH^-}) = (-2.835 \pm 0.315) + (0.401 \pm 0.524)\log(p_{H_2O})$$

The regression lines are plotted together in Fig. 3 without data points for clarity and to indicate the relationship of solubility at the three temperatures. Solubility is seen to decline with increasing temperature. Preliminary findings from the measurements with H_2 suggest that there might be need to re-interpret the solubility data. Further comment is premature, except to caution that these solubilities are still tentative. However, for matters as they stand, the heat of solution may be estimated from these isotherms to be -5.5 kcal per mole OH-. Isobars for H_2O partial pressure of 10^{-6}, 10^{-5}, and 10^{-4} atm are shown in Fig. 4. Linearity in these curves supports the corrections that were applied for residual hydroxide.

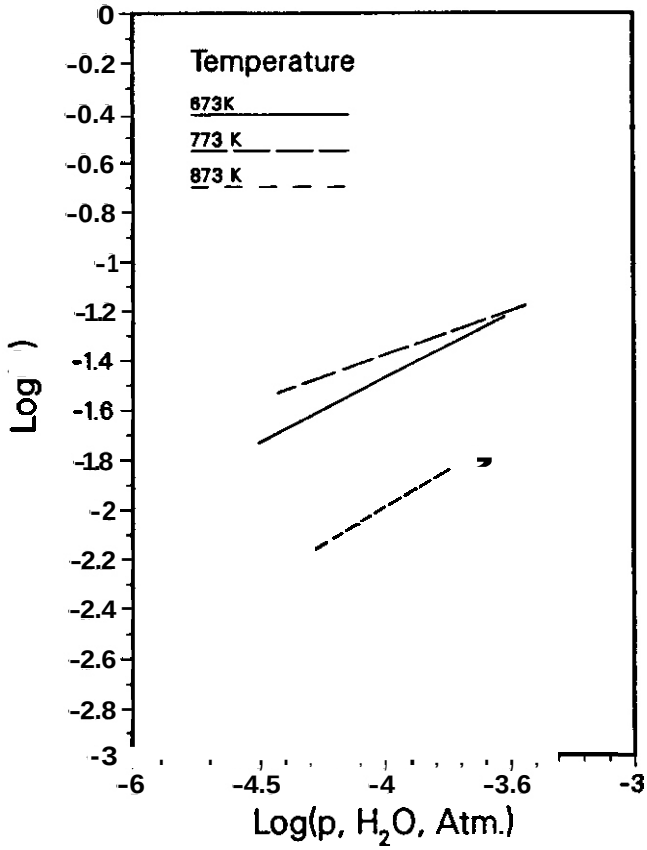

Fig. 1. Adsorption Isotnerms for OH- on $LiAlO_2$. e = fraction of surface covered.

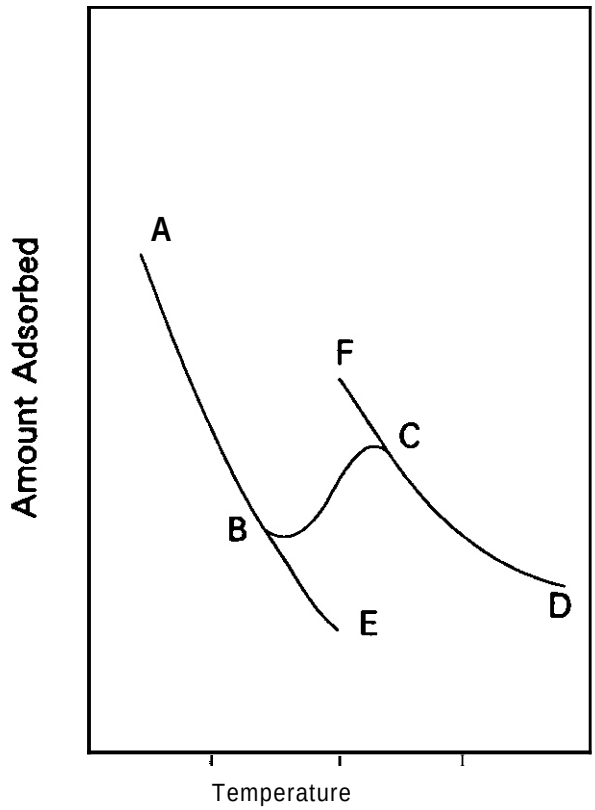

Fig. 2. Schematic Adsorption Isobars for Two Activated Processes.

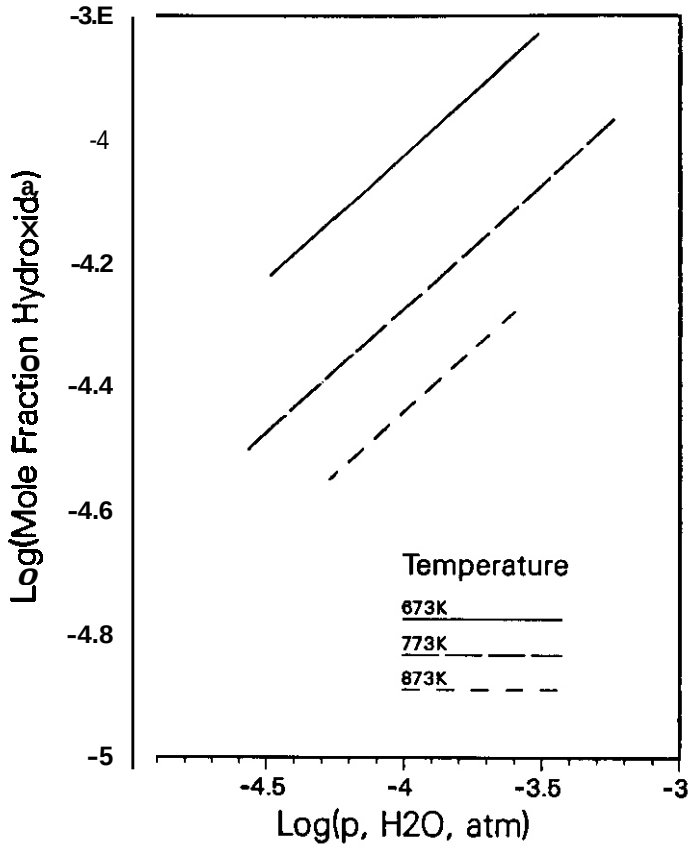

Fig. 3. Isotherms for Solubility of Hydroxide in $LiAlO_2$.

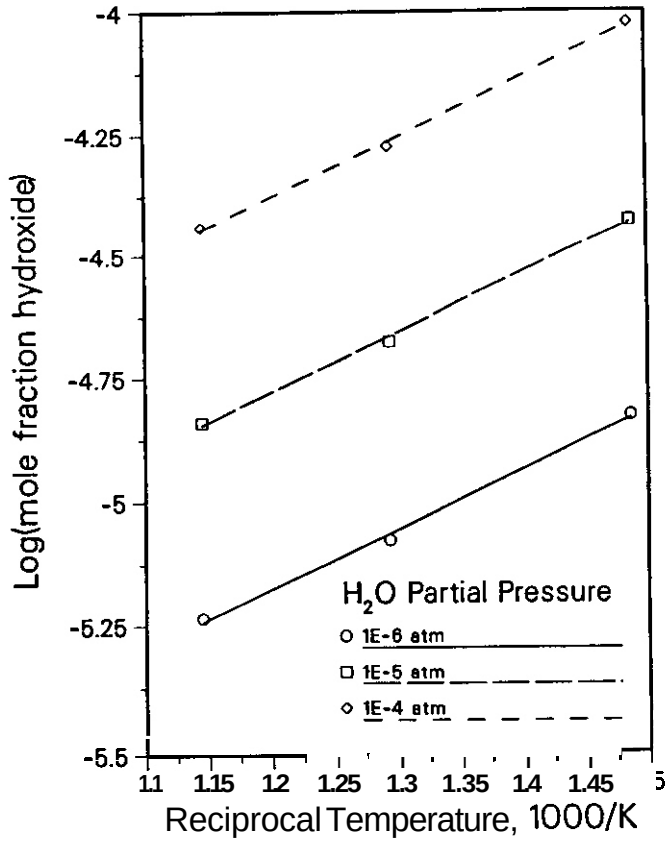

Fig. 4. Isobars for Solubility of Hyaroxide in $LiAlO_2$.

MODELING OF TRITIUM TRANSPORT IN CERAMIC BREEDER MATERIALS

J. P. Kopasz and C. E. Johnson (Argonne National Laboratory)

OBJECTIVE

The objective of this work is to develop a comprehensive model of tritium transport through a ceramic breeder material. The model will enable one to compare the relative contributions of the different transport processes: such as bulk diffusion, grain boundary diffusion, desorption, permeation and trapping, to the total tritium inventory and to the release kinetics. It may also suggest ways in which the tritium inventory can be reduced.

A computer program for tritium release determined by diffusion and desorption has been developed. This model gives better agreement with experimental data than does a pure diffusion model. An investigation of the tenperature and grain size dependence of the diffusion-desorption model indicates that for Li_2O diffusion dominates the tritium release at high temperatures for large grain radius samples and desorption dominates at low temperatures for samples with a small grain radius.

PROGRESS AND STATUS

Tritium release from ceramic breeder materials was, until recently, interpreted as either diffusion controlled[1-3] or desorption controlled.[4,5] These one mechanism models were unable to satisfactorily describe much of the data obtained in tritium release experiments. This led to our development of a diffusion-desorption model which we found to be a significant improvement over previous models. The details of the model were reported in the proceedings of the ICFRM-3 conference.[6] In that report were also published the results of several attempts to fit data from the LISA experiment to the diffusion-desorption model and a pure diffusion model. Better fits to the observed data were obtained with the diffusion-desorption model than for the diffusion model. For the lithium aluminate samples neither the diffusion nor diffusion-desorption model gave a good fit to the observed data. This suggests that for lithium aluminate some other mechanism may be involved in determining the tritium release.

Due to the large dependence of tritium release on temperature and the sample grain radius we examined the dependence of the diffusion and diffusion-desorption models on these two parameters. For the purpose of these calculations we modeled lithium oxide using the diffusivity determined by Guggi et al.,[7] and the desorption rate constant observed by Okuno and Kudo.[8] The difference between the predicted tritium release for the diffusion and diffusion-desorption models was calculated as a function of temperature and grain radius. The temperature dependence of this function is illustrated in Fig. 1 for a sample with a 50 micron grain radius. At low temperatures the overestimation of the release by the pure diffusion model increases with time. This will eventually reach a maximum and decrease to zero as the release approaches steady state. At high temperatures there is less of an overestimation by the diffusion model and the maximum overestimation is reached sooner. The dependence on the grain size is illustrated in Fig. 2 for a sample at 500°C. For small grains the diffusion model is a poor approximation to the diffusion-desorption release and gives a large overestimation of the tritium release at small times. For large grain samples the diffusion model appears to give a good approximation to the diffusion-desorption release. These graphs suggest that for Li_2O, if the diffusion and desorption rate constants used are correct, diffusion dominates the tritium release for large grains and at high temperatures while for small grains and low temperatures desorption controls the tritium release.

In order to determine the relative importance of other mechanisms. such as trapping, grain boundary diffusion, and permeation, in the tritium transport mechanism a more sophisticated program was needed. We have decided to use the OISPL computer software package for solving second order systems of nonlinear partial differential equations to handle these more complicated problems. This program should enable us to model diffusion-desorption-permeation problems as well as problems involving diffusion with trapping in the solid by radiation damage or gas bubbles. Initial attempts to utilize the DISPL program uncovered a bug in the program when dealing with spherical geometry. The DISPL package has been debugged and tested against the simple diffusion-desorption model. A model for diffusion, desorption and permeation is now being tested.

FUTURE WORK

The DISPL program will be used for scoping calculations investigating the importance of grain boundary diffusion and trapping to the total tritium inventory. Results from the CRITIC experiment will be analyzed using the current models to determine which mechanisms are important in determining tritium release.

REFERENCES

1) R. G. Clemmer et al., "The TRIO Experiment," ANL-84-55. Argonne National Laboratory (1984).

2) K. Okuno and H. Kudo, J. Nucl. Mater. 138 (1986) 210.

3) T. Kurasawa, H. Watanabe, G. Hollenberg, Y. Ishi, A. Nashimira, H. Yoshida, Y. Narusa, M. Aizawa, H. Ohno. and S. Konishi J. Nucl. Mater. 141-3 (1986) 265.

4) M. Dalle Donne, Fusion Tech. 9 (1986) 503.

5) T. Tanifuji, K. Noda, S. Nasu, and K. Uchida J. Nucl. Mater. 95 (1980) 108.

6) J. P. Kopasz, S. W. Tam, and C. E. Johnson, Proc. ICFRM-3, Karlsruhe, F. R. Germany, Oct. 4-10, 1987.

7) D.. Guggi, H.R. Ihle, D. Bruning, U. Kurz, S. Nasu, K. Noda, and T. Tanifuji, J. Nucl. Mater. 118 (1983) 100.

8) H. Kudo and K. Ohno, J. Nucl. Mater. 133-4 (1985) 192.

9) G. K. Leaf and M. Minkoff "DISPL1: A Software Package for One and Two Spatially Dimensioned Kinetics-Diffusion Problems," ANL-84-56. Argonne National Laboratory, 1984.

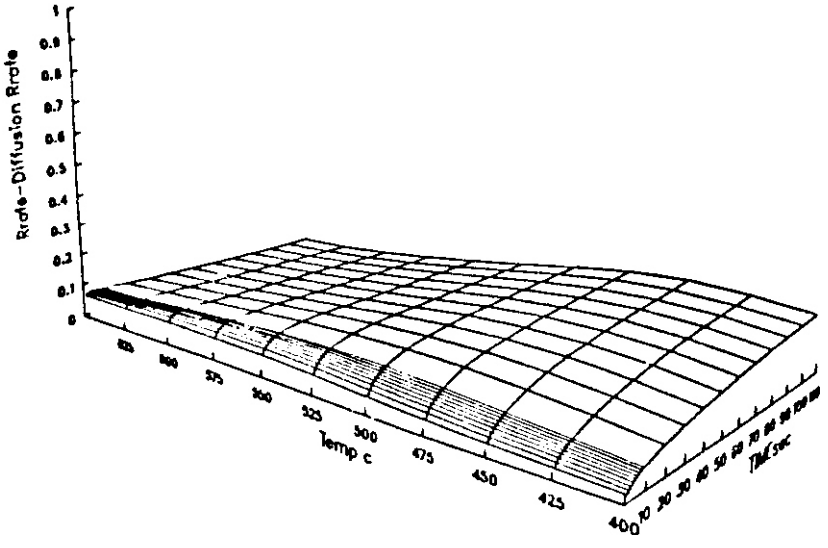

Fig. 1. Fractional Release from Diffusion Model Minus Fractional Release from Diffusion-Desorption Model as a Function of Time and Temperature for a Sample with a 50 Micron Grain Radius.

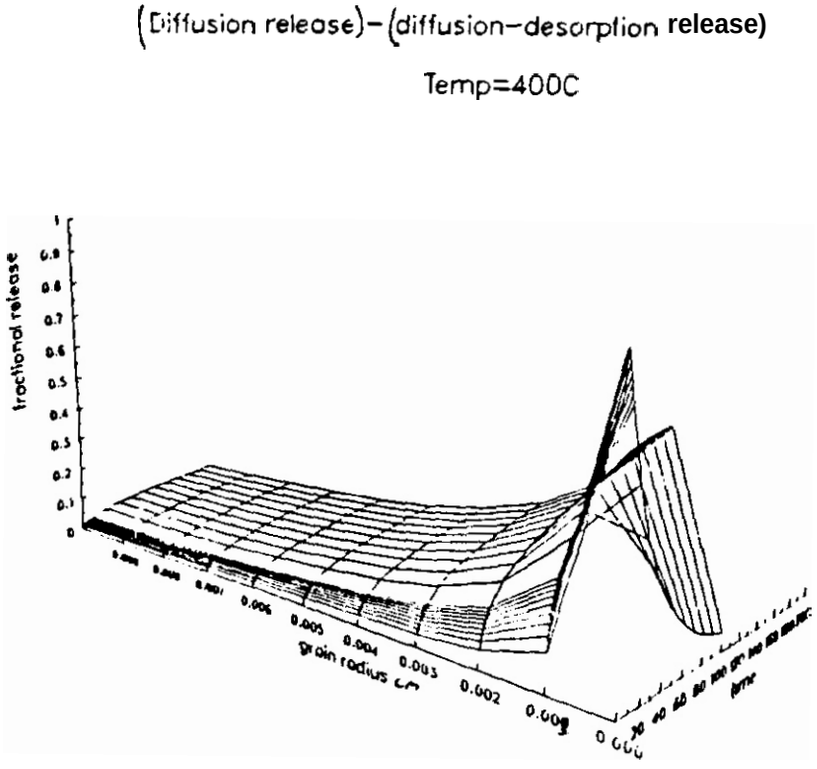

Fig. 2. **Fractional Release from Diffusion Model Minus Fractional Release from Diffusion-Desorption Model as a Function of Time and Grain Radius for a Sample at 400°C.**

EFFECT OF IRRADIATION ON THE THERMAL CONDUCTIVITY OF $LiAlO_2$ AND Li_2O = G. W. Hollenberg (Pacific Northwest Laboratory) and J. L. Ethridge and D. E. Baker (Westinghouse Hanford Company)

OBJECTIVE

The objective of this study is to determine the effect of fast neutron irradiation on the post irradiation thermal conductivity of $LiAlO_2$ and Li_2O.

SUMMARY

$LiAlO_2$ and Li_2O are two candidates for tritium breeder materials in fusion reactors which must operate within specific design temperature windows. Although irradiation may cause large reductions in thermal conductivity at room temperature. the effect at operating temperatures (T > 400°C) is much less. Hence. these solid breeder materials are expected to maintain temperatures within their initial temperature windows durfng operation.

PROGRESS AND STATUS

Introduction

Thermal properties of solid breeder materials are critical to not only blanket design activities, but also the selection and optimization of solid breeder materials. With the range of conditions provided by thermal properties and irradiation investigations. it was the purpose of this investigation to obtain a data base relating the change in thermal conductivity of Li_2O and $LiAlO_2$ to high temperature irradiation Conditions. Presented are thermal conductivity data derived from thermal diffusivity measurements via the flash-method. Samples were taken from pellets irradiated in the Hanford Engineering Development Laboratory's FUBR-1A experiment.[1-3]

EXPERIMENTAL DETAILS

Thermal Diffusivity Measurements

Pellets (0.95-cm diameter) of lithium aluminate and lithium oxide (85% TD) were irradiated in sealed capsules in the Experimental Breeder Reactor No. 2 (EBR-II).[3-5] These materials were irradiated at three different temperatures and reactor exposures. resulting in three different lithium burnup levels as shown in Table I. Thin cylindrical samples (0.075 cm thick) were cut from pellets using a diamond wafering saw. Extreme care was necessary in cutting and handling the samples since nearly all of the pellets were severely cracked. Oiffusivity samples were cut from the middle of the short four-pellet column to avoid the effects of temperature gradients at the ends of the pellet column during irradiation.

Since the samples contained tritium. measurements were conducted in an airtight chamber. The exterior of the chamber was cooled with flowing water to prevent diffusion of tritium through the chamber walls and release to the laboratory environment. The radiological hazard required all sample preparation. positioning and loading to be conducted in a glovebox filled with dry helium. Following sample loading. the test chamber was back-filled with helium to 300 Torr at room temperature and transferred to the thermal diffusivity apparatus. Located within the chamber was the nickel-chrome element furnace (1,000 watts) which allowed temperatures greater than 1273 K to be achieved. The energy pulses. provided by an Apollo Ruby. Model 22 laser (30 Joules - 800 microsecond pulse) penetrated the test chamber via a sapphire window at the bottom. Energy from the upper surface of the samples radiated through a second sapphire window located at the top of the test chamber and was focused through two CaF_2 lenses on to a liquid nitrogen-cooled InSb infrared detector. The signal from the detector was recorded with a Tektronix 7704A oscilloscope. digitized by a Tektronix P7001 Digitizer and analyzed by a Tektronix 4052 minicomputer. The time required to reach half the maximum temperature rise on the upper surface of the sample was determined from a least-square fit of the temperature waveform.

To maximize absorption of the laser energy. both surfaces of each sample were coated with a thin layer of metallic silver. Generally. five measurements at 100 K increments were made to provide good statistical analysis. Measurements were also taken on several samples during cool-down from 1173 K.

Parker, et al[6] discussed the flash-method for determining thermal diffusivity and thermal conductivity. In general. thermal conductivity is calculated from experimentally-measured thermal diffuslvity:

$$a = 1.38\ DC\ L^2\ \pi^2\ t_{1/2} \qquad [1]$$

where: a = thermal diffusivity
D = density
C = heat capacity
L = sample thickness. and
$t_{1/2}$ = time required for near surface to reach one-half its maximum value

Equation 1 assumes constant material properties. uniform sample heating, and no heat losses. Radiation and other sources of heat loss (gas conduction and conduction to sample holders) were modelled using the heat transfer canputer code HEATING5.[7] The thin, infrared-absorbing silver coating was also included in the model. These temperature-dependent effects were accounted for in Equation 1 by adjusting the $t_{1/2}$ determined from the experiment.

Thermal conductivity measurements on unirradiated archive samples of Li_2O and $LiALO_2$ were made and canpared with those of Takahashi[8], and Schulz[9], Gurwell[10] and Rasneur[11]. For lithium oxide the measurements were higher than Takahashi's data at low temperatures. but at high temperatures. Takahashi's data is lightly higher. The measured lithium aluminate data was in excellent agreement with those of Schulz, though Gurwell and Rasneur reported lower values at all temperatures. The good canparison of measured data with literature values. especially in the case of lithium aluminate, supports the results of the irradiated samples given below. Except for effects associated with Irradiation, i.e., high irradiation temperatures. retained tritium, swelling, etc., the irradiated and unirradiated archive samples were nearly identical.

Irradiated Lithium Oxide

In Figure 1, the measured thermal conductivity data is shown as a function of temperature for lithium oxide irradiated at 773, 973 and 1173 K with an exposure of 297 FPD's. The curve derived from the unirradiated data (adjusted to 85% TD) is included for canparison. Data fran irradiated samples generally followed the characteristic 1/(AT+B) temperature dependence. No differences were observed between the data collected during heat-up and cool-down. The distinction between different irradiation temperatures is apparent in these data at low measurement temperatures. However. the data at all irradiation temperatures approach similar, low values of conductivity at high measurement temperatures. Similar behavior was observed at lower burn-up levels, 105 and 142 FPD.

With a few exceptions, the measured thermal conductivity data was lower than unirradiated values. Low temperature conductivity values for the samples Irradiated at 1173 K were reasonably consistent, showing lower values at higher burnups - a manifestation of increased damage due to irradiation. However. data from the sample irradiated at 733 K (Figure 1) to high burnup (297 FPD) was different in that the conductivity was close to unirradiated values suggesting little burnup dependence. The burnup independence may be the result of grain growth in the sample.

Because grain boundaries offer increased scattering centers for phonons, materials with larger grain sizes can have high thermal conductivities. Hollenberg[2] reported grain sizes for samples irradiated to lithium burnups of 4 x 10^{20} capts/cm^3 (105FPD). He observed significant grain growth in lithium oxide at 1173 K, but very little at 773 or 973 K. Similar grain growth was observed for samples irradiated to higher burnup levels as shown in Table 1, except for Li_2O irradiated at 773 K to 11.7 x 10^{20} capts/cm^3 (297 FPD). The large grain size observed in this sample may explain the higher thermal conductivity values observed in Figure 1.

TABLE I

PARTIAL FUBR-1B TEST MATRIX AND OBSERVED AVERAGE GRAIN SIZE

SAMPLE	IRRADIATION TEMPERATURE (K)	BURNUP (10^{20} CAPTS/CM^3)	AVERAGE GRAIN SIZE (μm)*
Li_2O	773	3.9	3.4
Li_2O	973	3.7	7.1
Li_2O	1173	4.1	17.1
Li_2O	773	7.0	5.8
Li_2O	973	7.3	7.2
Li_2O	1173	7.3	14.4
Li_2O	773	11.7	11.3
Li_2O	973	11.3	6.7
Li_2O	1173	11.3	16.3
$LiALO_2$	773, 973, 1173	-3.0, 5.5, 8.5	<1.0

- Determined by Linear Intercept Method Fran Reference 2

The abnormally-large relative grain size for this case is yet unexplained. However. If the observed grain sizes from Table I are canpared at similar temperatures. only the grain size of the pellets at 773 K at 11.7 x 10^{20} captures/cm^3 data shows a statistically significant increase. The 973 K and 1173 K data, respectively, display a relatively constant grain size, within the estimated error of measurement. This suggests that an equilibrium grain size was achieved within the pellets during irradiation prior to reaching a lithium burnup of 4 x 10^{20} capts/cm^3. Pre-irradiation grain sizes for all of the lithium oxide samples were reported to be within the range of 2 to 10 μm[12]. The larger grain size (i.e., fewer

grain boundaries) of this sample may help explain the relatively high measured conductivity. The effect of grain size on conductivity may have obscured the effect related to irradiation damage.

Irradiated Lithium Aluminate

The thermal conductivity of irradiated lithium aluminate material in Figure 2 displayed an interesting response to temperature. The thermal conductivity during heatup measurements for all of the samples at all burnups is nearly independent of temperature for all lithium burnups. Data collected during this phase suggests a saturation of the thermal conductivity similar to observations made by Tam[13] and Hurley[14] for other materials at high measurement temperatures. This behavior was expected since it is known that the phonon mean free path decreases with temperature and irradiation damage. From the kinetic theory of gases. the thermal conductivity can be estimated by:

$$k = 113\ C v \ell \qquad (2)$$

where. k = thermal conductivity,
C = heat capacity.
v = average phonon velocity in the lattice. and
ℓ = average phonon mean free path.

The average phonon mean free path is given by:

$$1/\ell = 1/\ell_{phonon} + 1/\ell_{defects} \qquad (3)$$

where. ℓ_{phonon} = phonon mean free path associated with phonon-to-phonon collisions. and
$\ell_{defects}$ = phonon mean free path associated with defects.

From Equations 2 and 3, the thermal conductivity can be reduced by a decrease in the mean free path due to the introduction of material defects from irradiation. e.g., lattice defects. bubbles. voids. etc.[13]

For lithium aluminate at low measurement temperatures, the high concentration of stable lattice defects limit the normally-long mean free path of unirradiated materials to some shorter value. At higher temperatures. a further reduction in the mean free path does not occur because the mean free path is maintained at a low value by irradiation defects. The lattice defects in $LiALO_2$ have saturated at a lithium burnup level less than 3.0 x 10^{20} capt.cm^3 (105 FPD) which is consistent with the burnup independent behavior of the thermal conductivity. Continued irradiation beyond this point did not result in any further reduction in conductivity. The slight increase in thermal conductivity at 673 K for the sample irradiated at 973 K to 297 FPD (Figure 2) is unexplained even though repeated runs were made. This anomaly is not thought to be associated with swelling since very little was observed[4] in any of the lithium aluminate samples. Pre-irradiation grain size for these samples was reported to be less than 1μm and results given in Table I confirmed that grain growth was not measurable even at the highest irradiation temperature.

For $LiALO_2$ samples at low burnup (105 FPD), cool-down data were collected and significant recovery of the conductivity at low measurement temperatures was observed for all irradiation temperatures. This recovery of conductivity may be attributed to annealing of the irradiation defects while the samples were exposed to high measurement temperatures. thus providing a longer mean free path. Evidently. defect and damage annihilation reduced the number of phonon scattering centers resulting in recovery of the thermal conductivity. The thermal conductivity data from the cool-down experiments represent a more characteristic 1/(AT+B) relationship than the as-irradiated material. More study of the kinetic behavior of defects in $LiALO_2$ under these conditions is necessary to quantify the observed recovery in thermal conductivity during cool-down.

CONCLUSIONS

An apparatus and measurement methodology were developed which allowed measurement of thermal diffusivity from radioactive ceramic materials at temperatures up to 1173 K. This equipment and measurement technique minimized tritium exposure.

Significant decreases in thermal conductivity were observed in Li_2O irradiated in a fast neutron environment to lithium burnups of $\leq$ 12 x 10^{20} capt/cm^3. Significant reductions in thermal conductivity at low measurement temperatures were observed for lithium oxide samples as a result of radiation-induced lattice damage. The reduction ranged from about 40% and 28% at 373 K for samples irradiated from 4 x 10^{20} to 12 x 10^{20} capts/cm^3, respectively. At the high measurement temperatures (1073-1173 K), the thermal conductivity of all irradiated samples approached values only slightly below those of unirradiated lithium oxide. Grain growth and swelling during irradiation were considered to play a role in understanding the observed changes in conductivity.

The thermal conductivity of irradiated lithium aluminate samples remained relatively constant with temperature at a value of about 3.5-4.0 W/m-K, for all irradiation times and temperatures. This value is only slightly lower than observed values for unirradiated $LiALO_2$ at high measurement temperatures. After

subjecting the samples to sufficiently high measurement temperatures (>650 K), an increase in low temperature thermal conductivity was observed for all aluminate samples for which measurements were made during cool-down. The low burnup sample irradiated at 1173 K showed a significant improvement in conductivity reaching values comparable to unirradiated values.

REFERENCES

1. G.W. Hollenberg and O.E. Baker, "Thermal Properties of Lithium Ceramics for Fusion Applications," presented at the 84th Annual Meeting of the American Ceramic Society, Cincinnati. OH, May 2-5, 1982.

2. G.W. Hollenberg. "Fast Neutron Irradiation Results in Li_2O, Li_4SiO_4, Li_2ZrO_3, and $LiAlO_2$," J. Nuc. Mat. 141-143 (1986) 305-310.

3. G.W. Hollenberg and O.L. Baldwin, "The Effect of Irradiation on Four Solid Breeder Materials." J. Nuc. Mat. 133-134 (1985) 242-245.

4. G.W. Hollenberg. "Swelling of Lithium Ceramics During Irradiation," in Advances in Ceramics, March 1988, American Ceramic Society.

5. O.L. Baldwin and G.W. Hollenberg, "Measurement of Tritium and Helium in Fast Neutron Irradiated Lithium Ceramics Using High Temperature Vacuum Extraction," J. Nuc. Mat. 141-143 (1986) 305-310.

6. W.J. Parker, et al, "Flash Method of Determining Thermal Oiffusivity. Heat Capacity. and Thermal Conductivity." J. Appl. Phys. 32 (1961) 1679-1684.

7. W.O. Turner, et al, "HEATING 5 - An IBM 360 Heat Conduction Program," ORNL/CSD/TM-15, Oak Ridge National Laboratory. Oak Ridge. Tennessee. no date.

8. T. Takahashi and T. Kikuchi, "Porosity Dependence on Thermal Diffusivity and Thermal Conductivity of Lithium Oxide LI_2O from 200 to 900°C," J. Nuc. Mat. 91 (1980) 93-102.

9. B. Schulz. "Thermophysical Properties of Potential Breeder Materials for Fusion Technology." presented at the International Symposium on Fusion Reactor Blanket and Fuel Cycle Technology. October 27-29. 1986, University of Tokyo. Tokai-mura, Ibaraki. Japan.

10. W.E. Gurwell, "Characterization of Commercial Alluminates. Silicates, and Zero X Materials," BNW-CC-474, January 1966. Battelle Northwest Laboratories. Richland, WA.

11. B. Rasneur. "Tritium Breeding Material: $LiALO_2$," presented at the Sixth Topical Meeting on the Technology of Fusion Energy, March 3-7, 1985. San Francisco. CA.

12. C.N. Wilson, "Fabrication of Lithium Ceramics by Hot Pressing." presented at the Annual Meeting of the American Ceramic Society. May 2-5, 1982, Cincinnati. Ohio.

13. S.W. Tam, et al, "Saturation Phenanena and Percolatlve Transitions in High Temperature Thermal Conductivity of Gamma-$LiALO_2$, "J. Nuc. Mat. (1985) 234-237.

14. G. F. Hurley and F. W. Clinard, "Thermal Diffusivity of Neutron Irradiated Ceramics." Special Purpose Materials Annual Progress Report. DOE/ET-0095, U. S. Department of Energy (1979) 59.

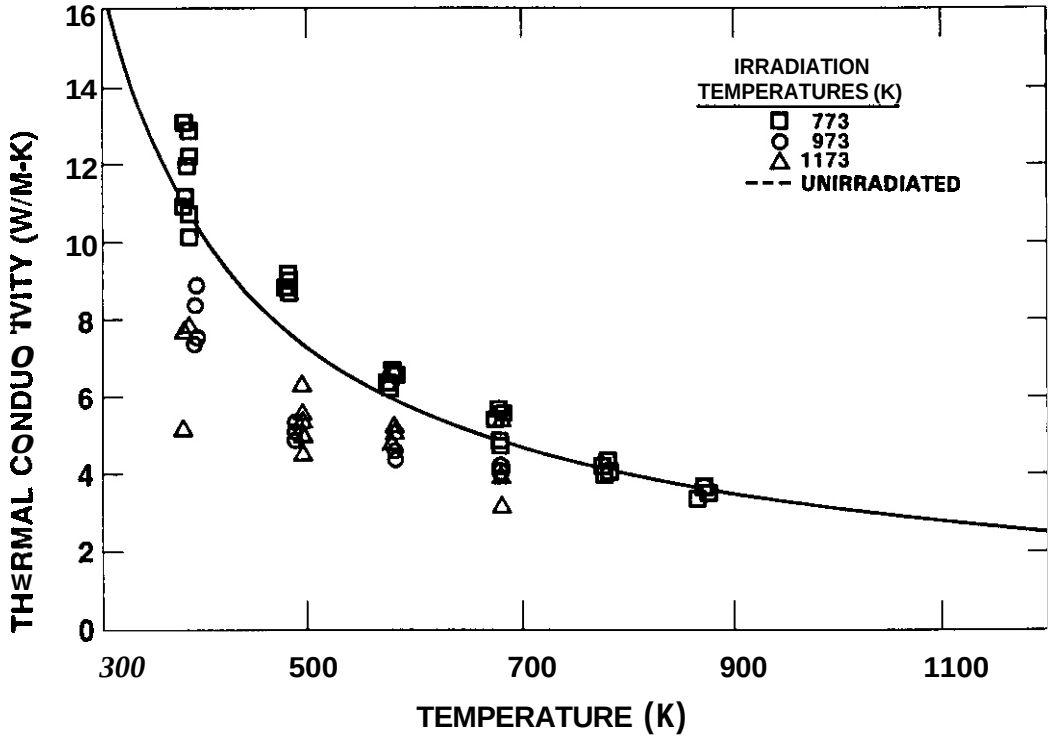

Fig. 1. Thermal Conductivity of Li_2O at Different Irradiation Temperatures 297 Full Power Days

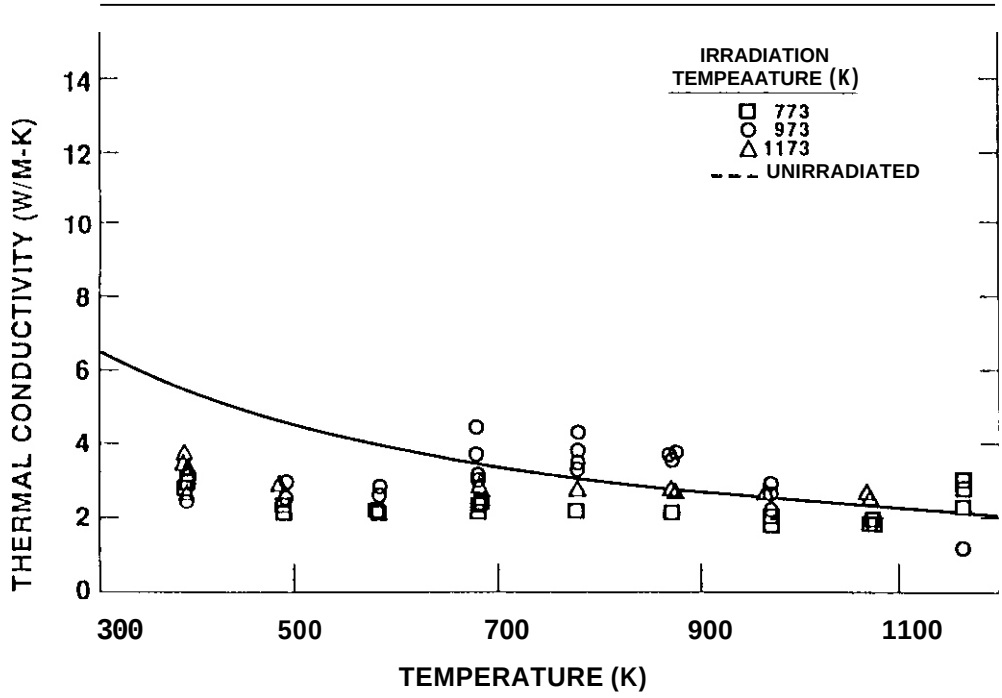

Fig. 2. Thermal Conductivity of $LiAlO_2$ at Different Irradiation Temperatures 297 Full Power Days

8. CERAMICS

MECHANICAL RELIABILITY OF FUSION CERAMICS FOR ECRH IN THE CONTEXT OF RADIATION DAMAGE

H. M. Frost and F. W. Clinard, Jr. (Los Alamos National Laboratory)

OBJECTIVE

To develop and apply an analytical approach for assessing the impact on service lifetime of radiation damage in ceramics intended for magnetic fusion energy (MFE) applications entailing electron cyclotron resonance heating (ECRH) of fusion plasmas.

SUMMARY

Most reports of radiation-induced changes in dielectric properties and thermal conductivities of insulating ceramics for HFE applications do not include quantitative assessments of the impact of such changes on material or device failure. We present details here on calculations based an a model published for some time but not applied until very recently to radiation damage. It incorporates the Weibull distribution for fracture statistics, such as used in the mid 1980's for gyrotron windows in a 'radiationless' environment. A major consequence of applying this and another model in the context of an alumina (α-Al_2O_3) or beryllia 'rf' window subject (during ECRH use) to dielectric and thermal-conductivity damage and strength changes, as induced by fast neutrons, involves reductions in service lifetimes by orders of magnitude.

PROGRESS AND STATUS

Introduction

The fracture models are described and discussed in enough detail to permit other investigators to evaluate them in connection with their own radiation-damage assessments. Our departure point in this respect consists of two key papers dealing with mechanical reliability of ceramic windows for gyrotrons not subject to neutron and other MFE radiation.[1] Discussions of the model will be based on published test data available on alumina and beryllia ceramics which were irradiated with fast neutrons ($E > 0.1$ MeV) at 385°C to a fluence of 10^{26} n/m^2 in the EBR-II fast fission reactor.[2]

Fracture models

It is well known that a flaw such as a void or a microcrack can act as a stress concentrator in a brittle material which can initiate fracture when its size is greater than some critical value. The Griffith criterion for fracture involves a dependence of the fracture strength on the inverse square root of the flaw sire. Normally, the flaws involved display a range or distribution of sizes, with the probability of the occurrence of a flaw of critical sire --for a given applied stress -- increasing with the volume of the test specimen. With the Weibull distribution, the probability P_f of failure through fracture in an inert environment relates to stress as follows:

$$\ln (1 - P_f) + (\sigma_{IC}/\sigma_o)^m = 0, \qquad \text{Eq.(1)}$$

where σ_{IC} and σ_o, respectively, are the inert fracture strength and a normalizing stress parameter, and m is the Weibull modulus.

For the type of fracture involved in the failure of rf windows in a reactive environment, i.e., slow crack growth via 'static fatigue,' the time to failure (lifetime) t_f relates to the applied stress σ_a as follows:

$$\ln (t_f) + n \ln (\sigma_a/\sigma_{IC}) - A = 0, \qquad \text{Eq.(2)}$$

where n and A characterize the reactive testing environment. For alumina and beryllia. $A = 0$, while for an rf window. σ_a corresponds to the hoop stress on the window edge. Then Eq.(2) can be more conveniently expressed as

$$t_{f,I} = t_{f,C} [(\sigma_{IC,I}/\sigma_{IC,C})(\sigma_{a,C}/\sigma_{a,I})]^n, \qquad \text{Eq.(3)}$$

with the notation "I" and "C" denoting the irradiated and control states for the material, and the assumption $n_I = n_C$ being made. As σ_{IC} appears in bath Eq.(1) and Eq.(2), a service stress $\sigma_s = \sigma_a$ can he calculated in terms of assumed values of t_f and P_f:

$$\sigma_s \simeq \sigma_o \, (t_f)^{-1/n} \, \{\ell n \, [1/(1 - P_f)]\}^{1/m}. \qquad \text{Eq.(4)}$$

Our procedure for estimating the effect of radiation on lifetime of the material is then as fallows:

- Determine the applied stress $\sigma_a = \sigma_{a,C}$ from Eq.(4) after deciding on what lifetime $t_{f,C}$ is desired at a given failure probability level for the control material; this quantity links the lifetime calculation to the actual engineering situation encountered.

- Estimate how the irradiation affects the two ratios of stress that appear in Eq.(3), then calculate $t_{f,I}$.

The second step in the preceding is the one emphasized in this report

The ratio of "σ_{IC}" stresses can be estimated from the values of tensile or rupture Stresses measured on specimens before and after irradiation. The ratio of "σ_a" (applied) stresses can be estimated from the proportionality --as expected from the steadv-state. inhomogeneous heat conduction equation --between the stress σ_a within the window and the quantities k, tanδ, ℘, and K, vie.

$$\sigma_a \propto k \tan\delta \, (f\wp) \, / \, K. \qquad \text{Eq.(5)}$$

Here, k is the dielectric constant and tan6 is the loss tangent -- with $k\tan\delta$ being the loss factor -- and B/K is the incident MMW power divided by the thermal conductivity. The frequency of the MMW's is f. Implicitly assumed here is the resonant condition of the rf window being an integral number of (material) half wavelengths both before and after irradiation. If this were not true, then the dependence of σ_a on k would be much more complex. Such a condition is known to apply to high-purity alumina after intense fast neutron irradiation but not to beryllia, although for simplicity and brevity this effect is ignored in this report. Further assumed is that the measured tan6 consists entirely of contributions from absorption processes. This is probably true for cavity techniques for the measurements and perhaps also for the in-waveguide techniques for long aspect-ratio specimens as involved in this report. Free-space techniques. especially for thin low-loss specimens. however, in principle yield tan6 values sensitive to scattering as well as absorption processes. so the use of such values can lead to systematic errors in the lifetime predictions.

Also, the temperature dependence of the material properties represented in Eq.(5) is ignored, which is reasonable as long as the window cooling keeps the temperature rises due to dielectric and radiation heating to within the order of magnitude of 100°C. With this assumption, the time rate at which heat is converted from the MMW's is constant, and for a given temperature gradient, the heat flow (thermal current density) from one point to another in the material is also constant. Thus, the temperature distributions that determine the thermal-mechanical stresses σ_a in the material are solutions to a linear heat conduction equation (with temperature-independent source) and absolute (vs. relative) values of σ_a are relatively easily calculable and therefore available in the literature.

For temperature rises much larger than 100°C, however, the heat conduction equation can become nonlinear in character, particularly because the quantity $\tan\delta/K$ is strongly temperature dependent for elevated temperatures above room temperature, the temperature dependences of tan6 and K for an insulating ceramic such as alumina complementing each other in this regard. When second-order derivative terms in the steady-state but inhomogeneous heat conduction equation for a (disc-shaped) window are ignored, then the stress-producing temperature gradient $\partial T/\partial r$ is proportional to $r\sigma_a$, with r the radial position of observation on the disc. Since σ_a itself is proportional to $\tan\delta/K$ via Eq.(5), then the thermal-mechanical stresses have a parametric dependence on temperature rather than being independent of it.

Discussion

It was recently reported that both a 99.5% alumina and also a beryllia-based ceramic experienced a doubling in the dielectric loss factor at room temperature and 90-100 GHz as a

result of the intense fast neutron exposure mentioned in the **Introduction.**[2] Assumed initial lifetimes of 1 yr for both materials led via **Eq.(3)** and **Eq.(5)** to 'irradiated' values of 2 sec for Al_2O_3 and 20 min for BeO, ignoring, however. the following two considerations. One concerns the significant measured reductions in strength that also resulted from this irradiation, the other the reductions in thermal conductivity likewise expected to have occurred. The materials and material constants involved in these irradiated values **are** represented in the following table, with 'ktanδ' values given in the format of 'before/after' irradiation:

Table 1. Material constants used in calculating 'irradiated' lifetimes

Material	Density (g/cm^3)	m	σ_o (MPa)	n	ktanδ (10^{-3})
Alumina, WESGO AL995	3.84	14.4	286	24.15	3.8/8.1
Beryllia, Ceradyne Thermalox 9959	2.90	13.3	193	14.85	4.0/8.3

Note: Data are **from** Refs. [1,2].

In the preceding. the values of ktanδ were measured at **room** temperature for an irradiation at 385°C. If the roughly 50% increases of ktanδ for temperature raised from room temperature to 385°C .. increases which are known to **occur** for unirradiated Al_2O_3 and BeO[3] .. **are** assumed to also apply for irradiated material, then the ratio of unirradiated to irradiated ktanδ values is the same at either temperature. This reasoning applies to other temperatures as well, as long as the point and/or extended defects produced by the irradiation and responsible for the altered property values do not 'anneal out' relative to the defect concentrations at **room** temperature. **Similar** reasoning can be applied to the temperature insensitivity of the corresponding ratios for K and for σ_{IC} appearing via Eq.(3) and Eq.(5).

The above lifetime estimates are altered when non-unity values of the ratios in **Eq.(3)** for σ_{IC} and K are taken into account. Interpolating data on K for WESGO AL995 alumina irradiated **with fast** neutrons at 50 and 700°C yields a conservative halving of K at 385°C as induced by 10^{22} n/cm[2] of fluence.[4] Other thermal conductivity data[3] indicate that this halving is also **a** conservative estimate for BeO. In contrast, though, the rupture strength **for** alumina decreases by only **26%**[5] but for beryllia probably by over an order **of** magnitude (via microcracking induced by anisotropic swelling in the hexagonal lattice).[7] for the irradiation conditions mentioned in the Introduction. **When** these estimates are taken into account, the 2 sec (actually, 1.69 sec) lifetime for alumina is reduced to about 70 psec .. or just a few cycles of MMW power at 100 GHz! For BeO, the 20 min (actually. 1068 sec) also reduces to essentially **zero** (actually. 5×10^{-17} sec!).

From Eq.(3) and **Eq.(5)**, plus the condition $t_{f,C} = t_{f,I}$, the following relation applies for determining by how much to decrease the applied power $\mathcal{P}_I$ relative to the value $\mathcal{P}_C$ that the rf window can tolerate at given values of failure time and probability which **are** taken to be constant throughout the irradiation:

$$\mathcal{P}_I/\mathcal{P}_C = (\sigma_{IC,I}/\sigma_{IC,C})\ (k_C/k_I)\ (\tan\delta_C/\tan\delta_I)\ (K_I/K_C). \qquad \text{Eq.(6)}$$

A schedule for decreasing the MMW power through the rf window (in an MFE reactor) **as** the performance of the latter degrades via radiation damage may be an appropriate operating protocol to consider **as** long as the power ratio does not vary too much from unity.

The Weibull statistics implicit in Eq.(1) **are** assumed to be valid for the ceramics mentioned in this report. However. nondestructive testing (NDT) of a Coors AD995 alumina disk, similar to the one from which the alumina specimens for exposure in EBR-II were **cut**, revealed macroscopic defects far larger than the critical flaw sizes required for fracture.[8] These tests included microfocus x-ray in which inclusions of the order of 100 μm **were** found. plus ultrasonic 'C-scans' in which voids about 2 mm in diameter were found. Variations of over 10% in the localized values of the ratio of elastic modulus divided by mass density **were** also found.

The predicted lifetimes **can** be affected not only by including the complete set of relevant

properties in materials free of macroscopic processing-related flaws, but also by including inaccuracies and imprecision in the dielectric and other data. Take WESGO AL995 alumina as a case material with the reported 'n' value of 24.15. If the total systematic and random error in the combined quantity in square brackets [ ] in Eq.(3) is either plus or minus 10%. then the '[ ]' quantity is 1.1 or 0.9 of what it should be and $t_{f,I}/t_{f,C}$ accordingly differs by factors of 10 and 0.08 respectively. of what it should be. Other than finding an alumina with a lower 'n' value, the only remedy (with alumina) seems to be to make better measurements -- considerably better than +lo% in order to allow for the propagation and subsequent accumulation Of errors in Eq.(3).

CONCLUSIONS

The combined use of models for both inert ('Weibull') and reactive fracture for assessing radiation damage in rf windows can yield predictions of service lifetimes that are very sensitive to even small, radiation-induced changes in dielectric, thermal, end strength properties. To assure the validity of such models, however. these windows need quality control screening via NDT for detection of windows containing unacceptably large defects. This type of screening is also needed before and after specimen preparation in connection with fission reactor studies. In the area of radiation damage studies, at least of rf windows. this is the first time apparently such models and testing have been used together.

Besides encouraging expanded use of such approaches, other recommendations for future work include:

- Paying enough attention, in the 'difficult' MMW dielectric measurements, to the accuracy and precision required for allowing at least order-of-magnitude 'accuracies' in predicting window lifetimes.

- Finding ceramics with relatively low 'n' values via inert fracture tests. as in four-point flexure under conditions that eliminate slow crack growth behavior. Such ceramics will have more stable lifetimes when subjected to irradiation.

- Making 'in situ' measurements of ktanδ, K, and σ_{IC} in order to see if the corresop-nding σ_a and σ_{IC} ratios in Eq.(3) differ from those evaluated simply through the use of pre- and post-irradiation data.

- Better understanding the nature of the defects -- e.,g., point defects vs. dislocation loops -- produced by the irradiation in order to facilitate extrapolations of available test data taken at 'inconvenient' temperatures to values expected at actual operating temperatures for rf windows.

- Measuring the effect of irradiation on the m, n, A, and σ_o parameters of Eq.(l) and Eq.(2). Such data are severely lacking.

Besides rf windows per se, the preceding conclusions can be applied to other rf insulating requirements in MFE reactors such as insulated coaxial leads terminating at a ceramic-and-metal antenna for ion cyclotron resonance heating (ICRH) of plasmas and ceramic-filled waveguides for plasma heating at intermediate frequencies, for example.

REFERENCES

1. M.X. Ferber. H.D. Kimrey, and P.F. Becher, "Mechanical reliability of ceramic windows in high frequency microwave heating systems - Part 1," J. Mater. Sci. 19 (1984) 3767-3777; P.F. Becher and M.K. Ferber, same title - Part 2," J. Mater. Sci. 19 (1984) 3778-3785.

2. M.M. Frost and F.W. Clinard. Jr., "Dielectric changes in neutron-irradiated rf window materials," J. Nucl. Mater. (1988), in press; H.M. Frost and C.D. Kise, "In-waveguide measurements of MMW dielectric properties of candidate fusion ceramics," pp. 384-388 in Fusion Reactor Materials Semiannual Progress Report for Period Ending September 30, 1986, DOE/ER-0313/1, U.S. Department of Energy, Washington, D.C.. June 1987.

3. W.W. Ho, "High temperature millimeter wave characterization of the dielectric properties of advanced window materials." Final Report, AMMRC TR 82-28, Army Materials and Mechanics Research Center, Watertown, Massachusetts, May 1982; W.W. Ho, "Millimeter wave dielectric property measurement of gyrotron window materials," Technical Report, ORNL/SUB/83-51926/1, Oak Ridge National Laboratory, Oak Ridge, Tennessee, April 1984.

4. W.H. Reichelt. et al., "Radiation induced damage to ceramics in the EBR-II reactor." pp. 39-44 in proceedings of 1970 Thermionic Conversion Specialists Conference, October 26-29, 1970, Miami, Florida.

5. B.S. Hickman and A.W. Pryor, "The effect of neutron irradiation on beryllium oxide,"

J. Nucl. Mater. 14 *(1964)* 96-110.

6. D.S. Tucker, C.D. Kise, and J.C. Kennedy, "Effects of neutron irradiation on $MgAl_2O_4$ and Al_2O_3," pp. 9-10 in Eighth Annual Progress Report on Special Purpose Materials for Magnetically Confined Fusion Reactors, DOE/ER-0113/5, U.S. Department of Energy, Washington, D.C., March 1986.

7. B.S. Hickman, "Radiation effects in beryllium and beryllium oxide," pp. 72-158 in Studies in Radiation Effects, series A, Physical and Chemical, vol. 1, G.J. Dienes (ed.), (Gordon and Breach, New York, 1966).

8. T.N. Claytor, Los **Alamos** National Laboratory, private communication (1987).

9. SUPERCONOUCTING MAGNET MATERIALS

No contributions received this period.

DOE/ER-0313/4
Distribution
Categories
UC-423. -424

DISTRIBUTION

1–13. Argonne National Laboratory, 9700 South Cass Avenue, Argonne, IL 60439

M. C. Billone
O. K. Chopra
R. G. Clemmer
D. R. Diercks
P. A. Finn
A. K. Fischer
Y. Y. Liu
B. A. Loomis
R. F. Mattas
L. A. Niemark
S. W. Tam
E. R. Van Deventer
H. Wiedersich

14. Argonne National Laboratory, EBR-II Division, Reactor Materials Section, P.D. Box 2528, Idaho Falls, ID 83403-2528

D. L. Porter

15. Arizona State University, Department of Mechanical and Aerospace Engineering, Tempe, A2 85281

W. A. Coghlan

16. Auburn University, Department of Mechanical Engineering, Auburn, AL 36849

E. A. Chin

17–30. Battelle-Pacific Northwest Laboratory, P.D. Box 999, Richland, WA 99352

J. L. Erimhall
D. G. Doran (5)
M. D. Freshley
F. A. Garner
D. G. Gelles
M. L. Hamilton
H. L. Heinisch
G. W. Hollenberg
B. D. Shipp
O. D. Slagle

31. EG&G Idaho, Inc., Fusion Safety Program, P.D. Box 1625, Idaho Falls, ID 83415-3523

D. F. Holland

32–33. Carnegie Institute of Technology, Carnegie-Mellon University, Schenley Park, Pittsburgh, PA 15213

W. M. Garrison, Jr.
J. C. Williams

34–37. GA Technologies, Inc.. P.O. Box 85608, San Diego, CA 92138

J. Baur
G. R. Hopkins
T. A. Lechtenberg
D. [redacted]-Roberts

38–39. General Dynamics Corporation, 5001 Kearny Villa Road. San Diego, CA 92138

T. L. Cookson
V. Stegar

40. General Electric, Advanced Nuclear Technology Operation, 310 Deguine Drive, Sunnyvale, CA 94088

S. Vaidyanathan

41. Georgia Institute of Technology, School of Textile Engineering, Atlanta, GA 30332

D. S. Tucker

42. Grumman Aerospace Corporation, c/o TFTR Project, Princeton Plasma Physics Laboratory, Princeton University, A. Site, Building 1-E, Princeton, NJ 08540

R. G. Micich

43–45. Lawrence Livermore National Laboratory, P.D. Box 808, Livermore, CA 94550

E.N.C. Dalder
M. Guinan
J. Perkins

46–53. Los Alamos National Laboratory, P.O. Box 1663, Los Alamos, NM 87545

J. L. Andersen
L. Caudel
D. J. Dudziak
H. M. Frost
G. Hurley
C. D. Kise
R. Liepens
T. Zocco

54. Manlabs, Inc., 231 Erie Street, Cambridge, MA 02139

D. Tognarelli

55. Massachusetts Institute of Technology, Department of Metallurgy and Materials Science, Cambridge, MA 02139

L. W. Hobbs

56. Massachusetts Institute of Technology, 138 Albany Street, Cambridge, MA 02139

O. K. Harling

57–58. Massachusetts Institute of Technology, 77 Massachusetts Avenue, Cambridge, MA 02139

I-Wei Chen
N. J. Grant

59-60. Massachusetts Institute of Technology, Plasma Fusion Center Headquarters, Cambridge, MA 02139

H. D. Becker
D. B. Montgomery

61. McDonnell-Douglas Astronautics Company, East, P.O. Box 516, Bldg. 92, St. Louis, MO 63166

J. W. Davis

62–63. National Bureau of Standards, Boulder, CO 80302

F. R. Fickett
M. B. Kasen

64. National Materials Advisory Board, 2101 Constitution Avenue, Washington, DC 20418

K. M. Zwilsky

65. Naval Research Laboratory, Washington, OC 20375

J. A. Sprague

66–131. Oak Ridge National Laboratory, P.O. Box 2008, Oak Ridge, TN 37831

Central Research Library
Document Reference Section
Laboratory Records Department (2)
Laboratory Records – RC
Patent Section
D. J. Alexander
J. Bentley
L. A. Berry
E. E. Bloom
D. N. Braski
W. P. Eatherly
M. L. Grossbeck
S. Hamada
R. L. Klueh
Eal Lee
R. A. Lillie
K. C. Liu
A. W. Longest
L. K. Mansur
P. J. Maziasz
T. K. Roche
A. F. Rowcliffe (35)
R. L. Senn
R. E. Stoller
M. S. Suzuki
K. R. Thoms
P. T. Thornton (2)
P. F. Tortorelli
F. W. Wiffen
S. J. Zinkle

132–134. Princeton Plasma Physics Laboratory, Princeton University, P.O. Box 451, Princeton, NJ 08540

J.P.F. Conrads
H. Furth
Long-Poe Ku

135. Rensselaer Polytechnic Institute, Troy, NY 12181

D. Steiner

136. Rockwell International Corporation, NA02, Rocketdyne Division, 6633 Canoga Avenue, Canoga Park, CA 91304

D. W. Kneff

137–138. Sandia National Laboratories, P.O. Box 5800, Albuquerque, NM 87185

M. J. Davis
W. B. Gauster

139–140. Sandia National Laboratories, Livermore Division 8316, Livermore, CA 94550

W. Bauer
W. G. Wolfer

141–142. University of California, Department of Chemical and Nuclear Engineering, Santa Barbara, CA 93106

G. E. Lucas
G. R. Odette

143–145. University of California, Department of Chemical, Nuclear and Thermal Engineering, Los Angeles, CA 90024

H. A. Abdou
R. W. Conn
N. M. Ghoniem

146. University of California, Los Alamos National Laboratory, P.O. Box 1663, Los Alamos, NM 87545

T. Zocco

147. University of Michigan, Oepartment of Nuclear Engineering. Ann Arbor, HI 48109

T. Kammash

148. University of Missouri, Department of Nuclear Engineering, Rolla, MO 65401

A. Kumar

149–153. Westinghouse Hanford Company, P.O. Box 1970, Richland, WA 99352

A. H. Ermi
G. D. Johnson
F. H. Mann
R. J. Puigh
R. L. Simons

154. Department of Energy, Oak Ridge Operations Office. P.O. Box 2001, Oak Ridge, TN 37831

Assistant Manager for Energy Research and Development

155–158. Department of Energy, Department of Fusion Energy, Washington, DC 20545

S. E. Berk
J. F. Clarke
M. M. Cohen
T. C. Reuther

159–208. Department of Energy, Office of Scientific and Technical Information, Office of Information Services, P.O. Box 62, Oak Ridge, TN 37831

For distribution as shown in DOE/TIC-4500, Distribution Categories UC-423 (Magnetic Fusion Reactor Materials) and UC-424 (Magnetic Fusion Energy Systems)